

Light Harvesting using
Metal-Organic and Organic Sensitizers
in Hybrid Solar Cells:
Synthesis, Characterisation and Application.

DISSERTATION

zur Erlangung des akademischen Grades
eines Doktors der Naturwissenschaften (Dr. rer. nat.)
im Fach Chemie der Fakultät für
Biologie, Chemie und Geowissenschaften der Universität Bayreuth

vorgelegt von
Katja Erika Gräf, geb. Willinger

geboren in Haßfurt / Deutschland

Bayreuth, 2012

Die vorliegende Arbeit wurde in der Zeit von August 2008 bis August 2012 am Lehrstuhl für Makromolekulare Chemie I / Angewandte Funktionspolymere der Universität Bayreuth unter der Betreuung von Prof. Dr. Mukundan Thelakkat angefertigt.

Vollständiger Abdruck der von der Fakultät für Biologie, Chemie und Geowissenschaften der Universität Bayreuth genehmigten Dissertation zur Erlangung des akademischen Grades eines Doktors der Naturwissenschaften (Dr. rer. nat.)

Dissertation eingereicht am:	22.08.2012
Zulassung durch die Promotionskommission:	13.09.2012
Wissenschaftliches Kolloquium:	12.12.2012

Prüfungsausschuss:

Prof. Dr. Mukundan Thelakkat	(Erstgutachter)
Prof. Dr. Hans-Werner Schmidt	(Zweitgutachter)
Prof. Dr. Carlo Unverzagt	(Vorsitzender)
Prof. Dr. Stephan Förster	

Amtierende Dekanin: Prof. Dr. Beate Lohnert

Für meine Familie

*"I'd put my money on the sun and solar energy. What a source of power!
I hope we don't have to wait until oil and coal run out before we tackle that."*

by *Thomas Alva Edison* in **1931**

(As quoted in *Uncommon Friends: Life with Thomas Edison, Henry Ford,
Harvey Firestone, Alexis Carrel & Charles Lindbergh* by James Newton)

TABLE OF CONTENTS

SUMMARY / ZUSAMMENFASSUNG	1
1. INTRODUCTION	9
1.1 SOLID-STATE DYE-SENSITIZED SOLAR CELLS	11
1.2 SENSITIZERS	16
1.3 DEVICE CONCEPTS	26
2. OBJECTIVE OF THE THESIS	39
3. OVERVIEW OF THE THESIS	41
4. INDIVIDUAL CONTRIBUTIONS TO JOINT PUBLICATIONS	61
5. SYNTHESIS, SPECTRAL, ELECTROCHEMICAL AND PHOTOVOLTAIC PROPERTIES OF NOVEL HETEROLEPTIC POLYPYRIDYL RUTHENIUM(II) DONOR-ANTENNA DYES	65
6. MULTICHROMOPHORE LIGHT HARVESTING IN HYBRID SOLAR CELLS	99
7. EFFICIENT PANCHROMATIC CO-SENSITIZATION FOR SOLID-STATE DYE-SENSITIZED SOLAR CELLS USING TRIPHENYLDIAMINE AND SQUARINE SENSITIZERS	119
8. SYNTHESIS AND PROPERTIES OF PANCHROMATIC BODIPYS WITH DONOR-ANTENNA GROUPS: A NEW SYNTHETIC ROUTE TOWARDS <i>meso</i> -ETHYNYLPHENYL BODIPYS	151
9. ENERGY TRANSFER IN SOLID-STATE DYE-SENSITIZED SOLAR CELLS: COMBINING BODIPYS AND TRIPHENYLDIAMINE ENERGY DONOR DYES	207
10. APPENDIX: PHOTSENSITIZERS IN SOLAR ENERGY CONVERSION	239
LIST OF PUBLICATIONS	337
LIST OF CONTRIBUTIONS	339
DANKSAGUNG	341
ERKLÄRUNG	343

SUMMARY

This thesis addresses the question how to improve light harvesting with novel tailor-made metal-organic and organic sensitizers for solid-state hybrid solar cell applications. Two approaches are in the focus: 1) the design and synthesis of sensitizers featuring high extinction coefficients over a broad wavelength range and 2) modern device concepts to further enhance or extend the absorption by the combination of two sensitizers. In short: The primary goal was to broaden and boost the optical density of hybrid solar cells. To reach this, novel sensitizer with extended conjugated π -system providing excellent optical properties had to be designed and synthesised in complex multi-step reaction sequences. For ideal sensitizers, further aspects had to be taken into account such as structural demands, electronic properties, and the tendency towards aggregation.

The first part of this thesis deals with the synthesis, characterisation and application of a series of metal-organic ruthenium(II) donor-antenna complexes. In addition to the typically broad absorption of Ru(II)bis(bipyridyl)(NCS)₂ complexes in the blue-green region arising from MLCT, these dyes feature much higher extinction coefficients ($\epsilon > 50\,000\text{ M}^{-1}\text{ cm}^{-1}$) in comparison to a commercially available reference dye lacking any donor-antenna groups ($\epsilon \sim 12\,000\text{ M}^{-1}\text{ cm}^{-1}$). By the application of these Ru(II) complexes in solid-state dye-sensitized solar cells, we found a clear structure-property relationship. The performance - especially the photocurrent density - was significantly improved with increasing extension of the delocalized system of the donor-antenna groups. The photocurrent density of the best performing donor-antenna complex was approximately doubled compared to the reference dye proving the positive effect of highly delocalized donor-antenna ligands.

To further boost the optical density in hybrid solar cells sensitized with a donor-antenna ruthenium dye (Ru-TPA-NCS), we developed an innovative and technically relevant concept of multichromophore sensitization involving a second sensitizer (TPD-dye). The latter absorbs up to $\sim 530\text{ nm}$ with absorption maximum in the region where Ru-TPA-NCS weakly absorbs. The solar cells were fabricated according to a novel method developed by us. A blend of sensitized TiO₂-particles and the hole transport material was prepared and simply doctor bladed on a conducting substrate that was previously coated with a blocking layer to get an active layer of nanocomposite blend. Due to the convenient preparation without the need for high

temperature sintering steps and the possibility to combine two or even more sensitizers in any desired ratio, this is a technologically highly interesting technique. The current density of the multichromophore hybrid blend solar cell (1.46 mA cm^{-2}) was approximately the sum of the photocurrents delivered by the devices sensitized with either of the dyes. However, the power conversion efficiencies of multichromophore hybrid blend solar cells were initially low due the weak interconnectivity of the TiO_2 particles. This issue was addressed by an optimization of the TiO_2 :spiro-OMeTAD ratio, so that a current density of 2.13 mA cm^{-2} could be achieved. By addition of PCBM as an organic electron transport material, the percolation of electrons and therefore the current density could be increased further to 3.6 mA cm^{-2} .

A further concept dealing with the combination of two sensitizers in a single device was accomplished by co-sensitization of a triphenyldiamine-based dye (TPD-dye) absorbing in the blue region and squaraine dye (SQ-dye) mainly absorbing the red part of the visible spectrum in a standard solid-state dye-sensitized solar cell. In this way, the optical response of the device was extended up to 700 nm. By optimizations regarding the thickness of the mesoporous layer, the solvent used for chemisorption and the chemisorption time, the current density of the co-sensitized hybrid solar cell could be increased from 2.03 to 5.86 mA cm^{-2} resulting in a power conversion efficiency of 2.41 %.

To accomplish the desired panchromaticity or even an extension of the absorption up to the NIR region with a single sensitizer, novel BODIPY dyes with excellent optical properties were designed and synthesised. We prepared BODIPYs with donor-groups to extend the delocalized system and integrated a *meso*-ethynyl bridge between the BODIPY core and the anchoring group to improve the electronic connection between them. For comparison, we also synthesised the corresponding BODIPYs without donor-moieties and without ethynyl bridge. The multi-step synthetic routes were optimized, the mechanism of the donor-attachment was clarified and the introduction of the ethynylphenyl group in the *meso*-position was accomplished for the first time. The optical characterisation of the compounds disclosed an impressively broad and intensive spectral response, especially for one *meso*-ethynylphenyl BODIPY with donor-groups, which absorbs up to 1030 nm with $\epsilon > 10^4 \text{ M}^{-1}\text{cm}^{-1}$ up to 940 nm. This makes suitable functionalised BODIPYs promising candidates for solar cell applications.

The next part took advantage of the excellent optical properties of BODIPYs and expanded the topic towards the concept of energy transfer in combination with an unattached energy donor dye to a sensitizing acceptor dye. To identify suitable dye combinations for energy transfer, we

performed comprehensive systematic investigations on the fulfilment of the requirements of energy transfer in solid-state dye-sensitized solar cells by steady-state UV/vis and fluorescence spectroscopy, by cyclic voltammetry, fluorescence quenching experiments in solution and in the solid state and by fluorescence lifetime measurements. Indeed, for appropriate combinations an additional contribution to the external quantum efficiency was found in the absorption region of the energy donor dye.

Furthermore, a review chapter was accomplished on all aspects of dye-sensitized solar cells and the sensitizers. As a part of the review, the requirements and design principles of sensitizers were highlighted, the sensitizers were classified and their photovoltaic performances were summarised to present a more comprehensive idea on the whole topic.

In summary, this thesis presents the successful design, synthesis and characterisation of both metal-organic and organic sensitizers including ruthenium complexes, triphenyldiamine-based dyes, a squaraine sensitizer and BODIPY dyes. The sensitizers (either individually or in combination with complementary sensitizers) provide excellent optical properties for the application in solar cells. The applicability of these sensitizers was successfully demonstrated in standard solid-state dye-sensitized solar cells, in newly developed multichromophore hybrid blend solar cells, co-sensitized solar cells or in solid-state dye-sensitized solar cells taking advantage of energy-transfer.

ZUSAMMENFASSUNG

Diese Dissertation behandelt die Fragestellung, wie die Lichtsammlung von Feststoff-Hybridsolarzellen mit neuen maßgeschneiderten metallorganischen und organischen Farbstoffen verbessert werden kann. Im Fokus stehen zwei Ansätze: 1) Das Design und die Synthese von Farbstoffen, die sich durch hohe Extinktionskoeffizienten über einen breiten Wellenlängenbereich auszeichnen und 2) moderne Konzepte für die Präparation von Hybridsolarzellen, die eine Verstärkung oder Ausdehnung der Absorption durch die Kombination von zwei Farbstoffe gewährleisten. Kurz gesagt: Das primäre Ziel war die Verbreiterung und Erhöhung der optischen Dichte von Hybridsolarzellen. Um das zu erreichen, mussten neue Farbstoffe mit exzellenten optischen Eigenschaften konzipiert und über komplexe Reaktionssequenzen synthetisiert werden. Mit dem Ziel möglichst ideale Farbstoffe herzustellen mussten auch zusätzliche Aspekte wie strukturelle Anforderungen, elektronischen Eigenschaften und die Tendenz zur Bildung von Aggregaten berücksichtigt werden.

Der erste Teil dieser Dissertation behandelt die Synthese, Charakterisierung und Anwendung einer Serie von metallorganischen Ruthenium(II) Donor-Antennen Komplexen. In Erweiterung zu der üblichen breiten MLCT Absorption von Ru(II)bis(bipyridyl)(NCS)₂ Komplexen im blauen bis grünen Bereich, bieten diese Farbstoffe wesentlich höhere Extinktionskoeffizienten ($\epsilon > 50\,000\text{ M}^{-1}\text{ cm}^{-1}$) als die kommerziell erhältlichen Referenzfarbstoffe, die keine Donor-Antennen Gruppen tragen ($\epsilon > 12\,000\text{ M}^{-1}\text{ cm}^{-1}$). Infolge der Anwendung dieser Ru(II) Komplexe in farbstoffsensibilisierten Feststoffsolarzellen konnte eine eindeutige Struktur-Eigenschaftsbeziehung festgestellt werden. Die Leistung der Solarzellen - insbesondere die Photostromdichte - konnte durch die Vergrößerung des delokalisierten Systems der Donor-Antennen Gruppen signifikant verbessert werden. Die Photostromdichte des effizientesten Donor-Antennen Komplexes konnte im Vergleich zum Referenzfarbstoff ohne Donor-Antennen Gruppen ungefähr verdoppelt werden. Dies ist ein eindeutiger Beweis für den positiven Effekt der stark delokalisierten Donor-Antennen Liganden.

Um die optische Dichte von Hybridsolarzellen auf der Basis eines Ruthenium(II) Donor-Antennen Farbstoffs (Ru-NCS-TPA) weiter zu steigern, entwickelten wir ein innovatives und technisch relevantes Konzept zur Multichromophorsensibilisierung. Dieses Konzept beinhaltet die Verwendung eines zweiten Farbstoffs (TPD-dye), der bis $\sim 530\text{ nm}$ absorbiert und über ein

Absorptionsmaximum in dem Bereich verfügt, in dem Ru-TPA-NCS nur schwach absorbiert. Die Solarzellen wurden gemäß einer neuartigen, von uns entwickelten Methode gefertigt. Dazu wurde eine Mischung bestehend aus sensibilisierten TiO_2 -Partikeln und dem Lochtransportmaterial hergestellt. Diese Mischung wurde durch Rakeln auf ein leitfähiges Substrat aufgebracht, welches zuvor mit einer blockenden Schicht versehen wurde. Dadurch konnte auf simple Weise eine aktive Schicht, bestehend aus einer Nanokomposit Mischung, hergestellt werden. Aufgrund der einfachen Präparation ohne die Notwendigkeit zur Anwendung von Hochtemperatur-Sinterschritten, sowie der Möglichkeit zur Kombination von zwei oder sogar mehr Farbstoffen in jedem beliebigen Verhältnis, ist diese Methode technologisch hoch interessant. Die Photostromdichte der multichromophoren Hybridsolarzellen entsprach ungefähr der Summe der Stromdichten, die von den Hybridsolarzellen geliefert wurden, welche mit jeweils nur einem Farbstoff sensibilisiert wurden. Allerdings waren die Wirkungsgrade von multichromophoren Solarzellen anfänglich sehr niedrig, da die einzelnen Partikel nur über eine geringe Interkonnektivität verfügen. Auf dieses Problem wurde durch eine Optimierung des TiO_2 :spiro-OMeTAD Verhältnisses eingegangen. Dadurch konnte die Stromdichte auf 2.13 mA cm^{-2} gesteigert werden. Des Weiteren konnte durch die Zugabe von PCBM, als organisches Elektronentransportmaterial, die Perkolation der Elektronen verbessert werden und somit eine Steigerung der Stromdichte auf 3.6 mA cm^{-2} erreicht werden.

Ein weiteres Konzept, das auf der Kombination von zwei Farbstoffen in einer Solarzelle beruht, ist Cosensibilisierung. Dazu wurde ein blau-absorbierender Triphenyldiamin-basierter Farbstoff (TPD-dye) mit einem rot-absorbierenden Squarain Farbstoff (SQ-dye) in einer Standard farbstoffsensibilisierten Feststoffsolarzelle kombiniert. Auf diese Weise konnte die optische Empfindlichkeit der Solarzelle über den sichtbaren Bereich bis 700 nm ausgedehnt werden. Durch Optimierungen bezüglich der Dicke der mesoporösen Schicht, des zur Chemisorption verwendeten Lösungsmittels und der Chemisorptionszeit konnte die Stromdichte der cosensibilisierten Hybridsolarzelle von 2.03 auf 5.86 mA cm^{-2} gesteigert werden. Damit wurde eine Effizienz von 2.41 % erzielt.

Um das angestrebte panchromatische Verhalten oder sogar eine Ausdehnung der Absorption bis hin zum NIR-Bereich mit einem einzelnen Farbstoff zu erreichen, wurden neue BODIPY Farbstoffe mit exzellenten optischen Eigenschaften konzipiert und synthetisiert. Dazu stellten wir BODIPY Farbstoffe her, deren delokalisiertes System durch die konjugierte Anbindung von Donor-Gruppen vergrößert wurde. Zudem wurde erstmals eine zusätzliche *meso*-Ethin-Brücke zwischen dem BODIPY Grundkörper und der Ankergruppe eingeführt, um die elektronische

Verbindung zwischen diesen Gruppen zu verbessern. Zu Vergleichszwecken haben wir des Weiteren die korrespondierenden BODIPY Analoga ohne Donor-Gruppen und ohne Ethin-Brücke synthetisiert. Die mehrere Stufen umfassenden Syntheserouten wurden optimiert, der Mechanismus der Donor-Anbindung untersucht und die Einführung einer Ethinylphenylgruppe erstmals realisiert. Die optische Charakterisierung der Verbindungen zeigte eine beeindruckend breite und intensive spektrale Empfindlichkeit. Die spektrale Empfindlichkeit war besonders ausgeprägt für einen meso-Ethinylphenyl BODIPY, der Donor-Gruppen trägt. Dieser absorbiert über den gesamten sichtbaren Bereich bis 1030 nm und bietet dabei bis 940 nm Extinktionskoeffizienten $\epsilon > 10^4 \text{ M}^{-1}\text{cm}^{-1}$. Dies zeichnet BODIPYs mit geeigneten funktionellen Gruppen als vielversprechende Kandidaten für die Anwendung als Sensibilisatoren in Hybridsolarzellen aus.

Im nächsten Teil wurde der Vorteil der exzellenten optischen Eigenschaften, den die BODIPYs bieten, ausgenutzt und um das Konzept des Energietransfers von einem nicht geankerten Energie-Donor-Farbstoff zu einem geankerten Akzeptor-Farbstoff erweitert. Um geeignete Farbstoffkombination zu identifizieren, haben wir umfassende systematische Untersuchungen durchgeführt. Dadurch sollte überprüft werden, ob die Anforderungen für Energietransfer in farbstoffsensibilisierten Feststoffsolarzellen erfüllt sind. Dazu wurden stationäre UV/vis- und Fluoreszenzmessungen, Cyclovoltammetrie-Experimente, Fluoreszenzlöschungsversuche in Lösung und im Feststoff sowie Fluoreszenzlebensdauermessungen durchgeführt. Für geeignete Kombinationen wurde in der Tat ein zusätzlicher Beitrag zur externen Quanteneffizienz im Absorptionsbereich des Energie-Donor-Farbstoffs gemessen.

Des Weiteren beinhaltet diese Dissertation einen in Buchform veröffentlichten Literaturüberblick, welcher alle Aspekte von farbstoffsensibilisierten Solarzellen und die diversen Farbstoffklassen abdeckt. Im Zuge dessen wurden besonders die Anforderungen und Designrichtlinien bezüglich der Farbstoffe hervorgehoben, sowie eine Klassifizierung der Farbstoffe vorgenommen. Ferner wurden Tabellen erstellt, um die Kenngrößen der Solarzellen (Kurzschlussstrom, Leerlaufspannung, Füllfaktor und Effizienz) in Abhängigkeit von den verschiedenen Farbstoffen zu sammeln. Damit soll ein umfassender Einblick in das gesamte Thema gegeben werden.

Zusammenfassend präsentiert diese Dissertation das erfolgreiche Design, die Synthese und Charakterisierung von diversen metallorganischen und organischen Farbstoffen. Dazu zählen Rutheniumkomplexe, Triphenyldiamine-basierte Farbstoffe, ein Squarain Farbstoff und BODIPY

Farbstoffe. Die einzelnen Farbstoffe, sowie die Kombinationen aus komplementären Farbstoffen, bieten exzellente optische Eigenschaften für die Anwendung in Solarzellen. Die Anwendbarkeit dieser Farbstoffe wurde erfolgreich demonstriert in Standard farbstoffsensibilisierten Feststoffsolarzellen, den neu entwickelten multichromophoren Hybridsolarzellen, cosensibilisierten Solarzellen und farbstoffsensibilisierten Feststoffsolarzellen unter Einbeziehung von Energietransfer.

1 INTRODUCTION

The development of novel technologies for energy conversion is forced by the growing energy demand, climate change and depleting of fossil resources. In 1839, long before these issues were considered, Becquerel discovered a process to convert sunlight into electric energy.¹ The photoelectric effect observed by Becquerel was explained by Einstein in 1905 (Nobel Prize 1921).² This paved the pathway for the invention of optoelectronic devices.

The present solar cell technology can be divided into three generations. The first generation comprises silicon solar cells made from crystalline or multicrystalline silicon wafers in cost-intensive processes. The first p-n-junction silicon solar cell, reaching an efficiency of already 6 %, was reported by Chapin, Fuller and Pearson in 1954.³ Only four years later, silicon solar cells came into application as energy source of the Vanguard 1 satellite.⁴ Today, they are common commercial products and reach certified efficiencies of 25.0 ± 0.5 %.⁵ In modules, efficiencies of up to 22.9 ± 0.6 % were reported for crystalline silicon.⁵ With this performance, first generation solar cells come close to the efficiency limit of 30 % calculated for single-junction solar cells by Shockley and Queisser in 1961.⁶ Additionally, no significant cost reduction is expected for this generation technology due to the energy intensive production of the highly purified silicon and the high material costs involved in the devices.

The second generation solar cells are inorganic thin film solar cells, which were already invented in 1883. Fritts used selenium and a thin layer of gold to prepare a solar cell device yielding an efficiency of 1%.⁷ Nowadays, thin film solar cells are characterised by their reduced production costs due to the lower consumption of material and lower manufacturing temperatures compared to the first generation solar cells.⁸ Additionally, their transparency allows the preparation of highly efficient, but very cost-intensive, multijunction devices (43.5 %).⁵ The conventional materials used for thin film solar cells are inorganic semiconductors like amorphous silicon, cadmium telluride (CdTe), gallium arsenide (GaAs) and copper indium gallium diselenide (CuInGaSe₂, CIGS). Module efficiencies of 8.2, 15.3 and 23.5 % have been reached for thin film solar cells on basis of silicon, CdTe and GaAs, respectively.⁵ Considering the shorter energy payback period of thin film solar cells and the meanwhile reasonably high efficiencies, they are strong competitors to the first generation solar cells.⁸

The latest generation of solar cells (third generation) is basically still in the research stage and can be categorized into: organic solar cells (OSC) and hybrid solar cells among which the best known representatives are the dye-sensitized solar cells (DSCs). The first OSCs was introduced by Tang who reported a two layer organic photovoltaic device comprising small molecules in 1986.⁹ With the first publication on electric conductivity in conjugated polymers by Heeger, MacDiarmid and Shirakawa in 1977 (Nobel prize 2000), polymers became increasingly important for OSCs.¹⁰ In 1995 Heeger reported the first polymeric bulk heterojunction (BHJ) OSC.¹¹ Since then, this novel type of solar cells gained a lot of research interest. The currently highest certified efficiency of a polymeric OSC under laboratory conditions is 8.37 %.¹² For small molecules, an efficiency of even 10.7 % was reported in an organic tandem solar cell.¹³

DSCs had their breakthrough in 1991. O'Regan and Grätzel published the first efficient DSC (7.1 %) using a mesoporous TiO₂ electrode sensitized by a ruthenium dye in contact with an iodine/iodide redox shuttle.¹⁴ Due to the liquid nature of the redox electrolyte, this type of DSCs is denoted as liquid-state dye-sensitized solar cells (LDSCs). To overcome the key problems of LDSCs, *viz.* the leakage of electrolyte, the evaporation of solvents and the aggressive nature of the redox shuttle causing dye degradation and corrosion of the electrode, solid-state dye-sensitized solar cells (SDSCs) were developed.¹⁵⁻¹⁷ Modern SDSCs make use of an organic, amorphous, small molecule semiconductor (spiro-OMeTAD, Figure2) that can regenerate the dye and transport charges *via* polaron hopping processes.¹⁸ Up to now, the highest efficiencies reached in DSC devices are 12.3 and 7.2 % for LDSCs and SDSCs, respectively.^{19, 20}

Both types, OSCs and DSCs, are promising low-cost alternatives to the first and second generation solar cells due to the high diversity of materials, the low material consumption, the low fabrication temperature and the possibility to construct the solar cells on flexible substrates in roll-to-roll processes. However, to realize these visions and to commercialize third generation solar cells world-wide, further fundamental research is necessary. This concerns on the one hand the tuning of the optical/electrochemical properties of materials and the elucidation of structure-property relationships. On the other hand, the perspectives and limitations of the established devices concepts need to be entirely understood and novel device concepts have to be developed.

1.1 SOLID-STATE DYE-SENSITIZED SOLAR CELLS

This thesis addresses solar cells of the third generation, more precisely solid-stated dye-sensitized solar cells. In the following, the standard setup, the operating principle, the characterisation methods of SDSCs will be presented.

Standard setup

Figure 1 shows the assembly of a standard SDSC. On a glass substrate covered with a transparent conducting oxide (TCO), usually a fluorinated tin oxide (FTO), a thin blocking layer (~ 100 nm) of dense TiO_2 is deposited by spray pyrolysis.²¹ On top of this, a commercial available TiO_2 paste consisting of TiO_2 nanocrystals and binder components is deposited by screen printing. This layer has to be sintered at 500°C to remove the binder components and to generate a well-connected mesoporous, crystalline TiO_2 network providing a large surface area at a thickness of ~ 1.5 - 2 μm . This electrode is sensitized by chemisorption of sensitizers from solution. After the dye loading, a solution of the hole transport material (HTM) is applied. This comprises spiro-OMeTAD (Figure 2) and additives (bis(trifluoromethylsulfonyl)amine lithium salt and 4-*tert*-butylpyridine) in chlorobenzene. The solution is cast onto the sensitized TiO_2 electrode and allowed to soak into the pores. Then the spin coating process is started to remove the solvent and to generate a very thin overstanding layer of the HTM. The process of pore-filling is a crucial step because hole injection and recombination rates are strongly influenced by the pore-filling fraction. This issue was comprehensively investigated by McGehee *et al.* and will be addressed in the next section.²²⁻²⁴ On top of the thin overstanding layer of the HTM, a gold contact (cathode) is deposited by thermal evaporation. An additional gold contact is deposited as counter electrode (anode).

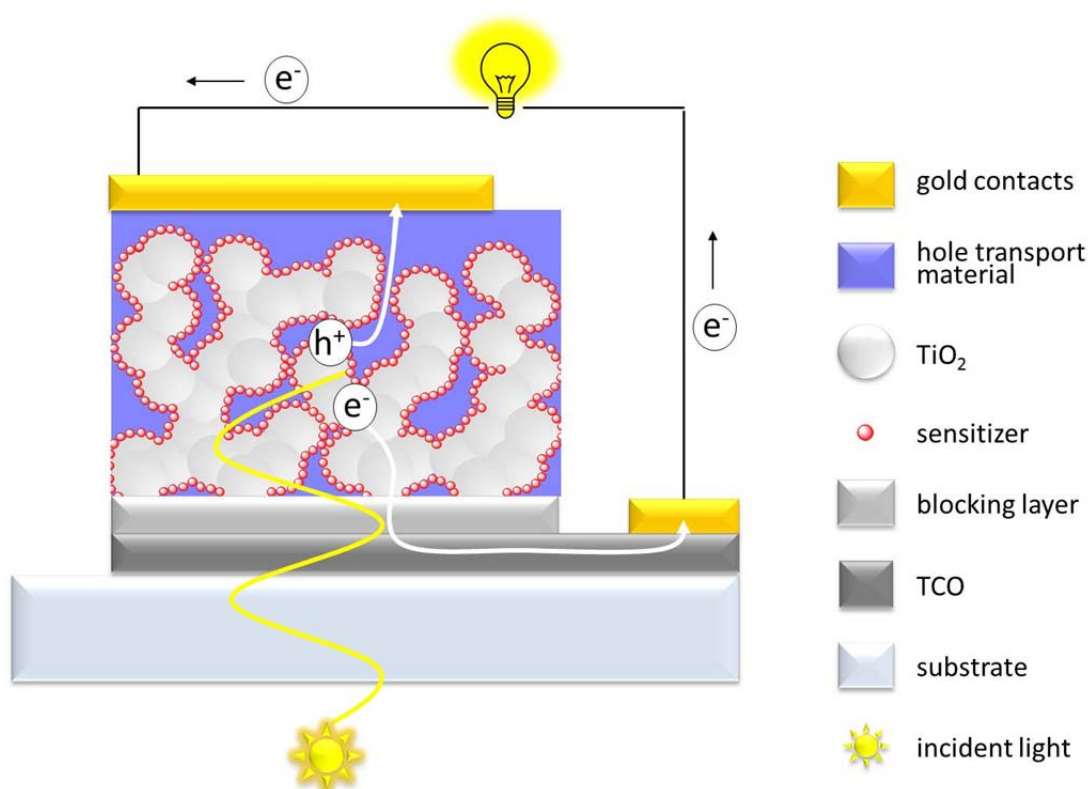


Figure 1. Schematic setup of a standard SDSC (cross section) comprising a transparent substrate (glass) covered with a thin layer of a transparent conducting oxide (TCO, typically fluorine doped tin oxide, thickness ~ 500 nm). On top of this, a thin blocking layer of compact TiO_2 (~ 100 nm) is deposited by spray pyrolysis. This layer is covered by the active layer of a well-connected mesoporous TiO_2 network that is sensitized in a dense monolayer of a sensitizer and filled with a hole transport material (thickness of the active layer $\sim 1.5\text{--}2\ \mu\text{m}$). The contacts (cathode and anode) are formed by a thin layer of gold (~ 50 nm). Light incidents through the glass substrate.

Operating principle

The diverse layers of SDSCs fulfil tasks to promote processes that contribute to the generation of photocurrent or to hinder processes that reduce the photocurrent or the voltage of SDSCs. In Figure 2, these processes are shown schematically.

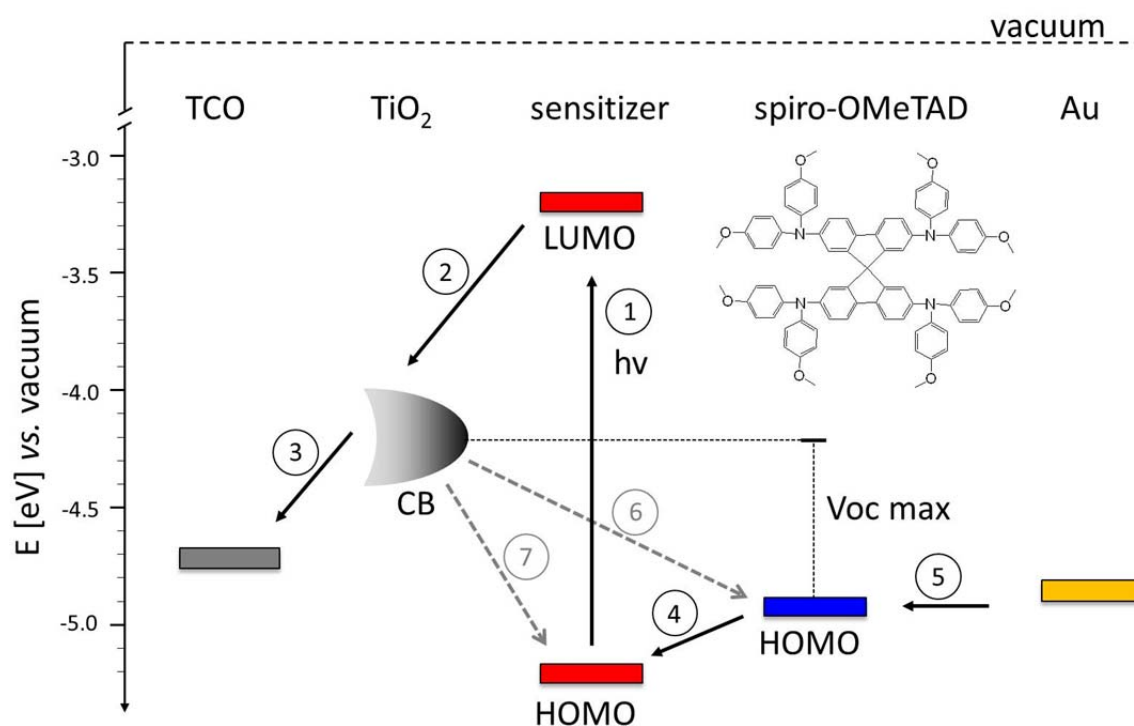


Figure 2. Schematic representation of the electronic processes in SDSCs. The processes contributing to the photocurrent generation are depicted in black, the main loss mechanisms are shown in grey. Upon excitation (1), an electron is injected into the conduction band (CB) of TiO_2 (2), transported to the TCO (3) and then to the anode contact. In parallel, the oxidized sensitizer is regenerated by the HTM spiro-OMeTAD (4), which transports the holes to the Au cathode (or respectively the electrons to the sensitizer) via polaron hopping processes (5). However, the recombination of injected electron with the oxidized sensitizer (6) and with the hole transport material (7) are loss processes that reduce the performance.

The photocurrent generation process starts with the excitation of the sensitizer by the incident light (1). An electron is excited from the highest occupied molecular orbital (HOMO) to the lowest unoccupied molecular orbital (LUMO). The excited electron is directly injected into the conduction band (CB) of TiO_2 . To provide a driving force for the injection, the LUMO level of the sensitizer has to be reasonably higher than the CB of TiO_2 . Injected electrons are afterwards transported through the TiO_2 network to the TCO (3). This electron transport in mesoporous polycrystalline titania is still not fully understood.^{18, 25} This is mainly due to the distinctively different properties of mesoporous TiO_2 networks of sintered particles compared to the compact or single crystalline analogues. Additionally, the properties of the network structure also depend on individual parameter such as the particle size. However, it is clear that the electron mobility in a mesoporous network is distinctively lower than in compact or single crystalline structures.^{18, 25} By the electron transfer processes the oxidized sensitizer is

regenerated by the HTM (spiro-OMeTAD) (4). To reach efficient regeneration and also an efficient hole transport to the cathode contact (5), the degree of pore-filling with spiro-OMeTAD has to be sufficiently high. McGehee *et al.* found that the degree of pore-filling is much higher than the concentration of spiro-OMeTAD in solution because the wet overstanding layer acts as a reservoir during the spin coating and solvent evaporation process.²² However, only films up to 2.5 μm could be entirely filled with spiro-OMeTAD while simultaneously keeping the overstanding layer thin.²² For thicker films the pore-filling fraction decreases. A low degree of pore-filling enhances recombination of holes in the HTM with injected electrons (6) as the holes cannot diffuse away.²³ A linear correlation was found between the pore-filling fraction and the recombination time.²³ Moreover, for thin active layers (2 μm) the charge collection efficiency was nearly quantitative. However, even if it would be possible to maintain a high pore-filling fraction for thicker films, the charge collection efficiency would be lower because the transport lifetime is proportional to the square of the film thickness.²³ Hence, pore-filling, recombination and charge collection issues limit the thickness of SDSCs to $\sim 2 \mu\text{m}$ although this is not sufficient for efficient light harvesting.

Additionally, recombination processes reducing the performance of the solar cells have to be considered. The mentioned recombination process between injected electrons and holes in the HTM, is the most striking loss process in SDSCs. Compared to LDSCs where this type of recombination is hindered by the formation of an $\text{I}_2^{\cdot -}$ intermediate, process 6 in SDSCs is a one-step reaction that happens very easily, *i.e.* this recombination is considerably fast and has a high rate.²⁶ A second recombination process is possible between injected electrons and the oxidized sensitizers (7). This is a minor loss process in SDSCs due to the fast dye regeneration (regeneration rate of sensitizers in SDSCs is in the range of nanoseconds, whereas the regeneration occurs in the microsecond time scale for LDSCs).¹⁸ A further crucial recombination process is not shown in Figure 2 because it is completely prevented by the introduction of the blocking layer. This layer impedes the contact between the HTM and the TCO, *i.e.* the contact between the material where the holes are transported and the material where the electrons are transported. Without the blocking layer, an ohmic contact would be formed between these materials which would result in such a high recombination rate that only a negligible output power would be obtained.²¹

As shown in Figure 2, the voltage of SDSCs is mainly determined by the energetic difference between the conduction band of TiO_2 and the HOMO level of the HTM. However, the voltage is also influenced by the additives.²⁷

Characterisation methods

The performance of solar cells is determined by measuring the current-voltage characteristics (I-V curve, Figure 3a) under standard conditions (AM 1.5 G, 100 mW/cm²). In addition to that, the measurement of the external quantum efficiency (EQE, also often denoted as incident-photon-to-current conversion efficiency, IPCE) gives information on the percentage of incident photons that are converted into photocurrent as function of the excitation wavelength (Figure 3b).

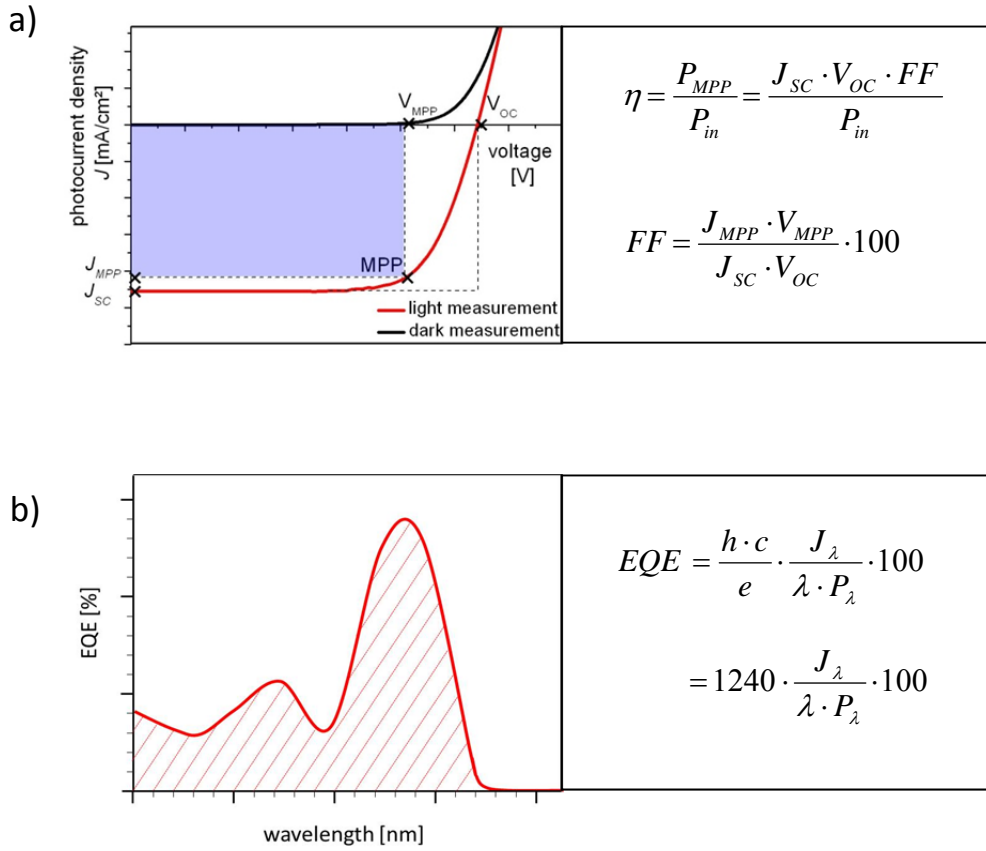


Figure 3. Characterisation methods of solar cells. a) The I-V curve of a solar cell is obtained by measuring the photocurrent density as function of applied counter-voltage under standard conditions (AM 1.5 G, 100 mW/cm²). The power conversion efficiency (η) of a solar cells is determined by the ratio between the power at the maximum power point (P_{MPP}) and the power of the incident light (P_{in}). P_{MPP} can be calculated by measuring the photocurrent density (J_{sc}), the open-circuit voltage (V_{oc}) and the fill factor (FF). For the calculation of the FF , the photocurrent density at the maximum power point (J_{MPP}) and the voltage at the maximum power point (V_{MPP}) are required. b) The external quantum efficiency spectrum is obtained by measuring the photocurrent density as function of the excitation wavelength. To get the EQE as percentage of the incident photons converted into photocurrent, the given equation has to be used (J_{λ} : photocurrent density at λ , h : Planck constant, c : light velocity and P_{λ} : power density of monochromatic light at λ).

1.2 SENSITIZERS

The inorganic semiconductor TiO_2 , which is typically used for DSCs, is not sensitive towards visible light due to its wide band gap. Hence, TiO_2 has to be sensitized by a metal-organic or organic sensitizer that is able to absorb light in the visible region of the electromagnetic spectrum and transfer excited electrons to TiO_2 .

An efficient sensitizer for DSCs has to meet specific key requirements that have to be considered for the design: 1) First of all, sensitizers have to provide excellent light harvesting properties. This includes a broad absorption in the visible region accompanied by high extinction coefficients. The better the light harvesting, the higher is the photocurrent that can be theoretically reached. 2) For an intimate contact with the semiconductor, the sensitizer has to be chemisorbed *via* an anchoring group. Usually, carboxylic acid groups are employed which anchor in a bidentate or bridging way.²⁸ 3) Sensitizers have to provide suitable energy levels of the frontier orbitals. That implies on the one hand, that the LUMO level of the sensitizer is sufficiently higher than the conduction band of TiO_2 to enable electron injection from the sensitizer to the inorganic semiconductor. On the other hand, the HOMO level of the sensitizer has to be lower than the HOMO level of the solid HTM in SDSCs (or lower than the redox level of the redox shuttle in LDSCs) to facilitate regeneration of the oxidized sensitizer. 4) Sensitizers should comprise a donor and an acceptor part, typically connected by a conjugated bridge. Such a donor- π bridge-acceptor or “push-pull” structure favours i) intramolecular charge transfer causing a positive effect on the optical properties²⁹, ii) unidirectional electron flow directed towards TiO_2 providing efficient electron injection³⁰ and iii) an increased spatial separation between injected electrons and holes increasing the recombination lifetimes³¹. 5) Furthermore, sensitizers should show a low tendency towards aggregation as this may cause quenching of the excited states of the sensitizer which reduces the electron injection rate and hence the photocurrent density. 6) For SDSCs a polarity match between the sensitizer and the HTM is favourable because this increases the wetting of the sensitizer with the HTM which can in turn support regeneration of the sensitizer. 7) Finally, high photostability, electrochemical and thermal stability are indispensable for long lifetimes of the devices.

To date, plenty of sensitizers fulfilling these demands have been synthesised and successfully applied in SDSCs. High efficiencies were reached for metal-organic sensitizers such as ruthenium complexes ($\sim 5\%$ ^{32, 33}) and porphyrins (3.6% ³⁴) as well as for organic sensitizers like thiophene bridged triphenylamines (6.8% ³⁵, 6.9% ³⁶), indolines (4.2% ³⁷), perylenes (3.8% ³⁸) and squaraines

(3.16 %³⁹). Although metal-organic ruthenium sensitizers have been extensively studied in the last decades, organic sensitizers started to complement them. Organic sensitizers can reach higher efficiencies as a consequence of their high extinction coefficients and their large structural variety allowing a tailor-made design and adapted optical/electrochemical properties. Additionally, they are cheaper as they do not contain any rare metals. In depth information on the diverse sensitizer classes applied in DSCs is provided in comprehensive reviews and in the appendix of this thesis.^{40, 41}

In the next sections, the sensitizer classes which are the subject of this thesis will be outlined briefly.

Ruthenium complexes

Metal-organic ruthenium(II) complexes are the best-known and most commonly used sensitizers for DSCs. After intensive optimizations of their structure, the devices setup and additives, impressive efficiencies of $\sim 5\%$ ^{32, 33} and $> 11\%$ ⁴²⁻⁴⁴ have been reached for SDSCs and LDSCs, respectively.

In the 1980's, sensitization of TiO_2 started with tris(2,2'-bipyridyl-4,4'-dicarboxylic acid) ruthenium(II) complexes⁴⁵ which absorb only up to 520 nm.⁴⁶ In 1991, a bulky CN-bridged trinuclear ruthenium complex providing a broader spectral response gave an efficiency of already 7.1 %¹⁴ in an LDSC.^{47, 48} The optimization of the structure of ruthenium complexes is still going on and follows some key concepts which will be highlighted in the following:

The basic representatives of ruthenium sensitizers are N3 and N719 (Figure 4). These complexes carry two NSC ligands and two 2,2'-bipyridyl-4,4'-dicarboxylic acid ligands which differ only in the degree of protonation. With these ruthenium complexes carrying non-functionalized ligands, LDSC efficiencies of 10 % were already reached in 1993, only shortly after the invention of DSCs in 1991.⁴⁹ This performance was unsurpassed until 2001. The so-called black dye, a ruthenium sensitizers with three NSC ligands and one 2,2':6',2''-terpyridine ligand, reached an slightly improved efficiency of 10.4 % due to a broadening of the absorption up to the near-infrared region.⁵⁰ Although these ruthenium sensitizers achieved impressive efficiencies in LDSCs under highly optimised conditions, their performance in SDSCs is quite low. This inferior performance is attributed to the low molar extinction coefficients and restricted absorption only in the blue-green region, since the SDSCs are fabricated comparatively thin to reduce recombination rates.

A striking innovation to improve the light harvesting of ruthenium sensitizers was the covalent attachment of electron-rich donor-antenna groups to one bipyridine ligand (*e.g.* Ru-TPA-NCS,⁵¹ Figure 4). The aim of ruthenium donor-antenna sensitizers is to reach higher extinction coefficients and thus a higher optical density of the device by the extended delocalized π -system of the donor groups. This is especially important for SDSCs, because the optimum thickness of the mesoporous layer is a compromise between light harvesting and pore-filling/recombination/charge transport issues. An increase in the optical density enhances the light harvesting especially for thin mesoporous layers. Moreover, charge transport losses and recombination can be reduced by the use of thinner mesoporous layers.⁵² A further beneficial effect of donor-antenna groups is the enhanced compatibility between the dye and the solid-state HTM due to a polarity match which improves the wetting of the sensitizer with the HTM.⁵¹ Additionally, the spatial separation between injected electrons in the n-type semiconductor and the radical cation localized at the donor-antenna group is increased. This separation significantly reduces the recombination half-times and leads to improved solar cell efficiency.^{31, 51, 53-55}

Further fine-tuning of the structure of ruthenium complexes was accomplished by the introduction of hydrophobic (*e.g.* Z907⁵⁶, C101⁵⁷, Figure 4) and ion-coordination functionalities (*e.g.* K51⁵⁸, Ru-TPA-EO-NCS⁵⁹, Figure 4). Hydrophobic alkyl chains are known to act as insulating barriers reducing the recombination between injected electrons and holes in the HTM.⁶⁰ Additionally, the stability of solar cells can be positively influenced due to a suppression of water induced desorption.⁶¹ The attachment of ion-coordinating groups like oligo ethylene oxide chains in K51 aims to fix lithium ions which are actually added to the HTM to increase the hole mobility.^{18, 62} Lithium ions cause various effects in SDSCs; some of them are positive, some negative and some even not yet completely understood. The most negative effect is the lowering of the open-circuit voltage due to a negative shift of the band edge of TiO₂ caused by the adsorption of lithium ions on the TiO₂ surface and by the intercalation of lithium ions into the anatase structure of TiO₂.⁶³ This adsorption/intercalation can be hindered by ion-coordinating functionalities.^{33, 63} Additionally, reduced recombination rates were observed for ion-coordinating sensitizers by screening the injected electrons from the holes in the HTM.⁶⁴

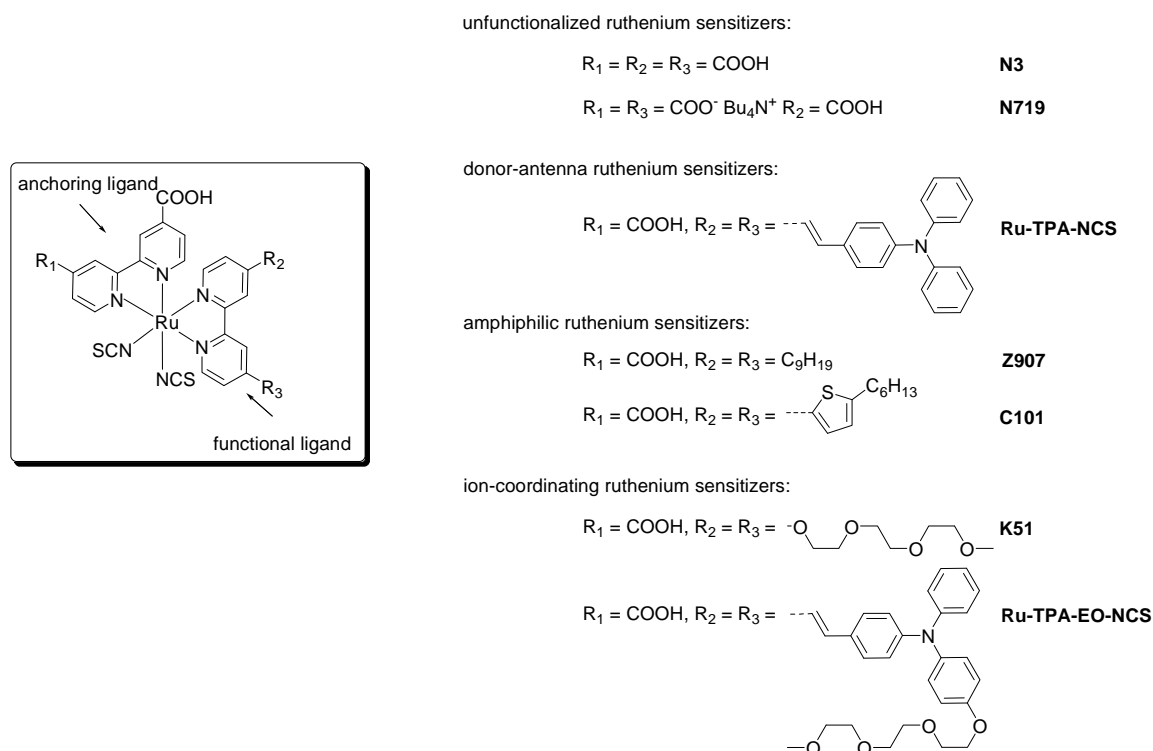


Figure 4. Basic structure of metal-organic ruthenium sensitizers (left) and selection of typical representatives of the different types of ruthenium sensitizers (right). The types of ruthenium sensitizers comprise unfunctionalized derivatives (N3, N719), donor-antenna derivatives that provide increased extinction coefficients (Ru-TPA-NCS), amphiphilic derivatives bearing hydrophobic chains to create a barrier layer between sensitized TiO_2 and the HTM (Z907), ion-coordinating derivatives that are able to prevent the adsorption/intercalation of lithium ions (K51) and derivatives that combine donor-antenna groups and further functional moieties (C101, Ru-TPA-EO-NCS).

TPD dyes

N,N,N',N'-Tetraphenylbenzidine derivatives, also denoted as triphenyldiamines (TPDs), are only rarely applied as sensitizers in DSCs.^{65, 66} TPD derivatives and even polymeric TPDs are better known as hole transport materials for organic light emitting diodes (OLEDs)⁶⁷ due to their high hole transport mobilities in the order of 10^{-3} and 10^{-4} $\text{cm}^2/\text{V s}$ for low molecular weight TPDs and TPD side-chain polymers, respectively.^{53, 68, 69} Additionally, they feature a low tendency towards aggregation and crystallisation due to the propeller-shape arrangement of the phenyl groups around the central nitrogen atoms.⁷⁰ They are electrochemically stable if the *para* positions are occupied, can easily be synthesised and are highly soluble in common solvents.⁷¹ These properties distinguish TPDs not only as suitable materials for OLEDs but also as promising hole transport material for DSCs. The first proof of this idea was given by Hagen *et al.* in 1997.¹⁶ With

the use of *para*-dimethoxytriphenyldiamine as solid-state hole transport material, the first SDSC on basis of an organic hole transport material was constructed. Later, further low molecular weight TPDs and polymeric TPDs were investigated as organic hole transport materials in DSCs.⁵³ However, they could not establish themselves against spiro-OMeTAD which performs superior in SDSCs due to optimized charge transport and due to the presence of additives.

In addition to the mentioned favourable characteristics, TPD-dyes feature suitable energy levels for DSCs applications. Moreover, their optical properties can be tuned by the attachment of electron withdrawing acceptor groups creating a D- π -A structure to shift the absorption to the visible region. This makes TPD-dyes also interesting for sensitization in DSCs. Sensitizers applied in DSCs are shown in Figure 5.

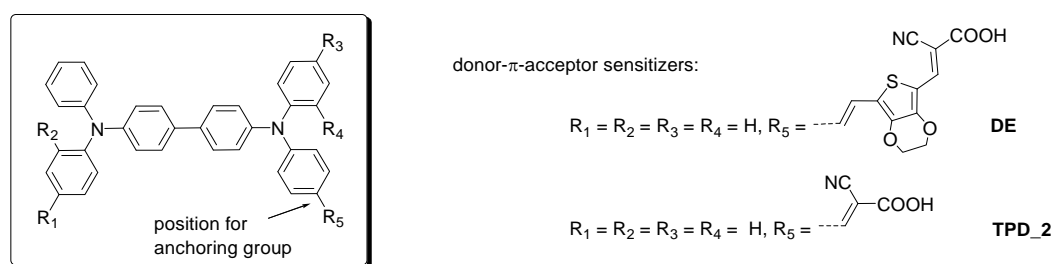


Figure 5. Basic structure of organic *N,N,N',N'*-tetraphenylbenzidines (left) and selection of donor- π -acceptor TPD-sensitizers used in DSCs (right).

However, the efficiencies of TPDs are currently quite low. For example, compounds DE and TPD_2 exhibited an efficiency of 5.63 % (LDSC) and 0.97 % (SDSC), respectively.^{65, 66} One reason for the low efficiency of TPD_2 might be the limited absorption only in blue region of the electromagnetic spectrum. However, this drawback can be turned into an advantage if TPDs are combined with red-absorbing sensitizers in so-called co-sensitized DSCs. (This concept will be focused in chapter 1.3)

Squaraines

Squaraines are resonance stabilized zwitterionic derivatives of the squaric acid that were first reported by Treibs and Jacob in 1965.⁷² These molecules typically comprise an electron deficient four-membered core flanked by two electron-rich donor groups creating a fully conjugated

D-A-D structure (Figure 6). This specific structure facilitates an intramolecular charge transfer. This charge transfer and the extended delocalized system of the donor groups are responsible for the strong absorption of squaraines in the red part of the electromagnetic spectrum. By a suitable choice of the donor groups, the absorption can be shifted even up to the near infra-red region. Squaraines are further characterised by their strong fluorescence. Due to these properties, squaraines have emerged as attractive materials for various interesting applications *e.g.* ion sensing, nonlinear optics, and photovoltaics. The properties, synthesis and scopes of application of squaraines are further highlighted in comprehensive reviews.^{73, 74}

In the context of this thesis, the ability of squaraines to sensitize n-type semiconductors like TiO₂ is the central point of interest. In recent years, different squaraines have been successfully applied as sensitizers in DSCs.^{39, 75-79} The current record efficiencies of squaraine sensitized DSCs are 6.29 %⁷⁵ (YR6, Figure 6) and 3.16 %³⁹ (JD10, Figure 6) for LDSC and SDSC devices, respectively. Besides the undisputed excellent optical properties of squaraines, there are two aspects under discussion that have to be considered when using squaraines as sensitizers for DSCs: 1) the advantages of unsymmetrical squaraines over their symmetrical analogues and 2) the aggregation behaviour of squaraines as adsorbed on mesoporous TiO₂.

The widely accepted estimation regarding the discussion on unsymmetrical vs. symmetrical squaraines is, that the unsymmetrical structure causes an inherent directionality. Upon excitation, this promotes an unidirectional electron flow of electrons from the donor part to the anchoring group which favours the injection of electrons.^{80, 81} However, Park *et al.* recently reported a comparative study on a symmetrical and an unsymmetrical squaraine (VG1_G and SQ01, Figure 6) evidencing comparable efficiency for both types.⁷⁹ Interestingly, FT-IR studies revealed that the symmetrical compound (VG1_G) carrying two anchoring groups, anchors with both of them; no free C=O stretching arising from unattached aromatic carboxylic acids was detected. This enables injection of electrons from both sides of the molecule. Nevertheless, the highest efficiencies up to now were reached with unsymmetrical push-pull squaraines carrying just one anchoring group.⁷⁵⁻⁷⁷

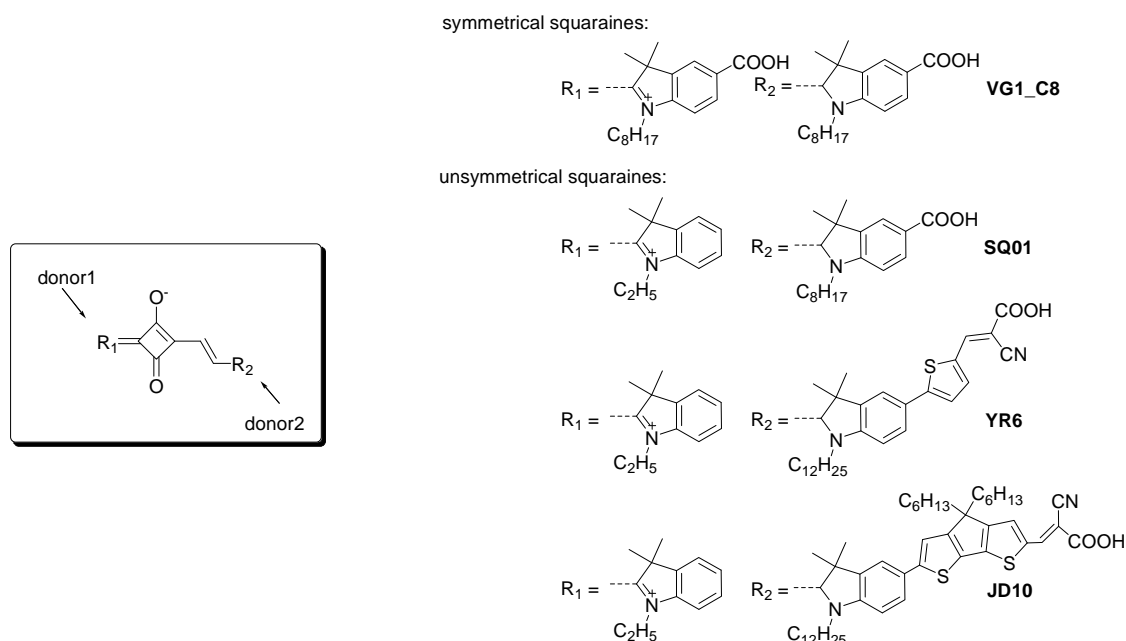


Figure 6. Basic structure of squaraines (left) and a selection of efficient squaraine sensitizers for DSCs (right).

The second issue to be considered is the aggregation of squaraines. Depending on the orientation of the molecules to each other (“plane-to-plane” or “head-to-tail”), squaraines are able to form blue-shifted H-aggregates or red-shifted J-aggregates or both types in solution and in the solid state.⁸²⁻⁸⁵ Aggregation is assumed to cause a negative effect on the performance of DSCs and is therefore reduced/suppressed by the additive chenodeoxycholic acid (CDCA).⁸⁶ CDCA additionally adsorbs on TiO₂ separating the squaraine molecules from each other, but it does not contribute to current generation. Taking a closer look on the influence of CDCA on the device performance, CDCA appears to improve the efficiency sometimes greatly (2.82 and 4.23 % without and with 10 mM CDCA, respectively⁸⁶), but in other cases the influence on the performance is marginal (4.16, 4.47 and 4.10 % with 0, 10 and 30 mM CDCA, respectively⁷⁷). Most often, aggregation of squaraines as adsorbed on TiO₂ is not further investigated, but directly suppressed/reduced by CDCA. However, fundamental research on the types of aggregates formed on TiO₂ and the aggregate formation process is still missing. This issue will be a part of this thesis.

BODIPYs

4,4-Difluoro-4-bora-3a,4a-diaza-s-indacene dyes (BODIPYs) were invented by Treibs and Kreuzer in 1968.⁸⁷ Since then, BODIPYs were for example exploited as biochemical labeling agents⁸⁸ or laser dyes.⁸⁹⁻⁹¹ Recently, BODIPYs gained increasing attention as sensitizers for DSCs and as photoactive donor materials for BHJ solar cells. Although, the number of BODIPY sensitizers tested in DSCs is very limited and the efficiencies are still low (0.68 % for SDSC⁹² and 2.46 % for LDSCs⁹³), BODIPYs are promising candidates for solar cell applications due to their tuneable optical properties, their electrochemical, thermal and photochemical stability, and their high solubility.

To synthesise novel, tailor-made BODIPYs with excellent optical properties for sensitization of SDSCs, a basic understanding on the modification pathway to vary the structure and thus the optical properties of BODIPYs is crucial. An overview on this issue is presented here. The BODIPY core structure and the resonance structures are shown in Figure 7a and 7b, respectively. Modification reactions reported in literature are summarised in Figure 7c.

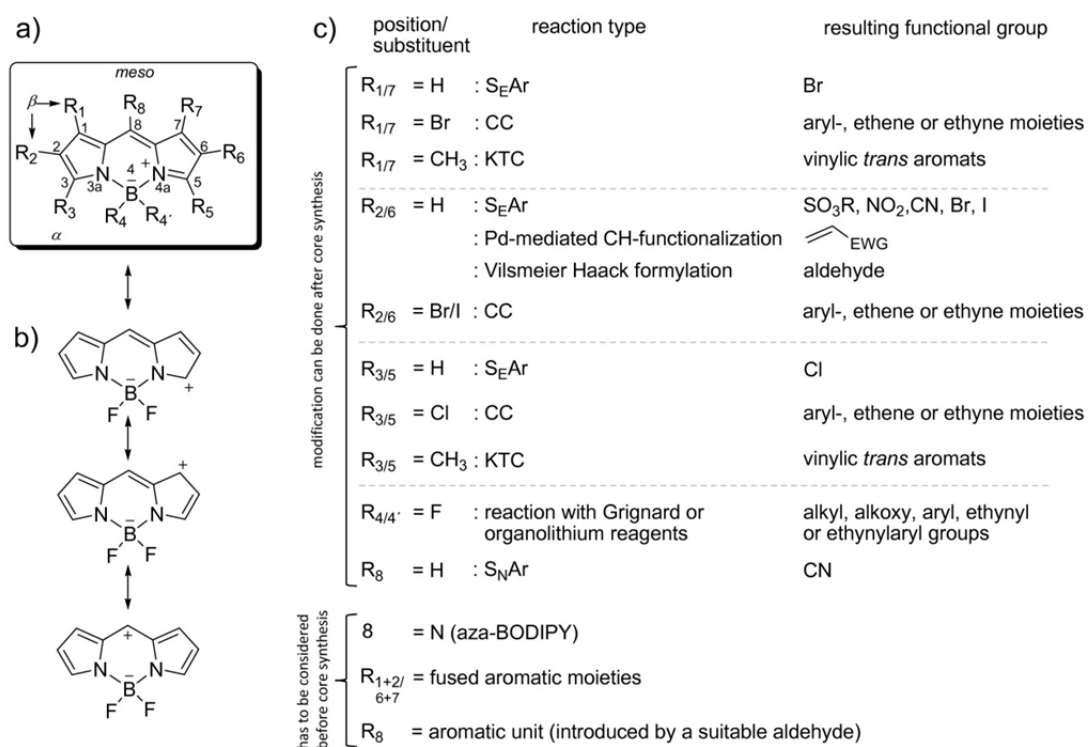


Figure 7. a) BODIPY framework with IUPAC atom numbering. b) BODIPY resonance structures. c) Overview of the reactions reported in literature to modify the BODIPY framework including the resulting functional groups. ($S_E\text{Ar}$: electrophilic aromatic substitution; CC: cross coupling reactions such as Suzuki, Stille, Heck or Sonogashira coupling; KTC: Knoevenagel-type condensation. $S_N\text{Ar}$: nucleophilic aromatic substitution.)

Protons in positions 1,7 and 3,5 can undergo electrophilic aromatic substitutions (S_EAr) to yield the 1,7-dihalogenated⁹⁴ and 3,5-dihalogenated^{95, 96} BODIPY derivatives. They can be further subjected to transition metal catalysed cross coupling (CC) reactions (*e.g.* Sonogashira, Suzuki, Heck and Stille coupling).⁹⁶ After cross coupling with aromatic compounds, a bathochromic shift is observed due to the extension of the aromatic system. This is less pronounced for 1,7-disubstituted compounds than for 3,5-disubstituted ones.⁹⁴ In both cases the largest bathochromic shift was noticed after Heck coupling reactions creating a vinylic connection between the BODIPY core and the aromatic units.^{94, 96}

The most straightforward electrophilic aromatic substitution can be done in positions 2 and 6, because these are, according to the resonance structures, the most negative positions of the BODIPY framework. A large variety of different electrophiles has already been introduced in sulfonation, nitration or halogenation reactions.^{90, 97, 98} An interesting feature of the sulfonation is the water-solubility of the resulting BODIPYs. Certainly, the optical properties are only marginally influenced by sulfonation and nitration. Halogenation at the positions 2 and 6 causes a red-shift of the absorption and enables the synthesis of BODIPY polymers *via* Sonogashira polymerisation which are, however, more interesting for BHJ solar cells.^{90, 99}

Although it is known, that the charge density upon excitation is increased at the *meso*-carbon atom, which distinguishes this as excellent position for an anchoring group,¹⁰⁰ only a few attempts have been made regarding nucleophilic substitutions at the *meso*-position.¹⁰¹ The common route to insert a functional group at the *meso*-position is the use of substituted aromatic aldehydes for the BODIPY core synthesis. Unfortunately, arylation at the *meso*-position only marginally affects the optical and electrochemical properties due to the orthogonal configuration of the *meso*-aryl group relative to the BODIPY core which prevents a good conjugation between both units.¹⁰²

The most pronounced change of the optical properties of BODIPYs is gained by the introduction of aromatic groups at the positions 3 and 5 in Knoevenagel-type condensations. This reaction creates a vinylic connection between the BODIPY core and the aromatic unit like after Heck-coupling of iodide substituted BODIPYs. Up to now, a large variety of different substituted benzenes,^{103, 104} thiophenes¹⁰⁵ as well as triphenylamines¹⁰⁰ or even more complicated aromatic moieties^{106, 107} have been introduced. In 2009 Akkaya *et al.*¹⁰⁸ reported the first synthesis of 1,3,5,7-tetra-styryl BODIPYs and, very recently, even asymmetric tri- and tetra-substituted BODIPYs have been synthesised by Ziessel *et al.*^{109, 110} It turned out that the positions 3 and 5 are

more susceptible towards Knoevenagel-type condensations¹⁰⁸ and that mono- and di-substitutions lead to a more pronounced bathochromic shift than tris- and tetra-substitutions.¹⁰⁸

In the early 1990s¹¹¹ Boyer and Morgan reported on a new derivative of the BODIPYs family: the 4,4-difluoro-4-bora-3a,4a,8-triaza-s-indacenes (aza-BODIPYs). These dyes feature a bathochromic shift of the absorption and emission. It is assumed that the red shift is caused by the contribution of the lone electron pair to the actual cyanine framework, reducing the HOMO-LUMO energy gap.⁹¹ Regrettably, no further modification is possible on the *meso*-position of aza-BODIPYs.

Another method to influence the optical properties of BODIPYs is the integration of additional aromatic moieties fused to the pyrrole rings. This also leads to a bathochromic shift, but complicates the synthesis distinctly. Ring-fused, or di(iso)indomethene BODIPYs can be prepared by retro Diels-Alder reactions or from substituted 2-hydroxyacetophenones and hydrazines.⁹⁰

Murase, Ulrich, Zissel and co-workers established a modification route which is based on reactions between Grignard or organolithium compounds and 4,4-difluoro-BODIPYs to replace the fluorine atom(s) either by ethynyl-, aryl-, or ethynylaryl derivatives.⁹¹ However, the photophysical properties of BODIPYs are not affected by the attached naphthalene,¹¹² pyrene^{113, 114} or perylene¹¹⁴ chromophores. These chromophores can be rather understood as an independent ancillary light harvesters.⁹¹

On the basis of the presented aspects, potentially ideal BODIPY sensitizers can be designed that provide excellent optical properties and fulfil the general requirements of sensitizers for SDSCs. An essential requirement is an extended absorption up to the near infrared region. Therefore, disubstituted BODIPYs with aromatic donor groups attached to the positions 3 and 5 by a vinylic bridge are most promising. Suitable donor groups are *e.g.* 4,4'-disubstituted-triphenylamines because they provide good light harvesting properties, a suitable HOMO level, good charge transporting properties¹¹⁵ and a higher stability against oxidative coupling compared to unsubstituted triphenylamine.⁷¹ In favour of the solubility, alkyl chains should be integrated at positions 2 and 6. However, the substitution of the fluorine atoms by additional chromophores is not worthwhile because they are obviously electronically not connected to the BODIPY framework. Additionally, an anchoring moiety has to be attached to the target compound to provide an intimate contact between the dye and the electron acceptor material in dye-sensitized solar cells. Due to the inherent directionality of the charge redistribution after excitation, the *meso*-position is most appropriate for this group.¹⁰⁰ To improve the conjugation

between the BODIPY core and the adjacent phenyl anchoring moiety, it would be beneficial to integrate an ethynyl bridge between these parts. Ethynyl bridges are known to enable an efficient electronic connection due to the comparatively diffuse nature of the π -bonds creating a cylindrical electron cloud around the σ -bond.¹¹⁶ Attempts to introduction of a *meso*-ethynylphenyl group have already been made, but have so far not been successful.¹¹⁷ The synthesis of such sensitizers is addressed in this thesis.

1.3 DEVICE CONCEPTS

In extension to the standard DSC concept, further strategies and device concepts were developed to *e.g.* adapt the manufacturing process to lower temperatures or to improve the spectral response of the devices by the combination of two sensitizers. The novel device concepts relevant for this thesis will be presented in the following.

Hybrid blend solar cells

Hybrid blend solar cells are the link between SDSCs and organic BHJ solar cells (Figure 8). In SDSCs (Figure 8a), electron transport occurs *via* a well-connected network of an inorganic metal oxide (TiO_2) whereas holes are transported *via* small molecules (spiro-OMeTAD) that have to be entirely filled into the pores of the inorganic network. Light absorption is accomplished by the adsorbed sensitizer. In contrast, in organic BHJ solar cells (Figure 8c), hole and electron transport as well as light absorption occur in small organic molecules or polymers.^{118, 119} Here, the active layer is prepared by blending a donor and an acceptor material. Depending on the system and the mixing ratio, different morphologies are generated by phase separation. In contrast to SDSCs, excitation of organic BHJ solar cells leads to the formation of strongly bound electron hole pairs, the so-called excitons.¹²⁰ These excitons have to diffuse to an interface between donor and acceptor to be separated and contribute to the current generation. If the distance to an interface is longer than the exciton diffusion length, the energy gets lost by radiative and non-radiative recombination processes. This problem in combination with transport and morphology issues limits the thickness of the devices to only around 100 nm; much less than needed for a sufficient light harvesting.

The recently devolved hybrid blend solar cells (Figure 8b) links these two concepts. Hybrid blend solar cells make use of polymers as light absorber and hole transport materials, but, in contrast to organic BHJ solar cells, inorganic particles (TiO_2 , ZnO, CdSe, CdS etc.) are as used as electron transport media.¹²¹⁻¹²³ The advantages of inorganic materials compared to their organic counterparts are their intrinsically high electron mobility, the high dielectric constants, their high electron affinity and the outstanding physical and chemical stability.¹²³ The main drawback of this concept is the lack of morphology control as the inorganic particles tend to aggregate and the low percolation of electrons *via* non-connected particles. Although the efficiencies of hybrid blend solar cells are currently low ($\sim 2-3\%$),^{121, 124} the intrinsic advantages of the high dielectric constant of inorganic particles, which helps to dissociate the excitons more efficiently, give rise to the expectation of more efficient hybrid blend solar cells.

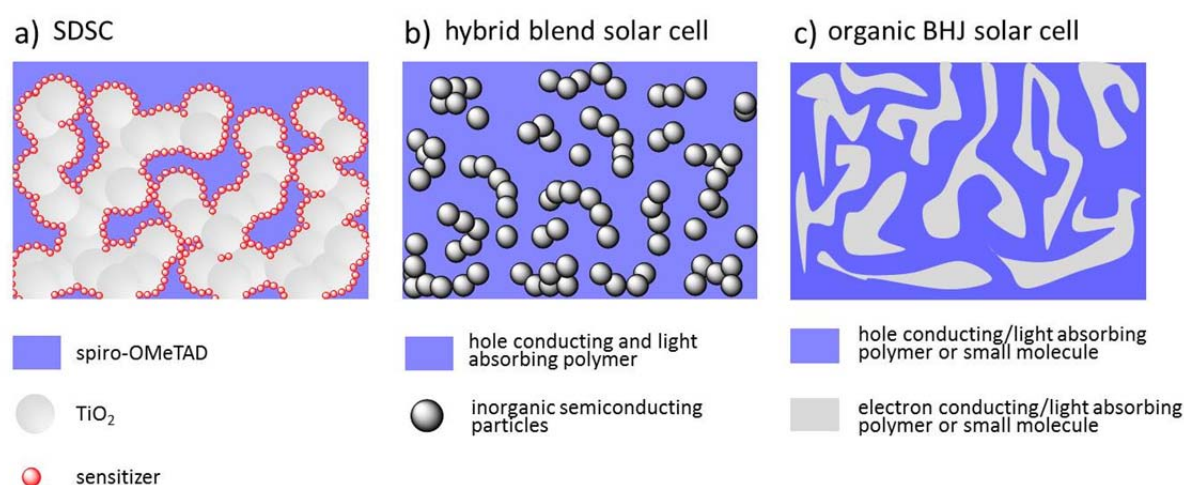


Figure 8. Schematic representation of the active layers in a) a solid-state dye-sensitized solar cell, b) a hybrid blend solar cell and c) an organic bulk heterojunction solar cell. Depending on the materials and the preparation technique, different types of solar cells can be constructed that differ in the operating processes, assets and drawbacks. (a) In DSCs light absorption is promoted by a sensitizer, electron transport occurs via a sintered, well-connected network of TiO_2 and hole transport is managed by spiro-OMeTAD. SDSCs are characterised by the good electron transport via the TiO_2 network but suffer from pore-filling issues. (b) In hybrid blend solar cells, light absorption and hole transport are performed with a polymer. Electrons are transported via semiconducting particles that are blended with the polymer. Hybrid blend solar cells benefit from the high electron mobility and high dielectric constant, but suffer from the lack of control of morphology (connectivity between the inorganic particles). (c) Organic BHJ solar cells comprise two materials that accomplish light absorption, electron and hole transport. However, both can contribute to light absorption, but BHJ suffer from morphology issues and short exciton diffusion length.

New concepts in hybrid blend solar cells are addressed in this thesis using a novel approach. Instead of using polymers as light absorber and hole transporter material, the applicability of

sensitized inorganic particles blended with a low molecular weight hole transport material was investigated. By this way, we wanted to overcome the issue of pore-filling in SDSCs and the problem of exciton diffusion in organic BHJ and conventional hybrid blend solar cells.

Co-sensitization

Co-sensitization is a well-known approach to extend the absorption of standard DSCs over the whole visible region. This panchromatic behaviour is realized by stepwise or simultaneous adsorption of two^{39, 125-128} or more¹²⁹ complementary absorbing sensitizers on the surface of the mesoporous TiO₂ network. In consequence, the main drawback of many organic sensitizers, the narrow absorption, can be overcome (Figure 9).

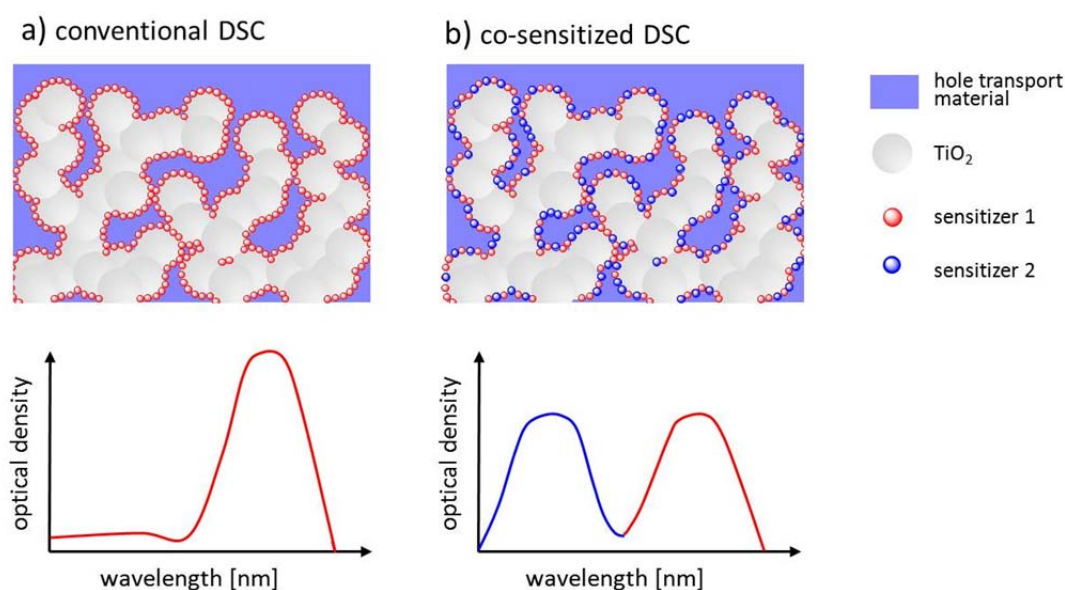


Figure 9. Schematic representation of the active layers and the corresponding absorption spectra of a) a conventional DSCs and b) a co-sensitized DSCs. By co-sensitization, the overall absorption of the device can be broadened, but the number and thus the optical density of sensitizer 1 is reduced due to the space demand of sensitizer 2.

Typically, absorption in the red region is achieved by squaraines,^{126, 127} porphyrins¹²⁵ or phthalocyanines¹²⁸ which are commonly combined with blue absorbing triphenylamine based sensitizers. The potential of the co-sensitization concept in SDSCs and LDSCs has been shown in several reports.^{126, 129, 130} For example, the performance of an LDSC with a ruthenium complex as

sensitizer could be improved by co-sensitization with an organic dye.¹³⁰ Here, the efficiency of the co-sensitized LDSC was 11.6 % (23.49 mA/cm²) compared to the single sensitized samples reaching efficiencies of 4.73 % (9.94 mA/cm²) and 10.0 % (20.61 A/cm²) for the organic and the ruthenium complex sensitizers, respectively. A comparable positive effect was observed for a combination of a red absorbing squaraine and a triphenylamine based sensitizer. The efficiencies of LDSCs were improved from 4.23 % (10.2 mA/cm²) and 7.0 % (13.2 mA/cm²) for the squaraine and the triphenyldiamine based sensitizers to 7.38 % (16.1 mA/cm²) for the co-sensitized device.¹²⁶ A tri-sensitized SDSC comprising a ruthenium complex (N719) and two triphenylamine derivatives as sensitizer performed with efficiency of 6.5 % (13.04 mA/cm²) compared to 1.2 % (2.64 mA/cm²), 3.4 % (8.43 mA/cm²) and 5.6 % (13.1 mA/cm²) for the single dye-sensitized devices.¹²⁹ A closer look at the photocurrent densities of these representative examples reveals that the photocurrent density of the co-sensitized solar cells is significantly lower than the sum of the photocurrents obtained by the individual sensitized cells. It is worth noting that co-sensitization does not lead to an improved performance in every case. Intramolecular interactions like charge or energy transfer and quenching of excited states *etc.* can diminish the expected improvements or even impair the photovoltaic output compared to single sensitized DSCs.¹³¹ An additional key problem especially for the thinner SDSCs is the confined surface area of the mesoporous TiO₂ network. As shown in Figure 9, the co-adsorption of sensitizer 2 limits the number of free adsorption sites available for sensitizer 1. Hence, the light harvesting by sensitizer 1 is lower in a co-sensitized device than in the single-sensitizer-device. The broadening of the absorption is thus realized on the expense of optical density.

Energy transfer

The application of energy transfer principles in solar cells is an emerging approach to improve the spectral response of standard DSCs by an additional energy donor. In contrast to co-sensitization, the additional donor chromophore is not anchored on the TiO₂ surface, but is embedded in the hole transport media of LDSCs and SDSCs. Upon light absorption, the non-anchored energy donor dye (EDD, also denoted as energy relay dye ERD) transfers its excitation energy to a sensitizing acceptor dye (SAD) by dipole-dipole interactions without affecting the optical density of the SAD. Thus, the external quantum efficiency is theoretically enhanced in the absorption region of the EDD without reducing the response of the SAD. This additional

contribution should improve the photocurrent density and thus, the power conversion efficiency. Here is no competition of chemisorption of two different dyes as in co-sensitization.

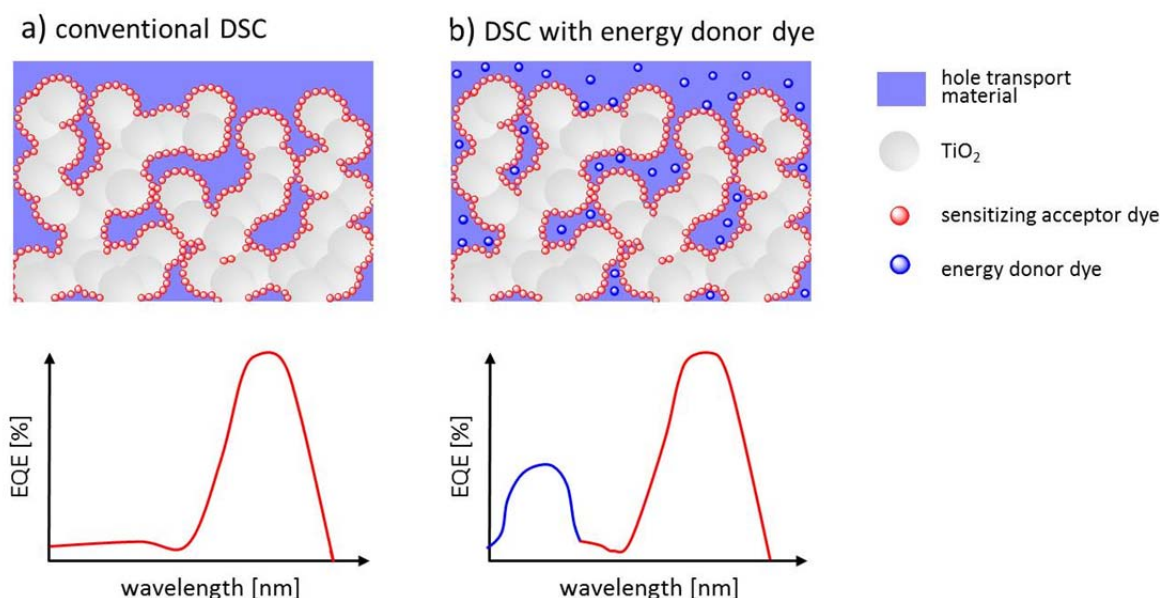


Figure 10. Schematic representation of the active layers and the corresponding EQE spectra of a) a conventional DSC and b) DSC with an additional energy donor dye (EDD). With the introduction of an EDD, an additional contribution to the photocurrent is induced in the absorption region of the EDD (shown in blue) without significantly influencing the EQE in the absorption region of the sensitizing acceptor dye.

To take advantage of energy transfer in DSCs, the EDD has to meet some requirements given by the theory of Förster resonance energy transfer:¹³²⁻¹³⁴ 1) The EDD has to provide a complementary absorption to the SAD, 2) the HOMO-LUMO gap of the EDD has to be larger than that of the SAD, 3) the overlap integral between the EDD emission and the SAD absorption should be high, 4) the distance between the EDD and the SAD should be short (*i.e.* the distance should only be a few nm because energy transfer is inversely proportional to the sixth power of the distance between EDD and SAD), 5) the orientation of the transition dipole moments has to be suitable to enable energy transfer by dipole-dipole interactions. Additionally, the HOMO/LUMO energy levels of the EDD and the SAD relative to each other and relative to the electron transport material and the HTM have to be well adjusted to ensure efficient electron injection into TiO_2 and regeneration of the oxidized sensitizer(s) by the HTM.

Since 2008, only a few reports proved the feasibility of the concept of energy transfer in LDSCs¹³⁵⁻¹³⁸ and SDSCs¹³⁹⁻¹⁴⁴. Most often squaraines and phthalocyanines absorbing in the red region are applied as SADs which were combined with organic EDDs absorbing in the blue region. Driscoll *et al.* reported an SDSC using a spiro-linked EDD in combination with a phthalocyanine SAD. Although they provide an unfavourable energy level alignment (the HOMO level of the EDD was slightly lower than that of the SAD),¹⁴¹ the beneficial effect of energy transfer was observed in the EQE measurements. During optimization of the EDD:spiro-OMeTAD ratio, they observed an increase in the EQE in the absorption region of the EDD up to a ratio of 60:40 (wt%:wt%). However, for high EDD amounts (> 40 wt%) the EQE signal arising from the SAD was reduced as a consequence of the inappropriate energy level alignment which causes a reduction of the dye regeneration rate. Additionally, the fill factor was reduced for EDD > 20 wt% due to a more complex transport through the EDD/spiro-OMeTAD blend. The best performance was found at a ratio of 20:80 (EDD:spiro-OMeTAD, wt%:wt%). This clearly demonstrates both, the advantages and the limitations of energy transfer in DSCs.

Despite the first promising results of this novel concept, still some critical issues have to be considered. Depending on the specific properties of each EDD (values of the energy levels, hole transport mobility, optical properties *etc.*), the amount of EDD in the hole conductor matrix has to be optimized for each system individually. Additionally, high quenching rates of the excited states of the EDD were observed in LDSCs in the presence of an iodine/iodide redox shuttle caused by collision of the EDD with the redox shuttle.^{135, 136, 138} For SDSCs, especially the regeneration of the dye and the charge transport in the HTM can be affected unfavourably by the EDD. In consequence, further fundamental research is required regarding suitable materials for energy transfer in SDSCs. The identification of appropriate EDD/SAD combinations for energy transfer in SDSCs is a subject of discussion in this thesis.

BIBLIOGRAPHY

- 1 E. Becquerel, *Comptes rendus hebdomadaires des séances de l'Académie des sciences*, **1839**, 9, 561-567.
- 2 A. Einstein, *Annalen der Physik*, **1905**, 17, 132-148.
- 3 D. M. Chapin, C. S. Fuller, G. L. Pearson, *Journal of Applied Physics*, **1954**, 25, 676-677.
- 4 Available via Database Provider, <http://nssdc.gsfc.nasa.gov/nmc/masterCatalog.do?sc=1958-002B>, accessed 20-08-2012.
- 5 M. A. Green, K. Emery, Y. Hishikawa, W. Warta, E. D. Dunlop, *Progress in Photovoltaics: Research and Applications*, **2012**, 20, 606-614.
- 6 W. Shockley, H. J. Queisser, *Journal of Applied Physics*, **1961**, 32, 510-519.
- 7 C. Fritts, *American Journal of Science*, **1883**, 26, 465-467.
- 8 C. S. Solanki, *Solar Photovoltaics: Fundamentals Technologies And Applications*, Prentice-Hall Of India Pvt. Limited, **2009**.
- 9 C. W. Tang, *Applied Physics Letters*, **1986**, 48, 183-185.
- 10 C. K. Chiang, C. R. Fincher, Y. W. Park, A. J. Heeger, H. Shirakawa, E. J. Louis, S. C. Gau, A. G. MacDiarmid, *Physical Review Letters*, **1977**, 39, 1098-1101.
- 11 G. Yu, J. Gao, J. C. Hummelen, F. Wudl, A. J. Heeger, *Science*, **1995**, 270, 1789-1791.
- 12 Z. He, C. Zhong, X. Huang, W.-Y. Wong, H. Wu, L. Chen, S. Su, Y. Cao, *Advanced Materials*, **2011**, 23, 4636-4643.
- 13 Available via Database Provider, <http://www.heliatek.com/?p=1923&lang=en>, accessed 20-08-2012
- 14 B. O'Regan, M. Grätzel, *Nature*, **1991**, 353, 737-740.
- 15 K. Tennakone, K. P. Hewaparakkrama, M. Dewasurendra, A. H. Jayatissa, L. K. Weerasena, *Semiconductor Science and Technology*, **1988**, 3, 382-387.
- 16 J. Hagen, W. Schaffrath, P. Otschik, R. Fink, A. Bacher, H.-W. Schmidt, D. Haarer, *Synthetic Metals*, **1997**, 89, 215-220.
- 17 U. Bach, D. Lupo, P. Comte, J. E. Moser, F. Weissörtel, J. Salbeck, H. Spreitzer, M. Grätzel, *Nature*, **1998**, 395, 583-585.
- 18 H. J. Snaith, L. Schmidt-Mende, *Advanced Materials*, **2007**, 19, 3187-3200.
- 19 A. Yella, H.-W. Lee, H. N. Tsao, C. Yi, A. K. Chandiran, M. K. Nazeeruddin, E. W.-G. Diao, C.-Y. Yeh, S. M. Zakeeruddin, M. Grätzel, *Science*, **2011**, 334, 629-634.
- 20 J. Burschka, A. Dualeh, F. Kessler, E. Baranoff, N.-L. Cevey-Ha, C. Yi, M. K. Nazeeruddin, M. Grätzel, *Journal of the American Chemical Society*, **2011**, 133, 18042-18045.
- 21 B. Peng, G. Jungmann, C. Jäger, D. Haarer, H.-W. Schmidt, M. Thelakkat, *Coordination Chemistry Reviews*, **2004**, 248, 1479-1489.
- 22 I.-K. Ding, N. Tétreault, J. Brillet, B. E. Hardin, E. H. Smith, S. J. Rosenthal, F. Sauvage, M. Grätzel, M. D. McGehee, *Advanced Functional Materials*, **2009**, 19, 2431-2436.
- 23 J. Melas-Kyriazi, I.-K. Ding, A. Marchioro, A. Punzi, B. E. Hardin, G. F. Burkhard, N. Tétreault, M. Grätzel, J.-E. Moser, M. D. McGehee, *Advanced Energy Materials*, **2011**, 1, 407-414.
- 24 I.-K. Ding, J. Melas-Kyriazi, N.-L. Cevey-Ha, K. G. Chittibabu, S. M. Zakeeruddin, M. Grätzel, M. D. McGehee, *Organic Electronics*, **2010**, 11, 1217-1222.

- 25 A. Hagfeldt, G. Boschloo, L. Sun, L. Kloo, H. Pettersson, *Chemical Reviews*, **2010**, 110, 6595-6663.
- 26 N. W. Duffy, L. M. Peter, R. M. G. Rajapakse, K. G. U. Wijayantha, *Electrochemistry Communications*, **2000**, 2, 658-662.
- 27 J. Krüger, R. Plass, L. Cevey, M. Piccirelli, M. Grätzel, U. Bach, *Applied Physics Letters*, **2001**, 79, 2085-2087.
- 28 C. Pérez León, L. Kador, B. Peng, M. Thelakkat, *The Journal of Physical Chemistry B*, **2006**, 110, 8723-8730.
- 29 W. Zeng, Y. Cao, Y. Bai, Y. Wang, Y. Shi, M. Zhang, F. Wang, C. Pan, P. Wang, *Chemistry of Materials*, **2010**, 22, 1915-1925.
- 30 J.-H. Yum, P. Walter, S. Huber, D. Rentsch, T. Geiger, F. Nüesch, F. De Angelis, M. Grätzel, M. K. Nazeeruddin, *Journal of the American Chemical Society*, **2007**, 129, 10320-10321.
- 31 S. A. Haque, S. Handa, K. Peter, E. Palomares, M. Thelakkat, J. R. Durrant, *Angewandte Chemie, International Edition*, **2005**, 44, 5740-5744.
- 32 M. Wang, J. Liu, N.-L. Cevey-Ha, S.-J. Moon, P. Liska, R. Humphry-Baker, J.-E. Moser, C. Grätzel, P. Wang, S. M. Zakeeruddin, M. Grätzel, *Nano Today*, **2010**, 5, 169-174.
- 33 H. J. Snaith, A. J. Moule, C. Klein, K. Meerholz, R. H. Friend, M. Grätzel, *Nano Letters*, **2007**, 7, 3372-3376.
- 34 W. M. Campbell, K. W. Jolley, P. Wagner, K. Wagner, P. J. Walsh, K. C. Gordon, L. Schmidt-Mende, M. K. Nazeeruddin, Q. Wang, M. Grätzel, D. L. Officer, *The Journal of Physical Chemistry C*, **2007**, 111, 11760-11762.
- 35 N. Cai, S.-J. Moon, L. Cevey-Ha, T. Moehl, R. Humphry-Baker, P. Wang, S. M. Zakeeruddin, M. Grätzel, *Nano Letters*, **2011**, 11, 1452-1456.
- 36 A. Dualeh, F. De Angelis, S. Fantacci, T. Moehl, C. Yi, F. Kessler, E. Baranoff, M. K. Nazeeruddin, M. Grätzel, *The Journal of Physical Chemistry C*, **2011**, 116, 1572-1578.
- 37 H. J. Snaith, A. Petrozza, S. Ito, H. Miura, M. Grätzel, *Advanced Functional Materials*, **2009**, 19, 1810-1818.
- 38 H. Wonneberger, N. Pschirer, I. Bruder, J. Schöneboom, C.-Q. Ma, P. Erk, C. Li, P. Bäuerle, K. Müllen, *Chemistry - An Asian Journal*, **2011**, 6, 1744-1747.
- 39 A. Dualeh, J. H. Delcamp, M. K. Nazeeruddin, M. Grätzel, *Applied Physics Letters*, **2012**, 100, 173512-173514.
- 40 A. Mishra, M. Fischer, P. Bäuerle, *Angewandte Chemie International Edition*, **2009**, 48, 2474-2499.
- 41 Y. Ooyama, Y. Harima, *European Journal of Organic Chemistry*, **2009**, 2009, 2903-2934.
- 42 C.-Y. Chen, M. Wang, J.-Y. Li, N. Pootrakulchote, L. Alibabaei, C.-h. Ngoc-le, J.-D. Decoppet, J.-H. Tsai, C. Grätzel, C.-G. Wu, S. M. Zakeeruddin, M. Grätzel, *ACS Nano*, **2009**, 3, 3103-3109.
- 43 M. K. Nazeeruddin, F. De Angelis, S. Fantacci, A. Selloni, G. Viscardi, P. Liska, S. Ito, B. Takeru, M. Grätzel, *Journal of the American Chemical Society*, **2005**, 127, 16835-16847.
- 44 Y. Cao, Y. Bai, Q. Yu, Y. Cheng, S. Liu, D. Shi, F. Gao, P. Wang, *The Journal of Physical Chemistry C*, **2009**, 113, 6290-6297.
- 45 A. J. McEvoy, M. Grätzel, *Solar Energy Materials and Solar Cells*, **1994**, 32, 221-227.
- 46 A. Juris, V. Balzani, F. Barigelli, S. Campagna, P. Belser, A. Von Zelewsky, *Coordination Chemistry Reviews*, **1988**, 84, 85-277.

- 47 M. K. Nazeeruddin, P. Liska, J. Moser, N. Vlachopoulos, M. Grätzel, *Helvetica Chimica Acta*, **1990**, 73, 1788-1803.
- 48 R. Amadelli, R. Argazzi, C. A. Bignozzi, F. Scandola, *Journal of the American Chemical Society*, **1990**, 112, 7099-7103.
- 49 M. K. Nazeeruddin, A. Kay, I. Rodicio, R. Humphry-Baker, E. Müller, P. Liska, N. Vlachopoulos, M. Grätzel, *Journal of the American Chemical Society*, **1993**, 115, 6382-6390.
- 50 M. K. Nazeeruddin, P. Péchy, T. Renouard, S. M. Zakeeruddin, R. Humphry-Baker, P. Comte, P. Liska, L. Cevey, E. Costa, V. Shklover, L. Spiccia, G. B. Deacon, C. A. Bignozzi, M. Grätzel, *Journal of the American Chemical Society*, **2001**, 123, 1613-1624.
- 51 C. S. Karthikeyan, K. Peter, H. Wietasch, M. Thelakkat, *Solar Energy Materials and Solar Cells*, **2007**, 91, 432-439.
- 52 J. Bandara, M. Thelakkat, *Journal of the National Science Foundation of Sri Lanka*, **2011**, 39, 35-42.
- 53 C. S. Karthikeyan, M. Thelakkat, *Inorganica Chimica Acta*, **2008**, 361, 635-655.
- 54 H. J. Snaith, C. S. Karthikeyan, A. Petrozza, J. Teuscher, J. E. Moser, M. K. Nazeeruddin, M. Thelakkat, M. Grätzel, *The Journal of Physical Chemistry C*, **2008**, 112, 7562-7566.
- 55 S. Handa, H. Wietasch, M. Thelakkat, J. R. Durrant, S. A. Haque, *Chemical Communications*, **2007**, 1725-1727.
- 56 L. Schmidt-Mende, S. M. Zakeeruddin, M. Grätzel, *Applied Physics Letters*, **2005**, 86, 013504-013503.
- 57 M. Wang, S.-J. Moon, D. Zhou, F. Le Formal, N.-L. Cevey-Ha, R. Humphry-Baker, C. Grätzel, P. Wang, S. M. Zakeeruddin, M. Grätzel, *Advanced Functional Materials*, **2010**, 20, 1821-1826.
- 58 H. J. Snaith, S. M. Zakeeruddin, L. Schmidt-Mende, C. Klein, M. Grätzel, *Angewandte Chemie*, **2005**, 117, 6571-6575.
- 59 J.-H. Yum, S.-J. Moon, C. S. Karthikeyan, H. Wietasch, M. Thelakkat, S. M. Zakeeruddin, M. K. Nazeeruddin, M. Grätzel, *Nano Energy*, **2012**, 1, 6-12.
- 60 J. E. Kroeze, N. Hirata, S. Koops, M. K. Nazeeruddin, L. Schmidt-Mende, M. Grätzel, J. R. Durrant, *Journal of the American Chemical Society*, **2006**, 128, 16376-16383.
- 61 S. M. Zakeeruddin, M. K. Nazeeruddin, R. Humphry-Baker, P. Péchy, P. Quagliotto, C. Barolo, G. Viscardi, M. Grätzel, *Langmuir*, **2002**, 18, 952-954.
- 62 H. J. Snaith, M. Grätzel, *Applied Physics Letters*, **2006**, 89, 262114-262113.
- 63 D. Kuang, C. Klein, H. J. Snaith, J.-E. Moser, R. Humphry-Baker, P. Comte, S. M. Zakeeruddin, M. Grätzel, *Nano Letters*, **2006**, 6, 769-773.
- 64 J. Kroeze, N. Hirata, L. Schmidt-Mende, C. Orizu, S. Ogier, K. Carr, M. Grätzel, J. Durrant, *Advanced Functional Materials*, **2006**, 16, 1832-1838.
- 65 G. Li, Y.-F. Zhou, X.-B. Cao, P. Bao, K.-J. Jiang, Y. Lin, L.-M. Yang, *Chemical Communications*, **2009**, 2201-2203.
- 66 S. Erten-Ela, J. Brendel, M. Thelakkat, *Chemical Physics Letters*, **2011**, 510, 93-98.
- 67 C. Schmitz, M. Thelakkat, H.-W. Schmidt, *Advanced Materials*, **1999**, 11, 821-826.
- 68 R. A. Klenkler, G. Voloshin, *The Journal of Physical Chemistry C*, **2011**, 115, 16777-16781.
- 69 S. Hüttner, M. Sommer, U. Steiner, M. Thelakkat, *Applied Physics Letters*, **2010**, 96, 073503-073503.

- 70 M. Malagoli, M. Manoharan, B. Kippelen, J. L. Brédas, *Chemical Physics Letters*, **2002**, 354, 283-290.
- 71 E. T. Seo, R. F. Nelson, J. M. Fritsch, L. S. Marcoux, D. W. Leedy, R. N. Adams, *Journal of the American Chemical Society*, **1966**, 88, 3498-3503.
- 72 A. Treibs, K. Jacob, *Angewandte Chemie International Edition*, **1965**, 4, 694-694.
- 73 S. Sreejith, P. Carol, P. Chithra, A. Ajayaghosh, *Journal of Materials Chemistry*, **2008**, 18, 264-274.
- 74 L. Beverina, P. Salice, *European Journal of Organic Chemistry*, **2010**, 2010, 1207-1225.
- 75 S. Paek, H. Choi, C. Kim, N. Cho, S. So, K. Song, M. K. Nazeeruddin, J. Ko, *Chemical Communications*, **2011**, 47.
- 76 Y. Shi, R. B. M. Hill, J.-H. Yum, A. Dualeh, S. Barlow, M. Grätzel, S. R. Marder, M. K. Nazeeruddin, *Angewandte Chemie International Edition*, **2011**, 50, 6619-6621.
- 77 T. Geiger, S. Kuster, J.-H. Yum, S.-J. Moon, M. K. Nazeeruddin, M. Grätzel, F. Nüesch, *Advanced Functional Materials*, **2009**, 19, 2720-2727.
- 78 J.-H. Yum, S.-r. Jang, R. Humphry-Baker, M. Grätzel, J.-J. Cid, T. Torres, M. K. Nazeeruddin, *Langmuir*, **2008**, 24, 5636-5640.
- 79 J. Park, C. Barolo, F. Sauvage, N. Barbero, C. Benzi, P. Quagliotto, S. Coluccia, D. Di Censo, M. Grätzel, M. K. Nazeeruddin, G. Viscardi, *Chemical Communications*, **2012**, 48, 2782-2784.
- 80 S. Alex, U. Santhosh, S. Das, *Journal of Photochemistry and Photobiology A: Chemistry*, **2005**, 172, 63-71.
- 81 L. Beverina, R. Ruffo, G. Patriarca, F. De Angelis, D. Roberto, S. Righetto, R. Ugo, G. A. Pagani, *Journal of Materials Chemistry*, **2009**, 19, 8190-8197.
- 82 F. Würthner, T. E. Kaiser, C. R. Saha-Möller, *Angewandte Chemie International Edition*, **2011**, 50, 3376-3410.
- 83 S. Alex, M. C. Basheer, K. T. Arun, D. Ramaiah, S. Das, *The Journal of Physical Chemistry A*, **2007**, 111, 3226-3230.
- 84 U. Mayerhöffer, F. Würthner, *Chemical Science*, **2012**, 3, 1215-1220.
- 85 K. C. Deing, U. Mayerhöffer, F. Würthner, K. Meerholz, *Physical Chemistry Chemical Physics*, **2012**.
- 86 J.-H. Yum, S.-J. Moon, R. Humphry-Baker, P. Walter, T. Geiger, F. Nüesch, M. Grätzel, M. d. K. Nazeeruddin, *Nanotechnology*, **2008**, 19, 424005.
- 87 A. Treibs, F.-H. Kreuzer, *Justus Liebigs Annalen der Chemie*, **1968**, 718, 208-223.
- 88 J. O. Escobedo, O. Rusin, S. Lim, R. M. Strongin, *Current Opinion in Chemical Biology*, **2010**, 14, 64-70.
- 89 J. Bañielos Prieto, F. López Arbeloa, T. Arbeloa López, V. Martínez, I. López Arbeloa, in *Chromic Materials, Phenomena and their Technological Applications* (Ed.: P. R. Somani.), Applied Science Innovations Pvt. Ltd., India, **2012**, pp. 641-677.
- 90 A. Loudet, K. Burgess, *Chemical Reviews*, **2007**, 107, 4891-4932.
- 91 G. Ulrich, R. Ziessel, A. Harriman, *Angewandte Chemie International Edition*, **2008**, 47, 1184-1201.
- 92 S. Kolemen, Y. Cakmak, S. Erten-Ela, Y. Altay, J. Brendel, M. Thelakkat, E. U. Akkaya, *Organic Letters*, **2010**, 12, 3812-3815.

- 93 S. Kolemen, O. A. Bozdemir, Y. Cakmak, G. Barin, S. Erten-Ela, M. Marszalek, J.-H. Yum, S. M. Zakeeruddin, M. K. Nazeeruddin, M. Grätzel, E. U. Akkaya, *Chemical Science*, **2011**, 2, 949-954.
- 94 V. Leen, D. Miscoria, S. Yin, A. Filarowski, J. Molisho Ngongo, M. Van der Auweraer, N. Boens, W. Dehaen, *The Journal of Organic Chemistry*, **2011**, 76, 8168-8176.
- 95 J. Han, O. Gonzalez, A. Aguilar-Aguilar, E. Pena-Cabrera, K. Burgess, *Organic & Biomolecular Chemistry*, **2009**, 7, 34-36.
- 96 T. Rohand, W. Qin, N. Boens, W. Dehaen, *European Journal of Organic Chemistry*, **2006**, 2006, 4658-4663.
- 97 C. Thivierge, R. Bandichhor, K. Burgess, *Organic Letters*, **2007**, 9, 2135-2138.
- 98 L. Li, J. Han, B. Nguyen, K. Burgess, *The Journal of Organic Chemistry*, **2008**, 73, 1963-1970.
- 99 B. C. Popere, A. M. Della Pelle, S. Thayumanavan, *Macromolecules*, **2011**, 44, 4767-4776.
- 100 S. Erten-Ela, M. D. Yilmaz, B. Icli, Y. Dede, S. Icli, E. U. Akkaya, *Organic Letters*, **2008**, 10, 3299-3302.
- 101 G. Sathyamoorthi, J. H. Boyer, T. H. Allik, S. Chandra, *Heteroatom Chemistry*, **1994**, 5, 403-407.
- 102 Y. Chen, L. Wan, D. Zhang, Y. Bian, J. Jiang, *Photochemical & Photobiological Sciences*, **2011**, 10, 1030-1038.
- 103 R. Guliyev, A. Coskun, E. U. Akkaya, *Journal of the American Chemical Society*, **2009**, 131, 9007-9013.
- 104 S. Mula, G. Ulrich, R. Ziessel, *Tetrahedron Letters*, **2009**, 50, 6383-6388.
- 105 S. Rihn, P. Retailleau, N. Bugsaliewicz, A. D. Nicola, R. Ziessel, *Tetrahedron Letters*, **2009**, 50, 7008-7013.
- 106 T. Bura, R. Ziessel, *Tetrahedron Letters*, **2010**, 51, 2875-2879.
- 107 R. Ziessel, P. Retailleau, K. J. Elliott, A. Harriman, *Chemistry - A European Journal*, **2009**, 15, 10369-10374.
- 108 O. Buyukcakil, O. A. Bozdemir, S. Kolemen, S. Erbas, E. U. Akkaya, *Organic Letters*, **2009**, 11, 4644-4647.
- 109 T. Bura, P. Retailleau, G. Ulrich, R. Ziessel, *The Journal of Organic Chemistry*, **2011**, 76, 1109-1117.
- 110 T. Bura, D. Hablot, R. Ziessel, *Tetrahedron Letters*, **2011**, 52, 2370-2374.
- 111 L. R. Morgan, J. H. Boyer, US Patent 5446157, **1993**.
- 112 A. Haefele, C. Zedde, P. Retailleau, G. Ulrich, R. Ziessel, *Organic Letters*, **2010**, 12, 1672-1675.
- 113 A. Harriman, G. Izzet, R. Ziessel, *Journal of the American Chemical Society*, **2006**, 128, 10868-10875.
- 114 G. Ulrich, C. Goze, M. Guardigli, A. Roda, R. Ziessel, *Angewandte Chemie International Edition*, **2005**, 44, 3694-3698.
- 115 V. Mimaite, J. Ostrauskaite, D. Gudeika, J. V. Grazulevicius, V. Jankauskas, *Synthetic Metals*, **2011**, 161, 1575-1581.
- 116 V. Lin, S. DiMagno, M. Therien, *Science*, **1994**, 264, 1105-1111.
- 117 L. Bonardi, G. Ulrich, R. Ziessel, *Organic Letters*, **2008**, 10, 2183-2186.
- 118 G. Li, R. Zhu, Y. Yang, *Nature Photonics*, **2012**, 6, 153-161.

- 119 P. Peumans, S. Uchida, S. R. Forrest, *Nature*, **2003**, 425, 158-162.
- 120 B. Schweitzer, H. Bässler, *Synthetic Metals*, **2000**, 109, 1-6.
- 121 W. U. Huynh, J. J. Dittmer, A. P. Alivisatos, *Science*, **2002**, 295, 2425-2427.
- 122 W. J. E. Beek, M. M. Wienk, R. A. J. Janssen, *Advanced Materials*, **2004**, 16, 1009-1013.
- 123 J. Bouclé, P. Ravirajan, J. Nelson, *Journal of Materials Chemistry*, **2007**, 17, 3141-3153.
- 124 S. Dayal, N. Kopidakis, D. C. Olson, D. S. Ginley, G. Rumbles, *Nano Letters*, **2009**, 10, 239-242.
- 125 C.-M. Lan, H.-P. Wu, T.-Y. Pan, C.-W. Chang, W.-S. Chao, C.-T. Chen, C.-L. Wang, C.-Y. Lin, E. W.-G. Diau, *Energy & Environmental Science*, **2012**, 5, 6460-6464.
- 126 J.-H. Yum, S.-R. Jang, P. Walter, T. Geiger, F. Nüesch, S. Kim, J. Ko, M. Grätzel, M. K. Nazeeruddin, *Chemical Communications*, **2007**, 4680-4682.
- 127 D. Kuang, P. Walter, F. Nüesch, S. Kim, J. Ko, P. Comte, S. M. Zakeeruddin, M. K. Nazeeruddin, M. Grätzel, *Langmuir*, **2007**, 23, 10906-10909.
- 128 J.-J. Cid, J.-H. Yum, S.-R. Jang, M. Nazeeruddin, E. Martínez-Ferrero, E. Palomares, J. Ko, M. Grätzel, T. Torres, *Angewandte Chemie International Edition*, **2007**, 46, 8358-8362.
- 129 P. J. Holliman, M. Mohsen, A. Connell, M. L. Davies, K. Al-Salihi, M. B. Pitak, G. J. Tizzard, S. J. Coles, R. W. Harrington, W. Clegg, C. Serpa, O. H. Fontes, C. Charbonneau, M. J. Carnie, *Journal of Materials Chemistry*, **2012**, 22, 13318-13327.
- 130 H. Ozawa, R. Shimizu, H. Arakawa, *RSC Advances*, **2012**, 2, 3198-3200.
- 131 B. E. Hardin, A. Sellinger, T. Moehl, R. Humphry-Baker, J.-E. Moser, P. Wang, S. M. Zakeeruddin, M. Grätzel, M. D. McGehee, *Journal of the American Chemical Society*, **2011**, 133, 10662-10667.
- 132 E. T. Hoke, B. E. Hardin, M. D. McGehee, *Optics Express*, **2010**, 18, 3893-3904.
- 133 K. E. Sapsford, L. Berti, I. L. Medintz, *Angewandte Chemie International Edition*, **2006**, 45, 4562-4589.
- 134 G. D. Scholes, *Annual Review of Physical Chemistry*, **2003**, 54, 57-87.
- 135 J.-H. Yum, B. E. Hardin, E. T. Hoke, E. Baranoff, S. M. Zakeeruddin, M. K. Nazeeruddin, T. Torres, M. D. McGehee, M. Grätzel, *ChemPhysChem*, **2011**, 12, 657-661.
- 136 B. E. Hardin, J.-H. Yum, E. T. Hoke, Y. C. Jun, P. Péchy, T. Torres, M. L. Brongersma, M. K. Nazeeruddin, M. Grätzel, M. D. McGehee, *Nano Letters*, **2010**, 10, 3077-3083.
- 137 A. Makhal, S. Sarkar, T. Bora, S. Baruah, J. Dutta, A. K. Raychaudhuri, S. K. Pal, *The Journal of Physical Chemistry C*, **2010**, 114, 10390-10395.
- 138 B. E. Hardin, E. T. Hoke, P. B. Armstrong, J.-H. Yum, P. Comte, T. Torres, J. M. J. Fréchet, M. K. Nazeeruddin, M. Grätzel, M. D. McGehee, *Nature Photonics*, **2009**, 3, 406-411.
- 139 E. L. Unger, A. Morandeira, M. Persson, B. Zietz, E. Ripaud, P. Leriche, J. Roncali, A. Hagfeldt, G. Boschloo, *Physical Chemistry Chemical Physics*, **2011**, 13, 20172-20177.
- 140 N. Humphry-Baker, K. Driscoll, A. Rao, T. Torres, H. J. Snaith, R. H. Friend, *Nano Letters*, **2011**, 12, 634-639.
- 141 K. Driscoll, J. Fang, N. Humphry-Baker, T. Torres, W. T. S. Huck, H. J. Snaith, R. H. Friend, *Nano Letters*, **2010**, 10, 4981-4988.
- 142 G. K. Mor, J. Basham, M. Paulose, S. Kim, O. K. Varghese, A. Vaish, S. Yoriya, C. A. Grimes, *Nano Letters*, **2010**, 10, 2387-2394.
- 143 J.-H. Yum, B. Hardin, S.-J. Moon, E. Baranoff, F. Nüesch, M. McGehee, M. Grätzel, M. Nazeeruddin, *Angewandte Chemie International Edition*, **2009**, 48, 9277-9280.

144 K. Shankar, X. Feng, C. A. Grimes, *ACS Nano*, **2009**, 3, 788-794.

2 OBJECTIVE OF THE THESIS

The aim of this thesis is the design, synthesis and characterisation of novel tailor-made metal-organic and organic sensitizers for the application in different types of solid-state hybrid solar cells. The focus is on sensitizers and device preparation techniques that both contribute to improved light harvesting in hybrid solar cells.

The low optical density and the limited wavelength of absorption are the most performance-limiting factors in solid-state hybrid solar cells. The light harvesting cannot be improved just by increasing the thickness of the absorbing layer, since the thickness has to be kept low (~ 1.5 - $2\ \mu\text{m}$) to reduce recombination. Further aspects influencing the device performance such as the HOMO/LUMO energy level alignment of the materials, aggregation issues or the methods for the preparation of devices should also be considered. The main drawback of hybrid solar cells, *viz.* the low light harvesting in the device, will be addressed in this thesis with the help of two different approaches:

The first approach deals with the synthesis of novel sensitizers providing an extended absorption and high optical density in the visible region of the electromagnetic spectrum (panchromatic behaviour) up to the near infrared region. A particular focus will be laid on ruthenium(II) donor-antenna dyes and 4,4-dibora-3a,4a-diaza-s-indaces (BODIPYs). A series of ruthenium complexes carrying different donor-antenna groups will be compared regarding the spectral and electrochemical behaviour. Their structure-property relationship should be investigated regarding their photovoltaic performance. The second class of sensitizers, the BODIPYs, are in their infancy regarding solar cell applications. In fact, they are better known for biological labeling or as laser dyes where they typically provide a narrow but intensive absorption. It is the goal to tune their absorption behaviour by a tailor-made design in such a way that the resulting BODIPY dyes feature an extraordinary broad optical response. To reach this, synthetic strategies have to be developed enabling a strong electronic conjugation throughout the whole molecular structure.

The second approach to increase the optical density in hybrid solar cell devices deals with novel device concepts. It will be realized by the combination of two sensitizers featuring complementary optical properties in a single device. Here, two basic concepts are of special importance. The first concept deals with the combination of two sensitizers, which are both

anchored on the TiO_2 semiconductor material. In contrast, the second concept focuses on energy transfer from an unattached energy donor dye to an anchored sensitizing acceptor dye. Both concepts require suitable dyes that have to be designed, synthesised and characterised. Finally, the implementation of both concepts in hybrid solar cells will be demonstrated.

The performance of all the hybrid solar cells will be investigated by measuring the current-voltage characteristics under AM 1.5 G conditions and by external quantum efficiency measurements which give information regarding the conversion of incident photons to current for each wavelength.

3 OVERVIEW OF THE THESIS

The focus of this thesis is on light harvesting in solid-state hybrid solar cells (SDSCs) using tailor-made metal-organic and organic sensitizers. This thesis encompasses the synthesis of novel sensitizers, their optical and electrochemical characterisation as well as their application in different types of hybrid solar cells. The primary challenges are: 1) the design and synthesis of metal-organic and organic sensitizers that feature a broad absorption in the visible/NIR region with high extinction coefficients and 2) new concepts to further broaden and boost the absorption by combining complementary sensitizers. Figure 1 illustrates the different approaches by various types of sensitizers and key concepts in the individual chapters of this thesis.

In general, solid-state hybrid devices suffer from low optical density. Due to pore-filling and recombination issues associated with the solid hole transport material spiro-OMeTAD, the thickness of the devices is limited to only $\sim 2\mu\text{m}$ entailing the unfavourable low optical density of the device. As a consequence, the current density is affected negatively. The solution of this problem is obvious: to enhance the device performance, light harvesting of the device has to be increased. The central theme of this thesis concerns this issue, on the one hand by developing sensitizers with optimized optical properties. Hence, the main part of this dissertation covers the design, synthesis and characterisation of novel dyes belonging to the class of ruthenium donor-antenna complexes, triphenyldiamine derivatives, squaraines and BODIPYs. These dyes feature an extended absorption and high extinction coefficients. On the other hand, light-harvesting is improved by device-specific concepts which contribute to an enhancement of the optical density. These concepts relay on the combination of two complementary absorbing dyes by the means of multichromophore light harvesting, co-sensitization or energy transfer.

This thesis comprises six manuscripts. Five are presented in chapter 5-9 and one more appears as appendix in chapter 10. In the following, a short description on each single topic will be given to bridge the individual parts and to demonstrate the stepwise evolution of a broadened and boosted absorption as the central goal of this thesis.

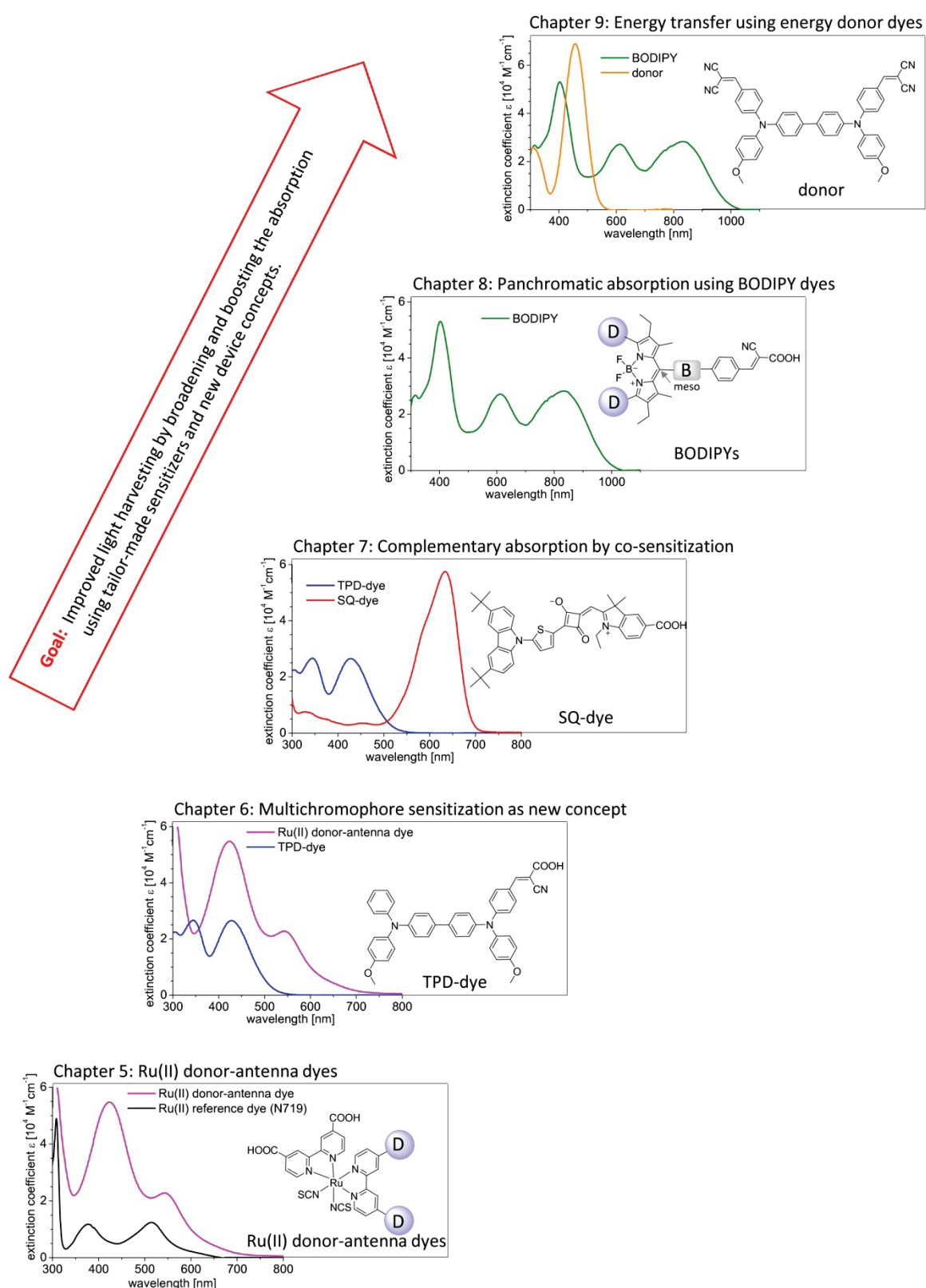


Figure 1. Diverse concepts for extended and boosted spectral response of single sensitizers and combinations of sensitizers for hybrid solar cells. The challenge of improved light harvesting was addressed by the synthesis and characterisation of tailor-made metal-organic and organic sensitizers and by device-specific concepts. The figure shows the absorption spectra and the molecular structures of the sensitizers presented in the single chapters. Further, the key concepts that determine the optical density of the device are introduced.

The first part of this thesis (chapter 5) concerns the synthesis and characterisation of a series of novel heteroleptic Ru(II) donor-antenna sensitizers. Ruthenium(II)bis(bipyridyl)(NCS)₂ complexes feature in general a metal-to-ligand-charge-transfer (MLCT) absorption band at ~ 550 nm. This band allows an extension of the absorption up to ~ 650 nm (Figure 1). In addition to that, the advantage of Ru(II) donor-antenna dyes is the high molar extinction coefficient of the donor-antenna ligand related absorption bands, which arise from the extended conjugated system of the ligands. Our systematic investigations on the structure-property relationships revealed that the photovoltaic performance of SDSCs sensitized with Ru(II) donor-antenna dyes strongly depends on the individual donor-antenna unit. With increasing extension of the conjugated system, the current density could be significantly increased proving the beneficial effects of tailor-made donor-antenna ligands.

The second part (chapter 6) takes advantage of these findings and extends the previous concept towards multichromophore sensitization. Multichromophore blend devices were prepared according to a novel and technologically interesting fabrication technique at room temperature. Here, TiO₂ particles are sensitized and subsequently blended with the hole transport material. This blend is coated on the substrate by doctor blading without the need for further sintering. For sensitization, we combined a metal-organic Ru(II) donor-antenna sensitizer (Ru-TPA-NCS) with an organic sensitizer, *viz.* a blue absorbing triphenyldiamine derivative (TPD-dye). The idea is to use two sensitizers with complementary absorption properties. TPD-dye shows two absorption maxima, at 345 nm and 428 nm in blue region, whereas Ru-TPA-NCS provides absorption maximum at 544 nm in the green region (Figure 1). Therefore, the TPD-dye is able to supplement the optical density of Ru-TPA-NCS in a device. The positive effect of combining those dyes can be clearly seen in the device performance. The current density of multichromophore sensitized hybrid devices is the sum of the individual single sensitized devices which results in a doubling of the power conversion efficiency.

A further approach addressing the combination of two sensitizers is presented in chapter 7. On the basis of the well-known concept of co-sensitization, two complementary absorbing sensitizers were simultaneously adsorbed on previously sintered mesoporous TiO₂ electrodes. Here, a squaraine sensitizer (SQ-dye) providing an intensive absorption in the red part of the electromagnetic spectrum was combined with the blue absorbing TPD-dye. This concept allows a remarkable extension of the absorption range up to 700 nm (Figure 1). External quantum efficiency measurements give clear evidence that both the SQ-dye and the TPD-dye contribute to the current generation achieving an overall power conversion efficiency of 2.4 %.

In chapter 8, the desired panchromaticity was realized in a single dye by developing novel structures of 4,4-difluoro-4-bora-3a,4a-diaza-s-indacene dyes (BODIPY). In this chapter a comprehensive study on the structure-property relationship of BODIPYs is accomplished. It is demonstrated how the optical and the electrochemical properties can be fine-tuned by variation of the substituents in the *meso*-position and by conjugated attachment of donor-antenna groups (D). Especially the donor-substituted BODIPYs exhibit extraordinary broad and intensive absorptions over the whole UV/visible range up to the NIR region. The best optical properties are found for a *meso*-ethynylphenyl BODIPY with TPA-donor-antenna groups providing absorption up to 1030 nm and $\epsilon > 10^4 \text{ M}^{-1} \text{ cm}^{-1}$ up to 940 nm (Figure 1). With these superior optical characteristics, the BODIPY sensitizer ranks among the best absorbing dyes.

Chapter 9 makes use of the investigations on the BODIPY compounds and expands the topic towards a recent concept to boost and broaden the absorption by Förster resonance energy transfer (FRET). Here, an additional energy donor dye is embedded in the solid hole transport material that is in close contact to the sensitizing dye which is chemisorbed on the n-type semiconductor TiO_2 . The advantage of this strategy over the concepts of multichromophore sensitization and co-sensitization is the fact that energy donor dyes can broaden and boost the spectral response by energy transfer without the need to be directly anchored on the TiO_2 surface. While the optical density of the adsorbed sensitizing acceptor dye remains constant, an additional contribution to the external quantum efficiency is achieved by FRET. To identify suitable donor-acceptor combinations for energy transfer in SDSCs, comprehensive experiments with BODIPY acceptor dyes and novel triphenylamine-based donor dyes are accomplished. Therefore, detailed steady-state UV/vis and fluorescence measurements, cyclic voltammetry studies and by fluorescence quenching experiments were done. For appropriate donor-acceptor combinations, we observed an increase of the external quantum efficiency in the absorption region of the energy donor dye.

To get a more comprehensive picture of recent developments of dye-sensitized hybrid solar cells in general, a review paper covering on the theoretical background of these solar cells, the design concepts of sensitizers (metal-organic and organic) and their performances in solar cells is presented in chapter 10 as appendix.

In the following, the individual chapters are summarized briefly and the main results are presented. An elaborated representation of the topics including experimental details can be found in the individual chapters and their supporting information.

SYNTHESIS, SPECTRAL, ELECTROCHEMICAL AND PHOTOVOLTAIC PROPERTIES OF NOVEL HETEROLEPTIC POLYPYRIDYL RUTHENIUM(II) DONOR-ANTENNA DYES

The focus of this investigation was the design, synthesis and characterisation of a series of novel heteroleptic Ru(II) (4,4'-dicarboxylic acid-2,2'-bipyridine)(*bipyridyl donor-antenna ligand*)(NCS)₂ complexes. The objective was to elucidate structure-property relationships between the donor-antenna ligands and the photovoltaic performance of the associated Ru(II) donor-antenna complexes in SDSCs. The molecular structures of the synthesised complexes are depicted in Figure 2.

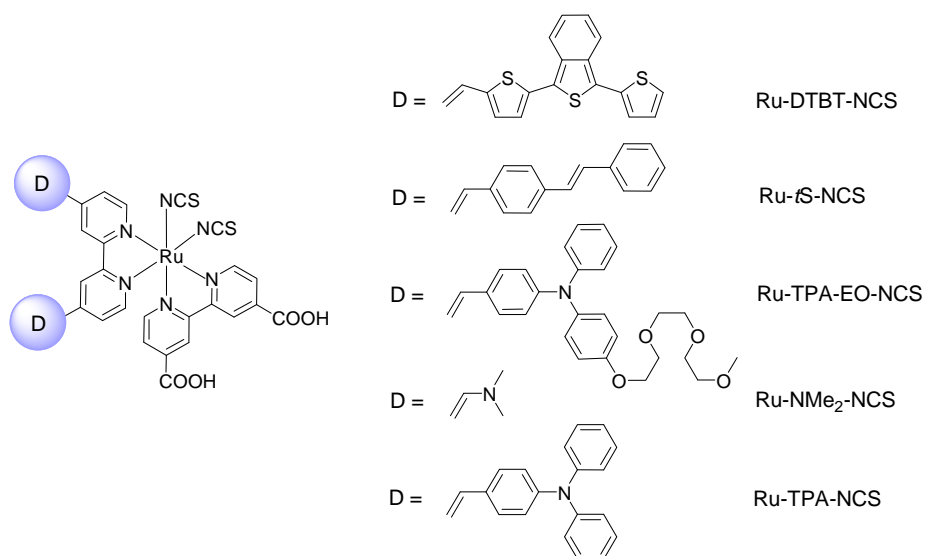


Figure 2. Overview of the molecular structures of the Ru(II) complexes carrying different donor-antenna groups (D).

After the successful synthesis of the bipyridyl donor-antenna ligands, the Ru(II) donor-antenna complexes were obtained in one-pot reactions under conventional or microwave assisted conditions. The electrochemical behaviour of the donor-antenna ligands and the Ru(II) complexes was investigated thoroughly by cyclic voltammetry in solution to ascertain the energy levels and to examine the role of the donor-antenna groups on electron transfer processes. The HOMO levels of the Ru(II) complexes were determined to be -5.13 ± 0.05 eV. On the basis of cyclic voltammetry experiments on the donor-antenna ligands and the commercially available reference dye N719 it could be stated that the HOMO levels of Ru-tS-NCS, Ru-TPA-NCS and Ru-TPA-EO-NCS are mainly delocalized over the ruthenium core and certain groups which are equal in all complexes like the NCS groups. In these cases, the second oxidation involves only the donor-ligands. For Ru-DTBT-NCS and Ru-NMe₂-NCS the HOMO level is assumed to be delocalized

over the ruthenium core and the bipyridyl donor antenna moiety. The values of the LUMO energy levels of all donor-antenna complexes and the reference dye are -3.13 ± 0.03 eV. The LUMO is mainly delocalized over the anchoring ligand. In conclusion, the values of the energy level determined for the complexes are ideal for electron injection into the n-type semiconductor TiO_2 and regeneration of the oxidized dye by the solid hole transport material spiro-OMeTAD.

To elucidate the influence of the donor-antenna groups on the optical properties of the complexes, steady-state UV/vis spectra were measured for all complexes. Figure 3 shows these spectra in comparison to the reference dye N719 which is lacking any donor groups.

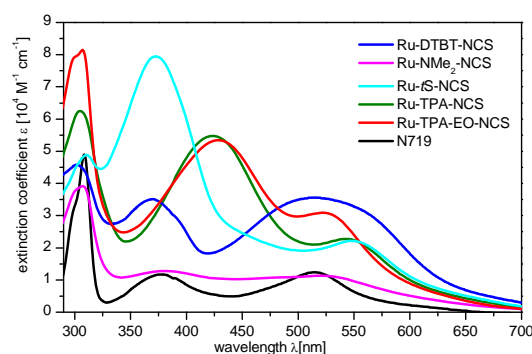


Figure 3. Comparison of the optical properties of a series of Ru(II) donor-antenna complexes and the complex N719 without donor-antenna groups. The calculated extinction coefficients of Ru-DTBT-NCS (in DMF, blue), Ru-NMe₂-NCS (in dioxane/H₂O/DMF 1:1:1 + 1 wt% KOH, purple), Ru-tS-NCS (in DMF, cyan), Ru-TPA-NCS (in MeOH + 1 wt% KOH, green), Ru-TPA-EO-NCS (in MeOH + 1 wt% KOH, red) and N719 (in MeOH + 1 wt% KOH, black) are shown as function of the wavelength.

The Ru(II) donor-antenna complexes and N719 exhibit three absorption bands leading to a broad absorption almost throughout the whole visible region. The maxima arise from ligand-centred (LC) and MLCT transitions. The high energy transition bands at 305 ± 5 nm were attributed to LC transitions in the anchoring and the donor-antenna ligand. The second absorption band is determined by two influences, LC $\pi\text{-}\pi^*$ transitions and MLCT $d\text{-}\pi^*$ transitions. The third low energy band with maxima between 515 and 550 nm is a MLCT transition associated with the introduction of NCS ligands. The most important aspect, however, is that all donor-antenna complexes provide higher extinction coefficients than the reference dye. This is a direct benefit from the extended delocalized π -systems of the donor-antenna ligands.

These superior optical properties make Ru(II) donor-antenna complexes interesting candidates as sensitizers in SDSCs. The current-voltage characteristics of the Ru(II) donor-antenna complexes are depicted in the following figure:

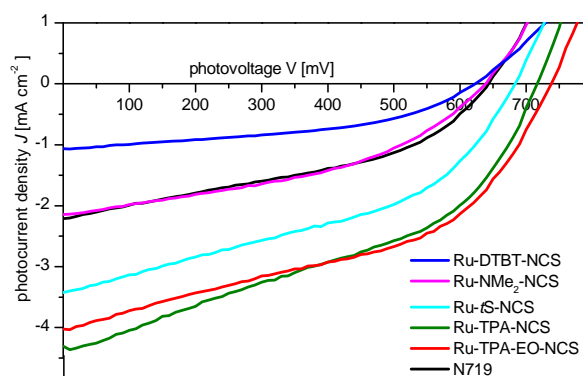


Figure 4. Current-voltage characteristics of Ru(II) donor-antenna dyes used as sensitizers in SDSCs in comparison to the performance of the reference dye N719.

It was clearly shown that especially the photocurrent density of the solar cells is strongly dependent on the respective donor group. As a general trend, a significant increase in the photocurrent density was observed with extension of the delocalized system (with exception of Ru-DTBT-NCS). The photocurrent density of solar cells sensitized with Ru-NMe₂-NCS, which is carrying the smallest donor groups, is rather the same as of N719-sensitized devices (2.15 and 2.21 mA cm⁻² for Ru NMe₂-NCS and N719, respectively). The optimum photocurrent density was achieved with Ru-TPA-NCS (4.30 mA cm⁻²). This dye features a large delocalized π -system and the highest optical density as adsorbed on mesoporous TiO₂. Although Ru-TPA-EO-NCS features the same conjugated system as Ru-TPA-NCS, its bulky side chains reduce the optical density as adsorbed on mesoporous TiO₂ and thus the current density is lower compared to Ru-TPA-NCS. However, the side chains were introduced with the aim to provide an ion-coordinating functionality. This causes an increase in the open-circuit voltage by preventing Li⁺-ions from reaching the TiO₂ surface, where they are supposed to lower the Fermi-level of TiO₂. For Ru-TPA-EO-NCS, the gain in voltage surpasses the loss in current density. Therefore, the highest efficiency of 1.37 % was achieved with Ru-TPA-EO-NCS in non-optimized devices.

MULTICHROMOPHORE LIGHT HARVESTING IN HYBRID BLEND SOLAR CELLS

This chapter deals with an innovative and technologically relevant preparation technique for multichromophore sensitized hybrid blend solar cells. Extended and strong light absorption as well as efficient pore-filling with hole conductor materials are important requirements to increase solar cell efficiencies. These issues are addressed by the combination of two sensitizers in multichromophore hybrid solar cells prepared by the new technique presented in Figure 5b.

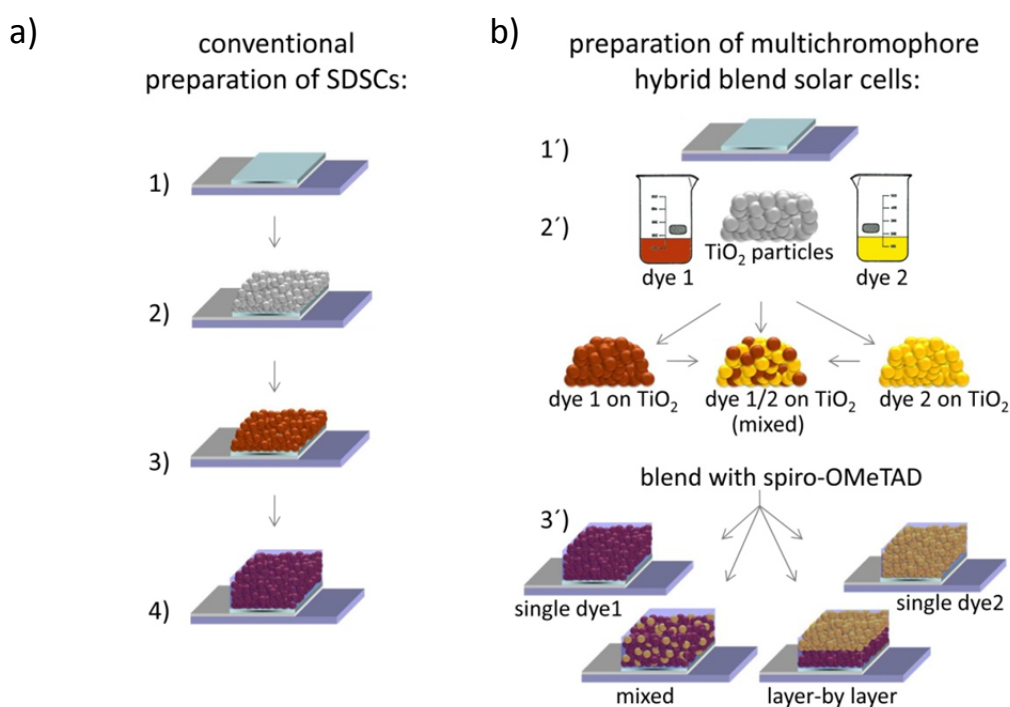


Figure 5. a) Conventional preparation process of SDSCs in comparison to b) the preparation technique of multichromophore hybrid blend solar cells. In the conventional approach (a), a partly etched FTO-coated glass substrate is covered with a blocking TiO₂ layer (1). On top of this layer, a mesoporous TiO₂ layer is applied by screen printing, spin-coating or doctor blading which subsequently is sintered at 500 °C (2). After dye-sensitization (3), the hole transport material is applied by spin-coating (4). Multichromophore hybrid solar cells (b) are prepared on similar substrates (1'), but here TiO₂ particles are sensitized with dye 1 and/or dye 2 (2'). In this way, single-dyed as well as co-sensitized particles can be prepared. Additionally, the single-dye sensitized particles can also be mixed in any desired ratio afterwards. In the last step, the sensitized particles are mixed with the hole transport material and subsequently coated on the substrate by doctor blading. Thereby different blend architectures can be generated (3').

The advantages of this concept are: 1) There is no need for a high temperature sintering step, hence the concept can be transferred to flexible substrates. 2) The application of TiO₂/spiro-OMeTAD blends circumvents the issue of incomplete pore-filling of mesoporous TiO₂ layers. 3) The chemisorption process of each dye can be optimized separately regarding the dyeing

solvent, time and co-adsorbents. 4) The combination of two or even more dyes is possible and the ratio of the dyes is adjustable by simply mixing the desired amount of single-dyed particles.

For a proof of principle, two dyes (Ru-TPA-NCS and TPD-dye, Figure 6a) were adsorbed on TiO_2 nanoparticles and blended with a mixture of spiro-OMeTAD and additives. The resulting paste was doctor bladed at room temperature, a smoothing hole injection layer and the electrode contacts were applied on top. The current-voltage characteristics of single-dye and multichromophore hybrid solar cells are given in Figure 6b.

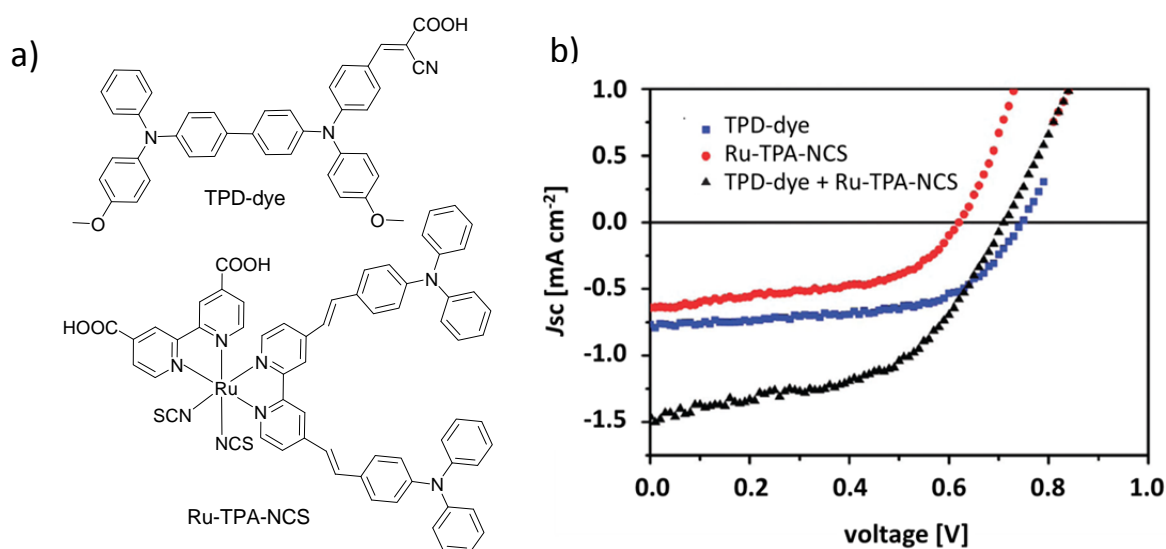


Figure 6. a) Molecular structures of the used sensitizers. b) Current-voltage characteristics for single-dye hybrid blend devices comprising TPD-dye (blue squares) or Ru-TPA-NCS (red circles) in comparison to the multichromophore sensitized devices (black triangles) under AM 1.5 G conditions (100 mW cm^{-2}).

The most striking feature of multichromophore hybrid solar cells is the increase in current density by combining two complementary sensitizers caused mainly by an increase in the spectral response. The current of the multichromophore device (1.46 mA cm^{-2}) was approximately the sum of the individual contributions of the single-dye devices (0.64 and 0.76 mA cm^{-2} for Ru-TPA-NCS and TPD-dye, respectively). However, the power conversion efficiency of this novel type of hybrid solar cells was low (0.54%) due to a low percolation of electrons *via* the TiO_2 particles. Nevertheless, the efficiency could be increased by an optimization of the TiO_2 : spiro-OMeTAD ratio. The optimum was found at a TiO_2 :spiro-OMeTAD ratio of 1:0.6 resulting in an increase of the current density from 1.46 to 2.13 mA cm^{-2} . A further increase to 3.6 mA cm^{-2} was achieved by addition of PCBM, which acts as an organic electron transport material and improved the percolation of electrons.

EFFICIENT PANCHROMATIC CO-SENSITIZATION FOR SOLID-STATE DYE-SENSITIZED SOLAR CELLS USING TRIPHENYLDIAMINE AND SQUARINE SENSITIZERS

The demand for panchromaticity in SDSCs is addressed by co-sensitization with two complementary absorbing sensitizers, viz. a blue-absorbing triphenyldiamine sensitizer (TPD-dye, Figure 7a) and a red-absorbing squaraine sensitizer (SQ-dye, Figure 7b). By mixing these dyes, the absorption could be extended to 700 nm with high extinction almost over the whole visible range (Figure 7c).

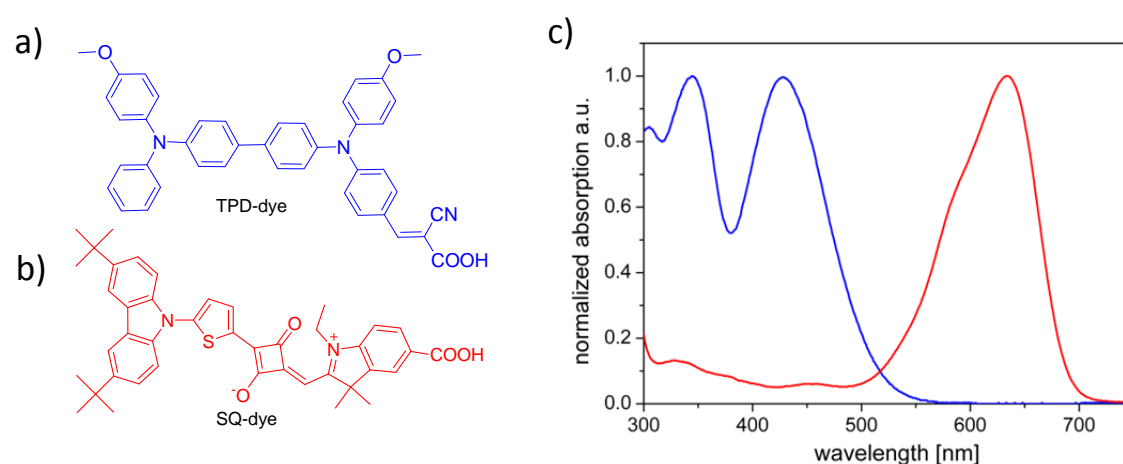


Figure 7. Molecular structures of a) SQ-dye and b) TPD-dye. c) Normalized steady-state absorption spectra of TPD-dye (blue) and SQ-dye (red) in CH_2Cl_2 .

However, squaraines are known for their tendency towards aggregation which can influence the solar cell performance. Therefore, fundamental studies on the aggregation behaviour of the SQ-dye in solution and as adsorbed on TiO_2 were performed. In solution, it was found that the shape and the position of the absorption bands strongly depend on the type of solvent (Figure 8a). The analysis of a dilution series in THF gave clear evidence that the absorption band in THF at 632 nm arises from J-aggregates and the band at 606 nm is attributed to the monomer species. The formation of H-aggregates (at 539 nm in toluene) could be induced by the addition of lithium iodide. By plotting the wavelength of the monomer absorption band as a function of the solvent polarity, a linear relationship was observed with a hypsochromic shift upon increasing the solvent polarity proving negative solvatochromism.

The absorption spectra of SQ-dye as adsorbed on mesoporous TiO_2 composes of three superimposed Gaussian functions (Figure 8b): one for H-aggregates (554 nm), one for the monomer species (594 nm) and one for the J-aggregates (642 nm).

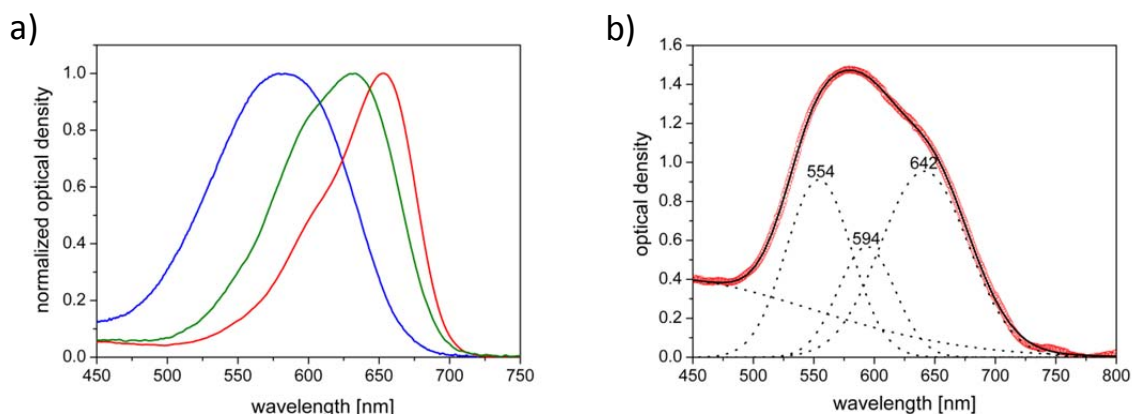


Figure 8. a) Normalized steady-state absorption spectra of SQ-dye in methanol (blue), tetrahydrofuran (green) and toluene (red). b) UV/vis spectrum of SQ-dye as adsorbed on mesoporous TiO_2 ($\sim 2.5 \mu\text{m}$) after chemisorption for 65 h (red circles). The approximation of this curve was done by Gaussian multi-peak fitting. The fitted curves with maxima at 554, 594 and 642 nm could be assigned to H-aggregates, the monomer species and J-aggregates, respectively.

Co-sensitized and single-dye SDSCs comprising TPD-dye and/or SQ dye were prepared according to a standard procedure (Figure 5a). The SDSCs performed with efficiencies of 0.80, 0.87 and 1.33 % for TPD-dye-sensitized, SQ-dye-sensitized and co-sensitized devices, respectively. The performance of the co-sensitized solar cell surpassed the single-dye devices. The most striking feature of our co-sensitized devices was an increase in the open-circuit voltage by 80 mV, which is attributed to a reduced recombination rate.

Upon optimizations of the solvent used for chemisorption and the thickness of the mesoporous layer, the power conversion efficiency of the co-sensitized device could be almost doubled to 2.41 %. The current-voltage characteristic of this solar cell is presented in Figure 9 together with the external quantum efficiency spectrum.

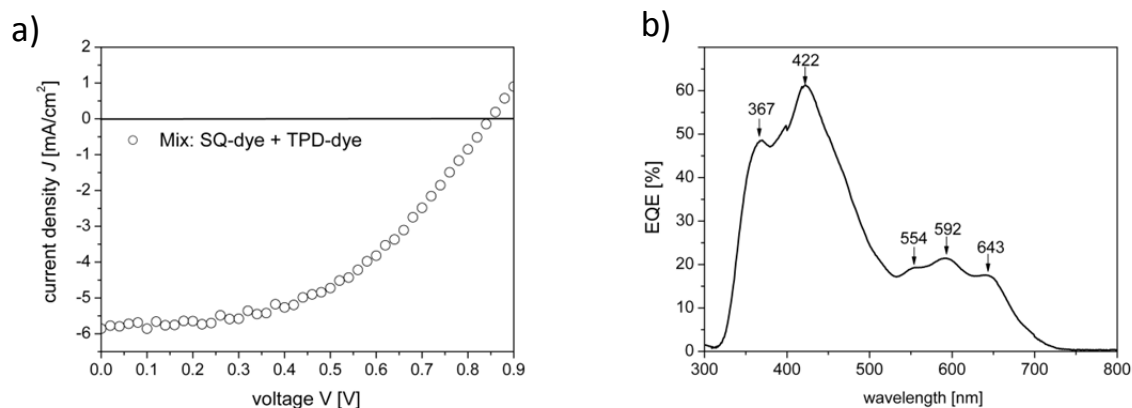
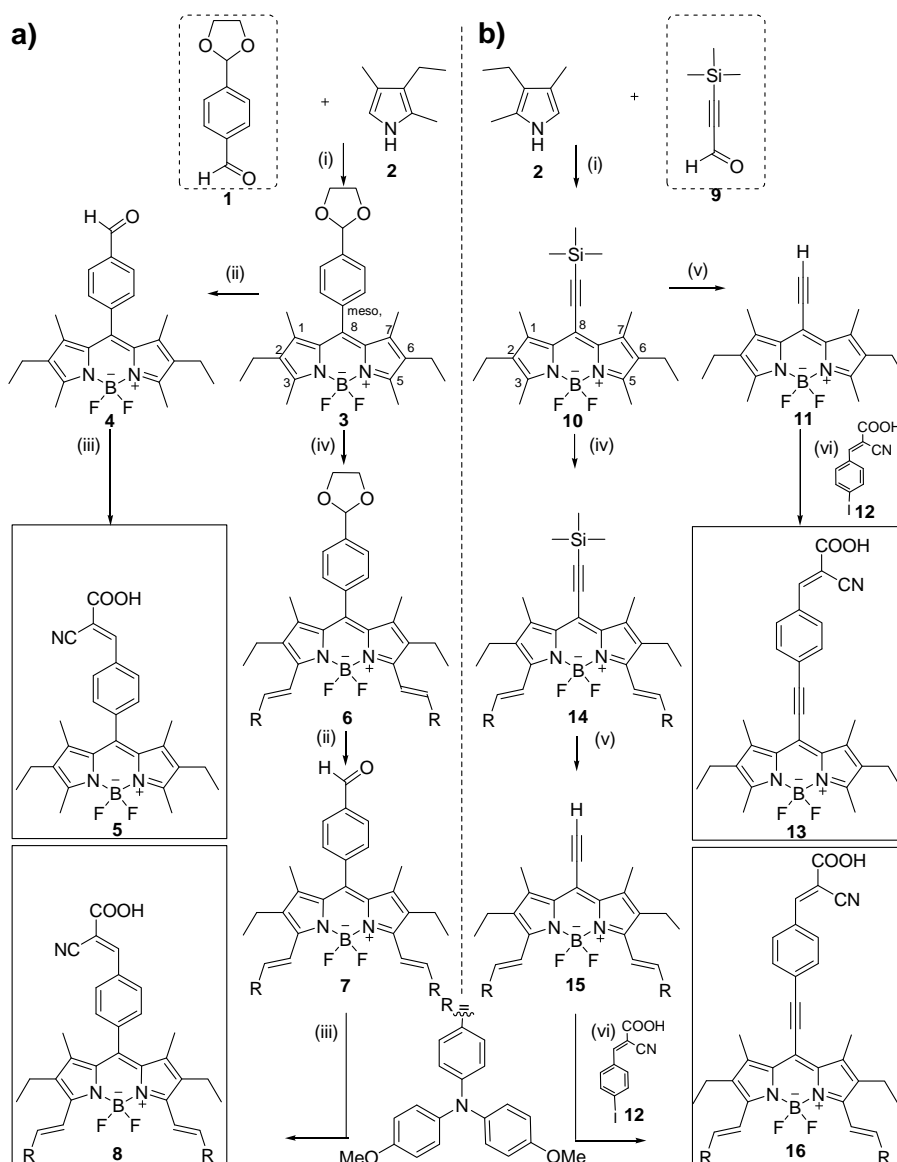


Figure 9. a) Current-voltage characteristics of the most efficient co-sensitized SDSC under AM 1.5 G conditions (100 mW cm^{-2}). b) External quantum efficiency spectrum as function of the excitation wavelength for the same device.

The EQE results are fully consistent with the findings for the aggregation behaviour of the SQ-dye and allow a clear assignment of the contributions of each species: The maxima at 643, 592, 554, 422 and 367 nm can be assigned to J-aggregates of the SQ-dye, the SQ-dye monomer species, H-aggregates of the SQ-dye, the TPD-dye and the hole transport material.

PANCHROMATIC BODIPYs WITH DONOR-ANTENNA GROUPS: A NEW SYNTHETIC ROUTE TOWARDS *meso*-ETHYNYLPHENYL BODIPYs

The design, synthesis and characterisation of novel BODIPY derivatives providing panchromaticity accompanied by high extinction coefficients are in the focus of the following investigation. Two types of BODIPYs are compared: *meso*-phenyl (route a) and *meso*-ethynylphenyl (route b) BODIPYs. The synthetic routes of both types without and with donor-antenna groups are depicted in Scheme 1.



Scheme 1. Synthetic routes a) for *meso*-phenyl BODIPYs **5** and **8**, b) for *meso*-ethynylphenyl BODIPYs **13** and **16**. i) Trifluoroacetic acid, 2,3-dichloro-5,6-dicyano-1,4-benzoquinone, NEt_3 , $\text{BF}_3 \cdot \text{OEt}_2$, in CH_2Cl_2 , RT. ii) 5% HCl_{aq} , in THF, RT. iii) 2-Cyanoacetic acid, piperidine, in acetonitrile, reflux. iv) 4-(di(4-methoxyphenyl)amino)benzaldehyde, piperidine, glacial acetic acid, in benzene, reflux. v) KF , in MeOH or MeOH: THF 1:1, RT. vi) $\text{Pd}(\text{PPh}_3)_4$, CuI , NEt_3 , in THF, RT.

Meso-phenyl BODIPYs are generally prepared by a condensation between kryptopyrrole **2** and an aromatic aldehyde like **1**. In contrast, we introduce the novel *meso*-ethynylphenyl BODIPYs, which were prepared from an aliphatic aldehyde (**9**) for the first time. The ethynyl bridge was inserted with the aim to improve the optical properties by a stronger electronic coupling between the phenyl group carrying the anchoring moiety and the BODIPY core. From *meso*-phenyl BODIPYs it is known that arylation and further derivatization of the phenyl group affects the optical properties only marginally due to the orthogonal configuration of the phenyl ring relative to the BODIPY core. This problem can be overcome by the ethynyl bridge. The σ -bond of the ethynyl bridge is surrounded by the cylindrical electron cloud of the π -bonds, which are supposed to enable strong electronic interactions. To understand the beneficial influence of the ethynyl bridge, compounds **5** and **13** were compared for their optical and electrochemical properties.

A further crucial step towards panchromaticity was the conjugated attachment of the donor-antenna group. This is done for both types of BODIPYs by a Knoevenagel condensation. We found that the reaction between 3,5-dimethyl BODIPYs like **3** or **10** and aldehydes in the presence of the secondary amine piperidine follows an organocatalytic mechanism. Piperidine primarily reacts as a nucleophile with the donor-antenna aldehyde to form a hemiaminal which can be either converted into an aminor or an iminium ion. These intermediates react with the methyl groups of the BODIPY derivative to form *trans*-substituted donor-antenna BODIPYs like **6** and **14**. Hence, a nucleophile such as piperidine that activates the donor-antenna aldehyde is indispensable. However, this caused a serious problem for BODIPYs carrying ethynyl groups because piperidine attacked the alkyne functionality in a very fast hydroamination reaction. To circumvent this, **10** was subjected to the Knoevenagel reaction. Here, the bulky trimethylsilyl groups prevented the triple bond from hydroamination. In this way compound **8** and **16** were synthesised.

Steady-state absorption measurements (Figure 10) show that the spectrum of **5** is dominated by a sharp and intensive band at 530 nm with $\epsilon = 4.20 \times 10^4 \text{ M}^{-1}\text{cm}^{-1}$. By introduction of the ethynyl bridge (**13**) the absorption experiences a bathochromic shift of 55 nm leading to λ_{max} of 585 nm, but the extinction coefficient is reduced. This behaviour is a direct consequence of the improved electronic interaction of the BODIPY core with the attached phenyl group due to the ethynyl bridge. The extended conjugation causes the broadening of the absorption, but the rearrangement of the molecular orbitals due to the change in electronic interaction increases the distance between the HOMO and the LUMO and reduces therefore the transition probability

of the low energy absorption band at 585 nm. However, upon the attachment of donor-antenna groups, *meso*-phenyl BODIPYs and *meso*-ethynylphenyl BODIPYs experience an enormous bathochromic shift. The lowest energy absorption band maximum appeared at 725 and 840 nm for **8** and **16**, respectively. In conclusion, the tailor-made design based on enhanced electronic interaction introduced by the *meso*-ethynyl bridge and additionally on the conjugated attachment of donor-antenna groups resulted in the conversion of the initially sharp optical response of **5** into the extreme broad and intensive absorption of **16** with $\epsilon > 10^4 \text{ M}^{-1}\text{cm}^{-1}$ up to 940 nm.

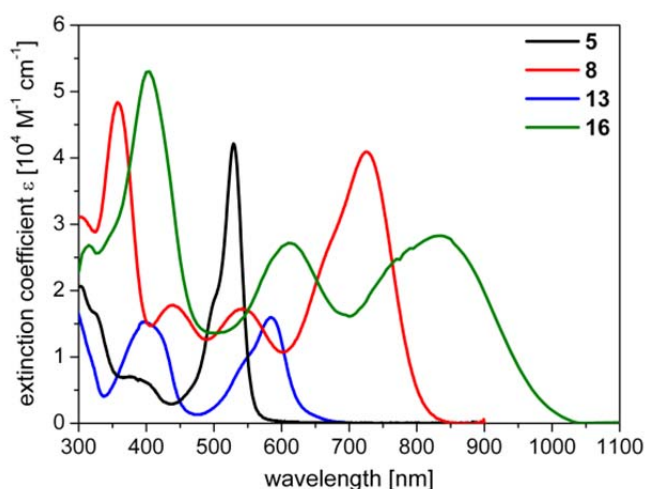


Figure 10. Steady-state UV/vis spectra of BODIPY sensitizers **5** (*meso*-phenyl/without donor-antenna, in CH_2Cl_2), **8** (*meso*-phenyl/with donor-antenna, in CH_2Cl_2), **13** (*meso*-ethynylphenyl/without donor-antenna, in $\text{CH}_2\text{Cl}_2/\text{THF}$ 1:1) and **16** (*meso*-ethynylphenyl/with donor-antenna, in CH_2Cl_2).

The influence of the *meso* moiety and the donor-antenna groups on the values of the energy levels was examined by cyclic voltammetry. Three general trends were identified: 1) For all BODIPY derivatives lacking additional donor-antenna groups, the value of the HOMO level is $-5.41 \pm 0.03 \text{ eV}$ regardless of the moiety in the *meso* position. 2) The HOMO value is determined by the donor moiety in positions 3 and 5. The donor-antenna groups shifted the HOMO value to -4.8 eV . 3) The LUMO level can be shifted to lower values with increasing electron withdrawing ability of the *meso* group. These guidelines provide an excellent basis for further tuning of the energy levels by suitable substitution.

ENERGY TRANSFER IN SOLID-STATE DYE-SENSITIZED SOLAR CELLS: COMBINING BODIPYs AND TRIPHENYLDIAMINE ENERGY DONOR DYES

This study concerns with BODIPY sensitizers towards energy transfer applications for improved light harvesting in SDSCs. Energy transfer is a sophisticated approach to boost or broaden the optical density of solar cells by an unattached energy donor dye (EDD) embedded in the hole transport material without reducing the optical density of the sensitizing acceptor dye (SAD). The fulfilment of the prerequisites of energy transfer between triphenyldiamine-based EDD compounds and BODIPY acceptors (Figure 11) was examined by cyclic voltammetry, steady-state UV/vis absorption and fluorescence measurements as well as by fluorescence quenching experiments in solution and transient (time-resolved) fluorescence quenching experiments in the solid state.

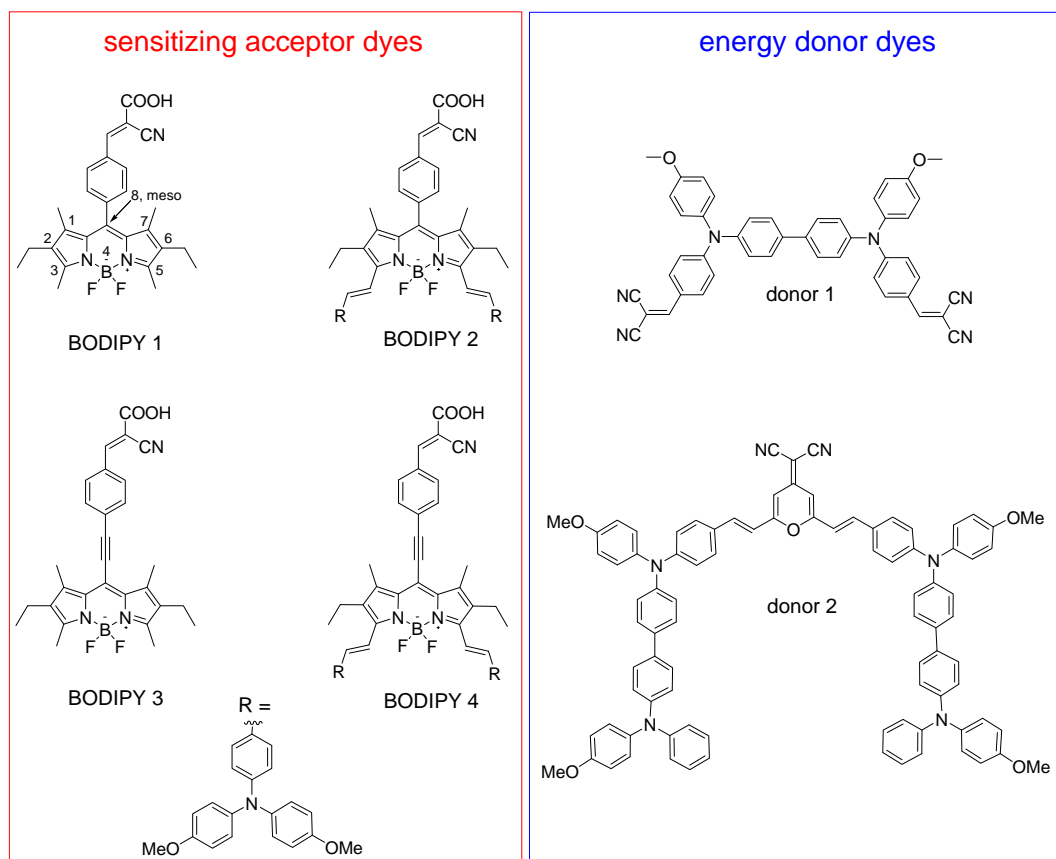


Figure 11. Molecular structures of the investigated sensitizing acceptor dyes and the energy donor dyes.

To take advantage of Förster resonance energy transfer from an donor dye to an acceptor dye in SDSCs the following fundamental requirements have to be fulfilled: 1) The HOMO-LUMO gap of

the SAD has to be smaller than the gap of the EDD to enable energy transfer. 2) The energy levels of the materials have to be aligned in such a way that efficient dye-regeneration by the hole transport material is feasible and that the generation of traps is excluded. Hence, the HOMO level of the EDD has to lie between that of the SAD and that of the hole transport material. 3) The EDD has to show an intensive absorption in the region, where the SAD shows only minor spectral response in order to enhance the light harvesting of the device. 4) In quenching experiments in solution and solid state both the fluorescence and the fluorescence lifetime of the EDD should be reduced in the case of energy transfer. The implementation of these requirements was scrutinized and suitable donor-acceptor combinations for energy transfer were identified. The results of the experiments are summarized in Table 1.

Table 1. Results of the energy transfer experiment of the acceptor/donor combinations. The column on the left side gives the respective combination. The other columns show how the specific requirement is fulfilled: + = very well fulfilled, o = not ascertainable, - = not fulfilled. The criteria include the size of the HOMO-LUMO gap of the acceptor relative to that of the donor, the alignment of the energy levels of the acceptor material relative to the donor, the overlap between the acceptor absorption and the donor emission and the success of quenching experiments in solution and in the solid state.

combination	HOMO-LUMO gap	energy level alignment	boost/broaden absorption	absorption/emission overlap	quenching in solution	quenching in solid state
BODIPY 1/ donor 1	+	+	+	+	o	+
BODIPY 2/ donor 1	+	-	+	+	+	+
BODIPY 3/ donor 1	+	+	+	+	+	+
BODIPY 4/ donor 1	+	-	+	+	+	+
BODIPY 1/ donor 2	-	+	+	-	-	-
BODIPY 2/ donor 2	+	-	+	+	+	+
BODIPY 3/ donor 2	+	+	+	+	+	+
BODIPY 4/ donor 2	+	-	+	+	+	+

By these experiments the most promising combinations were identified to be BODIPY 1/donor 1, BODIPY 3/donor 1 and BODIPY 3/ donor 2. However, the experiments also revealed that the combination BODIPY 1/ donor 2 is inapplicable. Further, regeneration problems can be expected for combinations involving BODIPY 2 and BODIPY 4 due to an unfavourable energy level

alignment although all other requirements are perfectly fulfilled. In further studies on the fluorescence lifetime of the EDDs in the solid state, it was found that donor 1 provides a considerably longer lifetime (317 ps) than donor 2 (104 ps). Considering that fluorescence relaxation rates are inverse proportional to the donor lifetime, the performance of donor 1 should exceed donor 2.

These deductions were proven by external quantum efficiency measurements on SDSCs with EDDs in comparison to reference devices without additional donor.

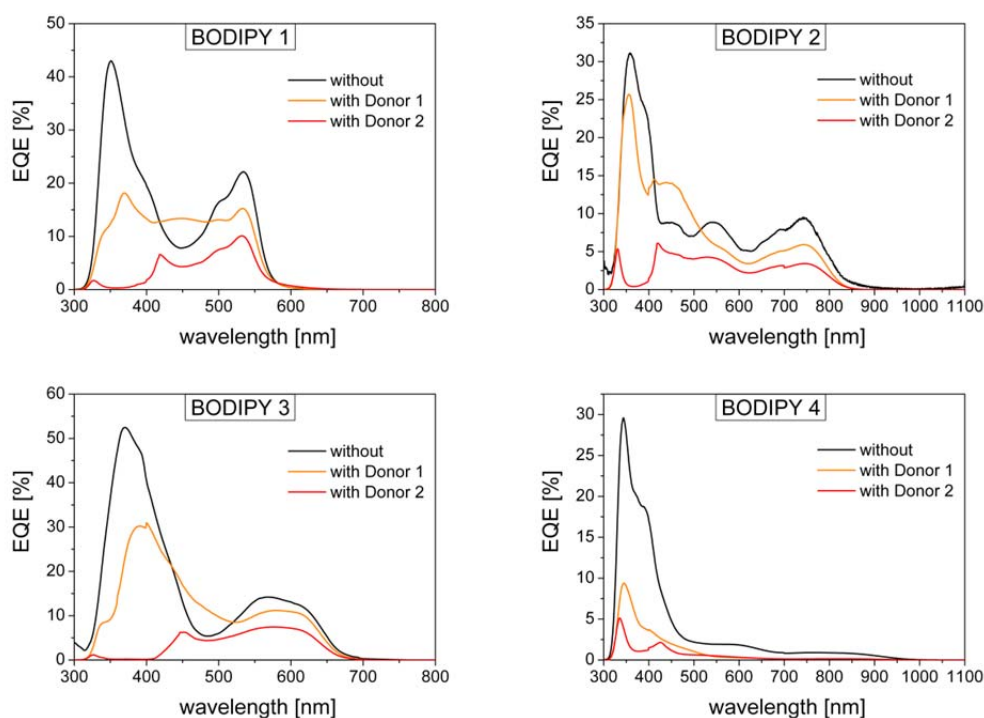


Figure 12. External quantum efficiency as function of the excitation wavelength of solid-state dye-sensitized solar cells sensitized with the different SADs without additional EDD (black), with donor 1 (orange) and with donor 2 (red).

Only for devices using donor 1 as energy donor dye a contribution to the external quantum efficiency could be measured whereas all devices with donor 2 failed. In particular the combinations BODIPY 1/donor 1 and BODIPY 3/donor 1 gave a contribution in the absorption region of the donor dye (at around 450 nm), but also for BODIPY 2 an improvement of the EQE was measured in this region. In conclusion, the most promising candidates for further optimizations are BODIPY 1/donor 1 and BODIPY 3/donor 1.

APPENDIX: PHOTOSENSITIZERS IN SOLAR ENERGY CONVERSION

In this part, a review of the evolution of dye-sensitized solar cells (DSCs), the materials used for the preparation, the theory behind the concept and the characterisation methods of solar cells are outlined. Special importance was attached to the sensitizers. They were divided into two main categories: metal-organic and organic sensitizers. The requirements for sensitizers and relevant design strategies to improve the performance were discussed. Additionally, each section on a special type of sensitizer is concluded by a table giving the respective dye, the used hole transport material and its performance in DSCs.

DSCs were divided into two types: liquid-state (L-DSCs) and solid-state dye-sensitized solar cells (S-DSCs). The former type comprises high volatile or less volatile electrolytes mainly on the basis of acetonitrile/valeronitrile or 3-methoxypropionitrile, respectively. These electrolytes act as hole transport materials and achieve higher power conversion efficiencies, because thicker sensitized mesoporous layers (providing a higher optical density) can be entirely filled with electrolytes and the recombination rate is lower. Nevertheless, long-term stability suffers from leakage and evaporation of the solvent as well as the corrosive nature of the redox shuttle iodine/iodide. To overcome these issues, solid hole transport materials were employed. The concept of SDSCs can increase the stability, but causes problems regarding pore-filling and recombination which compels the reduction of the thickness of the mesoporous layer and thus the optical density of the device. Therefore, the summarized efficiencies of L-DSCs and S-DSCs have to be considered independently.

The intension of this review is to identify design concepts and highlight requirements and critical issues in order to understand the basic guidelines influencing the performance of DSCs. One design strategy is, for example, the use of donor-antenna ligands for Ru(II) complexes as described in chapter 5. Here, the absorption could be efficiently increased by donor-antenna groups. This improves both the light harvesting and the efficiency. A strategy to increase the performance of organic sensitizers, which in general provide higher extinction coefficient, is based on a donor- π bridge-acceptor structure. This structure is supposed to cause an inherent directionality enabling intramolecular charge transfer from the donor moiety to the acceptor group which is responsible for electron injection. This design strategy reduces charge recombination due to a large distance between electrons and holes.

The light harvesting and photon management have to be entirely understood to develop new sensitizers and concepts capable of delivering high power conversion efficiencies.

4 INDIVIDUAL CONTRIBUTIONS TO JOINT PUBLICATIONS

This thesis incorporates six individual manuscripts. Two are published, one is submitted, two are prepared for submission and another one is published as book chapter and appears as appendix. In the following, the individual contributions of the authors to the manuscripts are specified.

Chapter 5

This work is published in *Journal of Materials Chemistry* (2009, 19, 5364-5376) under the title:

“Synthesis, spectral, electrochemical and photovoltaic properties of novel heteroleptic polypyridyl ruthenium(II) donor-antenna dyes”

by Katja Willinger, Katja Fischer, Roman Kisselev and Mukundan Thelakkat

I investigated the spectral properties, performed electrochemical studies on the materials, prepared the solid-state dye-sensitized solar cells and wrote the manuscript.

Katja Fischer and Roman Kisselev were involved in the synthesis of the ruthenium dyes.

Mukundan Thelakkat supervised the project and corrected the manuscript.

Chapter 6

This work is published in *Physical Chemistry Chemical Physics* (2011, 13, 12906–12911) under the title:

“Multichromophore light harvesting in hybrid solar cells”

by Jayasundera Bandara, Katja Willinger and Mukundan Thelakkat

I synthesised the sensitizers, performed the spectral characterisation in solution, was involved in the scientific discussion of the project and corrected the manuscript.

Jayasundera Bandara prepared the solar cells and wrote the first draft of the manuscript.

Mukundan Thelakkat supervised the project and corrected the manuscript.

Chapter 7

This work is submitted to *Energy & Environmental Science* under the title:

“Efficient panchromatic co-sensitization for solid-state dye-sensitized solar cells using triphenyldiamine and squaraine sensitizers”

by Katja Gräf, Moochikkadavath A. Rahim, Suresh Das and Mukundan Thelakkat

I synthesised and characterised the triphenyldiamine-based sensitizer (TPD-dye), investigated the aggregation behaviour by steady-state UV/vis spectroscopy, prepared and optimized the solar cells and wrote the manuscript.

Moochikkadavath A. Rahim performed the synthesis of the squaraine sensitizer, was involved in experiments on the aggregation behaviour and the preparation of solar cells as part of an exchange programme under EU-India project.

Suresh Das was involved in the scientific discussions on the project and corrected the manuscript.

Mukundan Thelakkat supervised the project and corrected the manuscript.

Chapter 8

This work is prepared for submission under the title:

“Synthesis and properties of panchromatic BODIPYs with donor-antenna groups: A new synthetic route towards *meso*-ethynylphenyl BODIPYs”

by Katja Gräf, Thomas Körzdörfer, Stephan Kümmel and Mukundan Thelakkat

I designed and synthesised the materials, did the structural, spectral and electrochemical characterisation, studied the mechanism of the donor-attachment and wrote the manuscript.

Thomas Körzdörfer performed the molecular orbital calculations.

Stephan Kümmel was involved in the scientific discussions on the project.

Mukundan Thelakkat supervised the project and corrected the manuscript.

Chapter 9

This work is prepared for submission under the title:

“Energy transfer in solid-state dye-sensitized solar cells: Combining BODIPYs and triphenylamine energy donor dyes”

by Katja Gräf, Nils Bösch, Jürgen Köhler and Mukundan Thelakkat

I synthesised the materials, did the optical and electrochemical characterisation, performed fluorescence quenching experiments in solution, prepared the solar cells and wrote the manuscript.

Nils Bösch performed time-resolved fluorescence quenching experiments in the solid state.

Jürgen Köhler supervised the work of Nils Bösch.

Mukundan Thelakkat supervised the project and corrected the manuscript.

Chapter 10 (Appendix)

This work is published as review in the book “Photosensitizers in medicine, environment, and security” (*Springer* **2012**, chapter 11 pp. 527-617, print ISBN 978-90-481-3870-8, online ISBN 978-90-481-3872-2, doi: 10.1007/978-90-481-3872-2) under the title:

“Photosensitizers in solar energy conversion”

by Katja Willinger and Mukundan Thelakkat

I did the literature research, data compilation and wrote the manuscript.

Mukundan Thelakkat corrected the manuscript.

Chapter 5

SYNTHESIS, SPECTRAL, ELECTROCHEMICAL AND PHOTOVOLTAIC PROPERTIES OF NOVEL HETEROLEPTIC POLYPYRIDYL RUTHENIUM(II) DONOR-ANTENNA DYES

*Katja Willinger, Katja Fischer, Roman Kisselev and Mukundan Thelakkat**

Department of Macromolecular Chemistry I, Applied Functional Polymers, Universität Bayreuth,
Universitätsstr. 30, 95440 Bayreuth, Germany.

Fax: +49 921 55 3206

E-mail: Mukundan.Thelakkat@uni-bayreuth.de

Published in *Journal of Materials Chemistry* **2009**, 19, 5364-5376.

Reproduced by permission of the Royal Society of Chemistry

ABSTRACT

A series of new heteroleptic Ru(II)(4,4'-dicarboxylic acid-2,2'-bipyridine)(bipyridyl donor-antenna ligand)(NCS)₂ complexes carrying different donor-antenna moieties was designed, synthesised and characterised. A general synthetic procedure was used for the covalent attachment of the donor-antenna units 1,3-di(2-thienyl)benzo[c]-thiophene (DTBT), trans-stilbene (tS) and 4-{2-[2-(2-methoxyethoxy)ethoxy]-ethoxy}-N,N-diphenylbenzenamine (TPA-EO) to 2,2'-bipyridine: First, a Vilsmeier-Haack reaction was applied to get the respective aldehyde-functionalised donor-antenna compounds which secondly reacted with 4,4'-bis(triphenylphosphonium-methyl)-2,2'-bipyridyl chloride under Wittig conditions to give the desired bipyridyl donor-antenna molecules. To create a dimethylamino (NMe₂) substituted donor-antenna compound a reaction between 4,4'-dimethyl-2,2'-bipyridine and the Brederick's reagent was carried out. The final Ru(II) complexes referred to as Ru-DTBT-NCS, Ru-tS-NCS, Ru-TPA-EO-NCS and Ru-NMe₂-NCS were obtained via one-pot reactions, starting from dichloro(p-cymene)ruthenium(II) dimer. The bipyridyl donor-antenna molecules as well as the complexes have been fully characterised and their optical and electrochemical properties were studied in detail. Preliminary tests of the novel Ru(II)bis(bipyridyl)(NCS)₂ dyes in solid-state dye-sensitized solar cells under AM 1.5 G conditions (100 mW cm⁻²) yielded short-circuit current densities of 1.06, 2.15, 3.42 and 4.03 mA cm⁻², open-circuit voltages of 625, 635, 685 and 735 mV and fill factors of about 45 % corresponding to overall efficiencies of 0.31, 0.58, 0.99 and 1.37 % for Ru-DTBT-NCS, Ru-NMe₂-NCS, Ru-tS-NCS and Ru-TPA-EO-NCS, respectively.

Keywords: solid-state dye-sensitized solar cell • Ru(II) complexes • donor-antenna dyes.

INTRODUCTION

Dye-sensitized solar cells (DSCs) have attracted considerable research interest because of their ability to convert sunlight into electrical energy at low costs and easy fabrication. Since the first report about DSCs¹, using the large band gap material TiO₂ as n-type semiconductor, a trimeric ruthenium complex as light absorber and a liquid redox electrolyte as hole transport material, extensive efforts towards highly optimised systems have been done to achieve record efficiencies above 10 %.^{2,3} The most serious drawbacks of such cells are inefficient sealing and leakage problems. Therefore solid hole-transport materials have been introduced to overcome the characteristic disadvantages. For that purpose, Grätzel *et al.*⁴ used an amorphous organic hole-transporter comprising of doped 2,2',7,7'-tetrakis-(*N,N*-di-4-methoxyphenyl amino)-9,9'-spiro-bifluorene (spiro-OMeTAD) which is almost a reference material due to its suitable redox potentials, respectable charge carrier mobility, high solubility and its ability to penetrate the pores of mesoporous TiO₂.⁵ However, the power conversion efficiencies of solid-state dye-sensitized solar cells (SDSCs) are still lower compared to liquid DSCs. Despite significant developments, fast charge recombination rates as well as insufficient light absorption are still considered to be the most limiting factors for the overall efficiencies of SDSCs. One approach to minimise these drawbacks is the well investigated concept of highly absorbing heteroleptic ruthenium(II)bis(bipyridyl)(NCS)₂ dyes carrying donor-antenna groups.⁶⁻⁸ In accordance with the donor-antenna dye concept and general considerations concerning the SDSC technology, efficient dyes for SDSC applications have to fulfil some key requirements: (a) They have to carry anchor groups (*e.g.* carboxylate or phosphonate units) to guarantee intimate contact with the semiconductor surface by chemisorption. (b) They must exhibit excellent light harvesting properties. This includes a broad absorption range as well as high extinction coefficients. Thus, thinner SDSCs can be produced in which transport losses are reduced. This is the main advantage of the donor-antenna dye concept in which bipyridyl donor-antenna ligands with extended conjugated π -systems provide high optical extinction coefficients. (c) Moreover, the LUMO level of an ideal sensitizer has to be sufficiently high enough to provide the opportunity of charge injection into the conduction band of the respective semiconductor and the HOMO level has to be sufficiently low enough to enable efficient regeneration of the oxidised dye by the hole conductor. (d) The electron injection into the conduction band of the semiconductor has to be rapid in comparison to the decay of the excited states of the dye. (e) Additionally, a polarity match between the donor-antenna groups and the hole conductor is desirable to improve the wetting of dye-coated titanium dioxide with the hole transporting material spiro-OMeTAD.

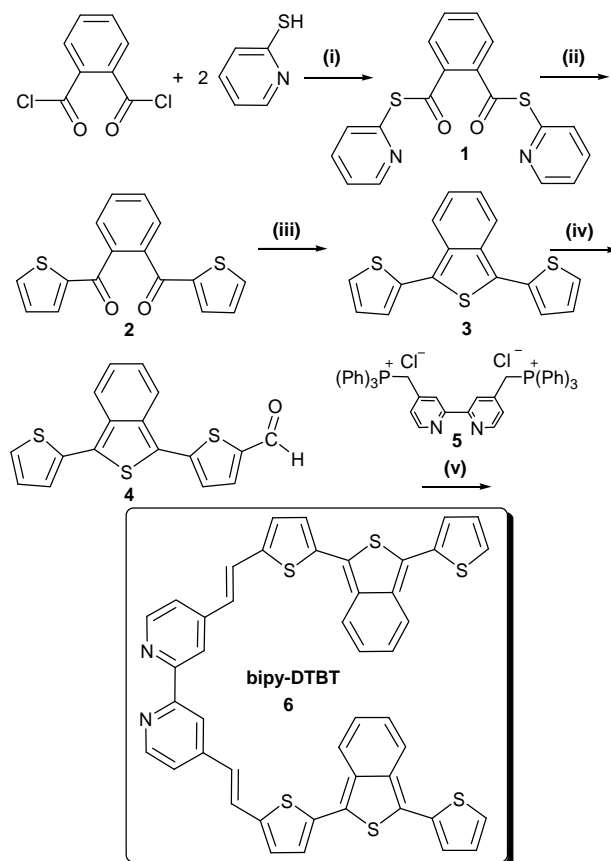
RESULTS AND DISCUSSION

In order to achieve these goals and to gain more insight into the properties of heteroleptic polypyridyl ruthenium(II) donor-antenna complexes, we synthesised a series of Ru(II)bis(bipyridyl)(NCS)₂ dyes carrying different donor-antenna moieties. The details of synthesis, spectral properties, electrochemical behaviour and preliminary results of the performance of these dyes in solid-state dye-sensitized solar cells are given in the following sections.

Synthesis of donor-antenna functionalised 2,2'-bipyridines. Our general synthetic strategy towards bipyridyl donor-antenna compounds was partly based on multi-step procedures. The target molecules **6**, **7**, **12** and bipy-TPA were obtained *via* Wittig reactions allowing the attachment of the donor-antenna moiety to the 2,2'-bipyridine core *via* a conjugated vinylene spacer. For that purpose, the particular aldehyde-functionalised donor-antenna unit was reacted with 4,4'-bis(triphenylphosphonium-methyl)-2,2'-bipyridyl chloride **5**. The triphenylphosphonium salt was prepared in accordance with published procedures starting from 4,4'-dimethyl-2,2'-bipyridine.^{6,9} Furthermore, the attachment of a dimethylamino donor unit to 2,2'-bipyridine *via* a conjugated vinyl spacer yielding the bipyridyl donor antenna compound **13** was achieved using the Brederick's reagent. The *trans*-configuration of every vinylene spacer guarantees that the donor-antenna ligands of the Ru(II) complexes used in SDSCs directly project away from the titanium dioxide surface towards the hole-transport material. Subsequent to the synthesis of the bipyridyl donor-antenna molecules, one-pot reactions were performed to yield three novel Ru(II) complexes *via* a conventional synthesis and two dyes *via* a microwave-assisted procedure.

The synthetic route for the preparation of the bipyridyl donor-antenna compound bipy-DTBT **6** is shown in Scheme 1. First, 1,2-di[*S*-(2-pyridinyl)]benzenedithioate **1**, was prepared *via* a trivial esterification of phthaloyl chloride with 2-mercapto-pyridine under the influence of triethylamine.¹⁰ A Grignard reaction of dithioester **1** and thiophen-2-yl-magnesium bromide yielded the diketone 1,2-di(2-thienoyl)benzene **2** in nearly quantitative yields.¹⁰ The subsequent ring closure yielded 1,3-di(2-thienyl)-benzo[*c*]-thiophene **3**. This reaction was carried out in the presence of the Lawesson's reagent which was used as a mild thionation agent.^{10,11} Subsequently, the formylation of **3** was done *via* a conventional Vilsmeier-Haack reaction, to yield the mono-

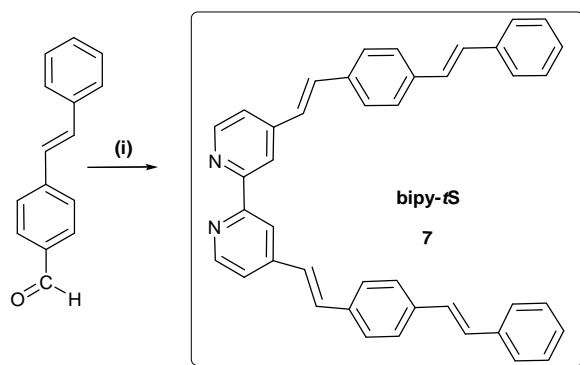
aldehyde 5-(3-thiophen-2-yl-benzo[c]thiophen-1-yl)thiophene-2-carbaldehyde **4**.^{12,13} Finally, the monoaldehyde **4** and the triphenylphosphonium salt **5** were reacted under Wittig conditions to yield 4,4'-bis[2-[5-(3-thiophen-2-yl-benzo[c]-thiophen-1-yl)thiophen-2-yl]vinyl]-2,2'-bipyridine **6**.



Scheme 1. Synthetic route for the preparation of donor-antenna compound **6**. (i) Esterification: Et_3N , THF, 0 °C, 1 min (quenched by HCl); (ii) Grignard reaction: thiophen-2-yl-magnesium bromide, THF, 0 °C, 30 min; (iii) Ring closure: Lawesson's reagent, CH_2Cl_2 , reflux, 30 min, ethanol, reflux, 30 min; (iv) Vilsmeier-Haack formylation: 1. POCl_3 , DMF, CH_2Cl_2 , 0 °C \rightarrow RT, 10 h, 2. $\text{NaOH}/\text{H}_2\text{O}$, steam bath, 1 h; (v) Wittig reaction: 1. NaH, THF, RT, 5 d, 2. glacial acetic acid/ H_2O , RT, 1 h.

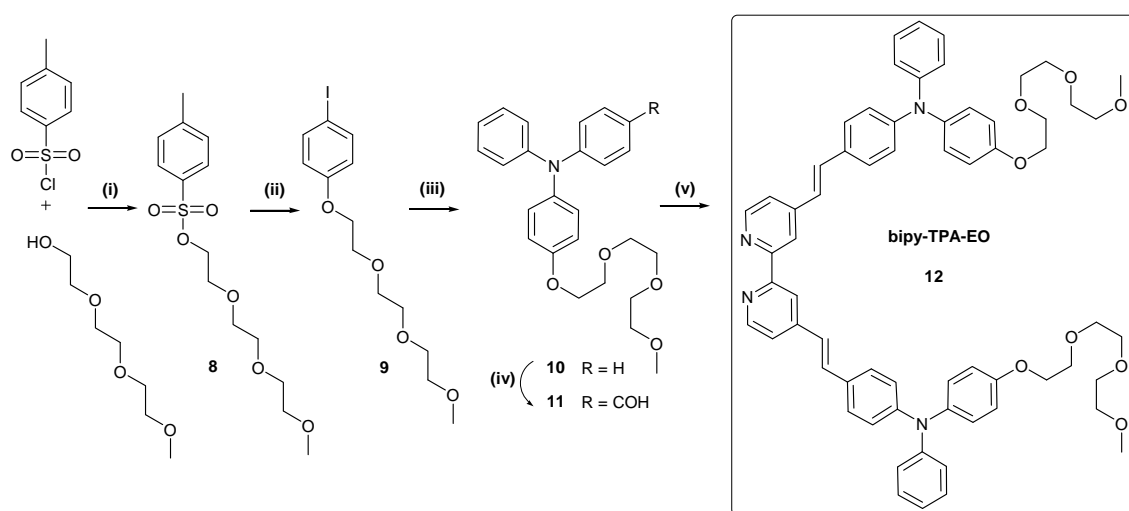
The synthesis of the bipyridyl donor-antenna molecule 4,4'-bis[4-(*p*-phenylvinyl)styryl]-2,2'-bipyridine **7** denoted as bipy-*t*S was performed according to Scheme 2 by coupling commercially available *trans*-stilbene-4-carbaldehyde with **5** via a Wittig reaction.

The reaction was carried out at room temperature in dry THF, using NaH as base, yielding the desired product together with traces of the monosubstituted derivative. The monosubstituted by-product was removed by boiling the raw product in methanol and cyclohexane, exploiting the difference in solubility of the two compounds.



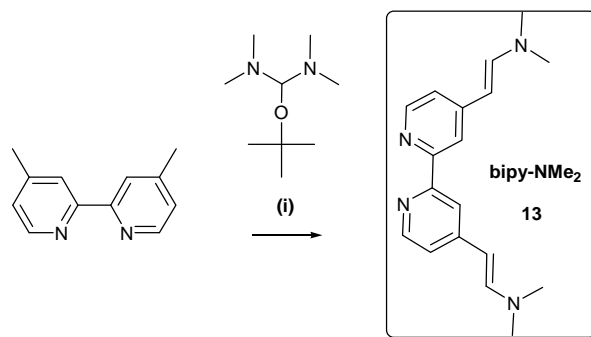
Scheme 2. Synthetic route for the preparation of donor-antenna molecule **7**. (i) Wittig reaction: 1. **5**, NaH, THF, RT, 4 d, 50 °C, 24 h, 2. acetic acid/H₂O, 5 °C, 1 h.

The donor-antenna molecule 4,4'-bis[4-*N*-{4-[2-[2-(2-methoxyethoxy)ethoxy]ethoxy}phenyl)-*N*-phenylamino-styryl]-2,2'-bipyridine **12** denoted as bipy-TPA-EO was synthesised as shown in Scheme 3. First, an esterification between triethylene glycol monomethyl ether and *p*-toluenesulfonyl chloride was performed in the presence of pyridine. Latter neutralised the accruing HCl to facilitate the nucleophilic attack of the alcohol which resulted in the formation of {2-[2-(2-methoxy)ethoxy]ethyl}-4-methyl-benzenesulfonate **8**. To use a tosylate as intermediate allows the substitution of the hydroxyl group of triethylene glycol monomethyl ether by almost every nucleophile. Therefore, the reaction of 4-iodophenol with **8** resulted in the formation of 1-{2-[2-(2-methoxyethoxy)ethoxy]ethoxy}-4-iodobenzene **9**. The subsequent synthetic step comprised of an Ullmann reaction^{14,15} between **9**, copper powder, potassium carbonate and 18-crown-6 in 1,2-dichlorobenzene at elevated temperature. This copper mediated nucleophilic substitution is a conventional method for the preparation of triaryl amines under the influence of a phase-transfer catalyst. Typically, a series of by-products is generated during the reaction. For that reason, an excess of the aryl iodide **9** was employed to synthesise 1-{2-[2-(2-methoxyethoxy)ethoxy]ethoxy}-4-(*N,N*-diphenylamino)benzene **10**. Afterwards, **10** was converted into the respective monoaldehyde 4-*N*-{4-[2-[2-(2-methoxy-ethoxy)ethoxy]ethoxy}phenyl)-*N*-phenylamino}benzaldehyde **11** via a Vilsmeier-Haack formylation. Subsequently, a Wittig reaction was accomplished to yield the donor-antenna molecule bipy-TPA-EO **12**.



Scheme 3. Synthesis of donor-antenna compound **12**: (i) Esterification: pyridine, 0 °C, 2-3 h; (ii) nucleophilic substitution: 4-iodophenol, K_2CO_3 , MEK, reflux, 4 h; (iii) Ullmann reaction: Cu-powder, K_2CO_3 , 18-crown-6, diphenylamine, o-dichlorobenzene, 120 °C, 1 h, 180 °C, 36 h; (iv) Vilsmeier-Haack reaction: 1. $POCl_3$, DMF, 0-5 °C, 30 min, 2. **10** + 1., CH_2Cl_2 , 0-5 °C, 15 min, 80-85 °C, 2.5 h 3. NaOAc/ H_2O , RT, overnight; (v) Wittig reaction: 1. **5**, KOtBu, THF, RT, 18 h, 2. acetic acid/ H_2O , RT, 30 min.

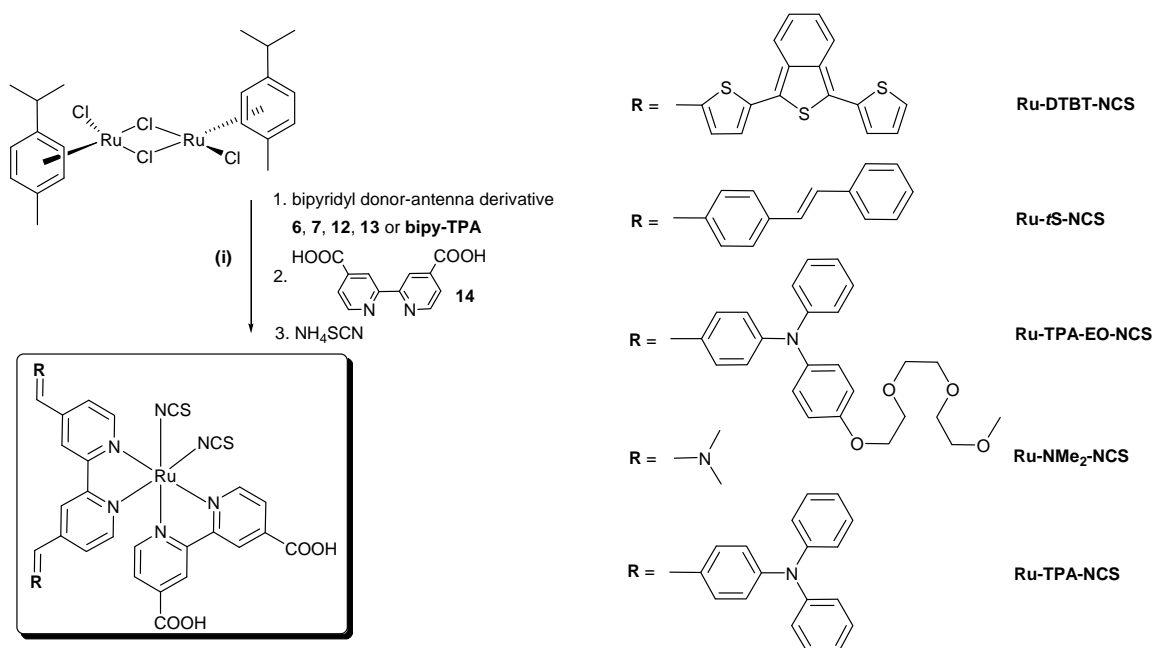
The donor-antenna compound 4,4'-bis[(*N,N'*-dimethyl-aminovinyl)-2,2'-bipyridine] **13**, denoted as bipy-NMe₂ was synthesised according to Bozec *et al.* using a one-pot reaction.¹⁶ This enamination between 4,4'-dimethyl-2,2'-bipyridine and *tert*-butoxy bis(diethylamino)methane, known as Bredereck's reagent, is shown in Scheme 4. The mechanism of the enamination in a polar solvents is discussed in detail by Wahl *et al.*¹⁷ The desired product **13** was formed after dissociation of the Bredereck's reagent followed by deprotonation of the educt 4,4'-dimethyl-2,2'-bipyridine and a β -H elimination. This results in the vinylic spacer with *trans*-configuration between the 2,2'-bipyridine core and the donor-antenna group -NMe₂.



Scheme 4. Synthesis of donor-antenna compound **13**. (i) Enamination: Bredereck's reagent, DMF, 140 °C, 22 h.

Additionally, the reference donor-antenna compound 4,4'-bis[4-(diphenylamino)styryl]-2,2'-bipyridine denoted as bipy-TPA was synthesised according to a published procedure.^{6,9,18}

Synthesis of donor-antenna dyes. As shown in Scheme 5, all bipyridyl donor-antenna derivatives (**6**, **7**, **12**, **13** and bipy-TPA) were converted into the desired complexes by using dichloro(*p*-cymene)ruthenium(II) dimer as reagent for the metallation reaction. This particular Ru(II) precursor provides the opportunity to obtain the desired heteroleptic octahedral ruthenium(II)bis(bipyridyl)(NCS)₂ complexes *via* an efficient one-pot synthesis by subsequent addition of the prospective ligands (**6**, **7**, **12**, **13** or bipy-TPA followed by the anchoring molecule **14**¹⁹ and finally adding an excess of NH₄SCN).²⁰



Scheme 5. One-pot synthesis and molecular structures of the donor-antenna ruthenium(II) sensitizers Ru-DTBT-NCS, Ru-tS-NCS, Ru-TPA-EO-NCS, Ru-NMe₂-NCS and Ru-TPA-NCS. (i) Complex formation reaction: I. Conventional method to synthesise Ru-DTBT-NCS, Ru-tS-NCS and Ru-TPA-EO-NCS: 1. bipyridyl donor-antenna derivative **6**, **7** or **12**, DMF, 100 °C, 4 h; 2. **14**, DMF, 150 °C, 5 h; 3. NH₄SCN, DMF, 150 °C, 4-5 h. II. Microwave assisted method to synthesise Ru-NMe₂-NCS and Ru-TPA-NCS: 1. bipyridyl donor-antenna derivative **13** or bipy-TPA, DMF, μ w, 70 °C, 20-25 min; 2. **14**, DMF, μ w, 135-150 °C, 20 min; 3. NH₄SCN, DMF, μ w 135-150 °C, 30-40 min.

The metallation reaction to assemble the heteroleptic octahedral cis-di(isothiocyanato)(2,2'-dicarboxylic acid-2,2'-bipyridyl)(bipyridyl donor-antenna ligand)ruthenium(II) dyes was

accomplished by different reaction conditions. The general procedure for the conventional preparation of Ru-DTBT-NCS, Ru-*t*S-NCS, Ru-TPA-EO-NCS started with dissolving dichloro(*p*-cymene)ruthenium(II) dimer in dry DMF, followed by adding the particular bipyridyl donor-antenna compound (**6**, **7** or **12**) and heating by a conventional external heat source. In this step, the coordination of the donor-antenna compound to the ruthenium center proceeded *via* cleavage of the chlorine double-bridged structure of the Ru(II)dimer to yield a mononuclear complex.²¹ After full consumption of the donor-antenna compound in 4 h, the anchoring compound of the prospective dye 4,4'-dicarboxylic acid-2,2'-bipyridine **14** was added to the reaction mixture and the reaction was continued for 5 h under reflux. Finally, an excess of NH₄NCS was added to be coordinated to the Ru(II) center atom in 4-5 h under reflux. The reaction was terminated by cooling the solution to room temperature and vacuum distillation of the solvent to obtain the respective raw product. Ru-DTBT-NCS was purified by reprecipitation. Ru-*t*S-NCS was isolated by precipitation from THF into diethyl ether. Ru-TPA-EO-NCS could be obtained as pure product after washing with water and diethyl ether. The novel heteroleptic Ru(II) complexes were obtained as violet or black powders.

This time-consuming synthetic procedure could be remarkably improved by using a microwave assisted method. This method was applied to obtain the novel complex Ru-NMe₂-NCS and the reference donor-antenna dye Ru-TPA-NCS which was synthesised here for the first time in a microwave oven. Thus, the metallation procedure was only modified with respect to the heat source and the time. The ruthenium(II) precursor, the steps of subsequent addition of ligands and the solvent were not changed. The use of microwave equipment implicates the advantage of a more efficient heating by direct transfer of the irradiated energy on the reaction mixture as a consequence of dielectric heating. This phenomenon is based on the ability of the molecules to absorb microwaves and transfer this energy directly into heat resulting in an extremely fast heating of all compounds in the reaction solution. For this reason, the microwave assisted heating is more efficient, leads to less wall effects and side reactions than the conventional heating in an oil bath where heat transfer depends on thermal conductivity.^{22,23} The positive influence of the microwave assisted method for preparing polypyridyl ruthenium(II) complexes can be directly seen by the remarkable acceleration of the reactions and the nearly quantitative yields for Ru-NMe₂-NCS and Ru-TPA-NCS. All dyes were characterised by FT-IR, UV-vis and cyclic voltammetry (CV).

Spectral properties. Fourier transform infrared (FT-IR) spectra of all complexes were measured after embedding the substance into potassium bromide pellets. The prominent bands are summarised in Table 1. All FT-IR spectra show the characteristic signal of the NCS-unit which is visible as an intense band at $\sim 2100\text{ cm}^{-1}$. This can be attributed to the N-coordinated isothiocyanate group proving the successful coordination of the NCS moiety to the ruthenium(II) center atom. The bands appearing at $\sim 1240\text{ cm}^{-1}$ can be assigned to the $\nu(\text{C-O})$ stretching of carboxylic acid groups. Furthermore, the presence of COOH-groups can be proven by the appearance of a $\nu(\text{C=O})$ stretching band present in the FT-IR spectrum of each complex between 1711 and 1722 cm^{-1} . Additionally, the typically broad band at about 3440 cm^{-1} indicates the existence of OH-groups. Beside these signals, the FT-IR spectrum of Ru-NMe₂-NCS shows prominent bands at 1479 and 1367 cm^{-1} , arising from asymmetric and symmetric bending vibrations of CH₃-N-moieties. The medium absorption peak at 1109 cm^{-1} in the FT-IR spectrum of Ru-TPA-EO-NCS indicates the existence of ethylene oxide moieties and the broadness of the band indicates the disorder of the side chains. Moreover, a weak but broad peak at 2879 cm^{-1} appears arising from the aliphatic CH-groups of the ethylene oxide groups.

Table 1. Prominent absorption bands appearing in the FT-IR spectra of Ru-DTBT-NCS, Ru-NMe₂-NCS, Ru-tS-NCS, Ru-TPA-NCS and Ru-TPA-EO-NCS indicating the existence of N-coordinated isothiocyanate groups and the presence of COOH anchor groups.

Dye	$\nu(\text{C=N})$ [cm ⁻¹]	$\nu(\text{C-O})$ [cm ⁻¹]	$\nu(\text{C=O})$ [cm ⁻¹]	$\nu(\text{OH})$ [cm ⁻¹]
Ru-DTBT-NCS	2098	1227	1711	3446
Ru-NMe ₂ -NCS	2099	1232	1722	3428
Ru-tS-NCS	2098	1231	1712	3443
Ru-TPA-NCS	2103	1254	1719	3440
Ru-TPA-EO-NCS	2103	1241	1718	3448

FT-IR-spectra were recorded after embedding the solid substances into potassium bromide pellets.

Figure 1 shows the ultraviolet-visible (UV-vis) spectra of all complexes and the standard dye N719 in solution. It is obvious that the polypyridyl complexes, including N719, show very broad and intense absorption bands throughout almost the whole absorption region extended up to the near UV range. All donor-antenna Ru(II)bis(bipyridyl)(NCS)₂ dyes exhibit higher extinction coefficients compared to the standard dye N719 over the whole investigated region. This can be

understood by the influence of the different delocalised π -systems integrated in the bipyridyl donor-antenna ligands. Furthermore, all dyes (including N719) show three characteristic absorption maxima caused by ligand-centred (LC) electronic transitions and/or metal-to-ligand-charge-transfer (MLCT) transitions.

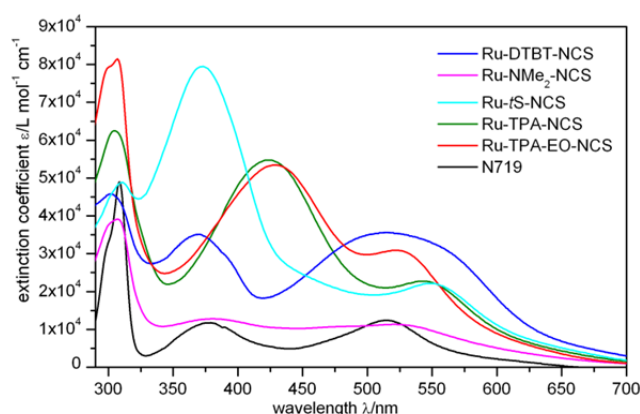


Figure 1. UV-vis spectra of Ru-DTBT-NCS (in DMF, blue), Ru-NMe₂-NCS (in dioxan/H₂O/DMF 1:1:1 + 1 wt% KOH, magenta), Ru-tS-NCS (in DMF, cyan), Ru-TPA-NCS (in MeOH + 1 wt% KOH, green), Ru-TPA-EO-NCS (in MeOH + 1 wt% KOH, red) and N719 (in MeOH + 1 wt% KOH, black).

The high energy bands in the UV region between 301 and 310 nm (Table 2, $\lambda_{\text{max}1}$) can be attributed to LC transitions arising from 4,4'-dicarboxylic acid-2,2'-bipyridine and the particular donor-antenna ligand, respectively. The second absorption band series with wavelength maxima between 369 and 429 nm (Table 2, $\lambda_{\text{max}2}$) can be assigned to two different influences. First, this absorption band results partly from LC π - π^* transitions because the single bipyridyl donor-antenna compounds used for metallation absorb in almost the same region (λ_{max} at 358, 355, 363, 398 and 395 nm for bipy-DTBT, bipy-NMe₂, bipy-tS, bipy-TPA and bipy-TPA-EO, respectively). The bathochromic shift of 11 to 34 nm of this second dye absorption band compared to the absorption band of the single bipyridyl donor-antenna compounds can be seen as a consequence of the coordination of the bipyridyl donor-antenna derivative to the ruthenium core. The second factor affecting the absorption bands with maxima between 369 and 429 nm is caused by one spin allowed d- π^* MLCT transitions. All dyes, except Ru-NMe₂-NCS, show extraordinary high extinction coefficients (Table 2, $\epsilon_{\text{max}2}$) for this absorption band depending on the nature of the donor-antenna moiety and its conjugated π -system. The reason for the low absorption of the standard dye N719 in this region is the absence of any donor-antenna groups; thus its absorption is just governed by the d- π^* MLCT transitions. The characteristic low energy absorption band of Ru(II)bis(bipyridyl)(NCS)₂ dyes with absorption

maxima between 515 and 550 nm (Table 2, $\lambda_{\max 3}$) is a direct consequence of the coordination of the NCS moiety to the ruthenium(II) center. Investigations of Ru(II)tris-(bipyridyl)s showed that in the absence of this functional group no low energy MLCT transition appeared under standard conditions because this transition is spin-forbidden for tris(bipyridyl) dyes.^{6,18,24} Regarding Ru-DTBT-NCS, the low energy band is exceptionally broad and intensive ($\epsilon = 35\,600\text{ L mol}^{-1}\text{ cm}^{-1}$ at 515 nm). The reason for this behaviour is based on an additional absorption contribution of the bipy-DTBT ligand **6** to this MLCT band. In contrast to all other donor-antenna ligands, this ligand shows a strongly bathochromic shifted low-energy absorption band with a wavelength maximum of 486 nm. As a consequence of this, the absorption band of Ru-DTBT-NCS at $\lambda_{\max} = 515\text{ nm}$ can be seen as an overlap of ligand-centred $\pi\text{-}\pi^*$ transitions occurring in bipy-DTBT **6** and the characteristic ruthenium-to-NCS MLCT transition. Both factors enhance and enlarge the low-energy absorption band.

Table 2. Molar extinction coefficients (ϵ) at the respective absorption maxima (λ_{\max}) calculated according to Beer-Lambert law for Ru-DTBT-NCS, Ru-NMe₂-NCS, Ru-*t*S-NCS, Ru-TPA-NCS, Ru-TPA-EO-NCS and N719, respectively in solution.

Dye	$\lambda_{\max 1}$ [nm]	$\epsilon_{\max 1}$ [L mol ⁻¹ cm ⁻¹]	$\lambda_{\max 2}$ [nm]	$\epsilon_{\max 2}$ [L mol ⁻¹ cm ⁻¹]	$\lambda_{\max 3}$ [nm]	$\epsilon_{\max 1}$ [L mol ⁻¹ cm ⁻¹]
Ru-DTBT-NCS ^{a)}	301	45 765	369	35 100	515	35 600
Ru-NMe ₂ -NCS ^{b)}	307	38 801	381	12 786	526	11 265
Ru- <i>t</i> S-NCS ^{a)}	310	48 561	373	79 485	550	22 150
Ru-TPA-NCS ^{c)}	304	62 462	423	54 700	544	22 700
Ru-TPA-EO-NCS ^{c)}	307	81 322	429	53 446	524	30 861
N719 ^{c)}	309	48 798	377	11 700	515	12 400

The dyes were dissolved in ^{a)} DMF, ^{b)} dioxane/H₂O/DMF 1:1:1 + 1 wt% KOH and ^{c)} MeOH + 1 wt% KOH.

Electrochemical investigations. The electrochemical properties of the bipyridyl donor-antenna compounds (**6**, **7**, **12**, **13** and bipy-TPA), the Ru(II) complexes (Ru-DTBT-NCS, Ru-NMe₂-NCS, Ru-*t*S-NCS, Ru-TPA-NCS and Ru-TPA-EO-NCS) and the standard dye N719 were studied by cyclic voltammetry (CV) in solution. Tetrabutylammonium hexafluorophosphate (Bu₄NPF₆, 0.1 M) was used as conducting salt, a glassy carbon disk electrode as working electrode and Ag/AgNO₃ as reference electrode. Each measurement was calibrated by the internal standard ferrocene (Fc^{0/+} (CH₂Cl₂) = 0.08 V, Fc^{0/+} (DMF) = 0.04 V, Fc^{0/+} (DMSO) = 0.04 V). The HOMO and LUMO levels were

calculated relative to the value of -4.8 eV for ferrocene with respect to the vacuum level. All measured values are summarised in Table 3.

Table 3. Summary of the electrochemical properties of all bipyridyl donor-antenna compounds and the respective complexes in comparison to N719.

donor-antenna compd / dye	E_{ox1} vs. $\text{Fc}^{0/+}$ [V]	HOMO [eV]	E_{ox2} vs. $\text{Fc}^{0/+}$ [V]	HOMO-1 [eV]	E_{red} vs. $\text{Fc}^{0/+}$ [V]	LUMO [eV]
bipy-DTBT ^{a)}	0.32	-5.12	0.51	-5.31	---	---
Ru-DTBT-NCS ^{b)}	0.28	-5.08	0.56	-5.32	-1.64	-3.16
bipy-NMe ₂ ^{a)}	0.36	-5.16	---	---	-2.20	-2.60
Ru-NMe ₂ -NCS ^{c)}	0.37	-5.17	---	---	-1.61	-3.19
bipy-tS ^{c)}	0.76	-5.56	---	---	-2.92	-1.88
Ru-tS-NCS ^{b)}	0.30	-5.10	0.70	-5.50	-1.61	-3.19
bipy-TPA ^{a)}	0.58	-5.38	---	---	---	---
Ru-TPA-NCS ^{b)}	0.32	-5.12	0.50	-5.30	-1.60	-3.20
bipy-TPA-EO ^{a)}	0.37	-5.17	---	---	-2.44	-2.36
Ru-TPA-EO-NCS ^{b)}	0.28	-5.08	0.47	-5.27	-1.67	-3.13
N719 ^{b)}	0.28	-5.08	---	---	-1.65	-3.15

Measured at 50 mV sec⁻¹ in ^{a)} CH₂Cl₂, ^{b)} DMF and ^{c)} DMSO, respectively with 0.1 M tetrabutylammonium hexafluorophosphate using a glassy carbon disk as working electrode and Ag/AgNO₃ as reference.

It is well known from the literature, that the HOMO of Ru(II)bis(bipyridyl)(NCS)₂ complexes without donor-antenna groups like N719 have a large amplitude on the NCS ligands.^{21,25} It is also known that oxidations of octahedral Ru(II) polypyridyl complexes usually involve a metal centred ($\pi_M(t_{2g})$) orbital under formation of the respective Ru(III) complex (low spin, 4 d⁵ configuration).²⁶ N719 showed in our investigation an oxidation potential of 0.28 V vs. Fc in DMF, corresponding to a HOMO level of -5.08 eV. Except Ru-DTBT-NCS and Ru-NMe₂-NCS, which have very similar first oxidation potentials both in Ru(II)-complex and donor-antenna ligand, all other Ru(II)-dyes exhibit first oxidation potentials relevant for Ru^{II/III} oxidation (at ~ 0.3 V vs. ferrocene). This is in agreement with the reported values in the literature.^{21,25} Thus the HOMO distribution for Ru-tS-NCS, Ru-TPA-NCS and Ru-TPA-EO-NCS is delocalised mainly over the ruthenium core and a certain group which is present in all dyes like the NCS ligand. However, in the case of Ru-DTBT-NCS and Ru-NMe₂-NCS, the HOMO can be assumed to be distributed over the ruthenium core and the bipyridyl donor-antenna moiety.

Furthermore, it is obvious that the HOMO-1 values of the dyes Ru-*t*S-NCS, Ru-TPA-NCS and Ru-TPA-EO-NCS agree with the HOMO values of the respective bipyridyl donor-antenna compounds within a maximum discrepancy of ± 0.1 eV (Table 3). This indicates that the second oxidation of the complexes most probably occurs in the bipyridyl donor-antenna compound. Earlier we reported that the first oxidation of the Ru-TPA-NCS complex occurs on the bipyridyl donor-antenna moiety, but based on our detailed electrochemical investigations presented here, it becomes obvious that not the first but the second oxidation takes place on the bipyridyl donor antenna moiety.²⁷

Earlier, it was observed that tris(bipyridyl) dyes carrying donor-antenna groups provide the possibility to reduce the recombination rate in SDSCs at the interface between TiO₂ and the hole conductor.²⁸ The reason for the suppression of recombination by spatial separation of charges in tris(bipyridyl) ruthenium(II) complexes is indeed a consequence of appropriate energy levels in these dyes. According to the literature, the Ru^{II/III} potential of the Ru(II)tris(bipyridine) prototype [Ru(2,2'-bipyridine)₃]²⁺ occurs at 0.85 V vs. Fc²⁶ which means that the oxidation of the bipyridyl donor-antenna compound, *e.g.* bipy-TPA appears at definitely lower potentials (E_{ox1} (bipy-TPA) vs. Fc = 0.58 V). In contrast to that, the Ru^{II/III} oxidation in bis(bipyridyl)(NCS)₂ dyes occurs at much lower potentials around 0.28-0.32 V vs. Fc. The reason for the shift of the Ru^{II/III} oxidation is due to the substitution of one bipyridyl ligand by two NCS ligands. This implies that only very easily oxidisable donor-antenna groups exhibiting oxidation potentials ≤ 0.3 V vs. Fc promote charge cascade transfer and thus increased spatial separation in charge separated state in Ru(II)L₂(NCS)₂ dyes. Since these values are solely based on cyclic voltammetric measurements in solution and appreciable shift of energy levels at interfaces can occur, a real picture of energetics and charge injection at TiO₂ dye interface can be elucidated only by further spectroscopic studies.

Furthermore, it is known that the LUMO amplitude in N719 is homogeneously distributed over the two 4,4'-dicarboxylic acid-2,2'-bipyridine anchoring ligands.^{21,25} The measured LUMO value for N719 was -3.15 eV corresponding to the reduction occurring primarily in the anchoring ligand. The measured LUMO levels of all the dyes lie in the same range (Table 3). Thus, it can be assumed, that the LUMO of these dyes is mainly located on the anchor ligand.

Performance of solid-state dye-sensitized solar cells. The extremely high molar extinction coefficients over an expanded wavelength region makes the complexes Ru-DTBT-NCS, Ru-NMe₂-NCS, Ru-*t*S-NCS, Ru-TPA-NCS and Ru-TPA-EO-NCS promising candidates for use as sensitizers in SDSCs. Therefore, we investigated the performance of these dyes in typical SDSC devices (Figure 2) and report hereby the first preliminary results. For cell preparation, a standard procedure optimised in our group was used. We used partly etched FTO coated glass as transparent conducting electrode covered by a compact TiO₂ film, acting as blocking layer to prevent direct contact between FTO and the hole-transport material.²⁹ The well-connected mesoporous TiO₂ network, exhibiting a huge surface-area for a high dye uptake, was prepared by screen printing and subsequent sintering of a nano-titanium dioxide paste. The respective sensitizers (Ru-DTBT-NCS, Ru-NMe₂-NCS, Ru-*t*S-NCS, Ru-TPA-NCS, Ru-TPA-EO-NCS and N719) were subsequently chemisorbed onto TiO₂. Afterwards, the hole-transport material spiro-OMeTAD and additives such as lithium salt (LiN(SO₂CF₃)₂) and 4-*tert*-butylpyridine were applied by spin coating and gold contacts were deposited under high vacuum.

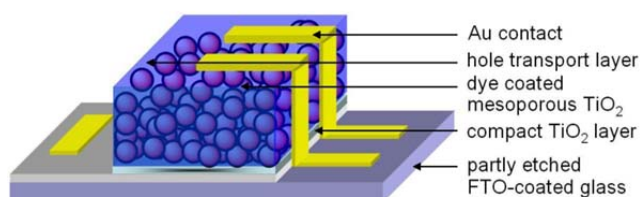


Figure 2. Schematic representation of a typical assembly of a solid-state dye-sensitized solar cell (total thickness: 2.7 μm).

The photovoltaic performance of the complexes Ru-DTBT-NCS, Ru-NMe₂-NCS, Ru-*t*S-NCS, Ru-TPA-NCS, Ru-TPA-EO-NCS and the standard sensitizer N719 chemisorbed on nanocrystalline TiO₂ (thickness: 2.3 μm) was studied under standard AM 1.5 G irradiation (100 mW cm⁻²). Figure 3 shows the results of the current-voltage measurements of the solar cells.

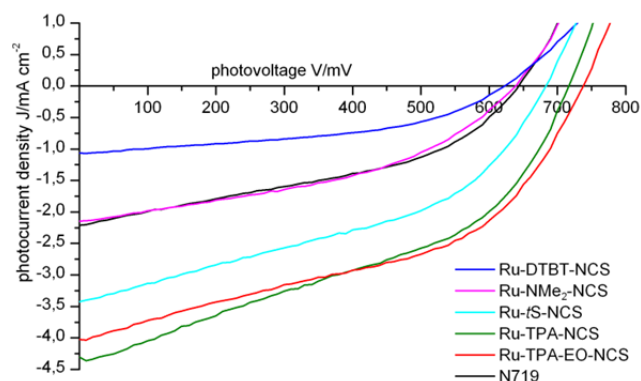


Figure 3. Current-voltage characteristics of SDSCs sensitized with Ru-DTBT-NCS, Ru-NMe₂-NCS, Ru-tS-NCS, Ru-TPA-NCS, Ru-TPA-EO-NCS and N719, respectively under standard AM 1.5 G conditions (100 mW cm⁻²).

The characteristic parameters, obtained from the current-voltage measurements such as photovoltage under open-current conditions (V_{oc}), photocurrent density under short-circuit conditions (J_{sc}), fill factor (FF) and the resulting power conversion efficiency (η) are listed in Table 4. For comparison, a N719 based devices was also prepared and measured under the same conditions. The higher current or efficiency values reported earlier for reference dyes N719 and Ru-TPA-NCS arise from differences in the used samples of nanocrystalline TiO₂ and thickness of active layers.⁶ In the comparative study here, we used a screen-printable TiO₂ paste bought from Dyesol, Australia and we observed large differences between this paste and that supplied by ECN, Netherlands in SDSC performance.

Table 4. Photovoltaic properties of SDSCs sensitized with Ru-DTBT-NCS, Ru-NMe₂-NCS, Ru-tS-NCS, Ru-TPA-NCS and Ru-TPA-EO-NCS in comparison with N719 under AM 1.5 G conditions (100 mW cm⁻²).

Dye	V_{oc} [mV]	J_{sc} [mA cm ⁻²]	FF [%]	η [%]
Ru-DTBT-NCS	625	1.06	46	0.31
Ru-NMe ₂ -NCS	635	2.15	42	0.58
Ru-tS-NCS	685	3.42	42	0.99
Ru-TPA-NCS	715	4.30	43	1.31
Ru-TPA-EO-NCS	735	4.03	46	1.37
N719	645	2.21	41	0.58

The photovoltaic results (Table 4) indicate, that the solar cell performance-especially the short-circuit photocurrent density-strongly depends on the particular secondary donor unit. This is in excellent agreement with the optical properties and the extinction coefficients of the various dyes (Figure 1, Table 2). The photocurrent density increases with increasing size of the conjugated π -system of the donor-antenna functionality (with exception of Ru-DTBT-NCS). By comparing the small-sized donor-antenna functionality $-NMe_2$ without additional conjugated π -system with the *trans*-stilbene unit having an enlarged delocalised system an increase of the photocurrent density from 2.15 to 3.42 mA cm⁻² was observed. By further extension of the π -system like in Ru-TPA-NCS and Ru-TPA-EO-NCS a further increase of the photocurrent density to 4.30 and 4.03 mA cm⁻², respectively was achieved. The optical density of chemisorbed Ru-TPA-EO-NCS is lower than that of Ru-TPA-NCS for the whole range of absorption (*cf.* Figure 4). This explains the slightly decreased photocurrent density of Ru-TPA-EO-NCS compared to Ru-TPA-NCS. This might be a consequence of the increased special demand of Ru-TPA-EO-NCS due to the oligo(ethylene oxide) side chains.

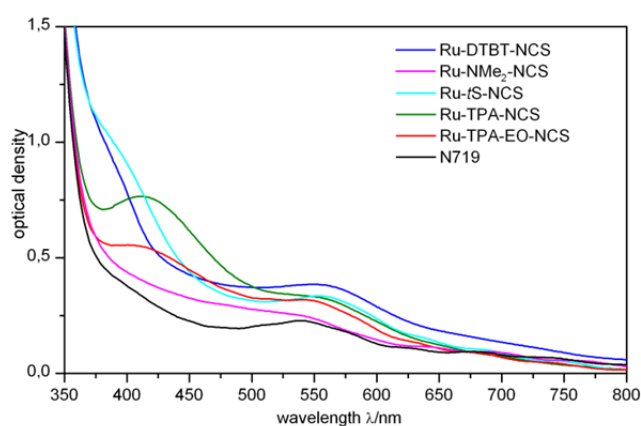


Figure 4. UV-vis spectra of Ru-DTBT-NCS, Ru-NMe₂-NCS, Ru-tS-NCS, Ru-TPA-NCS, Ru-TPA-EO-NCS and N719 adsorbed onto mesoporous TiO₂ (thickness: 2.3 μ m).

Nevertheless, the performance of Ru-DTBT-NCS is exceptional, indicating that the absorption behaviour is only one aspect for a good overall performance. Energetic properties of the dyes absorbed on TiO₂ as well as recombination processes have to be taken into account for a detailed understanding. Investigations in this direction are under way. The photovoltaic performance and absorption on TiO₂ of N719 and Ru-NMe₂-NCS is almost equal because both sensitizers miss the influence of an expanded π -system which enhances the absorption and as a consequence the photocurrent. These results indicate the importance of appropriate donor-

antenna moieties with extended delocalised π -systems. In accordance with this, the best overall results were obtained for the novel Ru-TPA-EO-NCS dye incorporating a highly conjugated delocalised π -system in combination with oligo(ethylene oxide) side chains acting as ion-coordinating functionalities. The positive effect of adding lithium salts in SDSCs to improve both J_{sc} and V_{oc} has been studied earlier.⁶ In order to increase the concentration of lithium ions at the interface, oligo(ethylene oxide) functionalities have been introduced in bipyridyl moieties.³⁰⁻³² These “ion-binding” groups can coordinate the lithium ions and partially block them from reaching the TiO_2 surface. This prevents the lowering of the photovoltage.³⁰ Thus the highest V_{oc} was obtained for Ru-TPA-EO-NCS. Hence, this dye combines two different approaches to enhance the efficiency of SDSCs. (1) The donor-effect of the conjugated π -system of TPA enhances the absorption and thus the photocurrent density. (2) The oligo(ethylene oxide) side chains improve the photovoltage in terms of ion-coordinating sensitizers for use in SDSCs.³⁰⁻³² These preliminary results of the donor-antenna dyes in comparison with the standard sensitizer N719 indicate the potential of the Ru(II)-dyes carrying donor-antenna moieties.

CONCLUSION

We successfully synthesised a series of bipyridyl donor-antenna compounds in multi-step procedures and used them for metallation reactions to obtain heteroleptic donor-antenna Ru(II)bis(bipyridyl)(NCS)₂ complexes *via* one-pot reactions. All complexes, denoted as Ru-DTBT-NCS, Ru-*t*S-NCS, Ru-TPA-EO-NCS, Ru-NMe₂-NCS and Ru-TPA-NCS comprised of a bipyridyl carboxylic acid anchor moiety, two NCS ligands coordinated to the Ru(II) center, and different secondary donor-antenna units covalently attached to the bipyridine core. Our main goal was to increase the molar extinction coefficients of sensitizers for SDSC application by appropriate donor-antenna groups attached to bipyridines *via* a vinylene spacer. This enables the use of thinner solar cells and thus reduces transport losses. Measurements of the spectral properties of all dyes except the less delocalised dye Ru-NMe₂-NCS demonstrated very high extinction coefficients over a broad range of the UV-vis spectra. In addition to that, detailed electrochemical investigations were performed. The oxidations were assigned to the Ru^{II/III} core and the donor-antenna groups. The reduction occurs in the anchor ligand. The obtained values for the frontier orbitals indicated, that the LUMO levels of the novel dyes were high enough for efficient charge injection into the conduction band of TiO₂ and the HOMO levels were low enough for proper regeneration of the oxidised dyes by spiro-OMeTAD. Furthermore, preliminary tests of these complexes as sensitizers in SDSCs were successfully accomplished and showed promising results in not yet optimised systems with potential for further improvement.

EXPERIMENTAL SECTION

Analytical measurements. UV-vis spectra were recorded with a HITACHI U-3000 spectrophotometer. The measurements were carried out in solution using quartz glass cuvettes with 1 cm thickness. Fourier transform infrared (FT-IR) spectroscopy was performed with a Bio-Rad Digilab FTS-40. The measurements were carried out after embedding solid substance into a potassium bromide pellet and liquid between NaCl plates using 32 scans and a resolution of 4 cm^{-1} (transmission mode). Proton nuclear magnetic resonance (^1H -NMR) spectra were obtained using a Bruker Avance AC-250 spectrometer (250 MHz). Mass spectra were recorded on a Finnigan MAT 8500 with a MAT 112 S Varian at an ionisation energy of 70 eV (electron-impact). Cyclic voltammetry (CV) was carried out under moisture- and oxygen-free conditions using a standard three-electrode assembly connected to a potentiostat (model 263A, EG&G Princeton Applied Research) and a PC at a scanning rate of 50 mV sec^{-1} . The working electrode was a glassy carbon disk electrode (area = 0.0314 cm^2), a platinum wire was used as auxiliary electrode and the quasi-reference electrode was Ag/Ag^+ composed of an Ag-wire and AgNO_3 in acetonitrile. Tetrabutylammonium hexafluorophosphate (Bu_4NPF_6 , 0.1 M) was used as conducting salt. Each measurement was calibrated with an internal standard (ferrocene/ferrocenium). The HOMO and LUMO values were determined from the value of -4.8 eV for ferrocene with respect to vacuum level.

Materials for synthesis. Commercial available chemicals were used as received without further purification with the exception of POCl_3 which was freshly distilled before use. Solvents for chromatography, reactions or extractions were purified by distillation. 4,4'-bis(triphenylphosphoniummethyl)-2,2'-bipyridyl chloride **5** was synthesised according to the literature^{6, 9} as well as the anchoring compound 4,4'-dicarboxylic acid-2,2'-bipyridine **14**.¹⁹ The bipyridyl donor-antenna compound 4,4'-bis[4-(diphenylamino)styryl]-2,2'-bipyridine bipy-TPA was synthesised analogical to a recently published multi-step reaction.^{6,9,18}

Synthesis of donor-antenna compounds for metallation. **1,2-Di[5-(2-pyridinyl)]benzenedithioate 1.** A solution of triethylamine (15 mL), THF (150 mL) and 2-mercaptopyridine (9.35 g, 84 mmol) was stirred at 0 °C for 15 min. Then a solution of *ortho*-phthaloyl dichloride (8.75 g,

42 mmol) in THF (60 mL) was added. The reaction was quenched instantly with 2 % HCl (200 mL, 146 mmol) and extracted with CHCl₃. The combined organic fractions were washed with 10 % NaOH and water until neutrality, dried over Na₂SO₄ and recrystallised from ethyl acetate/ether (10:1). The product was obtained as white crystals (10.08 g, 68 %).

FT-IR (KBr pellet): $\nu_{\text{max}}/\text{cm}^{-1}$ = 3050, 1690, 1664, 1572, 1451, 1420, 1209, 1191, 910, 770, 693; ¹H-NMR (250 MHz; CDCl₃; 20 °C; TMS): δ/ppm = 8.62 (d, 2H), 7.82-7.86 (m, 2H), 7.74-7.78 (d, m, 4H), 7.62-7.66 (m, 2H), 7.26-7.29 (m, 2H); MS (70 eV, EI): m/z = 242 (C₄H₄N-SCO-C₆H₄-CO⁺), 104 (C₆H₄-CO⁺), 78 (C₄H₄N⁺).

1,2-Di(2-thienoyl)benzene 2. 2-Bromothiophene (8.15 g, 50 mmol) was slowly added to a refluxing mixture of iodine activated magnesium (1.22 g, 50 mmol) in absolute THF (100 mL) to form the Grignard reagent in 3 h. Afterwards, the cold reagent was slowly added to a flask containing **1** (8.40 g, 23.8 mmol) in absolute THF (150 mL) at 0 °C and stirred for 30 min. Then, the reaction was quenched with 10 % HCl (200 mL) and extracted with ether. The combined organic fractions were washed with 2 M NaOH until neutrality, dried over Na₂SO₄ and the solvent was removed under reduced pressure. Purification by column chromatography (silica gel 60; cyclohexane/ethyl acetate 3:1) yielded the yellowish solid product (6.79 g, 95 %).

FT-IR (KBr pellet): $\nu_{\text{max}}/\text{cm}^{-1}$ = 1620, 1585, 1570, 1510, 1410; ¹H-NMR (250 MHz; CDCl₃; 20 °C; TMS): δ/ppm = 7.68-7.71 (m, 2H), 7.60-7.63 (d, m, 4H), 7.44 (d, 2H), 7.05 (pseudo t, 2H); MS (70 eV, EI): m/z = 298 (M⁺).

1,3-Di(2-thienyl)benzo[c]thiophene 3. A mixture of **2** (1.00 g, 50 mmol) and 2,4-bis-(4-methoxyphenyl)-1,3-dithia-2,4-diphosphetane-2,4-disulfide (20.00 g, 50 mmol) known as Lawesson's reagent was refluxed in CH₂Cl₂ (1 L) for 30 min. After evaporation of CH₂Cl₂, ethanol (1 L) was added and the mixture was refluxed for additional 30 min. Finally, water (2 L) was added and the product was extracted with ether. The combined organic fractions were extensively washed with 10 % NaOH and water, dried over Na₂SO₄ and concentrated under reduced pressure. The remaining solid was taken up in a small quantity of CHCl₃ and precipitated in *n*-hexane. The precipitate was filtered and the process was repeated several times. All fractions containing almost pure product were further purified by column chromatography (silica gel 60; *n*-hexane). The product was obtained as orange solid (9.98 g, 66 %).

UV-vis (CHCl_3): $\lambda_{\text{max}}/\text{nm} = 436$; FT-IR (KBr pellet): $\nu_{\text{max}}/\text{cm}^{-1} = 1530, 1216, 1182, 841, 738$; $^1\text{H-NMR}$ (250 MHz; CDCl_3 ; 20 °C; TMS): $\delta/\text{ppm} = 7.94\text{--}7.96$ (m, 2H), 7.33–7.35 (d, m, 4H), 7.14–7.15 (d, m, 4H); MS (70 eV, EI): $m/z = 298$ (M^+); CV (acetonitrile, Bu_4NPF_6): HOMO = -5.26 eV, LUMO = -2.63 eV.

5-(3-Thiophen-2-yl-benzo[c]thiophen-1-yl)thiophene-2-carbaldehyde 4. POCl_3 (2.6 mL, 28 mmol) was added to a solution of DMF (2.3 mL, 30 mmol) and CH_2Cl_2 (40 mL). The mixture was stirred at room temperature (RT) until a pale yellow colour appeared. Afterwards, it was added to a solution of **3** (6.75 g, 22.6 mmol) in CH_2Cl_2 (50 mL) at 0 °C and stirred at RT for 10 h. The solvent was removed under reduced pressure, aqueous NaOH (5.00 g in 100 mL) was added and the mixture was heated in a steam bath for 1 h. After cooling to RT, the product was filtered and dried. It was further purified by filtration through Alox, followed by recrystallisation from $\text{CH}_2\text{Cl}_2/n$ -hexane and washing with an excess of *n*-hexane. After repeating this process several times, the pure product was obtained as orange-red needles (6.18 g, 84 %).

$^1\text{H-NMR}$ (250 MHz; CDCl_3 ; 20 °C; TMS): $\delta/\text{ppm} = 9.96$ (s, 1H), 8.04 (dd, 2H), 7.74 (d, 1H), 7.51–7.36 (m, 2H), 7.34–7.10 (m, 4H); MS (70 eV, EI): $m/z = 326$ (M^+), 267 (M-CHO^+), 253, 221.

4,4'-Bis{2-[5-(3-thiophen-2-yl-benzo[c]thiophen-1-yl)-thiophen-2-yl]vinyl}-2,2'-bipyridine bipy-DTBT 6. In an argon flushed flask NaH (0.11 g, 4.6 mmol), **4** (1.07 g, 3.3 mmol) and 4,4'-bis(triphenylphosphonium-methyl)-2,2'-bipyridyl chloride **5** (1.16 g, 1.5 mmol) were dissolved in dry THF (30 mL) and stirred for 5 days at RT. Glacial acetic acid (20 mL) and H_2O (20 mL) were added and the reaction mixture was stirred for one hour at RT. The mixture was extracted with CH_2Cl_2 . The combined organic fractions were washed with an aqueous solution of NH_4OH and dried over Na_2SO_4 . Evaporation of the solvent yielded a dark reddish solid as raw product. This was almost completely dissolved in acetic acid (50 %) and precipitated by addition of an aqueous NH_4OH solution. The precipitate was filtered from the liquid and discarded. The aqueous NH_4OH solution was extracted with CH_2Cl_2 and the combined organic fractions were dried over Na_2SO_4 . After evaporation of the solvent a reddish-brown solid was obtained which was further purified by stirring in methanol. The solid was filtered, washed with methanol and dried to yield a reddish-brown powder (0.81 g, 67 %).

UV-vis (CHCl_3): $\lambda_{\text{max}}/\text{nm} = 286, 358, 486$; FT-IR (KBr pellet): $\nu_{\text{max}}/\text{cm}^{-1} = 3058, 3023, 2924, 1617, 1586, 1436, 1378, 1139, 1056, 990, 942, 809, 731, 688$; $^1\text{H-NMR}$ (250 MHz; CDCl_3 ; 20 °C; TMS): $\delta/\text{ppm} = 8.67$ (d, 2H), 8.48 (s, 2H), 7.72-6.74 (m, 24H); MS (70 eV, EI): $m/z = 800$ (M^+); CV (CH_2Cl_2 , Bu_4NPF_6): HOMO = -5.12 eV, HOMO-1 = -5.31 eV.

4,4'-Bis[4-(*p*-phenylvinyl)styryl]-2,2'-bipyridine bipy-ts 7. In an argon flushed flask NaH (0.18 g, 7.5 mmol), *trans*-stilbene-4-carbaldehyde (1.04 g, 5.0 mmol) and 4,4'-bis(triphenylphosphoniummethyl)-2,2'-bipyridyl chloride **5** (1.94 g, 2.5 mmol) were dissolved in dry THF (50 mL) and stirred for 4 days at RT. Then the reaction mixture was heated up to 50 °C and stirred for 24 h. The solution was neutralised with acetic acid (5 %), poured into ice water and stirred for 1 h. After extraction with CH_2Cl_2 , the combined organic fractions were washed three times with water before drying over Na_2SO_4 . Evaporation of the solvent yielded yellow crystals, which were further purified by recrystallisation from CH_2Cl_2 . Afterwards, monosubstituted by-product was removed by subsequent boiling the raw product in methanol and cyclohexane. Filtration and drying yielded a light yellow solid (0.90 g, 64 %).

UV-vis (CHCl_3): $\lambda_{\text{max}}/\text{nm} = 363$; FT-IR (KBr pellet): $\nu_{\text{max}}/\text{cm}^{-1} = 3056, 3024, 2926, 1630, 1583, 1542, 1460, 1417, 1374, 1330, 964, 827, 755, 691$; $^1\text{H-NMR}$ (250 MHz; $\text{CDCl}_3/\text{CF}_3\text{COOD}$; 20 °C; TMS): $\delta/\text{ppm} = 8.75$ (d, 2H), 8.44 (s, 2H), 7.02-7.69 (m, 28H); MS (70 eV, EI): $m/z = 564$ (M^+); CV (DMSO, Bu_4NPF_6): HOMO = -5.56 eV, LUMO = -1.88 eV.

{2-[2-(2-Methoxyethoxy)ethoxy]ethyl}-4-methylbenzene-sulfonate 8. Under inert gas atmosphere, triethylene glycol monomethyl ether (39.20 mL, 41.00 g, 250 mmol) and pyridine (10 mL) were cooled down to 0 °C. Meanwhile tosylchloride (51.00 g, 270 mmol) was dissolved in pyridine (40 mL) and added drop wise to the alcohol solution over 1 h. This mixture was stirred till the alcohol was fully used up (TLC control; cyclohexane/ethyl acetate 1:1). Afterwards, ice was added and the mixture was extracted with ethyl acetate. The combined organic fractions were subsequently washed with diluted HCl (20 mL), saturated Na_2CO_3 (20 mL) solution and water (50 mL). After drying over Na_2SO_4 and evaporation of the solvent, the product was obtained as yellow liquid (63.40 g, 80 %).

$^1\text{H-NMR}$ (250 MHz; CDCl_3 ; 20 °C; TMS): $\delta/\text{ppm} = 2.45$ (s, 3H, $\text{CH}_3\text{-Ph}$), 3.37 (s, 3H, O-CH_3), 3.48-3.73 (m, 10H, $\text{SO}_2\text{-O-CH}_2\text{-CH}_2\text{-O-CH}_2\text{-CH}_2\text{-O-CH}_2\text{-CH}_2\text{-OCH}_3$), 4.16 (t, $^3J(^1\text{H}, ^1\text{H}) = 5.05$ Hz, 2H,

SO₂-O-CH₂-CH₂), 7.34 (d, $^3J(^1\text{H}, ^1\text{H}) = 8.23$ Hz, 2H, H_{ar}: H-3 und H-5), 7.80 (d, $^3J(^1\text{H}, ^1\text{H}) = 8.20$ Hz, 2H, H_{ar}: H-2 und H-6); MS (70 eV, EI): $m/z = 318$ (1 %, M⁺), 303 (14, M-CH₃⁺), 226 (100), 227 (26, M-CH₃-Ph⁺), 199 (21, M-O-CH₂-CH₂-O-CH₂-CH₂-O-CH₃⁺), 183 (9), 172 (11), 155 (16), 106 (26), 93 (74), 91 (40, CH₃-Ph⁺), 80 (36), 79 (36), 59 (80, CH₂-CH₂-O-CH₃⁺), 45 (46, C₂H₅O⁺).

1-{2-[2-(2-Methoxyethoxy)ethoxy]ethoxy}-4-iodobenzene 9. 4-Iodophenol (22.00 g, 100 mmol) and K₂CO₃ (16.58 g, 120 mmol) were dissolved in dry MEK (50 mL) and heated to reflux under water- and moisture-free conditions. **8** (38.20 g, 120 mmol) was also dissolved in dry MEK (50 mL) and slowly added to the refluxing solution by a dropping funnel. The whole solution was refluxed for 4 h (TLC-control; cyclohexane/ethyl acetate 1:1). Afterwards, *n*-hexane (40 mL) was added and the solution was refluxed for additional 0.5 h. The reaction was quenched with ice water (30 mL), the organic phase was isolated, washed with water (2 x 40 mL), dried over Na₂SO₄ and concentrated under reduced pressure. The raw product was recrystallised from *n*-hexane and washed with cold petroleum ether. The pure product was obtained after drying it for 2 days under vacuum at 40 °C as light yellow liquid (12.82 g, 35 %).

¹H-NMR (250 MHz; CDCl₃; 20 °C; TMS): $\delta/\text{ppm} = 3.35$ (s, 3H, CH₃), 3.52 (t, $^3J(^1\text{H}, ^1\text{H}) = 2.55$ Hz, 2H, CH₂-O-CH₃), 3.58-3.73 (m, 6H, CH₂-CH₂-O-CH₂-CH₂-O-CH₃), 3.82 (t, $^3J(^1\text{H}, ^1\text{H}) = 2.55$ Hz, 2H, Ph-O-CH₂-CH₂), 4.06 (t, $^3J(^1\text{H}, ^1\text{H}) = 2.55$ Hz, 2H, Ph-O-CH₂-CH₂), 6.67 (d, $^3J(^1\text{H}, ^1\text{H}) = 8.85$ Hz, 2H, H_{ar}: H-2 and H-6), 7.51 (d, $^3J(^1\text{H}, ^1\text{H}) = 8.85$ Hz, 2H, H_{ar}: H-3 and H-5); MS (70 eV, EI): $m/z = 366$ (51 %, M⁺), 247/246 (26/9, I-Ph-O-CH₂-CH₂⁺), 220 (18), 203 (17, I-Ph⁺), 147 (35, CH₂-CH₂-O-CH₂-CH₂-O-CH₂-CH₂-O-CH₃⁺), 120 (25), 103 (26, CH₂-CH₂-O-CH₂-CH₂-O-CH₃⁺), 76 (14, Ph⁺), 59 (100, CH₂-CH₂-O-CH₃⁺), 45 (16, CH₂-O-CH₃⁺).

1-{2-[2-(2-Methoxyethoxy)ethoxy]ethoxy}-4-(*N,N*-di-phenylamino)benzene 10. **9** (10.9 g, 29.8 mmol), copper powder (2.77 g, 43.6 mmol), K₂CO₃ (12.08 g, 87.4 mmol), 18-crown-6 (577 mg, 2.2 mmol) and diphenylamine (3.7 g, 21.9 mmol) were consecutively dissolved in dry *ortho*-dichlorobenzene (50 mL). The solution was stirred under dry conditions at 120 °C for 1 h and then heated up to 180 °C for 36 h. (The progress of the reaction was followed by TLC; cyclohexane/ethyl acetate 9:1). After completion of the reaction, the mixture was cooled down to RT, THF was added and the suspension was filtered. The filtrate was dried under reduced

pressure. The remaining solid was dissolved in THF and the pure product was precipitated from methanol (8.40 g, 94 %).

$^1\text{H-NMR}$ (250 MHz; CDCl_3 ; 20 °C; TMS): δ/ppm = 3.38 (s, 3H, CH_3), 3.55 (t, $^3J(^1\text{H}, ^1\text{H})$ = 5.08 Hz, 2H, $\text{CH}_2\text{-O-CH}_3$), 3.59-3.78 (m, 6H, $\text{O-CH}_2\text{-CH}_2\text{-O-CH}_2\text{-CH}_2\text{-OCH}_3$), 3.85 (t, $^3J(^1\text{H}, ^1\text{H})$ = 5.05 Hz, 2H, $\text{Ph-O-CH}_2\text{-CH}_2$), 4.11 (t, $^3J(^1\text{H}, ^1\text{H})$ = 5.05 Hz, 2H, $\text{Ph-O-CH}_2\text{-CH}_2$), 6.60-7.58 (m, 14H, H_{ar}); MS (70 eV, EI): m/z = 407 (12 %, M^+), 366 (62), 260 (9, $\text{Ph}_2\text{N-Ph-O}^+$), 246 (37), 220 (26, $\text{Ph-N-Ph-O-CH}_2\text{-CH}_2^+$), 203 (39), 191 (17), 182 (14), 147 (51, $\text{CH}_2\text{-CH}_2\text{-O-CH}_2\text{-CH}_2\text{-O-CH}_2\text{-CH}_2\text{-O-CH}_3^+$), 120 (40, N-Ph-O-CH_2^+), 103 (35, $\text{CH}_2\text{-CH}_2\text{-O-CH}_2\text{-CH}_2\text{-O-CH}_3^+$), 91 (18, Ph-N^+), 77 (13, Ph^+), 76 (31, Ph^+), 59 (100, $\text{CH}_2\text{-CH}_2\text{-O-CH}_3^+$), 45 (71, $\text{CH}_2\text{-O-CH}_3^+$).

4-{N-[4-{2-[2-(2-Methoxyethoxy)ethoxy]ethoxy}phenyl]-N-phenylamino}benzaldehyde 11.

Freshly distilled POCl_3 (1.40 mL, 2.34 g, 15.25 mmol) was added to DMF (10 mL) under dry conditions, cooled down to 0 °C and stirred at 0-5 °C for 30 min. Afterwards, the ice bath was removed and the solution was stirred until the red colour vanished. Meanwhile, **10** (6.11 g, 15.0 mmol) was dissolved in dry CH_2Cl_2 (50 mL) and cooled down to 0-5 °C. Then the POCl_3 containing solution was added drop wise to the solution comprising **10** in CH_2Cl_2 . After stirring the resulting yellow solution for 15 min at 0-5 °C, it was heated up to 80-85 °C and stirred for 2.5 h (TLC-control; CH_2Cl_2 ; each sample was shaken with sodium acetate and diluted with CH_2Cl_2). After full conversion of **10**, the reaction mixture was cooled down to RT, added drop wise to a strongly stirring solution of sodium acetate in ice water (~ 50 mL) and stirred overnight. Afterwards, the organic layer was isolated and the aqueous was extracted with CH_2Cl_2 (5 x 70 mL). The combined organic fractions were dried over Na_2SO_4 and the solvent was removed under reduced pressure. The raw product was purified by column chromatography (silica gel 60; cyclohexane/ethyl acetate 1:1). The pure product was obtained as a yellow, highly viscous liquid (2.80 g, 43 %).

FT-IR (NaCl plates): $\nu_{\text{max}}/\text{cm}^{-1}$ = 3063 (w) and 3039 (w) (CH aromatic), 2877 (br m) (CH aliphatic), 2733 (m), 1695 (m), 1615-1558 (m), 1506-1436 (m), 1280-1220 (br m), 1070-1064 (br m) (CO), 946 (w), 826 (m), 759 (w) (CH aromatic out-of-plane), 725 (w), 697 (m), 616 (w), 547 (w); $^1\text{H-NMR}$ (250 MHz; DMSO-d_6 ; 20 °C; TMS): δ/ppm = 3.23 (s, 3H, CH_3), 3.41 (m, 2H, $\text{CH}_2\text{-O-CH}_3$), 3.46-3.63 (m, 6H, $\text{O-CH}_2\text{-CH}_2\text{-O-CH}_2\text{-CH}_2\text{-OCH}_3$), 3.74 (t, $^3J(^1\text{H}, ^1\text{H})$ = 5.05 Hz, 2H, $\text{Ph-O-CH}_2\text{-CH}_2$), 4.10 (t, $^3J(^1\text{H}, ^1\text{H})$ = 5.05 Hz, 2H, $\text{Ph-O-CH}_2\text{-CH}_2$), 6.79 (d, $^3J(^1\text{H}, ^1\text{H})$ = 8.85 Hz, 2H, H_{ar}), 7.05 (d, $^3J(^1\text{H}, ^1\text{H})$ = 8.85 Hz, 2H, H_{ar}), 7.18 (m, 5H, H_{ar}), 7.37 (m, 2H, H_{ar}), 7.68 (d, $^3J(^1\text{H}, ^1\text{H})$ = 8.85 Hz, 2H,

H_{ar}); MS (70 eV, EI): *m/z* = 435 (100 %, M⁺), 407 (22, M-COH⁺), 366 (30), 246 (15), 220 (11, Ph-N-Ph-O-CH₂-CH₂⁺), 203 (12), 191 (5), 147 (18, CH₂-CH₂-O-CH₂-CH₂-O-CH₂-CH₂-O-CH₃⁺), 120 (20, N-Ph-O-CH₂⁺), 103 (19, CH₂-CH₂-O-CH₂-CH₂-O-CH₃⁺), 91 (8, Ph-N⁺), 77 (5, Ph⁺), 76 (15, Ph⁺), 59 (35, CH₂-CH₂-O-CH₃⁺), 45 (23, CH₂-O-CH₃⁺).

4,4'-Bis[4-{N-{4-{2-[2-(2-methoxyethoxy)ethoxy]ethoxy}-phenyl}-N-phenylamino}-styryl]-2,2'-bipyridine bipy-TPA-EO 12. Under inert gas atmosphere KOtBu (1.12 g, 10.0 mmol) was added to dry THF (50 mL). **5** (1.94 g, 2.5 mmol) and **11** (2.18 g, 5.0 mmol) were added and the resulting suspension was stirred at RT for 18 h (TLC-control; cyclohexane/ethyl acetate 1:1; 5 % acetic acid was added to each sample). After full consumption of **11**, 5 % acetic acid (10 mL) was added and the solution was once again stirred at RT for 30 min followed by extraction of the organic layer with CH₂Cl₂ (5 x 70 mL). The combined organic fractions were dried over Na₂SO₄ and the solvent was removed under reduced pressure. The raw product was further purified by column chromatography (silica gel 60; cyclohexane/ethyl acetate 1:1; THF). Impurities were first eluted by cyclohexane/ethyl acetate and then the product was obtained by washing the column with THF. To remove the last impurities, the product was further purified by column chromatography (flash gel; acetonitrile) whereupon it was eluted with THF after all acetonitrile-soluble impurities were eluted. The pure product - an orange highly viscous liquid - was dried under high vacuum (0.58 g, 23 %).

UV-vis (MeOH): λ_{max}/nm = 291, 395; ¹H-NMR (250 MHz; CDCl₃; 20 °C; TMS): δ/ppm = 3.38 (s, 6H, 2 x CH₃), 3.49-3.59 (m, 4H, 2 x CH₂-O-CH₃), 3.59-3.79 (m, 12H, 2 x O-CH₂-CH₂-O-CH₂-CH₂-OCH₃), 3.79-3.89 (m, 4H, 2 x Ph-O-CH₂-CH₂-O), 4.02-4.17 (m, 4H, 2 x Ph-O-CH₂-CH₂-O), 6.75-7.90 (m, 32H, H_{ar}, H_{ol} and H_{bipy}: H-5 und H-5'), 8.28 (m, 2H, H_{bipy}: H-3 and H-3'), 8.56 (m, 2H, H_{bipy}: H-6 and H-6'); MS (70 eV, EI): *m/z* = 1018 (2 %, M⁺), 871 (5), 838 (3), 793 (7), 725 (12), 671 (14), 644 (3), 617 (5), 601, 587, 509 (14, M/2⁺), 503 (7), 470 (4), 454 (3), 421 (8), 363 (3), 289 (10), 279 (2), 277 (8), 230 (9), 226 (11), 167 (6), 77 (7, Ph⁺), 76 (11, Ph⁺), 59 (40, CH₂-CH₂-O-CH₃⁺), 45 (100, CH₂-O-CH₃⁺); CV (CH₂Cl₂, Bu₄NPF₆): HOMO = -5.17 eV, LUMO = -2.36 eV.

4,4'-Bis[(N,N'-dimethylaminovinyl)-2,2'-bipyridine] bipy-NMe₂ 13. Under inert gas atmosphere 4,4'-dimethyl-2,2'-bipyridine (2.30 g, 12.5 mmol) was dissolved in DMF (15 mL) and Brederick's reagent (11.86 mL, 57.4 mmol) was added. Afterwards, the light yellow solution was heated up

and stirred at 140 °C for 22 h. The reaction was stopped by addition of water (40 mL) whereupon the solution became brightly yellow and a yellow solid precipitated. The solid was dissolved by addition of in CH₂Cl₂ and the reaction mixture was extracted with CH₂Cl₂ (5 x 50 mL). The combined organic fractions were dried over Na₂SO₄ and the solvent was removed. The remaining solid was dissolved in a small amount of CH₂Cl₂ and precipitated in *n*-hexane. The pure product was obtained after collecting the yellow solid by filtration and drying it under reduced pressure (3.60 g, 98 %).

UV-vis (MeOH): $\lambda_{\text{max}}/\text{nm}$ = 232, 278, 355; FT-IR (KBr pellet): $\nu_{\text{max}}/\text{cm}^{-1}$ = 3112 (w) (CH, aromatic/vinylic), 1636 (s), 1575 (s), 1534 (w), 1461 (w) (CH₃ asym. bending), 1434 (w), 1416 (w), 1393 (m), 1362 (w) (CH₃ sym. bending), 1303 (w), 1226 (w), 1204 (w), 1110 (w), 1101 (w), 986 (w) (CH *trans*-alkene), 938 (w), 885 (w), 849 (w), 838 (w), 782 (w) (CH aromatic out-of-plane), 628 (w); ¹H-NMR (250 MHz; CDCl₃; 20 °C; TMS): δ/ppm = 2.78 (s, 12H, 2 x CH₃), 5.01 (d, ³*J*(¹H, ¹H) = 13.63 Hz, 2H, 2 x CH=CH-NMe₂), 6.89 (dd, ³*J*(¹H, ¹H) = 5.05 Hz, ⁴*J*(¹H, ¹H) = 1.60 Hz, 2H, H_{bipy}: H-5 and H-5'), 7.12 (d, ³*J*(¹H, ¹H) = 13.63 Hz, 2H, 2 x CH=CH-NMe₂), 8.06 (d, ⁴*J*(¹H, ¹H) = 0.99 Hz, 2H, H_{bipy}: H-3 and H-3'), 8.30 (d, ³*J*(¹H, ¹H) = 5.28 Hz, 2H, H_{bipy}: H-6 and H-6'); MS (70 eV, EI): *m/z* = 294 (100 %, M⁺), 279 (61, M-CH₃⁺), 264 (29, M-(2 x CH₃)⁺), 249 (16, M-(3 x CH₃)⁺), 234 (9, M-(4 x CH₃)⁺), 224 (7, M-Me₂N-CH=CH⁺), 207 (11, M-(Me₂N-CH and 2 x CH₃)⁺), 147 (16, M/2 (Py-CH=CH-NMe₂)⁺), 70 (29, M-Me₂N-CH=CH⁺), 42 (72); CV (CH₂Cl₂, Bu₄NPF₆): HOMO = -5.16 eV, LUMO = -2.60 eV.

One-pot syntheses of Ru(II)bis(bipyridyl)(NCS)₂ donor-antenna dyes. General procedure for the conventional one-pot synthesis: In an argon flushed three-neck flask dichloro(*p*-cymene)-ruthenium(II) dimer (2 equivalents) was dissolved in dry DMF. The respective donor-antenna bipyridyl compound (**6**, **7** or **12**, 1 equivalent) was added and the reaction mixture was stirred at 100 °C until the donor-antenna bipyridyl compound was fully consumed (TLC-control; Alox sheet; toluene/acetonitrile 9:1). 4,4'-Dicarboxylic acid-2,2'-bipyridine **14** (1 equivalent) was added and the solution was stirred at 150 °C for 5 h. After addition of NH₄SCN (25 equivalents) the reaction mixture was stirred at 150 °C for 4 – 5 h. Then, DMF was removed from the reaction flask by vacuum distillation.

General procedure for the microwave assisted one-pot synthesis: In an argon flushed Schlenk tube dichloro(*p*-cymene)ruthenium(II) dimer (2 equivalents) was dissolved in dry DMF. The respective donor-antenna bipyridyl compound (**13** or bipy-TPA, 1 equivalent) was added and the

reaction mixture was stirred under microwave irradiation at 70 °C for 20-25 min until the donor-antenna bipyridyl compound was fully consumed (TLC-control; Alox sheet; toluene/acetonitrile 9:1). 4,4'-Dicarboxylic acid-2,2'-bipyridine **14** (1 equivalent) was added and the solution was irradiated with microwaves at 135-150 °C for 20 min. After addition of NH₄SCN (25 equivalents), the reaction mixture was irradiated again at 135-150 °C for 30-40 min. Then, DMF was removed from the reaction flask by vacuum distillation.

Ru-DTBT-NCS. After the metallation reaction (*vide supra*: general conventional procedure) diethyl ether was added and a black sticky precipitate was obtained. After addition of THF/methanol the product precipitated. Filtration yielded the raw product as black powder which was further purified by reprecipitation from methanol in THF/diethyl ether to obtain the product as a dark violet solid (878 mg, 74 %).

UV-vis (DMF): $\lambda_{\text{max}}/\text{nm}$ = 301, 369, 515; FT-IR (KBr pellet): $\nu_{\text{max}}/\text{cm}^{-1}$ = 3446 (OH), 3063, 2098 (C=N, N-coordinated), 1967, 1711 (C=O), 1597, 1523, 1423, 1372, 1227 (C-O), 1019, 942, 816, 742, 697; ¹H-NMR (250 MHz; THF-d₅; 20 °C; TMS): δ/ppm = 6.70-9.30 (m, 36H); CV (DMF, Bu₄NPF₆): HOMO = -5.08 eV, HOMO-1 = -5.32 eV, LUMO = -3.16 eV.

Ru-tS-NCS. Subsequent to the complex formation reaction (*vide supra*: general conventional procedure), the residue was dissolved in THF/methanol and a black solid precipitated after addition of diethyl ether. The precipitate was filtered and reprecipitated from THF in diethyl ether. The product was obtained as a black powder (1.02 g, 60 %).

UV-vis (DMF): $\lambda_{\text{max}}/\text{nm}$ = 310, 373, 550; FT-IR (KBr pellet): $\nu_{\text{max}}/\text{cm}^{-1}$ = 3443 (OH), 3024, 2098 (C=N, N-coordinated), 1712 (C=O), 1607, 1596, 1510, 1447, 1423, 1366, 1231 (C-O), 1177, 1019, 960, 805, 752, 690; ¹H-NMR (250 MHz; DMSO-d₆; 20 °C; TMS): δ/ppm = 7.09-9.48 (m, 40H); CV (DMF, Bu₄NPF₆): HOMO = -5.10 eV, HOMO-1 = -5.50 eV, LUMO = -3.19 eV.

Ru-TPA-EO-NCS: Following the metallation reaction (*vide supra*: general conventional procedure), the black raw product was stirred for 25 min with tepid water. The remaining solid was collected and washed intensively with water and diethyl ether. This procedure (stirring with

water and subsequent washing) was repeated twice. Afterwards, the black solid (0.55 g, 67 %) was dried under vacuum at 40 °C overnight.

UV-vis (MeOH + 1 wt% KOH): $\lambda_{\text{max}}/\text{nm}$ = 307, 429, 524; FT-IR (KBr pellet): $\nu_{\text{max}}/\text{cm}^{-1}$ = 3448 (br m) (OH), 3113-3189 (w) (CH aromatic/vinyl), 2879 (br w) (CH aliphatic), 2103 (m) (C=N, N-coordinated), 1975 (w), 1718 (w) (C=O), 1585 (s), 1506 (s), 1457 (w), 1317 (w), 1241 (m) (C-O), 1191 (w), 1117 (w), 1109 (br w) (C-O-C, the broadness indicates the disorder of the chains), 1022 (w), 835 (w), 810 (w), 697 (w); $^1\text{H-NMR}$ (250 MHz; DMSO- d_6 ; 20 °C; TMS): δ/ppm = 2.89-4.18 (m, 30H), 7.65-7.97 (m, 34H), 8.12-9.29 (m, 8H); MS (70 eV, EI): m/z = 615 (12 %), 601 (9), 490 (21), 421 (11), 236 (9), 184 (13), 156 (91), 77 (13, Ph^+), 59 (84, $\text{CH}_2\text{-CH}_2\text{-O-CH}_3^+$), 58 (11, NCS^+), 125 (30), 77 (25), 44 (100, COOH^+); CV (DMF, Bu_4NPF_6): HOMO = -5.08 eV, HOMO-1 = -5.27 eV, LUMO = -3.13 eV.

Ru-NMe₂-NCS. After the complexation reaction (*vide supra*: general microwave assisted procedure), acetone was added to the oily raw product whereupon the product precipitated as a black solid which was collected and stirred with tepid water for 30 min. The remaining solid was collected and washed intensively with water and diethyl ether. After drying, the solid was dissolved in DMF and precipitated in diethyl ether. The product was obtained as a black solid (0.74 g, 96 %).

UV-vis (DMF): $\lambda_{\text{max}}/\text{nm}$ = 254, 307, 381, 526; FT-IR (KBr pellet): $\nu_{\text{max}}/\text{cm}^{-1}$ = 3428 (br w) (OH), 3063 (br w) (CH, aromatic/vinyl), 2099 (br s) (C=N, N-coordinated), 1988 (br m), 1722 (m) (C=O), 1611 (m), 1548 (w), 1479 (w) (CH_3 , asym. bending), 1407 (m), 1367 (m) (CH_3 , sym. bending), 1297 (w) 1264 (m), 1232 (m) (C-O), 1142 (w), 1019 (w), 901 (w), 825 (w), 767 (w) (CH aromatic out-of-plane), 682 (w); MS (70 eV, EI): m/z = 755 (4 %, M^+), 595 (3), 539 (3), 502 (5), 354 (7), 294 (5), 279 (4), 244 (4), 200 (21), 156 (29), 57 (29, NCS^+), 44 (100, COO or NMe_2^+); CV (DMSO, Bu_4NPF_6): HOMO = -5.17 eV, LUMO = -3.19 eV.

Ru-TPA-NCS. Subsequent to the one-pot synthesis (*vide supra*: general microwave assisted procedure), water was added to the remaining dark red solid. The suspension was stirred for 15 min at RT. The insoluble solid was collected and washed intensively with water. After drying at 40 °C under vacuum, the black solid was dissolved in DMF and precipitated in diethyl ether.

The precipitate was washed intensively with diethyl ether and dried under vacuum at 40 °C overnight. The product was obtained as a black solid (220 mg, 95 %).

UV-vis (DMF): $\lambda_{\text{max}}/\text{nm}$ = 224, 304, 423, 544; FT-IR (KBr pellet): $\nu_{\text{max}}/\text{cm}^{-1}$ = 3440 (br w) (OH), 3150-2994 (w) (CH, aromatic/vinylic), 2923 (w), 2834 (w), 2103 (m) (C=N, N-coordinated), 1975 (w), 1735 (w), 1719 (w) (C=O), 1586 (s), 1508 (m), 1492 (m), 1329 (w), 1304 (w), 1284 (w), 1254 (w) (C-O), 1190 (w), 1176 (w), 1020 (w), 945 (w), 838 (w), 755 (w) (CH, aromatic out-of-plane), 698 (w), 617 (w); $^1\text{H-NMR}$ (250 MHz; DMF- d_7 ; 20 °C; TMS): δ/ppm = 6.93-7.28 (m, 20H), 7.28-7.53 (m, 12H), 7.53-7.85 (m, 8H), 8.80-9.35 (m, 6H); MS (70 eV, EI): m/z = 694 (2 %), 437 (3, M- $\text{Ph}_2\text{NPh-CH}^+$), 379/378 (4/11), 224 (3, Ph_2NPh^+), 200 (100), 156 (38), 59 (80), 58 (12, NCS^+), 45 (100, COOH^+); CV (LM, Bu_4NPF_6): HOMO = -5.12 eV, HOMO-1 = -5.30 eV, LUMO = -3.20 eV.

Materials for SDSCs. Glass substrates (Tec15, 26 Ω/cm^{-1} , 1 inch x 1 inch), covered with fluorine-doped tin oxide (FTO), were purchased from Hartford Glass Co. Inc., Indiana, USA. Diisopropoxytitanium bis(acetylacetonate) solution (Aldrich) was used as received. The screen printable nano-titanium dioxide paste DSL 90-T was supplied by Dyesol, Queanbeyan NSW, Australia. The solid hole conductor 2,2',7,7'-tetrakis-(*N,N*-di-4-methoxy-phenyl amino)-9,9'-spiro-bifluorene (spiro-OMeTAD) was purchased by Merck KGaA, Darmstadt, Germany. 4-*Tert*-butylpyridine (Aldrich) was used as received. Lithium bistrifluoromethanesulfonimide ($\text{LiN}(\text{SO}_2\text{CF}_3)_2$) (Aldrich) was purchased, dried under vacuum and stored under N_2 till use. The standard dye N719 purchased by Solaronix SA, Aubonne, Switzerland was used as received.

Solar cell preparation. FTO-covered glass substrates were partly etched (to create a non-conducting area for the cathode contacts), cleaned and covered with a compact TiO_2 blocking layer by spray pyrolysis deposition.²⁹ After screen-printing and sintering the mesoporous nanocrystalline titanium dioxide, the respective dye was adsorbed from a 0.5 mM DMF (dry) solution with the exception of Ru-NMe₂-NCS which was adsorbed from a 0.5 mM DMSO (dry) solution. The hole-transport layer was 0.16 M concerning spiro-OMeTAD, 30.3 mM concerning the lithium salt $\text{LiN}(\text{SO}_2\text{CF}_3)_2$ and 0.23 M concerning 4-*tert*-butylpyridine. This hole transport layer solution was deposited by spin coating. To complete the solar cells, gold contacts were deposited under high vacuum.

Solar cell measurements. Current-voltage characteristics were measured under a standard light source (xenon arc lamp) equipped with suitable filters to get AM 1.5 G spectral conditions at an intensity of 100 mW cm^{-2} . The lamp was regularly calibrated with ISE Call lab, Freiburg silicon solar cell (WPVS cell). I/V values were recorded using a Keithley 6517 source measure unit.

ACKNOWLEDGMENT

This work was financially supported by the “Deutsche Forschungsgemeinschaft, Sonderforschungsbereich SFB 481”.

BIBLIOGRAPHY

- 1 B. O'Regan, M. Grätzel, *Nature*, **1991**, 353, 737-740.
- 2 M. Nazeeruddin, F. De Angelis, S. Fantacci, A. Selloni, G. Viscardi, P. Liska, S. Ito, B. Takeru, M. Grätzel, *Journal of the American Chemical Society*, **2005**, 127, 16835-16847.
- 3 M. Nazeeruddin, P. Péchy, T. Renouard, S. Zakeeruddin, R. Humphry-Baker, P. Comte, P. Liska, L. Cevey, E. Costa, V. Shklover, L. Spiccia, G. Deacon, C. Bignozzi, M. Grätzel, *Journal of the American Chemical Society*, **2001**, 123, 1613-1624.
- 4 U. Bach, D. Lupo, P. Comte, J. Moser, F. Weissörtel, J. Salbeck, H. Spreitzer, M. Grätzel, *Nature*, **1998**, 395, 583-585.
- 5 L. Schmidt-Mende, M. Grätzel, *Thin Solid Films*, **2006**, 500, 296-301.
- 6 C. Karthikeyan, M. Thelakkat, *Inorganica Chimica Acta*, **2008**, 361, 635-655.
- 7 S. Handa, H. Wietasch, M. Thelakkat, J. Durrant, S. Haque, *Chemical Communications*, **2007**, 1725-1727.
- 8 H. Snaith, C. Karthikeyan, A. Petrozza, J. Teuscher, J. Moser, M. Nazeeruddin, M. Thelakkat, M. Grätzel, *Journal of Physical Chemistry C*, **2008**, 112, 7562-7566.
- 9 K. Peter, M. Thelakkat, *Macromolecules*, **2003**, 36, 1779-1785.
- 10 R. Kiebooms, P. Adriaenssens, D. Vanderzande, J. Gelan, *Journal of Organic Chemistry*, **1997**, 62, 1473-1480.
- 11 I. Thomsen, K. Clausen, S. Scheibye, S.-O. Lawesson, *Organic Syntheses*, **1984**, 62, 158-164.
- 12 A. Vilsmeier, A. Haack, *Berichte der Deutschen chemischen Gesellschaft*, **1927**, 60, 119-122.
- 13 A. Mohanakrishnan, M. Lakshmikantham, C. McDougal, M. Cava, J. Baldwin, R. Metzger, *Journal of Organic Chemistry*, **1998**, 63, 3105-3112.
- 14 P. Fanta, *Synthesis*, **1974**, 9-21.
- 15 J. Hassan, M. Sévignon, C. Gozzi, E. Schulz, M. Lemaire, *Chemical Reviews*, **2002**, 102, 1359-1470.
- 16 O. Maury, J.-P. Guégan, T. Renouard, A. Hilton, P. Dupau, N. Sandon, L. Toupet, H. Bozec, *New Journal of Chemistry*, **2001**, 25, 1553-1566.
- 17 H. Bredereck, G. Simchen, R. Wahl, *Chemische Berichte*, **1968**, 101, 4048-4056.
- 18 C. Karthikeyan, K. Peter, H. Wietasch, M. Thelakkat, *Solar Energy Materials and Solar Cells*, **2007**, 91, 432-439.
- 19 A. Oi, R. Morgan, *Synthetic Communications*, **1995**, 25, 4093-4097.
- 20 P. Wang, S. Zakeeruddin, J. Moser, M. Nazeeruddin, T. Sekiguchi, M. Grätzel, *Nature Materials*, **2003**, 2, 402-407.
- 21 N. Hirata, J.-J. Lagref, E. Palomares, J. Durrant, M. Nazeeruddin, M. Grätzel, D. Di Censo, *Chemistry - A European Journal*, **2004**, 10, 595-602.
- 22 C. O. Kappe, *Angewandte Chemie*, **2004**, 116, 6408-6443; C. O. Kappe, *Angewandte Chemie International Edition*, **2004**, 43, 6250-6284.
- 23 E. Sayed, H. El Ashry, A. Kassem, *Arkivoc*, **2006**, 9, 1-16.

- 24 S. Campagna, F. Puntoriero, F. Nastasi, G. Bergamini, V. Balzani, in *Photochemistry and Photophysics of Coordination Compounds I*, ed. V. Balzani, S. Campagna, Springer, Berlin, 1st edn, **2007**, vol. 280, p. 117-214.
- 25 C.-Y. Chen, S.-J. Wu, C.-G. Wu, J.-G. Chen, K.-C. Ho, *Angewandte Chemie International Edition*, **2006**, 45, 5822-5825.
- 26 A. Juris, V. Balzani, F. Barigelletti, S. Campagna, P. Belser, A. von Zelewsky, *Coordination Chemistry Reviews*, **1988**, 84, 85.
- 27 C. Karthikeyan, H. Wietasch, M. Thelakkat, *Advanced Materials*, **2007**, 19, 1091-1095.
- 28 S. Haque, S. Handa, K. Peter, E. Palomares, M. Thelakkat, J. Durrant, *Angewandte Chemie International Edition*, **2005**, 44, 5740-5744.
- 29 B. Peng, G. Jungmann, C. Jäger, D. Haarer, H.-W. Schmidt, M. Thelakkat, *Coordination Chemistry Reviews*, **2004**, 248, 1479-1489.
- 30 D. Kuang, C. Klein, H. Snaith, J.-E. Moser, R. Humphry-Baker, P. Comte, S. Zakeeruddin, M. Grätzel, *Nano Letters*, **2006**, 6, 769-773.
- 31 H. Snaith, A. Moule, C. Klein, K. Meerholz, R. Friend, M. Grätzel, *Nano Letters*, **2007**, 7, 3372-3376.
- 32 D. Kuang, C. Klein, H. Snaith, R. Humphry-Baker, S. Zakeeruddin, M. Grätzel, *Inorganica Chimica Acta*, **2008**, 361, 699-706.

Chapter 6

MULTICHROMOPHORE LIGHT HARVESTING IN HYBRID SOLAR CELLS

*Jayasundera Bandara ^{[a][b]}, Katja Willinger ^[a] and Mukundan Thelakkat ^[a]**

^[a] Department of Macromolecular Chemistry I, Applied Functional Polymers, Universität Bayreuth, Universitätsstr. 30, 95440 Bayreuth, Germany.

Fax: +49 921 55 3206

E-mail: Mukundan.Thelakkat@uni-bayreuth.de

^[b] Institute of Fundamental Studies, Hantana Road, DP 20000, Kandy, Sri Lanka

Published in *Physical Chemistry Chemical Physics* **2011**, 13, 12906–12911.

Reproduced by permission of the PCCP Owner Societies

ABSTRACT

A new technologically relevant method for multichromophore sensitizing of hybrid blend solar cells is presented here. Two dyes having complementary absorption in the UV-visible regions are individually adsorbed on nanocrystalline TiO₂ powder separately. These dyed TiO₂ nanoparticles are blended with an organic hole-conductor (HC) spiro-OMeTAD in desired composition and applied on conducting substrate by doctor-blading at room temperature to fabricate multichromophore hybrid blend solar cells. The external quantum efficiency (EQE) of the single hybrid layer system fabricated with two dyes, that absorb mainly UV (TPD dye) and visible regions (Ru-TPA-NCS dye) exhibited a clear panchromatic response with the sum of the EQE characteristics of each single dye cell. The first results of a multichromophore-sensitized solid-state solar cell showed J_{sc} of 2.1 mA cm⁻², V_{oc} of 645 mV, FF of 47 % and efficiency of 0.65 % at AM 1.5 G, 100 mW cm⁻² illumination intensity. The J_{sc} of the multichromophore cell is the sum of the individually dyed solar cells. The process described here is technically very innovative and very simple in procedure. It has potentials to be adopted for panchromatic sensitization using more than two dyes in a single hybrid layer or layer-wise fabrication of a tandem structure at room temperature.

Keywords: Solid-state dye-sensitized solar cell • TiO₂ • thin film • multichromophore • hybrid solar cell • blend solar cell.

INTRODUCTION

There are different concepts for realizing solid-state organic-inorganic hybrid solar cells. The methods range from an adaptation of dye-sensitized solar cells in which a solid-state hole conductor is filled into a previously sintered mesoporous titania network¹⁻³ up to simple blending of polymeric hole conductors and metal oxides (TiO_2 , ZnO , *etc.*)^{4, 5} or inorganic semiconductors (CdSe , CdS , *etc.*)⁶. Other attempts include an *in situ* synthesis of the inorganic semiconductor in a polymer hole conductor matrix.^{7, 8} The first method of filling a mesoporous layer suffers from inefficient filling, especially with polymeric hole conductors, whereas blending usually results in low percolation for the electron transport *via* particles. Another issue in hybrid solar cells is how to increase the light harvesting. Ideally, the dye should be panchromatic, that is, it absorbs photons over the entire visible region of the solar spectrum while maintaining sufficient thermodynamic driving force for both the electron injection and dye regeneration process.^{9, 10} The single ideal dye that absorbs all visible light and smoothly transfer electron is very difficult to realize.¹¹ Molecular design of such an ideal sensitizer to absorb visible light of all colours presents a challenging task. The problem is that when using a single dye possessing a low band gap (usually low LUMO: lowest unoccupied molecular orbital) absorption spectrum, it is difficult to inject electrons from the dye to the n-type semiconductor because the LUMO of the dye approaches the conduction band of the semiconductor. To overcome this problem, several multichromophore light harvesting methods have been attempted.¹²⁻¹³ One such attempt was the co-sensitization using a cocktail of dyes with complementary absorption.¹⁴⁻¹⁷ The major problem in co-sensitization is that the number of free sites available on the titania surface for the dye attachment is limited and unfavourable adsorption and desorption interactions between two dye molecules often resulted in decrease in photovoltaic performances. On the other hand, tandem dye-sensitized solar cells (DSSC) have been introduced in liquid electrolyte based systems to minimize the unfavourable dye-dye interactions present in co-sensitized devices.¹⁸⁻²⁰ Though tandem DSSC is a promising approach for multichromophore devices, the fabrication of monolithic tandem solar cells remains largely challenging.^{11, 21} Furthermore the present high temperature preparation methods limit the fabrication of hybrid devices on flexible substrate as high temperature sintering is usually necessary for the preparation of mesoporous metal oxide (*e.g.* TiO_2) electrodes. Moreover, the second mesoporous TiO_2 layer that is necessary on the first dyed TiO_2 layer to fabricate the tandem device cannot be prepared by the same method. To overcome these difficulties, novel concepts of multichromophore sensitization and room temperature fabrication of hybrid solar cells are urgently required.

In this investigation we addressed most of the above issues encountered in this field and present a new fabrication concept for multichromophore light harvesting in hybrid devices using TiO_2 nanocrystals and an organic hole conductor. The dyes 1, 2, etc. (in principle we can use several dyes as we wish) having complementary absorption in the UV-visible regions are individually adsorbed on nanocrystalline TiO_2 powder separately. These dyed TiO_2 particles are mixed with an organic hole-conductor (e.g. spiro-OMeTAD or any p-type polymer) in any desired composition and this blend was applied on conducting substrate by doctor-blading method at room temperature. Finally an additional hole injection smoothing layer (PEDOT:PSS) was coated onto the blend layer. The two possible device structures are schematically shown in Figure 1.

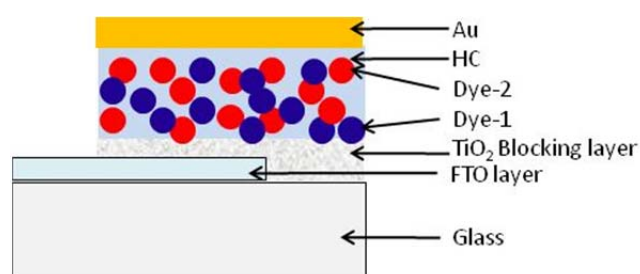


Figure 1a

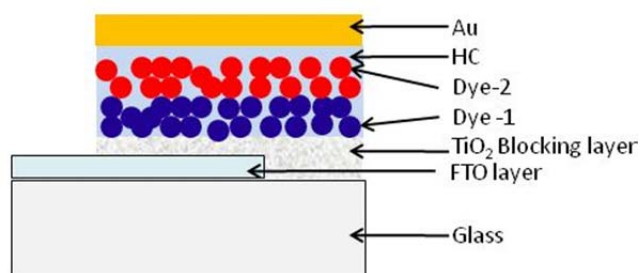


Figure 1b

Figure 1. Schematic diagram of a multichromophore sensitized hybrid solar cell with (a) randomly and (b) layer-wise dyed- TiO_2 thin films for the case of two different dyes.

Thus these solar cells can be fabricated either using a random mixture of differently dyed- TiO_2 (Figure 1a) or with subsequent layers of selectively dyed- TiO_2 (Figure 1b). The method described here is very simple and cost effective but technologically very relevant. The layer-wise

fabrication of two differently dyed layers at room temperature can be extended to panchromatic (multichromophoric) sensitization using more than two dyes in a tandem structure. In the following section, the proof of principle is shown for a) a single mixed dye hybrid device and b) a two-dye layer-wise assembly, while the latter method can be adopted for tandem cells very easily. It is important to note that the active layers were prepared at ambient conditions using the doctor-blading method, which is suitable for flexible device fabrication on plastic substrates.

RESULTS AND DISCUSSION

Light absorption in a broad wavelength region by dye molecules is a prerequisite for high solar cell efficiency. However lack of such a single dye makes it necessary to use a mixture of two or more dyes for panchromatic sensitization of nanocrystalline TiO_2 . In this investigation we introduced a novel fabrication concept that avoids most of the problems encountered in fabrication of multichromophore sensitized solar cells. To prepare multichromophore sensitized solar cell, different dyes having complementary absorption in the UV-visible regions are adsorbed on nanocrystalline TiO_2 powder and these dyed- TiO_2 particles are mixed with an organic hole-conductor spiro-OMeTAD to get a suspension. Finally, this paste was applied on a conducting substrate by doctor-blading method to fabricate thin film electrodes at room temperature. Figure 1 depicts schematically the different ways of fabrication of active layer, whereas Figure 10 (experimental section) shows the major steps of preparation. For this experiment, we used two dyes, dye-1 (TPD-dye) and dye-2 (Ru-TPA-NCS).

Their molecular structures are shown in Figure 2 and their absorption spectra in DMSO solution are compared with that of the equimolecular mixture in Figure 3. The TPD-dye absorbs mainly in the UV/blue region of the solar spectrum having absorption maximum around 400 nm and the colour of the dye is yellow. The Ru-TPA-NCS absorbs mainly in the green visible region of the solar spectrum having absorption maximum at 550 nm and the colour of the dye is dark brown. The dye mixture possesses the absorption contributions of the individual dyes and exhibits a broad absorption spectrum covering from 300 nm to 600 nm. The molar extinction coefficient for the absorption maximum for TPD-dye at 400 nm is $27\,500\text{ M}^{-1}\text{ cm}^{-1}$, whereas Ru-TPA-NCS has a value of $20\,500\text{ M}^{-1}\text{ cm}^{-1}$ at 544 nm. The former corresponds to the π - π^* transitions of the conjugated dye molecule, whereas the latter arises from an MLCT transition.

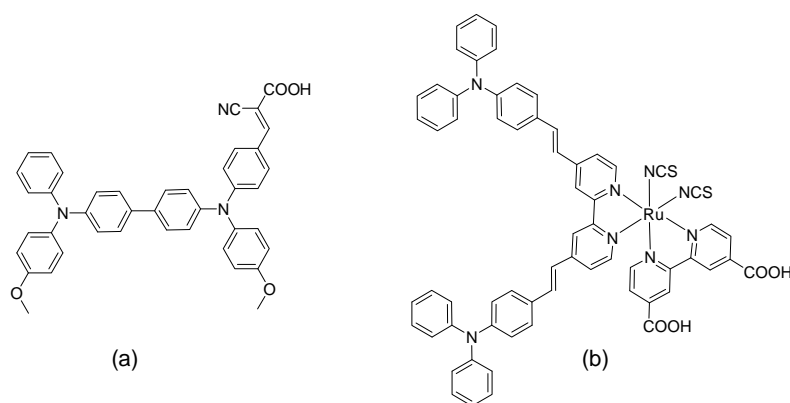


Figure 2. Chemical structures of (a) Dye-1: TPD-dye and (b) Dye-2: Ru-TPA-NCS.

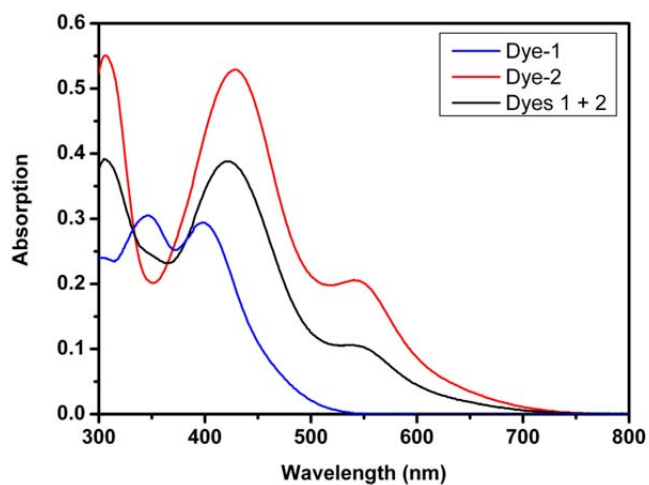


Figure 3. UV-vis absorption spectra of dye-1 (1.0×10^{-5} M), dye-2 (1.0×10^{-5} M) and the mixture of dye-1 and dye-2 (0.5×10^{-5} M each) in DMSO solution.

The solid-state absorption of thin films of TiO_2 nanoparticles on FTO glass coated with dye-1, dye-2 and dye mixture are shown in Figure 4, whereas the pictures of the dyed-electrodes and dyed particles are given in Figure 5.

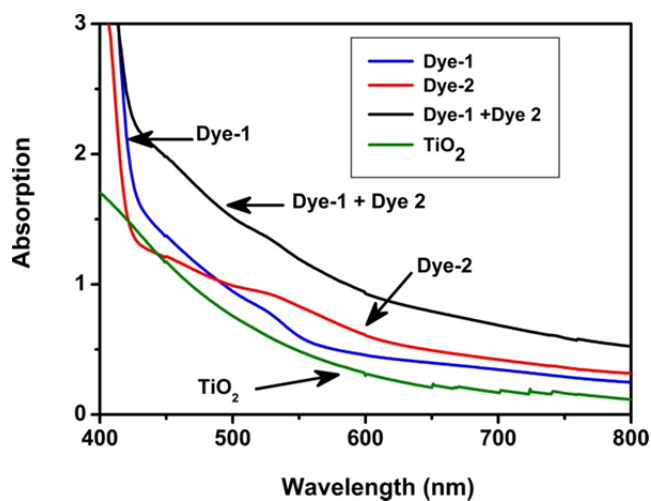


Figure 4. UV-vis spectra of different active layers obtained by dye adsorption on TiO_2 nanoparticles compared with the pristine TiO_2 .



Figure 5. Images of various dye coated TiO_2 thin films on FTO glass (top) and dyed TiO_2 nanocrystals (bottom).

A detailed description of dye-coating is given in the experimental part. In all the three cases, the amount of dyes used to absorb onto a definite amount of nanocrystals (75 mg) was completely adsorbed and the supernatant solution was colourless. As absorbed on titania, the absorption peaks of Ru-TPA-NCS and TPD dyes are blue shifted and exhibit broadened spectrum compared to those in DMSO solution. This implies the formation of dye aggregates on TiO_2 surface. However for the dye mixture, the absorption bands are not clearly visible owing to broadened absorption in 300-600 nm region. The broadened absorption spectra on TiO_2 surface can enhance the light harvesting ability. The most striking feature of this dye adsorption method is the ability to incorporate high amounts of dyes onto the TiO_2 surface. In a conventional liquid electrolyte DSSC, the reported adsorbed dye amount is in the range of 10^{16-19} molecules per cm^2 ,^{2, 27-28} however in our case the adsorbed dye amount is in the range of 10^{20-21} molecules per cm^2 which is roughly two orders of magnitude higher than the reported adsorbed dye amounts on mesoporous TiO_2 thin films. As explained above, the co-adsorption or multi-adsorption of the dyes on TiO_2 electrodes led to an efficient light harvesting over a wide spectrum region covering the whole UV-visible part which is a desirable feature for solar cells.

The power conversion efficiencies of single dye and multichromophore sensitized photovoltaic devices are shown in Figure 6. For these experiments, spiro-OMeTAD concentration was kept at 282 mg mL^{-1} and $170 \text{ }\mu\text{L}$ of the HC solution was mixed with 60 mg of dyed- TiO_2 . This results in a TiO_2 :spiro-OMeTAD ratio of 1 : 0.8 (wt/wt). The solar cell with dye-1 shows J_{sc} of 0.76 mA cm^{-2} , V_{oc} of 750 mV, FF of 45 % and 0.26 % efficiency, while devices using dye-2 shows J_{sc} of 0.64 mA cm^{-2} , V_{oc} of 620 mV, FF of 59 % and 0.23 % efficiency. The multi-dye sensitized device shows J_{sc} of 1.46 mA cm^{-2} , V_{oc} of 715 mV, FF of 51 % and an efficiency of 0.54 %.

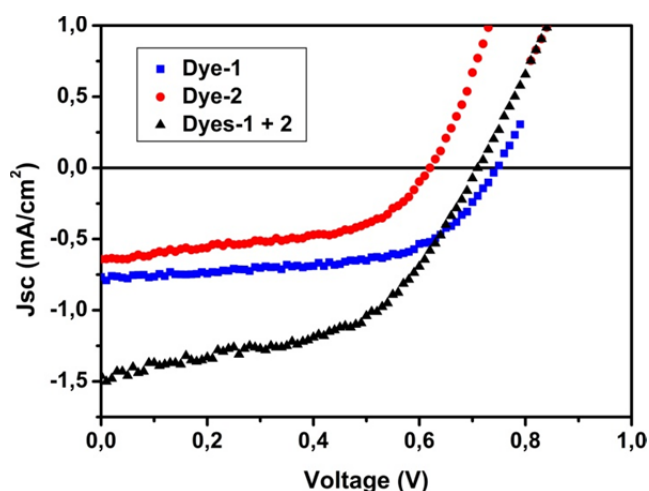


Figure 6. IV characteristics of devices for dye-1, dye-2 and for the dye mixture at illumination intensity of 100 mW cm^{-2} at AM 1.5 G condition. The TiO_2 :spiro-OMeTAD composition is 1 : 0.8 (wt/wt).

It is clearly evident that the efficiency and J_{sc} of the multi-dye sensitized solar cell are equal to or higher than the collective efficiencies and short-circuit current densities of the individual solar cells, respectively. The most striking feature of multi-sensitized solar cell is that it adds up the currents of the individual contributing cells as if in a parallel connected tandem cell. Thus the feasibility of efficient multichromophore light harvesting is demonstrated here. For the sequentially layer-wise deposited devices (see Figure 1b), we observed a similar performance improvement (J_{sc} of 1.62 mA cm^{-2} , V_{oc} of 710 mV, FF of 52 % and an efficiency of 0.59 %). This clearly supports the adaptability of the fabrication method described here towards tandem solar cells. Even though the absolute device efficiency reported in these first results is not very high compared to reported values in solid-state hybrid devices, the photovoltaic performance can be improved further as described below.

The IPCE spectra of devices with single dye and multi-dyes plotted as a function of excitation wavelength are presented in Figure 7. For the individual dye devices, the photocurrent action spectra were found to match the absorption spectra of the individual dyes. The Ru-TPA-NCS dye device shows the maximum value of IPCE at 550 nm and TPA-dye device shows the maximum IPCE at 430 nm which corresponds to the characteristic absorption of Ru-TPA-NCS and TPD dyes respectively. Similarly, for the multichromophore-sensitized device, the photocurrent action spectrum was found to match the absorption spectra of the mixtures of the two dyes with two maximum IPCE values at 550 nm and 430 nm. It is also clearly noticeable that

multichromophore-sensitized device exhibits higher IPCE in the 300-600 nm region than any single-dye sensitized devices though the adsorbed amount of each dye is only half the amount in multichromophore-sensitized device. Such a cooperative effect can be assigned to effective compact coverage of the TiO_2 surface by the presence of more dye molecules and the enhanced charge injection due to formation of dye aggregates. This shows that the multi-sensitization using two dyes investigated here extended the spectral response to the UV and visible domains and consequently enhanced the photocurrent and photovoltaic performance. The advantage using this method is that it has the potential to incorporate several dyes in a single layer electrode to cover the whole UV-visible-IR region.

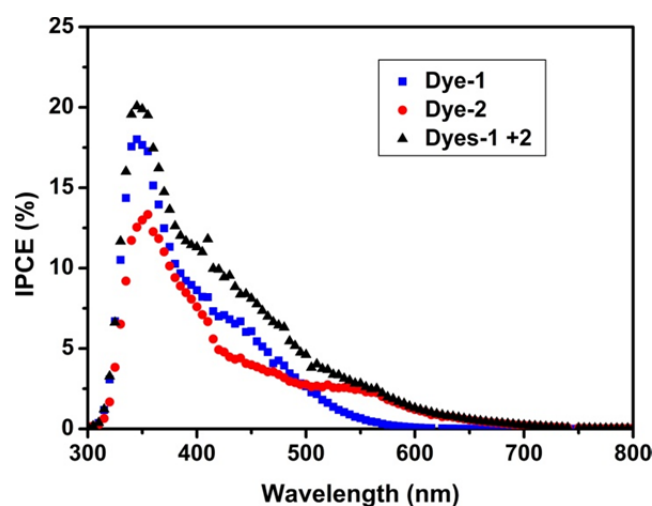


Figure 7. IPCE spectra of devices with individual dye-1, dye-2 and dye mixture for the active layer prepared containing a TiO_2 :spiro-OMeTAD composition of 1:0.8 (wt/wt).

We observed that the solar cell performance is highly dependent on the weight ratio of TiO_2 :spiro-OMeTAD. This can be expected since the composition decides the charge transfer and charge transport efficiencies. Especially the charge percolation *via* the nanocrystals in a nanocrystals-organic blend depends on the connectivity of the particles. The *IV* characteristic of the solar cells for different TiO_2 : spiro-OMeTAD ratios in the blend are shown in Figure 8 and Table 1. It can be observed that the best solar cell performance was obtained when the TiO_2 : spiro-OMeTAD ratio is equal to 1:0.6 and observed V_{oc} , J_{sc} , FF and efficiency are 645 mV, 2.1 mA cm^{-2} , 47 % and 0.65 % respectively.

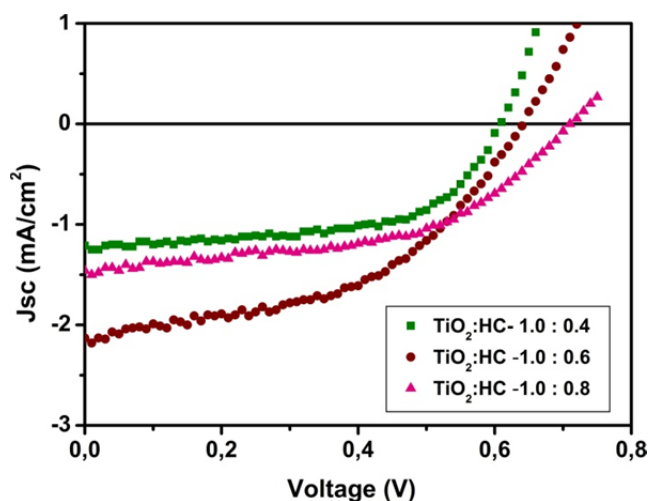


Figure 8. IV characteristics of devices with a dye mixture for the variation of TiO_2 : spiro-OMeTAD ratios (wt/wt); (■) 1.0: 0.4, (●) 1.0: 0.6 and (▲) 1.0:0.8.

Table 1. Device parameters for solar cells with different compositions of TiO_2 :spiro-OMeTAD (wt/wt).

TiO_2 :spiro-OMeTAD (wt/wt)	Voc [V]	Jsc [mA cm ⁻²]	FF [%]	η [%]
1:0.8	0.71	1.46	51	0.53
1:0.6	0.64	2.13	47	0.65
1:0.4	0.60	1.14	57	0.39

It is further interesting to study the bulk morphology of the active layer prepared by blending dyed- TiO_2 and HC under ambient conditions. To study especially the distribution of dyed- TiO_2 particles in the blended system, we investigated the cross-sections of blended devices by SEM. Figure 10 shows the SEM images of these systems with the different TiO_2 :spiro-OMeTAD ratios (Figure 10a-c) and for the purpose of comparison, we have included the SEM of the double layer device in Figure 10d as well. In all cases, the HC completely covers the dyed- TiO_2 nanoparticles in the blended system as shown in Figure 10a-c for TiO_2 :spiro-OMeTAD ratios of 1:0.4, 1:0.6 and 1:0.8, respectively. It is evident that the interconnections of the TiO_2 particles are different for different amounts of spiro-OMeTAD used. Analyses of the cross section SEM images of different TiO_2 :spiro-OMeTAD ratios revealed that more space is filled by the spiro-OMeTAD in the case of high spiro-OMeTAD amount (Figure 10c) resulting in dismal contact between TiO_2 particles that leads to inefficient electron transport. However, when the spiro-OMeTAD concentration is low (Figure 10a), space is filled mostly by TiO_2 particles giving better electron paths, but less amount of spiro-OMeTAD may cause weak charge generation and negatively influences the hole

transport. As mentioned earlier, thus the best solar cell performance was observed for the TiO_2 : spiro-OMeTAD ratio of 1:0.6 and as shown in Figure 10b, packing of TiO_2 particles and amount of spiro-OMeTAD are balanced here, which facilitates an optimum device performance. Still an improved percolation *via* interconnected particles is not yet achieved, which requires additional engineering methods such as pressing or lamination. It is common that in conventional dye-sensitized devices, a mesoporous layer is fabricated at high temperature (400-500 °C) and the dye is adsorbed afterwards and finally spiro-OMeTAD is filled in the pores of the mesoporous TiO_2 electrode. Pore-filling of spiro-OMeTAD is a common problem in these devices and incomplete filling of HC in pores resulted in lower solar cell performance and poor dye regeneration leading to dye degradation.²⁹⁻³² On the other hand, the blended system we described in this investigation does not suffer from this bottleneck.

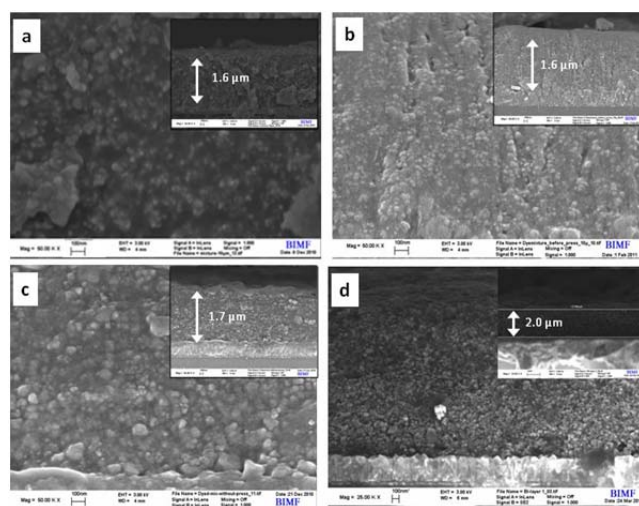


Figure 9. Cross sectional SEM images of solar cells with different TiO_2 :spiro-OMeTAD (wt/wt) compositions of (a) 1.0 : 0.4, (b) 1.0 : 0.6, (c) 1.0 : 0.8 and (d) cross sectional image of bi-layer device.

The above observations suggest the importance of having optimum TiO_2 :spiro-OMeTAD ratio to facilitate charge percolation and good device performance. Despite the fact that we could achieve an efficient interface area by blending the HC and the dyed TiO_2 particles, it appeared that the limiting factor of these blended solar cells is the weak contact between TiO_2 particles which hinders smooth electron transport. To verify this hypothesis and to enhance electron transport, we introduced PCBM, an efficient organic electron transport material to the system. It is interesting to note that the introduction of PCBM to the blended system resulted in increase

in J_{sc} to 3.6 mA cm^{-2} from 2.1 mA cm^{-2} indicating enhanced electron transport (since the absorption due to PCBM is negligible).

Though, various types of new organic hole-conductors with higher charge carrier mobility have been reported recently, it is known that their difficulty in efficient pore-filling and wetting of the dyed-TiO₂ layer in conventional fabrication method of filling a porous titania layer hinders the real progress of the solid-state hybrid devices with new HCs. Hence the blended system described in this investigation opens up new venues for the exploration of various new HCs for solid-state hybrid devices. Additionally, since a blended system can be adopted very easily to introduce a second layer on top of the first device without disturbing the first layer, this method is more suitable for fabrication of monolithic hybrid tandem solar cells.

CONCLUSION

We have developed a facile method to fabricate multichromophore sensitized hybrid blend devices using a solution casting process that avoids high temperature sintering steps. Efficient charge separation, transport and collection could be achieved in this dyed-TiO₂-spiro-OMeTAD blend system. An advantage of this method is that desired amounts and compositions of complementary dye-coated titania powders can be loaded onto a single hybrid layer or in several sequential layers by placing them on top of each other without disturbing the previous deposited layers. In this way the light harvesting can be complementarily improved leading to additive contributions in current and efficiency. Thus there is a high potential for realization of monolithic tandem cells with complementary absorption using this fabrication method. We believe that the dyed-TiO₂/spiro-OMeTAD blend devices will be a promising method to harvest a wider range of solar spectra and the concept is applicable to any HCs. Insufficient contacts between TiO₂ particles still limits the electron transport that lowers the efficiency. We believe that this issue can be surmounted by introducing additional electron pathways to the system, by increasing the aspect ratio of the nanoparticles using nanorods/nanowires, by optimizing the composition of the blend and by additional engineering methods.

EXPERIMENTAL SECTION

Titanium(IV)bis(acetoacetonato)-di(isopropanoxylate) (TAA) (Aldrich), TiO_2 (P25 Degussa), spiro-OMeTAD (Merck) and PEDOT:PSS (Aldrich) were purchased and used as received. Glass substrates (Tec 8) covered with fluorine-doped tin oxide (FTO) layer having sheet resistances of 8Ω per square were purchased from Hartford Glass Co. Inc., Indiana, USA. The TiO_2 blocking layer (bl- TiO_2) was prepared by spray pyrolysis deposition technique and the method has been discussed in detail by Peng *et al.* and hence only a brief account is mentioned here.²² The TiO_2 precursor, TAA, diluted with ethanol to a concentration of 0.2 M was used as the spraying solution and the pyrolysis was carried out at 400 °C. After the required number of spraying cycles under optimized conditions were done, the substrates were annealed at 400 °C for another hour before cooling down to room temperature. The substrates were kept in an inert atmosphere for further layer preparation. A similar compact blocking layer may also be prepared under low temperatures using published methods in literature.^{23, 24}

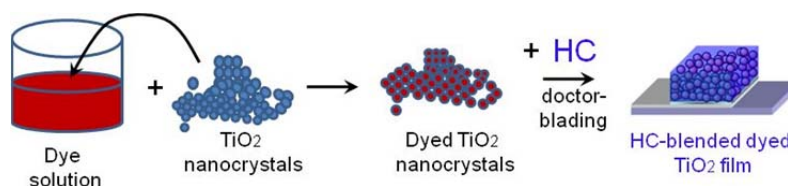


Figure 10. Schematic sketch of the fabrication steps of active layer of the solid-state hybrid blend solar cell at room temperature.

For multichromophore dye adsorption, two methods were employed; in the first case, dyes were adsorbed on TiO_2 particles separately and the dyed particles were mixed later. In the second case, a mixture of dyes was adsorbed on TiO_2 particles simultaneously. In both cases, similar solar cell efficiencies were observed. Therefore, to keep the fabrication method identical for all the experiments, we used the second method for the fabrication and the results from these are discussed in details as described below. The syntheses of dye-1, (*E*)-2-cyano-3-(4-((4-methoxyphenyl)(4'-((4-methoxyphenyl) (phenyl)amino) biphenyl -4-yl)amino) phenyl) acrylic acid [TPD-dye] and dye-2, *cis*-di(thiocyanato)(2,2'-bipyridyl-4,4'-dicarboxylic acid)-(2,2'-bipyridyl-4,4'-bis(vinyl triphenylamine) ruthenium(II) [Ru-TPA-NCS] have been described elsewhere.^{25, 26} Dye-2 was dissolved in an equal mixture of *tert*-butanol and acetonitrile, while for dye 1, the same solvent mixture was used with the addition of 10 % DMSO. For individual dye adsorption,

75 mg of TiO_2 powder was mixed with 7.5 mL of 0.5 mM solution of dye-1 or dye-2 separately. For multichromophore sensitization, 75 mg of TiO_2 powder was mixed with a dye mixture containing equimolar amounts of dye 1 and dye 2 in 7.5 mL of 0.5 mM concentration. All the suspensions were stirred well for dye adsorption for one hour and filtered to obtain dyed- TiO_2 nanocrystals. After the physisorbed dye molecules were rinsed away by washing the dyed- TiO_2 powder by the same solvent mixture, the samples were subsequently dried in air. To get pastes suitable for doctor-blading, 60 mg of the respective dyed- TiO_2 was stirred with 170 μL HC solution (containing additives) for 1-2 hours and the final paste was applied on the TiO_2 -coated FTO substrates. 140 μL of HC in chlorobenzene solution contain 48 mg of spiro-OMeTAD, 6 μL of *tert*-butylpyridine (tbp) and 5.1 μL of *N*-Lithiofluoromethane sulfonamide (Li salt). Li salt solution was normally prepared separately by dissolving 17 mg of *N*-Lithiofluoromethane sulfonamide in 100 μL of acetonitrile. This composition of the HC is maintained, but for optimization of solar cell performance, the concentration was varied. For obtaining randomly dyed- TiO_2 thin films as shown in Figure 1a, a mixture of dyes was adsorbed on TiO_2 particles simultaneously and mixed with HC as explained earlier. To fabricate layer-wise devices (Figure 1b), dye-1 coated TiO_2 -HC blend was first doctor-bladed on FTO glass and dried followed by dye-2 coated TiO_2 -HC blend. On top of the active layer, a hole injection and smoothening layer of PEDOT:PSS was spin-coated. As a final step, 40 nm Au-layer was vapor-deposited by sublimation in a vacuum chamber BA 510 type from Balzers (Lichtenstein) under vacuum with the help of a mask with active surface of 0.12 cm^2 .

The photovoltaic current–voltage measurements were carried out by a Keithley 6517 Source-Measure unit under AM 1.5 G conditions (Solar simulator-A grade from Newport). The intensity of the light was calibrated with a standard Si-reference cell from the Fraunhofer Institut für Solare Energiesysteme (ISE), Freiburg as 100 mW cm^{-2} . All efficiency values reported in this work were not corrected by the spectral mismatch factor. The IPCE values were measured using a lock-in amplifier (SR830, Stanford Research Systems) with a current preamplifier (SR570, Stanford Research Systems) under short-circuit conditions after illuminating the devices with monochromatic light from a Xenon lamp passing through a monochromator (Spectra-model). UV-vis spectra were recorded with a Hitachi 3000 spectrometer. Surface morphology of TiO_2 nanoparticles were examined using LEO 1530 Gemini field emission scanning electron microscope (FE-SEM).

ACKNOWLEDGMENT

Jayasundera Bandara would like to acknowledge the financial support from the NRC grant (Grant No. 07-46) and Alexander von Humboldt Foundation. We also acknowledge financial support from DFG (SFB 840).

BIBLIOGRAPHY

- 1 H. J. Snaith, A. J. Moule, C. Klein, K. Meerholz, R. H. Friend, M. Grätzel, *Nano Letters*, **2007**, 7, 3372-3376.
- 2 S. Kolemen, Y. Cakmak, S. Erten-Ela, Y. Altay, J. Brendel, M. Thelakkat, E. U. Akkaya, *Organic Letters*, **2010**, 12, 3812-3815.
- 3 C. S. Karthikeyan, M. Thelakkat, *Inorganica Chimica Acta*, **2008**, 361, 635-655.
- 4 W. J. E. Beek, M. M. Wienk, R. J. Janssen, *Advanced Materials*, **2004**, 16, 1009-1013.
- 5 J. Boucle, P. Ravirajana, J. Nelson, *Journal of Materials Chemistry*, **2007**, 17, 3141-3153.
- 6 W. U. Huynh, J. J. Dittmer, A. P. Alivisatos, *Science*, **2002**, 295, 2425-2427.
- 7 S. D. Oosterhout, M. M. Wienk, S. S. van Bavel, R. Thiedmann, L. J. A. Koster, J. Gilot, J. Loos, V. Schmidt, R. A. J. Janssen, *Nature Materials*, **2009**, 8, 818-824.
- 8 H. C. Leventis, S. P. King, A. Sudlow, M. S. Hill, K. C. Molloy, S. A. Haque, *Nano Letters*, **2010**, 10, 1253-1258.
- 9 A. Islam, H. Sugihara, M. Yanagida, K. Hara, G. Fujihashi, Y. Tachibana, R. Katoh, S. Murata, H. Arakawa, *New Journal of Chemistry*, **2002**, 26, 966-968.
- 10 M. Guo, P. Diao, Y.J. Ren, F. Meng, H. Tian, S.-M. Cai, *Solar Energy Materials and Solar Cells*, **2005**, 88, 23-35.
- 11 J. Yum, E. Baranoff, S. Wenger, Md. K. Nazeeruddin, M. Grätzel, *Energy and Environmental Science*, **2011**, 4, 842-857.
- 12 A. Islam, A., H. Sugihara, H. Arakawa, *Journal of Photochemistry and Photobiology A: Chemistry*, **2003**, 158, 131-138.
- 13 T. Funaki, M. Yanagida, N. Onozawa-Komatsuzaki, K. Kasuga, Y. Kawanishi, H. Sugihara, *Chemistry Letters*, **2009**, 38, 62-63.
- 14 R.Y. Ogura, S. Nakane, M. Morooka, M. Orihashi, Y. Suzuki, K. Noda, *Applied Physics Letters*, **2009**, 94, 073308-073308-3.
- 15 M. Guo, P. Diao, Y.J. Ren, F. Meng, H. Tian, S. M. Kai, *Solar Energy Materials and Solar Cells*, **2005**, 88, 23-35.
- 16 K. Sayama, S. Tsukagoshi, T. Mori, K. Hara, Y. Ohga, A. Shinpou, Y. Abe, S. Suga, H. Arakawa, *Solar Energy Materials and Solar Cells*, **2003**, 80, 47-71.
- 17 K. Lee, S. W. Park, M. J. Ko, K. Kim, N. G. Park, *Nature Materials*, **2009**, 8, 665-671.
- 18 W. Kubo, A. Sakamoto, T. Kitamura, Y. Wada, S. Yanagida, *Journal of Photochemistry and Photobiology A: Chemistry*, **2004**, 164, 33-39.
- 19 M. Dürr, A. Bamedi, A. Yasuda, G. Nelles, *Applied Physics Letters*, **2004**, 84, 3397-3399.
- 20 M. Murayama and T. Mori, *Thin Solid Films*, **2008**, 516, 2716-2722.
- 21 M.J. Scott, J.J. Nelson, S. Caramori, C.A. Bignozzi, C.M. Elliott, *Inorganic Chemistry*, **2007**, 46, 10071-10078.
- 22 B. Peng, G. Jungmann, C. Jäger, D. Haarer, H.-W. Schmidt, M. Thelakkat, *Coordination Chemistry Reviews*, **2004**, 248, 1479-1489.
- 23 S. Cho, K. Lee, A. J. Heeger, *Advanced Materials*, **2009**, 21, 1941.
- 24 M. R. Lilliedal, A. J. Medford, M. V. Madsen, K. Norrman, F. C. Krebs, *Solar Energy Materials and Solar Cells*, **2010**, 94, 2018.
- 25 C.S. Karthikeyan, H. Wietasch, M. Thelakkat, *Advanced Materials*, **2007**, 19, 1091-1095.

- 26 K. Gräf, M. A. Rahim, S. Das, M. Thelakkat submitted to *Energy & Environmental science*
- 27 A. Peic, D. Staff, T. Risbridger, B. Menges, L.M. Peter, A.B. Walker, P.J. Cameron, *Journal of Physical Chemistry C*, **2011**, 115, 613-619.
- 28 K.-J. Hwang, S.-H. Jung, D.-W. Park, S.-J. Yoo, J.-W. Lee, *Current Applied Physics*, **2010**, 10, 184-186.
- 29 I.-K. Ding, N. Tétreault, J. Brillet, B. E. Hardin, E. H. Smith, S. J. Rosenthal, F. Sauvage, M. Grätzel, M. D. McGehee, *Advanced Functional Materials*, **2009**, 19, 2431-2436.
- 30 L. Qi, J. D. Sogge, *Journal of the American Ceramic Society*, **2009**, 92, 1921-1925.
- 31 H. Han, U. Bach, Y.-B. Cheng, R.A. Caruso, *Applied Physics Letters*, **2007**, 90, 213510-213510-3.
- 32 L. Schmidt-Mende, M. Grätzel, *Thin Solid Films*, **2006**, 500, 296-301.

Chapter 7

EFFICIENT PANCHROMATIC CO-SENSITIZATION OF SOLID-STATE DYE-SENSITIZED SOLAR CELLS USING TRIPHENYLDIAMINE AND SQUARAIN SENSITIZERS

Katja Gräfe^[a], Moochikkadavath A. Rahim^[b], Suresh Das^[b] and Mukundan Thelakkat^{[a]}*

^[a] Department of Macromolecular Chemistry I, Applied Functional Polymers, Universität Bayreuth, Universitätsstr. 30, 95440 Bayreuth, Germany.

Fax: +49 921 55 3206

E-mail: Mukundan.Thelakkat@uni-bayreuth.de

^[b] Photosciences and Photonics Section, Chemical Science and Technology Division, National Institute for Interdisciplinary Science and Technology (CSIR), 695019 Trivandrum, India.

ABSTRACT

We address panchromatic response of solid-state dye-sensitized solar cells (SDSCs) by co-sensitization with two complementary absorbing sensitizers, viz. a triphenyldiamine and an unsymmetrical squaraine dye. The aggregation behaviour of the squaraine sensitizer was studied by steady-state UV/vis spectroscopy in solution as well as in the adsorbed state on mesoporous TiO₂ films. It was observed that the squaraine forms H- and J-aggregates, both in solution and adsorbed on TiO₂. Besides, the squaraine shows a pronounced negative solvatochromism in solution. The squaraine and the triphenyldiamine compound were used as sensitizers for single-dye and co-sensitized SDSCs. The performance of the SDSCs was optimized regarding the dyeing solvent, chemisorption time, and the thickness of the mesoporous layer. The best result was obtained for a co-sensitized SDSC after chemisorption for 3 h from a tert-butanol/acetonitrile solution on a 1.4 μm thick mesoporous TiO₂ layer with Voc of 848 mV, Jsc of 5.86 mA/cm² and FF of 48.6 % resulting in an overall efficiency of 2.4 %. The external quantum efficiency studies clearly indicate that the monomer species as well as the H- and J- aggregates contribute to the current generation.

INTRODUCTION

The near-UV and visible radiation up to 750 nm accounts for more than 50 % of the whole incident solar power reaching the earth under air mass 1.5 global (AM 1.5 G) conditions.¹ Hence, sensitizers with excellent optical properties combining high extinction coefficients and the ability to absorb the whole near-UV/vis part of the sunlight are in demand for high efficient dye-sensitized solar cells (DSCs). Additionally, the dyes should carry strong electron-withdrawing anchoring groups and feature ideal electronic properties to enable charge injection to TiO₂ and dye regeneration by a hole conductor. To fulfil these key requirements with only one single dye is a very challenging task. A more straightforward approach is to combine two complementary absorbing sensitizers known to function effectively in DSCs. Among the large variety of efficient organic sensitizers for DSCs which include indolines,^{2, 3} perylenes⁴ and coumarines,⁵ dyes of the arylamine family⁶⁻⁸ and squaraine sensitizers^{9, 10} provide a perfect starting pair for panchromatic co-sensitization. Many of the organic sensitizers feature high extinction coefficients and a high structural variety providing the possibility for molecular design and tailoring the optical/electronic properties. Beyond that, they show ideal complementary absorption behaviour. Co-sensitization is a concept which can improve the performance of DSCs by a broadened response to the solar spectrum.^{11, 12} However, the combination of two dyes adsorbed on TiO₂ reduces the intensity of absorption of the individual dyes due to limitation in the available surface area. Additionally, the interplay between the sensitizers regarding intermolecular charge and energy transfer can affect the device performance in a positive or negative way.¹³ Besides, the aggregation behaviour of squaraines constitutes additional complex issues in using them in devices. Regarding DSCs this has not been examined so far in closer detail, but aggregation is believed to cause an adverse effect on the dye-sensitized solar cell performance. Therefore, the aggregation tendency is reduced by the usage of chenodeoxycholic acid (CDCA) as co-adsorbent which is usually used in very large amounts.¹⁴ This co-adsorbent occupies the TiO₂ surface without contributing to light absorption. In general, squaraine derivatives are able to form both H-aggregates and J-aggregates. This makes aggregation of squaraines an interesting phenomenon that has been studied in solution,¹⁵⁻¹⁸ films¹⁹ and also recently in squaraine/PC₆₁BM bulk heterojunctions.²⁰ Most of the reported dyes possess symmetrical structures, whereas for DSC applications an unsymmetrical push-pull structure is preferred.^{21, 22} However, the advantages of unsymmetrical squaraines over their symmetric analogues are still under discussion.²³

We have synthesised a triphenyldiamine sensitizer 2-cyano-3-(4-((4-methoxyphenyl)(4'-((4-methoxyphenyl)(phenyl)amino)-[1,1'-biphenyl]-4-yl)amino)phenyl)acrylic acid (denoted as TPD-dye) absorbing in the blue region and the unsymmetrical squaraine dye 4-((5-carboxy-1-ethyl-3,3-dimethyl-3H-indol-1-ium-2-yl)-methylene)-2-(5-(3,6-di-*tert*-butyl-9H-carbazol-9-yl)-thiophen-2-yl)-3-oxocyclobut-1-enolate (denoted as SQ-dye) absorbing in the red region. The structures are shown in Fig. 1. Details of the synthesis are provided in the ESI. The aggregation behaviour of SQ-dye was investigated thoroughly in solution and as adsorbed on TiO₂. It was observed that the SQ-dye is able to form both, H- and J-aggregates in solution as well as on adsorption on TiO₂. Finally, both TPD-dye and SQ-dye were applied as sensitizers for single-dye and co-sensitized SDSCs. It was observed that the performance of co-sensitized SDSCs surpasses the single-dye SDSCs. On the basis of detailed steady-state UV/vis studies, a clear assignment of the individual contribution from each species (monomer, H- and J-aggregates) to the external quantum efficiency could be made.

RESULTS AND DISCUSSION

Design principles and physical properties of the sensitizers. In general, triphenylamine and triphenyldiamine derivatives provide high extinction coefficients and absorb in the blue to green part of the electromagnetic spectrum. They feature suitable energy levels for efficient electron injection into the acceptor material TiO_2 and the regeneration by the solid hole transport material spiro-OMeTAD. We have synthesised a TPD-dye with additional methoxy groups in the *para*-positions of the phenyl groups to improve the stability against oxidative coupling compared to unsubstituted triphenylamines.²⁵ A cyanoacrylic acid group with a strong electron-withdrawing character was introduced as anchoring group. This guarantees an intimate contact between the sensitizer and the TiO_2 semiconductor by coordination onto the surface. This structural design also imports a push-pull system. TPD-dye shows two prominent absorption bands at 344 nm and 428 nm with extinction coefficients of $2.7 \times 10^4 \text{ M}^{-1} \text{ cm}^{-1}$ in dichloromethane (Fig. 2). By cyclic voltammetry measurements in solution (Fig. S1), TPD-dye proved to be highly stable against repeated oxidation and rereduction cycles with energy levels of -5.10 eV (HOMO) and -2.92 eV (LUMO) which are suitable for SDSC applications.

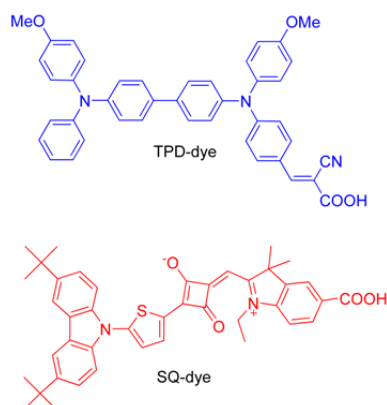


Figure 1. Molecular structures of the triphenyldiamine sensitizer TPD-dye and the squaraine sensitizer SQ-dye.

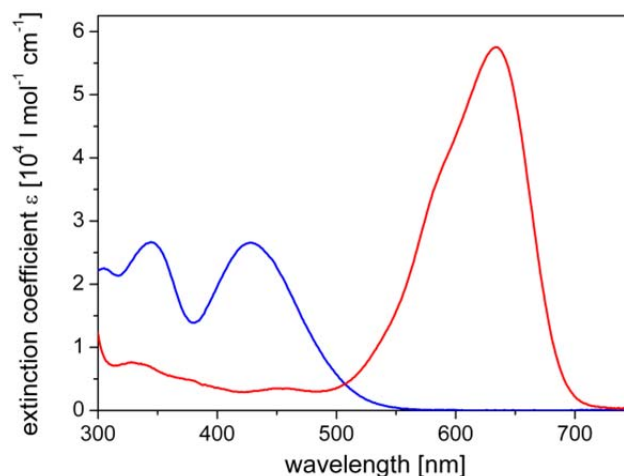


Figure 2. Absorption spectrum of TPD-dye (blue) and SQ-dye (red) in dichloromethane at a concentration of $1 \times 10^{-5} \text{ M}$.

In comparison to that, squaraines feature a resonance stabilized zwitterionic structure, classically comprising an electron deficient ring derived from squaric acid and two electron

donating groups.²⁶ In our synthetic strategy for an unsymmetrically substituted squaraine dye, adjacent to the four membered ring are a thiophene bridged carbazole and an indolium that carries a carboxylic acid anchoring group. This unsymmetrical structure of SQ-dye results in an inherent directionality that is assumed to promote an unidirectional flow of electrons upon photoexcitation.²¹ The extended π -electron system of SQ-dye combined with the typical intramolecular charge transfer characteristics of squaraines impart excellent optical properties. Thus, it exhibits an absorption in the red region with a maximum at 634 nm having an extinction coefficient of $5.7 \times 10^4 \text{ M}^{-1}\text{cm}^{-1}$ in dichloromethane. The energy values of the HOMO and LUMO levels of SQ-dye were determined by cyclic voltammetry in solution to be -5.21 eV and -3.33 eV, respectively (Fig. S2).

The combination of these sensitizers offers an elegant way to extend the absorption up to 700 nm with high extinction coefficients almost over the whole visible spectrum (Fig. 2). Apart from the good light harvesting properties, both sensitizers carry suitable anchoring groups and feature suitable energetic levels. The distinctive difference between them is the tendency towards aggregation. The affinity of TPDs to form aggregates is very low due to the propeller-shape conformation of the three aromatic rings at the nitrogen atoms.²⁷ This is in agreement with the steady-state absorption measurements of TPD-dye in solution and absorbed on TiO_2 . In both cases, we did not observe any indication for aggregation (Fig. S3, S4). In contrast to that, squaraines readily form aggregates.

Aggregation of SQ-dye in solution. Squaraines are particularly interesting as they form both H- and J-aggregates in solution and adsorbed on TiO_2 . The respective absorption bands corresponding to monomer and both aggregate types can clearly be distinguished by steady-state UV/vis spectroscopy. The reason for the pronounced shift in absorption is the rather high transition dipole moment of each squaraine molecule.^{20, 28} In accordance with the molecular exciton theory, this causes a large splitting of the excitonic states upon the interaction of transition dipoles.²⁰ Which type of aggregate is formed, depends solely on the arrangement of the transition dipoles relative to the molecule axis. A parallel orientation (“plane-to-plane”) of the molecules causes a blue-shift of the absorption (H-aggregates) and a collinear (“head-to-tail”) arrangement promotes a red-shift (J-aggregates) (Fig. S5).²⁹ In order to address the issue of aggregation, the absorption behaviour of SQ-dye was measured in different solvents (Fig. 3a). Depending on the solvent, the shape and the position of the absorption curve changed. To

interpret this, both aggregation and solvatochromism have to be taken into account. In a less polar solvent like toluene, the main absorption band was found at 653 nm and a shoulder at 610 nm. For this spectral absorption behaviour, there are three conceivable explanations: (1) the high-energy absorption band is a vibronic shoulder, (2) the shoulder can be assigned to H-aggregates and the main absorption band arises from the monomer species, (3) the shoulder can be assigned to the monomer species and the main absorption band to J-aggregates. The most straightforward way to clarify this is the spectroscopic characterisation of a dilution series (Fig. 3b). This was done in THF as solvent because SQ-dye shows a pronounced shoulder and features simultaneously a high solubility. It was observed, that with decreasing concentration the low-energy absorption band at 632 nm disappeared completely, whereas the high-energy shoulder at 606 nm increased. Hence, the high energy absorption band at 606 nm can be clearly assigned to the monomer species and the low-energy band to the formation of J-aggregates since it shows the typical red-shift relative to the monomer absorption band. In high polar solvents no aggregation was observed. By plotting the wavelength of the monomer absorption against the polarity of the solvent expressed by the $E_T(30)$ value, a linear behaviour with a hypsochromic shift upon increasing the solvent polarity was observed. This gave evidence for negative solvatochromism (Fig. S6) and indicates a more polar nature of the ground state compared to the excited state, *i.e.* a decrease of the dipole moment upon excitation.

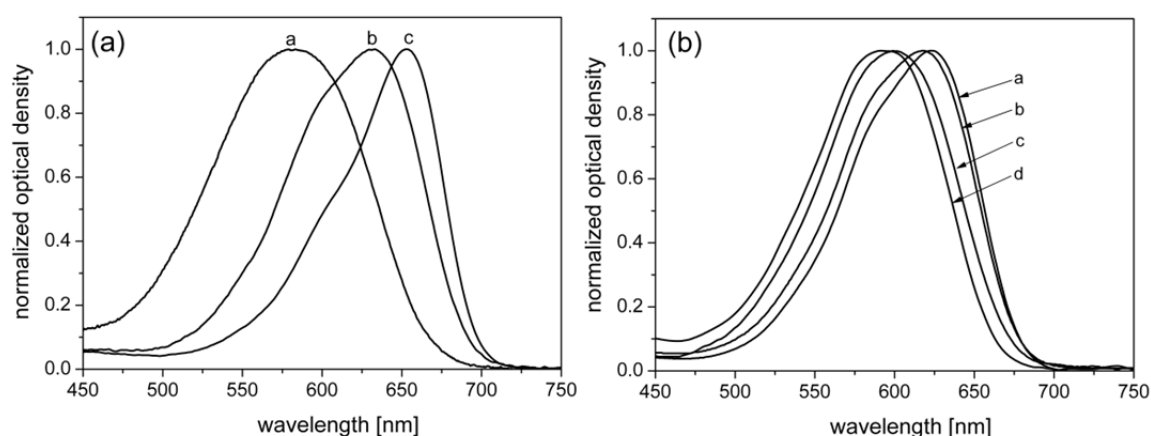


Fig. 3 (a) Normalized UV/vis absorption spectra of SQ-dye in a) MeOH, b) THF and c) Toluene. (b) Normalized dilution series of SQ-dye in THF at concentrations of a) 1×10^{-4} M, b) 1×10^{-5} M, c) 1×10^{-6} M, d) 1×10^{-5} M + ultrasonication for 30 min. The J-aggregate absorption band (632 nm) disappears with increasing dilution as the monomer absorption band (606 nm) gradually dominates the spectra. It can be further seen that the deaggregation process can be triggered by ultrasonication (black line). Here, even at a high concentration (1×10^{-5} M) aggregation can be completely removed.

In the course of these absorption studies in solution, there was no indication for the formation of H-aggregates. However, considering the fact that H-aggregates consist of a plane-to-plane alignment of molecules, this arrangement is supposed to dominate for molecules with little steric and electrostatic repulsion.³⁰ Hence, the short ethyl chain at the nitrogen-atom (low steric repulsion) and the unsymmetrical structure of SQ-dye with only one carboxylic acid group (low electrostatic repulsion) should enable the formation of H-aggregates. To induce H-aggregation, an increasing amount of lithium iodide was added to a solution of SQ-dye in toluene.

The absorption spectra of SQ-dye with varying concentration of LiI are depicted in Fig. 4. In SDSC devices, Li-salts are usually added to increase the conductivity of the hole transport material.³¹ Therefore, it was also interesting to understand the effect of dye aggregation in presence of Li-salts. With increasing amount of LiI the absorption of the J-aggregate band (653 nm) and the monomer shoulder (610 nm) were reduced, whereas a new blue-shifted absorption band appeared at 539 nm. An isosbestic point was observed at 587 nm. We attribute this high energy band to the formation of H-aggregates in the presence of LiI.

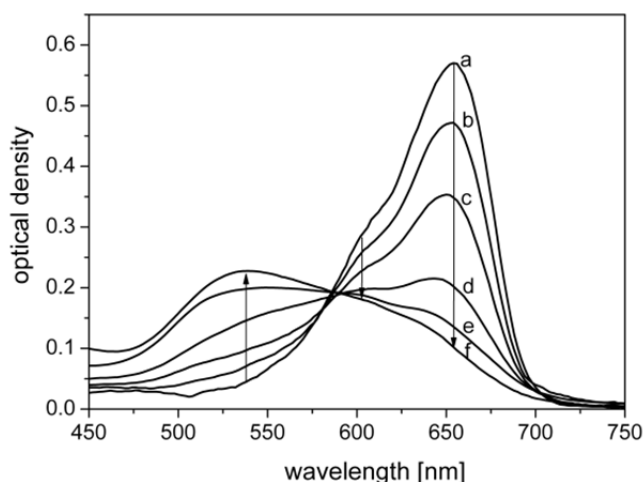


Figure 4. UV/vis absorption spectra of SQ-dye in toluene (1×10^{-5} M) upon addition of LiI (10 mg/ml in THF): a) without LiI, b) with 0.37 μmol LiI, c) with 0.75 μmol LiI, d) with 0.90 μmol LiI, e) with 1.50 μmol LiI, f) with 4.50 μmol LiI.

Aggregation of SQ-dye as adsorbed on TiO_2 . The aggregation behaviour of SQ-dye was further investigated in the chemisorbed state by anchoring on mesoporous TiO_2 (Fig. 5). The deconvolution of this absorption spectrum was done by three Gaussian functions: One that can be assigned to the H-aggregates (at 554 nm), one for the monomer species (at 594 nm) and one for the J-aggregates (at 642 nm). An additional fit function was used for background correction.

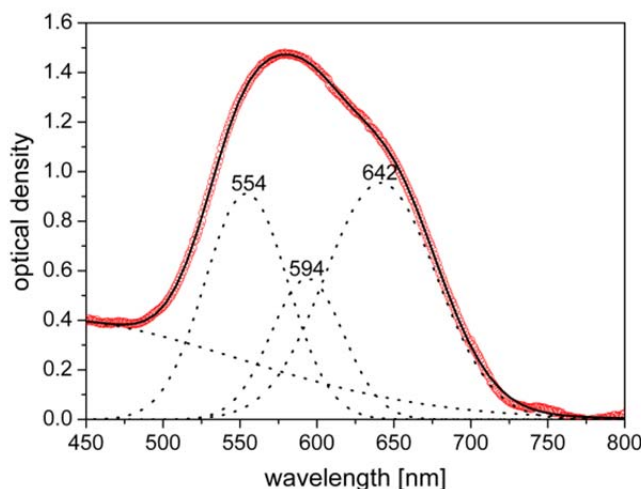


Figure 5. UV/vis spectrum of SQ-dye on mesoporous TiO_2 ($\sim 2.5 \mu\text{m}$) after 65 h chemisorption time from a dichloromethane solution (red, o symbols). The figure further shows the approximation of the absorption curve by a Gaussian multi-peak fitting function (black, dotted lines). The fitted curves centred at 554, 594 and 642 nm can be attributed to H-aggregates, monomer species and J-aggregates, respectively. A further fitting curve was introduced for background correction. The superposition of the fitted curves (black, solid line) matches perfectly with the measured spectrum of SQ (red, o symbols).

The assignments of the absorption bands was fully supported by a further chemisorption experiment using SQ-dye ($0.25 \times 10^{-4} \text{ M}$) and CDCA (10 mM) as co-adsorbent. CDCA is known to suppress/reduce aggregation.¹⁴ After chemisorption of SQ-dye for 30 min on TiO_2 only one broad monomer absorption band without any shoulder was observed at 600 nm (Fig. S7a). In our case, aggregation could only be completely suppressed for a very short time. After 2 h chemisorption time with CDCA a distinctive contribution of J-aggregation became apparent accompanied by a very low optical density due to co-adsorption of CDCA (Fig. S7b).

In order to elucidate the progress of aggregation on TiO_2 without any additives, the optical density of SQ-dye adsorbed from dichloromethane ($0.25 \times 10^{-4} \text{ M}$) was measured as a function of the chemisorption time. After only 15 min chemisorption time (Fig. 6, curve a) a distinct contribution of the monomer species (594 nm) and the J-aggregates (642 nm) was observed. This indicates that SQ-dye anchors on TiO_2 directly as both monomer and in an aggregated state. With increasing chemisorption time, the monomer species (at 594 nm) still dominates the spectra (Fig. 6, curve f). This is a rare and interesting behaviour.³² Generally, only monomers are adsorbed at an early stage and aggregation prevails with time due to the increasingly confined surface area. But here, initially monomer and J-aggregates are adsorbed from solution and even

after dipping overnight (16 h), the monomer species is dominating. However, a slight broadening of the absorption curve in the blue region after dipping overnight indicates the beginning growth of the H-aggregates (Fig. S10). This proves, after dipping overnight a high optical density as well as a high contribution of the monomer species can be reached without CDCA for this squaraine dye.

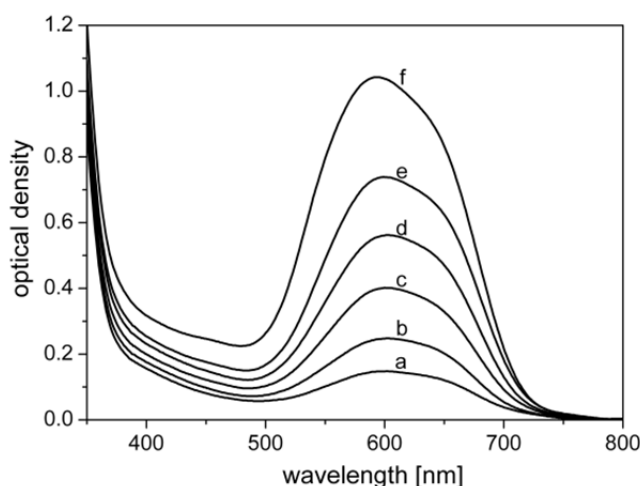


Figure 6. UV/vis absorption spectra of SQ-dye on TiO_2 ($\sim 2 \mu\text{m}$) after different chemisorption times. a) 15 min, b) 30 min, c), 65 min, d) 2 h, e) 3.5 h and f) 16 h.

Solar cell performance. The characteristics of the single-dye and co-sensitized SDSCs under different conditions are summarized in Table 1. The single-dye SDSCs (Table 1, entry 1 and 2) after overnight chemisorption show an efficiency of 0.80 and 0.87 % for TPD-dye and SQ-dye, respectively. In comparison, entries 3-5 for different times of chemisorption the beneficial effect of the co-sensitization can be clearly seen. Here, both SQ-dye and TPD-dye were mixed in a 1:1 molar ratio in dichloromethane (each $0.25 \times 10^{-4} \text{ M}$) and the TiO_2 electrodes were immersed in this solution for 1, 2, and 3 h, respectively. (Fig. 7) The absorption spectra as function of the chemisorption time show as expected an increase in optical density regarding the TPD-dye without any change in the position of the absorption maximum. In contrast to that, the SQ-dye absorption increases only up to 2 h. Upon longer chemisorption time, the optical density decreases again. This is associated with the ability of TPD-dye to desorb SQ-dye (Fig. S8). Further, the contribution of H-aggregates increases with chemisorption time. This is evident from the hypsochromic shift of the absorption maximum of the SQ-dye absorption band. The maximum overall optical density for the mixture is reached after 3 h.

Table 1. SDSC characteristics for different dyes, dipping conditions and thicknesses of the mesoporous TiO₂ layer.

entry	Dye	solvent, ^a dipping time	TiO ₂ [μm]	Voc [mV]	J _{sc} [mA/cm ²]	FF [%]	η [%]
1	TPD-dye	A, 16 h	2	715	2.30	48.6	0.80
2	SQ-dye	A, 16 h	2	715	2.82	43.3	0.87
3	Mix	A, 1 h	2	715	2.03	53.5	0.78
4	Mix	A, 2 h	2	765	2.12	55.2	0.90
5	Mix	A, 3 h	2	795	2.98	56.2	1.33
6	TPD-dye	B, 16 h	2	825	3.30	44.4	1.21
7	TPD-dye	B, 16 h	1.4	835	5.03	51.5	2.16
8	SQ-dye	B, 16 h	1.4	778	5.20	42.6	1.72
9	Mix	B, 3 h	1.4	848	5.86	48.6	2.41

^a Solvent A = dichloromethane/acetonitrile 9:1 vol/vol, B = acetonitrile/*tert*-butanol 1:1 vol/vol.

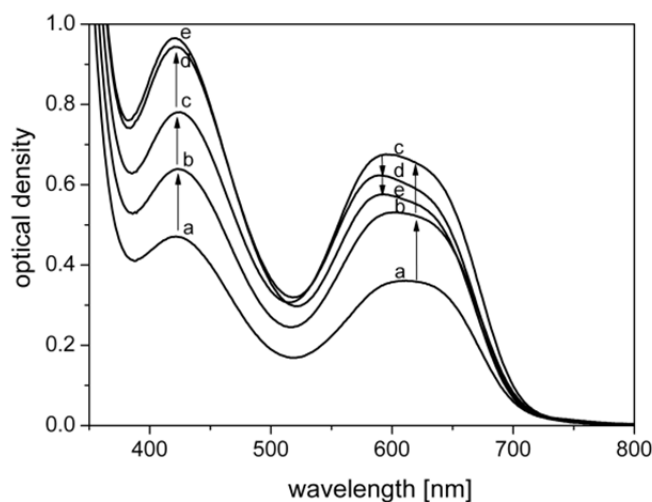


Figure 7. UV/vis absorption spectra of SQ-dye and TPD-dye on TiO₂ (~2 μm) during a simultaneous chemisorption process from a 1:1 mol/mol solution after dipping times of a) 30 min, b) 1 h, c) 2 h, d) 3 h, e) overnight.

For devices prepared with increasing dipping time, the voltage experienced a pronounced shift from 715 to 795 mV and the current increased from 2.03 to 2.98 mA/cm² resulting a maximum efficiency of 1.33 %. We attribute the improvement of the solar cell performance with increasing dipping time mainly due to an increase in the surface covering which reduces the recombination sites. Further improvement can be achieved by some optimizations. First, a change of the

chemisorption solvent from dichloromethane/acetonitrile 9:1 vol/vol (solvent A) to *tert*-butanol/acetonitrile 1:1 vol/vol (solvent B) caused an enhancement of the open-circuit voltage as well as of the short-circuit current density (compare entry 1 and 6). So far, the influence of the solvent used for chemisorption has not been exhaustively investigated. However, it is evident that an increase of the specific dielectric constant of the solvent decreases the amount of adsorbed dye significantly.³³ This is with the absorption data we obtained upon a change from solvent A to B (Fig. S9). Although the optical density is significantly reduced by the change of the solvent from A to B the performance of the solar cell is improved. We believe that this can be attributed to the beneficial effect of acetonitrile. Acetonitrile is known to adsorb on TiO₂ and passivate the (101) surface of anatase phase.³⁴ A further gain in the short-circuit current density could be reached by a reduction of the thickness of the mesoporous layer. The optimum thickness of SDSCs is always determined as a compromise between two opposing factors: light harvesting and charge collection. In our case the optimum was found at a thickness of 1.4 μm (compare entry 6 and 7, Fig. S11). Under these conditions the performance of the single-dye SDSCs could be enhanced to 2.16 (entry 7) and 1.72 % (entry 8) for TPD-dye and SQ-dye, respectively. The co-sensitized solar cell reached an efficiency of 2.41 % (entry 9). The photocurrent-voltage curve of this SDSC is shown in Fig. 8a.

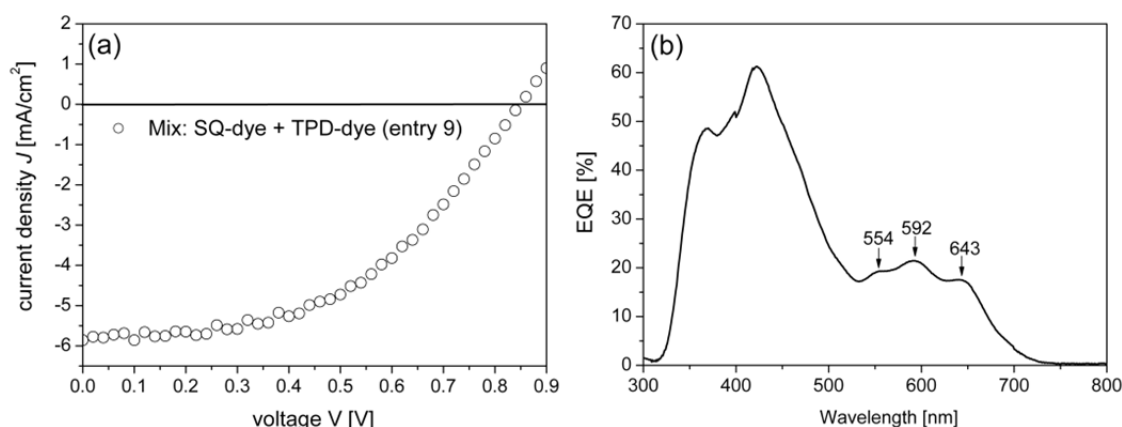


Figure 8. (a) Photocurrent-voltage characteristics of the highest efficient co-sensitized SDSC under AM 1.5 G conditions (100 mW/cm^2). (b) External quantum efficiency obtained with a $1.4 \mu\text{m}$ nanocrystalline TiO₂ thin film simultaneously co-sensitized with SQ-dye and TPD-dye.

The external quantum efficiency (EQE) of the best performing co-sensitized solar cell is shown in Fig. 8b. The contributions to the EQE at 368 can be assigned to energy transfer from the hole transport material spiro-OMeTAD and the contribution at 422 nm to the absorption of the TPD-

dye. Further contributions to the EQE (500-700 nm) are only understandable considering the previous aggregation studies. We observed three individual EQE maxima in the absorption region of the SQ-dye. In full agreement with absorption studies on TiO_2 , these maxima can be assigned to the contribution of H-aggregates (554 nm) the monomer species (592 nm) and J-aggregates (643 nm). It can be concluded that all three species contribute to the current generation.

CONCLUSION

In conclusion, we have shown that TPD-dye and SQ-dye provide a complementary absorption behaviour accompanied by high extinction coefficients. It was observed that the absorption of SQ-dye in different solvents exhibits a change in the shape of the absorption curve that can be attributed to aggregation with a monomer shoulder and a J-aggregate main absorption band in low polar solvents. H-aggregation could also be observed by addition of Li^+ salts. It was found, the spectral shift of the absorption curve is a result of negative solvatochromism. In the adsorbed state on TiO_2 , also three overlapping absorption bands could be identified for SQ-dye, which were attributed to H-aggregates, the monomer species and J-aggregates. On the basis of the steady-state UV/vis experiments it was possible to identify all contributions to the external quantum efficiency. The co-sensitized SDSCs using TPD-dye and SQ-dye surpassed the single-dye SDSCs and resulted under optimized conditions in an efficiency of 2.41 %.

EXPERIMENTAL SECTION

Details of the synthesis of TPD-dye and SQ-dye are provided in the ESI. Steady-state UV/vis spectra were recorded on a Hitachi U-3000 spectrophotometer. For the preparation of SDSCs, FTO-coated glass substrates (Pilkington, Tec 15) were partly etched, cleaned and covered with a compact blocking TiO₂ layer (134 nm).²⁴ The mesoporous layer was made by doctor blading of a TiO₂ paste (Solaronix, T20/SP) which was subsequently sintered. In order to reduce the thickness of the mesoporous layer, the paste was diluted with α -terpineol and the gap of the doctor blade was varied (Fig. S12). The thickness of the mesoporous layer was determined by a surface profilometer (Veeco, Dektak 150). The substrates were exposed to the dye solutions (0.25×10^{-4} M) for given time intervals. The stock solution for the solid hole transport layer contained 0.13 M spiro-OMeTAD, 0.02 M lithium salt LiN(SO₂CF₃)₂ and 0.23 M 4-*tert*-butylpyridine in chlorobenzene. Directly before the hole transport layer was prepared by spin coating (2500 rpm), the substrates were treated with acetonitrile (140 μ L) for 1 min and spun at 2500 rpm for 45 sec. The gold contacts were deposited under high vacuum using an electron-beam evaporator (BOC Edwards, Auto 306, FL 400). Current-voltage characteristics were measured under standard AM 1.5 G spectral conditions at an intensity of 100 mW/cm² using a setup equipped with a solar simulator (Newport-Oriel, 92250A-1000) and an electrometer (Keithley, Model 6517). The light source was regularly calibrated using a silicon solar cell (WPVS cell, ISE Call lab, Freiburg). For accuracy, the device area not covered by electrodes was removed and the devices were additionally equipped with a mask (active cell area: 0.20 cm²). External quantum efficiencies were measured with a PVE300 photovoltaic device characterisation system (Bentham) under white bias light.

ACKNOWLEDGMENT

We thank Department of Science and Technology, New Delhi and the Indo-European collaborative project, LARGECELLS for financial support. Research fellowship from UGC (R.M.K.A) and research grant from GAP:133339 are gratefully acknowledged.

BIBLIOGRAPHY

- 1 G. P. Smestad, F. C. Krebs, C. M. Lampert, C. G. Granqvist, K. L. Chopra, X. Mathew, H. Takakura, *Solar Energy Materials & Solar Cells*, **2008**, 92, 371-373.
- 2 H. J. Snaith, A. Petrozza, S. Ito, H. Miura, M. Grätzel, *Advanced Functional Materials*, **2009**, 19, 1810-1818.
- 3 X. Liu, W. Zhang, S. Uchida, L. Cai, B. Liu, S. Ramakrishna, *Advanced Materials*, **2010**, 22, E150-E155.
- 4 U. B. Cappel, M. H. Karlsson, N. G. Pschirer, F. Eickemeyer, J. Schöneboom, P. Erk, G. Boschloo, A. Hagfeldt, *Journal of Physical Chemistry C*, **2009**, 113, 14595-14597.
- 5 Z.-S. Wang, Y. Cui, Y. Dan-oh, C. Kasada, A. Shinpo, K. Hara, *Journal of Physical Chemistry C*, **2007**, 111, 7224-7230.
- 6 J. Bandara, K. Willinger, M. Thelakkat, *Physical Chemistry Chemical Physics*, **2011**, 13, 12906-12911.
- 7 S. Erten-Ela, J. Brendel, M. Thelakkat, *Chemical Physics Letters*, **2011**, 510, 93-98.
- 8 J. Burschka, A. Dualeh, F. Kessler, E. Baranoff, N.-L. Cevey-Ha, C. Yi, M. K. Nazeeruddin, M. Grätzel, *Journal of the American Chemical Society*, **2011**, 133, 18042-18045.
- 9 S. Das, K. G. Thomas, M. V. George, in: V. Ramamurthy, K. S. Schanze (Eds.), *Molecular and Supramolecular Photochemistry: Organic Photochemistry*, **1997**, vol. 1, pp. 467-517.
- 10 Y. Shi, R. B. M. Hill, J.-H. Yum, A. Dualeh, S. Barlow, M. Grätzel, S. R. Marder, M. K. Nazeeruddin, *Angewandte Chemie International Edition*, **2011**, 50, 6619-6621.
- 11 J.-H. Yum, S.-R. Jang, P. Walter, T. Geiger, F. Nüesch, S. Kim, J. Ko, M. Grätzel, M. K. Nazeeruddin, *Chemical Communications*, **2007**, 4680-4682.
- 12 D. Kuang, P. Walter, F. Nüesch, S. Kim, J. Ko, P. Comte, S. M. Zakeeruddin, M. K. Nazeeruddin, M. Grätzel, *Langmuir*, **2007**, 23, 10906-10909.
- 13 B. E. Hardin, A. Sellinger, T. Moehl, R. Humphry-Baker, J.-E. Moser, P. Wang, S. M. Zakeeruddin, M. Grätzel, M. D. McGehee, *Journal of the American Chemical Society*, **2011**, 133, 10662-10667.
- 14 J.-H. Yum, S.-J. Moon, R. Humphry-Baker, P. Walter, T. Geiger, F. Nüesch, M. Grätzel, M. d. K. Nazeeruddin, *Nanotechnology*, **2008**, 19, 424005-424011.
- 15 S. Das, K. G. Thomas, K. J. Thomas, V. Madhavan, D. Liu, P. V. Kamat, M. V. George, *Journal of Physical Chemistry*, **1996**, 100, 17310-17315.
- 16 A. J. McKerrow, E. Buncel, P. M. Kazmaier, *Canadian Journal of Chemistry*, **1995**, 73, 1605-1615.
- 17 S. Alex, M. C. Basheer, K. T. Arun, D. Ramaiah, S. Das, *Journal of Physical Chemistry A*, **2007**, 111, 3226-3230.
- 18 U. Mayerhöffer, F. Würthner, *Chemical Science*, **2012**, 3, 1215-1220.
- 19 O. P. Dimitriev, A. P. Dimitriyeva, A. I. Tolmachev, V. V. Kurdyukov, *Journal of Physical Chemistry B*, **2005**, 109, 4561-4567.
- 20 K. C. Deing, U. Mayerhöffer, F. Würthner, K. Meerholz, *Physical Chemistry Chemical Physics*, **2012**, 14, 8328-8334.
- 21 S. Alex, U. Sanathosh and S. Das, *Journal of Photochemistry and Photobiology A*, **2005**, 172, 63-71.

- 22 T. Geiger, S. Kuster, J.-H. Yum, S.-J. Moon, M. K. Nazeeruddin, M. Grätzel, F. Nüesch, *Advanced Functional Materials*, **2009**, 19, 2720-2727.
- 23 J. Park, C. Barolo, F. Sauvage, N. Barbero, C. Benzi, P. Quagliotto, S. Coluccia, D. Di Censo, M. Grätzel, M. K. Nazeeruddin, G. Viscardi, *Chemical Communications*, **2012**, 48, 2782-2784.
- 24 B. Peng, G. Jungmann, C. Jäger, D. Haarer, H.-W. Schmidt, M. Thelakkat, *Coordination Chemistry Reviews*, **2004**, 248, 1479-1489.
- 25 E. T. Seo, R. F. Nelson, J. M. Fritsch, L. S. Marcoux, D. W. Leedy, R. N. Adams, *Journal of the American Chemical Society*, **1966**, 88, 3498-3503.
- 26 S. Sreejith, P. Carol, P. Chithra, A. Ajayaghosh, *Journal of Materials Chemistry*, **2008**, 18, 264-274.
- 27 M. Malagoli, M. Manoharan, B. Kippelen, J. L. Brédas, *Chemical Physics Letters*, **2002**, 354, 283-290.
- 28 K. Yesudas, G. K. Chaitanya, C. Prabhakar, K. Bhanuprakash, V. J. Rao, *Journal of Physical Chemistry A*, **2006**, 110, 11717-11729.
- 29 F. Würthner, T. E. Kaiser, C. R. Saha-Möller, *Angewandte Chemie International Edition*, **2011**, 50, 3376-3410.
- 30 G. de Miguel, M. Ziólek, M. Zitnan, J. A. Organero, S. S. Pandey, S. Hayase, A. Douhal, *Journal of Physical Chemistry C*, **2012**, 116, 9379-9389.
- 31 H. J. Snaith, M. Grätzel, *Applied Physics Letters*, **2006**, 89, 262114-262113.
- 32 A. Ehret, L. Stuhl, M. T. Spitler, *Journal of Physical Chemistry B*, **2001**, 105, 9960-9965.
- 33 T. Ono, T. Yamaguchi, H. Arakawa, *Journal of Solar Energy Engineering*, **2010**, 132, 021101-021107.
- 34 F. Schiffrmann, J. VandeVondele, J. Hutter, A. Urakawa, R. Wirz, A. Baiker, *Proceedings of the National Academy of Sciences*, **2010**, 107, 4830-4833.

SUPPORTING INFORMATION

for the manuscript:

EFFICIENT PANCHROMATIC CO-SENSITIZATION OF SOLID-STATE DYE-SENSITIZED SOLAR CELLS USING TRIPHENYLDIAMINE AND SQUARINE SENSITIZERS

Katja Gräfe^[a], Moochikkadavath A. Rahim^[b], Suresh Das^[b] and Mukundan Thelakkat^{[a]}*

^[a] Department of Macromolecular Chemistry I, Applied Functional Polymers, Universität Bayreuth, Universitätsstr. 30, 95440 Bayreuth, Germany.

^[b] Photosciences and Photonics Section, Chemical Science and Technology Division, National Institute for Interdisciplinary Science and Technology (CSIR), 695019 Trivandrum, India.

Table of Contents

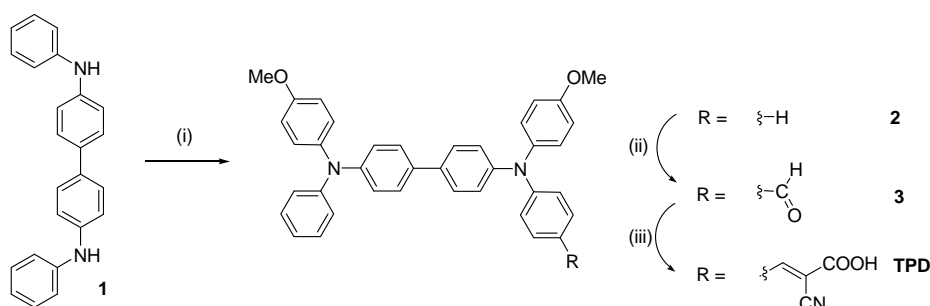
1. Synthesis and Characterisation of TPD-dye and SQ-dye
2. Cyclic Voltammetry Measurements of TPD-dye and SQ-dye
3. Characterisation by Steady-State UV/vis Measurements
 - 3.1 Absorption of TPD-dye in Solution and on TiO₂
 - 3.2 Influence of the Molecule Arrangement on the Absorption
 - 3.3 Solvatochromism of SQ-dye in Solution
 - 3.4 Absorption of SQ-dye on TiO₂
4. Thickness Optimization of the Mesoporous Layer
5. References

1. Synthesis and Characterisation of TPD-dye and SQ-dye

Methods. Proton nuclear magnetic resonance ($^1\text{H-NMR}$) data were recorded on a Bruker Avance 300 spectrometer at a transmitter frequency of 300 MHz or on a Bruker Avance 500 at a frequency of 500 MHz. The spectra were calibrated to the chemical shift of the respective solvent residue signal. Tetramethylsilane was used as internal standard. The chemical shifts are given in ppm. The abbreviations used for splitting patterns are s = singlet, sb = broad singlet, d = doublet, dd = doublet of doublets, m = multiplet. FAB mass spectra were obtained on a JEOL SX-120/DA6000 spectrometer using argon (6 kV, 10 mA) as the FAB gas.

Materials. All commercial available starting materials and reagents were used as received without further purification, except POCl_3 which was freshly distilled before use. Solvents used for precipitation and column chromatography were purified by distillation under ambient pressure. Column chromatography was performed on silica gel 60M (0.04-0.063 mm) by Macherey Nagel with the given eluents.

Synthesis of TPD-dye



Scheme S1. Synthetic route for TPD-dye. (i) 4-Iodoanisole, Na_2CO_3 , Cu, 18-crown-6, *o*-dichlorobenzene, reflux, 3 days, (ii) 1. DMF, POCl_3 , 1,2-dichloroethane, 80°C , 3 h, 2. $\text{Na}(\text{CH}_3\text{COO})$, ice water, r.t., overnight, (iii) cyanoacetic acid, piperidine, THF/MeOH (1:1 vol/vol), 40°C , 5 days.

Synthesis of **2¹.** N,N' -Bis(4-dimethoxyphenyl)- N,N' -diphenylbenzidine **2** was synthesised according to a published method¹ from N,N' -diphenylbenzidine **1** and 4-iodo-anisol with anhydrous potassium carbonate, copper powder and 18-crown-6 in *o*-dichlorobenzene (5.8 g, 70.5 %).

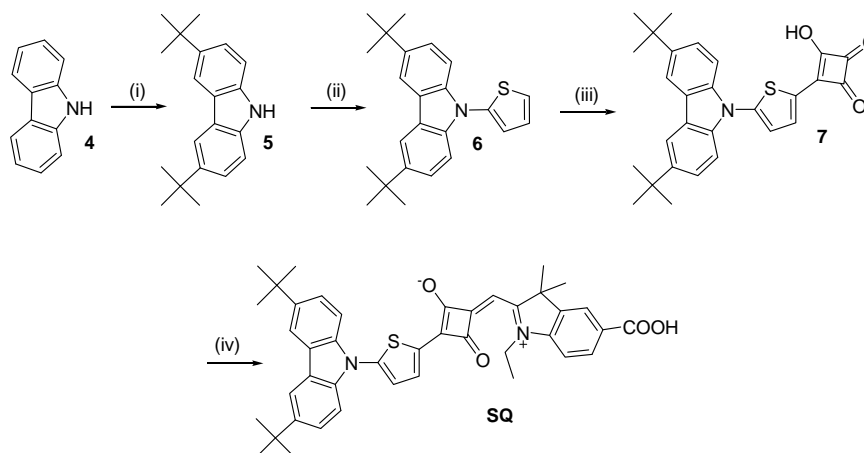
Synthesis of 3. Dimethylformamide (5 mL) was cooled to 0-5 °C and POCl₃ (0.50 g, 3.26 mmol) was added. The solution was stirred for 30 min at 0-5 °C and was then allowed to warm to room temperature. Compound **2** (2.60 g, 4.74 mmol) was dissolved in 1,2-dichloroethane (75 mL) and cooled to 0-5 °C. The first solution was slowly added to the second and the temperature was increased to 80 °C. The resulting solution was stirred at 80 °C for 3 h, cooled to room temperature and slowly poured into a well-stirred solution of Na(CH₃COO) (5.0 g) and ice water (50 mL). Stirring was continued overnight. The organic layer was separated, washed with water (3 x 100 mL), dried over Na₂SO₄ and the solvent was removed under reduced pressure. The pure product was isolated by column chromatography on silica gel with dichloromethane as eluent (1.50 g, 55 %).

¹H-NMR (300 MHz; acetone-d₆; Me₄Si): δ 3.82 (s, 3H), 3.85 (s, 3H), 6.90-7.15 (m, 13 H), 7.20-7.35 (m, 6H), 7.56 (d, 2H), 7.66 (d, 2H), 7.72 (d, 2H) and 9.82 (s, 1H).

Synthesis of TPD-dye. Compound **3** (1.50 g, 2.60 mmol) and cyanoacetic acid (1.55 g, 18.21 mmol) were dissolved in dry THF/MeOH (1:1, 80 mL) and piperidine (0.1 mL) was added. The solution was stirred at 40 °C for 5 days. The solvent was removed under reduced pressure. The crude product was dissolved in dichloromethane and washed with water (5 x 100 mL). After drying over Na₂SO₄, the product was purified by column chromatography using silica gel with toluene/MeOH (6:1) as eluent (1.20 g, 72 %).

¹H-NMR (300 MHz, DMSO-d₆, Me₄Si): δ 3.76 (s, 3H), 3.77 (s, 3H), 6.88 (dd, 2H), 6.90-7.00 (m, 9H), 7.06 (d, 2H), 7.14 (dd, 4H), 7.28 (dd, 2H), 7.55 (dd, 4H), 7.75 (d, 2H) and 7.85 (s, 1H).

Synthesis of SQ-dye



Scheme S2. Synthetic route for SQ-dye. (i) *t*-BuCl, ZnCl₂, MeNO₂, r.t., 2 h, (ii) 2-iodothiophene, *t*-BuONa, dioxane, 110 °C, 6 h, (iii) 1. 3,4-dichlorocyclobut-3-ene-1,2-dione, benzene, reflux, 6 h, 2. Et₃N, acetone, 5 % HCl, r.t., 6 h, (iv) 5-carboxy-1-ethyl-2,3,3-trimethyl-3H-indolium, benzene, butanol, quinoline, 100 °C, 8 h.

Synthesis of 5.² Carbazole **4** (5.0 g, 30 mmol), 150 mL nitromethane and ZnCl₂ (12.1 g, 90 mmol) were added to a three neck flask under argon atmosphere. *Tert*-butyl chloride (6.5 mL, 60 mmol) was added dropwise under stirring. The mixture was stirred at room temperature for 2 h and then hydrolysed with water (100 mL). The product was washed with water (2 x 150 mL), dried over anhydrous MgSO₄, and the solvent was removed under reduced pressure to yield the product as off-white solid (5.2 g, 92 %).

MS: *m/z* 279 (M⁺). ¹H-NMR (500 MHz, CDCl₃, Me₄Si): δ 1.45 (s, 18H), 7.32-7.34 (dd, 2H), 7.45-7.47 (dd, 2H), 7.85 (sb, 1H) and 8.08 (d, 2H) ppm.

Synthesis of 6.³ Compound **5** (1.00 g, 3.58 mmol), 2-iodothiophene (2.25 mL, 10.75 mmol), CuI (170 mg, 0.90 mmol), 1,2-*trans*-cyclohexdiamine (1.1 mL, 8.96 mmol) and *t*-BuONa (515 mg, 5.37 mmol) were dissolved in 1,4-dioxane (30 mL) and refluxed for 6 h. The pure product was separated using silica gel with 5 % chloroform-hexane as the eluent (0.80 g, 62 %).

MS: *m/z* 362.05 (M+1). ¹H-NMR (500 MHz, CDCl₃, Me₄Si): δ 1.46 (s, 18H), 7.15-7.16 (m, 3H), 7.33-7.35 (m, 1H), 7.35-7.39 (d, 2H), 7.47-7.49 (dd, 2H) and 8.10(s, 1H).

Synthesis of 7.^{4, 5} Squaric acid (3.00 g, 26 mmol) on reaction with thionyl chloride (6.20 g, 52 mmol) in dry benzene gave the squarilium chloride (3.16 g, 80 %). Squarilium chloride (830 mg, 5.53 mmol) and compound **6** (1.0 g, 2.77 mmol) were dissolved in dry benzene (50 mL) and refluxed for 6 h. After cooling, the reaction mixture was poured in to ice water (100 mL) and the two layers formed were separated. The organic layer was washed with water (50 mL), dried, and the solvent was removed under reduced pressure. The residue obtained was subjected to a column chromatography using silica gel with chloroform as eluent. The product obtained was immediately converted into the corresponding semisquaraine. The red precipitate was thus dissolved in dry acetone (30 mL) and triethylamine (0.5 mL) was added. After 6 h stirring at room temperature, the solvent was removed and the brown residue was taken up with water. The solution was filtered to remove any insoluble material. 5 % HCl was added dropwise till precipitation of a brown solid. The solid was collected and dried till constant weight (0.51 g, 40 %).

The compound was characterized only by FAB-Mass. MS: m/z 458 (M+1).

Synthesis of 5-carboxy-1-ethyl-2,3,3-trimethyl-3H-indolium.⁶ Glacial acetic acid (15 mL) was added to a mixture of 4-hydrazinobenzoic acid (1.0 g, 6.6 mmol), methyl isopropyl ketone (1.1 mL, 9.9 mmol), and sodium acetate (1.1 g, 13.2 mmol) in a round bottom flask fitted with a condenser. The brown suspension was refluxed for 8 h, and the solvent was removed under reduced pressure. The residue was redissolved into a clear solution using water and methanol (9:1). Insoluble material was filtered off. The filtrate was allowed to stand at room temperature, and the crystals of 2,3,3-trimethyl-3H-indole-5-carboxylic acid (0.94 g, 70 %) were collected by filtration.

¹H-NMR (500 MHz, CD₃OD, Me₄Si): δ 1.37 (s, 6H), 2.35 (s, 3H), 7.50 (d, 1H) and 8.00 (m, 2H).

2,3,3-Trimethyl-3H-indole-5-carboxylic acid (1.0 g, 4.9 mmol) and iodoethane (1.1 g, 7.4 mmol) were dissolved in acetonitrile (25 mL) and refluxed under argon for 10 h. The solvent was evaporated and the crude product was washed with diethyl ether three times (0.78 g, 68 %).

$^1\text{H-NMR}$ (500 MHz, DMSO- d_6 , Me_4Si): δ 1.53 (t, 3H), 4.45 (q, 2H), 8.07 (d, 1H), 8.15 (d, 1H) and 8.38 (s, 1H).

Synthesis of SQ-dye. Compound **7** (250 mg, 0.55 mmol) and 5-carboxy-1-ethyl-2,3,3-trimethyl-3H-indolium (200 mg, 0.86 mmol) were dissolved in a benzene/butanol (1:1) mixture and stirred well at 100 °C for 8 h. The solvents were removed under reduced pressure and the pure compound was separated using silica gel with chloroform/ methanol 95:5 as eluent (0.11 g, 30 %).

MS: m/z 671 ($M+1$). $^1\text{H-NMR}$ (500 MHz, CDCl_3 , Me_4Si): δ 1.46 (s, 18H), 1.53 (q, 3H), 1.90 (s, 6H), 4.34 (t, 2H), 6.405 (s, 1H), 7.29-7.31 (d, 1H), 7.40-7.09 (d, 1H), 7.51-7.53 (dd, 2H), 7.75-7.76 (d, 2H), 8.09 (s, 2H), 8.16-8.16 (d, 1H), 8.20 (s, 1H) and 8.22-8.24 (d, 1H).

2. Cyclic Voltammetry Measurements of TPD-dye and SQ-dye

Cyclic voltammetry on TPD-dye

Method. Cyclic voltammetry was performed under moisture- and oxygen-free conditions. A standard three-electrode assembly connected to a potentiostat (model 263A, EG&G Princeton Applied Research) was used at a scanning rate of 50 mV sec⁻¹. The working electrode was a Pt milli-electrode (model G0228, AMETEK Advanced Measurement Technology). A platinum wire in the respective solvent plus conducting salt (tetrabutylammonium hexafluorophosphate, 0.1 M) was used as counter electrode and the quasi-reference electrode consisted of an Ag wire in an AgNO₃/acetonitrile solution (0.1 M). Each measurement was calibrated with the internal standard ferrocene/ferrocenium. For the calculation of the energy levels, we used the following empirical relation:

$$E(\text{HOMO or LUMO}) = [-e(E_{1/2}^{1/2}(\text{x vs. Ag/AgNO}_3) - E_{1/2}^{1/2}(\text{Fc/Fc}^+ \text{ vs. Ag/AgNO}_3))] - 4.80 \text{ eV}.$$

The half wave potential of ferrocene/ferrocenium in dichloromethane was determined to be

$$E_{1/2}(\text{Fc/Fc}^+ \text{ vs. Ag/AgNO}_3) 0.10 \text{ V}.$$

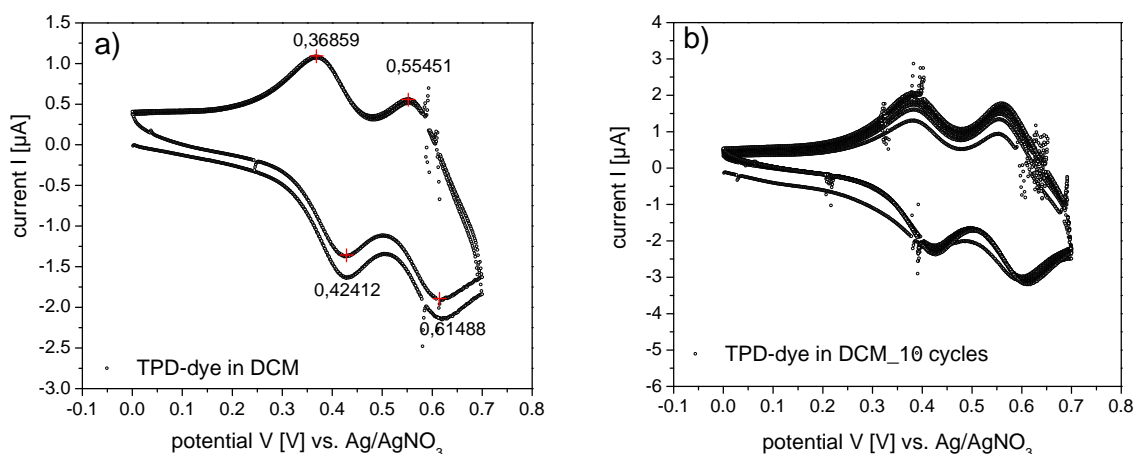


Figure S1. Cyclic voltammograms of TPD-dye in dichloromethane during a) 2 cycles and b) 10 cycles.

Table S1. Measured and calculated energy levels on the basis of cyclic voltammetry experiments carried out at 50 mV/sec in CH₂Cl₂ with 0.1 M tetrabutylammonium hexafluorophosphate using ferrocene as reference.

	E_{pa} [V]	E_{pc} [V]	$E_{ox \text{ vs. Fc/Fc}^+}$ [V]	HOMO [eV]	LUMO ^a [eV]
TPD-dye	0.42	0.37	0.30	-5.10	-2.92

^a Calculated from the absorption band edge (568 nm).

Cyclic voltammetry on SQ-dye

Method. Redox potentials of the all the derivatives were recorded using a BAS CV50W voltammetric analyser. Solution of the dye (1×10^{-3} M) in dichloromethane (DCM) containing 0.1 M tetra-*n*-butylammonium hexafluorophosphate (TBAFP₆) as supporting electrolyte were thoroughly deaerated before use. A glassy carbon electrode was used as the working electrode, a platinum wire was used as counter electrode, the potentials were measured using Ag/AgCl. Ferrocene was used as the internal standard and for the calculation of the energy levels, we used the following empirical relation:

$$E(\text{HOMO or LUMO}) = [-e \cdot (E^{1/2}_{(x \text{ vs. Ag/AgCl})} - E^{1/2}_{(\text{Fc/Fc}^+ \text{ vs. Ag/AgCl})})] - 4.80 \text{ eV}.$$

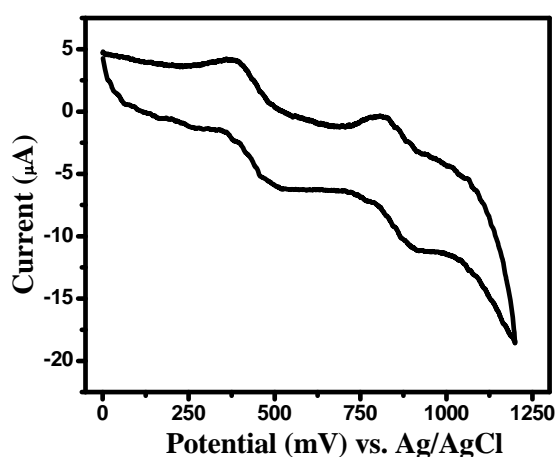


Figure S2. Cyclic voltammograms of SQ-dye in DCM (1 cycle).

Table S2. Measured and calculated energy levels on the basis of cyclic voltammetry experiments carried out at 100 mV/sec in CH₂Cl₂ with 0.1 M tetrabutylammonium hexafluorophosphate using ferrocene as reference.

	$E_{\text{ox}} (\text{Fc/Fc}^+) \text{ vs. Ag/AgCl}$	$E_{\text{ox}} (\text{SQ-dye}) \text{ vs. Ag/AgCl}$	$E_{\text{ox}} \text{ vs. Fc/Fc}^+$	HOMO	LUMO
	[V]	[V]	[V]	[eV]	[eV]*
SQ-dye	0.448	0.860	0.412	-5.212	-3.332

* calculated from the absorption band edge

3. Characterisation by Steady-State UV/vis Measurements

Method. Steady-state absorption measurements were performed on a Hitachi U-3000 spectrometer.

3.1 Absorption of TPD-dye in Solution and on TiO_2

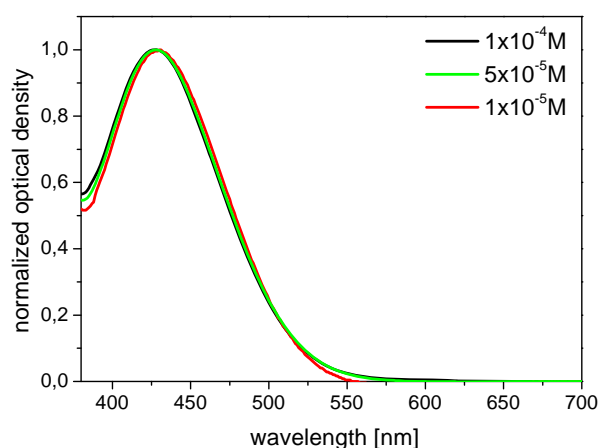


Figure S3. Normalized absorption spectra of TPD-dye in dichloromethane at different concentrations. Here, neither a change in the position nor in the shape of the absorption curve appears. Hence, TPD-dye does not form aggregates in solution.

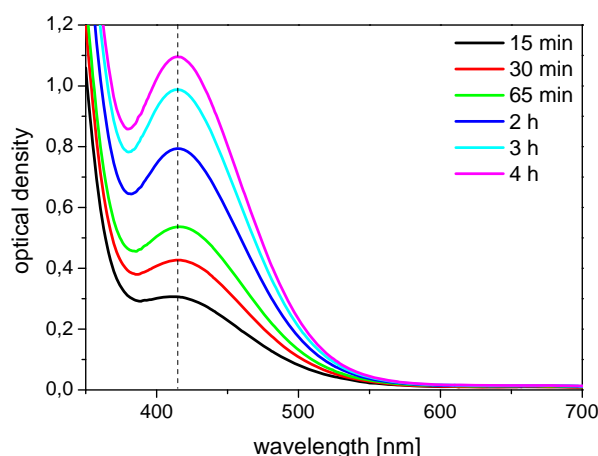


Figure S4. Absorption of TPD-dye on mesoporous TiO_2 (2 μm) as function of the chemisorption time. TPD-dye was adsorbed from dichloromethane/acetonitrile 9:1 at a concentration of $0.25 \times 10^{-4} \text{ M}$. With increasing chemisorption time the optical density increases continuously without any hint towards aggregate formation.

3.2 Influence of the Molecule Arrangement on the Absorption

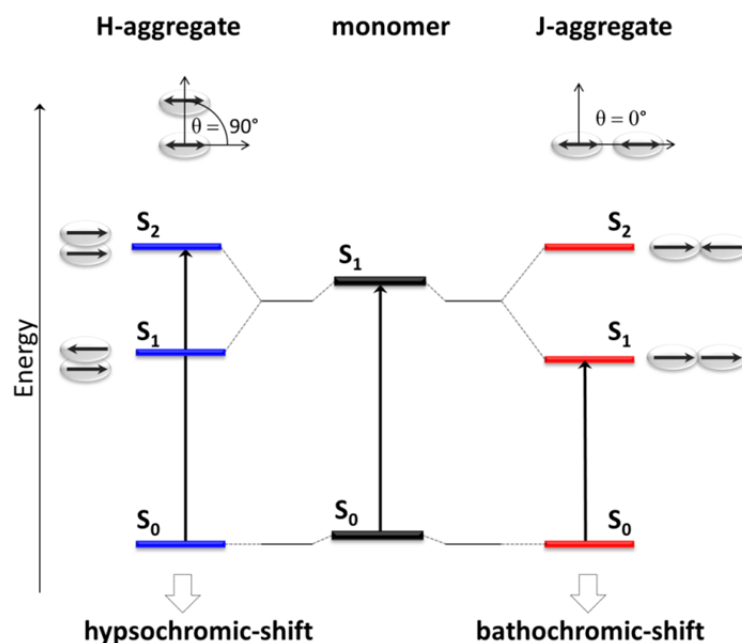


Figure S5. Schematic representation of the influence of the molecule arrangement on the spectral shift of H- and J-aggregates relative to the monomer species.

Based on Kasha's exciton theory,⁷ the interaction between transition dipoles (shown as short black arrows) causes a splitting of the excited state into two energy levels (S_1 and S_2). The arrangement of molecules is expressed by the angle θ . This is given by the direction of the transition dipoles with the line of the molecular centres. Depending on this angle two distinctive behaviours can be observed: (1) For a large angle ($\theta > 54.7^\circ$) with a "parallel" orientation (H-aggregate), a hypsochromic shift of the absorption band relative to the monomer absorption can be observed. Here, the equal preferential direction of transition dipoles results not only in higher energy (S_2), but also in a higher total dipole moment and hence high oscillator strength (allowed transition: $S_0 \rightarrow S_2$). (2) For a small angle ($\theta < 54.7^\circ$) with a "collinear" orientation (J-aggregate), a bathochromic shift of the absorption relative to the monomer absorption can be observed. Here, the equal preferential direction of transition dipoles results in both a lower energy (S_1) and a higher total dipole moment and hence higher oscillator strength (allowed transition: $S_0 \rightarrow S_1$).

3.3 Solvatochromism of SQ-dye

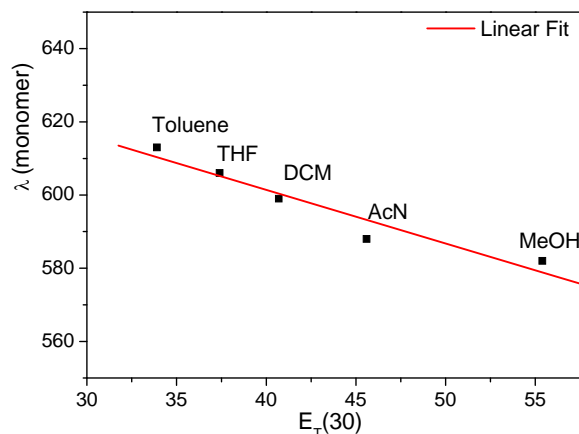


Figure S6. Absorption maximum of the SQ-dye monomer species as function of the solvent polarity expressed by the $E_T(30)^8$ value. The linear behaviour combined with a hypsochromic shift of the absorption maximum proves negative solvatochromism.

3.4 Absorption of SQ-dye on TiO_2

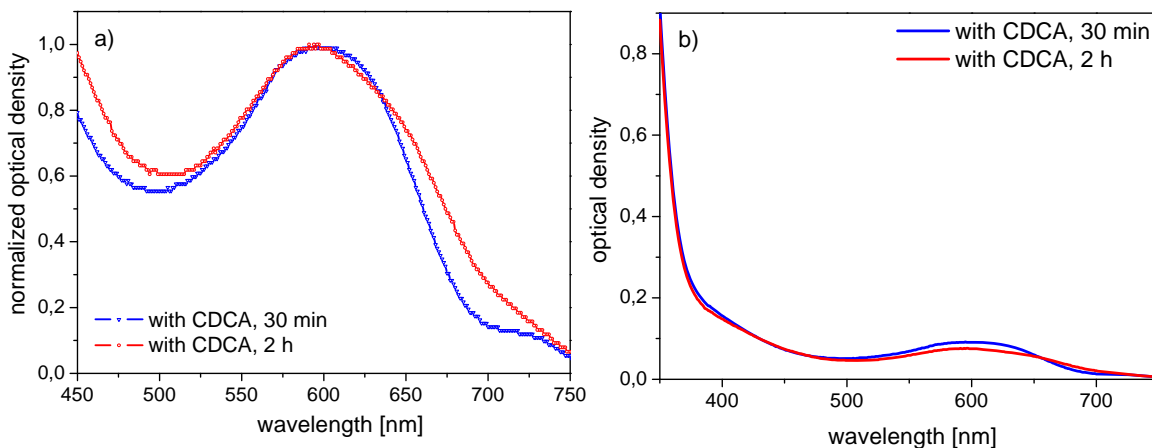


Figure S7. Absorption of SQ-dye on mesoporous TiO_2 (2 μm) under the influence of the additive CDCA after different dipping times. For chemisorption, SQ-dye and CDCA were dissolved in dichloromethane/ethanol 1:1 at a concentration of 0.25×10^{-4} M and 10 mM, respectively. Figure a) shows that the monomer species has an absorption maximum at 600 nm. Further it illustrates, that there is a strong contribution of J-aggregates even after 2 h chemisorption time. Figure b) reveals a very low optical density under the influence of CDCA (O.D. after 2 h with CDCA < 0.1, O.D. after 2 h without CDCA = 0.56).

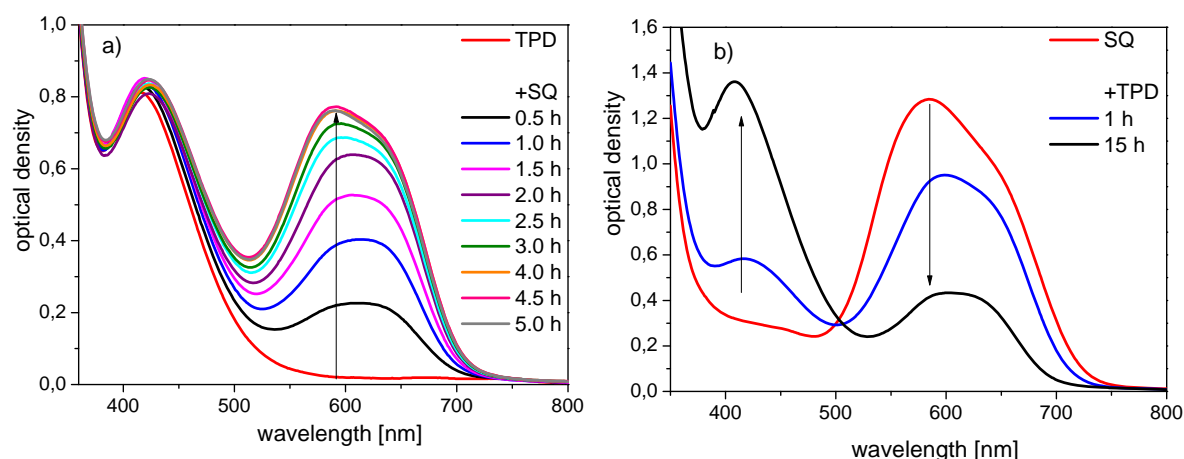


Figure S8. Absorption spectra of sequential chemisorption processes. In the case of a), the substrate was immersed in a solution of TPD-dye for 4 h (red curve), washed and subsequently immersed in a solution of SQ-dye for the given time intervals (0.5 to 5 h). In the case of b), the substrate was immersed in a solution of SQ-dye for 4 h (red curve), washed and subsequently immersed in a solution of TPD-dye solution for the given time intervals (1 to 15 h). The experiments were performed on mesoporous TiO_2 (2 μm) and chemisorption was done from dichloromethane/acetonitrile 9:1 at a concentration of $0.25 \times 10^{-4} \text{ M}$. It can be concluded from the spectra, that TPD-dye cannot be desorbed by SQ-dye, but SQ-dye can be desorbed by TPD-dye very easily.

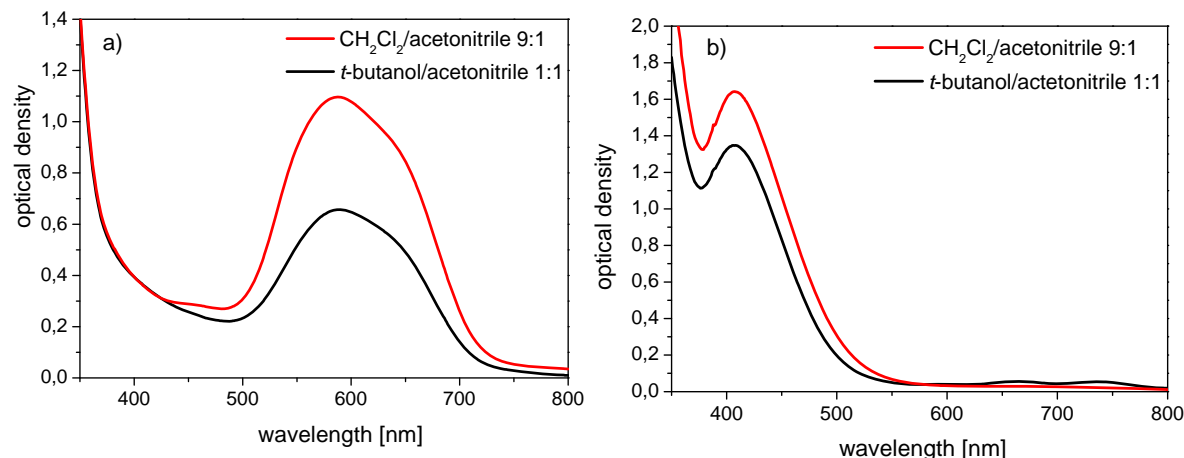


Figure S9. Influence of the chemisorption solvent on the optical density. The graphs show the absorption curves for a) SQ-dye and b) TPD-dye adsorbed on mesoporous TiO_2 either from dichloromethane/acetonitrile 9:1 (red line) or *t*-butanol/acetonitrile 1:1. In all cases chemisorption was done for 16 h and the thickness of the mesoporous layer was kept constant at 2 μm . The trend is clear: By a change of the solvent from dichloromethane/acetonitrile 9:1 to a solvent with a higher total dielectric constant (*t*-butanol/acetonitrile 1:1) the optical density is remarkably reduced.

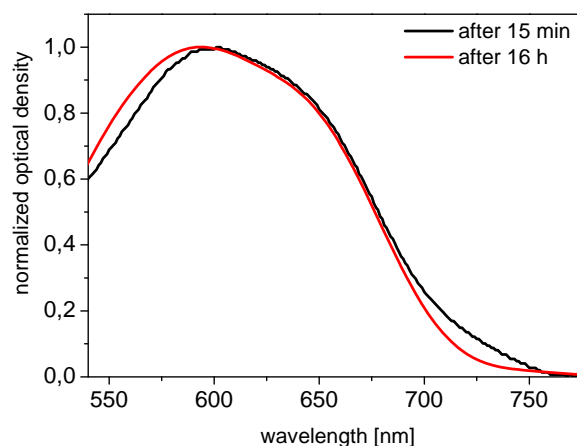


Figure S10. Normalized UV/vis spectra of SQ-dye on mesoporous TiO_2 ($\sim 2 \mu\text{m}$) adsorbed from dichloromethane/ acetonitrile 9/1 ($0.25 \times 10^{-4} \text{ M}$) after 15 min and 16 h chemisorption time. The broadening of the curve at the high-energy side after 16 h chemisorption time indicates the higher contribution of H- aggregates after longer dipping times.

4. Thickness Optimization of the Mesoporous Layer

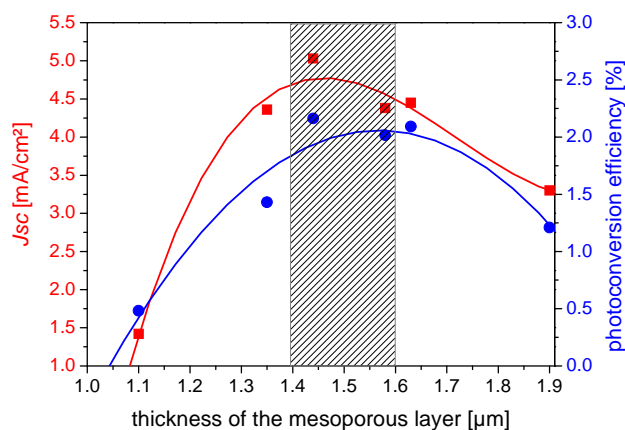


Figure S11. Optimization of the thickness of the mesoporous TiO_2 layer. The graph shows the photocurrent density of SDSCs sensitized with TPD-dye from tert-butanol/acetonitrile 1:1 ($0.25 \times 10^{-4} \text{ M}$) as a function of the thickness of the mesoporous layer. Here, the optimum of the photocurrent can be achieved at a thickness in the range of 1.4 to 1.6 μm .

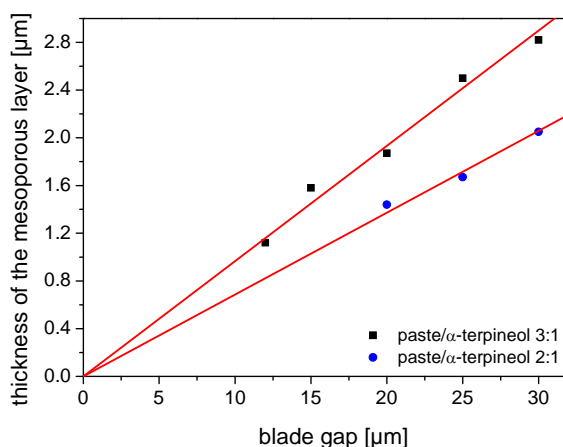


Figure S12. Variation of thickness of the mesoporous layer prepared by doctor blading. The thickness of the mesoporous layer can be adjusted by dilution of the commercial TiO_2 paste (Solaronix, T20/SP) with α -terpineol and with the gap of the blade.

5. References

- 1 a) S. Gauthier, J. M. J. Fréchet, *Synthesis*, **1987**, 1987, 383-385.
b) C. Schmitz, M. Thelakkat, H.-W. Schmidt, *Advanced Materials*, **1999**, 11, 821.
- 2 Y. Liu, M. Nishiura, Y. Wang, Z. Hou, *Journal of the American Chemical Society*, 2006, 128, 5592–5593.
- 3 J. Lu, P. F. Xia, P. K. Lo, Y. Tao, M. S. Wong, *Chemistry of Materials*, **2006**, 18, 6194-6203.
- 4 D. Keil, H. Hartmann, *Dyes and Pigments*, **2001**, 49, 161–179.
- 5 L. Beverina, R. Ruffo, G. Patriarca, F. D. Angelis, D. Roberto, S. Righetto, R. Ugoc, G. A. Pagani, *Journal of Materials Chemistry*, **2009**, 19, 8190–8197.
- 6 W. Pham W, W. F. Lai, R. Weissleder, C. H. Tung, *Bioconjugate Chemistry*, **2003**, 14, 1048-1051.
- 7 M. Kasha, H. R. Rawls, M. Ashraf El-Bayoumi, *Pure and Applied Chemistry*, **1965**, 11, 371-392.
- 8 C. Reichardt, *Chemical Reviews*, **1994**, 94, 2319-2358.

Chapter 8

SYNTHESIS AND PROPERTIES OF PANCHROMATIC BODIPYs WITH DONOR-ANTENNA GROUPS: A NEW SYNTHETIC ROUTE TOWARDS *meso*-ETHYNYLPHENYL BODIPYs

Katja Gräfe^[a], Thomas Körzdörfer^[b], Stephan Kümmel^[b] and Mukundan Thelakkat^{[a]}*

^[a] Department of Macromolecular Chemistry I, Applied Functional Polymers, Universität Bayreuth, Universitätsstr. 30, 95440 Bayreuth, Germany.

Fax: +49 921 55 3206

E-mail: Mukundan.Thelakkat@uni-bayreuth.de

^[b] Department of Theoretical Physics IV, Universität Bayreuth, Universitätsstr. 30, 95440 Bayreuth, Germany.

Prepared for submission.

ABSTRACT

We synthesised meso-ethynylphenyl BODIPYs with and without donor-antenna groups from an aliphatic aldehyde and the corresponding meso-phenyl BODIPYs from an aromatic aldehyde. The condensation of an aliphatic aldehyde with pyrrole opens up a new synthetic route for BODIPY core. All the four new dyes carry strongly electron-withdrawing cyano acrylic acid anchor groups making them suitable as sensitizer dyes for metal oxides. An essential part of the synthesis is the Knoevenagel-type condensation for the covalent attachment of donor-antenna groups to the BODIPY framework. The condensation follows an organocatalytic mechanism involving the nucleophilic attack of the piperidine catalyst on the aromatic donor aldehyde forming an aminor which reacts with the methyl groups of the BODIPY framework. We also investigated the concurring reaction of piperidine with alkyne group during the Knoevenagel-type condensation on meso-ethynylphenyl BODIPYs and show how to circumvent this problem. The final products were fully characterized regarding their configuration, optical and electrochemical properties by NMR, UV-vis absorption measurements and cyclic voltammetry experiments. The donor substituted BODIPYs show an excellent panchromatic behaviour with high molar extinction coefficients over the whole UV-vis up to the near-IR region; in one case even up to 1030 nm. Furthermore, all compounds are electrochemically stable and reversible under repeated oxidations and reductions. It was observed that the LUMO level is strongly influenced by the meso-substituent and the HOMO level is mainly influenced by the donor group, which is supported by DFT calculations.

Keywords: BODIPY • *meso*-ethynylphenyl • Knoevenagel condensation • panchromatic.

INTRODUCTION

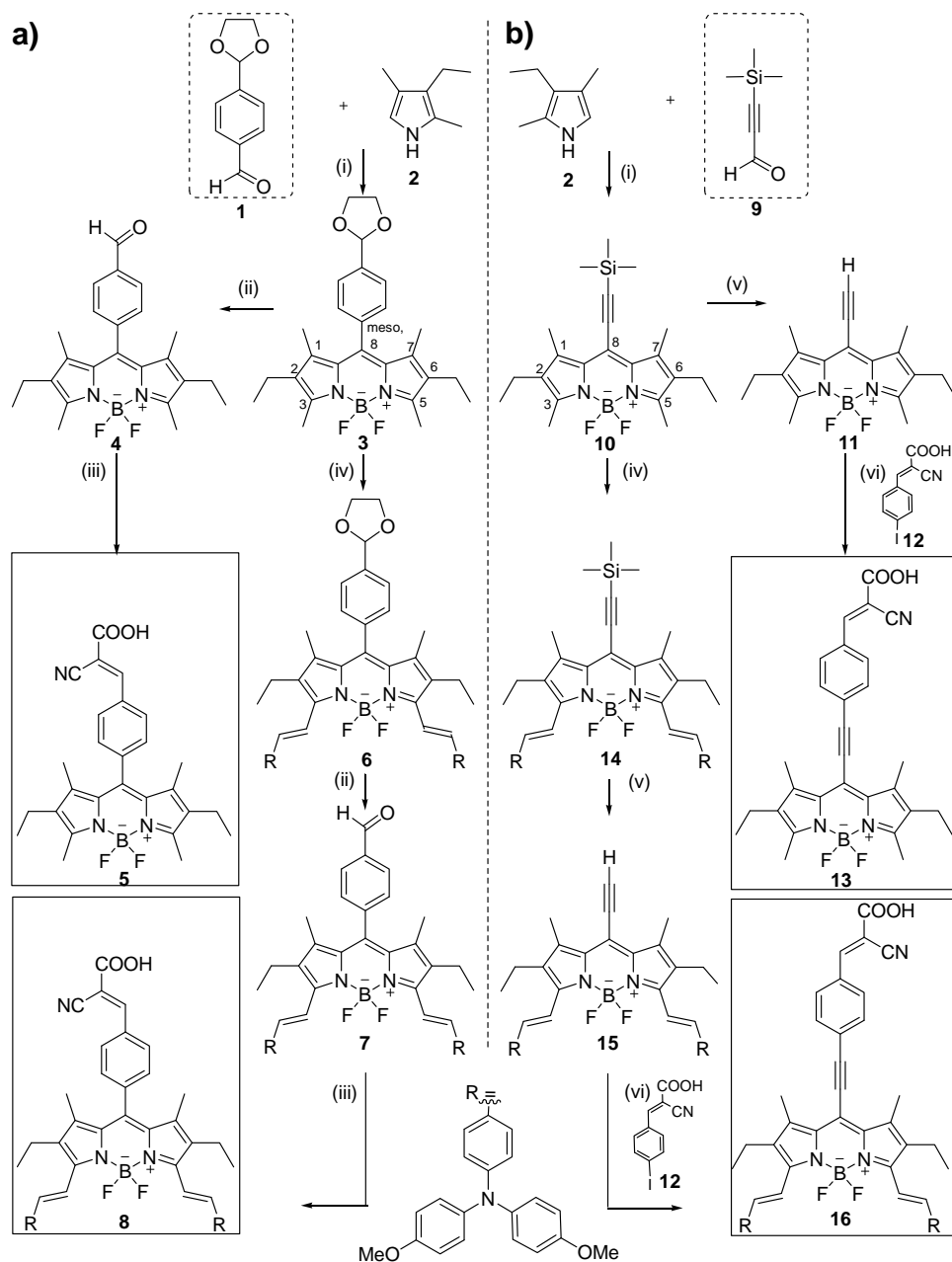
The class of 4,4-difluoro-4-bora-3a,4a-diaza-s-indacene derivatives, better known as BODIPYs, was discovered in 1968 by Treibs and Kreuzer.¹ Since this time, BODIPYs have attracted broad interest in different areas of science such as chemistry, physics, and biology. Their applications include the field of laser dyes²⁻⁴, biochemical labeling^{5, 6}, fluorescence sensors⁷/switches⁸, electroluminescent materials⁹⁻¹¹, molecular photonics¹², singlet oxygen sensitizers.¹³ Although, the use of BODIPY dyes in solar cell is in its infancy, there is increasing interest in investigating BODIPY derivatives as sensitizers in liquid electrolyte dye-sensitized solar cells.¹⁴⁻¹⁶ It has also been demonstrated that BODIPYs can be successfully used in solid-state dye-sensitized solar cells and in organic bulk heterojunction solar cells.^{17, 18} The large variety of applications and the scientific relevance of this class of dyes are based on the outstanding optical and physical properties such as thermal and photochemical stability as well as insensitivity against the polarity and pH of their environment. BODIPYs are further known for their tuneable absorption up to the infra-red region, thus making them suitable for biological applications.^{13, 19, 20}

In this paper, we focus on the design, synthesis and properties of two newly developed *meso*-ethynylphenyl BODIPY dyes and compare them with the corresponding *meso*-phenyl derivatives. Our goal was to design BODIPYs with excellent optical properties combining high extinction coefficients and a panchromatic behaviour. It is well known that the maximum attainable short-circuit photocurrent can be increased by a shift of the absorption edge to longer wavelength on condition of high extinction coefficients over the whole absorption region.²¹ Additionally, all the four dyes carry strongly electron-withdrawing cyano acrylic acid anchor groups making them suitable for possible applications in dye-sensitized solar cells. From literature it is known that arylation at the *meso* position affects the optical and electrochemical properties only marginally. The reason for this is the orthogonal configuration between the *meso*-phenyl moiety and the BODIPY core resulting in less conjugation between the two units.²² To overcome this issue, we introduced an ethynyl bridge between the *meso*-phenyl group and the BODIPY core. We assume, that the ethynyl bridge can enable an efficient delocalization due to the comparatively diffuse nature of the π -bonds creating a cylindrical electron cloud around the σ -bond. Moreover, it is known from the porphyrin chemistry that ethynyl type bridges guarantee strong electronic interactions between the two connected moieties.²³ To realize the *meso*-ethynylphenyl BODIPYs, we successfully utilized the condensation of an aliphatic aldehyde with pyrrole for the first time. To further increase the extend of absorption, a donor-antenna group was attached to the

BODIPY core *via* a vinylic bond. For this purpose 4,4'-dimethoxytriphenylamine was selected because it provides good light harvesting properties, a high lying HOMO level, a higher stability against oxidative coupling compared to unsubstituted triphenylamine²⁴ and good charge transporting properties. In order to introduce 4,4'-dimethoxytriphenylamine donor-antenna groups, we focus in particular on the Knoevenagel-type condensation for the conjugated attachment of the donor-antenna group to the BODIPY framework. Although this is the most widely used method to extend the conjugation and hence increase the absorption range of BODIPYs, the real mechanism of this particular reaction has not yet been studied. We verify which of the two possible proposed mechanisms for Knoevenagel-type condensations, *viz.* Hann-Lapworth or organocatalytic mechanism is valid here. We also studied the reasons for the failure of the standard procedures for the donor attachment in *meso*-ethynylphenyl BODIPYs using piperidine as catalyst. This has very much to do with the nucleophilic nature of the commonly used piperidine and its affinity to the triple bond. Thus the main synthetic challenge here was to introduce the *meso*-ethynylphenyl group as well as donor groups at 3,5-positions. Additionally, all target compounds were labelled with a 2-cyano-3-phenylacrylic acid anchoring moiety at the *meso* position (see structures **5**, **8**, **13** and **16** in Scheme 1). It is already demonstrated that the *meso* position is most appropriate for attaching the anchor groups because BODIPYs show an inherent directionality of the charge redistribution after excitation increasing the charge density at the *meso* position.¹⁶ Finally, the *meso*-ethynylphenyl BODIPYs without and with donor-antenna groups were characterized in comparison to the corresponding *meso*-phenyl BODIPYs by NMR, and their optical and electrochemical properties were investigated in detail.

RESULTS AND DISCUSSION

Synthetic strategy. Scheme 1 depicts the synthetic procedure for the target dyes **5**, **8**, **13** and **16**. We followed the conventional coupling method using an aryl aldehyde and a pyrrole for the synthesis of *meso*-phenyl derivatives (route a), whereas a new route involving an alkynyl aldehyde was used for the *meso*-ethynylphenyl BODIPYs (route b). Dyes **5** and **8** were synthesised starting from the aromatic aldehyde **1** and kryptopyrrole **2**. Deprotection of **3** and subsequent Knoevenagel condensation with 2-cyanoacetic acid resulted in the formation of compound **5**. In a similar manner, **8** was obtained from compound **3** with the difference that two units of 4,4'-dimethoxytriphenylamine donor groups were attached at the positions 3 and 5 of the BODIPY core by a Knoevenagel-type condensation before the deprotection of the aldehyde functionality followed by condensation with 2-cyanoacetic acid. Thus far, the direct synthesis of the *meso*-ethynylphenyl BODIPY sensitizers such as **13** and **16** was very difficult to accomplish, even though reports of BODIPYs substituted with aryl acetylene or trialkylsilylacetylene groups in various positions are known in the literature.²⁵ To the best of our knowledge, no aliphatic alkanyl, alkenyl or alkynyl aldehydes have been used for the coupling with pyrroles to obtain the BODIPY core. This may be due to the low reactivity of aliphatic aldehydes and the fact that alkenyl aldehydes tend to react in an unexpected way. According to the principle of vinylogy, the vinyl rather than the carbonyl group reacts with the pyrrole. That means, the reaction between α , β -unsaturated aldehydes and pyrroles does not result in the formation of BODIPY dyes with *meso*-alkenyl groups but in the formation of alkanal substituted pyrroles.²⁶ This is not the case for alkynyl aldehydes. We report the first synthesis of two *meso*-ethynylphenyl BODIPYs one without additional donor groups (**13**) and one with 4,4'-dimethoxytriphenylamine donor groups (**16**). Both were synthesised starting from kryptopyrrole **2** and 3-(trimethylsilyl)-2-propynal **9** in good yields. After deprotection of **10** and subsequent Sonogashira coupling with **12** the final *meso*-ethynylphenyl BODIPY **13** was isolated in moderate yields. In order to obtain the donor-antenna substituted *meso*-ethynylphenyl compound **16**, a Knoevenagel-type condensation of the TMS-protected *meso*-ethynyl BODIPY **10** and 4-(di(4-methoxyphenyl)amino)benzaldehyde was performed to yield **14** which was subsequently deprotected (**15**) and reacted with 2-cyano-3-(4-iodophenyl)acrylic acid **12** in a Sonogashira coupling to afford **16**. This was necessary to avoid undesired hydroamination reactions between the ethynyl group and piperidine (Figure S18). In general, the new synthetic route of condensation of an alkynyl aldehyde with pyrrole reported here paves the way for easy structural diversity in *meso*-ethynyl BODIPYs.



Scheme 1. Synthetic routes a) for *meso*-phenyl BODIPYs **5** and **8**, b) for *meso*-ethynylphenyl BODIPYs **13** and **16**. i) Trifluoroacetic acid, 2,3-dichloro-5,6-dicyano-1,4-benzoquinone, NEt_3 , $\text{BF}_3 \cdot \text{OEt}_2$, in CH_2Cl_2 , RT. ii) 5% HCl_{aq} , in THF, RT. iii) 2-Cyanoacetic acid, piperidine, in acetonitrile, reflux. iv) 4-(di(4-methoxyphenyl)amino)benzaldehyde, piperidine, glacial acetic acid, in benzene, reflux. v) KF , in MeOH or MeOH: THF 1:1, RT. vi) $\text{Pd}(\text{PPh}_3)_4$, CuI , NEt_3 , in THF, RT.

Mechanism of the Knoevenagel-type condensation. As already mentioned, the usual synthetic strategy to extend the π -conjugation of BODIPYs is the attachment of aromatic donor groups using Knoevenagel-type condensations. This is known to cause an extreme bathochromic shift of the absorption. In particular, an aromatic aldehyde is used to react with the methyl groups in

position 3 and 5 of the BODIPY framework creating a styryl-type substituted BODIPY. Although, this is a common modification route, its mechanism has not yet been studied. It is only considered as Knoevenagel-type condensation involving a deprotonation of the acidic methyl groups in position 3 and 5 as they can be deprotonated under mild conditions and will readily react with electron rich aromatic aldehydes.^{13, 19}

To gain a better understanding of this condensation reaction, we verified which of the two possible proposed mechanisms for Knoevenagel-type condensations, *viz.* Hann-Lapworth (Figure S1) or organocatalytic mechanism is valid here (Figure 1). With the used educts (3,5-dimethyl BODIPY, aromatic donor aldehyde and secondary amine), both reaction mechanisms are conceivable. The Hann-Lapworth mechanism,²⁷ includes the deprotonation of the reactive methyl/methylene compound by an amine base. The resonance stabilized carbanion is able to attack the electropositive carbon atom of the aldehyde in a nucleophilic reaction. Thus, a new C-C bond with an alkoxide functionality will be formed which has to be protonated either by the protonated base or by the solvent. Hence, protic solvents are advantageous for this kind of reaction. In the last step, the β -hydroxy compound undergoes dehydration to afford the unsaturated product. The mechanism can be proven by the isolation of the β -hydroxy intermediate. However, in reactions between 3,5-dimethyl BODIPYs and aromatic aldehydes in presence of the secondary base piperidine we could not find any evidence for the formation of such a β -hydroxy intermediate. Instead, an aminor (Figure 1, product B) was isolated (See supporting information Figure S16 for the NMR spectra of the aminor. Comparable structures were also found for the conversion of thiophene-2-carbaldehyde with piperidine Figure S17). The identification and isolation of this aminor proves that the Hann-Lapworth version of the mechanism is not valid in this case. Hence, the second mechanism studied by different research groups on the condensation between malonic acid derivatives and aromatic aldehydes in the presence of secondary amines has to be proven for its validity regarding the reaction between BODIPYs and aromatic aldehydes.²⁸ This mechanism is a rather an organocatalytic way of condensing a methyl/methylene compound with an aldehyde in the presence of primary or secondary amines. Here, the amine (in our case piperidine) acts primarily as a nucleophile. The proposed reaction sequences modified and adapted from ref. 28 as applied to the condensation reaction between an aromatic aldehyde and a BODIPY compound in the presence of piperidine/glacial acetic acid is shown in Figure 1.

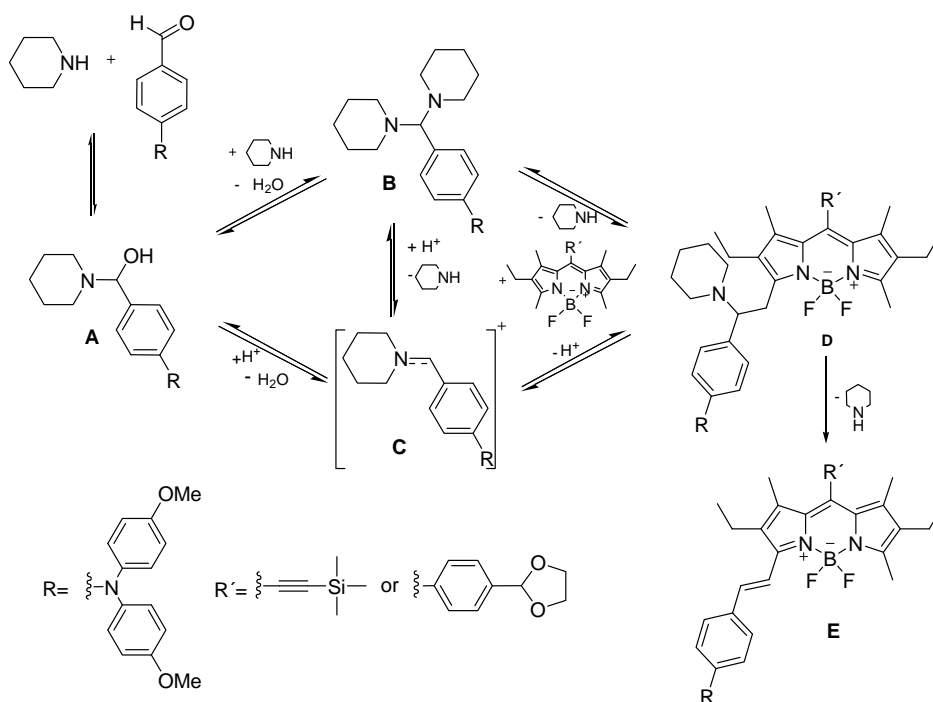


Figure 1. Proposed mechanism of the Knoevenagel-type condensation of 3,5-dimethyl BODIPYs with aromatic aldehydes catalysed by piperidine in a non-polar aprotic solvent (modified in accordance with²⁸).

In the first step, the amine is supposed to react with the electropositive carbonyl carbon of the aromatic aldehyde forming the hemiaminal **A** which can undergo a second nucleophilic reaction with an additional amine to form the aminal **B** under condensation. On the one hand, one piperidine molecule can be eliminated from **B** under acidic condition (to form an iminium ion **C**) on the other hand, **B** can directly react with the methyl groups of the BODIPY compound under splitting off one piperidine molecule creating the β -amino intermediate **D**. We assume that the formation of **D** is facilitated by the basic character of piperidine. In the last step one more piperidine molecule is split off and the mono-substituted product **E** is released and can participate in a new catalysis cycle. The fact that this condensation always results in the formation of exclusively *trans*-substituted BODIPYs (see for example Figure S7 and S15) can be understood from the mechanism. The intermediate **D** is supposed to be preferably formed in such a configuration that the steric demanding groups (donor group and BODIPY) are oriented antiperiplanar to each other. During the elimination of piperidine the *trans* orientation is sustained. Further, it is known that the deamination step of **D** is rate determining and can be accelerated in the presence of protons.²⁸ This explains the importance of the commonly added

acid (glacial acetic acid or *p*-toluenesulfonic acid). The isolation of the aminor B proves the validity of the organocatalytic mechanism for the reaction between 3,5-dimethyl BODIPYs and aromatic aldehydes in the presence of piperidine.

The mechanism strongly depends on the basicity and nucleophilicity of the used amine. For instance, the Hann-Lapworth mechanism is the only valid mechanism for reactions including tertiary amines because they cannot perform a nucleophilic attack on the carbonyl carbon of aldehydes as required in the organocatalytic mechanism.²⁸ For reactions using primary or secondary amines either mechanism are conceivable. Thus, instead of piperidine, we performed the reaction with 2,2,6,6-tetramethylpiperidine (TMP) which is a secondary amine that is as basic as piperidine but much more bulky. We observed completely no reaction (even after one week under reflux), because TMP is sterically hindered to react with the aldehyde. Similarly, by using the tertiary base NEt₃ (which has also a comparable basicity), we did not observe a condensation reaction. From these results it can be deduced, that only the organocatalytic mechanism is relevant here because bases with the comparable basicity as piperidine that are not able to activate the aldehyde (formation of A, B and C) did not promote the Knoevenagel condensation at all. To this end, the most efficient synthetic procedures for the reaction of aromatic aldehydes and 3,5-dimethyl BODIPYs are based on the piperidine/glacial acetic acid or the piperidine/*p*-toluenesulfonic acid catalyst systems in non-polar solvents such as benzene and toluene.

Nucleophilic attack on the ethynyl bridge. The Knoevenagel-type condensation on **3** with the donor aldehyde using both pathways, either the piperidine/glacial acetic acid catalyst system in benzene or piperidine/*p*-toluenesulfonic acid in toluene, resulted in the formation of the desired product **6** with comparable yields. However, both procedures did not work for **17** having a *meso*-ethynylphenyl moiety (Figure 2)

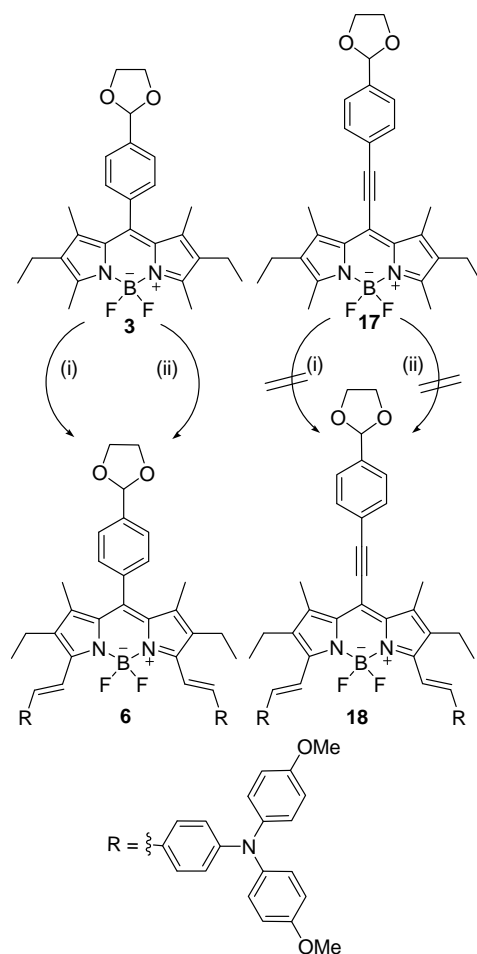


Figure 2. Synthetic pathways for the Knoevenagel-type condensation on *meso*-phenyl BODIPYs and *meso*-ethynylphenyl BODIPYs for the attachment of donor-antenna groups *R*. (i) 4-(Di(4-methoxyphenyl)-amino)benzaldehyde, piperidine/glacial acetic acid, in benzene, reflux. (ii) 4-(Di(4-methoxyphenyl)amino)-benzaldehyde, piperidine/*p*-toluenesulfonic acid, in toluene, reflux. i) and ii) could be successfully accomplished for **3** and yielded **6** but failed completely for **17** (**18** was not formed).

One would suggest that alkynes have a high tendency towards electrophilic addition because of the high electron density between the *sp*-hybridized carbon atoms. One might also think that this assumption is supported by the ^1H -NMR resonance signals of terminal alkyne protons that appear at a higher field (lower frequency) than alkenyl protons which indicates a higher shielding *viz.* a higher electron density around terminal alkyne protons. But in fact, it is basic knowledge that alkynes are more susceptible to nucleophilic reactions. Due to the *sp* hybridisation the positive charge of the atomic core is less shielded at the side of the single bond. This seems to be in conflict with the NMR observations. However, the shielding of alkynes observed in ^1H -NMR experiments is higher than those of alkenes because of the rotational symmetry nature of the triple bond causing a ring current with a magnetic field opposite to the external one. This lowers

the resonance frequency and gives the impression that the single bond sides of alkynes are less positive, but in fact they are fairly positive (which can also be seen in the acidity of terminal alkynes). Consequently, a nucleophile like piperidine can attack these positions resulting in hydroamination.²⁹

This is exactly what happens with *meso*-ethynylphenyl BODIPYs in the presence of piperidine. We observed, that even after a few minutes with piperidine at ambient conditions, the *meso*-ethynylphenyl BODIPY compound **17** is fully used up in a hydroamination reaction to form the corresponding enamine (Figure S18). Hence, the attachment of donor groups to BODIPY **17** is impossible under the usual Knoevenagel conditions but may be realizable under special conditions.³⁰ To solve this dilemma, **10** was selected for the standard Knoevenagel-type condensation instead of **17**. The bulky trimethylsilyl-group efficiently prevents the triple bond from hydroamination reactions with piperidine.

Characterization by NMR. The ¹H-NMR spectra of important intermediates and products are given in the supporting information. The main difference between *meso*-phenyl and *meso*-ethynylphenyl BODIPYs is the chemical shift of the resonance signal assigned to the 1,7-methyl groups of BODIPY core. These occur at about 1.28 ppm (*e.g.* **3**) for the *meso*-phenyl derivatives, whereas for the *meso*-ethynylphenyl BODIPYs they occur at about 2.53 ppm (*e.g.* **17**). This gives clear evidence that the chemical/magnetic environment of these protons is strongly influenced by the substituent in the *meso*-position. Figure 3 shows a section of the ¹H-NMR spectra of **19**, **3** and **17** having a *meso*-proton, *meso*-phenyl and a *meso*-ethynylphenyl group, respectively. The signals of methyl groups at 1, 3, 5 and 7 positions and ethyl protons at 2 and 6 positions are depicted. Relative to the corresponding *meso*-proton compound **19**, the orthogonal phenyl moiety in **3** seems to increase the electron density and hence the shielding of the 1,7-methyl groups (Figure 3b, resonance signal appears at a distinctly lower ppm-value) whereas the electron withdrawing ethynyl bridge in **17** causes a strong deshielding (Figure 3c, resonance signal appears at a higher ppm-value).

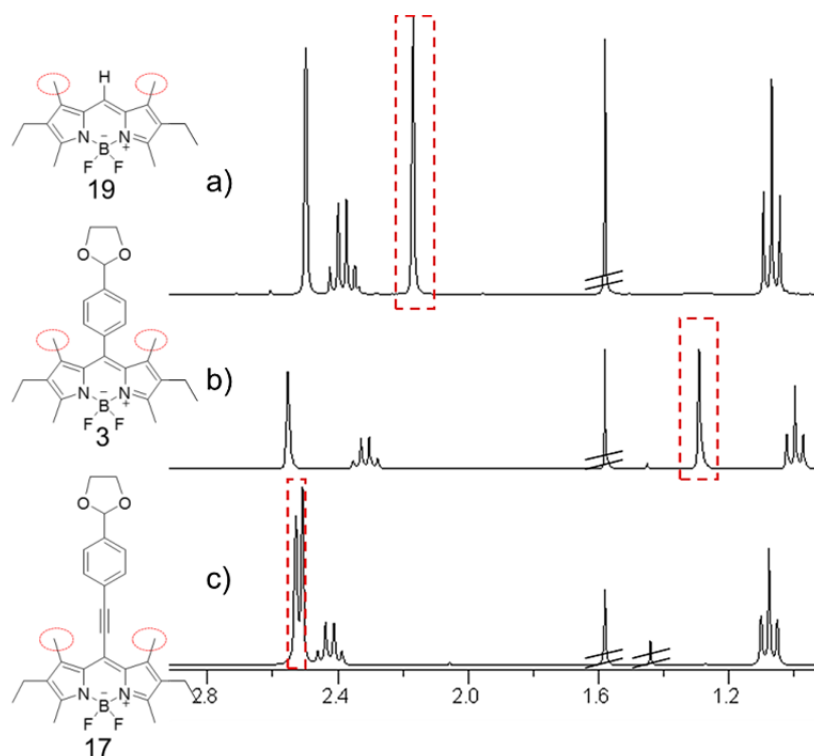


Figure 3. Excerpt of the ^1H -NMR spectra of a) the *meso*-proton BODIPY 1,3,5,7-tetramethyl-2,6-diethyl-4,4-difluoro-4-bora-3a,4a-diaza-*s*-indacene (**19**), b) the corresponding *meso*-phenyl BODIPY (**3**) and c) the *meso*-ethynylphenyl BODIPY (**17**). The red boxes mark the resonance signal attributed to the 1,7-methyl protons. (The signals at 1.56 and 1.44 ppm can be neglected because they arise from water and cyclohexane, respectively. The whole spectra are depicted in Figure S19.)

One might assume that the behaviour of the *meso*-phenyl compound can be ascribed to the strong +M-effect of the phenyl group increasing the electron density at the 1,7-methyl protons. Indeed, the +M-effect cannot be responsible for this because the orthogonal configuration of the phenyl ring relative to the BODIPY core interrupts the conjugation. We assume that the ring current of the *meso*-phenyl group and hence the resulting magnetic field causes this shift. So if the molecule with its delocalized π -electrons is exposed to a magnetic field, a ring current is induced in the phenyl group. This causes in turn a magnetic field with magnetic lines of force that are oriented opposed to the applied field in the center of the aromatic unit. Consequently, the generated magnetic field weakens the applied magnetic field at the 1,7-methyl groups which necessitates a higher external field. This equals a shift of the signal to lower ppm values. Therefore, it can be deduced that the *meso*-phenyl group does not influence the electron density at the 1,7-methyl groups, it only affects the magnetic environment. In contrast, the *meso*-ethynyl bridge group is able to reduce the electron density at these positions. These

observations are supported by the UV-vis measurements showing that the *meso*-ethynylphenyl BODIPY **17** causes a strong red shift due to the electron withdrawing ability of the *meso*-substituent whereas the corresponding *meso*-phenyl BODIPY **3** shows hardly any difference in the absorption relative to the *meso*-proton BODIPY **19** (Figure S28). However, the 3,5-methyl groups are only marginally influenced by the substituent in the *meso*-position. It can be argued that, if all methyl groups of *meso*-ethynylphenyl BODIPYs resonate closely, they also have an equal tendency to react with activated donor aldehydes in Knoevenagel-type condensations, whereas the methyl groups of *meso*-phenyl BODIPYs should show different reactivities.³¹ Nonetheless, under the chosen conditions exclusively the methyl groups in the positions 3 and 5 react with activated donor aldehydes in Knoevenagel-type condensations for both *meso*-phenyl and *meso*-ethynylphenyl BODIPYs. It is not distinguishable, if this is associated with reactivity issues or the bulkiness of the trimethylsilyl-group.

Further, the stereochemistry of the vinyl bond between the BODIPY core and the donor group was studied. On the basis of the ¹H-NMR spectra of **8** and **16** (Figure S7 and S15) the configuration can be clearly identified to be *trans* because the values for the vicinal ³J_{H/H} coupling are 16.6 Hz and 16.4 Hz for **8** and **16**, respectively. The proposed mechanism (Figure 1) supports the formation of exclusively *trans*-substituted BODIPYs.

Now only the geometry of the 4-(2-carboxy-2-cyanovinyl)phenyl units of **5**, **8**, **13** and **16** requires assignment. Here, the carboxyl group can be oriented either *cis* or *trans* relative to the phenyl group. Since this anchor group was synthesised in a comparable manner for all end-products and for **12**, we used detailed NMR-analysis of **12** for the investigation of the orientation. Unfortunately, for trisubstituted olefins this information cannot be deduced from the ¹H-NMR spectrum because there are no vicinal protons. In general, the configuration of such alkenes can be determined by measuring the nuclear Overhauser effect (NOE) and by performing proton coupled or gated decoupling experiments. In our case, the measurement of the NOE cannot be utilized for the determination of the configuration because the resonance signal of the proton of the carboxylic group is extremely broad in the ¹H-NMR spectrum (Figure S10). This indicates a very short relaxation time for this proton. Additionally, it is known that the NOE build-up time is very slow for small molecules. Hence, even if the carboxyl group would come close to the aromatic proton (*cis* configuration) no NOE would be measurable. Thus, we decided to perform a proton coupled ¹³C-NMR experiment on **12** (Figure 4). The spectrum shows the resonance signals for of the ten C-atoms and their splitting due to ¹J_{C/H}, ²J_{C/H} and ³J_{C/H} couplings. Of special interest are signal a with a vicinal ³J_{C/H} coupling constant of 6.7 Hz and signal f with vicinal ³J_{C/H}

coupling constant of 13.9 Hz arising from the carbon atoms of the COOH and CN group, respectively. As it is known from literature³² that *cis*-vicinal $^3J_{C/H}$ coupling constants of substituted alkenes are usually smaller than comparable *trans*-vicinal $^3J_{C/H}$ coupling constants, the double bond geometry of **12** was assigned as *trans*. This result is also supported by the DFT-calculations (Figure 6) showing that the carboxyl group is oriented *trans* relative to the phenyl ring.

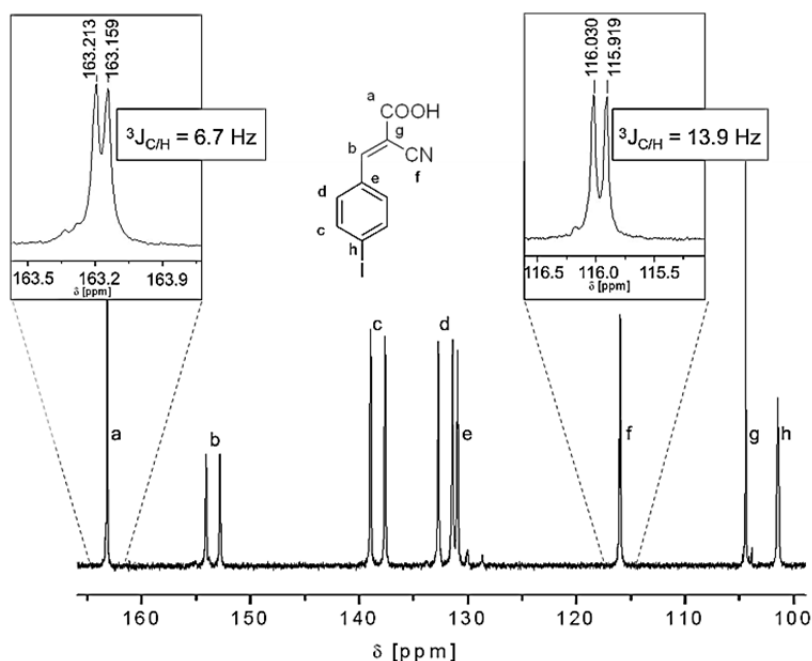


Figure 4. Proton coupled ^{13}C -NMR of **12**. The spectrum shows the ^{13}C resonance signals and their splitting due to the $^1J_{C/H}$, $^2J_{C/H}$ and $^3J_{C/H}$ couplings. The insets show an enlarged view of the resonance signals arising from the COOH group (a) and the CN group (f).

Optical properties. The electronic absorption spectra of **5**, **8**, **13** and **16** were recorded in solution and are depicted in Figure 5. Compound **5** shows the typical BODIPY absorption spectra with the sharp S_0 - S_1 transition at 530 nm and a high extinction coefficient ($4.20 \times 10^4 \text{ M}^{-1}\text{cm}^{-1}$). Additionally, a shoulder appears at 500 nm which is attributed to the 0-1 vibrational transition. In comparison to that, the S_0 - S_1 transition of its *meso*-ethynylphenyl derivative (**13**) is red shifted by 55 nm. The signal is broader and the extinction coefficient is reduced to $1.60 \times 10^4 \text{ M}^{-1}\text{cm}^{-1}$. The 0-1 vibrational transition was detected at 542 nm. The reason for the reduced extinction coefficient of **13** compared to **5** can be attributed to the larger spatial separation of the molecular orbitals involved in the transition. DFT calculations (Figure 6) indicate an increased distance between HOMO and LUMO with the introduction of the *meso*-ethynyl unit. This lowers the transition probability and hence the extinction coefficient is reduced. A further interesting

feature of **13** is the absorption band at 397 nm. The extinction coefficient of this band is much higher for **13** than for **5**. We found that this band is associated with the *meso*-phenyl/ethynylphenyl unit. The pronounced band of **13** indicates that the electronic interaction between the BODIPY core and the *meso*-substituted can be increased by the *meso*-ethynyl group.

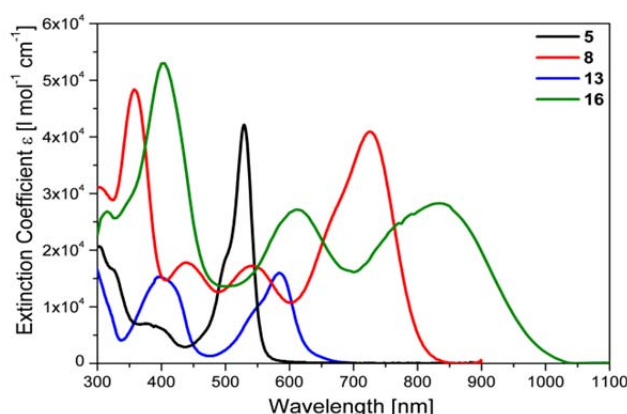


Figure 5. Electronic absorption spectra of the BODIPYs **3** (*meso*-phenyl/without donor-antenna, in CH_2Cl_2), **8** (*meso*-phenyl/with donor-antenna, in CH_2Cl_2), **13** (*meso*-ethynylphenyl/without donor-antenna, in CH_2Cl_2 :THF 1:1) and **16** (*meso*-ethynylphenyl/with donor-antenna, in CH_2Cl_2) measured at a concentration in the range of 1×10^{-5} M.

With the attachment of the donor groups, the absorption of **5** and **13** experience a strong bathochromic shift. Thus the absorption edge of **8** is at 840 nm and that of **16** is at 1030 nm. The absorption maxima appear at 725 nm ($\epsilon: 4.09 \times 10^4 \text{ M}^{-1}\text{cm}^{-1}$) and 835 nm ($\epsilon: 2.83 \times 10^4 \text{ M}^{-1}\text{cm}^{-1}$) for **8** and **16**, respectively. These are excellent absorption ranges and absorption coefficients for a panchromatic light harvesting. It is also interesting to note that the extinction coefficient of **8** is higher than $1 \times 10^4 \text{ M}^{-1}\text{cm}^{-1}$ over the whole visible spectrum (up to 787 nm) and regarding **16** it is higher than $1 \times 10^4 \text{ M}^{-1}\text{cm}^{-1}$ even into the IR region (up to 940 nm). This proves an excellent panchromatic behaviour of donor-antenna BODIPYs which is even more pronounced for *meso*-ethynylphenyl BODIPYs. The low energy band of **8** and **16** can be attributed to intramolecular charge transfer.

To investigate further the interaction of the ethynyl spacer and the donor substituents, steady-state emission measurements were done. Compared to **5**, the emission of **13** was remarkably reduced by the introduction of the ethynyl spacer. Additionally, the Stokes shift of **13** ($\Delta \text{Stokes} =$

22 nm) was almost double that of **5** (Δ Stokes = 14 nm). An explanation for both observations lies within the different freedom of rotation of the phenyl rings.^{22, 33} The increased distance due to the ethynyl bridge enables the free rotation of the phenyl group around the axis given by the *meso*-spacer. In contrast, the *meso*-phenyl ring in **5** is restricted to an almost orthogonal position by the 1,7-dimethyl groups. Consequently, the emission probability of **13** is reduced *via* non-radiative decay due to the motion of the phenyl ring.²² Additionally, the Stokes shift of **13** is increased due to stronger structural rearrangement. The donor-antenna BODIPYs **8** and **16** did not show any fluorescence in CH₂Cl₂. It is due to a possible intramolecular charge transfer.

Electrochemical properties and DFT calculations. Cyclic voltammetry was used to examine the redox properties of the BODIPY dyes in solution. The energy levels of the final products are given in Table 1. Cyclic voltammograms and a table summarizing the redox values of all BODIPY derivatives are included in the supporting information (Figure S31-42, Table S1).

Table 1. Summary of the energy levels calculated from cyclic voltammetry experiments measured at 50 mV/sec in CH₂Cl₂ with 0.1 M tetrabutylammonium hexafluorophosphate using ferrocene as reference.

compd	E _{HOMO1} [eV]	E _{HOMO2} [eV]	E _{HOMO3} [eV]	E _{LUMO} ^{a)} [eV]
5	-5.40	---	---	-3.18
13	-5.44	---	---	-3.48
8	-4.84	-4.97	-5.42	-3.28
16	-4.84	-4.98	-5.43	-3.59

a) The LUMO levels were calculated from the optical band gap.

A comparison of the HOMO/LUMO energy levels reveals two general trends. First, for all BODIPY compounds without donor substituent, the first oxidation (denoted as E_{HOMO1}) is almost unaffected by the substituent in *meso*-position, E_{HOMO1} is -5.41 ± 0.03 eV (Table 1 and Table S1 for all compounds). Thus, the HOMO of 1,3,5,7-tetramethyl BODIPYs is mainly delocalized over the BODIPY framework for both *meso*-phenyl and *meso*-ethynylphenyl BODIPYs **5** and **13**. Secondly, with increasing electron withdrawing ability of the *meso*-substituent (phenyl vs. ethynylphenyl), the energy level of the LUMO is shifted to lower values. Consequently, the LUMO is dependent on the *meso*-substituent. These findings are supported by published DFT

results and DFT calculations on **5** and **13**. From literature it is known, that the HOMO of *meso*-phenyl BODIPYs dyes without additional donor groups is delocalized over the BODIPY framework.^{22, 33} Our DFT calculations of **5** and **13** as typical examples (Figure 6) show in accordance with the literature results that the HOMO in both cases is delocalized exclusively over the BODIPY core. Furthermore, the LUMO of **5** is, delocalized mainly over the *meso*-substituent. For **13**, the LUMO is completely distributed over the *meso*-ethynylphenyl and anchor group. We attribute this behaviour to the strong electron withdrawing *para*-2-carboxy-2-cyanovinyl substituent. This is in accordance with the reported observation that LUMO of BODIPYs carrying strong electron withdrawing groups in *meso*-phenyl substituents are extensively delocalized into the *meso*-group.²² Thus in **13**, there is a decrease of orbital overlap which in turn lowers the molar extinction coefficient compared to **5**.

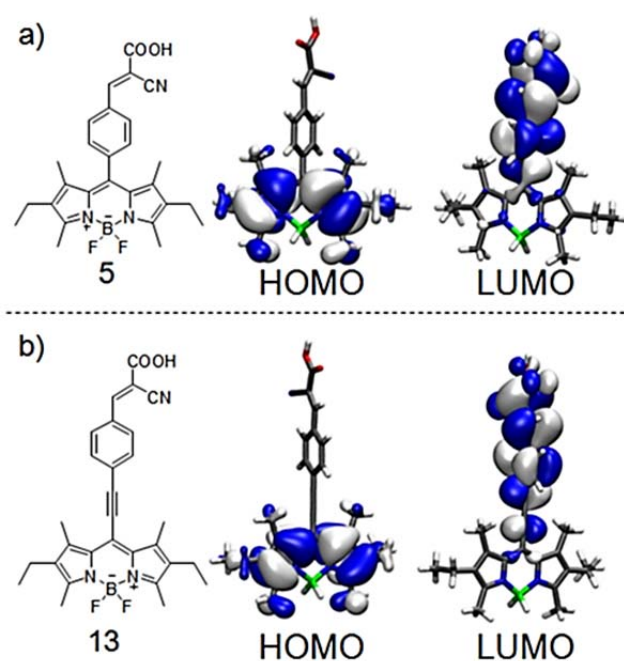


Figure 6. Orbital maps of the HOMO and LUMO of a) **5** and b) **13**.

By the attachment of the 4,4'-dimethoxytriphenylamine donor *via* a vinylic connection, the conjugated system is efficiently expanded. This can not only be seen in UV-vis measurement but also in the cyclic voltammetry experiments. The cyclic voltammograms of all 4,4'-dimethoxytriphenylamine substituted BODIPYs show three reversible oxidation signals (*e.g.*

Figure S34). In fact, for non-conjugated systems, only two oxidations would be expected. One arising from the independent 4,4'-dimethoxytriphenylamine moieties, and one from the BODIPY framework. However, we detected three reversible oxidations at -4.84 ± 0.01 eV, -4.97 ± 0.01 eV and around -5.43 eV. The shape of the first two peaks equals the cyclic voltammograms known from triphenyldiamine compounds.³⁴ This proves the conjugation of the 4,4'-dimethoxytriphenylamine moieties throughout the BODIPY core because the oxidation of one donor unit influences the electronic surrounding of the second one by the conjugation. The third oxidation is related to the BODIPY core. It was observed at values known from the BODIPYs without donor groups. As expected, the energy level deduced from the reduction peak appears in the same region as that of the donor-free BODIPYs.

An interesting feature of all BODIPY derivatives is their stability against repeated oxidation and reduction cycles. This can be attributed to the inherent redox stability of the BODIPY framework. Additionally, the *para*-methoxy groups of the donor-antenna BODIPY compounds inhibit radical coupling of the triphenylamines. *para*-Methoxy substituted triphenylamines are known for their reversible one-electron oxidation behaviour caused not simply by the occupation of the *para*-position but rather by their tendency to stabilize the radical cation and to prevent coupling.^{24, 35} In a nutshell, the LUMO level is strongly influenced by the *meso*-substituent and the HOMO is defined by the donor groups.

CONCLUSION

In this paper some novel *meso*-ethynylphenyl BODIPYs were successfully realized using a new synthetic approach. We have synthesised one *meso*-ethynylphenyl BODIPY without any donor groups (**13**) and one with two 4,4'-dimethoxytriphenylamine donor antenna groups (**16**) starting from an aliphatic aldehyde **9**. This access of condensation of aliphatic aldehyde with pyrrole opens up entirely novel structural variations in BODIPY chemistry. Additionally, the corresponding *meso*-phenyl compounds with and without donor groups (**8** and **5**) were synthesised and comparatively studied to get a general structure-property relationship for BODIPY sensitizers. Furthermore, the mechanism of the Knoevenagel-type condensation for the attachment of the donor groups was elucidated. This condensation follows an organocatalytic mechanism rather than a deprotonation of the methyl groups by piperidine as proposed earlier by other groups. Here, the piperidine catalyst does not behave like a base, but like a nucleophile. It reacts with the aromatic donor aldehyde forming an aminal or iminum ion which can in turn react with the methyl groups of the BODIPY framework. This was proven by the isolation of the aminal formed by the reaction of 4-(di(4-methoxyphenyl)amino)-benzaldehyde with piperidine. In the course of these investigations, we observed that the commonly applied Knoevenagel-type condensation using piperidine and an acid as catalyst system failed for *meso*-ethynylphenyl BODIPYs due to a nucleophilic attack of piperidine on the triple bond in a hydroamination reaction yielding the corresponding enamine. This issue could be circumvented by the use of the *meso*-(trimethylsilyl)ethynyl compound **10** instead of the *meso*-ethynylphenyl BODIPY **17**. The bulky trimethylsilyl-group can efficiently protect the triple bond from the hydroamination reaction. It was proved that the vinyl bond between the BODIPY framework and the donor group has always a *trans* configuration. Finally, proton coupled ^{13}C NMR measurements confirmed that the COOH group is in a *trans* configuration relative to the phenyl moiety. An investigation of the optical properties of the BODIPYs shows that the introduction of the ethynyl bridge between the BODIPY and the phenyl ring causes a strong bathochromic shift of the absorption. By the attachment of donor groups a panchromatic behaviour resulted for both the *meso*-phenyl and the *meso*-ethynylphenyl BODIPYs **8** and **16** with molar extinction coefficients $\epsilon > 1 \times 10^4 \text{ M}^{-1}\text{cm}^{-1}$ over the whole UV-vis region and up to near IR. In particular, the absorption edge of **16** is red-shifted to a value of 1030 nm. Furthermore, cyclic voltammetry experiments showed that BODIPYs without donor groups exhibit a HOMO level of $-5.41 \pm 0.03 \text{ eV}$ regardless of the substituents in the *meso*-position. However, the LUMO level depends on this substituent. Electron withdrawing substituents like the ethynyl group shift the level to lower values. As

expected, the HOMO levels of BODIPYs with donor groups are determined by the donor group. The HOMO/LUMO distributions are further supported by DFT calculations.

EXPERIMENTAL SECTION

Synthetic Details. The compounds 4-(1,3-dioxolan-2-yl)benzaldehyde (**1**)³⁶, 8-[4-(1,3-dioxolan-2-yl)phenyl]-1,3,5,7-tetramethyl-2,6-diethyl-4,4-difluoro-4-bora-3a,4a-diaza-s-indacene (**3**)¹⁶ and 4-(di(4-methoxy-phenyl)amino)benzaldehyde³⁷ were prepared according to slightly modified standard procedures. The synthetic procedures of all other compounds can be found in the Supporting Information.

Photophysical and electrochemical measurements. UV-vis spectra were recorded in CH₂Cl₂ (or in THF/CH₂Cl₂ 1:1 for **13**) on a Hitachi U-3000 spectrophotometer or in a Bentham DTR6 integrating sphere at a concentration in the range of 1 x 10⁻⁵ M. The extinction coefficients were calculated according to the Beer-Lambert law. The same solutions were also used for fluorescence measurement on a Shimadzu RF-5301PC spectrofluorometer. Cyclic voltammetry (CV) was carried out under moisture- and oxygen-free conditions using a standard three-electrode assembly connected to a potentiostat (model 263A, EG&G Princeton Applied Research) at a scanning rate of 50 mV sec⁻¹. A Pt milli-electrode (model G0228, AMETEK Advanced Measurement Technology) was used as working electrode. A platinum wire in the respective solvent plus conducting salt (tetrabutylammonium hexafluorophosphate, 0.1 M) was used as counter electrode. The quasi-reference electrode consisted of an Ag-wire in an AgNO₃/acetonitrile solution (0.1 M). Each measurement was calibrated with the internal standard ferrocene/ferrocenium. The energy levels were determined by the empirical relation E_{HOMO} or E_{LUMO} = [-e.(E^{1/2}_(x vs. Ag/AgNO₃) - E^{1/2}_(Fc/Fc⁺ vs. Ag/AgNO₃))] - 4.80 eV. Molecular geometries, energy levels, and orbitals were calculated from density functional theory at the B3LYP/cc-pVTZ level using the TURBOMOLE program package.³⁸

ACKNOWLEDGEMENT

We acknowledge financial support from the Graduiertenkolleg GRAKO 1640 (DFG).

BIBLIOGRAPHY

- 1 A. Treibs, F.-H. Kreuzer, *Liebigs Annalen der Chemie*, **1968**, 718, 208-223.
- 2 D. Zhang, V. Martin, I. García-Moreno, A. Costela, M. E. Pérez-Ojeda, Y. Xiao, *Physical Chemistry Chemical Physics*, **2011**, 13, 13026-13033.
- 3 J. Banuelos-Prieto, A. R. Agarrabeitia, I. Garcia-Moreno, I. Lopez-Arbeloa, A. Costela, L. Infantes, M. E. Perez-Ojeda, M. Palacios-Cuesta, M. J. Ortiz, *Chemistry - A European Journal*, **2010**, 16, 14094-14105.
- 4 T. L. Arbeloa, F. L. Arbeloa, I. L. Arbeloa, I. García-Moreno, A. Costela, R. Sastre, F. Amat-Guerri, *Chemical Physics Letters*, **1999**, 299, 315-321.
- 5 C. McCusker, J. B. Carroll, V. M. Rotello, *Chemical Communications*, **2005**, 996-998.
- 6 J. Karolin, L. B.-A. Johansson, L. Strandberg, T. Ny, *Journal of the American Chemical Society*, **1994**, 116, 7801-7806.
- 7 D. W. Domaille, L. Zeng, C. J. Chang, *Journal of the American Chemical Society*, **2010**, 132, 1194-1195.
- 8 K. Rurack, M. Kollmannsberger, J. Daub, *Angewandte Chemie International Edition*, **2001**, 40, 385-387.
- 9 L. Bonardi, H. Kanaan, F. Camerel, P. Jolinat, P. Retailleau, R. Ziessel, *Advanced Functional Materials*, **2008**, 18, 401-413.
- 10 A. Hepp, G. Ulrich, R. Schmechel, H. von Seggern, R. Ziessel, *Synthetic Metals*, **2004**, 146, 11-15.
- 11 R. Y. Lai, A. J. Bard, *Journal of Physical Chemistry B*, **2003**, 107, 5036-5042.
- 12 R. K. Lammi, R. W. Wagner, A. Ambroise, J. R. Diers, D. F. Bocian, D. Holten, J. S. Lindsey, *Journal of Physical Chemistry B*, **2001**, 105, 5341-5352.
- 13 G. Ulrich, R. Ziessel, A. Harriman, *Angewandte Chemie International Edition*, **2008**, 47, 1184-1201.
- 14 S. Kolemen, O. A. Bozdemir, Y. Cakmak, G. Barin, S. Erten-Ela, M. Marszalek, J.-H. Yum, S. M. Zakeeruddin, M. K. Nazeeruddin, M. Grätzel, E. U. Akkaya, *Chemical Science*, **2011**, 2, 949-954.
- 15 D. Kumaresan, R. Thummel, T. Bura, G. Ulrich, R. Ziessel, *Chemistry - A European Journal*, **2009**, 15, 6335-6339.
- 16 S. Erten-Ela, M. D. Yilmaz, B. Icli, Y. Dede, S. Icli, E. U. Akkaya, *Organic Letters*, **2008**, 10, 3299-3302.
- 17 S. Kolemen, Y. Cakmak, S. Erten-Ela, Y. Altay, J. Brendel, M. Thelakkat, E. U. Akkaya, *Organic Letters*, **2010**, 12, 3812-3815.
- 18 T. Rousseau, A. Cravino, E. Ripaud, P. Leriche, S. Rihn, A. De Nicola, R. Ziessel, J. Roncali, *Chemical Communications*, **2010**, 46, 5082-5084.
- 19 A. Loudet, K. Burgess, *Chemical Reviews*, **2007**, 107, 4891-4932.
- 20 R. Ziessel, G. Ulrich, A. Harriman, *New Journal of Chemistry*, **2007**, 31, 496-501.
- 21 H. J. Snaith, *Advanced Functional Materials*, **2010**, 20, 13-19.
- 22 Y. Chen, L. Wan, D. Zhang, Y. Bian, J. Jiang, *Photochemical and Photobiological Science*, **2011**, 10, 1030-1038.
- 23 V. Lin, S. DiMagno, M. Therien, *Science*, **1994**, 264, 1105-1111

- 24 E. T. Seo, R. F. Nelson, J. M. Fritsch, L. S. Marcoux, D. W. Leedy, R. N. Adams, *Journal of the American Chemical Society*, **1966**, 88, 3498-3503.
- 25 L. Bonardi, G. Ulrich, R. Ziessel, *Organic Letters*, **2008**, 10, 2183-2186.
- 26 A. Treibs, R. Wilhelm, E. Herrmann, *Liebigs Annalen der Chemie*, **1981**, 1981, 849-857.
- 27 A. C. O. Hann, A. Lapworth, *Journal of the Chemical Society, Transactions*, **1904**, 85, 46-56.
- 28 S. Bednarz, D. Bogdal, *International Journal of Chemical Kinetics*, **2009**, 41, 589-598.
- 29 R. Severin, S. Doye, *Chemical Society Reviews*, **2007**, 36, 1407-1420.
- 30 M. Makosza, D. N. Kozhevnikov, in *Russian Chemical Bulletin*, Vol. 50, Springer New York, **2001**, pp. 2236-2238.
- 31 O. Buyukcakil, O. A. Bozdemir, S. Kolemen, S. Erbas, E. U. Akkaya, *Organic Letters*, **2009**, 11, 4644-4647.
- 32 U. Vogeli, W. von Philipsborn, *Organic Magnetic Resonance*, **1975**, 7, 617-627.
- 33 H. L. Kee, C. Kirmaier, L. Yu, P. Thamyongkit, W. J. Youngblood, M. E. Calder, L. Ramos, B. C. Noll, D. F. Bocian, W. R. Scheidt, R. R. Birge, J. S. Lindsey, D. Holten, *Journal of the Physical Chemistry B*, **2005**, 109, 20433-20443.
- 34 M. Thelakkat, R. Fink, P. Pösch, J. Ring, H.-W. Schmidt, *Polymer Preprints of the American Chemical Society*, **1997**, 38, 394-395.
- 35 R. R. Nelson, R. N. Adams, *Journal of the American Chemical Society*, **1968**, 90, 3925-3930.
- 36 N. M. Loim, E. S. Kelbysheva, *Russian Chemical Bulletin*, **2004**, 53, 2080-2085.
- 37 M. Sommer, S. Hüttner, M. Thelakkat, *Advances in Polymer Science*, **2010**, 228, 123-153.
- 38 TURBOMOLE V6.3 2011, a development of University of Karlsruhe and Forschungszentrum Karlsruhe GmbH, 1989-2007, TURBOMOLE GmbH, since 2007; available from <http://www.turbomole.com>., **2007**.

SUPPORTING INFORMATION

for the manuscript:

SYNTHESIS AND PROPERTIES OF PANCHROMATIC BODIPYs WITH DONOR-ANTENNA GROUPS: A NEW SYNTHETIC ROUTE TOWARDS *meso*-ETHYNYLPHENYL BODIPYs

Katja Gräfe^[a], Thomas Körzdörfer^[b], Stephan Kümmel^[b] and Mukundan Thelakkat^{[a]}*

^[a] Department of Macromolecular Chemistry I, Applied Functional Polymers, Universität Bayreuth, Universitätsstr. 30, 95440 Bayreuth, Germany.

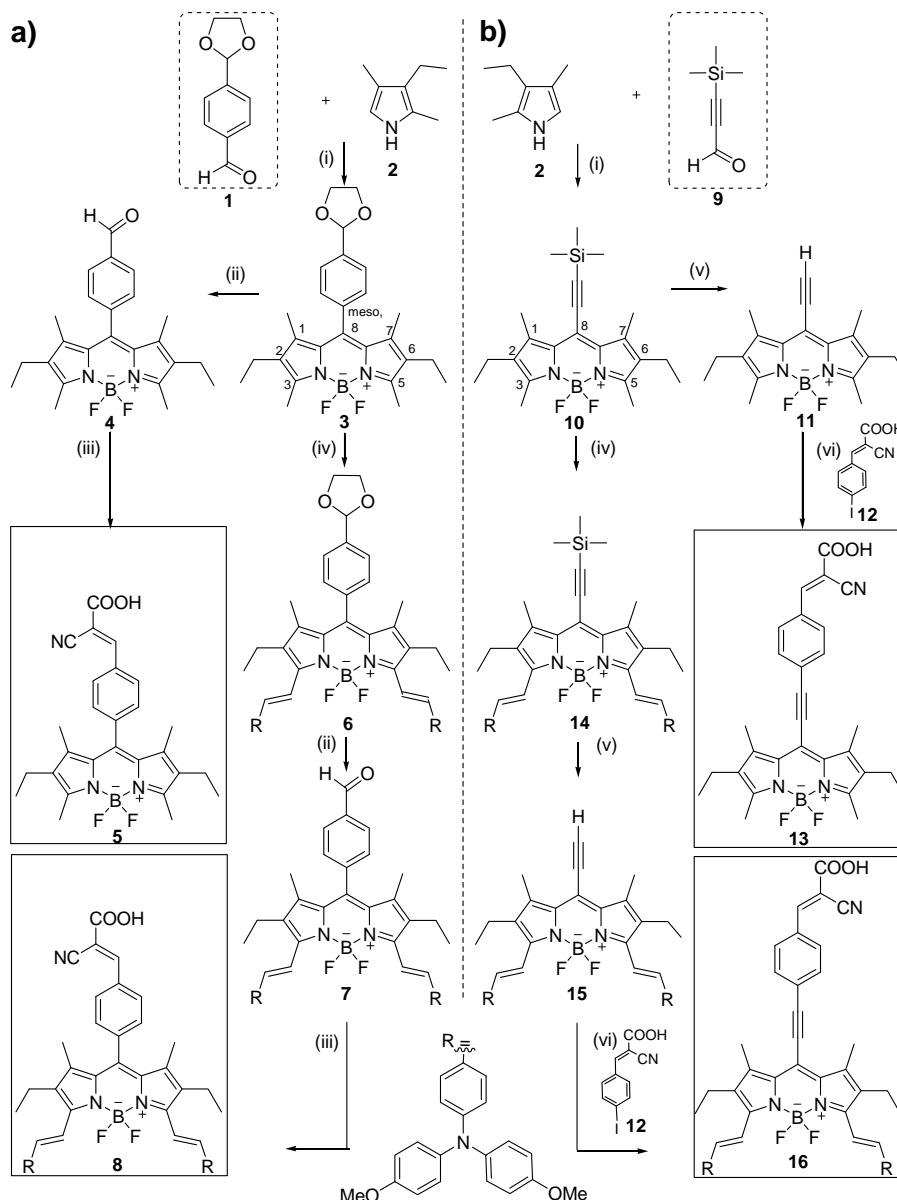
^[b] Department of Theoretical Physics IV, Universität Bayreuth, Universitätsstr. 30, 95440 Bayreuth, Germany.

Table of Contents

1. Synthesis Procedures
2. Hann-Lapworth Mechanism
3. NMR Spectra
4. FT-IR Spectra
5. UV-vis Spectra
6. CV Curves

1. Synthesis Procedures

A schematic presentation of the whole synthesis is depicted in Scheme S1.



Scheme S1. Synthetic routes a) for *meso*-phenyl BODIPYs (5, 8) and b) for *meso*-ethynylphenyl BODIPYs (13, 16).

Preparation of 8-(4-formylphenyl)-1,3,5,7-tetramethyl-2,6-diethyl-4,4-difluoro-4-bora-3a,4a-diaza-*s*-indacene 4. 3 (200.0 mg, 0.463 mmol) is dissolved in THF (50 mL) and 5 % HCl_{aq} (10 mL) is added. The solution is stirred for 3.5 h. Then CH₂Cl₂ (100 mL) is added and the solution is washed with diluted NaHCO₃ _{aq} (50 mL) and water (4 x 80 mL) until neutrality. The organic phase is dried over Na₂SO₄, filtered and the solvent is removed under vacuum to yield the pure product. Yield: 189 mg (red solid), 100 %.

$^1\text{H-NMR}$ (300 MHz, CDCl_3): δ = 1.00 (t, 6H; 2/6- CH_2CH_3), 1.27 (s, 6H; 1/7- CH_3), 2.32 (q, 4H; 2/6- CH_2CH_3), 2.56 (s, 6H; 3/5- CH_3), 7.53 (d, 2H; 8- H_{ar}), 8.04 (d, 2H; 8- H_{ar}), 10.14 (s, 1H; COH).

Preparation of 8-[4-(2-carboxy-2-cyanovinyl)phenyl]-1,3,5,7-tetramethyl-2,6-diethyl-4,4-difluoro-4-bora-3a,4a-diaza-s-indacene 5. 2-Cyanoacetic acid (218.7 mg, 2.572 mmol, 7 eq) and **4** (150.0 mg, 0.367 mmol, 1 eq) are dissolved in dry acetonitrile (35 mL) and piperidine (50 μL) is added. Then, the solution is heated to reflux for 3 h. The solvent is removed and the residue is dissolved in CH_2Cl_2 washed with water (4 x 80 mL), dried over Na_2SO_4 and is concentrated. The raw product is purified by column chromatography with toluene/methanol 5:1 as eluent. Yield after freeze-drying from 1,4-dioxane: 158 mg (red-orange solid, R_f (SiO_2 ; toluene/methanol 5:1) = 0.20), 90 %.

$^1\text{H-NMR}$ (300 MHz, DMSO-d_6): δ = 0.94 (t, 6H; 2/6- CH_2CH_3), 1.28 (s, 6H; 1/7- CH_3), 2.27 (q, 4H; 2/6- CH_2CH_3), 2.44 (s, 6H; 3/5- CH_3), 7.57 (d, 2H; 8- H_{ar}), 8.14 (d, 2H; 8- H_{ar}), 8.27 (s, 1H; Ph- $\text{CH}=\text{C}(\text{COOH})(\text{CN})$).

Preparation of 8-[4-(1,3-dioxolan-2-yl)phenyl]-1,7-dimethyl-3,5-di[4-(di(*p*-methoxyphenyl)-amino)styryl]-2,6-diethyl-4,4-difluoro-4-bora-3a,4a-diaza-s-indacene 6. To a solution of **3** (100.0 mg, 0.221 mmol, 1 eq) and 4-(di(4-methoxyphenyl)amino)-benzaldehyde (221.1 mg, 0.663 mmol, 3 eq) in benzene (20 mL) are added piperidine (0.3 mL) and glacial acetic acid (0.25 mL). After heating the solution to reflux over a glass frit containing molecular sieve (4 Å) for 11 h, the solvent is removed and the raw product is purified by column chromatography using cyclohexane/ethyl acetate 2:1 as eluent. Yield: 77 mg (green-black solid, R_f (SiO_2 ; cyclohexane: ethyl acetate 2:1) = 0.30), 32 %.

$^1\text{H-NMR}$ (300 MHz, CDCl_3): δ = 1.15 (t, 6H; 2/6- CH_2CH_3), 1.32 (s, 6H; 1/7- CH_3); 2.61 (q, 4H; 2/6- CH_2CH_3), 3.83 (s, 12H; OMe), 4.09-4.26 (m, 4H, O- CH_2CH_2 -O), 5.90 (s, 1H, Ph-CH), 6.86 (d, 8H; 3/5- H_{ar}), 6.93 (d, 4H; 3/5- H_{ar}), 7.10 (d, 8H; 3/5- H_{ar}), 7.19 (d, $^3J_{1\text{H}/1\text{H}}$ = 16.4 Hz, 2H; 3/5CH=CH), 7.36 (d, 2H; 8- H_{ar}), 7.42 (d, 4H; 3/5- H_{ar}), 7.64 (d+d, 2H+2H; 3/5CH=CH + 8- H_{ar}).

Preparation of 8-(4-formylphenyl)-1,7-dimethyl-3,5-di[4-(di(*p*-methoxyphenyl)amino)styryl]-2,6-diethyl-4,4-difluoro-4-bora-3a,4a-diaza-s-indacene 7. **6** (100.0 mg, 0.092 mmol) is dissolved

in THF (40 mL) and 5 % HCl_{aq} (5 mL) is added. The solution is stirred overnight. Then CH₂Cl₂ (100 mL) is added and the solution is washed with diluted NaHCO₃ _{aq} (50 mL) and water (4 x 100 mL) until neutrality. The organic phase is dried over Na₂SO₄, filtered and the solvent is removed under vacuum to yield the pure product. Yield: 95 mg (green-black solid), 99 %.

¹H-NMR (300 MHz, CDCl₃): δ = 1.16 (t, 6H; 2/6-CH₂CH₃), 1.30 (s, 6H; 1/7-CH₃); 2.61 (q, 4H; 2/6-CH₂CH₃), 3.83 (s, 12H; OMe), 6.87 (d, 8H; 3/5-*H_{ar}*), 6.93 (d, 4H; 3/5-*H_{ar}*), 7.10 (d, 8H; 3/5-*H_{ar}*), 7.20 (d, ³J_{1H/1H} = 16.6 Hz, 2H; 3/5CH=CH), 7.45 (d, 4H; 3/5-*H_{ar}*), 7.55 (d, 2H; 8-*H_{ar}*), 7.64 (d, ³J_{1H/1H} = 16.6 Hz, 2H; 3/5CH=CH), 8.04 (d, 2H; 8-*H_{ar}*), 10.15 (s, 1H; COH).

Preparation of 8-[4-(2-carboxy-2-cyanovinyl)phenyl]-1,7-dimethyl-3,5-di[4-(di(*p*-methoxyphenyl)amino)styryl]-2,6-diethyl-4,4-difluoro-4-bora-3a,4a-diaza-*s*-indacene 8. 2-Cyanoacetic acid (65.6 mg, 0.772 mmol, 7 eq) and **7** (114.3 mg, 0.110 mmol, 1 eq) are dissolved in dry acetonitrile (35 mL) and three drops of piperidine are added. Then, the solution is heated to reflux for 5 h. The solvent is removed and the residue is dissolved in CH₂Cl₂ washed with water (4 x 80 mL), dried over Na₂SO₄ and is concentrated. The raw product is purified by column chromatography with CH₂Cl₂/methanol 15:1 as eluent. Yield after freeze-drying from 1,4-dioxane: 72 mg (brown-black solid, R_f (SiO₂; CH₂Cl₂/methanol 15:1) = 0.45), 59 %.

¹H-NMR (300 MHz, DMSO-*d*₆): δ = 1.07 (t, 6H; 2/6-CH₂CH₃), 1.31 (s, 6H; 1/7-CH₃); 2.58 (q, 4H; 2/6-CH₂CH₃), 3.76 (s, 12H; OMe), 6.78 (d, 4H; 3/5-*H_{ar}*), 6.93 (d, 8H; 3/5-*H_{ar}*), 7.07 (d, 8H; 3/5-*H_{ar}*), 7.21 (d, ³J_{1H/1H} = 16.6 Hz, 2H; 3/5CH=CH), 7.41 (d + d, 2H + 4H; 3/5CH=CH + 3/5-*H_{ar}*), 7.56 (d, 2H; 8-*H_{ar}*), 8.10 (d, 2H; 8-*H_{ar}*), 8.16 (s, 1H; Ph-CH=C(COOH)(CN)).

Preparation of 8-[(trimethylsilyl)ethynyl]-1,3,5,7-tetramethyl-2,6-diethyl-4,4-difluoro-4-bora-3a,4a-diaza-*s*-indacene 10. Under dry conditions, 3-ethyl-2,4-dimethyl-1*H*-pyrrole (13.664 g, 110.909 mmol, 2 eq) is dissolved in dry CH₂Cl₂ (300 mL), cooled to -5 °C and degassed with argon for 30 min. Then **9** (7.000 g, 55.454 mmol, 1 eq) and one drop of trifluoroacetic acid is added. The solution instantly becomes orange, and changes the colour firstly to red and then to deep violet. After 1 h 2,3-dichloro-5,6-dicyano-1,4-benzoquinone (12.588 g, 55.454 mmol, 1 eq) is added at RT and stirring is continued overnight. NEt₃ (46.4 mL, 332.726 mmol, 6 eq) and 30 min later BF₃·OEt₂ (55.7 mL, 443.635 mmol, 8 eq) are added slowly. Stirring is continued for further 3 h. Then the solvent is removed under reduced pressure and the raw product is purified by

column chromatography using cyclohexane/ethyl acetate 13:1 as eluent. Yield: 9.66 g (pink-black solid, R_f (SiO₂; cyclohexane: ethyl acetate 13:1) = 0.49), 44 %.

¹H-NMR (300 MHz, CDCl₃): δ = 0.31 (s, 9H; Si(CH₃)₃), 1.06 (t, 6H; 2/6-CH₂CH₃), 2.41 (s, 6H; 1/7-CH₃), 2.41 (q, 4H; 2/6-CH₂CH₃), 2.51 (s, 6H; 3/5-CH₃).

Preparation of 8-ethynyl-1,3,5,7-tetramethyl-2,6-diethyl-4,4-difluoro-4-bora-3a,4a-diaza-s-indacene 11. **10** (400.0 mg, 0.999 mmol, 1 eq) is dissolved in methanol (80 mL), KF (290.2 mg, 4.995 mmol, 5 eq) is added and the reaction solution is stirred for 1.5 h at RT. After full consumption of the starting material, 1% CH₃COOH_{aq} (50 mL) is added. Then, CH₂Cl₂ (150 mL) is added and the organic layer is washed with water (4 x 80 mL) until neutrality. It is dried over Na₂SO₄ and the solvent is removed under vacuum. Yield: 327 mg (pink-black solid), 100 %.

¹H-NMR (300 MHz, CDCl₃): δ = 1.07 (t, 6H; 2/6-CH₂CH₃), 2.41 (s, 6H; 1/7-CH₃), 2.41 (q, 4H; 2/6-CH₂CH₃), 2.52 (s, 6H; 3/5-CH₃), 3.89 (s, 1H; \equiv H).

Preparation of 2-cyano-3-(4-iodophenyl)acrylic acid 12. Under dry conditions, 4-iodobenzaldehyde (7.400 g, 31.894 mmol, 1 eq) is dissolved in benzene (90 mL). Piperidine (0.90 mL), glacial acetic acid (0.75 mL) and 2-cyanoacetic acid (18.990 g, 0.223 mol, 7 eq) are added. The solution is heated to reflux over a glass frit containing molecular sieve (4 Å) for 40 h. Then, the solvent is removed and the raw product is purified by repetitive recrystallisation from CH₂Cl₂. Yield: 5.03 g (white solid), 53 %.

¹H-NMR (300 MHz, DMSO-d₆): δ = 7.79 (d, 2H; 2-*H_{ar}*), 7.98 (d, 2H; 3-*H_{ar}*), 8.30 (s, 1H; Ph-CH=C(COOH)(CN)), 14.04 (s (broad), 1H; COOH). ¹³C-NMR (125 MHz, DMSO-d₆): δ = 163.19 (d, ³*J*_{1H/13C} = 6.7 Hz; COOH), 153.46 (d, ¹*J*_{1H/13C} = 162.2 Hz; CH=C(COOH)(CN)), 138.29 (d, ¹*J*_{1H/13C} = 167.6 Hz; 3/5-*C_{ar}*), 132.06 (d, ¹*J*_{1H/13C} = 162.8 Hz; 2/6-*C_{ar}*), 130.91 (s; 1-*C_{ar}*), 115.97 (³*J*_{1H/13C} = 13.9 Hz; CN), 104.43 (s; CH=C(COOH)(CN)), 101.50 (s; 4-*C_{ar}*).

Preparation of 8-[(4-(2-carboxy-2-cyanovinyl)phenyl)ethynyl]-1,3,5,7-tetramethyl-2,6-diethyl-4,4-difluoro-4-bora-3a,4a-diaza-s-indacene 13. Under dry and oxygen-free conditions, **12** (820.0 mg, 2.742 mmol, 3 eq), Pd(PPh₃)₄ (63.4 mg, 0.055 mmol, 0.06 eq), CuI (6.9 mg,

0.036 mmol, 0.04 eq) and NEt₃ (0.60 mL, 4.296 mmol, 4.7 eq) are dissolved in dry THF (13 mL). Then, **11** (300.0 mg, 0.914 mmol, 1 eq) is dissolved in dry THF (20 mL) and added dropwise over 3 h at RT to the reaction solution. After further 60 min stirring at RT, the solvent is removed. The residue is dissolved in CHCl₃ and washed with water (4 x 100 mL). The organic fraction is dried over Na₂SO₄ and filtered. After removal of the solvent, the raw product is purified by column chromatography with cyclohexane/ethyl acetate 2:1 + 1% of glacial acetic acid, then the solvent is changed to CH₂Cl₂ followed by a change to CH₂Cl₂/methanol 20:1 with a gradient to 10:1. Yield: 218 mg (purple-black solid, R_f (SiO₂; CH₂Cl₂/methanol 10:1) = 0.50), 48 %.

¹H-NMR (300 MHz, DMF-d₇): δ = 1.07 (t, 6H; 2/6-CH₂CH₃), 2.46 (q, 4H; 2/6-CH₂CH₃), 2.53 (s, 6H; 3/5-CH₃), 2.58 (s, 6H; 1/7-CH₃), 7.87 (d, 2H; 8-*H_{ar}*), 8.09 (d, 2H; 8-*H_{ar}*), 8.29 (s, 1H; Ph-CH=C(COOH)(CN)).

Preparation of 8-[(trimethylsilyl)ethynyl]-1,7-dimethyl-3,5-di[4-(di(*p*-methoxyphenyl)amino)-styryl]-2,6-diethyl-4,4-difluoro-4-bora-3a,4a-diaza-*s*-indacene **14.** Under dry conditions 4-(di(4-methoxyphenyl)amino)benzaldehyde (1.873 g, 5.620 mmol, 3 eq) is dissolved in dry benzene (40 mL). Piperidine (0.30 mL), glacial acetic acid (0.25 mL) and then **10** (750.0 mg, 1.873 mmol, 1 eq) are added. The reaction solution is heated to reflux over a glass frit containing molecular sieve (4 Å) to remove the formed water. After complete consumption of the starting material (21 h), the solvent is removed and the raw product is purified by column chromatography using CH₂Cl₂/hexane 9:1 as eluent. Yield: 800 mg (blue-black solid, R_f (SiO₂; CH₂Cl₂/hexane 9:1) = 0.23), 41 %.

¹H-NMR (300 MHz, benzene-d₆): δ = 0.22 (s, 9H; Si(CH₃)₃), 1.07 (t, 6H; 2/6-CH₂CH₃), 2.36 (s, 6H; 1/7-CH₃), 2.55 (q, 4H; 2/6-CH₂CH₃), 3.37 (s, 12H; OMe), 6.75 (d, 8H; 3/5-*H_{ar}*), 6.84 (d, 4H; 3/5-*H_{ar}*), 7.04 (d, 8H; 3/5-*H_{ar}*), 7.38 (d, ³J_{1H/1H} = 16.6 Hz, 2H; 3/5CH=CH), 7.48 (d, 4H; 3/5-*H_{ar}*), 8.42 (d, ³J_{1H/1H} = 16.5 Hz, 2H; 3/5CH=CH).

Preparation of 8-ethynyl-1,7-dimethyl-3,5-di[4-(di(*p*-methoxyphenyl)amino)styryl]-2,6-diethyl-4,4-difluoro-4-bora-3a,4a-diaza-*s*-indacene **15.** **14** (790.0 mg, 0.766 mmol, 1 eq) is dissolved in THF/methanol 1:1 (80 mL of each), KF (222.6 mg, 3.831 mmol, 5 eq) is added and the reaction solution is stirred for 30 min at RT. Then 1 % CH₃COOH_{aq} (50 mL) and CH₂Cl₂ (150 mL) are added.

The organic layer is washed with water (4 x 100 mL) until neutrality, dried over Na₂SO₄, filtered and the solvent is removed under vacuum. Yield: 710 mg (blue-black solid), 97 %.

¹H-NMR (300 MHz, THF-d₈): δ = 1.24 (t, 6H; 2/6-CH₂CH₃), 2.53 (s, 6H; 1/7-CH₃), 2.78 (q, 4H; 2/6-CH₂CH₃), 3.80 (s, 12H; OMe), 4.69 (s, 1H; -≡H), 6.88 (d + d, 4H + 8H; 3/5-*H_{ar}*), 7.08 (d, 8H; 3/5-*H_{ar}*), 7.28 (d, ³*J*_{1H/1H} = 16.7 Hz, 2H; 3/5CH=CH), 7.41 (d, 4H; 3/5-*H_{ar}*), 7.63 (d, ³*J*_{1H/1H} = 16.6 Hz, 2H; 3/5CH=CH).

Preparation of 8-[(4-(2-carboxy-2-cyanovinyl)phenyl)ethynyl]-1,7-dimethyl-3,5-di[4-(di(*p*-methoxyphenyl)amino)styryl]-2,6-diethyl-4,4-difluoro-4-bora-3a,4a-diaza-s-indacene 16.

Under dry and oxygen-free conditions, **12** (280.1 mg, 0.939 mmol, 3 eq), Pd(PPh₃)₄ (21.7 mg, 0.019 mmol, 0.06 eq), CuI (2.4 mg, 0.013 mmol, 0.04 eq) and NEt₃ (0.20 mL, 1.408 mmol, 4.5 eq) are dissolved in dry THF (15 mL). Then, **15** (300.0 mg, 0.313 mmol, 1 eq) is likewise dissolved in dry THF (20 mL) and added dropwise over 3 h at RT to the reaction solution. After further 60 min stirring at RT, the solvent is removed. The raw product is purified by column chromatography starting with cyclohexane/ethyl acetate 2:1 + 1 % of glacial acetic acid, then the solvent is changed to CH₂Cl₂ followed by a change to CH₂Cl₂:methanol 20:1 with a gradient to 10:1. The product fractions are collected and concentrated. The pure product is precipitated from ethanol, washed with ethanol, methanol, hexane and water. Yield: 170 mg (green-black solid, R_f (SiO₂; CH₂Cl₂/methanol 10:1) = 0.41), 48 %.

¹H-NMR (300 MHz, DMSO-d₆): δ = 1.13 (t, 6H; 2/6-CH₂CH₃), 2.49 (s, 6H; 1/7-CH₃), 2.67 (q, 4H; 2/6-CH₂CH₃), 3.75 (s, 12H; OMe), 6.76 (d, 4H; 3/5-*H_{ar}*), 6.92 (d, 8H; 3/5-*H_{ar}*), 7.05 (d, 8H; 3/5-*H_{ar}*), 7.20 (d, ³*J*_{1H/1H} = 16.4 Hz, 2H; 3/5CH=CH), 7.38 (d, ³*J*_{1H/1H} = 16.9 Hz + d, 2H + 4H; 3/5CH=CH + 3/5-*H_{ar}*), 7.72 (d, 2H; 8-*H_{ar}*), 7.95 (d, 2H; 8-*H_{ar}*), 8.00 (s, 1H; Ph-CH=C(COOH)(CN)).

2. Hann-Lapworth Mechanism

For clarity, the Hann-Lapworth mechanism as applied to the reaction of 3,5-dimethyl-BODIPYs with aromatic aldehydes under the influence of piperidine is depicted here. It is pointed out that this mechanism is only shown for a better understanding and it is not valid for this reaction.

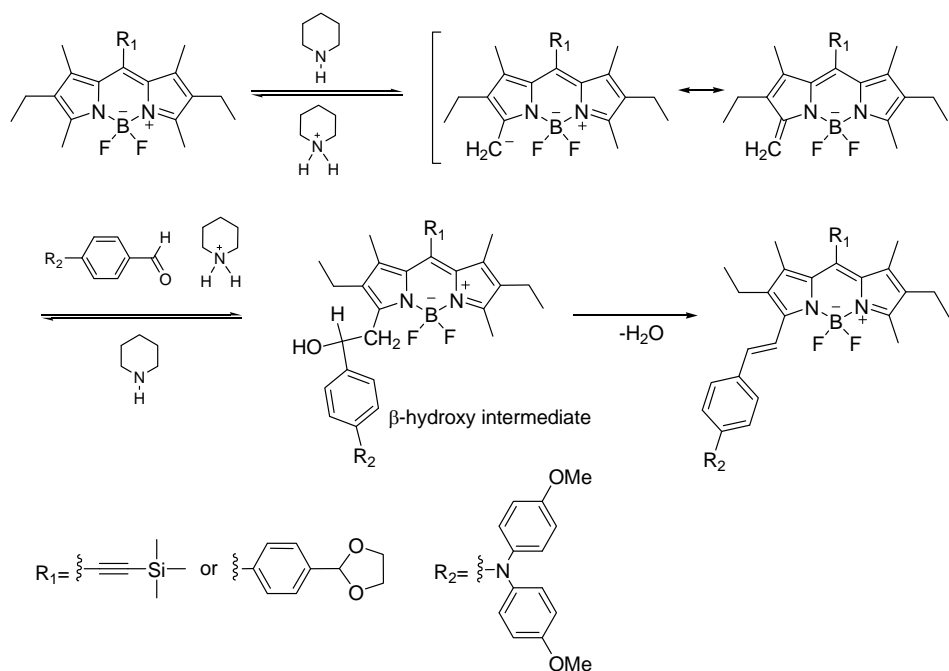


Figure S1. Hann-Lapworth mechanism as applied to the reaction of 3,5-dimethyl-BODIPYs with aromatic aldehydes under the influence of piperidine.

The validity of this mechanism was excluded by the fact the β -hydroxy intermediate was not formed. Instead animal B (Figure S16) was formed, proving the validity of the organocatalytic mechanism show in Figure 1.

3. NMR Spectra

^1H -NMR spectra were recorded on a Bruker Avance 300 spectrometer at a transmitter frequency of 300 MHz and ^1H - ^{13}C coupled NMR spectra were recorded at a frequency of 125 MHz. The spectra are calibrated to the chemical shift of the respective solvent residual signal.

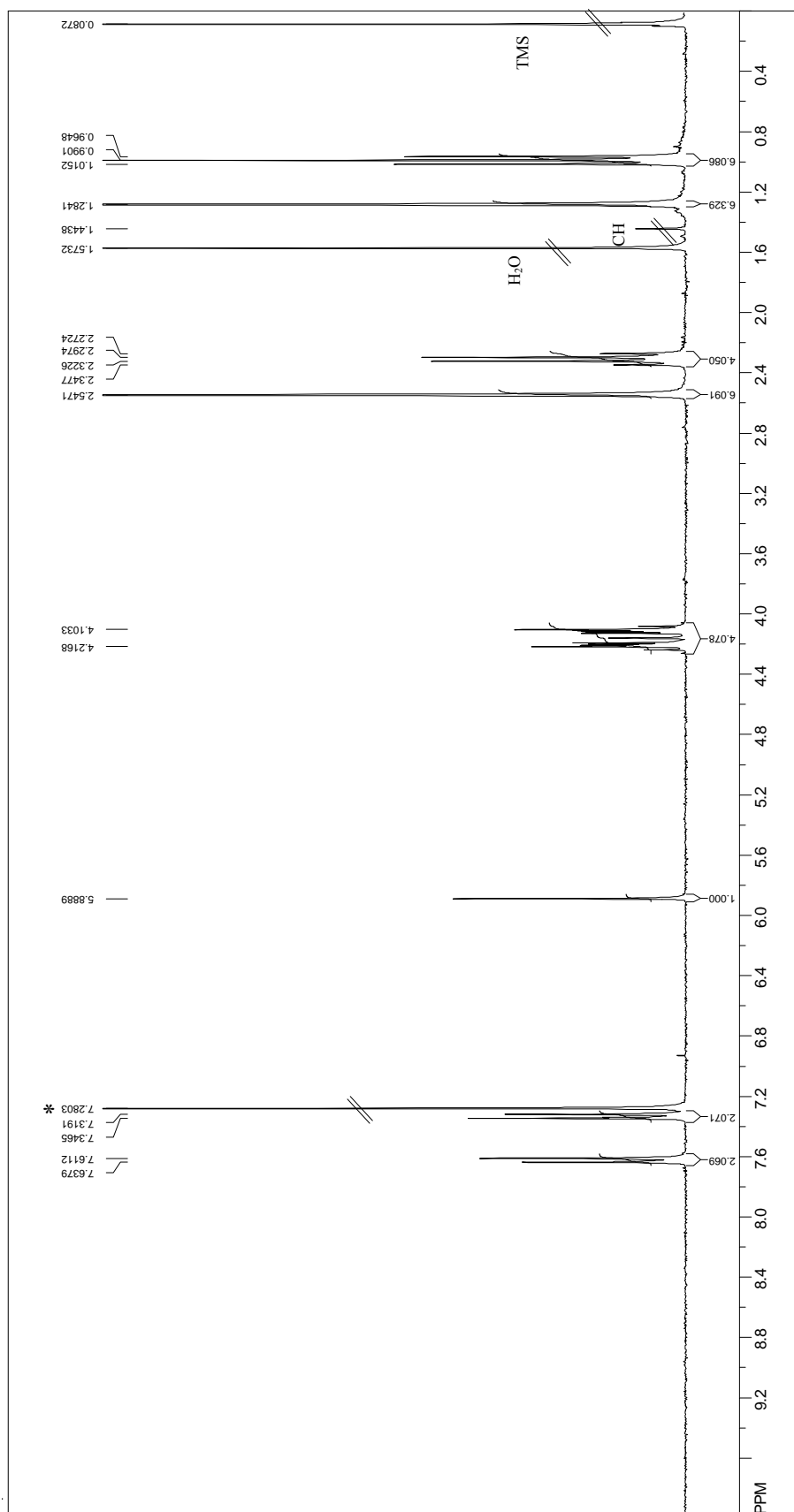


Figure S2. ^1H -NMR spectrum of compound **3** in CDCl_3 . (*: solvent residual signal; TMS: internal standard = tetramethylsilane; CH: cyclohexane)

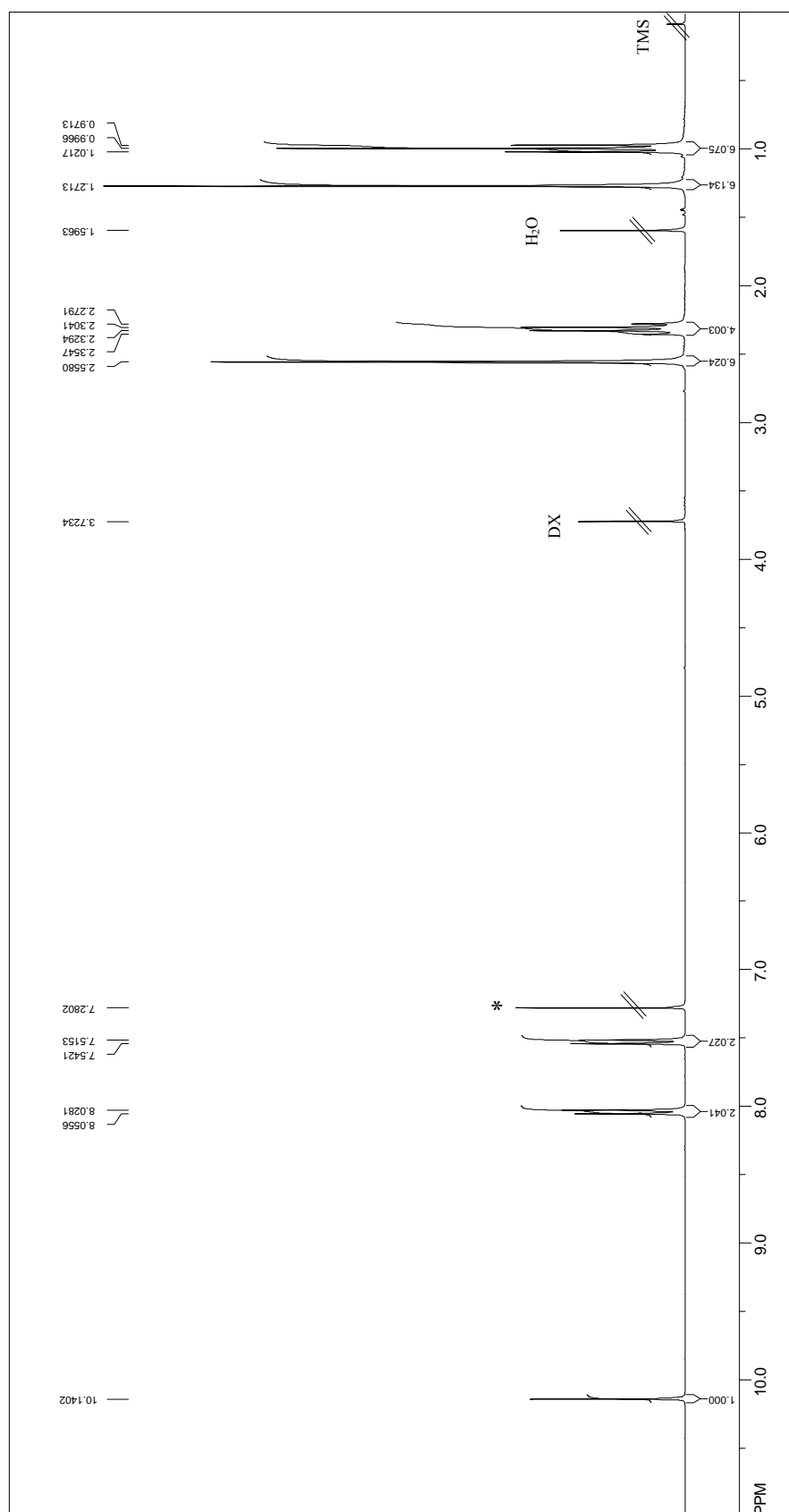


Figure S3. ¹H-NMR spectrum of compound **4** in CDCl₃. (*: solvent residual signal; TMS: internal standard = tetramethylsilane; CH: cyclohexane)

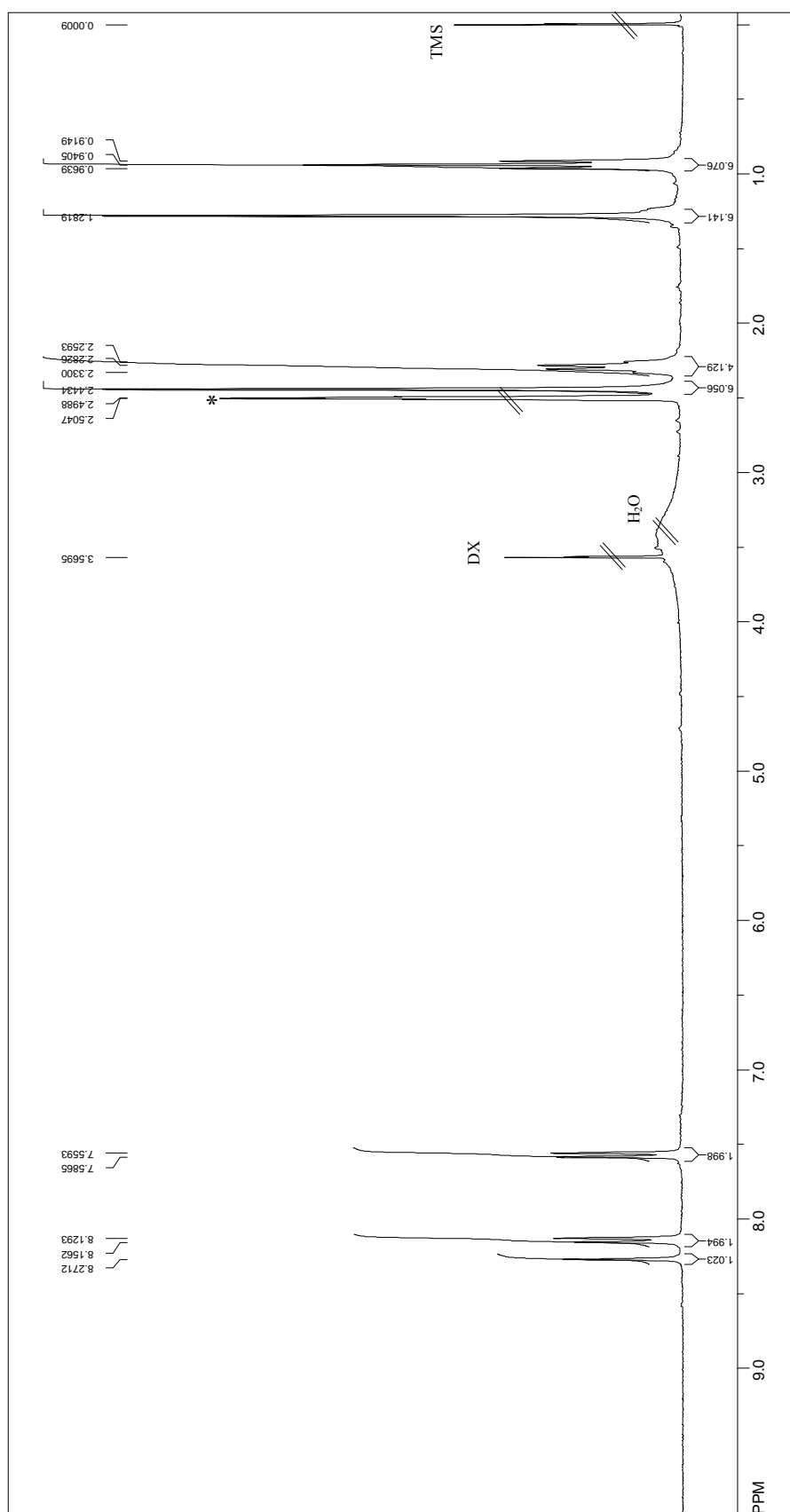
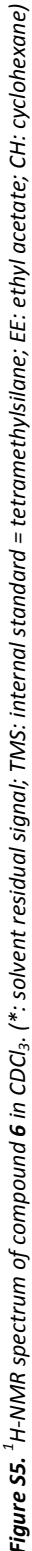
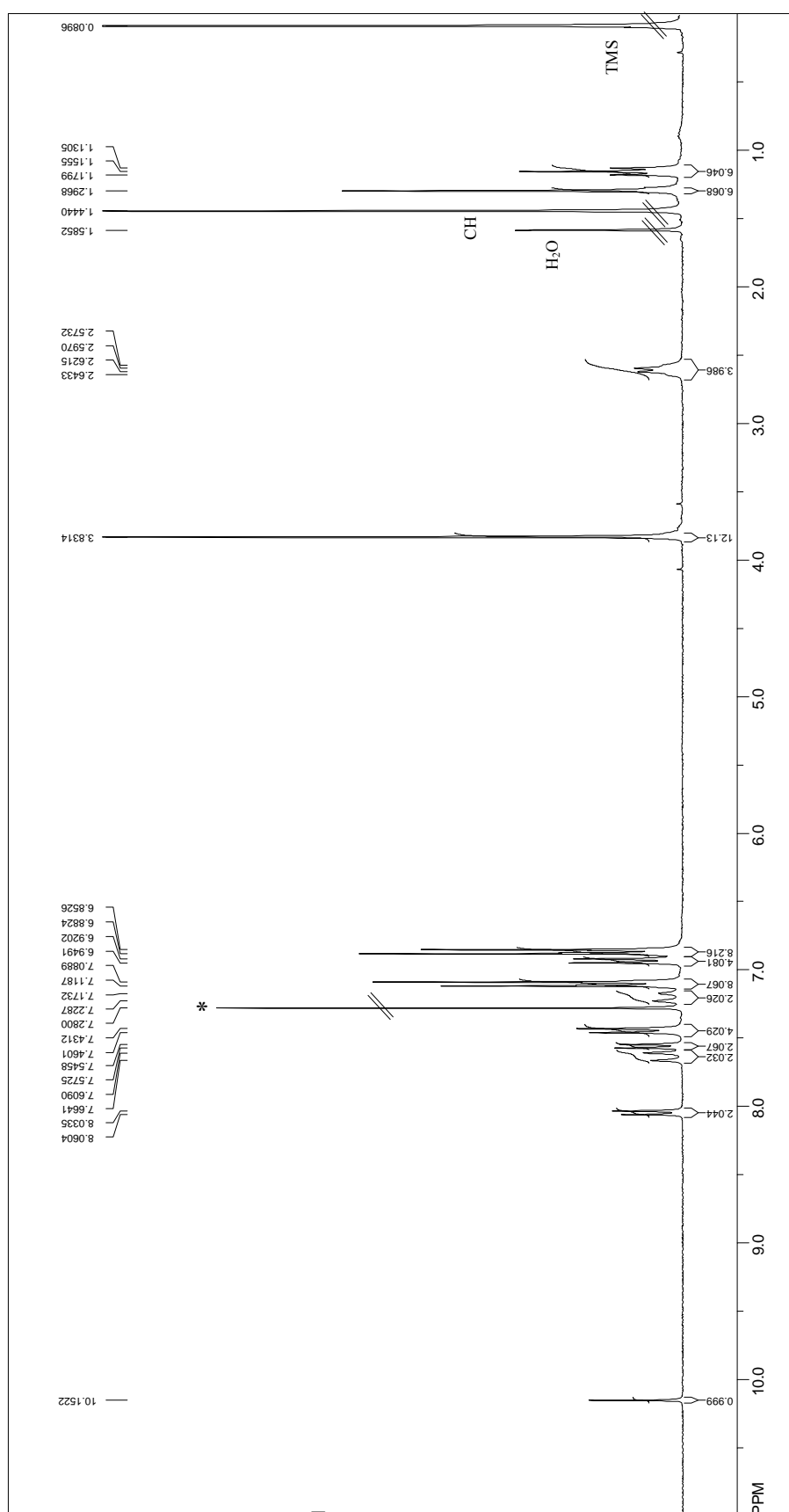


Figure S4. ¹H-NMR spectrum of compound **5** in DMSO-d₆. (*: solvent residual signal; TMS: internal standard = tetramethylsilane; DX: 1,4-dioxane used for freeze-drying)







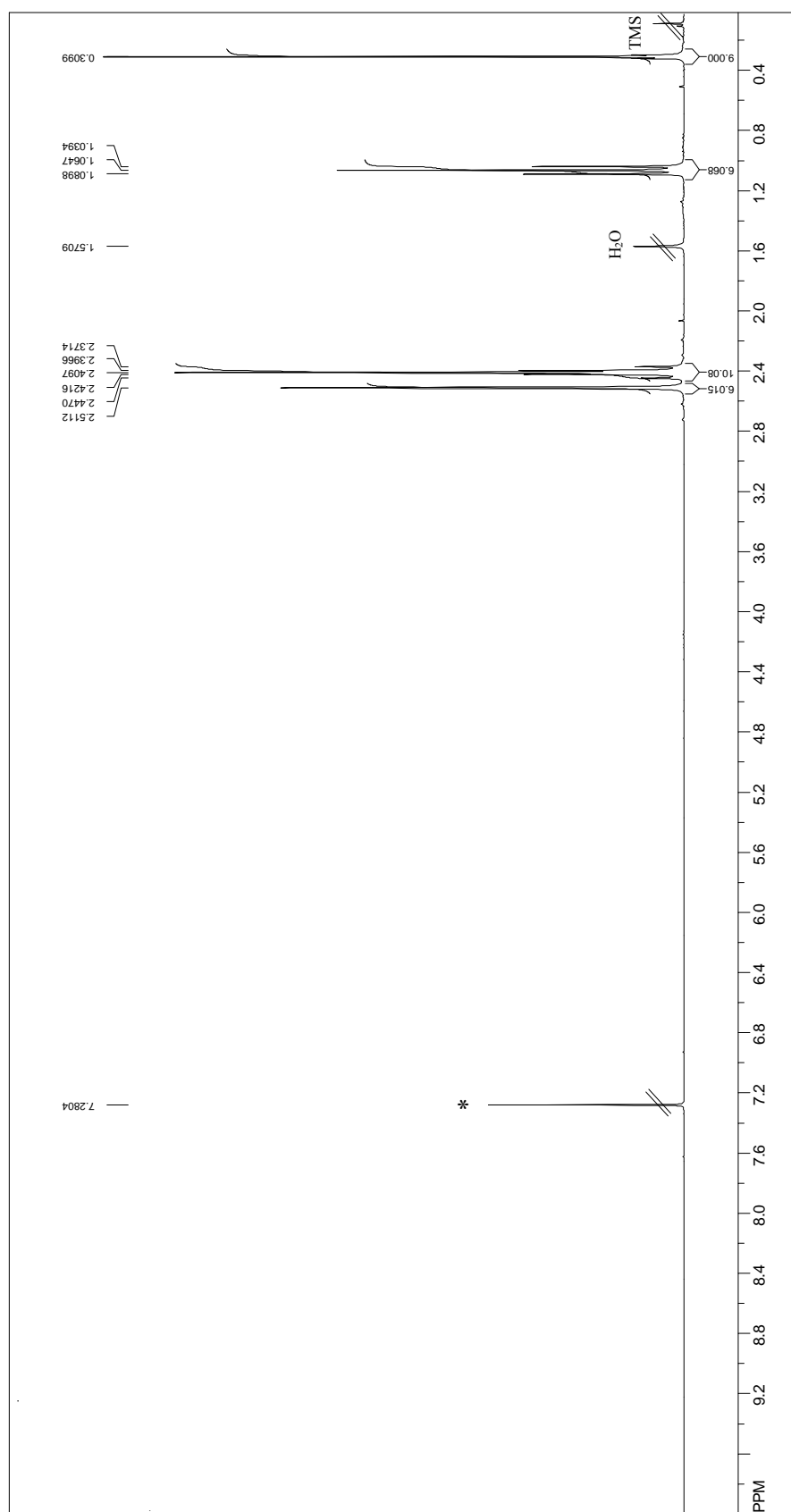


Figure S8. ¹H-NMR spectrum of compound **10** in CDCl₃. (*: solvent residual signal, TMS: internal standard = tetramethylsilane)

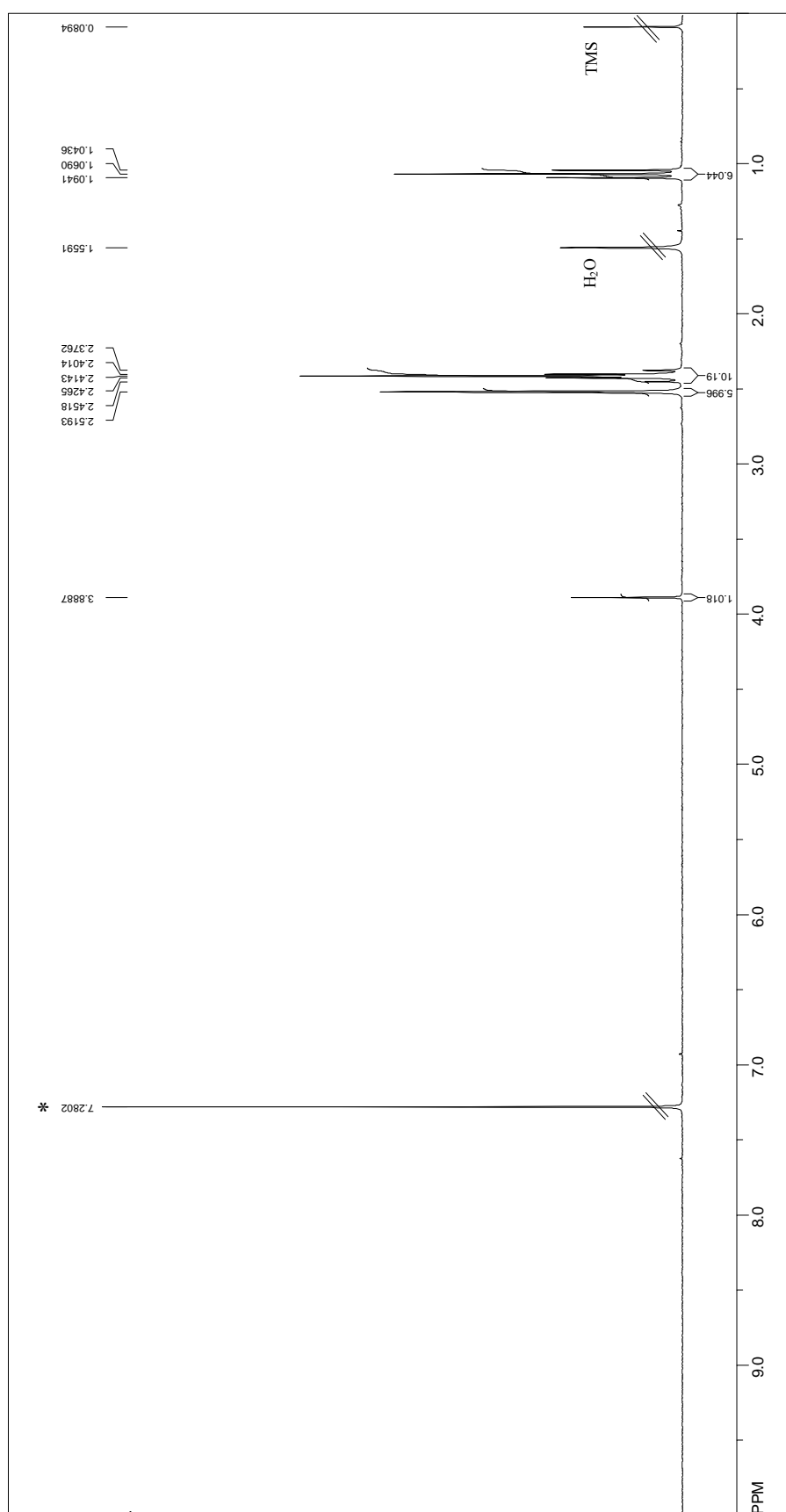


Figure S9. ¹H-NMR spectrum of compound **11** in CDCl₃. (*: solvent residual signal; TMS: internal standard = tetramethylsilane)

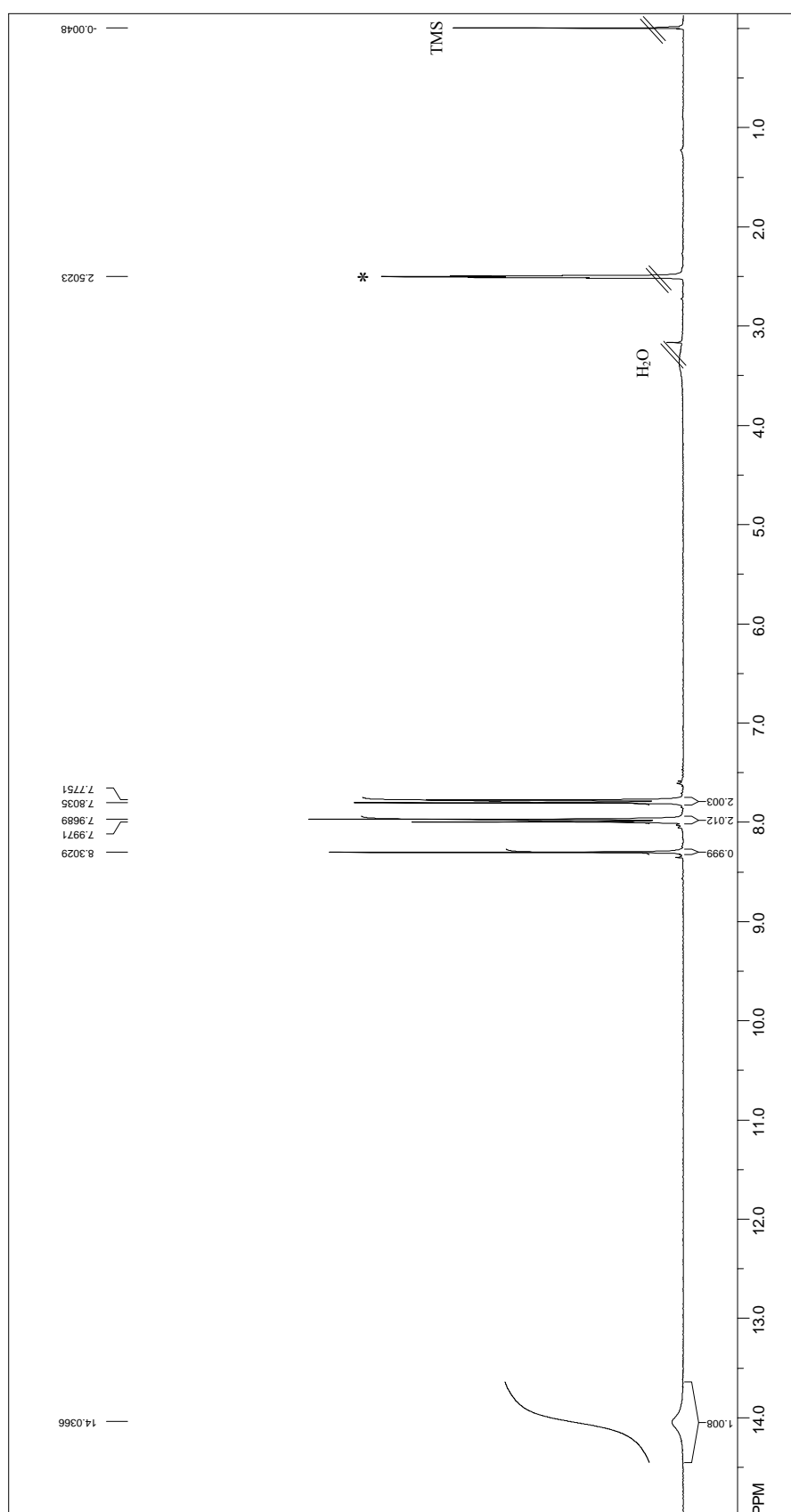


Figure. S10. ¹H-NMR spectrum of compound **12** in DMSO-d₆. (*: solvent residual signal; TMS: internal standard = tetramethylsilane)

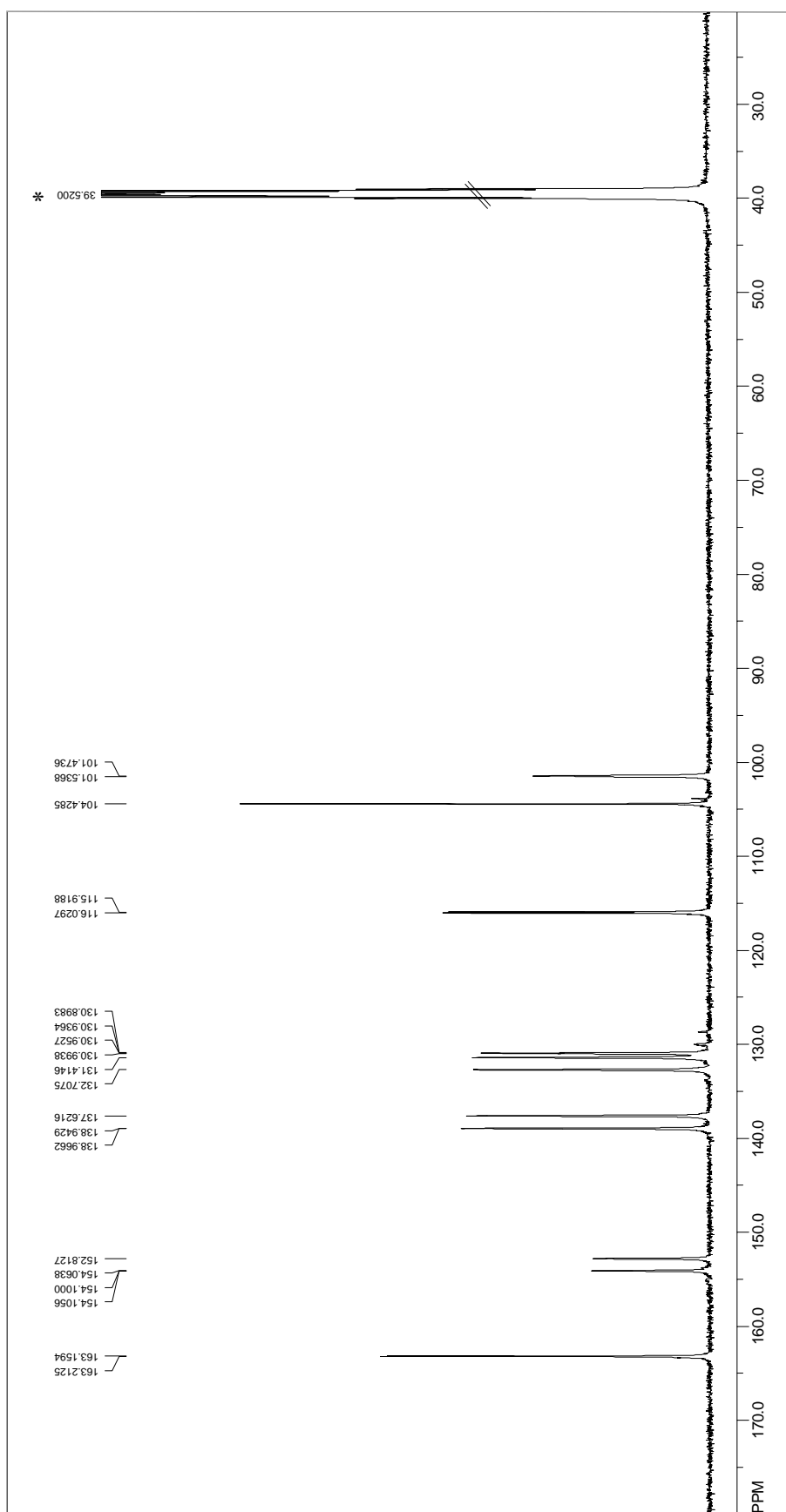


Figure S11. Proton coupled ^{13}C -NMR of compound **12** in DMSO- d_6 . (*: solvent residual signal)

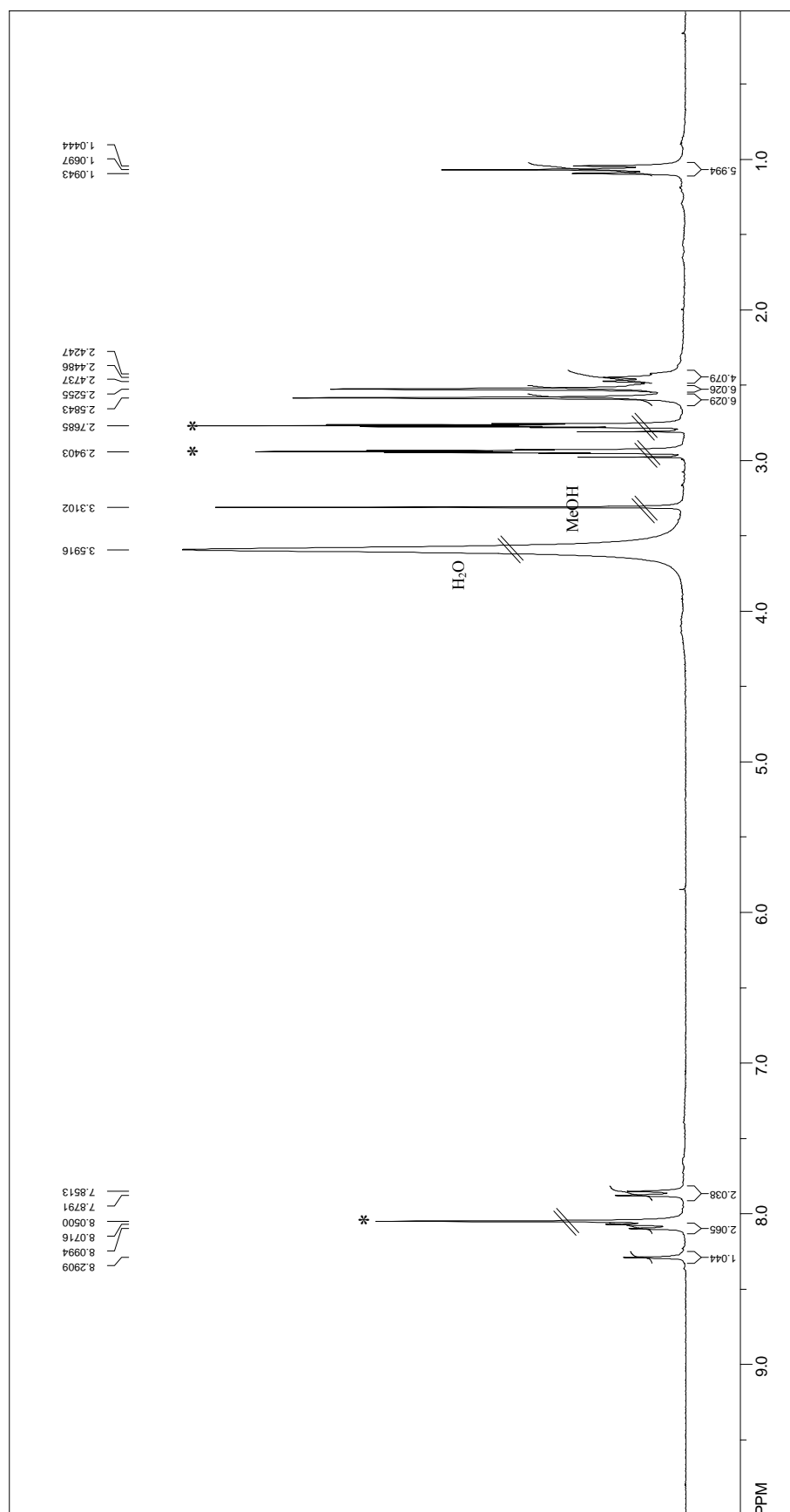


Figure S12. ¹H-NMR spectrum of compound **13** in DMF-d₇. (*: solvent residual signals)

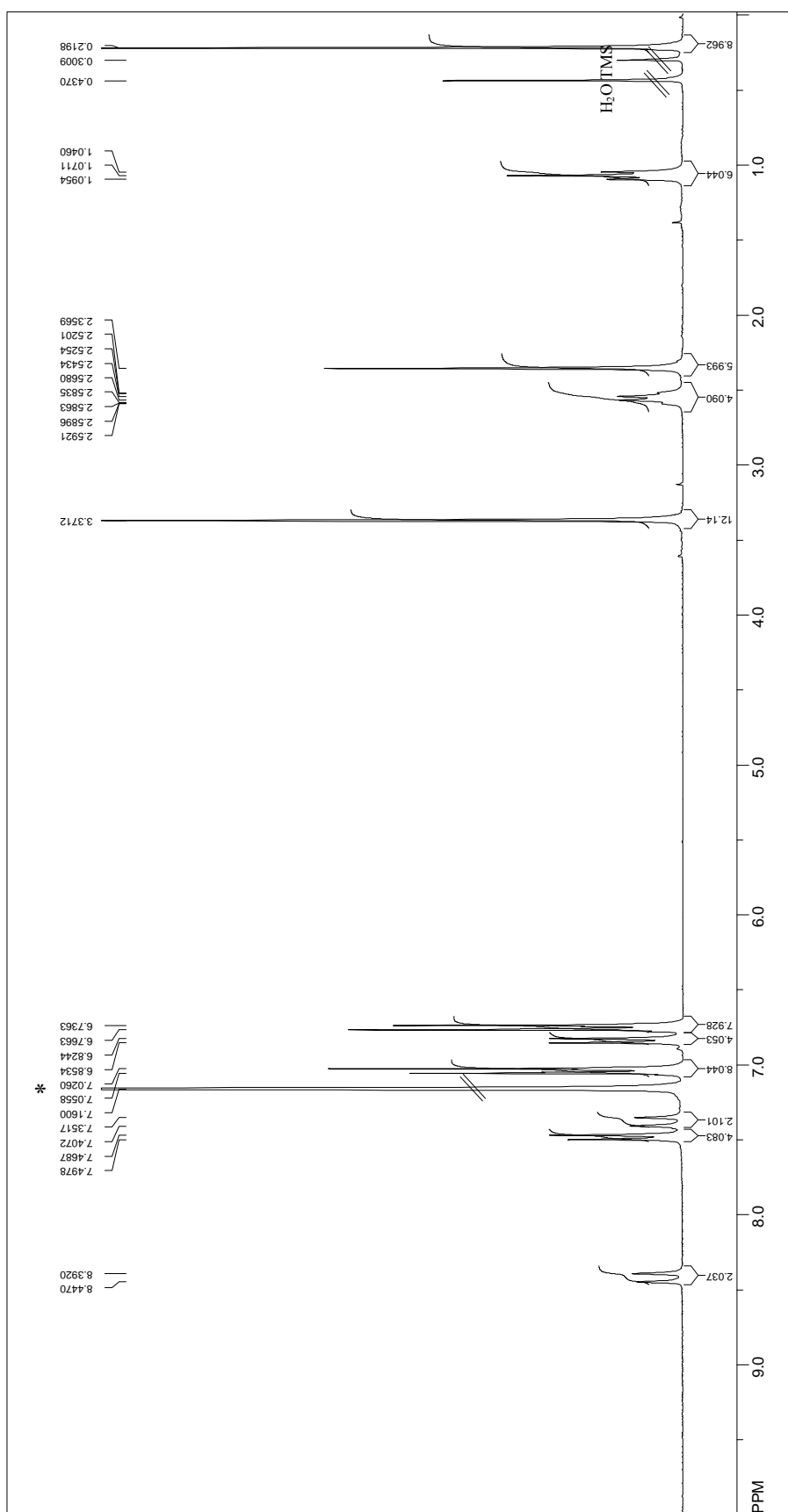


Figure S13. ¹H-NMR spectrum of compound **14** in benzene-d₆. (*: solvent residual signal; TMS: internal standard = tetramethylsilane)

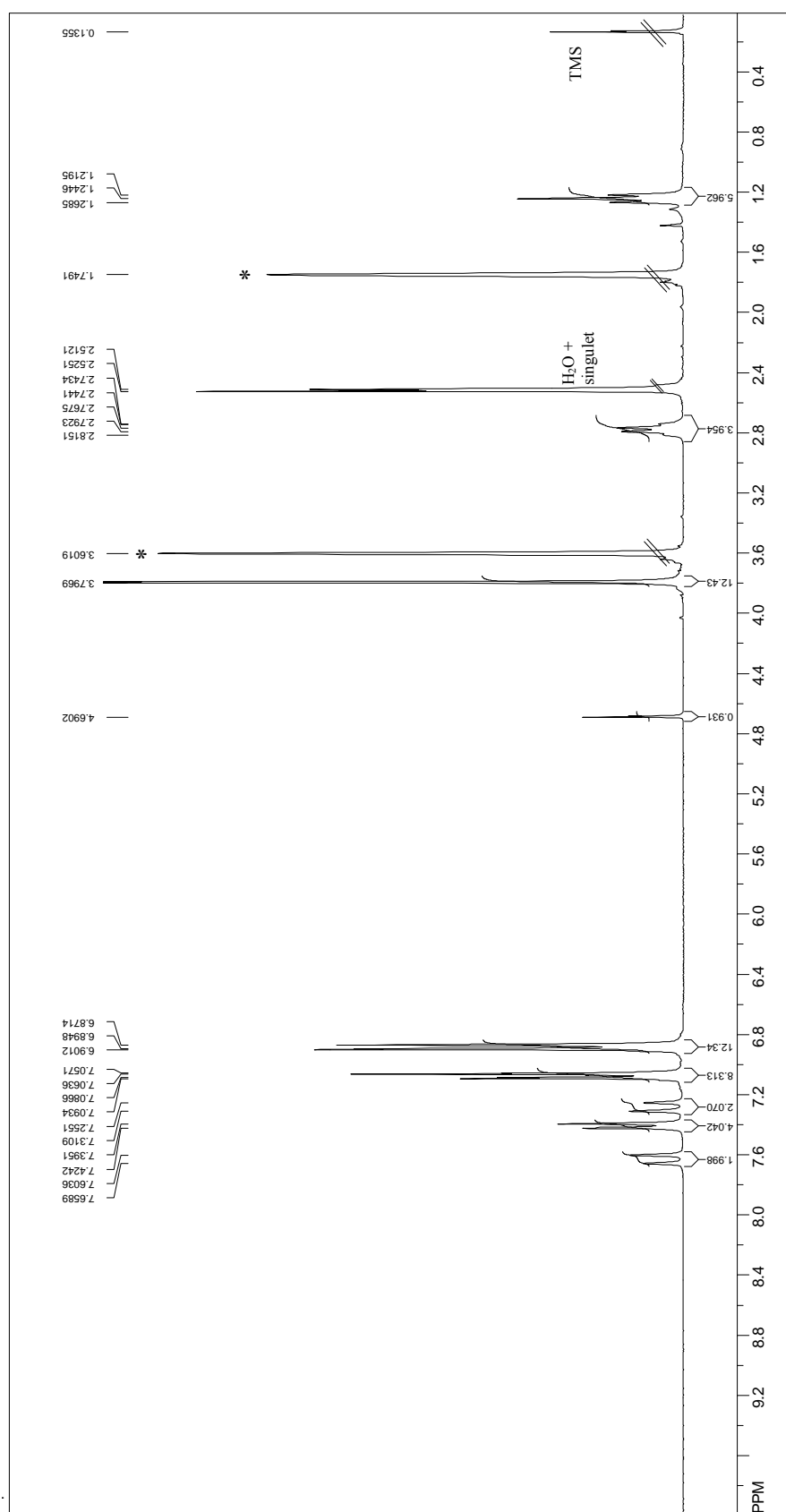


Figure S14. ¹H-NMR spectrum of compound **15** in THF-d₈. (*: solvent residual signal; TMS: internal standard = tetramethylsilane)

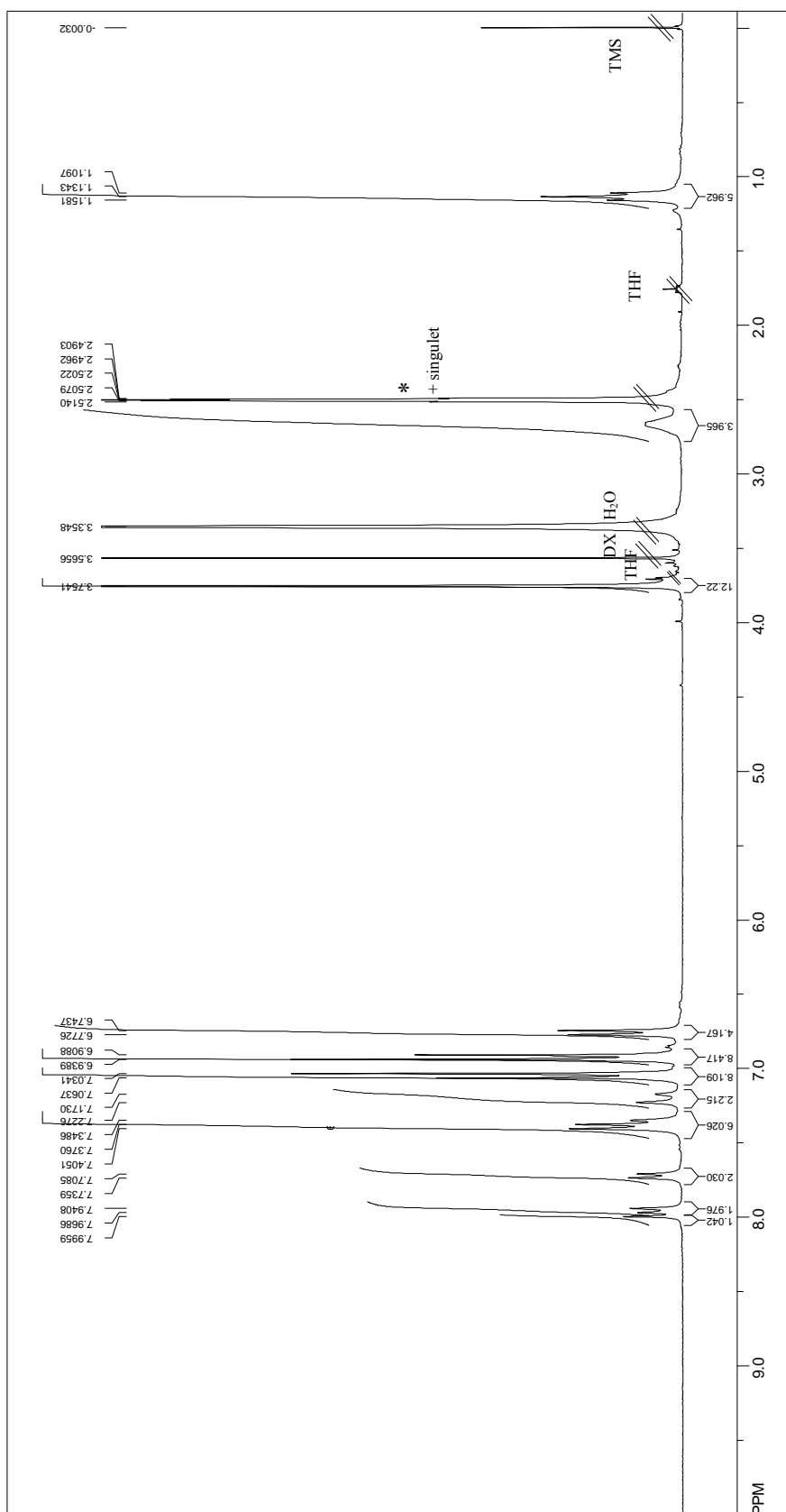


Figure S15. ¹H-NMR spectrum of compound **16** in DMSO-d₆. (*: solvent residual signal; TMS: internal standard = tetramethylsilane; THF: tetrahydrofuran; DX: 1,4-dioxane used for freeze-drying)

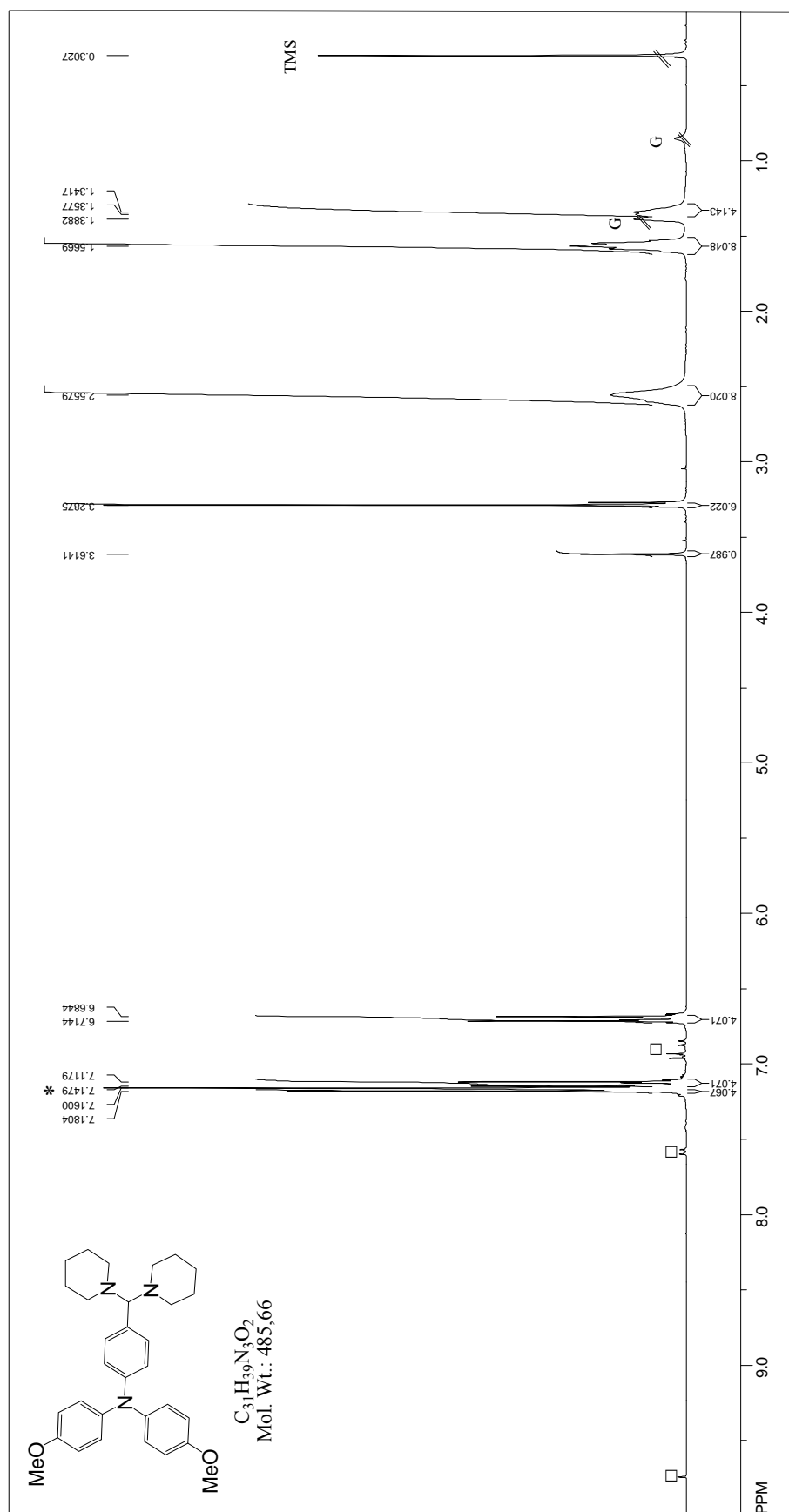
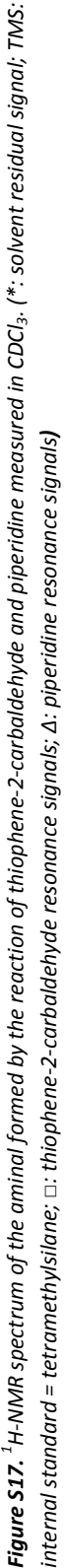
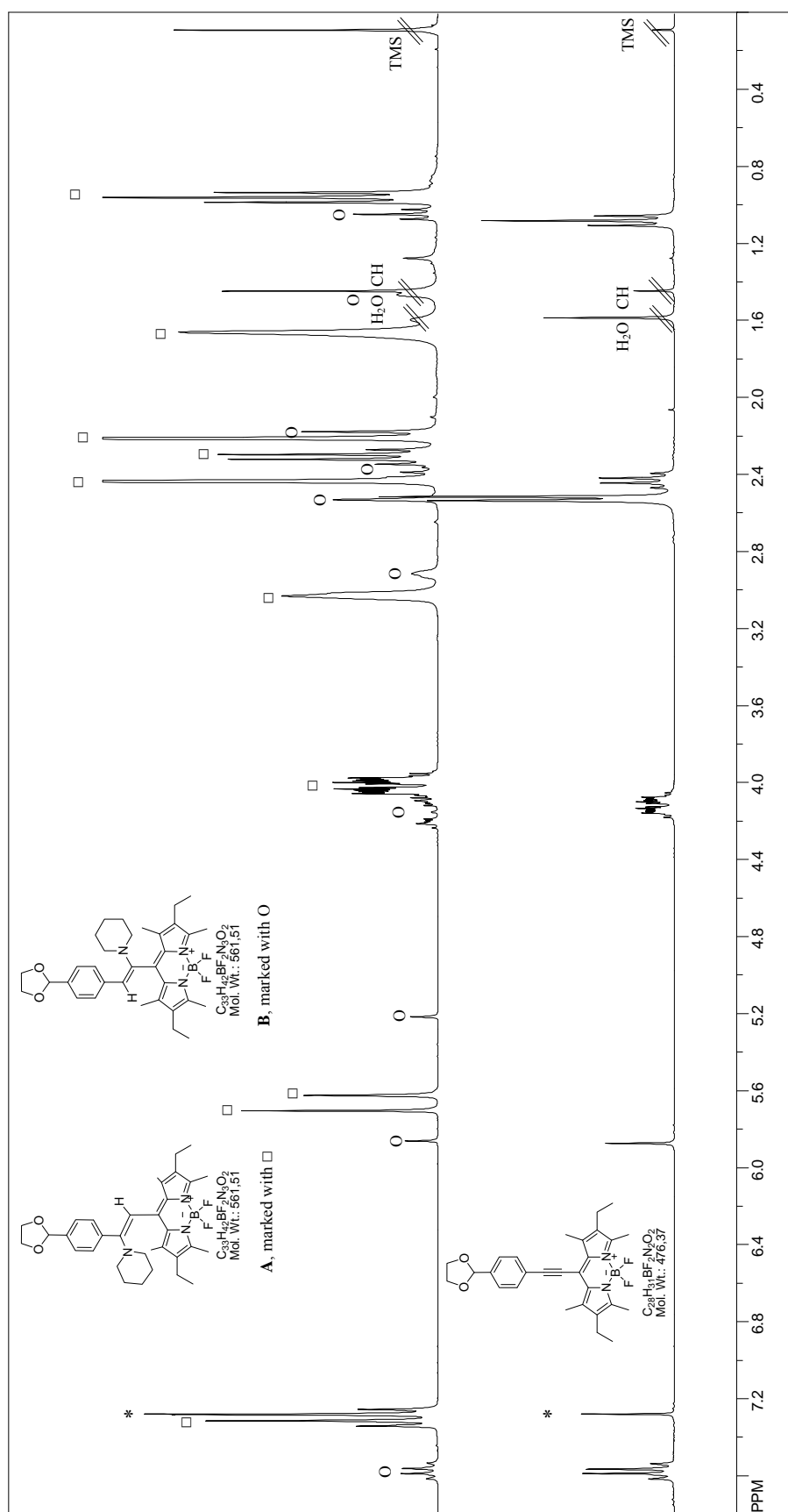


Figure S16. $^1\text{H-NMR}$ spectrum of the amination product formed by the reaction of 4-(di(4-methoxyphenyl)amino)benzaldehyde and piperidine measured in C_6D_6 (*: solvent residual signal; TMS: internal standard = tetramethylsilane; \square : 4-(di(4-methoxyphenyl)amino)benzaldehyde resonance signals; G: H-grease)





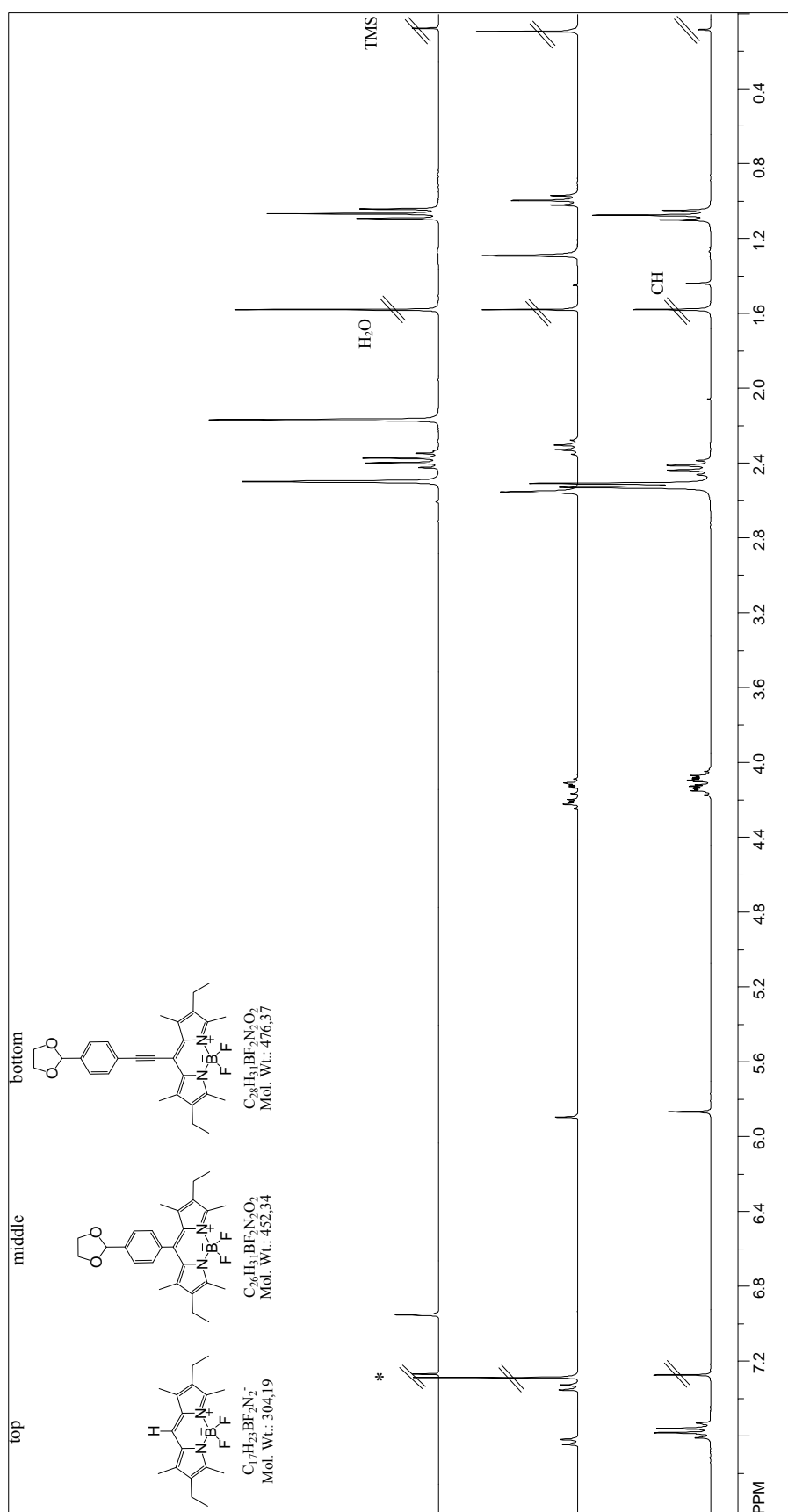


Figure S19. ^1H -NMR spectra of the *meso*-proton BODIPY 19 (top), the corresponding *meso*-phenyl BODIPY 3 (middle) and the *meso*-ethynylphenyl BODIPY 17 (bottom). (*: solvent residual signal; TMS: internal standard = tetramethylsilane; CH: cyclohexane)

4. FT-IR Spectra

Fourier transform infrared (FT-IR) spectra were measured on a Perkin Elmer spectrum 100 FT-IR spectrometer equipped with an ATR unit.

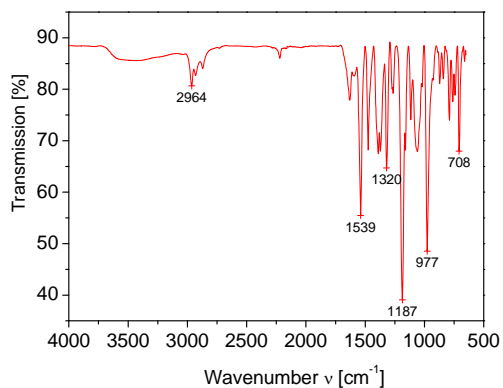


Figure S20. FT-IR spectrum of **5**.

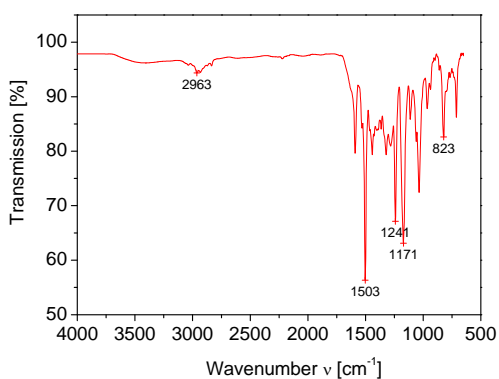


Figure S21. FT-IR spectrum of **8**.

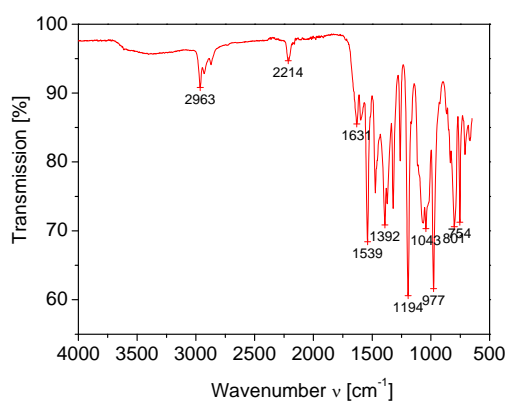


Figure S22. FT-IR spectrum of **13**.

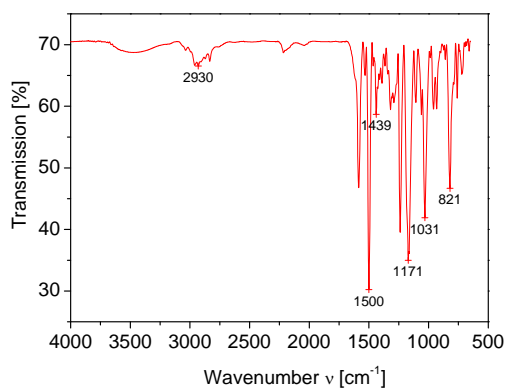


Figure S23. FT-IR spectrum of **16**.

5. UV-vis Spectra

UV-vis spectra were recorded in CH_2Cl_2 (or in $\text{THF}:\text{CH}_2\text{Cl}_2$ 1:1 for **13**) on a Hitachi U-3000 spectrophotometer or in a Bentham DTR6 Ulbricht sphere at a concentration in the range of 1×10^{-5} M. The extinction coefficients were calculated according to the Beer-Lambert law.

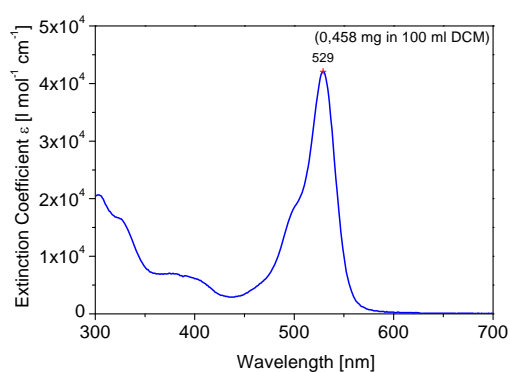


Figure S24: UV-vis spectrum of **5**.

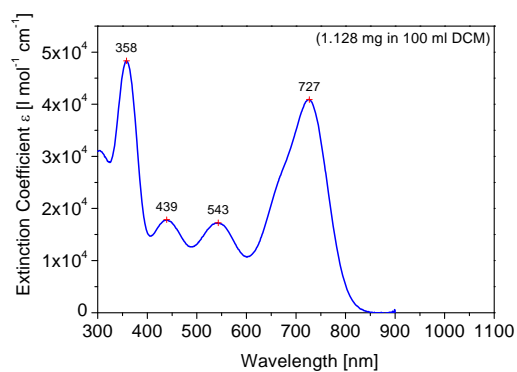


Figure S25: UV-vis spectrum of **8**.

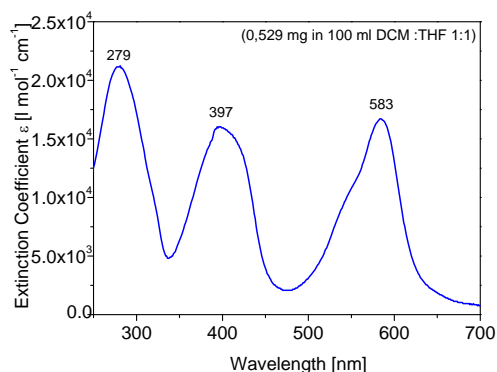


Figure S26: UV-vis spectrum of **13**.

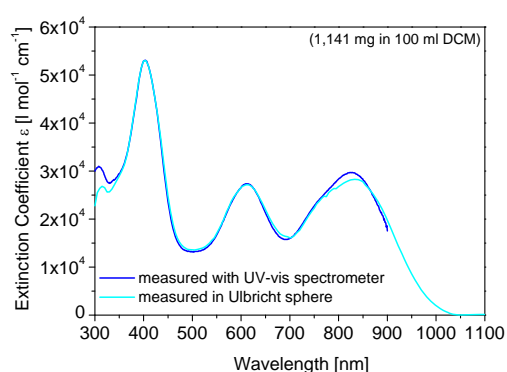


Figure S27: UV-vis spectrum of **16**.

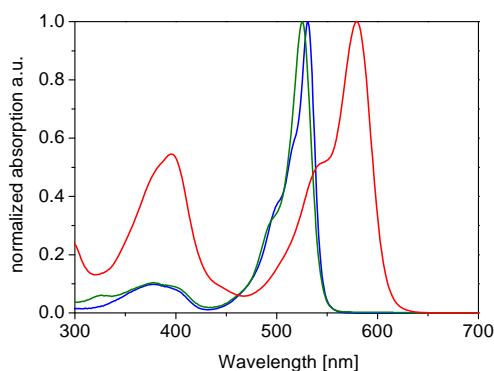


Figure S28: UV-vis spectra of **19** (blue), **3** (olive) and **17** (red).

6. CV Curves

Cyclic voltammetry (CV) was carried out under moisture- and oxygen-free conditions using a standard three-electrode assembly connected to a potentiostat (model 263A, EG&G Princeton Applied Research) at a scanning rate of 50 mV sec⁻¹. A Pt milli-electrode (model G0228, AMETEK Advanced Measurement Technology) was used as working electrode. A platinum wire in the respective solvent plus conducting salt (tetrabutylammonium hexafluorophosphate, 0.1 M) was used as counter electrode and the quasi-reference electrode consisted of an Ag-wire in an AgNO₃/acetonitrile solution (0.1 M). Each measurement was calibrated with the internal standard ferrocene/ferrocenium. The energy levels were determined by the empirical relation $E^{\text{HOMO or LUMO}} = [-e \cdot (E_{1/2}^{\text{(x vs. Ag/AgNO}_3\text{)}} - E_{1/2}^{\text{(Fc/Fc}^+\text{ vs. Ag/AgNO}_3\text{)}})] - 4.80 \text{ eV}$.

CV curves of ferrocene in DCM. Due to a change in the measurement setup, two slightly different calibration files have to be used for the calculation of the E_{HOMO} and E_{LUMO} levels of the compounds.

Calibration spectra I:

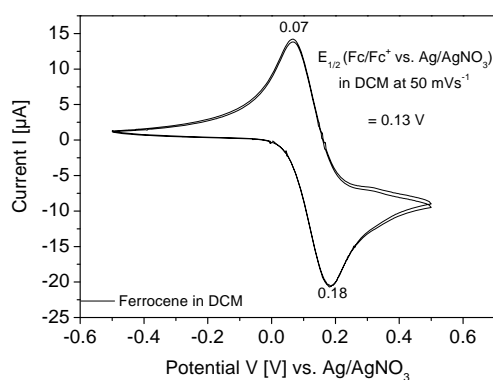


Figure S29. CV-curve of Ferrocene in DCM (calibration spectra I).

Calibration spectra II:

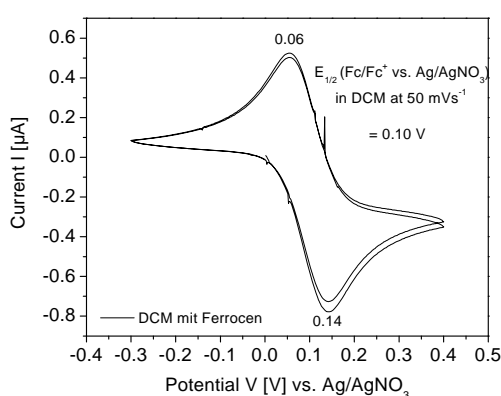


Figure S30. CV-curve of Ferrocene in DCM (calibration spectra II).

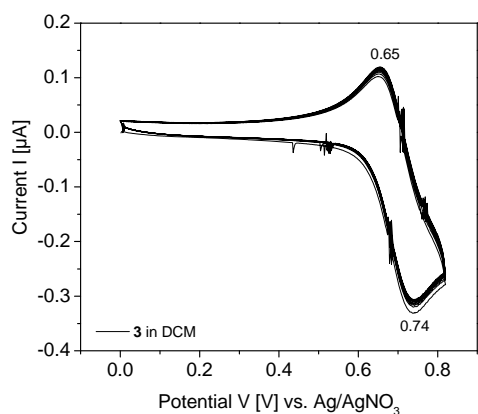


Figure S31. CV-curve for the HOMO level determination of **3**.
(Has to be calibrated with calibration II)

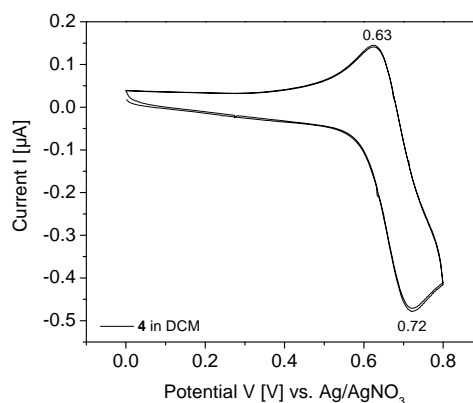


Figure S32. CV-curve for the HOMO level determination of **4**.
(Has to be calibrated with calibration II)

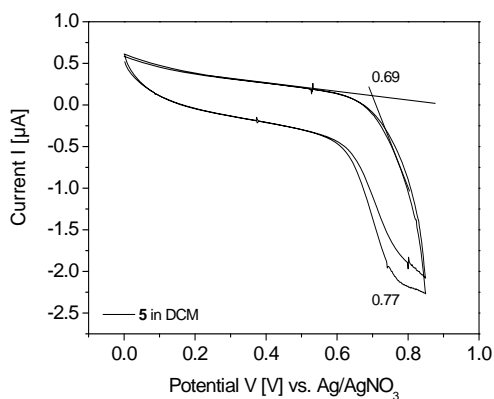


Figure S33. CV-curve for the HOMO level determination of **5**.
(Has to be calibrated with calibration I)

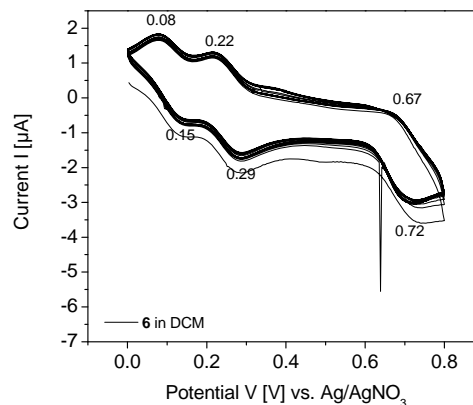


Figure S34. CV-curve for the HOMO level determination of **6**.
(Has to be calibrated with calibration II)

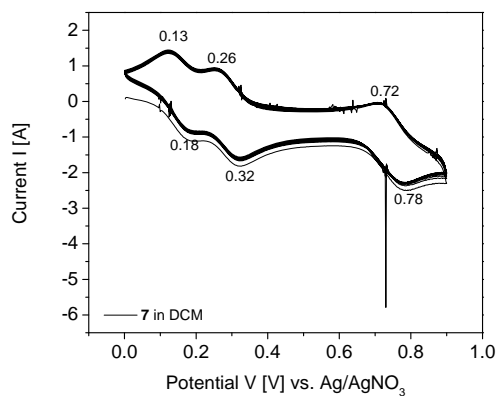


Figure S35. CV-curve for the HOMO level determination of **7**.
(Has to be calibrated with calibration I)

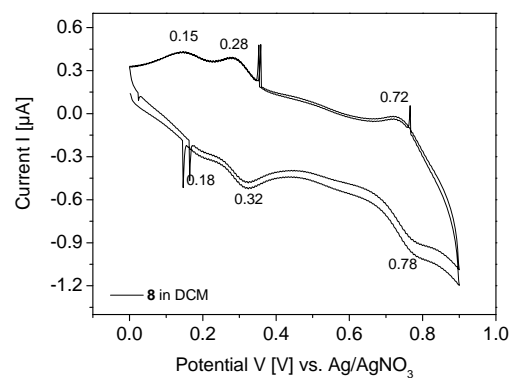


Figure S36. CV-curve for the HOMO level determination of **8**.
(Has to be calibrated with calibration I)

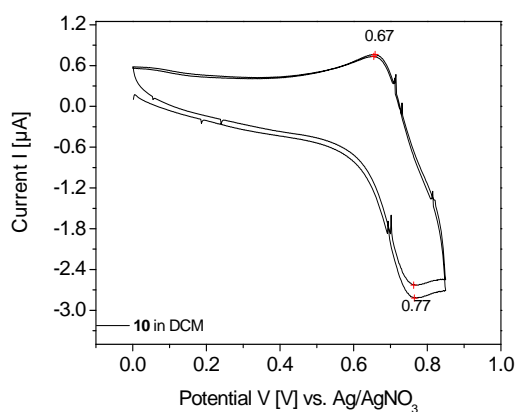


Figure S37. CV-curve for the HOMO level determination of **10**.
(Has to be calibrated with calibration II)

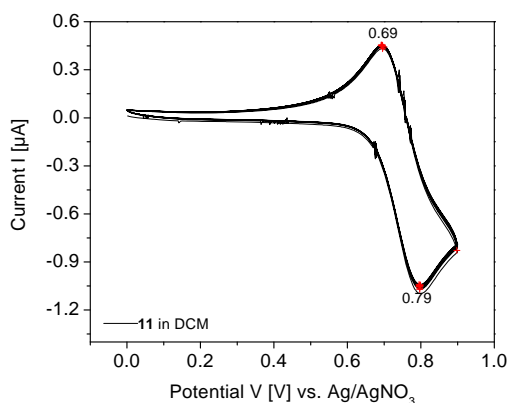


Figure S38. CV-curve for the HOMO level determination of **11**.
(Has to be calibrated with calibration II)

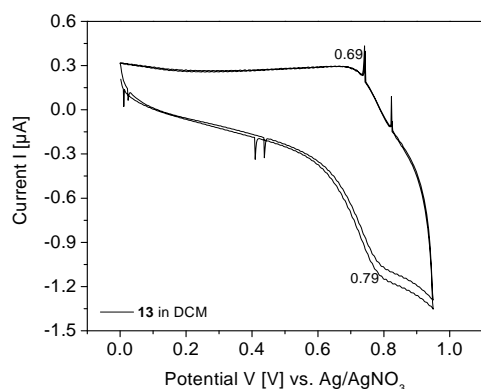


Figure S39. CV-curve for the HOMO level determination of **13**.
(Has to be calibrated with calibration II)

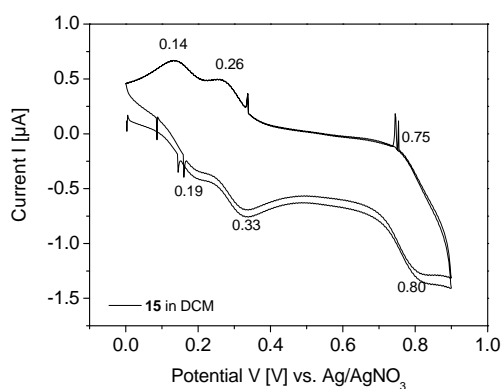


Figure S40. CV-curve for the HOMO level determination of **15**.
(Has to be calibrated with calibration I)

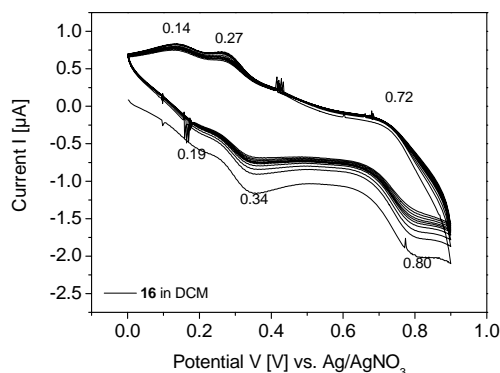


Figure S41. CV-curve for the HOMO level determination of **16**.
(Has to be calibrated with calibration I)

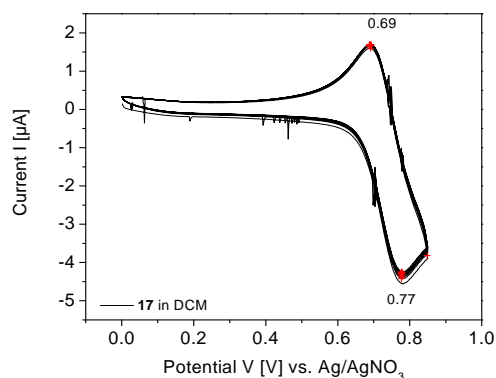
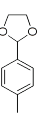
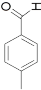
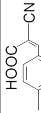
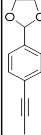
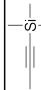
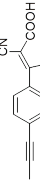
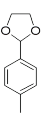
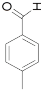
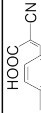



Figure S42. CV-curve for the HOMO level determination of **17**.
(Has to be calibrated with calibration II)

Table S1. Summary of the measured and the calculated energy levels on the basis of cyclic voltammetry experiments carried out at 50 mV/sec in CH_2Cl_2 with 0.1 M tetrabutylammonium hexafluorophosphate using ferrocene as reference.

compd	$E_{\text{OX1}}^{-1/2}$ [V]	E_{HOMO1} [eV]	$E_{\text{OX2}}^{-1/2}$ [V]	E_{HOMO2} [eV]	$E_{\text{OX3}}^{-1/2}$ [V]	E_{HOMO3} [eV]	$E_{\text{RED}}^{-1/2}$ [V]	E_{LUMO} [eV]	$E_{\text{LUMO}}^{\text{a)}$ [eV]	R in pos. 8	R in pos. 3 and 5
3	0.60	-5.40	---	---	---	---	-1.68	-3.12	-3.12		CH_3
4	0.58	-5.38	---	---	---	---	-1.65	-3.15	-3.12		CH_3
5	0.60	-5.40	---	---	---	---	---	---	-3.18		CH_3
17	0.63	-5.43	---	---	---	---	---	---	-3.39		CH_3
10	0.62	-5.42	---	---	---	---	-1.45	-3.35	-3.34		CH_3
11	0.64	-5.44	---	---	---	---	---	---	-3.36	---H	CH_3
13	0.64	-5.44	---	---	---	---	---	---	-3.48		CH_3
6	0.02	-4.82	0.16	-4.96	0.60	-5.40	-1.56	-3.24	-3.23		= - DIOMeTPA ^{b)}
7	0.03	-4.83	0.16	-4.96	0.62	-5.42	---	---	-3.26		= - DIOMeTPA ^{b)}
8	0.04	-4.84	0.17	-4.97	0.62	-5.42	-1.53	-3.27	-3.28		= - DIOMeTPA ^{b)}
15	0.04	-4.84	0.17	-4.97	0.65	-5.45	---	---	-3.40	---H	= - DIOMeTPA ^{b)}
16	0.04	-4.84	0.18	-4.98	0.63	-5.43	---	---	-3.59		= - DIOMeTPA ^{b)}

^{a)} The LUMO level was calculated from the optical band gap. ^{b)} 4,4'-dimethoxytriphenylamine. Note: 14 could not be measured because the protection group was removed by the conducting salt very fast. In contrast to that, the deprotection of 10 proceeded more slowly.

Chapter 9

ENERGY TRANSFER IN SOLID-STATE DYE-SENSITIZED SOLAR CELLS: COMBINING BODIPYs AND ENERGY DONOR DYES

Katja Gräf^[a], Nils Bösch^[b], Jürgen Köhler^[b] and Mukundan Thelakkat^{[a]}*

^[a] Department of Macromolecular Chemistry I, Applied Functional Polymers, Universität Bayreuth, Universitätsstr. 30, 95440 Bayreuth, Germany.

Fax: +49 921 55 3206

E-mail: Mukundan.Thelakkat@uni-bayreuth.de

^[b] Department of Experimental Physics IV, Universität Bayreuth, Universitätsstr. 30, 95440 Bayreuth, Germany.

ABSTRACT

Energy transfer in solid-state dye-sensitized solar cells (SDSCs) is a novel and promising concept to broaden and boost the light harvesting and thus the external quantum efficiency. Herein, this concept is tested by using promising donor-acceptor combinations. We used four BODIPYs as sensitizing acceptor dyes (SADs) and two triphenyldiamine derivatives as energy donor dyes (EDDs). The compliance of the prerequisites of energy transfer was investigated for each SAD-EDD combination by steady-state UV/vis and fluorescence experiments. Additionally, the alignment of the energy levels of the SADs and EDDs relative to TiO_2 and relative to the solid hole transport material was determined by cyclic voltammetry. To further investigate the potential of the materials for energy transfer, fluorescence quenching experiments were performed in solution as well as in the solid state. It appeared that the most promising SAD-EDD combinations are BODIPY 1/donor 1 and BODIPY 3/donor 1. BODIPY 1 and BODIPY 3 meet all prerequisites of energy transfer and feature a suitable energy level alignment for SDSC applications. On the contrary, the HOMO levels of donor-substituted-BODIPYs (BODIPY 2 and BODIPY 4) are too high for an efficient dye regeneration using spiro-OMeTAD as hole transport material. Compared to donor 2, donor 1 features a longer fluorescence lifetime which was more efficiently shorted by the SADs. Both facts indicate a more efficient energy transfer. A series of SDSCs was prepared using different amounts of the EDDs for each SAD-EDD pair. External quantum efficiency measurements on the SDSCs with EDDs in comparison to such devices without EDD prove an additional photoresponse in the absorption region of the EDD donor 1.

Keywords: solid-state dye-sensitized solar cell • energy transfer • FRET • BODIPY.

INTRODUCTION

Dye-sensitized solar cells (DSCs)¹ have been intensively studied as promising low-cost high-efficiency photovoltaic technology. DSCs based on liquid electrolytes (LDSCs) reached impressive efficiencies of > 12%.² However, long-time stability is affected by the volatility of the redox electrolyte and by encapsulation problems. This main drawback can be avoided by using a solid hole transport material like spiro-OMeTAD.³ Solid-state dye-sensitized solar cells (SDSCs) typically feature higher open-circuit voltages but also high recombination rates.⁴ This fact compels the thickness of the mesoporous layer that can be used to be about 2 μm (compared to $\sim 10\text{-}20\ \mu\text{m}$ for LDSCs). This limitation entails an unfavourable reduction of the optical density. To increase light harvesting, key pathways that provide the potential to boost and broaden the absorption are in demand. A possibility to boost the optical density is a change from ruthenium dyes to organic sensitizers that provide higher extinction coefficients. However, the absorption bands of organic dyes are often quite narrow. Here, co-sensitization is a possibility to extend the absorption breadth, but this concept suffers from the confined surface area.^{5, 6} By combining two complementary sensitizers on a semiconductor surface the optical density of the individual dyes is reduced. Hence, the extension of the absorption is realized at the expense of optical density. A more sophisticated concept to avoid the loss of optical density while simultaneously improving the spectral response is the use of energy donor dyes. Energy donor dyes (EDDs) are unattached dyes that can be added to liquid electrolytes and solid hole transport materials. They absorb high energy photons and transfer energy to the sensitizing acceptor dye (SAD) while latter is able to absorb low energy photons. The use of EDDs in DSCs can improve the spectral response by a broadening of the absorption range and boost the absorption in regions with low optical density of the SAD without reducing its optical density. The feasibility of this concept has already been shown for LDSCs⁷⁻¹⁰ and SDSCs.¹¹⁻¹⁴ In this way, red-absorbing SADs (*e.g.* phthalocyanines^{8, 12} or squaraines^{13, 14}) were combined with blue-to-green-absorbing EDDs (*e.g.* commercial available 4-(dicyanomethylen)-2,6-dimethyl-4H-pyran derivatives^{9, 13}). A clear increase in the external quantum efficiency (EQE) in the absorption region of the EDD shows the beneficial effect of this additional dye. It appeared that this concept is more important for SDSCs than for LDSCs because of the intrinsic lower optical density of SDSCs and the fact that the iodine/iodide redox couple is an efficient quencher for the EDD, thus reducing energy transfer.^{8, 15}

Here, we present energy transfer studies on 4,4-difluoro-4-bora-3a,4a-diaza-s-indacene dyes (BODIPYs) as SADs (BODIPY 1-4) and triphenyldiamine derivatives as EDDs (donor 1 and donor 2). The structures of the materials under study are depicted in Scheme 1 and Figure 2. The optical properties of the compounds were studied using steady-state and transient methods. It was found that the EDDs feature an absorption in the region where the SADs provides only poor optical density/low extinction coefficients. This provides the possibility to boost the EQE in the said region. In order to further investigate the potential of the donor-acceptor combinations for energy transfer in SDSCs, electrochemical measurements and steady-state as well as transient fluorescence quenching experiments were performed. It was observed that the fluorescence of the EDDs can be efficiently quenched and the lifetimes are radically reduced by addition of the SADs indicating energy transfer from the donor to the acceptor. Finally, SDSCs using the four different BODIPY SADs without and with two different EDDs were prepared and characterised. A contribution of the EDD to the current generation could be demonstrated for suitable donor-acceptor combinations.

RESULTS AND DISCUSSION

Theory and choice of the materials. The schematic energy diagram for SDSCs based on the concept of energy transfer using a SAD and an EDD is depicted in Figure 1.

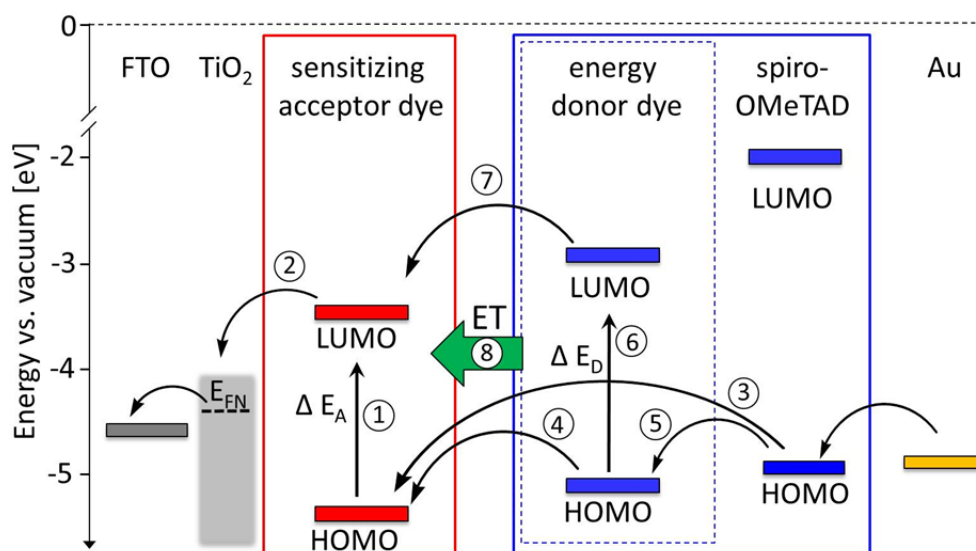


Figure 1. Idealized energy level diagram of SDSCs incorporating TiO₂ as semiconducting electron transport material, a SAD and an additional EDD embedded in the hole transport material (spiro-OMeTAD). The arrows indicated the conceivable electronic and energetic processes that contribute to current generation upon light exposure. 1: excitation of the SAD, 2: electron injection, 3: regeneration of the oxidized SAD by spiro-OMeTAD, 4: regeneration of the oxidized SAD by the EDD, 5: regeneration of the EDD, 6: excitation of the EDD, 7: electron transfer from the EDD to the SAD, 8: energy transfer (ET) from the EDD to the SAD. The additional arrows indicate the electron transfer to the FTO anode and the hole transfer to the Au cathode.

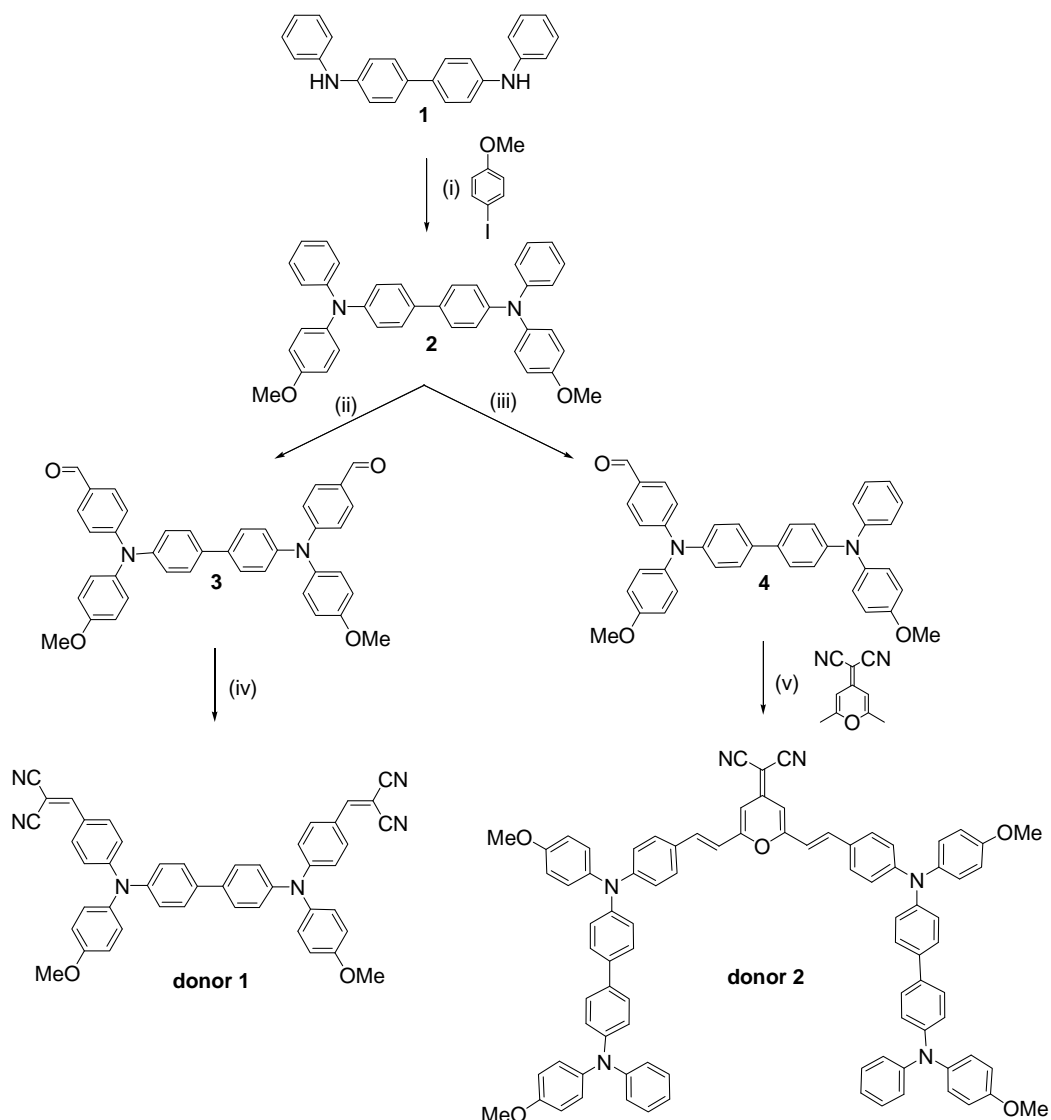
Three main photoinduced pathways that contribute to the current generation can be distinguished. Pathway 1: After excitation of the SAD with low energy photons (1), electron injection occurs (2). The oxidized SAD can be either directly regenerated by the hole transport material (3) or through the EDD (4, 5). Latter should be capable to transfer holes to the hole transport material and avoid the generation of traps for holes. Therefore, the HOMO (highest occupied molecular orbital) of the EDD has to be energetically localized between the HOMO of the SAD and that of the hole transport material. Pathway 2: After excitation of the EDD with high energy photons (6), the excited electron can be transferred to the LUMO (lowest unoccupied molecular orbital) of the SAD which is reduced and injects the electron into the conduction band of TiO₂ (2). The oxidized EDD has to be regenerated subsequently by the hole transport material (5) or directly from the Au electrode. Pathway 3: After excitation of the EDD (6) three more processes are possible. In the first process, excitation energy can be transferred to the SAD (8). If

this energy transfer occurs *via* dipole-dipole interactions, it is called Förster resonance energy transfer (FRET). For this non-radiative energy transfer some key requirements have to be fulfilled:¹⁶⁻¹⁸ i) the HOMO-LUMO gap of the acceptor (ΔE_A) has to be smaller than that of the donor dye (ΔE_D), ii) the overlap integral between the donor fluorescence and the acceptor absorption has to be high, iii) the distance between donor and acceptor has to be short and iv) the transition dipoles of both have to be in a suitable orientation. Besides, a second mechanism for the energy transfer is conceivable. Here, the excited electron of the EDD (after 6) can be transferred to the LUMO of the SAD (7) while an electron from the HOMO of the SAD is transferred to the HOMO of the EDD. This process is known as Dexter¹⁹ energy transfer. Thirdly, a less relevant energy transfer mediated *via* emission of the donor and reabsorption by the acceptor (radiative energy transfer) is possible. Herein, we concentrate exclusively on FRET. This is a long-range “through-space” energy transfer mechanism that involves coulomb interactions of transition dipoles (distance up to a few nm). In contrast, the Dexter mechanism is only a short range “through-bond” electron exchange process that necessitates the overlap of molecular orbitals (distance < 10 Å).^{17, 20}

To enable the concept of energy transfer in SDSCs, suitable donor-acceptor combinations have to be identified that fulfil the prerequisites of FRET and feature an appropriate energy level alignment for SDSC applications. For our experiments, we used BODIPYs as acceptor materials because of their high extinction coefficients and the tunability of their optical and electronic properties by the variation of the *meso*-group (*meso*-phenyl vs. *meso*-ethylphenyl) and the moieties in positions 3 and 5 (methyl vs. *N,N*-bis(4-methoxyphenyl)benzamine).²¹ As complementary donor materials, we chose triphenyldiamine compounds. Triphenyldiamines feature good hole transporting properties,²² exhibit photoluminescence and their electronic properties can be tuned very easily. The electrochemical stability can be further increased by the introduction of *para*-methoxy groups.²³ In particular, donor 1 was designed to have *para*-methoxy and *para*-dicyanovinyl groups (A-D-A structure). This provides an absorption in the blue region. Donor 2 is a (dicyanomethylene)pyran derivative, that is flanked by two triphenyldiamine units (D-A-D structure). This provides a broad absorption up to the green region, possible due to intramolecular charge transfer between D-A structured units.

Synthesis of the investigated compounds. Both EDDs (donor 1 and donor 2) were synthesised starting from *N,N'*-diphenylbenzidine **1** (Scheme 1). A Ullmann coupling with 4-iodoanisole was

performed to get *N,N'*-bis(4-dimethoxyphenyl)-*N,N'*-diphenylbenzidine **2** according to a published procedure.²⁴ Compound **2** was converted into the di-aldehyde derivative **3** and the mono-aldehyde **4** under classical Vilsmeier-Haack reaction conditions with different equivalents of POCl₃. To get donor 1, compound **3** was reacted with malononitrile in a Knoevenagel condensation with a yield of 86 %. Donor 2 was synthesised under Knoevenagel condition in a reaction between compound **4** and 4-dicyanomethylen-2,6-dimethyl-4H-pyran in a moderate yield of 59 %.



Scheme 1. Synthesis of the EDDs donor 1 and donor 2. Reagents and conditions: (i) K₂CO₃, Cu-powder, 18-crown-6, o-dichlorobenzene, reflux, 25 h, yield: 61 %; (ii) dimethylformamide, POCl₃ (3.3 eq), 1,2-dichloroethane, 80 °C, 20 h, yield: 88 %; (iii) dimethylformamide, POCl₃ (0.7 eq), 1,2-dichloroethane, 80 °C, 3 h, yield: 55 %; (iv) malononitrile, piperidine, glacial acetic acid, toluene, 70 °C, 25 h, yield: 86 %; (v) piperidine, acetonitrile, reflux, 27 h, yield: 59 %.

The synthesis of the BODIPYs is described elsewhere.²¹ The structures are shown in Figure 2.

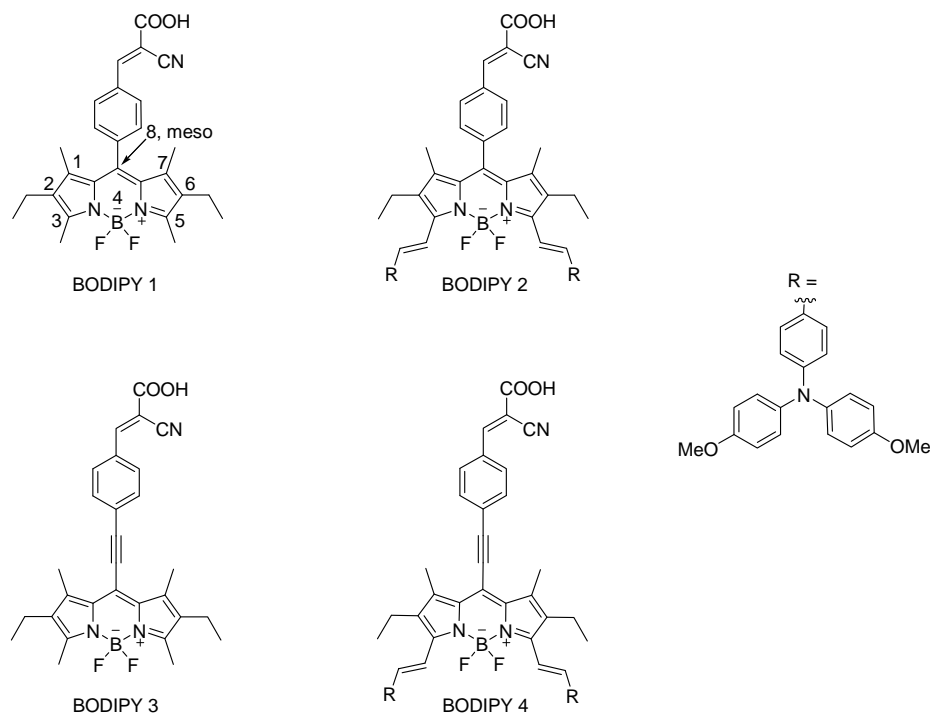


Figure 2. Molecular structures of the SADs BODIPY 1-4 used in this study.

Electrochemical measurements. The electronic energy levels of the molecules were determined from redox potentials using cyclic voltammetry experiments in solution. Figure 3 shows the cyclic voltammograms of donor 1 and donor 2.

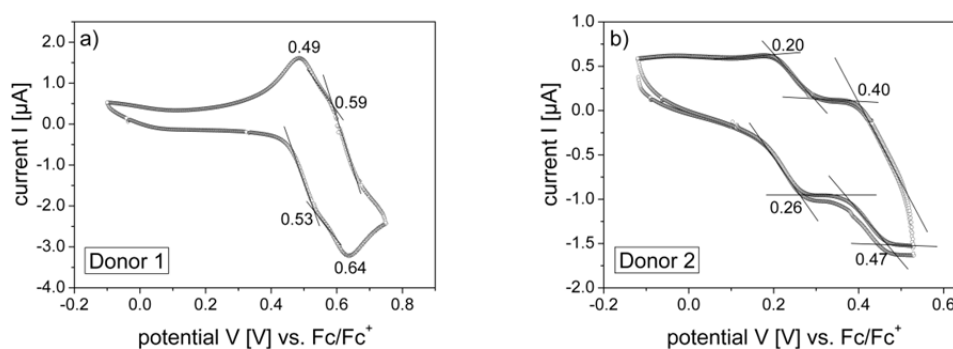


Figure 3. Cyclic voltammograms of a) donor 1 and b) donor 2. Both compounds were measured in CH_2Cl_2 with 0.1 mM TBAPF₆ at a scanning rate of 50 mV sec⁻¹. The potential is given relative to ferrocene/ferrocenium.

The electrochemical oxidation of both donors leads to two pairs of reversible cathodic and anodic signals. This is a typical behaviour for triphenyldiamine derivatives that is well studied in literature.^{25, 26} For donor 1, the oxidation peaks show only a small separation with half-wave potentials of 0.51 and 0.62 V, respectively. This indicates a small energetic difference in the first two electron transfer processes. The energy levels derived from the cyclic voltammogram were calculated to be -5.31 and -5.42 eV for donor 1. In comparison to that, the experiments on donor 2 reveal that the oxidations proceed at lower potentials and the separation between the peaks is larger. The half-wave potentials of donor 2 were determined to be 0.23 and 0.44 V. This results in energy levels of -5.03 and -5.24 eV. All energetic values of the SADs and the EDDs are summarized in Table 1. The redox potentials and the energy levels calculated from them, for the BODIPY dyes are given in reference 21. In Figure 4 the energy level (HOMO/LUMO) diagram is depicted.

Table 1. Summary of the measured half-wave potentials, the calculated energy levels and the HOMO-LUMO gaps ΔE . The values were obtained by cyclic voltammetry in CH_2Cl_2 with 0.1 mM TBAPF_6 at a scanning rate of 50 mV sec^{-1} and are given relative to the redox couple ferrocene/ferrocenium. The values for the BODIPY compounds are taken from ref. 21.

compd	$E^{1/2}_{\text{OX1}}$ [V]	E_{HOMO} [eV]	$E^{1/2}_{\text{OX2}}$ [V]	$E_{\text{HOMO-1}}$ [eV]	$E^{1/2}_{\text{OX3}}$ [V]	$E_{\text{HOMO-2}}$ [eV]	$E_{\text{LUMO}}^{\text{a)}}$ [eV]	$\Delta E^{\text{b)}}$ [eV]
donor 1	0.51	-5.31	0.62	-5.42	---	---	-2.98	2.33
donor 2	0.23	-5.03	0.44	-5.24	---	---	-2.85	2.18
BODIPY 1	0.60	-5.40	---	---	---	---	-3.18	2.22
BODIPY 2	0.04	-4.84	0.17	-4.97	0.62	-5.42	-3.28	1.56
BODIPY 3	0.64	-5.44	---	---	---	---	-3.48	1.96
BODIPY 4	0.04	-4.84	-0.18	-4.98	0.63	-5.43	-3.59	1.25

^{a)} Calculated from the point of intersection of the tangent to the absorption in solution with the x-axis ($E_{\text{LUMO}} = E_{\text{HOMO}} - h \cdot c / \lambda_{\text{tangent}}$). ^{b)} HOMO-LUMO gap ($\Delta E = |E_{\text{HOMO}}| - |E_{\text{LUMO}}|$).

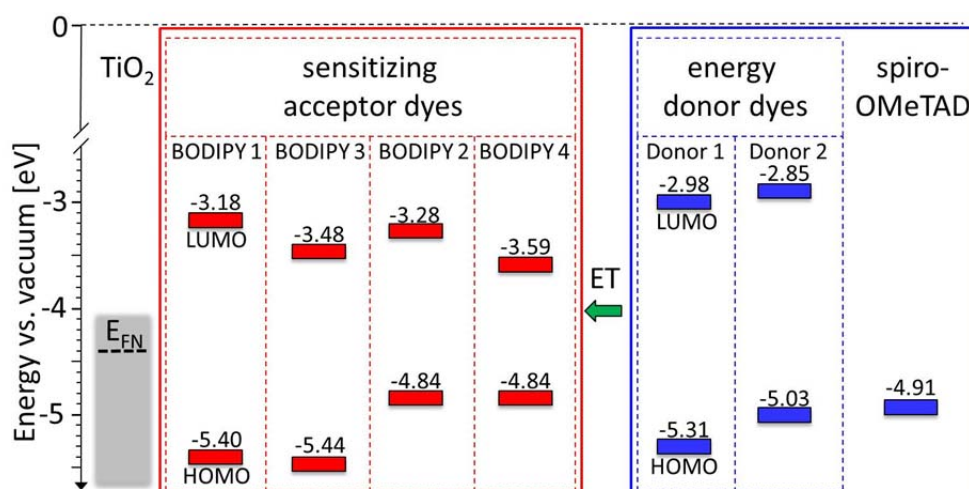


Figure 4. Schematic representation of the alignment of the energy levels of the SADs (red) and the EDDs (blue) relative to each other and relative to the Fermi level of the semiconductor TiO_2 (E_{FN}) and the HOMO level of the hole transport material spiro-OMeTAD.

It is apparent from Figure 4, that both EDDs feature HOMO levels that are lower than the HOMO level of the hole transport material (-4.91 eV^{27}). Additionally, the HOMO level of the EDD should be higher than that of the SAD to enable facile dye regeneration. This requirement is fulfilled for BODIPY 1 and BODIPY 3, but not for BODIPY 2 and BODIPY 4. In BODIPY 2 and BODIPY 4 even the direct dye regeneration by spiro-OMeTAD is not favourable. Therefore, the introduction of an additional EDD to the hole transport material may hamper dye regeneration even more. However, it has already been shown that even in cases with a slightly unfavourable energy landscape, an improvement in the photovoltaic performance can be reached by energy transfer, but only under the limitation of a low EDD loading to enable direct contact between the SAD and spiro-OMeTAD.^{12, 13} A further prerequisite of FRET accounts the HOMO-LUMO gap; the gap of the acceptor has to be smaller than that of the donor dye. This is fulfilled for all SAD-EDD combinations except BODIPY 1/donor 2 (Table 1).

Optical properties. Steady-state absorption and fluorescence measurements in solution (Figure 5) and also in the solid state (Figure S1) were performed. With these studies, two questions should be answered: i) are the EDDs able to absorb complementary to the SADs and ii) is there a distinct overlap between the EDD emission and the SAD absorption.

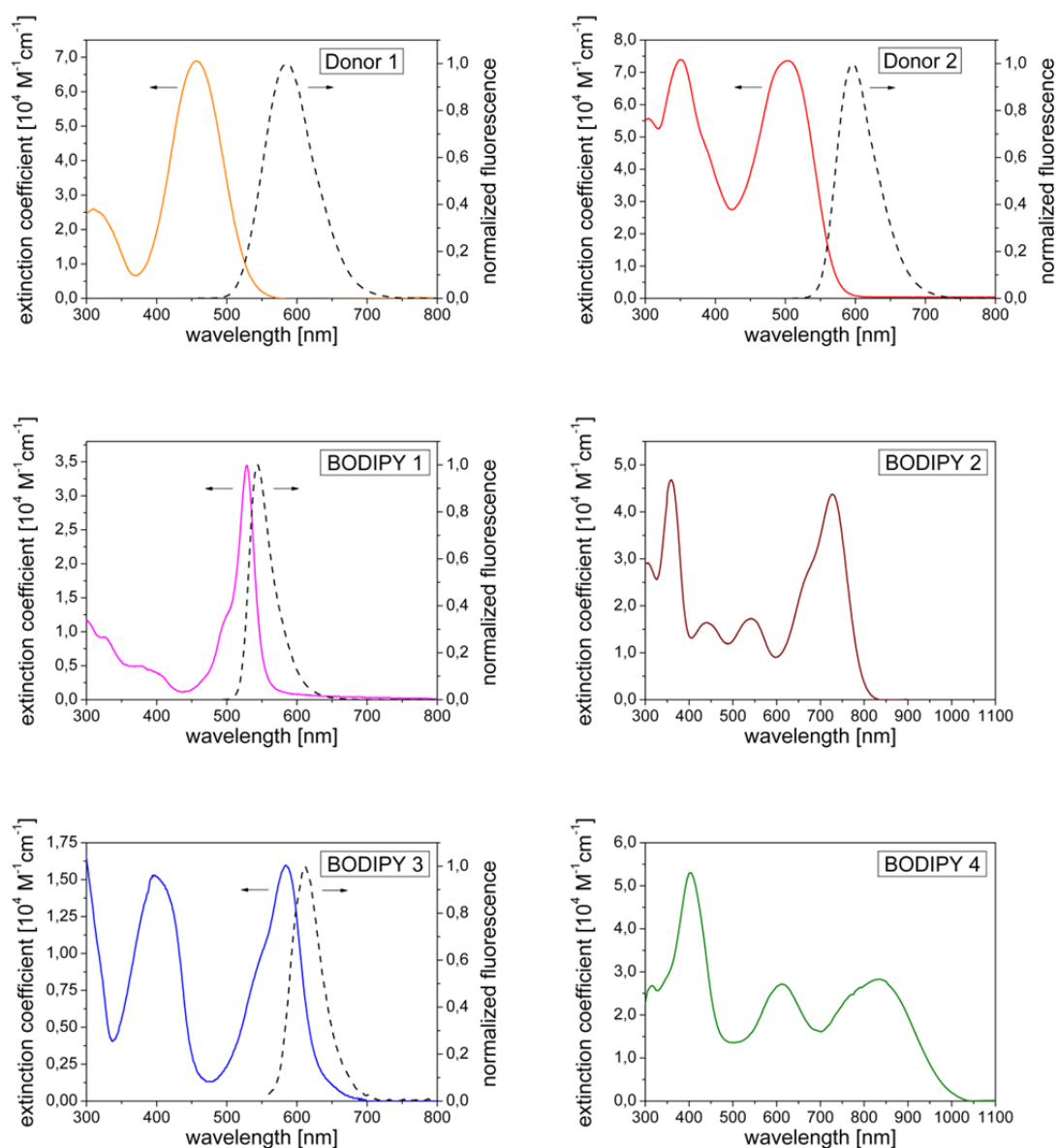


Figure 5. Steady-state absorption and fluorescence spectra of the EDDs (donor 1 and 2) and the SADs (BODIPY 1-4) in solution. The absorption spectra were measured in the range of $1 \times 10^{-5} \text{ M}$ in dichloromethane except BODIPY 3 which was measured in dichloromethane/tetrahydrofuran 1:1 due to solubility issues. The extinction coefficients were calculated according to the Beer-Lambert law. The fluorescence spectra were measured in toluene. BODIPY 2 and BODIPY 4 did not fluoresce.

A comparison of the absorption spectra of the EDDs and the SADs in solution shows that the EDDs absorb in regions where the SADs provide only low extinction coefficients. Donor 1 absorbs up to 550 nm with a maximum at 457 nm ($\epsilon = 6.9 \times 10^4 \text{ M}^{-1} \text{ cm}^{-1}$) and donor 2 absorbs up to 600 nm with a maximum at 503 nm ($\epsilon = 7.4 \times 10^4 \text{ M}^{-1} \text{ cm}^{-1}$). This is an excellent basis for providing a complementary absorption and hence to improve the EQEs in the regions with low optical density of the SAD for all donor-acceptor combinations.

Further, the overlap between the donor fluorescence and the acceptor absorption was studied. Except BODIPY 2 and BODIPY 4, all materials exhibit fluorescence in solution and in solid state. In BODIPY 2 and BODIPY 4 intramolecular charge transfer is possible between the BODIPY core and TPA donor substituents. Donor 1 emits between 500 and 700 nm with a maximum at 585 nm. This provides a moderate overlap with the absorption of BODIPY 1 and a perfect overlap with the absorption of BODIPYs 2-4. Donor 2 fluoresces between 550 and 700 nm with a maximum at 596 nm. Hence, there is only a negligible overlap with the absorption of BODIPY 1 but a good to perfect overlap with the absorption of BODIPYs 2-4. Comparable conclusions can be drawn by comparing the donor and acceptor spectra in the solid state (Figure S1).

Fluorescence quenching experiments. So far, the prerequisites of FRET for SDSC applications have been discussed and verified for the donors and the acceptors with regard to energetic and optical issues. Further, fluorescence quenching experiments were done to investigate the potential for energy transfer in mixed systems. An important indication for energy transfer is the ability of the acceptor materials to quench the fluorescence of the donor material, although quenching can also be due to further processes *e.g.* electron transfer from the donor to the acceptor. First, we performed preliminary investigations on the quenching ability of the SADs in solution (Figure 6).

As expected, the fluorescence of both donors could be efficiently reduced by the addition of the BODIPY acceptors. A deviating behaviour was observed only for quenching experiments involving BODIPY 1. In consideration of our energetic and optical investigations, the combination BODIPY 1/donor 1 should function as quenching system. However, both donor and acceptor fluoresce almost in the same region (Figure 5). Thus, quenching cannot be detected because it is not possible to distinguish between the donor and the acceptor fluorescence even if excitation was performed at the absorption minimum of the acceptor. Neither does the combination BODIPY 1/donor 2 show any indication for quenching. Previous experiments already identified this system as not suitable because of a lack of orbital overlap. Any quenching effects induced by the added solvent were excluded by a reference measurement without acceptor (Figure S2).

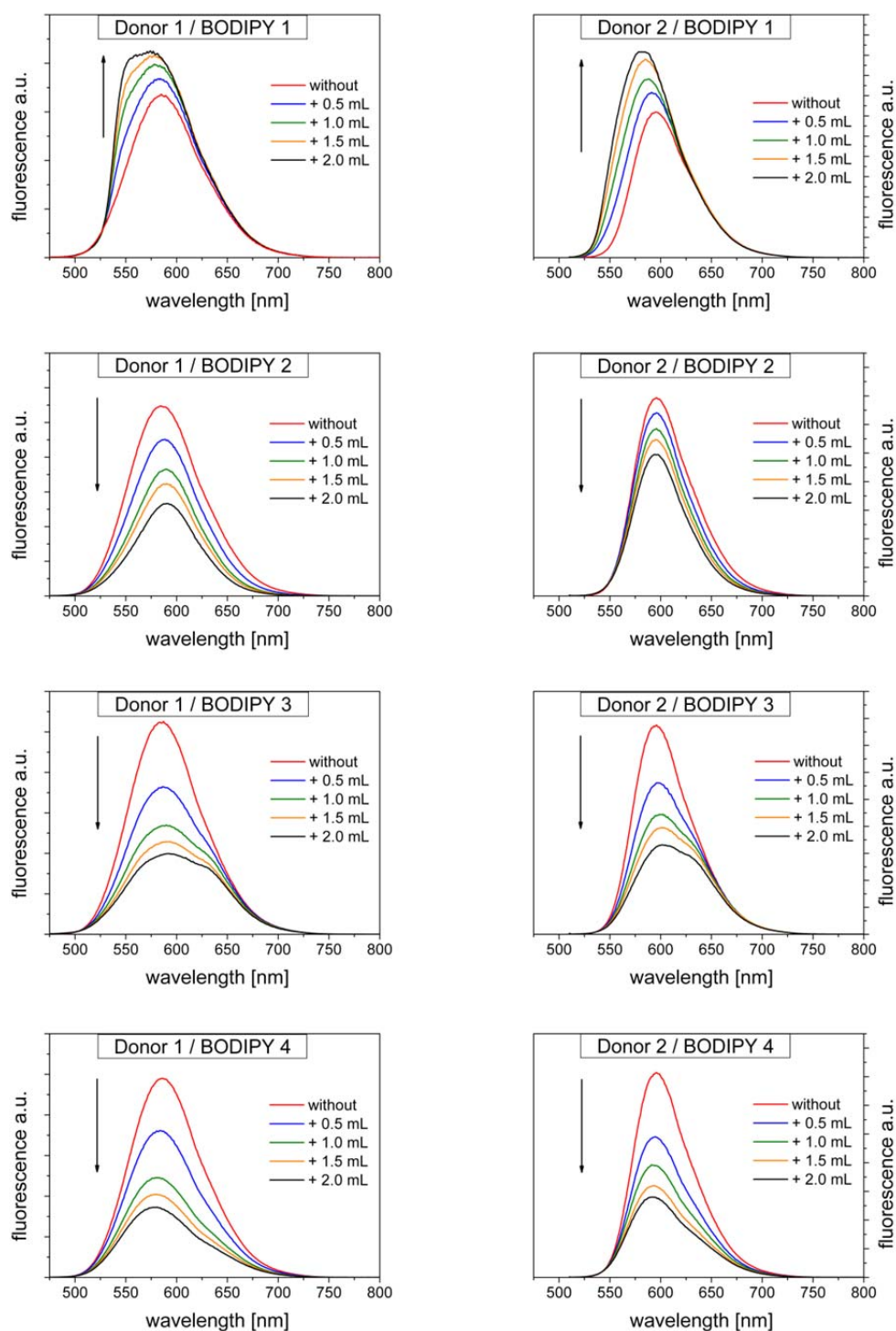


Figure 6. Fluorescence quenching experiments in solution. The materials were dissolved in toluene except BODIPY 3 which was dissolved in toluene/tetrahydrofuran 9:1 vol/vol due to solubility issues. The red curves show the fluorescence of 2 mL of the given donor at a concentration of 0.25×10^{-4} M without acceptor material. The other fluorescence spectra were obtained by adding 0.5 mL (blue), 1.0 mL (green), 1.5 mL (orange) and 2.0 mL (black) of the respective BODIPY solution with a stock concentration of 0.5×10^{-4} M. Excitation was done at the absorption maximum of the respective donor (437 and 503 nm for donor 1 and donor 2, respectively) except for the combination BODIPY 1/donor 1. Here, the solution was excited at the absorption minimum of BODIPY 1 (437 nm) to reduce the contribution of acceptor fluorescence. The arrows indicate the progression of the fluorescence upon addition of the acceptor.

To go a step further towards energy transfer in SDSCs, we performed additional fluorescence quenching experiments in the solid state. Donor thin films and donor-acceptor blends were prepared (donor/acceptor 1:1 mol/mol) and the fluorescence lifetime of the donors was measured. The blend films represent a simplified approximation to the conditions in SDSCs at the interface between SAD and EDD. Additionally, the blend setup ensures a short distance between donor and acceptor which is beneficial for FRET. The fluorescence lifetimes of pure donor films and donor-acceptor blend films are given in Table 2. The associated fluorescence spectra are shown in Figure S3. The time-resolved fluorescence spectra are given in Figure 7.

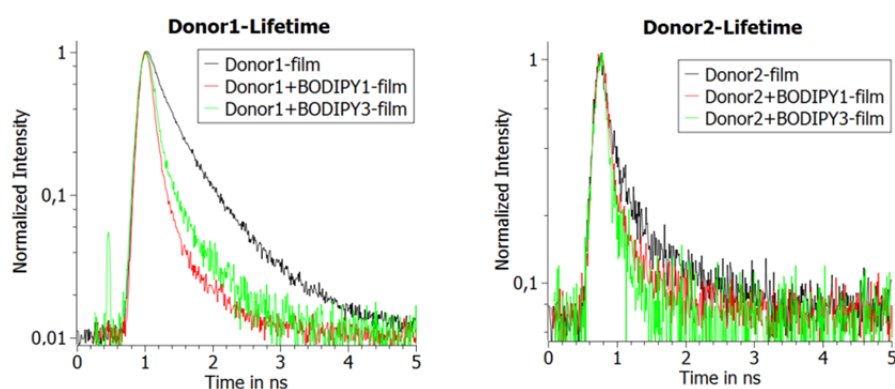


Figure 7. Time-resolved fluorescence spectra of pure donor thin films in comparison to donor-acceptor blend films involving the BODIPY 1 and BODIPY3. For the blend films with BODIPY 2 and BODIPY 4 the fluorescence of the donors was quenched completely.

Table 2. Summary of the measured fluorescence lifetimes of donor 1 and donor 2 in the absence and presence of BODIPYs in thin films. The films were prepared by spin coating (1000 rpm) of 4 wt% solutions of the pure donor material and 1:1 mol/mol mixtures of donor and acceptor.

acceptor	lifetime of donor 1 [ps]	reduction of the lifetime of donor 1 ^{a)} [%]	lifetime of donor 2 [ps]	reduction of the lifetime of donor 2 ^{a)} [%]
without	317	---	104	---
BODIPY 1	97	69	77	26
BODIPY 2	0	100	0	100
BODIPY 3	114	64	60	42
BODIPY 4	0	100	0	100

^{a)} The reduction of the lifetime of the donors was calculated by the equation: $[1 - (\tau_{\text{donor with acceptor}} / \tau_{\text{donor}})] \cdot 100$.

These experiments show that in presence of BODIPY 2 and BODIPY 4, the fluorescence of the donors is quenched completely (reduction of donor lifetime = 100%). Furthermore, the fluorescence lifetime of donor 1 without acceptor (317 ps) can be efficiently reduced by 69 and 64 % in blend films with BODIPY 1 and BODIPY 3, respectively. The lifetime of donor 2 without acceptor (104 ps) is reduced by 26 and 42 % in blend films with BODIPY 1 and BODIPY 3, respectively. Hence, the less pronounced reduction of the fluorescence lifetime of the donor was observed for combination BODIPY 1/donor 2 (26 %) which already emerged as inappropriate. However, the fluorescence was completely quenched in blend films incorporating 3,5-di(*N,N*-bis(4-methoxyphenyl)benzamine))-substituted BODIPYs (BODIPY 2 and BODIPY 4). Here, the energetic and optical prerequisites of FRET are fulfilled best. The fluorescence lifetime experiments on thin films further show that the lifetime of donor 2 is three times lower compared to the lifetime of donor 1. Long-lived excited states can have a beneficial effect on energy transfer because the rate of relaxation processes is inverse proportional to the lifetime of the donor excited state. This makes donor 1 more suitable for energy transfer in SDSCs.

Performance of solid-state dye-sensitized solar cells. The absorption of BODIPYs 1-4 on TiO₂ is depicted in Figure S5. A series of SDSCs was prepared for the different SAD-EDD pairs using 20 wt% and 50 wt% of the respective EDD in the hole conductor medium. The *J*-*V*-characteristics of the important devices without and with EDDs are given Table 3. A summary of the characteristics of all SDSCs is given in Table S1. The EQE spectra of all devices are depicted in Figure 8.

Table 3. *J*-*V* characteristics of SDSCs without and with 20 wt% of the different EDDs (donor1 and donor 2) measured under AM 1.5 G conditions (100 mW cm⁻²)

compd	J_{sc} [mA cm ⁻²]	V_{oc} [mV]	FF [%]	η [%]
BODIPY 1	2.19	677.5	47.6	0.71
BODIPY 1/donor 1 (20%)	1.72	762.5	45.4	0.59
BODIPY 1/donor 2 (20%)	0.80	757.5	38.0	0.23
BODIPY 2	2.93	632.5	38.6	0.71
BODIPY 2/donor 1 (20%)	2.33	765.0	36.7	0.65
BODIPY 2/donor 2 (20%)	0.96	747.5	39.5	0.28

Table 3 (continued)

BODIPY 3	2.98	667.5	39.6	0.79
BODIPY 3/donor 1 (20%)	2.18	695.0	31.4	0.48
BODIPY 3/donor 2 (20%)	1.04	692.5	29.2	0.21
BODIPY 4	0.71	457.5	41.5	0.14
BODIPY 4/donor 1 (20%)	0.31	622.5	46.9	0.09
BODIPY 4/donor 2 (20%)	0.18	612.5	51.6	0.06

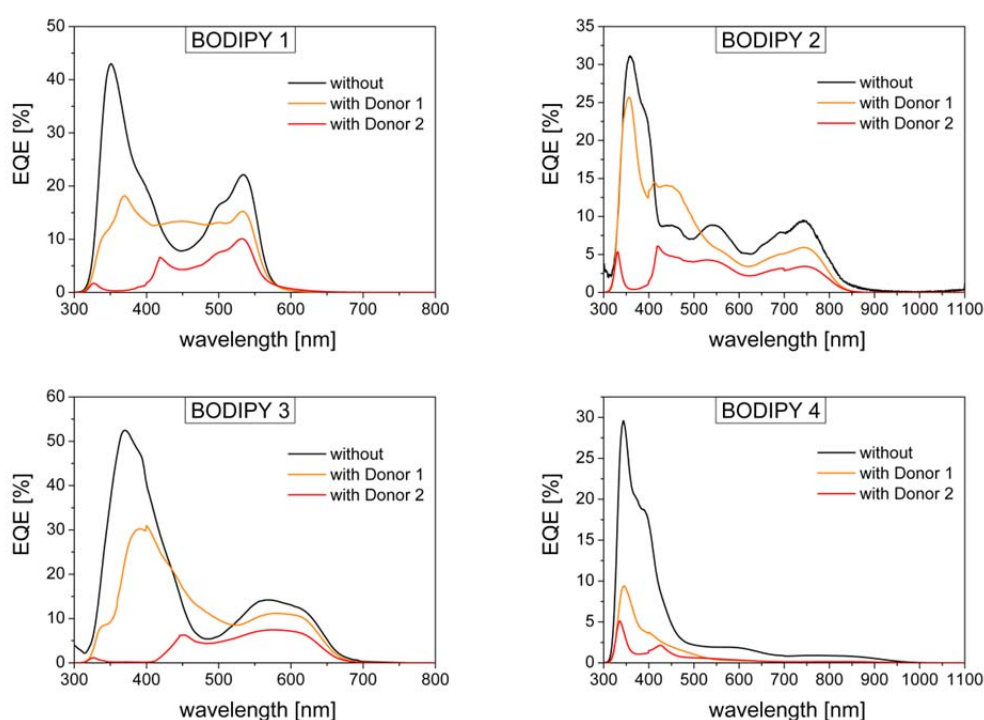


Figure 8. External quantum efficiency spectra of SDSCs using different BODIPYs as SADs without additional EDD (black), with 20 wt% of donor 1 (orange) and with 20 wt% of donor 2 (red) embedded in the hole transport material.

The EQE spectra of SDSCs incorporating donor 1 as EDD (Figure 8, orange lines) show a clear increase in the absorption region of the donor with a maximum at ~450 nm. This proves that donor 1 is an efficient energy donor that is able to boost the spectral response as expected. In contrast to that, the contribution of donor 2 (Figure 8, red lines) is negligible, although all preliminary investigations have been very promising. The reason for this behaviour is not yet understood and needs further investigations. Besides, the EQE of all SDSCs using a donor (regardless which) is reduced in the region between 330 and 420 nm. This effect is even more distinct for donor 2 than for donor 1. The high EQE in this region for SDSCs without additional

EDD can be attributed to energy transfer from the hole transport material spiro-OMeTAD to the SAD. Once a donor is involved, the energy of the excited states of spiro-OMeTAD can be transferred from spiro-OMeTAD to the donor (which acts in this special case as an acceptor) or it can be lost by deactivation induced by the donor. An indication for the validity of this hypothesis is given by quenching experiments in solution as depicted in Figure 8. The fluorescence of spiro-OMeTAD can be efficiently reduced by the addition of either EDD. Moreover, the direct light harvesting by the acceptor dyes in the 300-400 nm region is also lowered due to the absorption by the EDD in the same region. This indicates that the absorption of the EDD should be fine-tuned further to cause appreciable improvement using FRET.

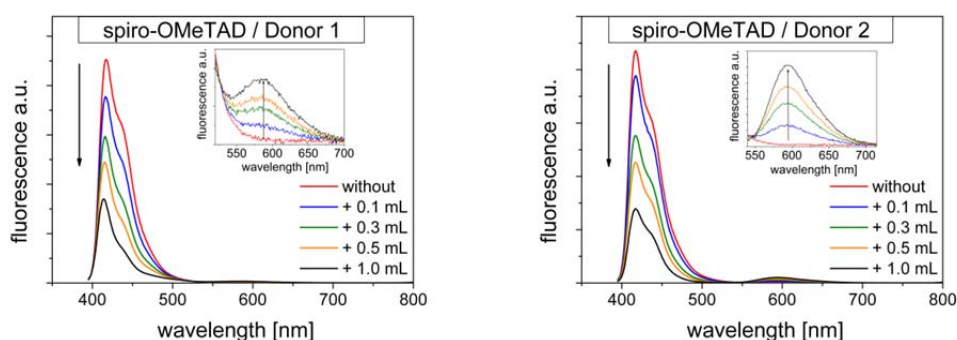


Figure 9. Fluorescence quenching experiments of spiro-OMeTAD with donor 1 and donor 2 in toluene. The red curves show the fluorescence of 2 mL of spiro-OMeTAD at a concentration of 0.25×10^{-4} M without acceptor material. The other fluorescence spectra were obtained by adding 0.5 mL (blue), 1.0 mL (green), 1.5 mL (orange) and 2.0 mL (black) of donor 1 and donor 2, respectively at a stock concentration of 0.5×10^{-4} M. The inset shows an enlarged view of the donor fluorescence. Excitation was done at 388 nm (= absorption maximum of spiro-OMeTAD).

A further issue negatively affecting the EQE of energy transfer SDSCs is the quenching of the excited donor states by the hole transport material spiro-OMeTAD.^{11, 12} This has nothing to do with energy transfer because neither the energetic nor the optical prerequisites of FRET are fulfilled for this combination. We measured the fluorescence lifetime in 1:1 mol/mol blend films of spiro-OMeTAD and the donors 1 and donor 2. The fluorescence intensity and the lifetime of the donors were remarkably reduced. The lifetimes in blend films are 68 ps and 61 ps for donor 1 and donor 2, respectively. This corresponds to a reduction of 79 and 41 % compared to pure donor films without spiro-OMeTAD. The origin of the reduced lifetimes was not further investigated. However, this energy is lost and cannot be used for current generation.

A major positive effect upon the use of these EDDs is an increase in the open-circuit voltage by more than 100 mV at comparable efficiencies (Table 3, Table S1 e.g. entry 6 and 7). This is a consequence of the lower lying HOMO level of the donors compared to that of spiro-OMeTAD.

The solar cell characteristics as shown in Table 3, indicate that the overall performance could not be improved by blending either donor 1 or donor 2 in the hole conductor media at amount of 20 wt%. Another alternative may be to physisorb the donors by spin-coating on the chemisorbed dye coated TiO₂. This may also avoid any negative influence in the hole conductor mobility of the spiro-OMeTAD layer due to the presence of donors.

CONCLUSION

We performed electrochemical and optical studies on BODIPYs as sensitizing acceptor dyes in combination with triphenylamine-based energy donor dyes to elucidate the potential of the SAD-EDD combinations for energy transfer in solid-state dye-sensitized solar cells. By measuring cyclic voltammetry in solution, the HOMO-LUMO band gaps as well as the energy levels were determined. It was found that the HOMO levels of BODIPY 2 and BODIPY 4 are higher than that of both donor compounds which may hinder dye regeneration. Because of that, BODIPY 2 and BODIPY 4 are less suitable for energy transfer in SDSCs in combination with donor 1 or donor 2 although all other prerequisites of FRET are perfectly fulfilled. The longer fluorescence lifetime of donor 1 (317 ps) compared to donor 2 (104 ps) reveals the higher potential of donor 1 for energy transfer due to an increase in the energy transfer rate. This is in perfect accordance with the EQE data. Here only donor 1 contributes to the current generation. Hence, the combinations BODIPY 1/donor 1 and BODIPY 3/donor 1 represent the most promising perspectives for further optimization.

Although the concept of increasing the EQE by energy transfer in SDSCs is simple at the first sight, a lot of complex issues have to be taken into account to identify suitable SAD-EDD combinations. This includes not only the prerequisites of FRET, the energy level alignment and fluorescence lifetimes of the donor materials, but also excited energy deactivation of the donor material and of the hole transport material by each other or by additives. Additionally, the amount of EDD embedded in the hole transport material has to be optimized for each SAD-EDD system separately to maintain the required hole carrier mobility of the medium. It has also to be investigated if methods other than simple blending can be used to bring the EDD in close contact to the SAD.

EXPERIMENTAL SECTION

Synthesis. Synthetic details and the characterisation of the EDDs donor 1 and donor 2 are provided in the electronic supporting information. The synthesis of the BODIPY SADs is published elsewhere.²¹

Characterisation methods. Cyclic voltammetry experiments were performed with a standard three-electrode setup connected to a potentiostat (model 263A, EG&G Princeton Applied Research). The measurements were carried out under moisture- and oxygen-free conditions. The working electrode consisted of a Pt milli-electrode (model G0228, AMETEK Advanced Measurement Technology). A platinum wire in the respective solvent plus conducting salt (tetrabutylammonium hexafluorophosphate TBAPF₆, 0.1 M) was used as counter electrode. An Ag-wire in an AgNO₃/ acetonitrile solution (0.1 M) was employed as quasi-reference electrode. Each measurement was calibrated with the internal standard ferrocene/ferrocenium (Fc/Fc⁺). The energy levels were determined by the empirical relation $E_{\text{HOMO}} = [-e \cdot (E^{1/2}_{\text{x vs. Fc/Fc}^+})] - 4.80 \text{ eV}$. Steady-state absorption spectroscopy was performed on a Hitachi U-3000 spectrophotometer. The extinction coefficients were calculated according to the Beer-Lambert law. Fluorescence spectra were recorded on a Shimadzu RF-5301PC spectrofluorometer. Fluorescence-lifetimes were calculated from time-resolved fluorescence spectra upon excitation with a pulsed titanium-sapphire-laser (Ti:Sa, Tsunami, Spectra Physics) equipped with a frequency doubler. Time-resolved fluorescence quenching was monitored with streak-system consisting of a spectrometer (250 Imaging Spectrograph, Bruker Optics), a streak-camera (C5680, Hamamatsu Photonics) and a CCD-camera (C4742, Hamamatsu Photonics).

Solar cell preparation and characterisation. Solid-state dye-sensitized solar cells were fabricated on transparent conducting FTO-coated glass substrates (Pilkington, Tec 15). The substrates were partially etched to create a non-conducting area for the cathode contact. After cleaning the substrates with different solvents (acetone, 2 wt% Hellmanex, water, ethanol), a compact blocking TiO₂ layer (134 nm) was deposited by spray pyrolysis²⁸ using titanium diisopropoxide bis(acetylacetonate) (Sigma-Aldrich, 75 wt% in isopropanol) in ethanol (2.4:21.6 mL/mL). The mesoporous TiO₂ layer was fabricated by screen printing a TiO₂ paste (Solaronix, T20/SP) which was subsequently sintered. A surface profilometer (Veeco, Dektak 150) was used to determine the thickness of the mesoporous layer which was found to be 1.8-2.0 μm . The substrates were immersed in the respective dye solutions (0.5 mM in acetonitrile/*tert*-butanol 1:1 vol/vol for BODIPY 1 and 3; 0.5 mM in acetonitrile/*tert*-butanol/DMSO 9:9:2 vol/vol/vol for BODIPY 2 and 4)

for 16 h. After entirely washing the substrates, they were treated with acetonitrile (140 μ l) for 1 min and spun at 3000 rpm for 45 sec. Then, the hole transport layer was applied by spin coating (3000 rpm). The stock solution of the hole transport material contained 0.13 M spiro-OMeTAD (Merck, livilux SHT-263), 0.02 M lithium salt $\text{LiN}(\text{SO}_2\text{CF}_3)_2$ and 0.23 M 4-*tert*-butylpyridine in chlorobenzene. For SDSCs incorporating energy donor dyes, the amount of spiro was reduced by 20 and 50 wt% and the same amount of the energy donor dye was added. The gold electrode contacts (50-60 nm) were deposited under high vacuum with a thermal evaporator (BOC Edwards, Auto 306, FL 400). External quantum efficiency measurements were performed with a PVE300 photovoltaic device characterisation system (Bentham) under white bias light.

ACKNOWLEDGMENT

Financial support from SFB 840 and GRAKO 1640 is kindly acknowledged.

BIBLIOGRAPHY

- 1 B. O'Regan, M. Grätzel, *Nature*, **1991**, 353, 737-740.
- 2 A. Yella, H.-W. Lee, H. N. Tsao, C. Yi, A. K. Chandiran, M. K. Nazeeruddin, E. W.-G. Diao, C.-Y. Yeh, S. M. Zakeeruddin, M. Grätzel, *Science*, **2011**, 334, 629-634.
- 3 U. Bach, D. Lupo, P. Comte, J. E. Moser, F. Weissörtel, J. Salbeck, H. Spreitzer, M. Grätzel, *Nature*, **1998**, 395, 583-585.
- 4 F. Fabregat-Santiago, J. Bisquert, L. Cevey, P. Chen, M. Wang, S. M. Zakeeruddin, M. Grätzel, *Journal of the American Chemical Society*, **2009**, 131, 558-562.
- 5 J.-H. Yum, S.-R. Jang, P. Walter, T. Geiger, F. Nüesch, S. Kim, J. Ko, M. Grätzel, M. K. Nazeeruddin, *Chemical Communications*, **2007**, 4680-4682.
- 6 D. Kuang, P. Walter, F. Nüesch, S. Kim, J. Ko, P. Comte, S. M. Zakeeruddin, M. K. Nazeeruddin, M. Grätzel, *Langmuir*, **2007**, 23, 10906-10909.
- 7 C. Siegers, U. Würfel, M. Zistler, H. Gores, J. Hohl-Ebinger, A. Hinsch, R. Haag, *ChemPhysChem*, **2008**, 9, 793-798.
- 8 B. E. Hardin, E. T. Hoke, P. B. Armstrong, J.-H. Yum, P. Comte, T. Torres, J. M. J. Fréchet, M. K. Nazeeruddin, M. Grätzel, M. D. McGehee, *Nature Photonics*, **2009**, 3, 406-411.
- 9 B. E. Hardin, J.-H. Yum, E. T. Hoke, Y. C. Jun, P. Péchy, T. Torres, M. L. Brongersma, M. K. Nazeeruddin, M. Grätzel, M. D. McGehee, *Nano Letters*, **2010**, 10, 3077-3083.
- 10 J.-H. Yum, B. E. Hardin, E. T. Hoke, E. Baranoff, S. M. Zakeeruddin, M. K. Nazeeruddin, T. Torres, M. D. McGehee, M. Grätzel, *ChemPhysChem*, **2011**, 12, 657-661.
- 11 J.-H. Yum, B. Hardin, S.-J. Moon, E. Baranoff, F. Nüesch, M. McGehee, M. Grätzel, M. Nazeeruddin, *Angewandte Chemie International Edition*, **2009**, 48, 9277-9280.
- 12 K. Driscoll, J. Fang, N. Humphry-Baker, T. Torres, W. T. S. Huck, H. J. Snaith, R. H. Friend, *Nano Letters*, **2010**, 10, 4981-4988.
- 13 G. K. Mor, J. Basham, M. Paulose, S. Kim, O. K. Varghese, A. Vaish, S. Yoriya, C. A. Grimes, *Nano Letters*, **2010**, 10, 2387-2394.
- 14 E. L. Unger, A. Morandeira, M. Persson, B. Zietz, E. Ripaud, P. Leriche, J. Roncali, A. Hagfeldt, G. Boschloo, *Physical Chemistry Chemical Physics*, **2011**, 13, 20172-20177.
- 15 J. Najbar, M. Mac, *Journal of the Chemical Society, Faraday Transactions*, **1991**, 87, 1523-1529.
- 16 K. E. Sapsford, L. Berti, I. L. Medintz, *Angewandte Chemie International Edition*, **2006**, 45, 4562-4589.
- 17 G. D. Scholes, *Annual Review of Physical Chemistry*, **2003**, 54, 57-87.
- 18 E. T. Hoke, B. E. Hardin, M. D. McGehee, *Optics Express*, **2010**, 18, 3893-3904.
- 19 D. L. Dexter, *Journal of Chemical Physics*, **1953**, 21, 836-850.
- 20 L.-J. Fan, W. E. Jones, in *Photochemistry and Photophysics of Polymer Materials*, John Wiley & Sons, Inc., **2010**, pp. 1-39.
- 21 K. Gräf, T. Körzdörfer, Kümmel Stephan, M. Thelakkat, **2012**, prepared for submission.
- 22 S. Heun, P. M. Borsenberger, *Chemical Physics*, **1995**, 200, 245-255.
- 23 E. T. Seo, R. F. Nelson, J. M. Fritsch, L. S. Marcoux, D. W. Leedy, R. N. Adams, *Journal of the American Chemical Society*, **1966**, 88, 3498-3503.
- 24 C. Schmitz, M. Thelakkat, H.-W. Schmidt, *Advanced Materials*, **1999**, 11, 821-826.
- 25 M. Thelakkat, R. Fink, P. Pösch, J. Ring, H.-W. Schmidt, *Polymer Preprints of the American Chemical Society*, **1997**, 1, 394-395.
- 26 M. Matis, P. Rapt, V. Lukes, H. Hartmann, L. Dunsch, *The Journal of Physical Chemistry B*, **2010**, 114, 4451-4460.
- 27 K. Peter, H. Wietasch, B. Peng, M. Thelakkat, in *Applied Physics A: Materials Science & Processing*, Vol. 79, Springer Berlin / Heidelberg, **2004**, pp. 65-71.

- 28 B. Peng, G. Jungmann, C. Jäger, D. Haarer, H.-W. Schmidt, M. Thelakkat, *Coordination Chemistry Reviews*, **2004**, 248, 1479-1489.

SUPPORTING INFORMATION

for the manuscript:

ENERGY TRANSFER IN SOLID-STATE DYE-SENSITIZED SOLAR CELLS: COMBINING BODIPYs AND ENERGY DONOR DYES

Katja Gräf^[a], Nils Bösch^[b], Jürgen Köhler^[b] and Mukundan Thelakkat^{[a]}*

^[a] Department of Macromolecular Chemistry I, Applied Functional Polymers, Universität Bayreuth, Universitätsstr. 30, 95440 Bayreuth, Germany.

Fax: +49 921 55 3206

E-mail: Mukundan.Thelakkat@uni-bayreuth.de

^[b] Department of Experimental Physics IV, Universität Bayreuth, Universitätsstr. 30, 95440 Bayreuth, Germany.

Table of Contents

1. General Information
2. Synthesis and Characterisation of Donor 1 and Donor 2
3. Optical Properties of the Materials in Thin Films
4. Reference Measurements for Fluorescence Quenching Experiments
5. Fluorescence Spectra of Donor Films and Donor-Acceptor Blend Films
6. Absorption Spectra of the BODIPYs on Mesoporous TiO₂
7. Solar Cell Performances
8. References

1. General Information

Proton nuclear magnetic resonance (^1H -NMR) spectra were recorded on a Bruker Avance 300 spectrometer at a transmitter frequency of 300 MHz. The spectra were calibrated to the chemical shift of the respective solvent residue signal. The chemical shifts are given in ppm and the coupling constants in Hz. The abbreviations used for splitting patterns are s = singlet, d = doublet, m = multiplet. Fourier transform infrared spectra were measured on a Perkin Elmer spectrum 100 FT-IR spectrometer equipped with an ATR unit. The frequency of the signals is given in cm^{-1} . The abbreviations used for the intensity of the signals are s = strong, m = medium, w = weak.

Steady-state absorption spectra were measured with a Hitachi U-3000 spectrophotometer. Fluorescence spectra were recorded on a Shimadzu RF-5301PC spectrofluorometer. For fluorescence quenching experiments on thin films, a pulsed titanium-sapphire-laser (Ti:Sa, Tsunami, Spectra Physics) equipped with a frequency doubler was used for excitation at 450 nm. Time-resolved fluorescence quenching was monitored with streak-system consisting of a spectrometer (250 Imaging Spectrograph, Bruker Optics), a streak-camera (C5680, Hamamatsu Photonics) and a CCD-camera (C4742, Hamamatsu Photonics).

Current-voltage characteristics were measured under standard AM 1.5 G spectral conditions at an intensity of 100 mW cm^{-2} using a solar simulator (Newport-Oriel, 92250A-1000) and an electrometer (Keithley, Model 6517). For accuracy, the light source was calibrated with a silicon solar cell (WPVS cell, ISE Call lab, Freiburg) and the device area not covered by electrodes was wiped away. The device was additionally furnished with a mask (active cell area: 0.20 cm^2 , mask aperture area: 0.30 cm^2).¹

2. Synthesis and Characterisation of Donor 1 and Donor 2

Materials. The starting material *N,N'*-diphenylbenzidine **1** and the reagents 4-iodoanisole, malononitrile and 4-(dicyanomethylen)-2,6-dimethyl-4H-pyran were purchased from Sigma-Aldrich or TCI and used as received without further purification. POCl_3 was freshly distilled prior use. Solvents used for precipitation and column chromatography were purified by distillation. Column chromatography was performed on silica gel 60M (0.04-0.063 mm) by Macherey Nagel

with the given eluents. *N,N'*-bis(4-dimethoxyphenyl)-*N,N'*-diphenylbenzidine **2** was synthesised according to a published method from compound **1** and 4-iodo-anisol with anhydrous potassium carbonate, copper powder and 18-crown-6 in *o*-dichlorobenzene.^{2, 3}

Synthesis. General Procedure for the Vilsmeier-Haack reaction: Dimethylformamide (DMF) was cooled to 0-5 °C and POCl₃ was added. The solution was stirred for 30 min at this temperature. Then it was allowed to warm to room temperature. **1** was dissolved in 1,2-dichloroethane (75 mL) and cooled to 0-5 °C. The first solution was slowly added to the second and the temperature was increased to 80 °C. The combined solutions were stirred at 80 °C for the given reaction times. After cooling to room temperature, the reaction solution was slowly poured into a well-stirred solution of Na(CH₃COO) (5.0 g) and ice water (50 mL). Stirring was continued overnight. The organic layer was separated, washed with water (3 x 100 mL), dried over Na₂SO₄ and the solvent was removed under reduced pressure. The pure product was isolated by column chromatography with dichloromethane as eluent.

4,4'-([1,1'-biphenyl]-4,4'-diylbis((4-methoxyphenyl)azanediyl))dibenzaldehyde **3.** DMF (3.50 mL), POCl₃ (1.50 g, 9.78 mmol) and **2** (1.65 g, 3.00 mmol) were allowed to react according to the above general procedure for 20 h. Compound **3** was freeze-dried from benzene and obtained as yellow solid (1.60 g, 88 %).

¹H-NMR (300 MHz, DMSO-d₆): δ/ppm = 3.76 (s, 6H, 2 OCH₃), 6.86 (d, ³J_{H/H} = 8.65 Hz, 4H, *H*_{ar}), 7.01 (d, ³J_{H/H} = 8.97 Hz, 4H, *H*_{ar}), 7.18 (d, ³J_{H/H} = 8.94 Hz, 4H, *H*_{ar}), 7.22 (d, ³J_{H/H} = 8.50, 4H, *H*_{ar}), 7.66 (d, ³J_{H/H} = 8.65 Hz, 4H, *H*_{ar}), 7.70 (d, ³J_{H/H} = 8.79 Hz, 4H, *H*_{ar}), 9.73 (s, 2H, 2COH).

4-((4-methoxyphenyl)(4'-((4-methoxyphenyl)(phenyl)amino)-[1,1'-biphenyl]-4-yl)amino)-benzaldehyde **4.** DMF (5 mL), POCl₃ (0.50 g, 3.26 mmol) and **2** (2.60 g, 4.74 mmol) were allowed to react according to the above general procedure for 3 h. Compound **4** was freeze-dried from benzene and obtained as yellow solid (1.50 g, 55 %).

¹H-NMR (300 MHz, acetone-d₆): δ/ppm = 3.82 (s, 3H, OCH₃), 3.85 (s, 3H, OCH₃), 6.90-7.15 (m, 13H, *H*_{ar}), 7.20-7.35 (m, 6H, *H*_{ar}), 7.56 (d, ³J_{H/H} = 8.78 Hz, 2H, *H*_{ar}), 7.66 (d, ³J_{H/H} = 8.64, 2H, *H*_{ar}), 7.72 (d, ³J_{H/H} = 8.86, 2H, *H*_{ar}), 9.82 (s, 1H, COH).

2,2'-((((1,1'-biphenyl)-4,4'-diylbis((4-methoxyphenyl)azanediyl))bis(4,1-phenylene))bis-(methan-yl-ylidene))dimalononitrile (donor 1). Malononitrile (0.13 g, 1.98 mmol) and **3** (0.40 g, 0.661 mmol) were dissolved in toluene (20 mL). Piperidine (45.2 μ L) and glacial acetic acid (52.4 μ L) were added. The reaction solution was stirred at 70 °C for 25 h. The solvent was removed under reduced pressure and the crude product was extracted with dichloromethane. After drying over Na₂SO₄ and removal of the solvent under vacuum, the crude product was further purified by column chromatography with toluene/acetonitrile 9:1 (v/v) as eluent. The final product was freeze-dried from benzene to afford donor 1 as orange solid (400 mg, 86 %).

¹H-NMR (300 MHz, DMSO-d₆): δ /ppm = 3.79 (s, 6H, 2 OCH₃), 6.87 (d, ³J_{H/H} = 9.02, 4H, H_{ar}), 7.05 (d, ³J_{H/H} = 8.88 Hz, 4H, H_{ar}), 7.26 (d, ³J_{H/H} = 8.88 Hz, 4H, H_{ar}), 7.32 (d, ³J_{H/H} = 8.66 Hz, 4H, H_{ar}), 7.73 (d, ³J_{H/H} = 8.60 Hz, 4H, H_{ar}), 7.83 (d, ³J_{H/H} = 9.04 Hz, 4H, H_{ar}), 8.21 (s, 2H, 2 H=(CN)₂). FT-IR (ATR): ν /cm⁻¹ = 3034 w, 2932 w, 2836 w, 2219 m (CN), 1612 w, 1597 m, 1564 s, 1488 s, 1439 m, 1319 m, 1292 m, 1239 m, 1181 s, 1164 w, 1106 w, 1030 w, 1004 w, 956 w, 924 w, 822 s, 794 w, 756 w, 725 w.

2-(2,6-bis((E)-4-((4-methoxyphenyl)(4'-((4-methoxyphenyl)(phenyl)amino)-[1,1'-biphenyl]-4-yl)amino)styryl)-4H-pyran-4-ylidene)malononitrile (donor 2). 4-(Dicyanomethylen)-2,6-dimethyl-4H-pyran (0.10 mg, 0.58 mmol), **4** (0.83 g, 1.45 mmol) and piperidine (50 μ L) were dissolved in acetonitrile (10 mL). The reaction solution was heated under reflux for 27 h. The solvent was removed under reduced pressure and the crude product was extracted with dichloromethane, dried over Na₂SO₄ and the solvent was removed. Purification was done by column chromatography with gradient elution using toluene/methanol 25:1 -> 75:1 (vol/vol). The final product was freeze-dried from 1,4-dioxane to afford donor 2 as red solid (440 mg, 59 %).

¹H-NMR (300 MHz, DMSO-d₆): δ /ppm = 3.83 (s, 6H, 2 OCH₃), 3.85 (s, 6H, 2 OCH₃), 6.59 (d, ³J_{H/H} = 16.04 Hz, 2H, 2 (Pyran)H=H(TPD)), 6.64 (s, 2H, H_{ar}), 6.84-7.30 (m, 38H, 2 (Pyran)H=H(TPD) + H_{ar}), 7.38-7.53 (m, 14H, H_{ar}). FT-IR (ATR): ν /cm⁻¹ = 3032 w, 2927 w, 2206 m (CN), 1637 m, 1586 s, 1538 m, 1504 w, 1485 s, 1412 m, 1318 m, 1282 m, 1238 s, 1202 w, 1163 m, 1105 w, 1031 m, 960 w, 944 w, 816 s, 761 w, 747 w, 725 w.

3. Optical Properties of the Materials in Thin Films

The following figures show the normalized optical density and the normalized fluorescence intensity of the different donor and acceptor thin films. The films were prepared by spin coating (2000 rpm, 120 sec) from 1 wt% solutions in chlorobenzene except BODIPY 3 which was dissolved in THF due to solubility problems.

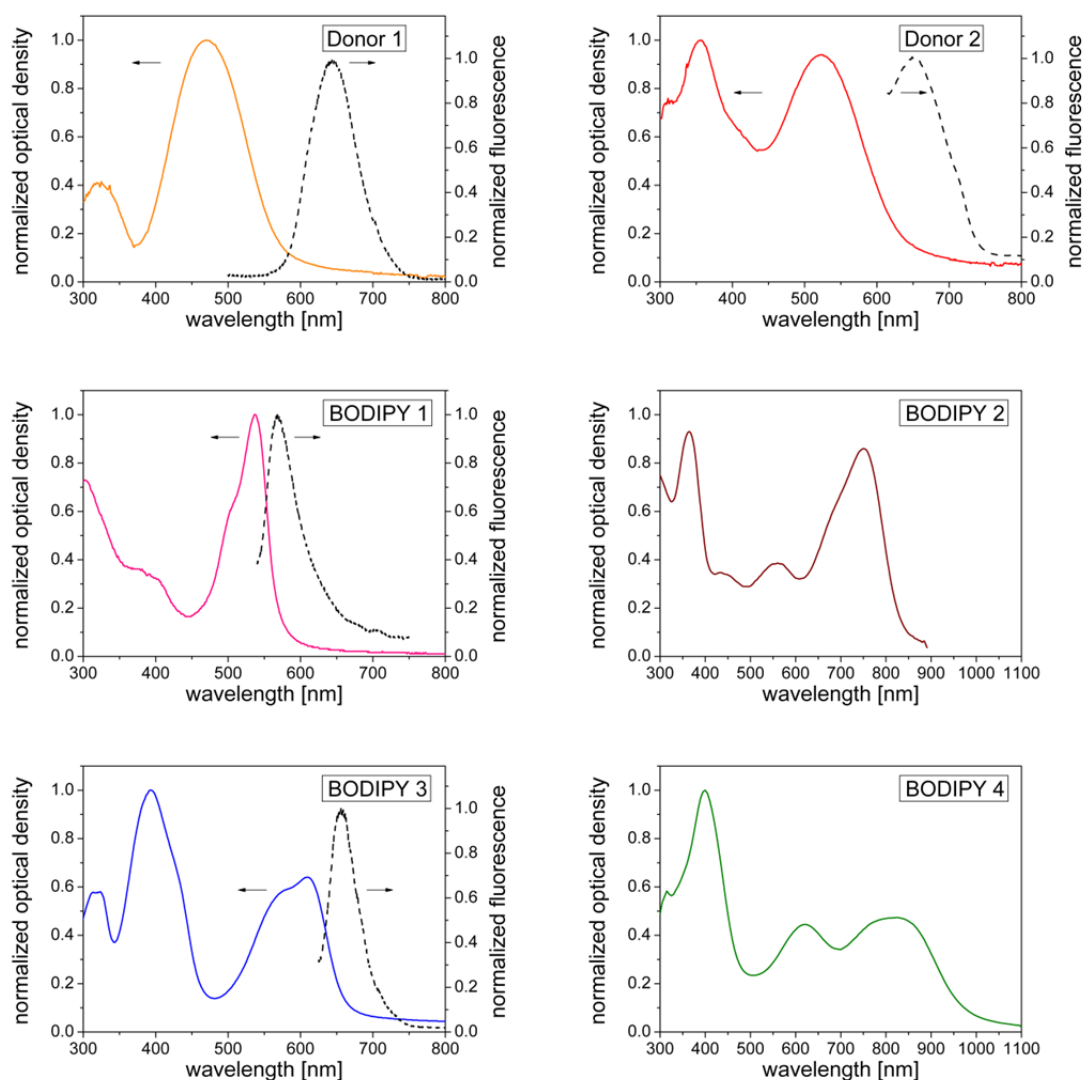


Figure S1. Steady-state absorption and fluorescence spectra of the energy donor dyes (donor 1 and 2) and the sensitizing acceptor dyes (BODIPY 1-4) in solid state as films on glass. The films were prepared by spin coating (1 wt%, 2000 rpm) from chlorobenzene except BODIPY 3 which was spin coated from tetrahydrofuran. BODIPY 2 and 4 did not fluoresce.

A comparison of these spectra with the solution spectra reveals a slight broadening of the absorption in thin films and red shift by 13 and 11 nm for donor 1 and donor 2, respectively. The absorption spectra of the acceptor materials have been hardly changed. In accordance with the measurements in solution, the donor materials absorb in regions where the acceptors show only low optical density and the overlap between the donor fluorescence and the acceptor absorption is still guaranteed.

BODIPY 2 and BODIPY 4 can exhibit internal charge transfer and therefore do not show any fluorescence in the solid state (and also in solution).

4. Reference Measurements for Fluorescence Quenching Experiments

To make sure that the solvent did not cause any quenching effects, the fluorescence quenching experiments were repeated without addition of the acceptor material by solely adding toluene.

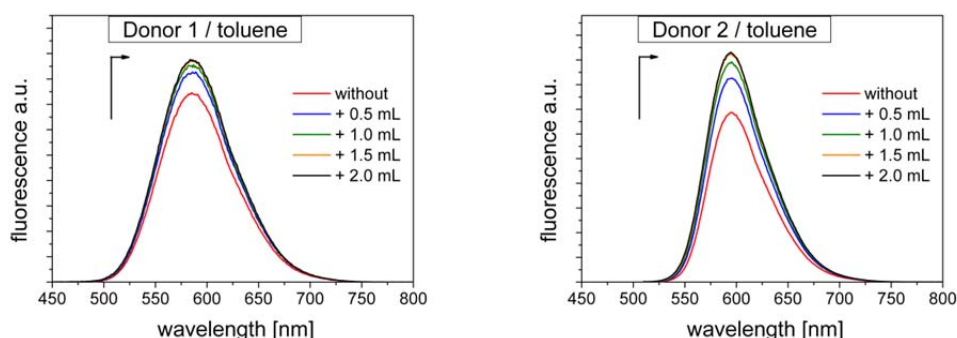


Figure S2. Reference measurements for the fluorescence quenching experiments in solution. Here, the quenching experiments were repeated but without any acceptor just by addition of toluene. The red curves show the fluorescence of 2 mL of the given donor in toluene at a concentration of 0.25×10^{-4} M without additional toluene. The other fluorescence spectra were obtained by adding 0.5 mL (blue), 1.0 mL (green), 1.5 mL (orange) and 2.0 mL (black) of toluene.

As expected, the fluorescence intensity was not reduced by the addition of toluene. The addition of toluene equals a dilution of the stock solution which results at first in a slight increase of the fluorescence due to less self-quenching of the donor molecules in solution. For higher dilutions, the fluorescence intensity stays constant (orange and black line).

5. Fluorescence Spectra of Donor Films and Donor-Acceptor Blend Films

The following spectra show the fluorescence and the time-resolved fluorescence of donor films in comparison to the donor-acceptor blend films. These measurements were used for the calculation of the fluorescence lifetimes given in Table 2. The films were prepared by spin coating (1000 rpm, 120 sec) from 4 wt% solutions in chlorobenzene except BODIPY 3 containing films which were prepared from THF due to solubility issues. The blend films comprise a 1:1 mol/mol ratio of donor to acceptor.

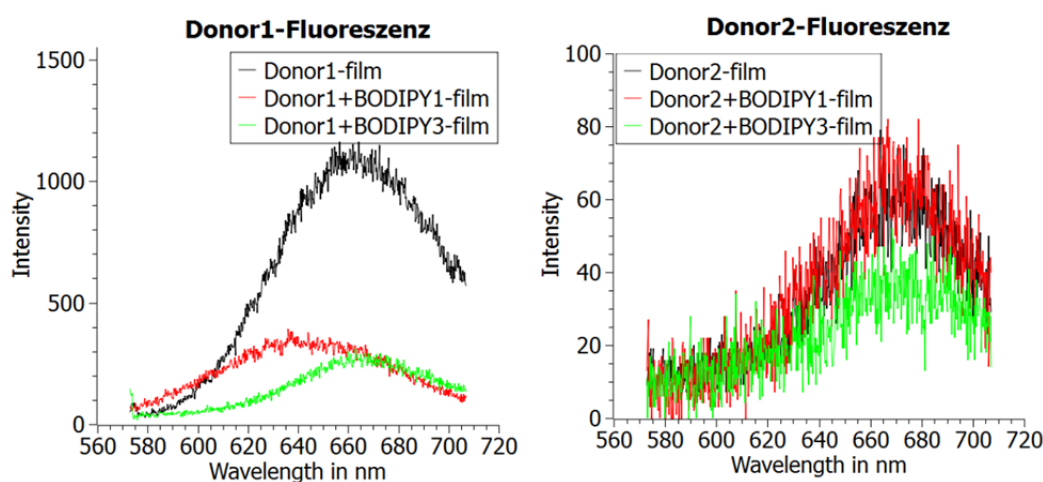


Figure S3. Fluorescence spectra of donor thin films in comparison to donor-acceptor blend films.

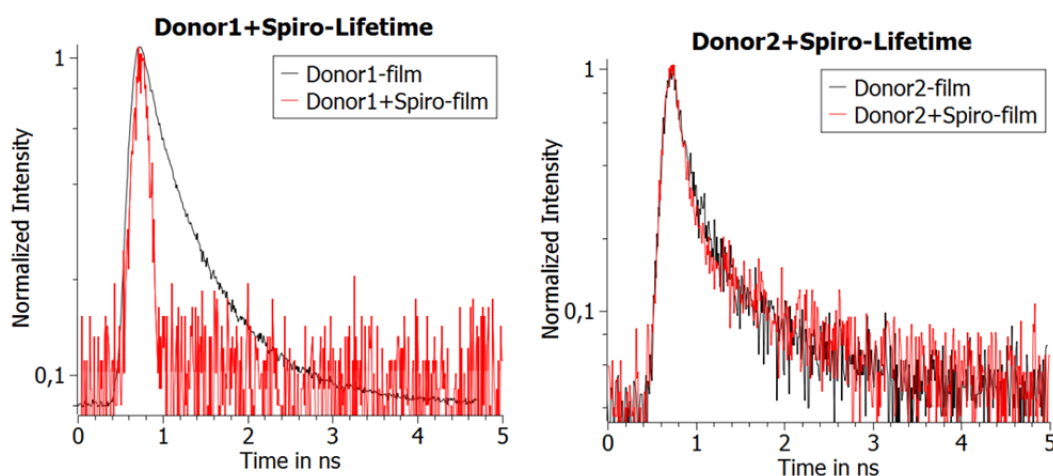


Figure S4. Time-resolved fluorescence spectra of donor thin films in comparison to donor-spiro-OMeTAD blend films.

6. Absorption Spectra of the BODIPYs on Mesoporous TiO₂

The following figure shows the optical density as a function of the wavelength for BODIPYs 1-4 in the adsorbed state anchored on mesoporous TiO₂. These sensitized TiO₂ layers were used for the preparation of solar cells.

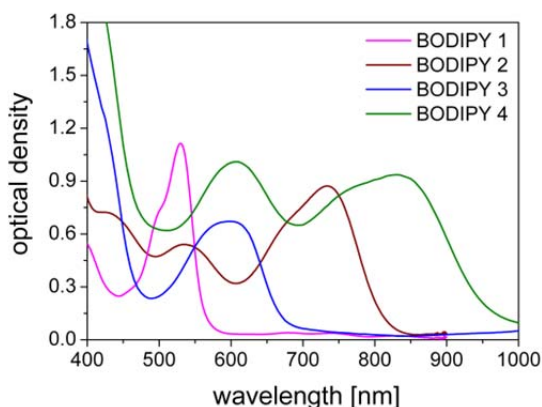


Figure S5. Steady-state absorption spectra of sensitized mesoporous TiO₂ thin films (2 μm) that were used for the preparation of SDSCs and energy transfer solar cells.

7. Solar Cell Performances

The short-circuit current density (J_{sc}), the open circuit voltage (V_{oc}), the fill factor (FF) and the resulting efficiency (η) of SDSCs using the BODIPY compounds as sensitizing acceptor dye without and with additional energy donor dyes are summarized in Table S1.

Table S1. J-V characteristics of SDSCs without and with energy donor dyes measured under AM 1.5 G conditions (100 mW cm⁻²)

entry	compd	J_{sc} [mA cm ⁻²]	V_{oc} [mV]	FF [%]	η [%]
1	BODIPY 1	2.19	677.5	47.6	0.71
2	BODIPY 1/donor 1 (20%)	1.72	762.5	45.4	0.59
3	BODIPY 1/donor 1 (50%)	0.46	792.5	39.6	0.15
4	BODIPY 1/donor 2 (20%)	0.80	757.5	38.0	0.23
5	BODIPY 1/donor 2 (50%)	0.35	782.5	40.8	0.11
6	BODIPY 2	2.93	632.5	38.6	0.71
7	BODIPY 2/donor 1 (20%)	2.33	765.0	36.7	0.65
8	BODIPY 2/donor 1 (50%)	0.37	757.5	39.6	0.11
9	BODIPY 2/donor 2 (20%)	0.96	747.5	39.5	0.28
10	BODIPY 2/donor 2 (50%)	0.11	777.5	43.7	0.04

Table S1 (continued)					
11	BODIPY 3	2.98	667.5	39.6	0.79
12	BODIPY 3/donor 1 (20%)	2.18	695.0	31.4	0.48
13	BODIPY 3/donor 1 (50%)	0.55	762.5	33.5	0.14
14	BODIPY 3/donor 2 (20%)	1.04	692.5	29.2	0.21
15	BODIPY 3/donor 2 (50%)	0.20	762.5	45.3	0.07
16	BODIPY 4	0.71	457.5	41.5	0.14
17	BODIPY 4/donor 1 (20%)	0.31	622.5	46.9	0.09
18	BODIPY 4/donor 1 (50%)	0.13	637.5	33.1	0.03
19	BODIPY 4/donor 2 (20%)	0.18	612.5	51.6	0.06
20	BODIPY 4/donor 2 (50%)	0.05	627.5	45.1	0.01

8. References

- 1 J. Park, H.-J. Koo, B. Yoo, K. Yoo, K. Kim, W. Choi, N.-G. Park, *Solar Energy Materials and Solar Cells*, **2007**, 91, 1749-1754.
- 2 S. Gauthier, J. M. J. Fréchet, *Synthesis*, **1987**, 1987, 383-385.
- 3 C. Schmitz, M. Thelakkat, H.-W. Schmidt, *Advanced Materials*, **1999**, 11, 821-826.

Chapter 10

APPENDIX: PHOTSENSITIZERS IN SOLAR ENERGY CONVERSION

*Katja Willinger and Mukundan Thelakkat**

Department of Macromolecular Chemistry I, Applied Functional Polymers, Universität Bayreuth,
Universitätsstr. 30, 95440 Bayreuth, Germany.

Fax: +49 921 55 3206

E-mail: Mukundan.Thelakkat@uni-bayreuth.de

Published as book chapter in *Photosensitizers in Medicine, Environment and Security*
Springer **2012** (ISBN 978-90-481-3870-8), chapter 11, 527-617.
with kind permission from Springer Science+Business Media B.V.

ABSTRACT

Today's energy problems arise from the predicted exhaustion of fossil energy resources and the negative aspects of climate change. Additionally, the increasing energy needs and the improved environmental awareness of people all over the world necessitate the utilization of environmental friendly energy sources. The most abundant energy source is the sun. The solar energy is largely available, surpassing our annual energy demand by the factor of 10 000. Each second the sun produces enough energy to cover the energy demand for the whole humanity for 1 000 000 years.¹ The dye-sensitized solar cell (DSC) concept is an interesting alternative to conventional silicon based solar cells due to its advantages of easy and fast fabrication, low production costs, short energy payback time and high photoelectric conversion efficiencies. In the following pages an overview shall be given of the operation principle of DSCs and the dyes used as sensitizers for solar energy conversion. The aim is to give an outline of the evolution of the DSC concept, the advantages and drawbacks of dye-sensitized systems and the different dyes (metal-organic and organic) applied in liquid and solid-state DSCs. Furthermore, the state of the art performance of the different types of dyes will be given.

OUTLINE

1 Historical Background of Dye-Sensitization	243
2 Dye-Sensitized Solar Cells	247
2.1 Assembly and Materials	248
2.1.1 Transparent Conducting Oxides	249
2.1.2 Compact Blocking Layer	250
2.1.3 Mesoporous Metal Oxide Semiconductors	251
2.1.4 Sensitizers – Requirements and Strategies	253
2.1.5 Hole Transport Materials	257
2.1.6 Counter Electrodes	259
2.2 Mechanisms	260
2.2.1 Key Processes	260
2.2.2 Recombination Processes	262
2.3 Characterization by Current/Voltage-Curves	263
2.4 Characterization by IPCE Measurements	264
3 Metal-Organic Sensitizers in Dye-Sensitized Solar Cells	265
3.1 Ruthenium Dyes	265
3.1.1 Unfunctionalized Ruthenium Dyes	268
3.1.2 Amphiphilic Ruthenium Dyes	271
3.1.3 Donor-Antenna Ruthenium Dyes	276
3.1.4 Donor-Antenna Ruthenium Dyes bearing Hydrophobic Chains	283
3.1.5 Ion-Coordinating Ruthenium Dyes	289
3.2 Phthalocyanine and Porphyrin Dyes	296
4 Organic Sensitizers in Dye-Sensitized Solar Cells	304
4.1 BODIPY Dyes	305
4.2 Polymer Sensitizers	306
4.3 Squaraine Dyes	307
4.4 Perylene Dyes	308
4.5 Cyanine Dyes	309
4.6 Coumarin Dyes	311
4.7 Indoline Dyes	313
4.8 Oligothiophene bridged Arylamine Donor Dyes	314
5 Conclusion	319
6 Bibliography	321

ABBREVIATIONS

AIST	advanced industrial science and technology
ATO	antimony doped tin oxide
ATR-FTIR	attenuated total reflectance - fourier transform infrared (spectroscopy)
AZO	aluminium doped zinc oxide
CB	conduction band
CDCA	chenodeoxycholic acid
DCA	deoxycholic acid
DFT	density functional theory
DPA	1-decylphosphonic acid
DSC	dye-sensitized solar cell
EDOT	3,4-ethylenedioxythiophene
EMIB(CN) ₄	1-ethyl-3-methylimidazolium tetracyanoborate
FTO	fluorinated tin oxide
GZO	gallium doped zinc oxide
HDMA	<i>n</i> -hexadecylmalonic acid
HOMO	highest occupied molecular orbital
HTM	hole transport material
ITO	indium tin oxide
LC	ligand centred
L-DSC	liquid-state dye-sensitized solar cell
LUMO	lowest unoccupied molecular orbital
MC	metal centred
MLCT	metal-to-ligand charge transfer
S-DSC	solid-state dye-sensitized solar cell
spiro-OMeTAD	2,2',7,7'-tetrakis(N,N-di- <i>p</i> -methoxyphenylamine)-9,9'-spirobifluorene
<i>t</i> BP	4- <i>tert</i> -butylpyridine
PEDOT	poly(3,4-ethylenedioxythiophene)
P3HT	poly(3-hexylthiophene)
P3TAA	poly(3-thiophenylacetic acid)
PMII	1-propyl-3-methylimidazolium iodide
RCPV	research center for photovoltaics
TCO	transparent conducting oxide
TPD	triphenyldiamine

1 HISTORICAL BACKGROUND OF DYE-SENSITIZATION

The photoelectric effect was first reported by A. E. Becquerel in 1839.² He used an electrolyte solution surrounding two platinum electrodes with one additionally covered with a thin layer of silver chloride. As a consequence of illumination of the silver chloride plate, an electric current resulted. Becquerel supposed that the current arose from a chemical reaction but the mechanism was not clarified until H. Hertz and W. Hallwachs accomplished systematic investigations in 1886.³ They explained that charge carriers can be emitted from matter (metals, solids, liquids or gases) upon absorption of high energetic (short wavelength) irradiation, such as visible or ultraviolet light. These results were confirmed by P. Lenard in 1900 who verified that the emitted charge carriers were electrons. Furthermore, he discovered that the maximum kinetic energy of the emitted photoelectrons depends on the frequency of the absorbed wavelength, but not on its intensity which defines the number of ejected electrons. Besides these developments, the photoelectric effect had to wait until 1905 for an exact explanation by A. Einstein.⁴ "For his service to Theoretical Physics, and especially for his discovery of the law of the photoelectric effect" Einstein was awarded the Nobel Prize in Physics of the year 1921.⁵ This was also the basis for the invention of the p-n junction silicon solar cell in 1954 by D. Chapin, C. Fuller, G. Pearson⁶ which culminated in the first application in 1958 as energy source in the Vanguard 1⁷ satellite. Although the information flow with this satellite is broken since 1964, the solar cells still work and hence Vanguard 1 is the world's oldest satellite still in orbit. As it is known, the energy conversion by semiconducting silicon solar cells on the basis of the inner photoelectric effect is currently one of the most promising renewable energy technologies. Built in 2008, the Olmedilla Photovoltaic Park in Spain is today the largest photovoltaic plant using silicon solar cells with a peak production of 60 megawatts. Unfortunately, the widespread use of silicon solar cells is somewhat hindered by the requirement of high-purity silicon, skilled manufacturing techniques and therefore high production costs.

In view of this, it is a serendipity that J. Moser opened up a second way for photocurrent generation in 1887, also partly using the inner photoelectric effect but with an inventive add-on. On the base of Becquerel's electrodes, Moser imbrued his halogenated silver plates in an erythrosine solution.⁸ In this way, he was able to enhance the photocurrent caused by the photoelectric effect significantly. Whereas Becquerel's silver chloride covered platinum electrode could just use the high energetic part of the incident light, Moser's dye covered electrodes could also use a large part of the visible light thanks to the absorption of the dye.

Later, metal electrodes were replaced by semiconductors to reduce recombination effects. In the following years, the theoretical understanding on the spectral sensitization of semiconductors by metal-organic/organic dyes steadily improved. Tributsch and co-workers, for example, investigated the sensitization effects occurring at the contact interface between the n-type semiconductor ZnO and a dye (fluorescein).⁹ They measured current/voltage characteristics for the sensitized single-crystal electrode with and without illumination by applying an increasing counter voltage. The same type of measurement is still used to characterize the performance of DSCs (*cf.* section 2.3). In 1970 H. Tributsch and M. Calvin studied the electrochemical reactions of excited molecules (chlorophyll) at a wide-band gap semiconductor surface (ZnO) in contact with an electrolyte in detail, measured anodic photocurrents and investigated the role of the regenerating electrolyte.¹⁰

With increasing understanding of the processes occurring in dye-sensitized systems, an application for the dye-sensitized photoelectrochemical cells drew scientists' attention, *viz.* the photoelectrolysis of water. A. Fujishima and K. Honda discussed an electrochemical photocell based on an n-type TiO₂ electrode in contact with an aqueous electrolyte and a platinum plate as counter electrode.¹¹ With this novel type of cell it was possible to decompose water into oxygen and hydrogen without application of any external voltage. Until this work of Fujishima and Honda, only little attention had been paid to the idea of an application for the dye-sensitized concept. The photoelectrochemical cells were rather used for mechanistic interpretations of processes and reactions occurring at semiconductor/dye interfaces.

Inspired by water splitting, H. Gerischer discussed the application of this type of cell for the conversion of light into electricity in 1975.¹² After that, the field of light energy conversion in dye-sensitized photoelectrochemical cells began to flourish. Scientists like Tributsch, Gerischer and Grätzel exerted effort on the improvement of the visible light response of wide band gap semiconductors, such as ZnO and TiO₂ by dye-sensitization at flat semiconductor electrolyte interfaces.¹³ During this time, the understanding of photoinduced effects at dye-coated semiconductor surfaces which are in contact to a liquid electrolyte steadily increased, not only due to the interest in light-harvesting systems for energy conversion, but also due to the importance of dye-sensitization in photography.

In 1988 K. Tennakone *et al.* invented a novel type of dye-sensitized solar cell.¹⁴ Besides, the known liquid-state dye-sensitized solar cells (L-DSC) comprising of a wide band gap semiconductor (*e.g.* TiO₂), a dye (commonly natural dyes) and a liquid electrolyte, they used a

solid hole transport material (p-CuCNS). Their aim was to overcome a major problem of L-DSCs, viz. the degradation of dye molecules. According to Tennakone, degradation takes place because the electron transfer and the excitation of the dye molecule occur in an environment containing reactive ions and molecules. Hence, the problem of dye degradation does not arise in DSCs where electrolytes are not employed. To realize their concept of solid-state dye-sensitized solar cells (S-DSC) they used thiocyanates of Rhodamine B and Methyl Violet as dyes to extend the spectral response of a semiconductor to visible light. The dye monolayer was sandwiched between two inorganic wide band gap semiconductors, the one of which exhibited a p-type while the other one exhibited an n-type conduction mechanism. After the excitation of the dye ($D + h\nu \rightarrow D^*$), charge separation happened at a semiconductor/dye/semiconductor interface ($D^* \rightarrow D + h^+ + e^-$). Whereupon hole transfer from the dye to the valence band of p-CuCNS and electron transfer to the conduction band of SnO_2 took place. The efficiency of DSCs using a solid inorganic hole transport material in this early stage of research was in the order of 10^{-7} - 10^{-8} under monochromatic light.¹⁴

Despite great achievements in the field of dye-sensitized photoelectrochemical cell for solar energy conversion in the 1980s, the light harvesting efficiency of such devices remained low and the concept was far away from any efficient device application. The milestone in the development of efficient DSC was made by B. O'Regan and M. Grätzel in 1991.¹⁵ They designed an L-DSC from low-to medium-purity materials through low cost processes which exhibited a commercially realistic energy conversion efficiency of 7.9 % (at 8.3 mW/cm^2) and 7.12 % (at 75 mW/cm^2) measured under simulated solar light. These results exceeded all existing L-DSC because of two main innovations: (i) Instead of a flat semiconductor surface, they used a $10\text{-}\mu\text{m}$ -thick mesoporous TiO_2 layer comprising of nanometer-sized TiO_2 particles. Sintered porous TiO_2 nanoparticles provide a 100-fold increased internal surface as compared to a compact and flat TiO_2 layer.¹⁶ This enhanced the light harvesting capability of the cell because a rough and porous TiO_2 -surface provides more space for dye molecules. Consequently, the dye surface concentration could be increased so that a larger quantity of dye molecules could absorb light and was simultaneously in contact with the electrolyte. (ii) Stability problems were partly overcome by newly developed charge-transfer dyes.^{17, 18} These CN-bridged trinuclear ruthenium complexes carrying "COOH-anchoring groups" could chemisorb on TiO_2 to give a proper connection between the dye and the electron conducting TiO_2 for efficient charge injection. Upon absorption of electromagnetic irradiation from the visible region of light, the ruthenium dye acts as an electron pump to convey an electron from the HOMO (highest occupied

molecular orbital) to the LUMO (lowest unoccupied molecular orbital). Afterwards the excited dye injects an electron into the wide band gap semiconductor titanium dioxide from where it reaches the photoanode. At the same time, the oxidized dye is regenerated by a hole transport material (an iodide/triiodide redox electrolyte) which transfers the holes to the cathode. Now the dye is ready for the next cycle and the charges are separated at the electrodes of the photoelectrochemical cell and can be used by a consumer load. After a turn over number of 5×10^6 cycles, which equals to two month under load, the change in photocurrent of O'Regan's and Grätzel's L-DSC was less than 10 %, showing the high stability of the novel ruthenium dyes.¹⁵

The effective concept of high surface porous TiO_2 was also transferred to S-DSCs. In 1995 K. Tennakone *et al.* used a nanoporous TiO_2 layer (thickness about 3 μm) deposited on conducting glass, sensitized it with a monolayer of the pigment cyanidine and filled the intercrystallite pores with p-type CuI (thickness about 6 μm).¹⁹ The use of thicker layers than a monolayer of dyes/pigments tends to result in electrical insulation and also cuts off light that should be incident to the dye molecules that are adsorbed directly at the semiconductor surface. With this assembly of an S-DSC, an impressive short-circuit photocurrent of 2.5 mA/cm^2 and an open-circuit voltage of 375 mV (at 80 mW/cm^2 in direct sunlight) could be reached.

When two semiconductors (a p-type and an n-type) form an interpenetrating network on the nanometer-scale, there are several problems to be addressed. For example, the crystal lattice mismatch of the different semiconductors will prevent a good contact at the interface. Additionally, the processability of inorganic hole transport materials is a serious issue. In contrast to that, low molecular weight compounds offer the advantages of easy processability in combination with a high variety of the chemical structure and hence an almost unlimited diversity. Furthermore, low-molecular weight materials like triphenyldiamines (TPDs) provide a good hole transport mobility and their amorphous structure can easily adapt to the n-type semiconductor surface. Hagen *et al.* used these advantages to assemble an S-DSC employing a low molecular weight hole transport material for the first time.²⁰ Unfortunately, the device displayed a low efficiency (0.2 %) because (i) the cells were prepared by evaporation of the TPD transport layer. Therefore, the pores were not entirely filled and an efficient regeneration of the oxidized dye was not possible. (ii) The high thickness

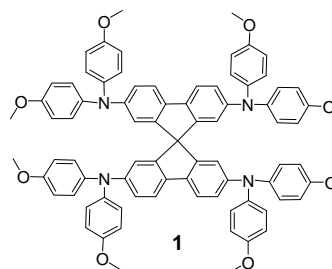


Figure 1. 2,2',7,7'-tetrakis(*N,N*-di-*p*-methoxyphenyl-amine)-9,9'-spiro-bifluorene (spiro-OMeTAD).

of the overstanding hole transport layer caused higher recombination losses due to longer trajectories between the inner surface and the counter electrode.

Grätzel and co-workers improved Hagen's concept by using the amorphous organic hole transport material 2,2',7,7'-tetrakis(*N,N*-di-*p*-methoxyphenylamine)-9,9'-spirobifluorene (spiro-OMeTAD) (Figure 1, **1**).²¹ The spiro-center improved the glass-forming properties and prevented crystallization, which would otherwise lead to a bad contact between the mesoporous surface of TiO₂ and the hole conductor. Spiro-OMeTAD in combination with different dopants such as Li[(CF₃SO₂)₂N], N(PhBr)₃SbCl₆^{21, 22} and 4-*tert*-butylpyridine²² (in the following denoted as *tBP*) is even today a popular and efficient hole transport material.

Parallel to the evolution of the concept of using low molecular weight semiconductors to overcome some of the typical drawbacks of L-DSCs, such as dye desorption/degradation, solvent evaporation and sealing issues, Cao and co-workers²³ reported about the application of a viscous polymer gel electrolyte and Yanagida and co-workers²⁴ were the first to utilize a polymer (*in situ* polymerized pyrrole) as hole transport material. The efficiency of the devices suffered from the strong absorption of the polymer in the visible region, hence impairing the light harvesting at the dye monolayer. As expected, the handling of such S-DSCs was more favourable, but the efficiency of the S-DSCs was lower than that of L-DSCs (*cf.* section 2.1.5).

In the last decade research was mainly focused on the development of more stable and high efficient dyes for L-DSCs according to Grätzel's example from 1991 and S-DSC on the basis of spiro-OMeTAD, in which the main concepts of L-DSC and S-DSC were not changed drastically. Accordingly, an introduction on the operation principle of DSCs (including materials and mechanisms) will follow. Moreover, special focus will be put on different sensitizers (metal-organic and organic) for the application in DSCs as an attractive and promising concept for solar energy conversion.

2 DYE-SENSITIZED SOLAR CELLS

The following section will give a short overview on the assembly of L-DSCs as well as S-DSCs and the different materials used for the manufacture. Furthermore, the processes and mechanisms that entail high performances and the ones which reduce the efficiency of DSCs will be outlined

and the characterisation methods will be presented. A detailed overview of DSCs regarding materials, characterisation and modules is also published recently.²⁵

2.1 Assembly and Materials

As shown in Figure 2, typical DSCs consist of an assembly of different functional layers. With regard to the slightly different demands of L-DSCs and S-DSCs, the materials, types of layers and their thicknesses vary somewhat.

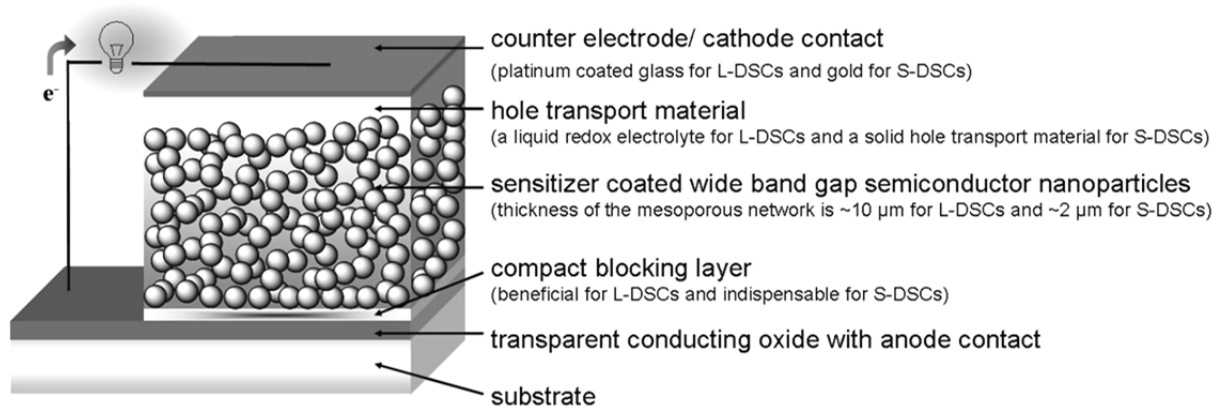


Figure 2. Schematic representation of the assembly of typical DSCs.

For both L- and S-DSCs a *substrate* (glass, a thin metal foil^{26, 27} or a flexible polymer²⁸⁻³⁰) covered by a *transparent conducting oxide* (TCO) is forming an electrode contact (anode). The next layer, which is indispensable for S-DSCs, is a thin and flat *compact blocking layer*. It prevents the holes travelling through the hole transport material (HTM) from recombination with electrons collected in the TCO layer. In contrast to that, this layer is optional for L-DSCs because the energetic conditions of the contact formed between a solid HTM and a TCO are completely different from the ones between a liquid electrolyte and a TCO. The latter causes only less recombination (*cf.* section 2.1.2). The adjacent layer – the *wide band gap semiconductor* layer – is the thickest layer in both types of DSCs (~ 10 μm for L-DSCs, ~ 2 μm for S-DSCs). It provides an extremely high surface due to its mesoporous nature and high electron conductivity due to its interconnected nanocrystalline structure. Typically, in L-DSCs, an additional mesoporous semiconductor layer is applied, the so called scattering layer. It consists of the same wide band

gap semiconductor as used for the mesoporous layer but the single particles are larger (~ 400 nm). The function of this layer is the scattering of incident photons to improve the light harvesting efficiency. Under ideal conditions, the whole semiconductor surface is covered by the most variable component of DSCs, the *sensitizer* (metal-organic, organic or inorganic quantum dots³¹⁻³⁶). It covers the surface in form of a monolayer and causes the light induced formation of an excited state, which results in charge separation at the semiconductor/dye interface, *i.e.* electron injection into the conduction band of the semiconductor and subsequent regeneration of the oxidized sensitizer by the HTM happen. The nature of the *hole transport material* characterises the most serious difference between liquid and solid-state DSCs. Regarding L-DSCs, generally an iodide/triiodide redox electrolyte dissolved in a non-protic solvent is used. It mediates the holes between the oxidized sensitizer and the counter electrode. In S-DSCs, the HTM is, as the name suggests, a solid material, *viz.* a p-type semiconductor (organic, inorganic or polymeric). However, the boundary between both DSC concepts is merging. The quasi-solidification is one approach to combine the advantages of liquid electrolytes and solid HTMs by adding a gelator to a liquid hole conductor. The last part to complete a DSC is the *counter electrode*. Its task is the reduction of the respective HTM. Under illumination, both assemblies (L- and S-DSC) can convert solar energy to electric energy which can be used to run a consumer.

The single layers of typical DSCs and their functions will be explained in detail in the next sections.

2.1.1 Transparent Conducting Oxides

The most commonly used substrate for DSCs is glass coated with TCOs,^{37, 38} such as FTO (fluorinated tin oxide, $\text{Sn}_2\text{O}_3\text{:F}$)^{38, 39} or ITO (indium tin oxide, $\text{In}_2\text{O}_3\text{:SnO}_2$);³⁸ rarely also used are ATO ($\text{SnO}_2\text{:Sb}$)⁴⁰ or AZO (ZnO:Al)⁴¹ and GZO (ZnO:Ga).³⁸ For highly efficient solar cells, the TCO has to meet some fundamental requirements, such as a high electrical conductivity, so that the efficiency of the cell is not diminished by the sheet resistance. This can be achieved by employing doped metal oxides. Furthermore, the positions of the energy levels of the TCO and the semiconductor layer in contact have to ensure that preferably all electrons are injected from the semiconductor layer into the TCO (*i.e.* the Fermi level of the TCO has to be lower than that of the semiconductor). Moreover, the TCO has to be transparent, so that as much light as possible reaches the dye monolayer. Additionally, the sheet resistance should be independent from the

temperature, because the covering semiconductor layer is commonly sintered at temperatures as high as 500 °C. ITO indeed shows the highest transparency (about 90 %⁴²) and conductivity, but at higher temperatures its resistance increases significantly and the stability decreases. Hence, FTO is usually the material of choice for DSCs mainly owing to its capability to fulfil above requirements and especially due to its temperature stability.

As substrate, glass has the advantages of long-time stability, planarity and transparency (maximum transmission 92 % which can be further enhanced²⁸). But its main drawback is its inflexibility. Especially for a commercial application of DSCs, flexible cells are advantageous due to inexpensive high throughput roll-to-roll processes, easy handling and installation. At the present stage of performance of DSCs, indoor applications in watches and calculators or outdoor DSC panels⁴³ and photovoltaic clothes⁴⁴ are interesting perspectives. For this purpose, polymer substrates covered with TCOs in particular are promising because such polymers (*e.g.* ITO-coated polyethylene terephthalate, PET)⁴⁵ can be used as flexible, thin and lightweight conducting electrodes. However, polymer substrates suffer from thermal instability, photooxidation, fatigue, insufficient barrier properties (due to permeability of moisture and oxygen) or the leaching out of plasticizers and stabilizers. Characteristically, the efficiencies of DSCs using a polymer substrate are lower than those using glass. The main reason for this can be the reduced sintering temperatures applied for the preparation of the mesoporous TiO₂ layer in order to avoid melting of the substrate. At moderate temperatures (about 150 °C) the organic additives in the semiconductor paste are not properly burned out.⁴⁶ Nevertheless, plastic-substrate DSCs have already reached an efficiency of 7.6 % by using a TiO₂-water paste and a non-thermal press method.³⁰ The results were validated by the RCPV, AIST in Japan under standard conditions (100 mW/cm², 25 °C) employing a ruthenium standard dye (**N719**, *cf.* Figure 7) and a liquid iodide/triiodide electrolyte. Some reports regarding flexible metal foils as substrates (*e.g.* Ti) have also appeared in recent years.^{26, 27} But they usually require a backside illumination due to the opaque nature of such films.

2.1.2 Compact Blocking Layer

As mentioned before, the compact electron conducting hole blocking layer is indispensable for S-DSCs but can also cause a slight improvement in the performance of L-DSCs. Each contact between the solid HTM and the TCO anode results in recombination and loss of photocurrent.

The reduction of the generated photocurrent (and voltage) leads to an extreme loss in the performance and can culminate in short-circuit of the cell. Therefore, the introduction of a compact blocking layer was put forward by Grätzel and Kavan.⁴⁷ They could enhance the current output by three to four orders of magnitude *via* suppressing this recombination in S-DSCs. For the preparation of a blocking layer, different methods can be used, such as electron beam evaporation,⁴⁸ chemical vapour deposition from precursors⁴⁹⁻⁵¹ or spray pyrolysis^{47,52} of an aerosol. The latter method was automated and investigated in detail by our group using an aerosol prepared from the common TiO₂-precursor titanium diisopropoxide bis(acetylacetonate) (TAA) in ethanol (0.2 M solution).⁵² The optimal thickness and morphology as well as the rectifying properties of this layer were scrutinized by ellipsometry, scanning electron microscopy and current/voltage measurements (*cf.* section 2.3). With increasing blocking layer thickness, the rectifying behaviour increased and hence recombination could be efficiently suppressed. The best overall performance was reached by a layer thickness of about 120-200 nm.

In contrast to S-DSCs, it is generally assumed that a blocking layer is not necessary for L-DSCs because the recombination at the TCO/redox electrolyte interface is negligible. This can be ascribed to the similarity between the Fermi level of the FTO and the redox Fermi level of the iodide/triiodide redox electrolyte.⁵³ For this reason, there is no driving forces for recombination under short-circuit conditions (*i.e.* no electric resistance encountered, voltage is zero). The situation changes under open-circuit conditions (*i.e.* infinite resistance encountered, current is zero). Typically, the Fermi level of FTO strongly rises under these conditions (by up to 0.7 eV, marginally beyond the conduction band level of TiO₂), so that a driving force for recombination at the electrolyte/FTO interface is established.⁵³ Therefore, the introduction of a blocking layer can theoretically prevent this recombination and thus enhance the suppression of leakage currents. The validity of this theory is being intensively discussed,^{53, 54} but an improvement of the open-circuit voltage was found in many cases.⁵⁵⁻⁵⁸

2.1.3 Mesoporous Metal Oxide Semiconductors

Among the diverse wide band gap semiconductors⁵⁹⁻⁶¹ such as SnO₂,^{62, 63} Nb₂O₅,⁶¹ In₂O₃,⁶¹ SrTiO₃⁶⁴ and NiO^{65, 66} or combinations of these,⁶³ titanium dioxide (TiO₂) and zinc oxide (ZnO) are the most commonly used and most intensively studied materials. Both show a good chemical stability under visible irradiation, are non-toxic as well as inexpensive, largely abundant and easy

to process. The essential requirements that an efficient mesoporous semiconductor has to fulfil are (i) a suitable conduction band energy level which facilitates the injection of electrons by a sensitizer, (ii) an interconnected nanocrystalline network of the semiconductor with efficient electron conduction, (iii) an optimum porosity for efficient pore-filling by the hole conductor and (iv) a high surface area for a high dye-uptake. Concerning nanocrystalline-TiO₂ the formation of a pure anatase phase is significant. It is reported that anatase-TiO₂ shows a higher efficiency compared to closely packed rutile-TiO₂ due to a higher surface area and faster electron transport.⁶⁷⁻⁶⁹

The mesoporous nanocrystalline semiconductor layer is commonly prepared by screen printing, doctor blading or spin coating of a suitable TiO₂-paste and a subsequent sintering step (up to 500 °C). For this purpose, nanocrystalline TiO₂-colloids are dispersed in water or alcohol, or in α -terpineol.⁷⁰ The former method can lead to aggregation, whereas the latter gives more stable and reproducible colloidal pastes. However, optimised semiconductor pastes are also commercially available.

The optimum thickness of the mesoporous layer for S-DSCs is approximately 2 μm ⁷¹, depending on the dye and the hole conductor used. This is less than the optical depth of the composite, which would be about 10 μm for 90 % absorption over a wide spectral region employing a standard ruthenium complex as sensitizer.⁷² Thus, a dye-coated 2 μm thick layer does not absorb all the incident light, a thicker layer would be favourable, but it is not possible to fill thicker layers efficiently by a solid hole transport material.⁷²⁻⁷⁴ It was reported that for thicker layers both, pore infiltration and short electron diffusion length cause the limit of about 2 μm .⁷³⁻⁷⁵ However, studies showed that the electron diffusion length is about 20 μm .⁷² Consequently, the pore infiltration causes the limit and the efficiency of S-DSCs could be significantly enhanced if an efficient pore-filling method for thicker films can be found.

Regarding L-DSCs, pore-filling is not a critical issue because the liquid redox electrolyte penetrates into even thicker mesoporous films and small pores. Thus, 10-20 μm thick films can be used. Taking the roughness factor (> 1000) into account, a mesoporous semiconductor film of 1 cm² (thickness about 10 μm) provides a surface area of 1 000 cm² for dye-sensitization.⁷⁶ This causes a light harvesting efficiency of about 100 % at the peak absorption wavelength of a standard ruthenium dye. To increase the light harvesting efficiency over a broader range of the visible region of the spectrum, an additional layer is introduced in L-DSCs, viz. the scattering

layer. It contains larger particles (400 nm), which cause a (back-)scattering of not absorbed light to enhance the absorption and thus the performance of the cell.

Instead of the conventional mesoporous metal oxides, also specific nanostructured semiconductor vertical arrays (usually as well consisting of TiO_2 or ZnO) can be used as electrodes for DSCs.^{59, 77, 78} Transition metal oxide nanostructure assemblies, such as nanotubes, nanowires and nanorods, which do not only feature a large surface, but also an aligned nature are supposed to direct charge transfer along the length of the vertically oriented tubes/rods/wires etc. straight to the conducting substrate.⁷⁹ This can be beneficial for the charge-collection efficiency.⁸⁰

2.1.4 Sensitizer – Requirements and Strategies

The sensitizer is an essential component of DSCs; it is continually excited by the incident light, injects an excited electron into the conduction band of a semiconductor and is subsequently regenerated by the hole transport material. Thus, it acts like an electron pump for the conversion of solar energy to electricity. Ideal sensitizers for DSCs should carry appropriate anchoring groups⁶⁹ (prevalently carboxylic acids, less frequently phosphonic acid,⁸¹ acetylacetonate,⁸² catechol,⁸³ silanol^{84, 85} or silyl⁸⁶ groups) to chemisorb on the semiconductor's surface and thus guarantee an excellent connection between dye and semiconductor. For sensitizers employed in L-DSC, desorption from the semiconductor surface is always a problem, thus sensitizers should additionally show a high stability towards water-induced desorption.⁸⁷ Ideal sensitizer must show excellent light harvesting properties including high extinction coefficients and a broad absorption area. This is especially important for S-DSCs because the cells are thinner ($\sim 2 \mu\text{m}$ compared to $\sim 10 \mu\text{m}$ for L-DSCs) and so an increase in the absorption coefficient or absorption cross section results in improved light harvesting which improves the performance of devices significantly. The molecular design of sensitizers should be so chosen that aggregation of dye molecules is suppressed, and consequently minimizing the loss through the associated deactivation of excited states. The LUMO level has to be sufficiently high enough for charge injection into the conduction band of the semiconductor and the HOMO level has to be sufficiently low enough for efficient regeneration of the oxidized dye by a liquid electrolyte or a solid hole transport material. By using the latter, the charge transfer rate of the dye regeneration depends strongly on the HOMO energy offset between the dye and the solid HTM. For instance, on the basis of the Marcus theory, an optimum energy offset at an energy gap of

0.79 eV was reported for a particular set of dyes and a series of hole conductors.⁶⁷ Further, it was reported,⁸⁸ that interfacial charge transfer process like this one are not kinetically controlled but thermodynamically and that the band gap must be at least 0.2 eV for a charge transfer yield of 85 %. Additionally, a polarity match between the dye and the solid HTM is favourable to facilitate a good electronic communication between both. Another requirement for sensitizers in both types of DSCs refers the electron injection into the conduction band of the semiconductor which has to be faster than the decay of excited state. Otherwise the absorbed photons are lost without current generation. Moreover, sensitizers should be stable for about 10^8 turnover cycles corresponding to 20 years under load.⁸⁹ Finally, the periphery of the dye should be hydrophobic to minimize direct contact between the electrolyte and the semiconductor surface, to prevent water-induced desorption and to increase the wettability with the solid HTM.^{87, 90}

Different strategies were developed to obtain new, efficient and stable sensitizers. Both metal-organic and organic dyes with suitable photophysical and electrochemical properties as well as a directed orientation and arrangement of the chemisorbed dye molecules were investigated and also summarized in elaborated reviews.⁹⁰⁻⁹² In the following, the diverse synthetic strategies for a suitable dye design will be briefly summarized. A detailed discussion of each class of dyes will be given in section 3 and 4.

Variation of ligands in ruthenium dyes: Already, at the beginning of the search for suitable sensitizers for the development of dye-sensitized semiconductor electrodes in the 1980s, ruthenium complexes attracted scientist's attention. The prototype used at this time was tris(2,2'-bipyridyl-4,4'-dicarboxylic acid)ruthenium(II).⁹³ The class of tris(bipyridyl)Ru(II) complexes remained attractive due to a unique combination of chemical stability, metal-to-ligand charge transfer (MLCT), suitable redox properties and long excited state lifetimes.⁹⁴ Thus, these dyes were further investigated for the use as sensitizer in DSCs, but they suffer from low extinction coefficients in the visible range (if no additional donor group is attached) and possess a less broad absorption range.⁹⁵ Therefore, one bipyridyl ligand was replaced by two NCS groups to shift the MLCT absorption band to longer wavelength regions.¹⁶ Additionally, the geometry of the two ligands is an important factor which has to be taken into account because *trans*-complexes typically show a broader absorption up to higher wavelengths (lower energies).⁹⁶ Also the use of terpyridyl ligands instead of bipyridyl can enhance the performance L-DSCs dramatically by the broadening of the absorption area (*cf.* "**black dye**", Figure 7 yielding over 10 % power conversion efficiency).⁹⁷

Introduction of hydrophobic chains: The attachment of hydrophobic chains to a bipyridyl ligand in ruthenium(II)bis(bipyridyl)(NCS)₂ complexes can improve the performance and stability of L-DSCs. The hydrophobic layer that can be formed between the semiconductor surface and the liquid hole transport material created by the long hydrophobic chains of the dye is attributed to minimize recombination between electrons from the semiconductor and holes from the electrolyte.⁹⁸ Besides, the hydrophobic layer may enhance the stability towards water-induced desorption, hence increasing the long term stability.⁸⁷ Regarding S-DSCs, ruthenium dyes carrying hydrophobic chains yielded very high efficiencies of ~ 4 %.⁷¹ Here, the long hydrophobic chains were expected to improve interfacial properties, viz. the wetting of the dye covered semiconductor and the solid HTM due to a polarity matching. This can accelerate the regeneration of oxidized dye molecules.^{90, 99} (For further information on amphiphilic dyes employed as sensitizers in DSCs cf. section 3.1.2)

Incorporation of donor-antenna groups: In a nutshell, the goal of the donor-antenna dye concept is the enhancement of the absorbance of ruthenium(II)bis(bipyridyl)(NCS)₂ by covalently connecting electron-rich donor moieties (e.g. triphenylamine groups) to a bipyridyl ligand. In comparison, extremely high molar extinction coefficients can be reached due to the extended π -electron delocalized system. This improves the light harvesting efficiency and thus the performance of DSCs. Furthermore, the push pull system created by the donor and the acceptor/anchor parts of the dye results in a longer distance between the HOMO (located on the donor) and LUMO (located on the anchoring group), is assumed to slow down recombination.¹⁰⁰⁻¹⁰² Additionally, the donor groups can improve the wetting with the solid hole conductor spiro-OMeTAD via a polarity matching. (This concept will be discussed in detail and the dyes which meet the demands of the concept will be presented in section 3.1.3.)

Introduction of ion-coordinating groups: The concept of incorporating ion-coordinating moieties in ruthenium(II)bis(bipyridyl)(NCS)₂ complexes is a design strategy which was developed for DSCs using the “magic salt” (Lithium bis(trifluoromethanesulfonyl)imide, LiN(SO₂CF₃)₂) or other Li⁺-salts as additives in the HTM. This sophisticated approach is based on the interaction of ion-coordinating functionalities and Li⁺ ions. Its aim is to fix the Li⁺-ions at the dye/TiO₂ interface, thus preventing them from reaching the TiO₂ surface and avoiding an unfavourable lowering of the TiO₂ conduction band edge (which equals a lowering of the open-circuit voltage) while enhancing the photocurrent output. (The different effects on DSCs will be discussed in section 3.1.5)

Donor- π Bridge-Acceptor structure for organic dyes: In the last years it was shown that organic dyes can act as efficient sensitizers and their absorbance and absorption range can be tuned by varying the chemical structure.^{90, 92} Donor- π bridge-acceptor sensitizers incorporate an electron-rich donor moiety as well as an electron-deficient acceptor group covalently connected by a π -conjugate bridge. After excitation of these dyes intramolecular charge transfer happens in such a way that electrons are efficiently transferred from the donor unit to the anchoring acceptor moiety from where the electrons can be easily injected into the semiconductor. This causes a large distance between holes (delocalized mainly over the donor unit) and injected electrons and thus recombination can be reduced. In addition, the energy gap and consequently the maximum absorption wavelength can be easily tuned by changing the electron-donating and electron-accepting abilities, *viz.* changing the donor and acceptor groups. Regrettably, donor- π bridge-acceptor sensitizers frequently suffer from aggregation which reduces the performance of DSCs. (The different organic dyes on the basis of this concept will be presented in section 4)

Suppression of aggregation: Aggregation on the semiconductor surface is in all classes of sensitizers (metal-organic and organic) a critical issue. If aggregation occurs, excited states can be deactivated by intermolecular energy transfer between the dyes. Thus the performance of the solar cell can decrease. Furthermore, aggregation can induce a shift in the energy level of the dye, which can be seen in a shift of the absorption. The changed electronic properties can affect electron injection efficiency and thus the energy conversion efficiency of the cell. To solve these problems, bulky groups (*e.g.* *tert*-butyl groups) can be attached to the dye molecules to prevent aggregation, or co-adsorbents can be used which also reduces the interaction between dye molecules.

Influence of the dipole moment: Organic dyes are capable of yielding higher voltages in DSCs than ruthenium complexes if their dipole moment on the semiconductor surface is suitably directed. A fluorene containing dye (**82**, Figure 37) for example reached an impressive voltage of 1 V in an S-DSC assembly.¹⁰³ This can be ascribed to the dipole moment of the dye which improves the rectifying behaviour if the dipole points away from the TiO₂ surface.⁹⁹ Investigations on benzoic acids having different dipole moments showed, that a suitable dipole moment has a positive effect on the work function of TiO₂ and the energy across the TiO₂/dye/HTM interface.¹⁰⁴

2.1.5 Hole Transport Materials

The tasks to be fulfilled by the HTM are (i) efficient and fast dye regeneration, (ii) transport of holes to the counter electrode and (iii) charge extraction at the cathode. HTMs for dye-sensitized solar cells can be roughly divided into two classes; viz. redox couple based HTMs (for L-DSCs) and solid HTMs (for S-DSCs).

The electrolyte medium for L-DSCs in which the redox couple is dissolved can be a volatile polar solvent (*e.g.* acetonitrile/valeronitrile) or a low volatile one (*e.g.* 3-methoxypropionitrile), an ionic liquid¹⁰⁵ or a gel.¹⁰⁶ The most frequently used electrolyte for L-DSCs consists of an organic solvent, a redox couple and additives. Commonly, the organic solvent electrolytes are nitriles such as acetonitrile, valeronitrile, 3-methoxypropionitrile or esters such as ethylene carbonate, propylene carbonate and γ -butyrolactone. These are highly polar, dissolve the redox couple and facilitate fast charge carrier transport by the redox couple.¹⁰⁷ The major redox couple is the iodide/triiodide couple. Its performance is unsurpassed by other redox couples such as $\text{Br}^-/\text{Br}_3^-$,^{107, 108} $\text{SCN}^-/(\text{SCN})_2$,^{109, 110} $\text{SeCN}^-/(\text{SeCN})_2$,^{109, 110} or $\text{Ni(III)/(IV) bis(dicarbollide)}$.¹¹¹ The counter ions used for the redox couple also influence the performance of solar cells because of their different ion conductivities in the electrolyte and because of the fact that these ions can adsorb on the semiconductor surface. This can induce a shift of the conduction band and hence a change in the open-circuit voltage. Alkyl imidazolium cations for example can adsorb on the TiO_2 surface, charge it positively and can form an additional blocking layer which prevents triiodide ions from reaching the TiO_2 surface and recombining there.¹¹² For a further improvement of the cell performance, additives can be used such as 4-*tert*-butylpyridine (tBP),¹¹³ guanidinium-derivatives¹¹⁴ and chenodeoxycholic acid (CDCA)¹¹⁵ which can cause an increase in the open-circuit voltage, reduce recombination, enhance the long term stability, or suppress dye aggregation. Thus the compositions as well as the mass fractions of the liquid electrolyte ensemble have to be optimized for each sensitizer to reach high efficiencies.

Since the diffusion of ions determines the charge transport in redox electrolytes, usually less dense viscous solvents are used to promote the ionic transport. Thus organic solvents employed in the electrolyte cell often are volatile and therefore the long term stability of L-DSCs is essentially inhibited because of the drying up of the solvents. Ionic liquids can replace organic solvent electrolytes. This implicates advantages which arise from the negligible vapour pressure of ionic liquids, their high electric conductivity supplemented by low-flammability and a very wide electrochemical stability window. Regrettably, the viscosity of ionic liquids is much higher

compared to standard organic solvents which reduces the short-circuit current drastically due to the limited mass transport. Recently, it was reported that it is possible to reach competitive efficiencies (about 7.6 %^{116, 117} and 8.5 %¹¹⁸) by ionic liquids with an optimized composition. Hence it seems to be possible to overcome the characteristic drawbacks of L-DSCs such as solvent leakage and evaporation of the solvent by the use of an appropriate ionic liquid electrolyte while preserving high efficiencies. But still corrosion caused by the aggressive nature of the iodide/triiodide redox couple can limit the long term stability of L-DSCs.¹¹⁹

Sealing is procedure which is applied for L-DSCs on the basis of volatile/low volatile electrolyte to prevent leakage of the electrolyte and evaporation of the solvent. This is still the most critical issue of L-DSCs which constrains the commercialization because of less long term stability. For L-DSCs prepared in laboratory scale, the dye-sensitized semiconductor electrode and the counter electrode were assembled into a sealed sandwich-type cell by heating a Surlyn® (DuPont™) film which simultaneously acts as a spacer between the electrodes. Surlyn® is a commercial thermoplastic ionomer resin consisting of the random copolymer poly(ethylene-co-methacrylic acid). After the introduction of the electrolyte through a drilled hole in the counter electrode, the latter is sealed using a Bynel® film (DuPont™) and a thin cover glass.⁷⁶

It is advantageous to replace liquid electrolytes by non-corrosive solid electronic transport materials, such as low molecular weight organic hole conductors, organic polymers and inorganic p-conductors. In contrast to liquid transport materials, where the infiltration of the mesoporous structure of the semiconductor is easily achieved, pore-filling is a critical issue for S-DSCs. An ideal solid hole conductor has to fulfil the following key requirements: (i) excellent pore-filling properties, (ii) capability of getting deposited at temperatures < 100 °C to avoid degradation the dye, (iii) absence of the tendency to be highly crystalline, (iv) good film forming capacity, (v) high hole transport mobility to guarantee fast dye regeneration and to suppress recombination, (vi) transparency in the region of the visible light to guarantee that the incident light reaches the sensitizer, (vii) photochemical stability and (viii) the HOMO energy level should be higher than the HOMO level of the respective dye for an efficient hole transfer.^{67, 88} Among the solid hole transport materials, the most established one *viz.* spiro-OMeTAD (Figure 1) (plus additives like *t*BP and LiN(SO₂CF₃)₂),^{21, 73, 120} belongs to the class of low molecular weight triphenylamine hole conductors. It shows moderate charge carrier mobility in the order of 10⁻⁴ cm²/Vs for spiro-OMeTAD⁷³ which can be enhanced by adding the “magic-salt”

$\text{LiN}(\text{SO}_2\text{CF}_3)_2$.⁷² Its good infiltration property has been shown to lead to a higher filling fraction of the pores of the semiconductor than with other hole transport materials.⁷³

So far, S-DSCs employing this material led to impressive efficiencies of 4.5 %, ^{121, 122} 4.6 %, ¹²³ 4.7 %¹²⁴ and 5.0 %¹²⁵ (measured at 100 mW/cm²). However, this is just nearly half of the record efficiency of L-DSCs (11.5 %¹²⁴, 100 mW/cm²). The intrinsically lower efficiency of S-DSCs compared to L-DSCs can be ascribed to (i) the lower hole transport mobility of organic semiconductors, (ii) high recombination between TiO_2 and the HTM, (iii) a bad electrochemical contact between dye and HTM and (vi) less efficient pore-filling and hence the use of thinner mesoporous layers which causes less light harvesting.⁶⁷

Polymers have a very high potential for the use as HTM in S-DSCs due to their good film forming properties and amorphous or partially crystalline nature.¹²⁶⁻¹²⁹ But for the pore-filling, novel concepts and strategies should be developed. From a technological standpoint, a polymer semiconductor nanocomposite solar cell prepared at low temperatures on a flexible substrate has all the potentials to compete with other flexible types of solar cells.

2.1.6 Counter Electrodes

At the counter electrode (cathode), the hole transport material is reduced. To do so, usually platinum coated glass is employed in L-DSCs. However, corrosion is the one main problem in L-DSCs.¹¹⁹ Metals such as platinum, copper, aluminium, or zinc which show enough electro catalytic activity to mediate the electron exchange suffer from corrosion. This influences the long term stability negatively. Therefore, novel approaches were developed to facilitate electron exchange and simultaneously corrosion stability. Recently, graphite¹³⁰ and carbon materials (carbon black,¹³¹ activated carbon¹³⁰ and carbon nanotubes¹³²) were reported. These materials are favourable due to low costs of the starting material, the possibility of roll-to-roll processing and their stability towards corrosion.

The top-contact of S-DSCs typically composes of gold due to its large work function. However, also silver is reported to be employed as counter electrode. In a direct comparison to gold contacts, silver can enhance the photocurrent without changing the other cell parameters. The reason for this observation is the reflection capability. The reflectivity for Au is 56 % whereas

that for Ag is 96 % (at 510 nm). Thus, less light is dissipated into the metal and more is guided back to the sensitizer enhancing the optical path length of the cell.¹²¹

2.2 Mechanisms

The following section will focus on the key processes of charge generation and transport in liquid and solid-state dye-sensitized solar cells as well as on the recombination process and the associated mechanisms.

2.2.1 Key Processes

The light induced processes as well as the energetic conditions of DSCs are depicted in the following figure:

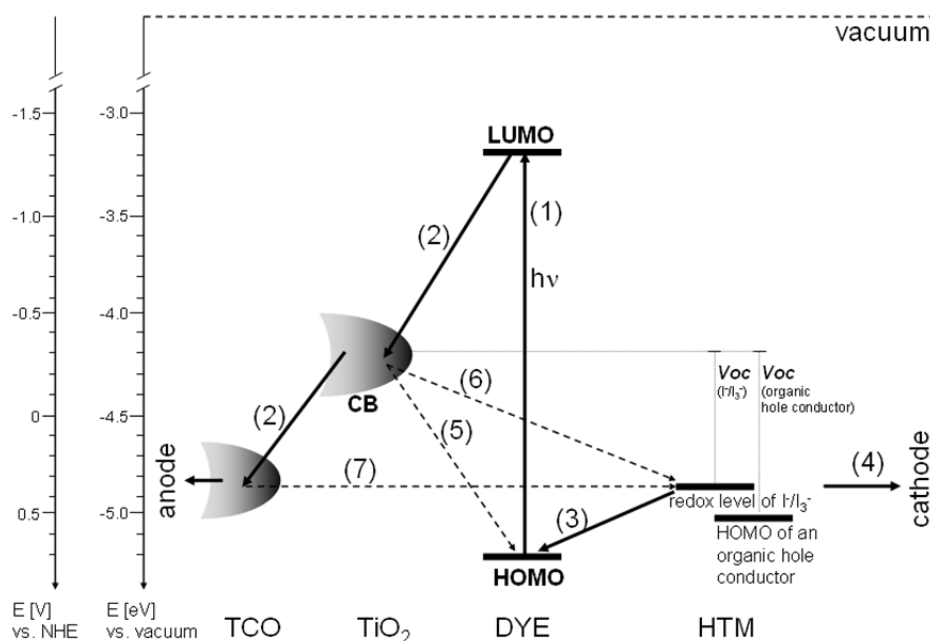


Figure 3. Schematic energy diagram for DSCs including the electronic processes that support the current and voltage generation (solid arrows) as well as the ones which reduce the solar cell performance (dashed arrows). (1) Excitation of the dye by absorption, (2) electron injection and conduction to the anode, (3) regeneration of the oxidized dye by the dissolved I[•]/I₃⁻ redox couple or a solid hole transport material whereas the energy level of the solid HTM is supposed to be lower, (4) hole transport to the cathode by diffusion controlled ionic conduction or polaron hopping for liquid and solid HTMs, respectively. (5) Recombination between electrons in the TiO₂ and the oxidized dye, (6) recombination between electrons in the TiO₂ and holes of the HTM (liquid/solid), (7) recombination between electrons in the TCO and holes of the HTM (liquid/solid). Note that the plotted energy levels are no absolute values. For instance, the energy level of the TiO₂ conduction band can shift appreciably with the media and additives.^{133, 134} (+cf. section 3.1.5) Furthermore, the I[•]/I₃⁻ system shows not just one redox level, rather different unstable radicals associated with a variety of different redox levels.¹¹⁹ Moreover, the Fermi level of the FTO coated substrate can shift (by about 0.7 eV) upon illumination under open-circuit conditions.⁵³

Under the influence of electromagnetic irradiation, the chemisorbed dye is excited ($D + h\nu \rightarrow D^*$) and forms an electron-hole pair. At the interface between dye and semiconductor, the excited electron is injected from the LUMO of the dye into the conduction band of the semiconductor. This process is extremely fast, it occurs in the femto- to picosecond time scale for both DSC types.^{72, 89, 135} Although, the mechanism for electron transport of injected charge carriers in mesoporous semiconductors is still under discussion, there is almost consensus that the electron lifetime in the mesoporous semiconductor network is limited.⁷² It can be calculated by the following equation:

$$L_D = \sqrt{D_e \cdot \tau_e} \quad (1)$$

L_D	electron diffusion length
D_e	electron diffusion coefficient
τ_e	electron lifetime

Under consideration that the electron lifetime as well as the electron diffusion coefficient depend on the light intensity, the electron diffusion length is in the range of 10-20 μm .⁸⁹ This limits the thickness of the mesoporous layer.

After the electron transfer from the dye to TiO_2 , the dye has to be regenerated as fast as possible by a liquid electrolyte or by a solid HTM. This process takes place within nanoseconds.^{72,89} For liquid electrolyte DSCs, iodide regenerates the oxidized dye (D^+) by reduction. In doing so, it is oxidized to triiodide (*i.e.* $2 D^+ + 3 I^- \rightarrow 2 D + I_3^-$). In comparison to that, a solid hole transport material regenerates the oxidized dye by injecting an electron from its HOMO level to the vacancy in the HOMO of the dye. Therefore, as it was explained before, it is important that the HOMO level of the HTM lies higher than the one of the dye to create an energetic drifting force for the regeneration.^{67, 88}

Depending on the type of HTM (liquid or solid), the transport of holes proceeds according to different mechanisms. In L-DSCs, the hole transport occurs *via* diffusion controlled ionic conduction whereas it occurs *via* a polaron hopping⁷² process for solid HTMs like spiro-OMeTAD. Ionic conductance in general is determined by speed and medium dependent friction. The rate of diffusion is dependent on the solvent, the radius of the ion, the field intensity, the pressure and the temperature.¹³⁶ Ion diffusion in L-DSCs is a fast and efficient way of charge transport. The charge transport in S-DSCs employing spiro-OMeTAD *via* polaron hopping depends on the hole transport mobility. The latter is quite low in pristine spiro-OMeTAD ($\sim 10^{-4} \text{ cm}^2 \text{ V}^{-1} \text{ s}^{-1}$),¹³⁷

but can be enhanced by adding $\text{LiN}(\text{SO}_2\text{CF}_3)_2$ (to $\sim 10^{-3} \text{ cm}^2 \text{ V}^{-1} \text{ s}^{-1}$).⁷² It was reported, that the hole mobility after addition of the Li-salt even exceeded the mobility of TiO_2 .¹³⁸ Consequently, the hole transport is not limiting the efficiency of S-DSC, but the poor pore infiltration by the HTM and recombination processes.

2.2.2 Recombination Processes

The possible channels of recombination in DSCs are (i) between electrons in the TiO_2 and the oxidized dye, (ii) between electrons in the TiO_2 and holes in the HTM, (iii) between electrons in the TCO and holes of the HTM (shown as processes 5, 6, 7 in Figure 3).

Recombination between electrons in the TiO_2 and the oxidized dye is a more important loss mechanism for L-DSCs than for S-DSCs. Under standard conditions, about 10-15 % of the oxidized dyes are lost by recombination before regeneration by the liquid electrolyte.¹³⁹ The regeneration of the oxidized dye by the HTM is characteristically faster in S-DSCs than in L-DSCs (regeneration rate for L-DSCs in microsecond time scale, for S-DSCs in nanosecond range).⁷² Hence, the recombination with the oxidized dye is slow in S-DSCs.¹³⁹

Recombination between electrons in the TiO_2 and holes in the HTM is less significant in L-DSCs. In general, if the oxidized dye is regenerated, the recombination is slow for L-DSCs. The reason for that is the formation of intermediate radical species $\text{I}_2^{\cdot-}$, which cannot recombine directly with injected electrons. It has to find an additional $\text{I}_2^{\cdot-}$ to generate I_3^- and I^- to facilitate recombination.¹⁴⁰ In contrast to that, this kind of recombination is a one-step process in S-DSCs which can occur much more easily. Hence the recombination rate is higher. It was reported that this recombination can be greatly reduced with a suitable dye design, *viz.* ion-coordinating ruthenium dyes.¹³⁹

Recombination between electrons in the TCO and holes of the HTM is negligible for L-DSCs under short-circuit conditions, but becomes relevant under open-circuit condition.⁵³ In contrast to that, for S-DSCs this is the most significant recombination channel which can completely annihilate the current generation of the solar cell. Fortunately, it is quite easy to prevent this recombination absolutely by the incorporation of an electron conducting hole blocking layer (*cf.* section 2.1.2).

2.3 Characterization by Current/Voltage-Curves

The most significant characteristic of solar cells is the current/voltage curve (I/V curve). The dependence of I vs. V under illumination as well as under dark conditions are measured. While doing so, an increasing variable counter bias is applied to the cell and the respective current is detected to plot the current density against the applied voltage:

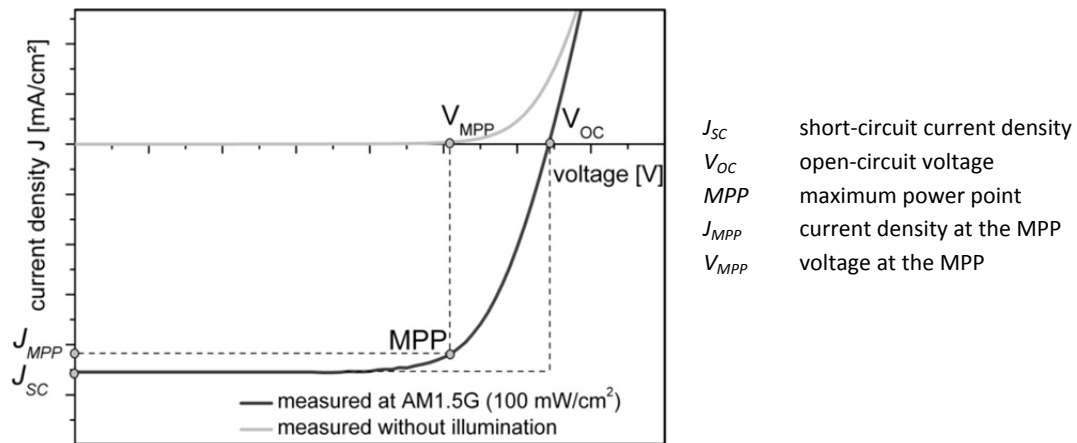


Figure 4. Typical I/V-curve under dark conditions and illumination including the characteristic parameters.

Under dark conditions the photocurrent should be zero, thus no current should be measured until the applied counter bias is larger than a threshold voltage, which is equal to the photovoltage generated by the solar cell under illumination. Then the applied electron pressure overcomes the energetic barrier of the cell and starts to inject heavily (the current rises extremely at further forward bias).

Under illumination and short-circuit conditions (*viz.* no electric resistance encountered, voltage is zero) the maximum generated photocurrent flows and the short-circuit current I_{SC} can be measured. Taking the cell area into account, the short-circuit current density J_{SC} can be determined. The photocurrent stays constant with increasing applied bias until the photogenerated current is balanced to zero by the counter voltage. Under these open-circuit conditions (*viz.* infinite resistance encountered, current flow is zero) the open-circuit voltage V_{OC} can be read off. From the shape of the I/V-curve under illumination, the maximum power point (*MPP*), the point at which the product of current and voltage is maximal, can be determined as well as the associated current density (J_{MPP}) and voltage (V_{MPP}). With these specifications the solar energy-to-electricity conversion efficiency of a solar cell can be calculated.

$$\eta = \frac{P_{MPP}}{P_{in}} = \frac{J_{SC} \cdot V_{OC} \cdot FF}{P_{in}} \quad (2)$$

$$FF = \frac{J_{MPP} \cdot V_{MPP}}{J_{SC} \cdot V_{OC}} \cdot 100 \quad (3)$$

η	solar energy-to-electricity conversion efficiency (expressed as percentage)
P_{MPP}	power density at the maximum power point [W/cm ²]
P_{in}	incident light power density [W/cm ²]
J_{SC}	short-circuit current density [mA/cm ²]
I_{SC}	short-circuit current [mA]
V_{OC}	open-circuit voltage [V]
FF	fill factor (expressed as percentage)
J_{MPP}	current density at the maximum power point [mA/cm ²]
V_{MPP}	voltage at the maximum power point [V]

To improve the accuracy, validity, reliability and reproducibility of reported power conversion efficiencies for solar cells, a universal specification standard was set.¹⁴¹ According to that, solar cell testing has to be accomplished under an Air Mass 1.5 Global (AM 1.5 G¹⁴²) solar spectrum for which the spectral intensity distribution equals that of the sun on the earth's surface at an incident angle of 48.2° including both direct and diffuse irradiation. The power of the lamp should be 100 mW/cm² (1 sun). Furthermore, a suitable mask has to be used during the measurement to ensure that light incidents only on the reported area.^{141, 143}

2.4 Characterization by IPCE Measurements

The incident photon-to-current conversion efficiency (IPCE) is defined as the number of electrons delivered to the external circuit divided by the number of incident photons. It can be calculated for each wavelength by the following equation:

$$\begin{aligned} IPCE &= \frac{h \cdot c}{e} \cdot \frac{J_{\lambda}}{\lambda \cdot P_{\lambda}} \cdot 100 \\ &= 1240 \cdot \frac{J_{\lambda}}{\lambda \cdot P_{\lambda}} \cdot 100 \end{aligned} \quad (4)$$

$IPCE$	incident photon-to-current conversion efficiency (expressed as percentage)
h	Planck constant [C V s]
c	light velocity [nm/s]
J_{λ}	short-circuit current density at λ [mA/cm ²]
e	elementary charge [C]
λ	wavelength [nm]
P_{λ}	power density of monochromatic light at λ [mW/cm ²]
1240	condensed coefficient [V nm]

When a photon is absorbed by the sensitizer, an electron-hole pair is generated, which can either contribute to the photocurrent produced by the cell, or can be annihilated through recombination. In the latter case, the absorbed photon is lost without contributing to the current production. The IPCE curve, *i.e.* the wavelength-dependent spectral response of the photocurrent, illustrates how efficient photons are converted into current by the sensitizer at each wavelength. Thus, it is not surprising that the IPCE curve (also called action spectrum) and the absorption of the sensitizer chemisorbed on the semiconductor fit together very well if the absorbed photons contribute towards photocurrent. If the optical depth of the solar cell is high enough (caused by high molar extinction of the sensitizer or by a large thickness of the cell) and the data are corrected for reflection and absorption loss by the substrate, the IPCE can be close to 100 % over a broad range of the absorption area of the dye.

3 METAL-ORGANIC SENSITIZERS IN DYE-SENSITIZED SOLAR CELLS

In the following, focus will be on metal-organic dyes used as sensitizers in DSCs. The sensitizers, which serve as solar energy absorbers and electron pumps, decide the light harvesting properties as well as the overall performance of DSCs significantly. Thus, a lot of research effort has been done on the design, synthesis and characterisation of novel sensitizers. For example, systematic studies on the effect of different metals, suitable ligands and different substituent groups have been carried out. These efforts resulted in the development of various mononuclear and polynuclear dyes based on transition metals, such as Ru^{II},⁹¹ Os^{II},^{144, 145} Pt^{II},^{146, 147} Re^I,⁹¹ Ir^{III},¹⁴⁸ Cu^I,¹⁴⁹ Zn^{II},^{92, 150, 151} and Fe^{II}.¹⁵² Transition metal ions are used as central atoms in dyes such as polypyridyl ruthenium complexes, porphyrins and phthalocyanines. These three classes are the most promising and most intensively investigated ones among the metal-organic sensitizers. Hereafter, they will be discussed in detail, *viz.* their general properties, design concepts and strategies as well as selected examples, proving the capability of such dyes in their function as sensitizers in DSCs will be given.

3.1 Ruthenium Dyes

Most of the ruthenium complex sensitizers have the general structure RuLL'(X)₂ (Figure 5). Here, L stands for the anchoring ligand (typically 2,2'-bipyridyl-4,4'-dicarboxylic acid) and L' for the

ancillary ligand (which commonly is a bipyridyl ligand substituted by simple carboxylic acid, amphiphilic, donor or ion-coordinating groups or combinations of these). X represents a monodentate ligand (halogen or pseudohalogen, most frequently isothiocyanate).¹⁶

The ruthenium(II) transition metal center ion is in principle capable of forming numerous homo- or heteroleptic complexes with various ligands such as bipyridine-derivatives, 2,2':6',2''-terpyridines, NCS⁻, NH₃, CO, CN⁻, H₂O etc., leading to a variety of different mono- or polynuclear¹⁵³⁻¹⁵⁵

complexes. Generally, ruthenium in the oxidation state +2 (d^6) is octahedrally surrounded by ligands and the complexes are diamagnetic due to the low-spin configuration t_{2g}^6 . Influenced by the Coulomb-repulsion in the presence of a symmetrical octahedral ligand field, the five d-orbitals of ruthenium are split into three energetically lower (t_{2g}) and two higher (e_g) orbitals. (In deformed octahedrons an additional splitting occurs, cf. Jahn-Teller effect.) The energetic distance between the t_{2g} - and e_g -orbitals is determined by the crystal field strength Δ_0 .

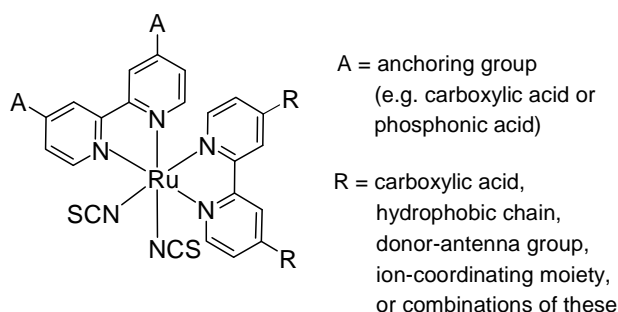


Figure 5. General structure of polypyridyl Ru(II) sensitizers.

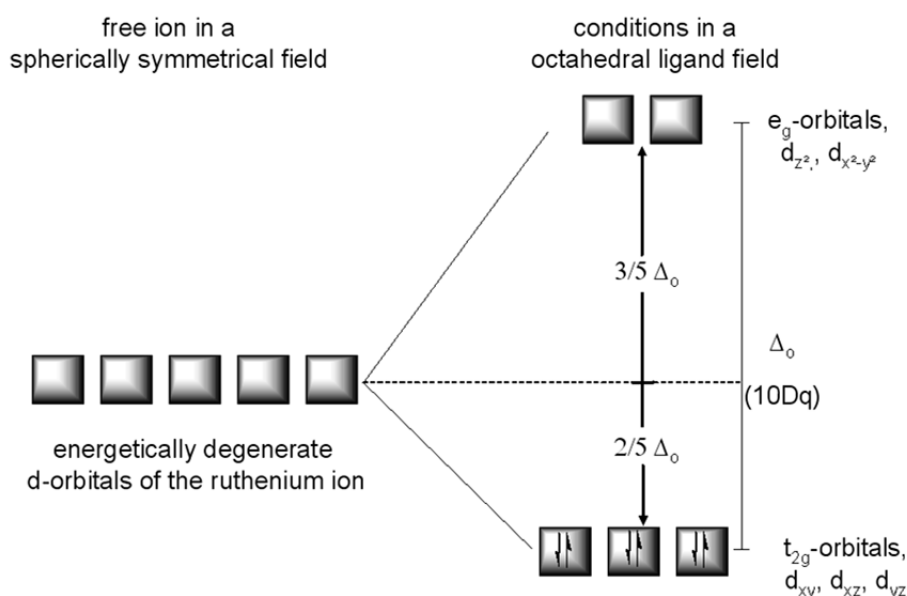


Figure 6. Schematic representation of the energetically degenerate d-orbitals of a free Ru^{2+} ion and the splitting of the energy levels due to the perturbation by a symmetrical octahedral ligand field. (Δ_0 : crystal field strength) Here, the low-spin configuration of Ru^{2+} (t_{2g}^6) is depicted, which is created by the influence of strong ligands such as bipyridines.

When a transition metal like ruthenium(II) has 4 to 7 electrons in the d-orbitals and tends to form octahedral complexes, two different electron distributions can be generated. If weak ligands, which cause only a weak splitting (small Δ_o), are coordinated to the transition metal center, the *high-spin configuration* occurs. Here, according to Hund's rules, the distribution with the highest number of unpaired electrons is generated. In contrast to that, the *low-spin configuration* (where the number of unpaired electrons is minimal) is generated, if a strong ligand, which causes a large splitting (large Δ_o), is coordinated to the center ion. The strength of the respective ligand can be derived from the so called spectrochemical series. Roughly said, π -acceptors (e.g. bipyridines) cause a large splitting and π -donors (e.g. I^- , Br^- , SCN^-) cause a weak splitting. Consequently, for typical Ru(II) complexes incorporating bipyridines, the electrons of Ru(II) are filled into the low energetic t_{2g} orbitals resulting in low-spin complexes. Due to the fact that the e_g -orbitals, which are antibonding regarding the metal-ligand bonds, are not filled, the bond between ligands and central ion is very strong. Hence, these complexes are chemically very stable and the ligands do not show any tendency towards dissociation even at elevated temperatures.

Besides the crystal field splitting arising from Coulomb-repulsion, there is another contribution influencing the orbitals in complexes, viz. the hybridization between orbitals of the transition metal ion and the orbitals of the ligand. Polypyridine ligands possess σ -donor orbitals localized on the nitrogen atom as well as π -donor and π^* -acceptor orbitals more or less delocalized on the aromatic rings.⁹⁴ By hybridization, a mixing of the metal associated and ligand associated orbitals occurs and the metal orbitals are split further. Then, the promotion of an electron from a π_{Metal} -orbital (which is mainly localized on the metal) to the π^*_{Ligand} -orbital (which is mainly located on the ligand) gives rise to metal-to-ligand charge transfer (MLCT) excited states, whereas promotion of an electron from π_{Metal} to σ^*_{Metal} gives rise to metal centered (MC) excited state. Ligand centred (LC) excited states can be obtained by promoting an electron from π_{Ligand} to π^*_{Ligand} .⁹⁴ Due to the MLCT absorption in the longer wavelength range in combination with MC and LC absorption bands, these complexes are capable to absorb over a wide range of the visible spectrum, but suffer usually from low extinction coefficients.

Moreover, if the complexes are applied as sensitizers in DSCs, they facilitate fast injection because of the fact that the absorption of photons places the excited electron on the anchoring ligand(s). The positive charge (hole) is thereby distributed over the metal and also to some extent over the NCS group causing a spatial separation between injected electrons and holes,

thus retarding the rate of recombination.^{156, 157} Furthermore, ruthenium(II) complexes show favourable photochemical, photophysical and electrochemical properties.⁹⁴

The best photovoltaic performances in terms of conversion yield and long-term stability for L-DSCs and S-DSCs on the basis of spiro-OMeTAD have so far been achieved with polypyridyl ruthenium(II) complexes, although organic dyes started to catch up especially for S-DSCs. Due to the overwhelming number of efficient ruthenium sensitizers, they are in the following classified according to their functional groups attached to the ancillary ligand. The design concepts and selected examples are presented and the performances of the different complexes in DSCs are summarized in tables at the end of each section.

3.1.1 Unfunctionalized Ruthenium Dyes

The class of unfunctionalized ruthenium dyes is limited to different protonation degrees of $\text{Ru}(2,2'\text{-bipyridyl-4,4'-dicarboxylic acid})_2(\text{NCS})_2$ denoted as **N3** and $\text{Ru}(4,4',4''\text{-tricarboxy-2,2':6',2''-terpyridine})(\text{NCS})_3$ denoted as **black dye** (Figure 7 structures 2-5). These sensitizers do not carry any functional groups, but just carboxylic acid/carboxylate groups attached to each pyridine moiety.

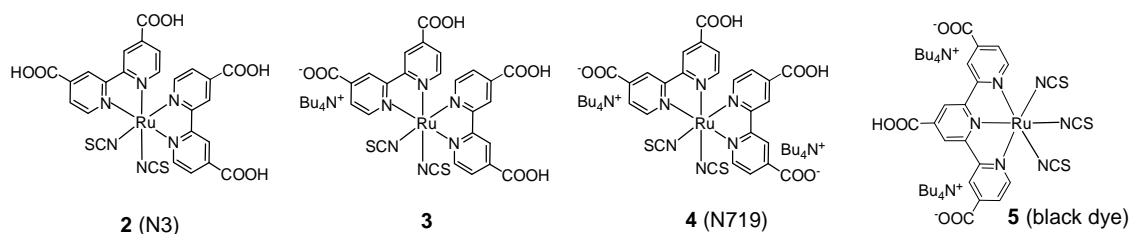


Figure 7. Molecular structures of unfunctionalized ruthenium(II) sensitizers (**2-5**) carrying protonated or deprotonated carboxylic acid groups on each pyridine moiety.

Nevertheless, the long-term stability of such unfunctionalized sensitizers is reasonable¹⁵⁸ and the attainable efficiencies are high especially for L-DSCs. For example polypyridyl ruthenium(II) complex **2** (Figure 7) was reported to deliver a short-circuit current density of more than 18 mA/cm² and an open-circuit voltage higher than 700 mV leading to a solar-to-electricity energy conversion efficiency of 10 % (see Table 1).¹⁶ The high overall efficiency is a consequence of optimization, suitable additives, and the outstanding properties of the redox sensitizer, *viz.* the absorption of a sufficient fraction of the incident light in combination with long excited-state

lifetimes. Since this first report of an L-DSC reaching 10 % in 1993, only slight improvements in the solar cell performance could be achieved. In 2001, the so called **black dye** (Figure 7, **5**) surpassed the performance of **2** marginally with an efficiency of 10.4 %.¹⁵⁹ In 2006, even 11.1 % could be reached with this dye.¹⁶⁰ The improvement in the performance of **5** compared to **2** is attributed to the strong spectral response in the red and near-IR region. The IPCE started to rise at 940 nm, more than 100 nm further shifted into the IR-region than **2** resulting in higher short-circuit photocurrents, even though the surface coverage and the extinction coefficient of **5** are significantly lower than **2**. In 2005 it was reported that **N719** (Figure 7, **4**) and the mono salt (Figure 7, **3**) exhibited power conversion efficiencies of 10.26 % and 11.18 %, respectively.¹⁶¹ In the case of sensitizers that do contain deprotonated carboxylic groups, the open-circuit voltage is observed to be higher while the short-circuit current is lower. In the case of sensitizers which contain free carboxylic acid anchoring groups, most of the protons may be transferred to the TiO₂ surface. This can cause a positive charging of the surface and shifts the Fermi level which can result in a decrease in the open-circuit voltage. Furthermore, a surface dipole is generated by the protons resulting in an electric field that enhances the adsorption and assists the electron injection which equals an increase in the short-circuit current. Hence, the appropriated degree of deprotonation is a crucial issue for high efficiencies.^{159, 161}

Today only a few new functional dyes exceeded the best performance of the above dyes. For example, the ruthenium sensitizers **C106**¹⁶² (Figure 17, **34**) and **CYC-B11**¹²⁴ (Figure 18, **36**) carrying extinction enhancing groups in combination with hydrophobic chains exhibit high short-circuit current densities and high efficiencies above 11.2 % (Table 4). It was reported, that, taking into account electrical and optical losses in the dye-sensitized system, the maximum power conversion efficiency attainable as a function of the optical band gap of the sensitizer and the “loss-in-potential” from the optical band gap to the open-circuit voltage is estimated to be 13.4 % for currently used sensitizers.¹⁶³ Accordingly, the upper limit of L-DSCs is almost reached and higher efficiencies can only be achieved by sensitizers that offer an absorption onset in the near-IR region or by reducing the loss-in-potential.

Due to the lack of functional groups that enhance the absorption or reduce recombination, the unfunctionalized polypyridyl ruthenium(II) dyes are less attractive for S-DSCs considering the fact that S-DSCs have an optimum thickness of ~ 2 μm . In the early stage of S-DSCs development, these sensitizers were mainly used for device optimization. For instance, the performance of S-DSCs based on **N719** and spiro-OMeTAD could be considerably improved by controlling charge

recombination losses across the interface and enhancing the hole transport mobility of the spiro-OMeTAD.²² To reach these goals, additives like *t*BP and Lithium bis(trifluoromethanesulfonyl)imide ($\text{LiN}(\text{SO}_2\text{CF}_3)_2$) were added to the hole transport material. The cooperative effect of both additives was investigated and a 100 % improvement in the open-circuit voltage and a considerable increase in the short-circuit current density was reached leading to an overall efficiency of 2.56 %. The additive *t*BP has a beneficial effect on the homogeneity of the hole conductor film and promotes the dissolution process of the Li-salt in the hole transporters matrix. Furthermore, it reduces recombination and so does the Li-salt.²² With increasing salt concentration the recombination was further slowed down. These results were confirmed by the National Renewable Energy Laboratories.²² A further improvement was reached by adding silver ions (silver nitrate) to the dye solution which was used to cover the surface of the mesoporous semiconductor.¹⁶⁴ The silver ions are assumed to bind to the isothiocyanate group *via* the sulphur which has been described in terms of the hard-soft acid-base concept. The formation of such silver complexes is suggested to result in a higher packing density increasing the surface concentration of dyes. This treatment increased the open-circuit voltage and the short-circuit current density leading to an efficiency of 3.2 % for a **N719** sensitized solar cell (compared to 2.1 % for an untreated cell).

Table 1. Overview of the performances of unfunctionalized sensitizers tested in L-DSCs as well as S-DSCs (measured under AM1.5, 100 mW/cm²).

Complex	Solar Cell type	Type of HTM ^a	J_{sc} [mA/cm ²]	V_{oc} [V]	FF [%]	η [%]	Ref
2	L-DSC	volatile	18.2	0.720	73	10.0	¹⁶
3	L-DSS	volatile	17.7	0.846	75	11.18	¹⁶¹
4	L-DSC	volatile	17.6	0.800	73	10.26	¹⁶¹
4	S-DSC	spiro-OMeTAD	5.1	0.910	55	2.56	²²
4	S-DSC	spiro-OMeTAD	4.6	0.931	71	3.2	¹⁶⁴
5	L-DSC	volatile	20.5	0.720	70	10.4	¹⁵⁹
5	L-DSC	volatile	20.9	0.736	72	11.1	¹⁶⁰

^a Volatile solvents for L-DSCs are on the basis of acetonitrile/valeronitrile.

To cause a further improvement in the performance while maintaining the general device concept, two approaches were developed, which are complementary to each other. The first is the optimization of additives and device engineering and the second is the optimization of the sensitizer including novel strategies and concepts by variation of the functional ligands coordinated to the ruthenium(II) core. The latter topic is the subject matter of the following sections.

3.1.2 Amphiphilic Ruthenium Dyes

One design strategy to improve the properties of standard sensitizers such as **N3** (Figure 7, 2) and its double-deprotonated analogue **N719** (Figure 7, 4) is the introduction of hydrophobic alkyl substituents to obtain amphiphilic ruthenium complexes. These amphiphilic dyes are supposed to offer several advantages which favour their use as sensitizers in DSCs: (i) The hydrophobic spacer provides an insulating barrier between the sensitized semiconductor and the hole transport material to avoid charge carrier recombination between injected electrons and the positive charges of the HTM,⁹⁸ (ii) the presence of the hydrophobic barrier increases the stability of solar cells towards water induced desorption of sensitizer molecules from the semiconductor surface,⁸⁷ (iv) the ground state pK_a value of the anchoring 2,2'-bipyridyl-4,4'-dicarboxylic acid is higher for amphiphilic complexes compared to standard sensitizers, this enhances the binding capability of the sensitizer onto the semiconductor surface,¹⁶⁵ (v) amphiphilic sensitizers show an increase in dye loading due to the decreased charge density on the sensitizer which attenuates the electrostatic repulsion¹⁶¹ and (vi) it is assumed, that the interaction between the dye and an organic HTM (*e.g.* hole conducting polymers) can be improved by hydrophobic chains which are capable to enhance the wettability and thus the electronic communication between dye and HTM.⁹¹

The number of amphiphilic dyes in the strict sense is quite low, because the possibilities of variation are limited to the modification of the length of the hydrophobic chains, their degree of branching and the anchoring group. Here, some examples of amphiphilic ruthenium complexes will be presented. The characteristic solar cell parameters can be found in Table 2.

To gain more insight into the effects of the different chain lengths, complexes **6–10** carrying C_1 , C_6 , C_9 , C_{13} and C_{18} chains (Figure 8) were systematically tested in devices.^{98, 165, 166} It could be demonstrated, that in L-DSCs the short-circuit current density as well as the open-circuit voltage and thus the efficiency increased with an increase in chain length from C_1 to C_{13} . (Or rather, the current rose from 14.6 to 16.2 mA/cm² and the voltage from 700 to 740 mV resulting in an efficiency increase from 6.7 to 8.6 %, from C_1 to C_{13}).¹⁶⁵

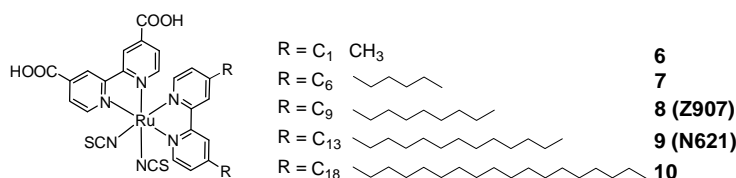


Figure 8. Structures of a series of amphiphilic sensitizers (**6–10**).

Furthermore, it was reported that the series of amphiphilic ruthenium dyes with varying hydrocarbon chain length were able to act as an insulating barrier for recombination in L-DSCs as well as in S-DSCs.⁹⁸ It is assumed, that the chains stretch out creating a aliphatic network (especially in the presence of a solid hole transporter) and increasing the distance between semiconductor and HTM.¹⁶⁶ Moreover, it was suggested that sensitizers with long alkyl chains are being oriented normal to the semiconductor surface.⁹⁸ By time-resolved emission spectroscopy (monitoring the dynamics of electron injection) and transient optical absorption spectroscopy (monitoring the charge recombination and regeneration), it was observed, that the increasing alkyl chain length resulted in slower recombination dynamics for both, the recombination of injected electrons with dye cation and that one with the hole transport material (solid and liquid).⁹⁸ Hence, the performance of DSCs improved with increasing alkyl chain length. An exception was the L-DSC on the basis of **10** carrying the longest alkyl chain (C_{18}). Here, the dye cation recombination dynamics exceed the dye regeneration speed resulting in a reduced performance. The same reduced performance was observed for the S-DSCs employing this sensitizer. The low S-DSC performance of the amphiphilic dye carrying the longest chain was ascribed to the collapse of too long chains reducing the effective distance and the blocking behaviour between into the semiconductor injected electrons and the holes in the HTM.¹⁶⁶

Among the amphiphilic ruthenium sensitizers, the most prominent representative is compound **8**, denoted as **Z907**. This amphiphilic heteroleptic sensitizer carrying two hydrophobic chains ($-C_9H_{19}$) was applied in DSCs using liquid electrolytes,^{165, 167, 168} a polymer gel electrolyte,¹⁶⁹ and solid organic HTMs.^{71, 166}

The L-DSC performance of **Z907** was improved by co-adsorbing amphiphilic molecules such as *n*-hexadecylmalonic acid¹⁶⁷ (HDMA) or 1-decylphosphonic acid¹⁶⁸ (DPA). The co-adsorption is

supposed to result in a more tightly packed mixed monolayer on the semiconductor surface providing a more effective insulating barrier and passivating the non-dye-adsorbed surface. The mixed monolayer seems to impair the recombination between injected electrons and the HTM very effectively, so that the losses due to decreased light harvesting caused by minor dye loading appear to be overridden. Compared to a device without co-adsorbent, the efficiency could be enhanced from 7.2 to 7.8 % and 6.8 to 7.3 % for HDMA and DPA, respectively. Additionally these devices were also very stable under thermal stress and light soaking.

In solid state devices, **Z907** reached an efficiency of 4.0 % under optimized conditions.⁷¹ The addition of silver ions¹⁶⁴ caused no further enhancement. Although the voltage was increased by 106 mV under the influence of silver ions, the current decrease significantly because of an unfavourable blue-shift of the absorption.⁷¹

It is known, that chemisorbed sensitizers are susceptible to desorption from the surface under the influence of trace amounts of water, having serious consequences for the long term stability of the cells.⁸⁷ It is assumed, that amphiphilic dyes can cause an enhanced stability towards desorption. A quasi-solid-state DSC employing **Z907** and a polymer gel electrolyte consisting of a photochemically stable fluorine polymer (poly(vinylidene fluoride-co-hexafluoropropylene, (PVDF-HFP)) which was used to solidify a 3-methoxypropionitrile based liquid electrolyte performed under both thermal stress and soaking with light equivalent to a DSC using a liquid electrolyte on the basis of 3-methoxypropionitrile.¹⁶⁹ This indicates that the gelation has no adverse effect on the conversion efficiency. The efficiency of ~ 6 % which was archived for both systems is much below the highest efficiencies reported for DSCs using for example **N719**. However, the quasi-solid device showed an excellent stability with a little drop of 5 % in efficiency under light soaking at 55 °C for 1000 h under a solar simulator (100 mW/cm² equipped with an ultraviolet filter). Even under heating for 1000 h at 80 °C the efficiency decreased just by 6 %. Actually, within the first week the efficiency was moderately enhanced. (For comparison, in the case of **N719** the efficiency decreased almost 35 % during the first week at 80 °C.)

Beside amphiphilic sensitizers carrying linear hydrophobic chains, also the branched derivatives like **11** were synthesised and the photovoltaic performance as well as the stability under special conditions were investigated.^{87, 170} However, while maintaining the comparable good stability, the branching did not result in any advantage over the linear amphiphilic sensitizers.⁸⁷

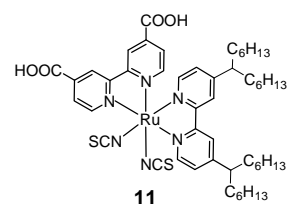


Figure 9. Structure of the amphiphilic, branched dye **11**.

Furthermore, amphiphilic sensitizers carrying the same functional aliphatic chains as **Z907** but different anchoring groups were used as sensitizers. In compound **12**, denoted as **Z955**, for example the two carboxylic acid groups are replaced by phosphonic acid anchoring groups while maintaining the hydrophobic C₉-chains of **Z907**.⁸¹

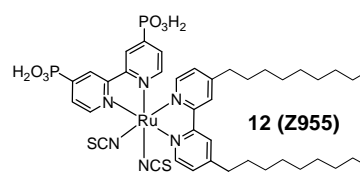


Figure 10. Molecular structure of **12**.

The H₂PO₃ anchoring groups caused an increase in stability by a stronger binding onto TiO₂ compared to carboxylic acid groups, but the overall conversion efficiency decreased from 6.8 % for **Z907** compared to 6.4 % for **12**. The new H₂PO₃ groups also caused an unfavourable blue-shift of the absorption and a disadvantage in the electron injection capability because the groups are not in conjugation to the polypyridyl plane due to their non-plane structure.¹⁰⁷ Furthermore, a decrease in the open-circuit voltage was observed for **12**.⁸¹

Further examples of amphiphilic dyes are **13**^{171, 172} and **14**.¹⁷² **13** incorporates carboxyvinyl acid anchoring moieties, whereas **14** contains 4-vinylbenzoic acid groups. Both are assumed to enhance the long wavelength spectral response and the extinction coefficients due to the increased delocalized system. The performances of the **13**, **14** and **Z907**

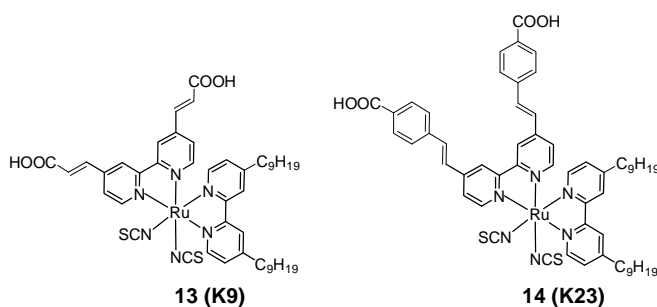


Figure 11. Structures of the amphiphilic sensitizer **13** and **14**.

sensitizers chemisorbed on a thin mesoporous TiO₂ layer (2.5 μm + 5 μm scattering layer) were investigated in L-DSCs. The measured photocurrents are 15.16, 15.73 and 15.09 mA/cm² respectively, showing just a little impact of the increased delocalized system. Nevertheless, the concept of increasing the delocalized π-system to improve the light harvesting efficiency is a promising approach (especially for thin S-DSCs) if the extended delocalization is realized in the ancillary ligand. This will be explained in the next section.

Table 2. Overview of the performances of amphiphilic sensitizers tested in L-DSCs as well as S-DSCs (measured under AM1.5, 100 mW/cm²).

Complex	Solar Cell type	Type of HTM ^b	J_{SC} [mA/cm ²]	V_{OC} [V]	FF [%]	η [%]	Ref
6^a	L-DSC	volatile	14.6	0.700	66	6.7	165
6	L-DSC	volatile	6.2	0.660	56	2.4	98
6	S-DSC	spiro-OMeTAD	5.4	0.714	60	2.3	166
7	L-DSC	volatile	15.5	0.700	68	7.4	165
7^a	L-DSC	volatile	6.4	0.690	58	2.6	98
7	S-DSC	spiro-OMeTAD	5.8	0.712	61	2.5	166
8	L-DSC	volatile	16.0	0.750	70	8.4	165
8	L-DSC	low volatile	15.2	0.764	68	7.8	167
8	L-DSC	low volatile	14.6	0.722	69	7.3	168
8	L-DSC	polymer gel	12.5	0.730	67	6.1	169
8	S-DSC	spiro-OMeTAD	6.3	0.738	61	2.8	166
8	S-DSC	spiro-OMeTAD	8.3	0.752	64	4.0	71
9	L-DSC	volatile	16.2	0.740	72	8.6	165
9^a	L-DSC	volatile	7.0	0.750	62	3.2	98
9	L-DSC	volatile	16.8	0.778	73	9.57	161
9	S-DSC	spiro-OMeTAD	6.3	0.744	66	3.1	166
10^a	L-DSC	volatile	3.5	0.670	56	1.3	98
10	S-DSC	spiro-OMeTAD	5.8	0.718	55	2.3	166
11	L-DSC	volatile	12.62	0.630	62	5.68	170
12	L-DSC	volatile	16.37	0.707	69	8.0	81
13	L-DSC	volatile	15.16	0.693	66	6.92	172
13	L-DSC	volatile	16.5	0.666	71	7.81	171
14	L-DSC	volatile	15.73	0.707	67	7.45	172

^a Note that in order to enable transient absorption measurements, transparent mesoporous TiO₂ films with a thickness of only 4 μm were applied. This reduces the amount of absorbed light, resulting in reduced J_{SC} values.

^b Volatile solvents for the electrolyte are on the basis of acetonitrile/valeronitrile and low volatile ones mainly rest upon 3-methoxypropionitrile.

3.1.3 Donor-Antenna Ruthenium Dyes

The term donor-antenna ruthenium dyes stands for ruthenium sensitizers incorporating an extended delocalized π -system. The main intention of this concept is the improvement of the light harvesting efficiency by increasing the molar extinction coefficient. This is addressed by the covalent connection of electron-rich donor groups to one bipyridyl ligand. Especially in S-DSCs, where the optimum thickness of the mesoporous semiconductor layer is a compromise between light absorption and charge transport/recombination, it is extremely favourable to use sensitizers providing a good light harvesting ability. The donor-antenna sensitizers offer an excellent opportunity to enhance the optical depth of sensitized mesoporous thin-films. Hence, an extremely strong absorbing sensitizer provides the possibility to prepare thinner DSCs, while enhancing or maintaining the optimum light harvesting efficiency. A reduction of the thickness of the mesoporous layer saves material and can considerably reduce charge transport losses in both DSC types. A further benefit of this concept is based on the spatial separation of the dye cation from the metal oxide surface. Charge recombination dynamics (in particular the recombination between photoinjected electrons and the oxidized sensitizer) is significantly influenced by the dye cation to TiO_2 distance which seems to be increased by donor-antenna ancillary ligands. More specifically, a linear correlation between the logarithm of the reciprocal charge recombination half-time ($t_{50\%}$) and the spatial separation r has been found.¹⁷³ Furthermore, an advantage of donor-antenna ruthenium dyes is the achievement of compatibility between donor-antenna groups and solid HTM which promotes an intimate electronic contact between sensitizer and HTM leading to higher regeneration rates. In the following, a selection of sensitizers based on the donor-antenna dye concept will be presented.

The Ru(II)tris(bipyridine) complexes **15**, **16**, and **17** are examples for ruthenium donor-antenna dyes providing high extinction coefficients, a large spatial separation (between dye cation and the semiconductor surface) in addition to a polarity match between donor-antenna groups and spiro-OMeTAD. Each of these dyes bears two identical bipyridyl anchoring ligands and one triphenylamine-based electron-rich bipyridyl donor-antenna ligand.^{67, 95, 100, 174}

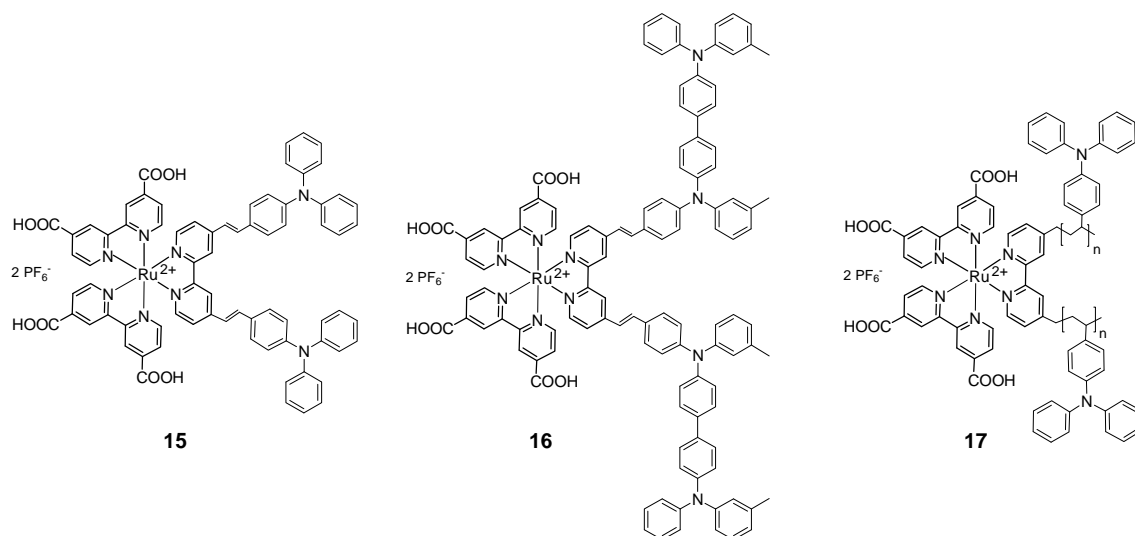


Figure 12. Structures of the Ru(II)tris(bipyridine) sensitizers **15**, **16** and **17** carrying donor-antenna groups.

Transient absorption spectroscopy of dye sensitized TiO₂ films was employed to monitor charge recombination dynamics by observing the decay of the photoinduced cation absorption of dye/TiO₂ films. Recombination half-times ($t_{50\%}$) of 350 μ s, 5 ms, and 4 s were measured for **15**, **16**, and **17**, respectively.¹⁰⁰ Compared to that, about 200 μ s were measured for **Z907** (Figure 8, 7).^{169, 175, 176} The decelerated charge recombination behaviour was attributed to an increased physical separation of dye cations from the semiconductor surface as a result of the suitable location of the HOMOs and a translation of the holes away from the ruthenium core to the donor functionalities.¹⁰⁰ Density functional theory (DFT) ab initio calculations, accompanied by cyclic voltammetry measurements, were performed to support this hypothesis. The HOMO of the reference compound [Ru^{II}(2,2'-bipyridyl-4,4'-dicarboxylic acid)₃] which does not carry any donor-antenna groups was found to be centred on the ruthenium core. However, the HOMO of **15** is additionally delocalized over the triphenylamine donor-antenna ligand. For **16** and **17**, the HOMO is exclusively located on the phenylamine moieties.¹⁰⁰ The spatial separations r of the dye cation from the TiO₂ surface derived from DFT calculations were 10.8, 15.6 and 16.7 Å for **15**, **16** and **17**, respectively.¹⁰⁰ As expected,¹⁷³ by plotting the logarithm of the reciprocal charge recombination half-time $\log(1/t_{50\%})$ against the calculated spatial separation r a linear correlation was found.¹⁰⁰ Furthermore, the cyclic voltammetry measurements showed that these donor-antenna ruthenium sensitizers indeed provide the possibility of creating a charge transfer cascade.⁹⁵ If the HOMO level of the donor group is energetically located between the HOMO level of the Ru-core and the HOMO or redox level of the HTM, a charge transfer cascade can be

envisaged. This is the case for complexes **15**, **16** and **17**. Here, after light absorption, an excited electron is shifted to the LUMO (delocalized over the anchoring group) whereas the hole is shifted to the HOMO which is mainly delocalised over the donor groups. This creates a large distance between (excited and injected) electrons and holes causing a lower recombination.

The relationship between the spatial distance and the recombination rate is not only valid for polypyridyl ruthenium dyes; it is also true for phthalocyanines and porphyrins.^{173, 177} However, there are some factors that have to be taken into account when discussing the distance dependency of the recombination dynamics. For instance, the DFT method to calculate the distribution of orbitals over a molecule is a technique that does not consider the real conditions of chemisorbed sensitizers generating a dense monolayer on a semiconductor surface. Additionally, the positioning of the sensitizer relative to the surface should not be disregarded, since the spatial separation between dye cation and semiconductor surface changes significantly when the relative orientation and conformation of the sensitizer change. Nevertheless, these calculations are used to estimate the distance between dye cation and semiconductor. Furthermore, the transient absorption spectroscopy measurements to determine the recombination half-times depend on experimental conditions, such as the intensity of the used light and the degree of dye adsorption.^{175, 176}

Despite the favourable long recombination half-times measured for **15**, **16** and **17**, the performance of such sensitizers in S-DSCs is rather low (*cf.* Table 3, **15**) due to the lack of absorption in the longer wavelength region. The replacement of one bipyridine anchoring ligand by two NCS-ligands leading to Ru(II)bis(bipyridine)(NCS)₂ complexes increases the light harvesting efficiency expressed by an additional MLCT absorption band around 550 nm.^{67, 95} The Ru(II)bis(bipyridine)(NCS)₂ counterparts to **15** and **16** are the complexes **18** and **19** which show a dramatic increase in absorption and

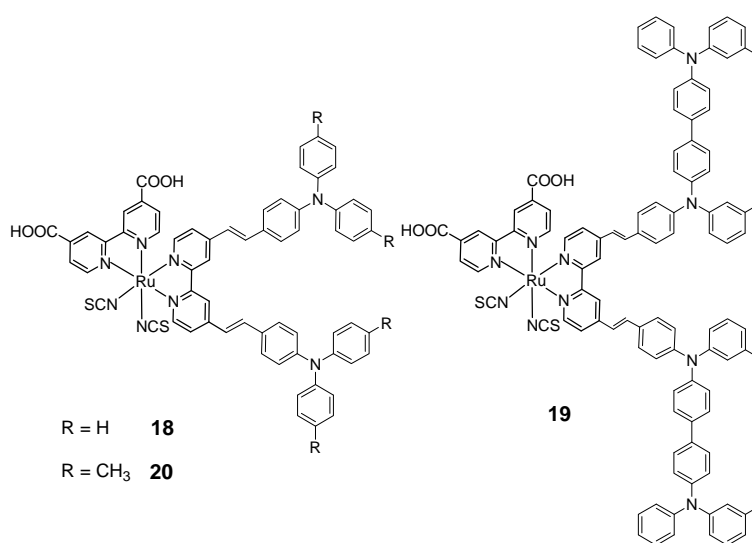


Figure 13. Molecular structure of the high extinction coefficient donor-antenna dyes **18**, **19** and **20**.

solar cell performance.^{67, 95, 175, 176, 178} The molar extinction coefficients of the additional MLCT band at 526 and 540 nm are 2.45×10^4 and $2.67 \times 10^4 \text{ M}^{-1}\text{cm}^{-1}$ for **18** and **19**, respectively.¹⁷⁸ Thus, for **18** an overall conversion efficiency of 3.2 % was measured for an S-DSC.¹⁷⁶ Dye **18** was also employed as sensitizer in vertically oriented TiO₂ nanotube arrays in conjugation with a liquid low volatile electrolyte.¹⁷⁹ By using **18** in combination with 14 μm long TiO₂ nanotubes instead of a mesoporous electrode, an efficiency of 6.1 % could be reached (with a volatile electrolyte and a mesoporous TiO₂ electrode, **18** reached 8.7 %¹⁸⁰). An extremely similar sensitizer compared to **18**, viz. complex **20** was applied in standard L-DSCs using mesoporous TiO₂ (thickness: 13 μm composed of 20 nm anatase TiO₂ particles, plus 4 μm composed of 400 nm light scattering anatase particles).¹⁸¹ CDCA was added to the sensitizer solution meanwhile the dye-coating process to reduce aggregation of dye molecules and thus leading to higher efficiencies. Additionally, also the composition of the volatile electrolyte was optimized to cause either a higher photocurrent density by employing LiI or a higher voltage by adding more tBP and guanidinium thiocyanate. However, both electrolytes led to a power conversion efficiency of 10.3 %.

The sensitizers **21**, **22**, and **23** (Figure 14) belong to a whole series of high extinction coefficient donor-antenna dyes.¹⁸² They were characterized concerning their electrochemical, spectral and photovoltaic properties. In cyclic voltammetry measurements, it was found that the first reduction occurred at about -1.6 eV vs. ferrocene for all sensitizers resulting in LUMO levels of about -3.2 eV. Taking into account, that the LUMO level of the

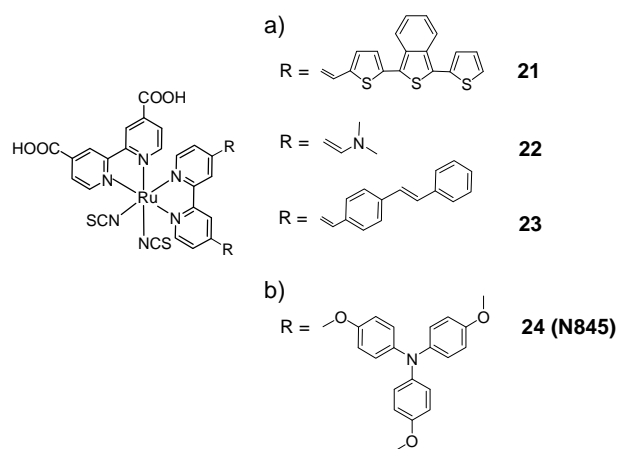


Figure 14. Structures of donor-antenna in which the donor is attached via a) a vinyl spacer (**21**, **22** and **23**) or b) a methylene group (**24**).

standard dye **N719** occurred at the same value and that this orbital is known to be distributed over the 2,2'-bipyridyl-4,4'-dicarboxylic acid ligands,^{161, 183} it is assumed that the LUMO of **21**, **22** and **23** is also distributed over the anchoring ligand. Concerning the spectral properties, it was found, that **21** and **23** showed extremely high extinction coefficients compared to the standard dye **N719**. For example, at about 370 nm, the molar extinction coefficient of **23** is almost seven times as high as that of **N719**. For the weakest π -electron delocalisation donor-antenna group, viz. the dimethylamino moiety (*cf.* complex **22**), the absorption behaviour is comparable to **N719**

and so is the photovoltaic performance. Under non optimized conditions, both sensitizers achieved comparable photocurrent densities, open-circuit voltages and fill factors resulting in equal efficiencies. Although the light harvesting efficiency and the position of the orbitals of **21** were found to be suitable for efficient solar cells, an S-DSC employing this sensitizer performed only less efficient. This shows clearly, that absorption and suitable energy level are not the only aspects affecting the solar cell performance. Nevertheless, the high extinction coefficient sensitizer **23** performed almost twice as good as **N719** in these preliminary tests.¹⁸²

The donor-antenna ruthenium sensitizer **24** (Figure 14.b) is a further example for the control of charge-transfer dynamics.¹⁰² Here, two *N,N*-(di-*p*-anisylamino)phenoxyethyl donor units are connected to a ruthenium complex *via* -CH₂-O- groups. Transient absorption spectroscopy monitoring the rate of recombination between electrons from the conduction band of the TiO₂ nanoparticles with the oxidized form of the ruthenium sensitizers showed a 1000-fold retardation of the recombination compared to a dye without donor-antenna groups ($t_{50\%}$ = 0.71 s and 0.85 ms for **24** and **N719**, respectively). This is also assumed to be caused by the increase in the spatial separation of the HOMO orbital from the TiO₂ surface, which was supported by semiempirical calculations. Despite the outstanding recombination behaviour and suitable position of the energy levels, until now no efficient DSC was reported using **24** as sensitizer. This may be due to the low absorption of **24**. Although a strong donor is attached to the bipyridyl ligand, the link is not conjugated to enable π -electron delocalization and hence the extinction coefficient stays low (to be precise, the absorption of **24** is even lower than that of **N719** except for the LC transition at about 300 nm).

In the next group of sensitizers (Figure 15, **25-30**), alkyl-, alkoxy- or alkylamino-substituted styryl moieties were used as donor-antenna groups to increase the molar extinction coefficient. DFT calculations of **25** and **26** illustrated that the HOMO orbitals of each dye are delocalized over the ruthenium metal and the NCS ligands. The LUMO is

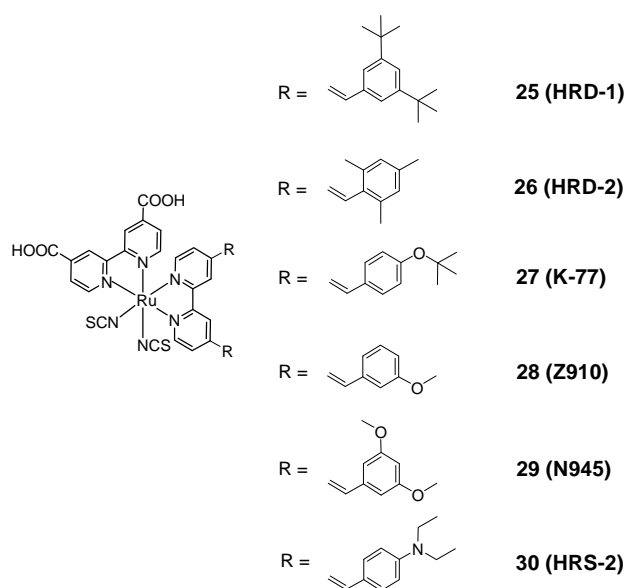


Figure 15. Donor-antenna sensitizers **25-30** carrying different alkyl-, alkoxy- or alkylamino-substituted styryl moieties to enhance the light harvesting efficiency.

localized on the carboxylic acid anchoring ligands.¹⁵⁶ The dyes **25**, **26** and **27** were used as sensitizers in L-DSC employing durable redox electrolytes, both, a low volatile and an ionic liquid one.^{116, 156, 184} As in the case of **20**, the high LiI concentration of the low volatile electrolyte decreases the open-circuit voltage, but increases the electron transport properties, whereas the electrolyte on the basis of ionic liquids benefits from employing guanidinium thiocyanates which improves the open-circuit voltage by reducing the dark current.¹⁸⁵ Additionally, the long term performance of L-DSCs using the low volatile electrolyte was high under light soaking and thermal stress. The devices on the basis of **25** and **26** maintained about 90 % of their initial photovoltaic performance in both stability tests. For **27**, in combination with the co-adsorbent 3-phenylpropionic acid, the volume ration of a solvent-free binary ionic liquid electrolyte on the basis of 1-propyl-3-methylimidazolium iodide (PMII) and 1-ethyl-3-methylimidazolium tetracyanoborate (EMIB(CN)₄) was optimized leading to a high efficiency of 7.6 % as well as a high stability. By electrochemical impedance spectroscopy, it was shown, that the I₃⁻ transport in the electrolyte and the charge transfer to the counter became more slowly with increasing PMII concentration due to the increase in viscosity.¹¹⁶ By using a low volatile electrolyte based on 3-methoxypropionitrile, **27** reached an efficiency of 9.0 % and by using a volatile electrolyte based on acetonitrile/valeronitrile, **27** achieved 10.5 %.¹⁸⁴ Comparable results were also accomplished by dye **28** using a volatile solvent for the electrolyte ($\eta = 10.2$ %).¹⁸⁶ For stability test, a low volatile ionic liquid electrolyte was used reaching an efficiency of about 7 % which, is higher than the value reached for **Z907** while the stability was similar.¹⁸⁶ In comparison to the unfunctionalized dye **N719**, **30** carrying the ancillary ligand 4,4'-bis[*p*-diethylamino] α -styryl]-2,2'-bipyridine showed a 400 % increase in the absorption at about 400 nm and a 100 % increase at about 540 nm (ϵ of **30** is 5.93×10^4 and $2.81 \times 10^4 \text{ M}^{-1} \text{ cm}^{-1}$ at 431 and 542 nm, respectively). Preliminary tests of this sensitizer in L-DSC resulted in an efficiency of 8.65 % although no blocking layer and no antireflection layer was introduced.¹⁸⁷

The enhancement of the molar extinction coefficient by suitable donor-antenna groups opens up the possibility to create thinner DSCs and thus construct more efficient DSCs because of reduced transport losses. In order to investigate the impact of high molar extinction coefficients on the photovoltaic parameters, L-DSCs employing **29** using transparent mesoporous TiO₂ films of various thicknesses were fabricated.¹⁸³ By increasing the thickness from 2, 5, 7 to 9 μm the efficiency rose from 5.72, 7.31, 8.04, to 8.31 %, respectively. With increasing thickness the photocurrent density increased drastically reaching a plateau value of almost 19 mA/cm² at 14 μm with an efficiency of 10.82 %. On the contrary, the open-circuit voltage decreased with

increasing thickness. The investigations demonstrate further, that the difference in performance between **29** and **N719** is strongly pronounced for thinner mesoporous layers ($\Delta I_{SC} = 30\%$) consistent with the higher molar extinction coefficient. However, for thicker TiO_2 layers, the disparity in efficiency between the two sensitizers decreases from 30 to less than 7 %. Hence, for thicker TiO_2 layers an upper limit is reached beyond which the influence of the high molar extinction coefficient is buffered.

Table 3. Overview of the performances of donor-antenna sensitizers tested in L-DSCs as well as S-DSCs (measured under AM1.5, 100 mW/cm²).

Complex	Solar Cell type	Type of HTM ^f	J_{SC} [mA/cm ²]	V_{OC} [V]	FF [%]	η [%]	Ref
15	S-DSC	spiro-OMeTAD	2.5	0.718	34	0.8	95
18 ^a	L-DSC	low volatile	13.44	0.723	63	6.1	179
18	L-DSC	volatile	16.75	0.727	72	8.70	180
18	S-DSC	spiro-OMeTAD	4.4	0.767	34	1.5	67, 95
18	S-DSC	spiro-OMeTAD	7.6	0.790	53	3.2	176
19	S-DSC	spiro-OMeTAD	9.6	0.757	35	3.4	67, 95
20 ^{b, c}	L-DSC	volatile	17.6	0.801	73	10.3	181
20 ^{b, d}	L-DSC	volatile	19.2	0.748	72	10.3	181
21	S-DSC	spiro-OMeTAD	1.06	0.625	46	0.31	182
22	S-DSC	spiro-OMeTAD	2.15	0.635	42	0.58	182
23	S-DSC	spiro-OMeTAD	3.42	0.685	42	0.99	182
25	L-DSC	low volatile	16.98	0.500	66	5.77	156
25	L-DSC	ionic liquid	10.90	0.590	78	4.93	156
26	L-DSC	low volatile	15.00	0.470	69	4.87	156
26	L-DSC	ionic liquid	10.50	0.600	78	4.91	156
27	L-DSC	low volatile	15.40	0.500	67	5.16	156
27	L-DSC	low volatile	17.5	0.737	79	9.0	184
27	L-DSC	ionic liquid	7.95	0.565	78	3.50	156

Table3 (continued)

27 ^e	L-DSC	ionic liquid	15.1	0.702	71	7.6	¹¹⁶
27	L-DSC	volatile	19.2	0.780	73	10.5	¹⁸⁴
28	L-DSC	volatile	17.2	0.777	76	10.2	¹⁸⁶
29	L-DSC	volatile	18.84	0.783	73	10.82	¹⁸³
30	L-DSC	volatile	17.47	0.697	71	8.65	¹⁸⁷

(Solvents for L-DSCs can be volatile such as acetonitrile/valeronitrile, low volatile such as 3-methoxypropio-nitrile or ionic liquids.) ^a The solar cell was prepared using an array of 14.4 μm long TiO_2 nanotubes on a Ti foil subjected to illumination in the backside geometry. ^b CDCA was used as co-adsorbent. ^c The volatile electrolyte involved a high concentration tBP and guanidinium thiocyanate and no LiI. ^d The volatile electrolyte contained LiI but less tBP and guanidinium thiocyanate. ^e 3-Phenylpropionic acid was used as co-adsorbent. ^f Volatile solvents for the electrolyte are on the basis of acetonitrile/valeronitrile and low volatile ones mainly rest upon 3-methoxypropionitrile.

3.1.4 Donor-Antenna Ruthenium Dyes bearing Hydrophobic Chains

In order to create sensitizer which provide an increased optical cross section and simultaneously facilitate long-term stability, the concepts of donor-antenna dyes and amphiphilic sensitizers were combined. This approach is currently addressed by novel ruthenium(II) sensitizers carrying ancillary bipyridyl ligands which are covalently connected to donor-antenna groups (such as phenyl, thiophene, or thieno[3,2-*b*]thiophene derivatives) that additionally carry hydrophobic chains. This does not only increases the molar extinction coefficient of the dye *via* the extended π -delocalized system, but also augments its hydrophobicity by the alkyl chains. Hence, recombination losses can be minimized by allowing the preparation of thinner TiO_2 films. Simultaneously, desorption of sensitizer molecules by water may be prevented stabilizing the device performance under long-term light soaking and thermal stress. In summary, donor-antenna ruthenium dyes bearing hydrophobic chains can provide the following key advantages: (i) high molar extinction coefficients, (ii) large spatial separation of the dye cation from the metal oxide surface, (iii) polarity match between the sensitizer and the solid standard hole transport material spiro-OMeTAD and (iv) the possibility to form an insulating barrier between the sensitized semiconductor and the HTM to diminish recombination losses and to prevent water induced desorption. (For a more detailed explanation of the single advantages of each concept *cf.* section 3.1.2 and 3.1.3)

The heteroleptic ruthenium(II) donor-antenna dyes bearing hydrophobic chains meet all the key demands of sensitizers for the application in high efficient DSCs. However, the synthetic procedure is very demanding because the ancillary ligands have to be prepared in multi-step synthesis. Nevertheless, the effort is worthwhile, since very high efficiencies were reached with such sensitizers.^{122, 123, 125, 162, 188}

The donor-antenna dye **31** bearing hexyl chains shows a molar extinction coefficient of $1.82 \times 10^4 \text{ M}^{-1}\text{cm}^{-1}$ at the low energy MLCT absorption band at 543 nm which is significantly higher than that of the standard dyes **N719** ($1.40 \times 10^4 \text{ M}^{-1}\text{cm}^{-1}$) and **Z907** ($1.22 \times 10^4 \text{ M}^{-1}\text{cm}^{-1}$).¹⁸⁹ The same order is represented by the photovoltaic measurements, where **31**, **N719**

and **Z907** reached an efficiencies of 7.0, 6.7 and 6.0 %, respectively. During thermal ageing tests for 1000 h at 80 °C, **N719** showed only a poor stability which is probably caused by desorption. In contrast, the amphiphilic sensitizers **Z907** and **31** retained over 92 % of their initial performance. Furthermore, a device containing **31** and a co-adsorbent (3-phenylpropionic acid) kept 93 % of its initial performance after the 1000 h light soaking test.¹⁹⁰

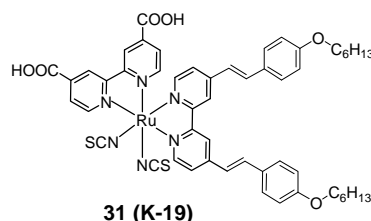


Figure 16. Structure of the amphiphilic high extinction coefficient sensitizer **31**.

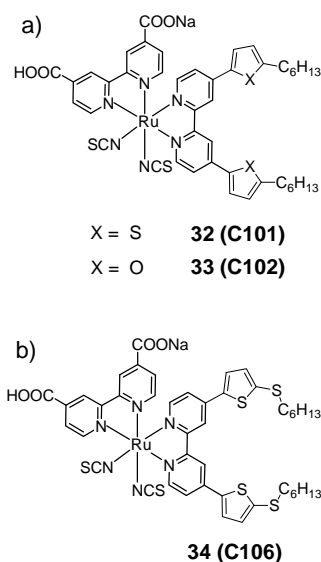


Figure 17. Chemical structures of amphiphilic donor-antenna dyes carrying a) hexyl thiophene/furan groups (**32**, **33**) or b) (hexylthio)-thiophene moieties (**34**).

Currently, remarkably high solar cell performances are reached with amphiphilic sensitizers incorporating thiophene moieties attached to the bipyridyl ligand without any spacer. A ruthenium(II) complex bearing a hexylthiophene-conjugated bipyridine as ancillary ligand is presented for the use in S-DSCs.¹²² Complex **32**, denoted as **C101**, is distinguished by its high absorption due to the π -conjugated system and the high hydrophobicity of stained TiO_2 films (determined by water-contact angle measurements). **32** is capable to reduce the recombination of injected electrons with holes from the HTM compared to its thiophene-free counterpart **Z907** and it can shift the band edge of TiO_2 by its high dipole moment leading to a higher open-circuit voltage. The entirety of the mentioned advantages of **32** leads to an outstanding performance of this dye, reflected by an efficiency of 4.5 % in

an S-DSC device. Furthermore, **32** was employed as sensitizer in L-DSCs using an acetonitrile-based volatile redox electrolyte, a low volatile electrolyte and a solvent-free ionic liquid leading to efficiencies of 11.0, 9.7 and 7.4 %, respectively.¹⁸⁸ The lower efficiency of the solvent-free ionic liquid device can be explained with the much shorter effective electron diffusion length due to the lower electron diffusion coefficient and shorter electron lifetimes in mesoporous TiO₂ which limit the photocurrent. However, the stability of DSCs on the basis of ionic liquids and low volatile electrolytes is enhanced, both retaining over 95 % of their initial performance after 1000 h full sunlight soaking at 60 °C. Hence, the low volatile electrolyte device represents the compromise between efficiency and stability. Considering the similar configuration, molecular size and anchoring mode of **33** compared to **32**, the photovoltaic performance should be similar, but actually it is lower. It was found that a lower surface coverage is responsible for this.

The molecular structure of the sensitizer **34** (Figure 17), denoted as **C106**, is very similar to **32**, with the difference, that a sulphur atom is inserted between the *n*-hexyl chain and the thiophene.¹⁶² This increases the absorption of a stained TiO₂ film. Hence, the performance of an L-DSC employing this sensitizer is slightly improved compared to **32** leading to a remarkably high overall efficiency of 11.29 % (and 11.4 % at 30 °C). By employing this high molar extinction coefficient ruthenium dye in an S-DSC using spiro-OMeTAD as organic hole transport material, a certificated electric power conversion efficiency of 5 % could be reached (measured at the National Renewable Energy Laboratory, USA).¹²⁵ To the best of our knowledge, this is currently the highest reported efficiency for a solid-state DSC using spiro-OMeTAD as HTM.

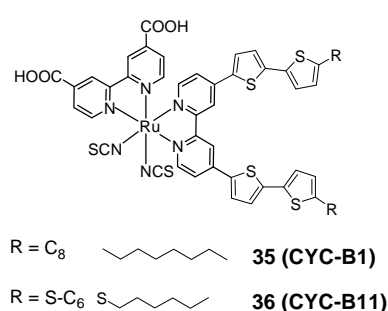


Figure 18. Structures of the octyl bithiophene and the (hexylthio)-thiophene substituted sensitizers **35** and **36**.

The ruthenium photosensitizer **35 (CYC-B1)** bears an ancillary ligand in which one bipyridine is substituted with alkyl bithiophene groups. Here, the oligothiophene moiety can be regarded as a *cis*-oligoacetylene chain bridged with sulphur atoms. It was reported, that the bridging sulphur atoms can provide aromatic stability compared to oligoacetylene while preserving high charge transport properties.^{191, 192} Furthermore, sulphur offers a greater radial extension in its bonding than for example carbon. Hence, thiophene is more electron-rich causing a high extinction coefficients and a red-shift of the absorption (ϵ of **35** is 4.64×10^4 and $2.12 \times 10^4 \text{ M}^{-1}\text{cm}^{-1}$ at 400 and 553 nm, respectively).¹⁹² The photo-to-current conversion efficiency of L-DSCs sensitized with **35** is in the region of 8.5 %.^{192, 193}

Following the development of **35**, a (hexylthio)bithiophene containing sensitizers was reported.¹²⁴ This complex, referred to as **CYC-B11**, showed an absorption improvement of about 14 % compared to its predecessor **35**. It is supposed, that this is directly related to the influence of the additional sulphur atom. Inserting a sulphur atom between bithiophene and the alkyl chain can augment the electronic transition dipole momentum and hence the extinction coefficient of the MLCT band. A careful optimization of the device engineering facilitated the preparation of high efficient L- and S-DSCs yielding impressive efficiencies of 11.5 and 4.7 %, respectively under AM 1.5 G simulated sunlight.¹²⁴ So far, 11.5 % efficiency is the highest reported value for L-DSCs based either on metal-organic or organic sensitizers.

Instead of simple 2,2'-bipyridines, also 2,2'-bipyridylamine ligands (*cf.* **37** and **38**) can be used as ligands to coordinate to the ruthenium center ion.¹⁹⁴ The alkyl-substituted bipyridylamines form six membered rings with less π -acceptor character on chelation than a five-membered ring of bipyridines. It is assumed, that the HOMO level of the corresponding complex is lifted due to more σ -donating power of the amine, resulting in a red-shifted MLCT band. Additionally, the well-established alkyl-thiophene (**37**) or alkyl-thienothiophene (**38**) moieties are attached for a better light harvesting efficiency. The analysis of the spectral properties of sensitizers **37** and **38** compared to **N719** showed that the low-energy MLCT band is just marginally red-shifted and extinction coefficients are only slightly increased or even lower. To be precise, the MLCT band of **37**, **38** and **N719** arises at 527, 525 and 521 nm, respectively corresponding to molar extinction coefficients of 1.02×10^4 , 1.56×10^4 and $1.40 \times 10^4 \text{ M}^{-1}\text{cm}^{-1}$. The same order is kept regarding the photovoltaic performance of L-DSC resulting in 7.66, 9.03 and 8.88 % overall efficiency for **37** and **38** and **N719**, respectively. Although, the L-DSCs of **37** and **38** using an electrolyte on the basis of the low volatile solvent 3-methoxypropionitrile showed outstanding long-term stability under thermal stress and light soaking, the novel coordination ligand itself did not cause any improvement. However, the combination of a standard 2,2'-bipyridine coordinating ligand with

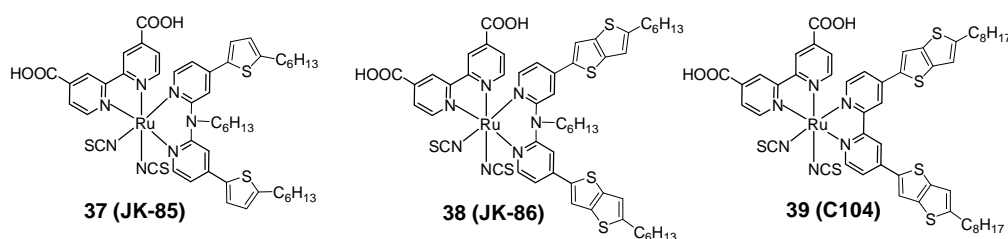


Figure 19. Structures of sensitizers **37**, **38** and **39**, carrying different bipyridyl ligands substituted by alkyl-thiophene or alkyl-thieno[3,2-*b*]thiophene.

an 5-octylthieno[3,2-*b*]thiophene-2-yl moiety (dye **39**) was more favourable since it resulted in a red-shifted absorption, a high extinction coefficient (ϵ of $2.05 \times 10^4 \text{ M}^{-1}\text{cm}^{-1}$ at 553 nm) and high power conversion efficiency of 10.53 %. This sensitizer also reached a conversion efficiency of 4.6 % in an S-DSC device using spiro-OMeTAD as HTM.¹²³

Sensitizers **40-42** featuring one or two electron-rich 3,4-ethylenedioxythiophene units, known as EDOT, in combination with long hydrophobic chains in their ancillary ligand facilitate high light harvesting capacity and good solubility. The low energy MLCT bands of **40**, **41** and **42** are centred at 550, 546, and 559 nm corresponding to extinction coefficients of about 1.88×10^4 , 1.87×10^4 and $2.74 \times 10^4 \text{ M}^{-1}\text{cm}^{-1}$, respectively.^{118, 195} The HOMO of each dye is distributed among the metal center and the NCS ligands, whereas the LUMO concentrates on the anchoring ligand. The insertion of EDOT units depresses the LUMO and evidently lifts the HOMO.^{195, 196} The sensitizers achieved efficiencies about 10 % in L-DSCs; with the highest absorbing dye **42** a maximum solar-to-electricity conversion efficiency of 10.7 % was reached employing a volatile redox electrolyte. Complex **41** was further examined as a sensitizer for plastic DSCs constructed at low temperatures. The effect of a compact blocking TiO_2 layer was investigated as well as the electrolyte composition and co-adsorbents. Under optimized conditions, **41** worked very well ($\eta = 6.31 \%$), while the flexible plastic device was more stable than the one incorporating **N719**.¹⁹⁷ (Note that EDOT groups may interact with Li^+ ions, as found for ion-coordinating sensitizers; cf. section 3.1.5.)

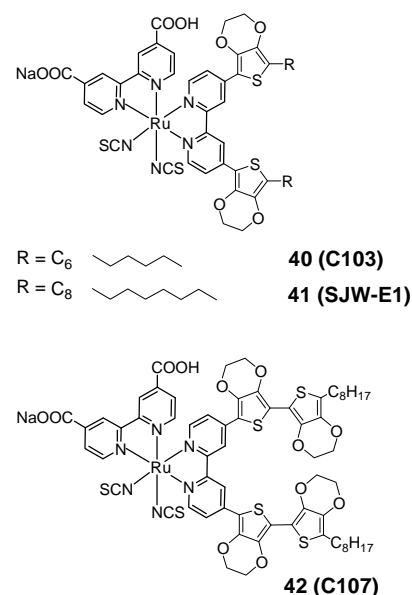


Figure 20. Molecular structures of sensitizers **40** and **41** carrying alkyl-3,4-ethylenedioxythiophene groups and structure of dye **42**, carrying 5-octyl-2,2'-bis(3,4-ethylenedioxy-thiophene moieties).

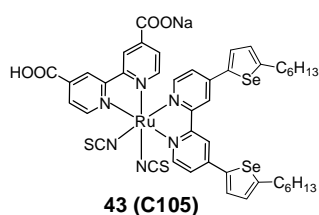


Figure 21. Selenophene based high molar extinction coefficient dye **43**.

The complexes **32** and **34-42** demonstrated the high potential of ruthenium dyes carrying thiophene based ancillary ligands. The DSCs showed excellent photovoltaic performances. Motivated by this and the lower band gap and broader photocurrent response of poly(3-hexylselenophene)^{198, 199} compared to poly(3-hexylthiophene), a hexylselenophene complex (**43**, coded as

C105) was synthesised for the use in L-DSC.²⁰⁰ The molar extinction coefficient of **43** was higher than these of the thiophene and furan analogues (**32** and **33**). The molar extinction coefficient increased in the order **33** (furan) < **32** (thiophene) < **43** (selenophene) corresponding to extinction coefficients of 1.68×10^4 , 1.75×10^4 and $1.84 \times 10^4 \text{ M}^{-1}\text{cm}^{-1}$ at 547, 547 and 550 nm. This order is also consistent with the electropositivity trend and the size of the heteroatom ($\text{O} < \text{S} < \text{Se}$). Sensitizer **43** reached an efficiency of 10.6 % in an L-DSC device using a volatile electrolyte.²⁰⁰

Table 4. Overview of the performances of donor-antenna sensitizers bearing hydrophobic chains tested in L-DSCs as well as S-DSCs (measured under AM1.5, 100 mW/cm²).

Complex	Solar Cell type	Type of HTM ^b	J_{sc} [mA/cm ²]	V_{oc} [V]	FF [%]	η [%]	Ref
31	L-DSC	low volatile	14.61	0.711	67	7.0	¹⁸⁹
32	S-DSC	spiro-OMeTAD	8.193	0.800	69	4.5	¹²²
32	L-DSC	volatile	17.94	0.778	79	11.0	¹⁸⁸
32	L-DSC	low volatile	17.98	0.746	74	9.7	¹⁸⁸
32	L-DSC	ionic liquid	14.77	0.681	74	7.41	¹⁸⁸
33	L-DSC	low volatile	17.80	0.730	73	9.5	¹⁸⁸
34	L-DSC	volatile	19.2	0.776	76	11.29	¹⁶²
34	S-DSC	spiro-OMeTAD	8.27	0.848	71	5.0	¹²⁵
35	L-DSC	volatile	19.5	0.669	66	8.55	¹⁹³
36	L-DSC	volatile	20.05	0.743	77	11.5	¹²⁴
36	S-DSC	spiro-OMeTAD	9.22	0.825	63	4.7	¹²⁴
37	L-DSC	volatile	16.50	0.710	65	7.66	¹⁹⁴
38	L-DSC	volatile	18.32	0.680	72	9.03	¹⁹⁴
39	L-DSC	volatile	17.87	0.760	78	10.53	²⁰¹
39	S-DSC	spiro-OMeTAD	8.386	0.814	69	4.6	¹²³
40	L-DSC	volatile	18.35	0.760	75	10.4	¹⁹⁵
40	L-DSC	low volatile	17.51	0.771	71	9.6	¹¹⁸

Table 4 (continued)

40	L-DSC	ionic liquid	15.93	0.710	75	8.5	¹¹⁸
41	L-DSC	volatile	21.6	0.669	63	9.02	¹⁹⁶
41 ^a	L-DSC	volatile	12.69	0.741	74	6.31	¹⁹⁷
42	L-DSC	volatile	19.18	0.739	75	10.7	¹⁹⁵
43	L-DSC	volatile	18.74	0.754	75	10.61	²⁰⁰

^a **41** was used as sensitizers for a plastic DSC constructed by a low-temperature electrode preparation method using binder-free TiO₂ paste on an ITO-polyethylene naphthalate substrate. ^b Volatile solvents for the electrolyte are on the basis of acetonitrile/valeronitrile and low volatile ones mainly rest upon 3-methoxypropionitrile.

3.1.5 Ion-Coordinating Ruthenium Dyes

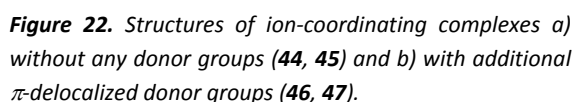
The approach of integrating the so-called ion-coordinating functionalities (*e.g.* oligo ethylene oxide moieties) in ruthenium(II) sensitizers either directly connected to a bipyridyl ligand (Figure 22.a) or to a π -delocalized donor-antenna bipyridyl ligand (Figure 22.b) is an innovative concept to augment the performance of DSCs. In order to understand the benefit of ion-coordinating groups as parts of the sensitizer, it is important to figure out the mode of action of lithium ions in L- and S-DSCs influencing the characteristic parameters of DSCs devices (J_{SC} , V_{OC} and FF). However, the presence of Li⁺-ions causes diverse effects which can act contrary to one another affecting the solar cell performance. Until now, not all impacts of incorporating lithium salt in the HTM of DSCs are understood. Nevertheless, the two main effects will be explained briefly in the following.

TiO₂ band gap effect: Lithium ions are known to adsorb onto the TiO₂ surface or even intercalate into the same.^{139, 202-204} While Li⁺ insertion in rutile-TiO₂ is negligible at room temperature; anatase-based electrodes tend to intercalate Li-ions.²⁰³ This can be ascribed to the different connectivity modes of TiO₆ octahedra. Anatase consists of edge sharing TiO₆ octahedra, providing sufficient space for Li intercalation. Upon Li⁺-insertion serious structural changes occur, *viz.* the original tetragonal anatase host is disordered orthorhombically.²⁰³ Depending on the intercalation/adsorption ratio a band edge shift away from the vacuum level occurs, hence the energetic distance between the redox or HOMO level of the hole transport material and the quasi-Fermi level of electrons in TiO₂ decreases, resulting in an undesired decrease in the open-

circuit voltage.²⁰⁵⁻²⁰⁷ This does not only affect the open-circuit voltage, it also affects the electron injection, charge transport time constants and recombination lifetime of electrons.^{208, 209} For instance, various studies have shown, that improvements of the photocurrent output arise partly from an increase in the efficiency of electron injection from the excited sensitizer after a downward shift of the conduction band.^{208, 210-213} This can be understood as due to the increase in the thermodynamic driving force for injection as a consequence of lowering the TiO₂ band edge relative to the excited state energy level of the sensitizer.²⁰⁸ Furthermore, it was verified that a shift of the band edge or quasi-Fermi level away from the vacuum level slows down the recombination of electrons owing to a decrease in trapped electron density.²¹⁴ In contrast to the downward shift caused by lithium-ions, other ions like Mg²⁺ can shift the Fermi level in the opposite direction, causing higher open-circuit voltages of about 1 V.²¹⁵ Moreover, amines (e.g. tBP) can shift the band edge causing an increase in the open-circuit voltage. The nitrogen containing compounds charge the TiO₂ surface negatively by deprotonating it²¹⁴ or they bring about a dipole moment normal to the TiO₂ surface plane.¹³³

Bulk-effect: Lithium-ions incorporated in the bulk-phase of the hole transport material (liquid or solid) are known to increase the photocurrent output.^{22, 67, 156, 181, 216, 217} In L-DSCs most frequently LiI is integrated in the “bulk” phase of a redox electrolyte delivering Li⁺ and simultaneously I⁻. Typically, an increase in the LiI concentration leads to an increase in the photocurrent density partly due to an increase in conductivity.²¹⁸ At higher concentrations (> 0.3 M), the photocurrent density decreases again due to an increase in the viscosity of the solution which decreases the ion mobility in the solution. The open-circuit voltage decreases as well with an increasing LiI concentration in L-DSCs due to band gap effects and the enhanced production of I₃⁻ (by addition of I⁻ the equilibrium $I^- + I_2 \rightleftharpoons I_3^-$ is shifted towards I₃⁻) which favours back electron transfer.²¹⁸ With regard to S-DSCs, it was reported that the mobility of pristine spiro-OMeTAD can be increased by an order of magnitude due to ionic additives like LiN(SO₂CF₃)₂. Furthermore, a 100-fold increase in conductivity through spiro-OMeTAD within a TiO₂ mesoporous network was observed due to the ionic additive.²¹⁹ It is assumed, that the Li-salt does not appear to p-dope the spiro-OMeTAD, it rather increases the conductivity by a more complicated mechanism whereby the potential landscape and the polarizability of the medium is altered by the ionic additives.^{72, 219} By increasing the conductivity, the internal series resistance is decreased resulting in higher FF values. This effect can be seen either by using standard spiro-OMeTAD^{22, 67} or in particular by using lithium ion binding hole transport materials.^{67, 220, 221}

was designed and synthesised in the hope that the attached alkyl chains imply the advantages of amphiphilic dyes (*cf.* 3.1.2) and prevent dye desorption.^{121, 223} The main drawbacks of **44** and **45**, *viz.* the low molecular extinction coefficient and the high solubility in organic solvents which favours dye desorption, were overcome by sensitizers **46 (K60)**²²⁴ and **47**.²²⁵ Both carry an extended π -conjugated system in combination with ion-coordinating chains.



291

surface and afterwards exposed to a solution of LiI in acetonitrile.^{139, 223, 224} The ATR-FTIR spectra before and after the exposure were monitored. It was observed, that the initial $\nu(\text{C-O})$ stretch peak was partly shifted to lower energies due to the coordination ($\text{C-O}^{\cdots}\text{Li}^+$). Additionally, the initial $\nu(\text{C-O})$ peak was diminished by about 50 % after the exposure, leading to an estimated average of one Li^+ per adsorbed dye molecule. After the films were rinsed with pure acetonitrile, the original spectra were retained. A hint towards coordination even by using a solid HTM was gained by current density measurements in the dark. Plotting the dark current density versus the applied bias, the current density through a Li-doped **Z907** device was approximately three times that of the Li-doped **44** device, although the initial ionic concentration in both devices was identical. The only difference between the **Z907** and **44** based devices is the ion-coordinating side chain. Consequently, the lower current directly indicates that a large portion of the ions are extracted from the bulk phase and immobilized on the surface by the ion-coordinating dye monolayer.²²²

Apart from mechanistic considerations arising from Li^+ and ion-coordinating functionalities, measurements on the recombination dynamics clearly show that ion-coordinating sensitizers are able to reduce recombination times. For instance, measurements of the transient decay of the open-circuit voltage were used to determine the overall charge lifetime of **44** and **Z907** based solid-state devices. The charge separation lifetime for a Li-free **Z907** sensitized device was determined to be 30 μs whereas an increase to 320 μs was observed by the addition of Li^+ -ions. By tethering the Li-ions to the **44** dye, the charge separation lifetime increased even further to 430 μs .²²² Transient absorption measurements on the dynamics of recombination of injected electrons with the oxidized dye were accomplished to estimate the half-reaction times of **44** and **Z907** to be 200 μs and 180 μs , respectively. In the presence of a Li-free redox electrolyte, the decay of the oxidized dye was accelerated. The half-times due to regeneration were measured to be 10 μs and 30 μs for **44** and **Z907**, respectively. Thus, for **44** about 5 % of the initial oxidized species recombine with conduction band electrons whereas the loss is 10-15 % for **Z907**.¹³⁹ The charge recombination rate constant (k_{rec}) was estimated from perturbation open-circuit voltage decay measurements. Here, for a better comparability, a reference dye carrying just methoxy groups (*cf.* Figure 22, R would be -O-Me) instead of ion-coordinating moieties. The k_{rec} decreases in the order reference dye > **44** > **45** indicating reduced recombination behaviour. Additionally, by the measurement of the open-circuit voltage perturbation, the relative position of the energy levels in the TiO_2 with respect to those in the spiro-OMeTAD was estimated to increase in the order reference dye < **44** < **45**. The photocurrent and the voltage also increased in this order.¹²¹

Regarding **46**, the lifetime of the excited state was determined to be 13.2 ns. Due to the fact that electron injection typically takes place within the femtosecond to picosecond time frame, the natural decay cannot compete kinetically with the interfacial charge transport. By nanosecond laser transient absorbance the regeneration of the oxidized dye (**46**) in the presence of a liquid redox electrolyte was estimated to be 10 μ s, whereas the recombination of injected electrons with the oxidized dye was determined to be 200 μ s (the same was measured for **44**).²²⁴ In conclusion, all measured ion-coordinating sensitizers show slower recombination times and faster regeneration compared to reference dyes without ion-coordinating functionalities.

How can these reduced recombination times be rationalized? If Li^+ -ions are really prevented from reaching the surface by ion-coordinating functionalities, there is no reason for a shift of the TiO_2 band edge. However, this not only influences the open-circuit voltage positively, as mentioned before it also affects the electron injection,²⁰⁸ charge transport time constants and recombination lifetime of electrons.²⁰⁹ As further noted, a shift of the band edge or quasi-Fermi level away from the vacuum level would slow down the recombination of electrons²¹⁴ and increase electron injection.^{208, 210-213} But this does not seem to be case for ion-coordinating sensitizers. Here it is assumed, that the tethering of Li^+ -ions to the ion-coordinating functionalities near the interface does not only prevent a decrease of the open-circuit voltage, it is likely to “coulombically” retard recombination by “screening” the electrons in the TiO_2 from the holes in the HTM, thus increasing the activation energy for recombination.^{121, 139, 222} The lithium salt is known to have the ability to screen the electrostatic interactions deriving from Coulomb interactions between photogenerated charges and interface dipoles resulting in an increased charge injecting and reduced recombination, and hence an increase in DSC performance.^{74, 226}

A further contribution to the increased performance of DSCs is expected to arise from the dipole moment.¹³⁹ Permanently adsorbed charge species in combination with the ion-coordinating dye molecule may acts as a dipole at the surface and causes a downward shift in the HOMO level of a solid HTM (e.g. spiro-OMeTAD) with respect to the Fermi level of TiO_2 thereby increasing the quasi energy gap and thus the open-circuit voltage.²²² An evidence for this hypothesis was reported.¹⁰⁴ The introduction of a suitable oriented surface dipole in TiO_2 solar cells has shown to increase the voltage by changing in the band bending at the TiO_2 spiro-OMeTAD interfaces.

Furthermore, under illumination of S-DSCs, it is assumed, that a net positive space charge is formed in the HTM. This induces the generation of a local field that impairs current flow. The

lithium salt is assumed to screen this field, thereby eliminating the space-charge control of the photocurrent.²¹ Additionally, the globally positive charge on the surface is assumed to increase the local concentration of iodide and hence increases the dye regeneration rate.¹³⁹ Both factors can enhance the photocurrent output.

There are two studies focusing on the influence of varying lithium salt concentrations in a redox electrolyte on the performance of L-DSCs.^{139, 223} Without lithium salt, a higher efficiency was reached for the Li⁺-coordinating dye **44** (7.80 %) compared to the amphiphilic dye **Z907** (6.60 %). This was assumed to be due to faster dye regeneration; half-life times of the dye regeneration in the same electrolyte were found to be 10 μ s and 30 μ s for **44** and **Z907**, respectively. By adding Li-salt and successively increasing the Li-concentration of the redox electrolyte, the current density increased for **44** and **Z907**. However, for **Z907** the increase in current density was counterbalanced by a decrease in voltage resulting in almost the same overall efficiency as without salt. Regarding **44**, the voltage also decreased but less leading to higher efficiency (8.10 %). This might be ascribed to the ion-coordinating ability of **44** preventing a fraction of the Li⁺ ions from contacting the surface. High Li⁺ concentrations further reduce the voltage of **Z907** and **44** based devices whereas the voltage of **44** sensitized cells always remained higher.¹³⁹ A similar behaviour was observed for **45**. Here, the current density slightly increased with increasing Li⁺-concentration in the redox electrolyte but decreased again at higher Li⁺ concentrations. Further, it was observed, that the open-circuit voltage successively decreased.²²³

In S-DSCs it was observed, that the open-circuit voltage of **44** based DSCs increased constantly with increasing Li⁺ concentration.¹³⁹ However, for **Z907** the open-circuit voltage was somewhat fluctuating but always remained lower than that of **44** based devices. The authors assumed that in solid-state devices the ion-coordinating sensitizers can hold a high concentration of Li⁺ ions. This prevents the Li⁺-ions from reaching the TiO₂ surface and causes a strong charge screening effect. The latter is believed to reduce recombination and increase the voltage.

The highest reported efficiency for S-DSCs sensitized with **44**, **45**, and **47** are 3.8,²²² 4.51¹²¹ and 3.30 %²²⁵ (the associated characteristic values are listed in Table 5). When compared to a reference dye carrying methoxy groups instead of ion-coordinating moieties, the efficiency of the sensitizers bearing oligo ethylene oxide substituents was enhanced by up to 83 %.¹²¹

Tests regarding the long term stability of **45**-based devices using a low volatile organic solvent electrolyte showed that over 94 % of the initial value was retained after 1 month at 80 °C in the

dark. However, **44**-based DSCs were not stable under similar high temperature accelerated ageing conditions.²²³ **46**-sensitized L-DSCs using also a low volatile electrolyte maintained 94 % of their initial value during 1000 h of ageing at 80 °C²²⁴ and **47**-sensitized L-DSCs using an ionic liquid electrolyte remained 95 % of their initial efficiency under long term accelerated ageing under light soaking conditions (100 mW/cm², 60 °C).²²⁵

Table 5. Overview of the performances of ion-coordinating ruthenium sensitizers tested in L-DSCs as well as S-DSCs (measured under AM1.5, 100 mW/cm²).

Complex	Solar Cell type	Type of HTM ^f	J_{sc} [mA/cm ²]	V_{oc} [V]	FF [%]	η [%]	Ref
44	L-DSC	low volatile	15.40	0.738	69	7.80	139
44 ^a	L-DSC	low volatile	16.60	0.715	68	8.10	139
44 ^b	L-DSC	low volatile	16.86	0.699	68	7.95	139
44 ^c	L-DSC	low volatile	17.71	0.681	66	7.75	139
44	L-DSC	low volatile	14.8	0.730	72	7.7	223
44	S-DSC	spiro-OMeTAD	7.1	0.810	63	3.6	121
44	S-DSC	spiro-OMeTAD	6.8	0.875	65	3.8	222
45	L-DSC	low volatile	14.4	0.762	69	7.6	223
45 ^a	L-DSC	low volatile	14.88	0.737	72	7.89	223
45 ^c	L-DSC	low volatile	15.64	0.689	69	7.44	223
45	S-DSC	spiro-OMeTAD	7.6	0.930	64	4.51	121
46 ^d	L-DSC	low volatile	16.28	0.720	68	8.02	224
46 ^e	L-DSC	low volatile	16.85	0.730	67	8.44	224
47	L-DSC	volatile	18.30	0.682	72	9.02	225
47	S-DSC	spiro-OMeTAD	4.03	0.735	46	1.37	182
47	S-DSC	spiro-OMeTAD	6.75	0.864	57	3.30	225

The electrolyte contained additionally ^a 50 mM, ^b 125 mM, or ^c 250 mM of LiClO₄. ^d Device without any co-adsorbent. ^e Device with the co-adsorbent DPA. The improvement in the performance is ascribed to the formation of a mixed monolayer of **46** and DPA. ^f Volatile solvents for the electrolyte are on the basis of acetonitrile/valeronitrile and low volatile ones mainly rest upon 3-methoxypropionitrile.

Note, that the presence of Li^+ -ions as additive to spiro-OMeTAD is indispensable for S-DSCs; without lithium salt the photocurrent density as well as the open-circuit voltage are extremely low.^{21, 67, 220} Concerning L-DSCs, efficient solar cells can be obtained without Li-salt.

3.2 Phthalocyanine and Porphyrin Dyes

Due to the fact that only very recently a few reviews^{92, 150, 151, 227, 228} about the application of phthalocyanines and porphyrins in DSCs were published, we just highlight here some highly efficient dyes of both classes.

Although, it is well known that polypyridyl ruthenium complexes are currently the best performing dyes among all sensitizer classes ($\eta = 11.5\%$ ¹²⁴ in L-DSCs), there are some disadvantages. Ruthenium is a rare and expensive metal; its complexes can cause undesirable environmental impacts and most importantly they suffer from the lack of absorption in the red/IR-region (ϵ low above $\sim 600\text{ nm}$). However, phthalocyanines and porphyrins are distinguished by their intense absorption in the red/IR-region (Q band). Additionally, mainly abundant and inexpensive metals (*e.g.* Cu and Zn) are used as central metals. Furthermore, the optical, photophysical and electrochemical properties can be systematically tailored by modifying the peripheral substituents, changing the symmetry of the macrocycles and/or the inner metal center.²²⁹ Moreover, phthalocyanines and porphyrins are known for their excellent chemical, light and thermal stability.^{227, 230} The core structures of metallo-phthalocyanines and -porphyrins are shown in Figure 23.

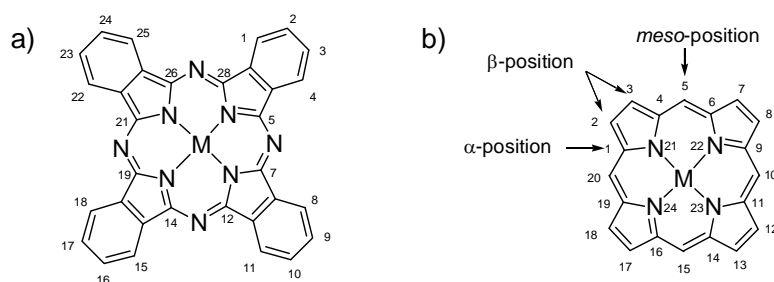


Figure 23. Core structures of a) metallo-phthalocyanines and b) metallo-porphyrins including the atom numbering. M represents the center metal.

In L-DSCs, efficiencies of 3-4 % were reached with phthalocyanines, whereas porphyrins performed more efficient with about 11 % efficiency.

Phthalocyanines do not only exhibit an intense absorption in the red/NIR region (at about 700 nm) due to the Q band, they also show strong absorption in the UV/blue region (at about 300 nm) due to the Soret band. Thus they are transparent over a large region of the visible spectrum. This provides the possibility to use them as sensitizers for “photovoltaic windows”.^{231, 232} The use of red/IR absorbing solar cells instead of simple windows makes it possible to harvest the incident energy of the red/IR region for energy conversion meanwhile the solar heating of buildings is reduced as well as the demand for air-conditioning.²³³ Furthermore, these dyes can be combined with blue/green absorbing dyes in tandem cells or energy transfer systems. Despite favourable absorption properties and suitable energy levels, the reported efficiencies of different metal phthalocyanine sensitized DSC were only about 1 % for a long time.²³⁴⁻²³⁸ This was mainly attributed to aggregation,^{237, 239-241} low solubility and the lack of directionality in the excited state²³³ which influences an efficient electron transfer from the excited dye to the semiconductor.

In order to address the latter issues, unsymmetrically substituted “push-pull” phthalocyanines were developed. The zinc phthalocyanine sensitizer **48** (Figure 24, coded as **PCH001**) is a predecessor of this concept. It was synthesised as an unsymmetrical complex with three bulky *tert*-butyl groups to act as electron-donors. Simultaneously, these groups enhance the solubility, tune the LUMO level and minimize aggregation. But the two electron withdrawing carboxylic acid anchoring groups of **48** are not directly connected to the macrocycle. By using sensitizer **48** in S-DSCs, an efficiency of 0.87 % (AM 1.5, 90 mW/cm²) was reached, whereas in L-DSCs using chenodeoxycholic acid (CDCA) as additive and a volatile electrolyte an efficiency of 3.05 % could be achieved.²³³ This was a breakthrough in the design and development of phthalocyanine-based DSCs.

Later, unsymmetrical push-pull phthalocyanines sensitizers (**49-51**) having conjugated connection between donor, core-complex and acceptor were successfully applied in DSCs. The asymmetry and the created push-pull system generate directionality. This is

important to provide an efficient electron transfer pathway from the excited sensitizer to the conduction band of the semiconductor by electronic coupling between the LUMO of the

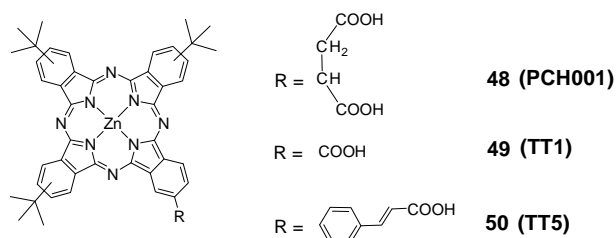


Figure 24. Structures of the phthalocyanine sensitizers **48**, **49** and **50** carrying different anchoring groups.

sensitizer and the Ti 3d orbitals.^{230, 233, 242} Sensitizer **49**, incorporated in an L-DSC with a volatile electrolyte achieved an efficiency of 3.5 %.^{242, 243} Here, the concentration of CDCA used as a co-adsorbent on TiO₂ was optimized.²⁴³ It was found, that CDCA not only reduced the adsorption causing a negative influence on the photocurrent output, but it also increased the open-circuit voltage due to a shift of the TiO₂ conduction band (measured by photovoltage decay) and a small increase in electron lifetime at high CDCA concentrations in the dye-coating solution (60 mM). The peak performance was found at 10 mM CDCA.

A second promising approach which was already successfully applied for DSC on the basis of different dye classes, viz. the combination of two or more dyes by co-sensitization^{90, 244-248} or multilayer co-sensitization,²⁴⁹⁻²⁵¹ was also used for phthalocyanine based DSCs. For this purpose two dyes with complementary absorption were combined; **49** and an the organic dye **82**^{103, 252, 253} denoted as **JK2** (*cf.* Figure 37).²⁴² The mesoporous TiO₂ film was sensitized for 1 and 3 h with solutions of the organic dye and **49**, respectively. The overall device efficiency increased from 3.52 %, for a pure **49** sensitized cell to 7.74 % for the co-sensitized L-DSC. But compared to an L-DSC based solely on the organic dye **82** which showed an efficiency of 7.08 % (under optimized conditions even 8.01 % could be reached²⁵²) the improvement using co-sensitization is negligible. The intrinsic disadvantage of this concept is the limited surface. Always, the available surface area for a second dye is limited by the adsorbed first dye. Hence, the absorptions of the two dyes are counterbalanced by each other so that almost no improvement can be reached. In contrast to that, multilayer co-sensitization seems to have better prospects (*cf.* dye **66**).²⁴⁹

In the course of a study about the structure-function relationship in Zn-phthalocyanines, sensitizer **50** (Figure 24) turned out to be the most efficient one (beside **49**).²⁵⁴ The spacer group between the chromophore and the TiO₂ surface was found to be essential for the performance because it influences the electron injection as well as recombination.²³⁴ By time-correlated single-photon-counting measurements, the yield of electron injection for this dye (and also for others carrying different spacers, including **49**) was determined to be higher than 90 % with electron injection times in the rage of 173-277 ps.²⁵⁴ Furthermore, transient absorption spectroscopy was used to investigate the electron recombination kinetics.²⁵⁴ For **50** an impressive recombination half-time $t_{50\%}$ of 3.9 ms was found (*cf.* about 200 μ s were measured for **Z907**^{169, 175, 176}). Although, another zinc-phthalocyanine sensitizer with a non-conjugated spacer showed in this study a $t_{50\%}$ value of even 11.7 ms, its solar cell performance was very poor (η = 0.4 %). Therefore it is difficult to pinpoint the reason for the good performance of dye **50**.

Currently, the highest efficiency among the phthalocyanines (4.6 %) was reached with sensitizers **51** (coded as **PcS6**).²⁵⁵ All phthalocyanines sensitizers presented before were substituted by *tert*-butyl groups, but the fact, that for efficient DSC still a co-adsorbent (*e.g.* CDCA) was needed to prevent aggregation arising from π - π stacking shows, that the bulkiness of these groups is not sufficient. Hence, bulkier groups like 2,6-diphenylphenoxy moieties were used to create highly sterically hindered Zn-phthalocyanines.²⁵⁶ The three dimensional enlargement of the molecular structure prevents aggregation almost completely without wasting surface space for co-adsorbents. This was proven by UV/vis spectroscopy. The absorption of **51** in solution as well as adsorbed on TiO₂ showed just a weak blue-shifted shoulder peak of the Q band around 630 nm which can be assigned to H-aggregate species.²⁵⁵

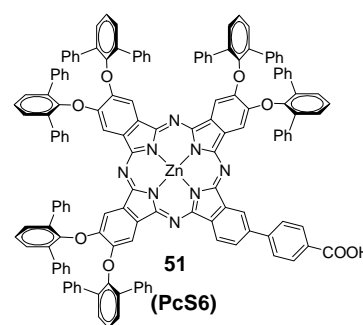


Figure 25. High efficient phthalocyanine sensitizer **51**.

Table 6. Overview of the performances of phthalocyanine sensitizers tested in L-DSCs as well as S-DSCs (measured under AM1.5, 100 mW/cm²).

Complex	Solar Cell type	Type of HTM ^d	J_{sc} [mA/cm ²]	V_{oc} [V]	FF [%]	η [%]	Ref
48 ^a	L-DSC	volatile	6.5	0.635	74	3.05	233
48 ^b	S-DSC	spiro-OMeTAD	2.1	0.72	52	0.87	233
49 ^a	L-DSC	volatile	7.60	0.617	75	3.52	242
49 ^a	L-DSC	volatile	7.78	0.611	75	3.56	243
49 ^c	L-DSC	volatile	16.20	0.666	72	7.74	242
50 ^a	L-DSC	volatile	6.80	0.613	74	3.10	254
51	L-DSC	volatile	10.4	0.630	70	4.6	255

^a CDCA was used as co-adsorbent to reduce aggregation. ^b Measured at 90 mW/cm². ^c Co-sensitized with **82** (Figure 37). ^d Volatile solvents for the electrolyte are on the basis of acetonitrile/valeronitrile.

Similar to phthalocyanines, *porphyrins* possess an intense Soret band at about 400 nm and a moderate Q band at about 600 nm. The porphyrin skeletal structure is symmetrical (D_{4h} symmetry) and the π -electrons are, in the ground state as well as in the excited state,

delocalized over the whole structure.¹⁵¹ In the beginning of using porphyrins as sensitizers in DSC, the efficiencies were quite low.^{151, 257-259} But it was known, that zinc improves the solubility and shifts the LUMO as well as HOMO to higher energy levels.¹⁵¹ Additionally, symmetrical porphyrins exhibit long-lived (>1 ns) π^* singlet excited states, only weak singlet/triplet mixing and appropriate HOMO/LUMO levels for electron injection and dye regeneration.²⁶⁰ Further it was known, that *meso*-phenyl groups extend the π -system and can act as spacer between anchoring group and chromophore to reduce the rate of recombination. Surprisingly, it was found that the rate of recombination as well as the rate of injection of symmetrical free base and zinc porphyrins are very similar to that of ruthenium complexes (**N3**, Figure 7) although the delocalization of the cation is very different and the redox potentials are not equal.²⁶¹ It was revealed, that the lower efficiencies of porphyrins is a result of the increased probability of excitation annihilation due to the strong transition dipole of porphyrin single excited state which allows rapid migration of the excited state between neighbouring dyes at a high dye coverage.²⁶¹ The poor performance was also assigned to the insufficient light harvesting capability of porphyrins and the effect of electronic coupling between the porphyrin and the TiO_2 surface as well as the formation of molecular aggregates.⁹² It was suggested, that low-symmetric structures are important for efficient charge separation. The loss of symmetry, not only creates directionality, but also caused a broadening as well as a red-shift of the absorption and an increase in the Q band relative to the Soret band. Today, unsymmetrical metal porphyrin sensitizers reach peak overall efficiencies of about 6-7 %.²⁶²⁻²⁶⁸ However, only lately a porphyrin with an impressive efficiency of 11 % was published.²⁶⁹

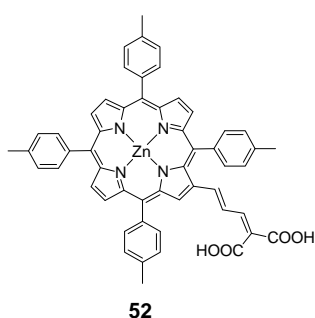


Figure 26. High efficient porphyrin sensitizer **52**.

Until recently, the best performance for porphyrin sensitized DSCs was reached with sensitizer **52**. The dye gave an efficiency of 7.1 % with a liquid volatile redox electrolyte and 3.6 % by using spiro-OMeTAD as solid HTM.²⁶² **52** emerged from a whole series of porphyrins with different aromatic (donor) substituents (*e.g.* 4-ethyl phenyl, 4-(*n*-butyl)phenyl and 4-(*n*-octyl)phenyl, or the here shown 4-methylphenyl group) attached to the *meso*-position while keeping the conjugated malonic acid anchoring group in one β -position. All dyes show a red-shift of the absorption

compared to a non-substituted porphyrin. The exact identity of the alkyl-phenyl group virtually influences neither the band position nor the molar extinction coefficient. Additionally negligible variations were observed for the HOMO (~ -5.16 eV) and LUMO (~ -3.08 eV) levels relative to the

vacuum level. Nevertheless, the efficiency decreased from 7.1 to 5.8 % by replacing the methyl groups of **52** with ethyl groups. Possibly, it is influenced by device preparation parameters as shown for sensitizers **53-55**.²⁶⁷

In a study concerning dyes **53-55** and also in other studies, it was demonstrated, that the efficiency strongly depends on the immersing time for dye-coating.^{267, 270, 271} For **54** it became obvious, that the efficiency at first increases rapidly with increasing immersion time and then decreased gradually (the peak value was reached below 1 h immersing time).²⁶⁷ This is not due to the surface concentration Γ , because Γ increases very rapidly

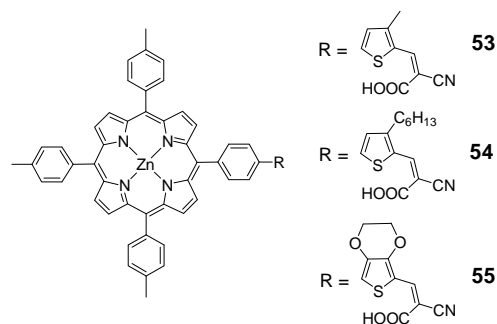


Figure 27. Structures of a series of thiophene-linked porphyrin sensitizers (**53-55**).

and remains constant. Hence, the decline of the efficiency seems to be due to a change in orientation at longer immersing times. The highest efficiencies for **53-55** were reached by immersing the TiO_2 electrode for 15 min. (Note that dye-coating with Ru-dyes usually takes place over night or at least some hours.) These sensitizers also follow the donor- π bridge-acceptor/push-pull concept, where the *meso*-tris(4-methylphenyl) porphyrin acts as donor, the cyanoacrylic acid as acceptor and the different thiophene derivatives as π -bridge. The thiophene derivatives were introduced to enhance light absorption and affect electron injection, whereas EDOT features a small torsion angle with the adjoining phenyl fragment. Again, for compounds **53-55** a broadening of the absorption accompanied by a red-shift was observed. The solar cell performance of these three dyes shows, that they differ just in the short-circuit current densities ($J_{sc} = 12.83, 13.71$ and 15.59 mA/cm^2 for **53**, **54** and **55**, respectively). The poor performance of the 3-*n*-hexylthiophene derivative **54** was ascribed to the lowest Γ value in this series (1.8×10^{-8} , 0.23×10^{-8} and $1.3 \times 10^{-8} \text{ mol/cm}^2$ for **53**, **54** and **55**, respectively). Despite the high Γ value of **53**, the photocurrent output is still low. For **55**, carrying the EDOT groups, Γ showed a moderate value, but the highest current value was measured.²⁶⁷ The degree of aggregation of these dyes under the applied condition of dye-coating is to be studied to quantify the performance differences.

Sensitizers **56-61** (Figure 28)

emerged as the most efficient dyes of comprehensive studies about asymmetrically *meso*-substituted zinc donor- π bridge-acceptor porphyrins published by Yeh, Diau and co-workers.^{263, 265, 266}

All these porphyrin sensitizers carry different alkyl-functionalized donor groups (*cf.* amphiphilic ruthenium-dyes) and one anchoring group at the *meso*-positions. For **56-58** the only difference is the π -bridge between chromophore and anchoring moiety.²⁶³ By replacing the phenyl π -bridge of **56** with naphthalene

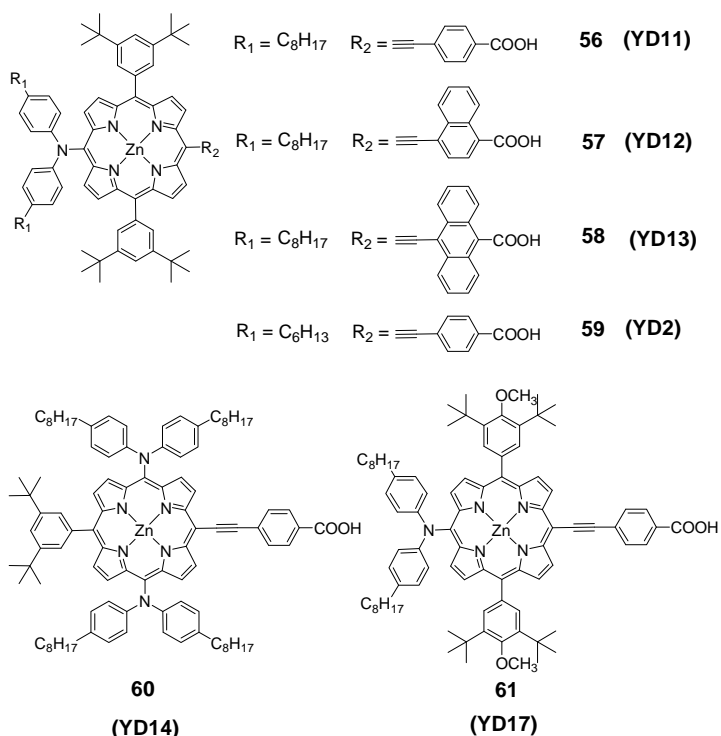


Figure 28. Selection of efficient donor- π bridge-acceptor porphyrins (**56-61**) belonging to the YD-series.

(**57**) and anthracene (**58**), an increasing broadening of the absorption spectra accompanied by a red-shift occurs, which reflects the increasing extension of the π -system. Additionally, the HOMO/LUMO levels of all sensitizers were found to be comparable. Nevertheless, the photovoltaic performance of **58** was far below that of **56** and **57**, whereas **56** and **57** performed very similar. The reason for that behaviour was revealed by femtosecond fluorescence decay measurements. The determined quantum yields for electron injection were found to be 83, 83 and 62 % for **56**, **57** and **58** respectively. The low electron injection caused low photocurrents and hence a low overall efficiency in **58** sensitized L-DSCs. There are two possible explanations for the reduced electron injection ability of **58**: Anthracene can either a) induce rapid intramolecular relaxation due to effective vibronic coupling and/or b) cause intermolecular relaxation due to aggregation. Time correlated single photon counting was used to determine the lifetime of the excited states of **56-58**, which were found to be equal, thus eliminating the possibility a). To verify the possibility b), photovoltaic measurements of the sensitizers co-adsorbed with a large amount of CDCA were performed. It was found, that for **56** and **57** the photocurrent output decreased (due to a lower dye uptake) whereas a significant increase was observed for **58** (due to reduced aggregation).²⁶³

Sensitizer **59**, also belonging to the YD-series, shows an almost negligible structural difference compared to **56**, viz. the length of the alkyl chain was changed from C₈ to C₆. This was also reflected by the comparable efficiency of about 7 %.^{263, 265, 266} But optimized by Grätzel and co-workers, **59** reached an impressive efficiency of about 11 %.²⁶⁹ To the best of our knowledge, this is the highest reported value for a porphyrin sensitized L-DSC.

In extension of the YD-series, different phenyl, diarylamino and/or triphenylamino moieties were induced at the *meso*-positions to create a push-pull framework for high efficient L-DSCs.²⁶⁵ Among these, **60** and **61** showed the best overall performance with an efficiency of ~ 7 %.

Table 7. Overview of the performances of porphyrin sensitizers tested in L-DSCs as well as S-DSCs (measured under AM1.5, 100 mW/cm²).

Complex	Solar Cell type	Type of HTM ^b	J_{sc} [mA/cm ²]	V_{oc} [V]	FF [%]	η [%]	Ref
52	L-DSC	volatile	14.0	0.680	74	7.1	²⁶²
52	S-DSC	spiro-OMeTAD	7.4	0.780	62	3.6	²⁶²
53	L-DSC	low volatile	12.83	0.640	68	5.55	²⁶⁷
54	L-DSC	low volatile	13.71	0.630	67	5.80	²⁶⁷
55	L-DSC	low volatile	15.59	0.640	65	6.47	²⁶⁷
56^a	L-DSC	volatile	14.01	0.716	68	6.79	²⁶³
57^a	L-DSC	volatile	14.23	0.717	68	6.91	²⁶³
58^a	L-DSC	volatile	4.12	0.630	72	1.86	²⁶³
59^a	L-DSC	volatile	13.40	0.710	69	6.56	²⁶⁶
59^a	L-DSC	volatile	14.80	0.714	67	7.1	²⁶⁵
59^a	L-DSC	volatile	18.6	0.770	76	10.9	²⁶⁹
60	L-DSC	volatile	14.27	0.712	67	6.8	²⁶⁵
61	L-DSC	volatile	13.99	0.722	69	7.0	²⁶⁵

^a CDCA was used as co-adsorbent to reduce aggregation. ^b Volatile solvents for the electrolyte are typically on the basis of acetonitrile/valeronitrile and low volatile ones mainly rest upon 3-methoxypropionitrile.

4 ORGANIC SENSITIZERS IN DYE-SENSITIZED SOLAR CELLS

Recently, comprehensive reviews on organic dyes for DSCs were published by Ooyama and Harima⁹² and by Bäuerle and co-workers.⁹⁰ We just concentrate here on the general properties of organic sensitizers and emphasise the high efficient dyes of the most promising classes of organic sensitizers in a compact form.

Organic dyes in general are very promising for the use as sensitizers for DSCs because (i) they can be synthesised and purified very easily at low costs, (ii) they do not contain rare and expensive metal, (iii) they have in particular extremely high extinction coefficients which facilitate a high light harvesting ability and hence reduce the optical depth so that organic dyes are suitable for thinner semiconductor electrodes, and (iii) a variety of possible functional groups and their facile modification provide the opportunity to tune the spectral, photophysical, photochemical and electrochemical properties very well considering structure-property relationships.^{90, 92, 272}

However, the performance of organic dyes for L-DSCs is currently still inferior compared to that of metal-organic dyes (which achieve η values about 11 %^{124, 160-162, 263}). Generally, S-DSCs follow this order except for S-DSCs using an indoline dye in combination with PEDOT as HTM.¹²⁷ This can be ascribed to some of the typical disadvantages of organic dyes such as (i) their narrow absorption bands in the visible region of the electromagnetic spectrum, which limits the light harvesting ability, (ii) their tendency towards π - π -stacking (aggregation), which reduces the electron injection rate by intermolecular energy transfer and excited state quenching, (iii) their lower stability, which may arise from the formation of excited triplet states and unstable radicals under illumination,^{273, 274} (iv) their short emission lifetimes of excited states, which are often shorter than those of metal complexes.^{91, 275, 276} The latter aggravates charge separation because the electron injection has to be faster than the dye's emission lifetime to achieve efficient charge separation.^{275, 277} A large electronic coupling between dye and semiconductor can facilitates fast injection.²⁷⁸

To match the general requirements of sensitizers (*cf.* section 2.1.4) and to overcome or minimize the disadvantages, an appropriate design concept for organic sensitizers is needed. Commonly, organic dyes follow the donor- π -bridge-acceptor concept. On the basis of the data obtained from literature, it was stated that electron-rich aryl amines like aminocoumarins, (difluorenyl)phenylamines, triphenylamines and indolines are ideally suitable as donor groups,

whereas cyanoacrylic acids and rhodanine-3-acetic acids are perfect acceptor and anchoring groups.⁹⁰ Additionally, it was found that the π -bridges are frequently based on thiophenes (*e.g.* oligothiophenes, thienylenevinylenes, or dithienothiophenes) or phenylenevinylenes due to their excellent charge transport properties.⁹⁰

At present, a large variety of different sensitizer classes are successfully applied in DSC such as BODIPYs ($\eta = 1.66\%$ ²⁷⁹ for L-DSC, volatile; $\eta = 0.68\%$ ²⁸⁰ for S-DSC, spiro-OMeTAD), polymer sensitizers ($\eta = 2.4\%$ ²⁸¹ for L-DSC, volatile; $\eta = 0.9\%$ ¹²⁸ for S-DSC, spiro-OMeTAD), squaraines ($\eta = 5.40\%$ ²⁸² for L-DSC, volatile; $\eta = 3.8\%$ ²⁸³ for S-DSC, P3HT), hemicyanines ($\eta = 6.3\%$ ²⁸⁴ for L-DSC, low volatile), perylenes ($\eta = 6.8\%$ ²⁸⁵ for L-DSC, volatile; 3.2% ²⁸⁶ for S-DSC, spiro-OMeTAD), cyanines ($\eta = 7.6\%$ ²⁸⁷ for L-DSC, volatile), coumarins ($\eta = 8.2\%$ ²⁸⁸ for L-DSC, volatile), indolines ($\eta = 9.5\%$ ²⁸⁹ for L-DSC, volatile; $\eta = 4.1\%$ ²⁹⁰ / 4.2% ²⁹¹ for S-DSC, spiro-OMeTAD; $\eta = 6.1\%$ ¹²⁷ for S-DSC, PEDOT) and oligothiophene bridged arylamine donor dyes ($\eta = 10.1\%$ ¹¹⁷ for L-DSC, volatile; $\sim 4.8\%$ ^{292, 293} for S-DSC, spiro-OMeTAD). (see Table 8) Note that this is only a selection of promising and efficient organic dye classes, a lot more were successfully tested in DSCs.^{90, 92, 294-296}

4.1 BODIPY Dyes

BODIPY dyes (4,4-difluoro-4-bora-3a,4a-diaza-s-indacens)²⁹⁷⁻²⁹⁹ were prepared for the first time in 1968 by Treibs and Kreuzer.³⁰⁰ Later, they were employed as laser dyes³⁰¹ and reagents for biological labeling.³⁰² Only very recently scientists started to regard them as interesting candidates for DSC^{279, 280, 303-305} and bulk heterojunction solar cells.³⁰⁶⁻³⁰⁸ Since these dyes are getting applied in DSCs the efficiency values reported did not yet exceed 2 %. However, the BODIPY complexes are promising due to their outstanding properties such as their excellent thermal and photochemical stability, chemical robustness, good solubility, absence of toxicity,³⁰⁴ suitable redox levels, inherent directionality,²⁷⁹ high fluorescence quantum yield, modest stokes shift, negligible triplet formation, long excited state lifetimes³⁰⁹ and their intense absorption profile.²⁹⁷ The latter can be easily influenced by substituents which can shift the absorption up to red/near IR region while keeping very high molar extinction coefficients. This emphasizes BODIPY derivatives as potential aspirants not only for L- but also for S-DSCs.

For L-DSCs, the highest reported efficiency (1.66 %) was reached by the BODIPY sensitizer **62** depicted in Figure 29.²⁷⁹ This sensitizer carries triphenylamine electron-donating groups and a 2-cyano-3-phenylacrylic acid electron-withdrawing unit at the *meso*-position (λ_{max} at about 700 nm, ϵ at peak value about $6.9 \times 10^4 \text{ M}^{-1}\text{cm}^{-1}$). It was found that an inherent asymmetry in charge redistribution occurs upon excitation (S_0 - S_1 transition) which increases the charge density on the *meso*-position while decreasing it in most other positions. Hence, the *meso*-carbon (C-8) seems to be the preferable position for attaching an anchoring group. Furthermore, the HOMO/LUMO levels were determined to be -5.09 and -3.52 eV, respectively and thus they are suitable for electron injection and dye regeneration. In a recent report, the same dye (**62**) was successfully applied as red absorbing sensitizer in an S-DSC device ($\eta = 0.68 \%$). These preliminary results of this emerging dye class are encouraging.

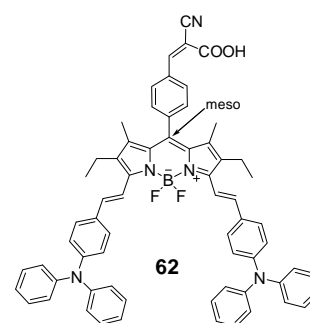


Figure 29. BODIPY dye **62** carrying two triphenylamine donor groups.

4.2 Polymer Sensitizers

Recently, polymeric sensitizers started to gain interest as an attractive alternative to commonly used low molecular weight dyes.^{128, 281, 310-316} Although, the performance of these sensitizers is quite low at the moment, conjugated polymers feature low costs, high absorption coefficients in the visible part of the spectrum, simple synthesis, capability for mass production and high charge carrier mobilities.³¹³ In combination with polymeric hole conductors, polymer sensitized DSCs offer a possibility for all-polymer and flexible S-DSCs.

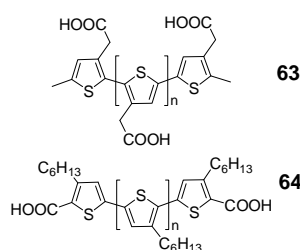


Figure 30. Structures of P3TAA (**63**) and regioregular, carboxylic acid end group functionalized P3HT (**64**) used as sensitizers for L- and S-DSCs, respectively.

Yanagida and colleagues reported polymer sensitized L-DSCs on the basis of poly(3-thiophenylacetic acid) (P3TAA, **63**) chemisorbed on TiO_2 or SnO_2 -ZnO electrodes.²⁸¹ P3TAA is a carboxylic acid functionalized derivative of one of the best known conjugated polymers poly(3-hexylthiophene) (P3HT); it possess an appropriate band matching with many inorganic semiconductors used in DSCs.³¹⁷ The best performance for a polymeric sensitizers ($\eta \sim 2.4 \%$ ²⁸¹) was reported for **63** sensitized TiO_2 DSCs employing a volatile

liquid electrolyte additionally containing an ionic liquid.^{313, 318} Although, the current density was quite high ($J_{SC} = 9.76 \text{ mA/cm}^2$), the open-circuit voltage was very low ($\sim 400 \text{ mV}$). This was assumed to be due to the protonation of the surface by the polymer.²⁸¹ Poly(3-thiophenemalonic acid) carrying two carboxylic acid groups per monomer delivered an even lower open-circuit voltage (365 mV).³¹³ Until now, there is only one report about a polymer sensitizer applied in a classical S-DSC on the basis of TiO_2 and spiro-OMeTAD.¹²⁸ Highly regioregular P3HT (**64**) with carboxylic acid end groups was synthesised in our group and tested as sensitizer ($\eta = 0.9 \%$). P3HT in general is known for its strong absorption between 450 and 600 nm and its high charge carrier mobility of up to $0.1 \text{ cm}^2 \text{ V}^{-1} \text{ s}^{-1}$.³¹⁹ Additionally, it carries alkyl side chains which facilitate its solubility and it can self-assemble on surfaces.³¹⁵ The low efficiency of polymer sensitizers may be ascribed to a lack of optimization, the fact that polymers suffer from their small absorption overlap with the solar spectrum and that the polymer chains can cause a clogging of the pores of the mesoporous TiO_2 electrode which can slow down regeneration.³¹⁵

4.3 Squaraine Dyes

Squaraines are a well investigated class of organic dyes which was first reported by Treibs and Jacob in 1965.³²⁰ Squaraines suitable for a broad range of applications such as nonlinear optics, imaging, photodynamic therapy, ion sensing and photovoltaics.³²¹ Typically, squaraine sensitizers contain an electron deficient central four membered ring (derived from the squaric acid) and two electron donating groups, resulting in a resonance stabilized planar zwitterionic structure. The strong absorption ($\epsilon > 10^5 \text{ M}^{-1} \text{ cm}^{-1}$) in the visible to near-IR region and the photostability favours these molecules to be used as sensitizers. On the basis of theoretical calculations it was proposed that the ground state and the excited singlet state of squaraines involve intramolecular charge transfer. Hence, the S_0 - S_1 excitation is a charge transfer transition. Combining this consideration with an extended π -donor framework gives an explanation for the featured absorption behaviour.³²¹

Squaraines achieve moderate photovoltaic performances in both, L- and S-DSCs, whereas the best performing squaraines are very similar to each other (*cf.* Figure 31).^{282, 283, 322} In general, unsymmetrical squaraines perform better than symmetrical ones.³²³ The unsymmetrical dye **65**, which reached an efficiency of 5.4 % in an L-DSC, shows a strong absorption in the far red region

($\lambda_{\text{max}} = 662$, $\epsilon = 3.2 \times 10^5 \text{ M}^{-1}\text{cm}^{-1}$), suitable HOMO/LUMO levels (-5.31 and -3.72 eV, respectively) but suffers from aggregation which can be partly suppressed by CDCA.²⁸² **66** shows a slightly diminished absorption in the far red region due to a less delocalized π -system ($\lambda_{\text{max}} = 647$, $\epsilon = 2.9 \times 10^5 \text{ M}^{-1}\text{cm}^{-1}$), but also suitable HOMO/LUMO levels (-5.33 and -3.73 eV, respectively).²⁸² **66** was

successfully employed in an S-DSC device where TiO_2 nanotube arrays and regioregular P3HT were used as electron transport material and HTM, respectively.²⁸³ It was assumed that the high efficiency ($\eta = 3.8\%$) arose from the combination of an organic dye and P3HT. Here, the normal process of excitation of the organic dye, electron injection and subsequent regeneration by the HTM (P3HT) is thought to be complemented by exciton generation in the P3HT phase, diffusion of the excitons to the P3HT/dye interface, dissociation of the excitons at the interface in electrons and holes whereas the electrons travel through the dye to the TiO_2 surface. Hence, both the complementary absorbing sensitizers contribute to the photocurrent generation. This was proven by IPCE measurements.²⁸³ Besides this, squaraines were also applied in co-sensitized DSC with the complementary absorbing low molecular weight dye **82** depicted in Figure 37.²⁴⁷⁻²⁴⁹ Here, efficiencies of up to 8.65% were reached by a novel way of co-sensitization where a primary monolayer of dye is spatially separated from a second monolayer of another dye using Al_2O_3 (resulting architecture: $\text{TiO}_2/\text{Dye1}/\text{Al}_2\text{O}_3/\text{Dye2}$).²⁴⁹

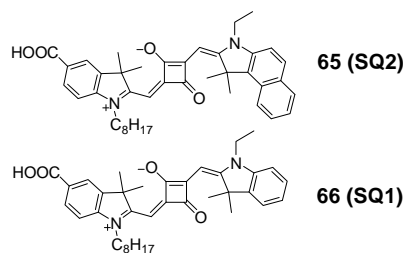


Figure 31. Molecular structures of the squaraine sensitizers **65** and **66**.

4.4 Perylene Dyes

Perylenes are distinguished for their outstanding chemical, thermal and photochemical stability,²⁸⁵ non-toxicity, high stability and broad absorption spectra.²⁸⁶ However, the power conversion efficiency of perylene derivatives used as sensitizers in DSCs remained low ($\eta < 2\%$)³²⁴⁻³²⁶ due to aggregation and energy-level matching issues.^{285, 327, 328} The low electron-donating ability of perylenes imides (*i.e.* the LUMO is energetically very close to conduction band of TiO_2) impedes efficient electron injection.³²⁷ Substituents at the bay positions are known to tune the HOMO/LUMO levels and thereby the absorption behaviour. Hence, strongly electron donating perylenes with electron-rich substituents at the perylene core (bay-positions) were synthesised and applied in DSCs.^{285, 327, 328}

The most well performing perylene dye reported in L-DSCs is **67**.²⁸⁵ It shows an efficiency of 6.8 % due to (i) a broad absorption (400-750 nm) with intramolecular charge transfer character, (ii) the high molar extinction coefficients (1.37×10^4 and $2.27 \times 10^4 \text{ M}^{-1}\text{cm}^{-1}$ at 462 and 620 nm, respectively), (iii) reduced aggregation as a consequence of the bulky side groups and (iv) the appropriate HOMO/LUMO location and levels for a

more efficient electron injection and dye regeneration.²⁸⁵ It is known, that upon adsorption on TiO_2 , perylene anhydrides like **67** show a blue-shift of the absorption. This is attributed to a ring opening of the anhydride group to form two carboxylates which indeed facilitate a strong coupling between the dye and TiO_2 , but concomitantly cause a further negative shift of the energy levels.²⁸⁵ Nevertheless, the energy levels of **67** bearing two thiophenol groups in the 1 and 6 positions are even after the ring opening suitable for efficient electron injection and regeneration by a liquid electrolyte.

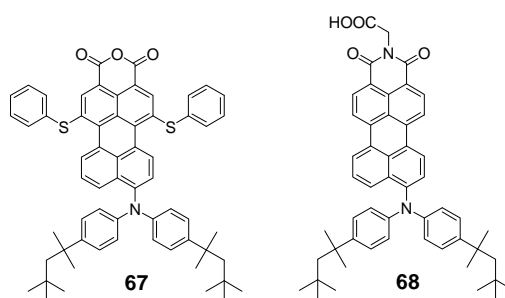


Figure 32. Chemical structures of the best performing perylene sensitizers **67** and **68** for L- and S-DSCs, respectively.

With regard to S-DSC applications, **68** was found to be an efficient sensitizer.²⁸⁶ To prevent the energetically negative effects caused by the adsorption of perylene anhydrides, the anhydride anchor was replaced by a carboxylic acid anchor attached to a perylene monoimide. By cyclic voltammetry in solution, it was found that the LUMO is about 0.14 eV more positive than the conduction band level which should provide an appropriate driving force for electron injection. Efficient DSCs could only be manufactured if the standard additive *t*BP was omitted because it is known to shift the conduction band to more positive potentials which can cause an increase in the open-circuit voltage but also causes a hindering of the electron injection into TiO_2 in perylene-sensitized DSCs.^{113, 133, 214} In fact, the dye worked well in *t*BP free S-DSCs ($\eta = 3.2 \%$) but not in L-DSCs. The observation suggests a different injection mechanism for L- and S-DSCs, which were discussed but not yet completely understood.^{286, 291, 329, 330}

4.5 Cyanine Dyes

By definition, cyanines comprise of an electron withdrawing quaternary ammonium group and a ternary electron donating amino group which are connected by methine ($-\text{CH}=\text{CH}-$) or other conjugated units. Depending on whether the nitrogen atoms are parts of heterocyclic rings or

carry aliphatic groups, the cyanines are classified as open chain cyanines, the so called streptocyanines ($R_2N^+=CH[-CH=CH]_n-NR_2$), hemicyanines ($Aryl=N^+=CH[-CH=CH]_n-NR_2$) and closed chain cyanines which are seen as the classical cyanines ($Aryl=N^+=CH[-CH=CH]_n-N=Aryl$). Attractive for DSCs are only the last two types. These cationic donor- π bridge-acceptor molecules feature high extinction coefficient absorption bands in the visible region (~ 450 - 600 nm, $\epsilon_{\max} \sim 10^5 \text{ M}^{-1}\text{cm}^{-1}$) which are of charge transfer character and their absorption will undergo a red-shift upon increasing the electron donating and withdrawing ability of the donor and acceptor groups, respectively.³³¹ Additionally, they are characterised by their tendency for aggregation in solution as well as at the solid-liquid interface.^{330, 332} A head-to-tail arrangement results in a formation of red-shifted J-aggregates, a plane-to-plane stacking causes blue-shifted H-aggregates and the formation of Herring-bone aggregates induces both a higher and lower wavelength band.³³² In various studies, the influence of aggregation of cyanines on the photosensitization was investigated.^{244, 330, 332, 333} It was found that besides the monomer form also the aggregated forms can contribute to photoinduced electron injection in TiO_2 , but how effective the aggregate based electron injection is, depends on the respective dye. Furthermore, it is known that cyanines can suffer from *cis-trans* photoisomerisation inducing a decay of excited states.²⁷⁶

Characteristically, the donor part of *hemicyanines* comprises of *p*-dialkylaminophenyls and for the cationic acceptor part often benzo- and naphthothiazolium, pyridinium and indolium salts are employed. Methine units ($-CH=CH-$) are used to connect both parts.⁹² As anchoring units sulfonate, carboxyl and hydroxy groups were found to be suitable. The efficiency of the DSC devices is strongly depended on the anchoring groups. It decreased in the order: carboxyl + hydroxyl > carboxyl > sulfonate + hydroxyl.³³¹ The best performing representatives of this class is **69**, it exhibited a high overall efficiency of 6.3 % (at 80 mW/cm^2 , white light from a Xe lamp) by using a liquid electrolyte based on propylene carbonate.²⁸⁴ The major structural difference to other less performing hemicyanines is the presence of the hydroxy group in **69**. Considering the anchoring capability of this group along with the sulfonate anchoring group, the contact area between the dye and the TiO_2 nanoparticles should be increased resulting in a decreased dye loading (which was confirmed by absorption measurements of the desorbed dye) and maybe an enhanced electron injection.²⁸⁴

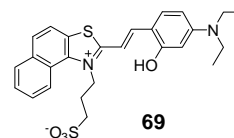


Figure 33. Molecular structure of the hemicyanine sensitizer **69**.

Regarding to *cyanines* it was found, that unsymmetrical derivatives perform superior compared to their symmetrical counterparts due to directionality which facilitates electron flow from the donor to the acceptor moiety carrying the anchoring group.³²³ As a reminder, the same was found for phthalocyanines, porphyrins and squaraines. Additionally, by systematic investigations it was found that (i) the absorption maxima of cyanines shifts (by about 100 nm) to longer wavelength with each increase of one methine unit (ii) the IPCE decreases with increasing number of methine units because the LUMO level shifts to more negative values (*i.e.* energetically closer to the conduction band level of TiO₂) with increasing number of methine units, (iii) the IPCE increases with decreasing distance between the cyanine skeleton and the TiO₂ surface due to a more stable charge transfer state and (iv) the photocurrent output of cyanine sensitized electrodes increased with a shift of the conduction band in the order NB₂O₅ < TiO₂ < ZnO < SnO₂.³³⁴

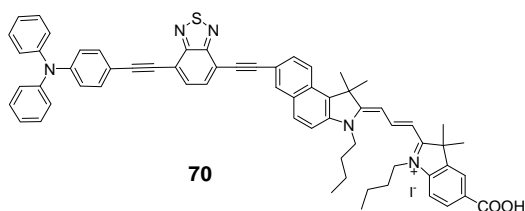


Figure 34. Structure of the efficient cyanine sensitizer **70**.

Regarding L-DSCs, the best performing cyanine dye **70** was reported by Tian and co-workers.²⁸⁷ It contains a carboxylic acid acceptor/anchoring group, a triphenylamine donor group and a bridging low-band-gap benzothiadiazole connecting the donor and the cyanine

skeleton. The HOMO/LUMO values were determined to be -5.73 eV and -3.82 eV, respectively and Herring-bone aggregates were assumed to broaden the absorption spectrum benefiting the photoelectrical conversion. The efficiency was found to be 7.62 % (measured under irradiation with a Xe lamp at 75 W/cm²) with an photocurrent output of 22.10 mA/cm² (Under the same conditions, the efficiency of the Ru(II) dye **N719** was found to be 9.5 %; J_{SC} = 27.25 mA/cm², V_{OC} = 0.640 V, FF = 41 %). Regarding S-DSCs cyanines are in their infancies and the reported efficiencies are still low.³³⁵

4.6 Coumarin Dyes

Coumarins are known for their good photoresponse in the visible region, the tunability of the absorption,³³⁶ good long-term stability³³⁷ and suitable HOMO LUMO levels/locations.³³⁸ They are based on the donor- π bridge-acceptor concept using the coumarin derivative 1,1,6,6-tetra-

methyl-10-oxo-2,3,5,6-tetrahydro-1H,4H,10H-11-oxa-3a-aza-benzo[de]anthracene-9-yl as donor and (cyano)acrylic acid as acceptor connected by different π -conjugated bridges (cf. Figure 35).

A cyanoacrylic acid anchoring group was found to be more beneficial than a simple acrylic acid group, because the cyano units are known to shift the LUMO level more positively due to their strong electron accepting ability. Furthermore, they decrease the HOMO/LUMO band gap resulting in an increased efficiency in L-DSCs. For example, the η value for the acrylic acid anchoring coumarin **72** is 3.4 %, ²⁷⁵ whereas the cyanoacrylic acid anchoring coumarin **73** delivers 4.1 %. ²⁷⁵

donor	π bridge	acceptor	denotation	η [%]
			71 (NKX-2700)	8.2
			72 (NKX-2398)	3.4
			73 (NKX-2388)	4.1
			74 (NKX-2311)	6.0
			75 (NKX-2586)	3.5
			76 (NKX-2593)	7.2
			77 (NKX-2677)	7.7
			78 (NKX-2697)	5.3

Figure 35. Selection of different coumarin donor- π bridge-acceptor sensitizers **71-78**. Note that the values for the L-DSC efficiencies are taken from different references.

Furthermore, it was found that the bridge significantly influences the absorption, photovoltaic performance and the stability. ^{288, 336} By increasing the number of bridging methine units (that is an increase in the conjugation length), the absorption can be step-wise red-shifted causing an increase in the efficiency. Regrettably, this increases also the instability and reduces the efficiency for dyes incorporating long methine bridges owing to the possibility of isomer formation. ³³⁶ Thus the η values **73**, **74** and **75** are 4.1, ²⁷⁵ 6.0 ³³⁹ and 3.5 %. ²⁷⁵ Further, π -conjugated rings (thiophenes) were introduced to enhance the stability, absorption and concomitantly the efficiency. Thus, the efficiencies increase in the order **74**, **76**, **77**, **71** with η values of 6.0, ³³⁶ 7.2, ³³⁶ 7.7 ³³⁶ and 8.2 %, ²⁸⁸ respectively. But note that with increasing number of thiophenes the intermolecular π - π stacking interactions increase and hence the efficiency decreases again (cf. oligothiophenes). For instance, the trithiophene dye **78** delivers a lower efficiency of 5.3 %. ³⁴⁰ In a detailed investigation about the interfacial electron transfer kinetics in DSC of coumarin dyes compared to a standard Ru dye (**N719**), Durrant and co-workers found: (i) a shorter lifetime of the electron injecting state for the coumarin dye compared to the Ru dye (resulting in a relative fast electron injection halftime of 60 ps for the coumarin dye compared to ~ 350 ps for the Ru dye), (ii) a faster rate constant for recombination between injected electrons

and the electrolyte for the coumarin dye (lowering the photocurrent output) and (iii) a greater tendency for the coumarin dye to aggregate (reducing the electron injection efficiency).³⁴¹ To reach such a high efficiency as the best performing coumarin dye **71**, high amounts of deoxycholic acid (DCA) in the dye solution to reduce aggregation and high concentrations of *t*BP in the redox electrolyte to reduce charge recombination and to raise the conduction band are indispensable.²⁸⁸

4.7 Indoline Dyes

The class of indoline sensitizers was established by Horiuchi and Uchida and is today dominated by three high extinction coefficient indoline based sensitizers (**79**, **80**, and **81** denoted as **D205**, **D102** and **D149**, respectively) reaching impressive power conversion efficiencies in L-DSCs as well as in S-DSCs. All these dyes have push-pull systems with an indoline derivative as donor and rhodanine units carrying anchor groups as acceptor. Sensitizer **79** carries an octyl group, whereas **81** has an ethyl moiety on the terminal rhodanine unit. The dye **81** has a second

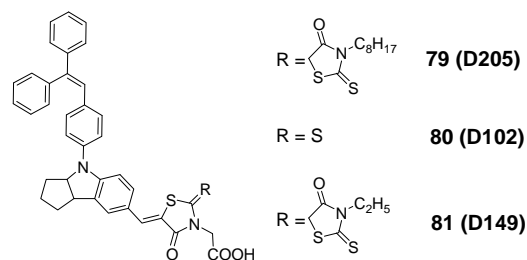


Figure 36. Molecular structure of the efficient indoline dyes **81-83**.

rhodanine unit compared to **80** to extend its π -conjugated system. **80** was the first indoline dye reported as sensitizers in DSCs by Horiuchi, Miura and Uchida in 2003.^{342, 343} By comparing the absorption of **79** (in THF: $\lambda_{\text{max}} = 532 \text{ nm}$, $\epsilon = 5.3 \times 10^4 \text{ M}^{-1}\text{cm}^{-1}$), **81** (in *tert*-butanol: $\lambda_{\text{max}} = 526 \text{ nm}$, $\epsilon = 6.9 \times 10^4 \text{ M}^{-1}\text{cm}^{-1}$) and **80** (in THF: $\lambda_{\text{max}} = 494 \text{ nm}$, $\epsilon = 6.1 \times 10^4 \text{ M}^{-1}\text{cm}^{-1}$) a red-shift upon incorporation of an additional rhodanine unit was observed, whereas the exchange of the alkyl chain changes the absorption only marginally.³⁴⁴ By electrochemical impedance spectroscopy, the electron lifetimes of L-DSC were found to increase in the order: **80** (6.4 ms) < **81** (10.9 ms) < **79** (23.0 ms) indicating a more effective suppression of recombination between injected electrons and the redox electrolyte for **79**.³⁴⁴ This may be an explanation for the high efficiencies reached by **79** in an L-DSC. Using a volatile electrolytes and CDCA to reduce aggregation, L-DSCs sensitized with **79** achieved an efficiency of 9.52 % (whereas the η value of **81** was 8.85 %).²⁸⁹ Even in L-DSCs using ionic liquid electrolytes, **79** led to a record efficiency of 7.18 % (compared to 6.38 and 4.86 % for **81** and **80**, respectively).³⁴⁴ Dyes **80** and **81** were found to perform very well in S-DSCs using spiro-OMeTAD as HTM. η values of 4.1²⁹⁰ and 4.2 %²⁹¹ were reached for **80**

and **81**, respectively and even 6.1 % were achieved by **81** at 10 W/cm². The photovoltaic performance of **81** with poly(3,4-ethylenedioxythiophene) (PEDOT) as HTM is also very impressive.¹²⁷ Here, due to the common critical issues of HTMs in penetrating and filling into the pores intensified by the large size of polymers, *in situ* polymerization of pre-penetrated monomers was performed.^{127, 345} Ramakrishna and co-workers manufactured in this way a solid-state DSC employing **81** as sensitizer yielding an unprecedented efficiency of 6.1 %. (**Z907** reached under the same conditions an efficiency of just 1.7 %. But note that the sensitizer plays an important role for *in situ* polymerized HTM-based S-DSCs, viz. it influences the polymerisation process which can greatly affect interface properties and the penetration depth.¹²⁷) The high S-DSC performance of **81** in combination with a polymer HTM is unmatched by any other sensitizer neither organic nor metal-organic. A comparison between the polymer-HTM based **81** or **Z907** sensitized DSCs shows an excellent light response owing to the broad absorption, low photoelectron recombination and good polymer penetration for the **81** based cell.¹²⁷ This indicates the great potential of polymers as hole transport materials on the way up to efficient solid-state dye-sensitized solar cells.

4.8 Oligothiophene bridged Arylamine Donor Dyes

Sensitizers incorporating (alkyl-substituted) thiophene bridges between donor (*i.e.* phenylamine, fluorenylamine, carbazoles and triphenylamine) and acceptor perform very well in L-DSCs^{274, 346-350} and S-DSCs.^{292, 293} In contrast to that, pure oligothiophenes without any donor groups gave η values of less than 4 % in L-DSCs due to strong intermolecular π - π interactions that impede high photocurrents.^{92, 351, 352} This tendency towards strong π - π interactions with increasing thiophene number leading to dye aggregation is the main disadvantages of oligothiophenes.^{349, 350} However, this impact is offset by the advantages of electron-rich π -conjugated oligothiophene spacers. The use of such spacers facilitates high stability,³⁵³ high polarizability,⁹⁰ high molar extinction coefficients and also the suppression of dark currents³⁵⁴ especially, if the thiophenes bear alkyl chains. They are assumed to increase the electron lifetimes by preventing acceptors (*i.e.* dye cations or I₃⁻ ions) from reaching the TiO₂ surface and/or by reducing the reorganization energy of the dye which is believed to increase the rate of dye cation regeneration.^{347, 355} The effects of the alkyl chain number/position and the thiophene number on aggregation, the photophysical, photochemical and electrochemical properties of the sensitizers, the solar-cell performance and the kinetics of electron injection and charge

recombination were investigated in detail by Hara and co-workers.³⁴⁹ They showed that the electron lifetime in TiO₂ can indeed be increased by the existence of alkyl side chains which causes a retardation of the charge recombination rate. Furthermore, it is suggested that the aggregation of oligothiophenes can be suppressed by the steric hindrance of the long alkyl chains.^{274, 355} Additionally to the benefits of oligothiophene bridges, arylamines and especially triphenylamine derivatives have been identified as highly efficient donors for L- and S-DSC applications.^{117, 292, 293, 296, 356-361}

Among the oligothiophene bridged arylamine sensitizers, dyes **82**, **83** and **84** have turned out to belong to the best performing ones for L-DSCs applications ($\eta = 8.01$,²⁵² 8.60 ²⁷⁴ and 10.1% ,¹¹⁷ respectively). It was found that in donor- π bridge-acceptor dyes of this type the HOMO is delocalized over the donor groups and partly on the thiophene bridge, and the LUMO is determined to be mainly delocalized over the cyanoacrylic anchoring group facilitating directionality and hence an efficient electron transfer to TiO₂.^{274, 350, 362} This was also found for **82**²⁵² and **83**.²⁷⁴ The dyes **82** and **83** consist of dimethylfluorenyl-amino donors which possesses a dipolar character that

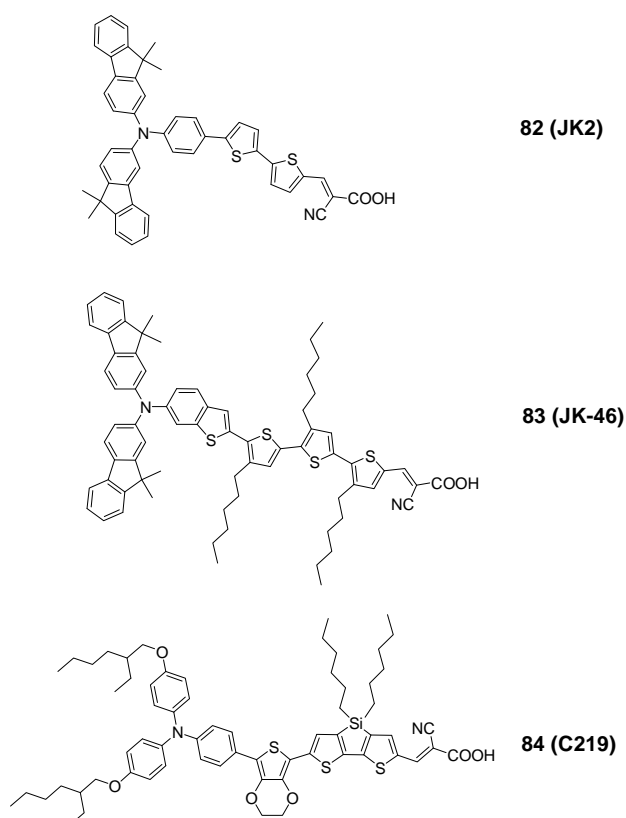


Figure 37. Oligothiophene bridged arylamine donor dyes **82-84** for efficient L-DSCs.

facilitates the formation of stable cation (and anion) radicals, a conducting thiophene bridge with or without *n*-hexyl chains and a cyanoacrylic acid acceptor/anchor. Although the absorption of **82** is slightly red-shifted compared to **83** ($\lambda_{\text{max}} = 452$ and 430 nm for **82** and **83**, respectively) and the molar extinction coefficient of **82** is higher ($\epsilon_{\text{max}} = 3.9 \times 10^4$ and 2.9×10^4 M⁻¹cm⁻¹ for **82** and **83**, respectively), the overall efficiency for **83** is higher using a volatile electrolyte ($\eta = 8.01$ and 8.60% for **82** and **83**, respectively).^{252, 363} By using a stable, solvent-free ionic-liquid electrolyte the measured efficiency for **83** was 6.82% which even increased slightly during a long term stability test (1000 h, visible light soaking under AM 1.5 G and 100 W/cm^2 at 60°C) to

7.03 %.²⁷⁴ A comparable stable device was manufactured on the basis of a similar dye but employing a fused dithienothiophene bridge which shows a low free energy of solution in the high polar standard electrolytes.³⁴⁸ Bäuerle and co-workers compared linear and branched oligothiophenes.³⁶² It was found that the branched dye, even though it bore two donor groups compared to one for the unbranched derivative, performed inferior in L- and S-DSCs because of a lower dye loading on the surface facilitating higher recombination rates. Nevertheless, the stability of the branched dye was superior. Currently the highest efficiency among all organic dyes was reached by the unbranched dye **84**.¹¹⁷ It reached an efficiency of 10.1 % using a volatile electrolyte and 7.6 % by using an ionic liquid.

The sensitizers **85** and **86** belong to the highest efficient organic dyes for S-DSC applications reaching efficiencies of 4.8²⁹² and 4.86 %, ²⁹³ respectively. They carry a triphenylamine derivative as donor, a thiophene based bridge combined with and cyanoacrylic anchoring group creating a high molar extinction coefficient push-pull system. In these dye systems, a spatial separation between the HOMO (mainly located on the donor) and LUMO (mainly located on the anchor) was reached while maintaining an overlap to enhance electronic transition.^{117, 292} The spatial separation is assumed to facilitate ultrafast electron injection and slow down recombination between injected electrons and the oxidized dye.¹⁷³

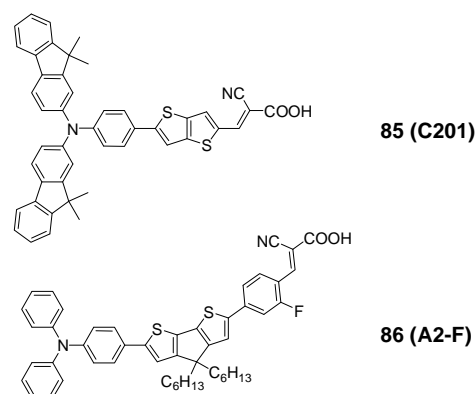


Figure 38. Oligothiophene bridged arylamine donor dyes **85** and **86** for efficient S-DSCs.

Table 8. Overview of the L- and S- DSC performances of efficient organic sensitizers of different dye classes (BODIPY: **62**; polymer sensitizers: **63** and **64**; squaraines: **65** and **66**; perylenes: **67** and **68**; hemicyanine: **69**; cyanine: **70**; coumarins: **71-78**; indolines: **79-81** and oligothiophene bridged arylamine donor dyes: **82-87**). Measured under AM1.5 G, 100 mW/cm² (except otherwise mentioned).

Complex	Solar Cell type	Type of HTM ^k	J_{sc} [mA/cm ²]	V_{oc} [V]	FF [%]	η [%]	Ref
62	L-DSC	volatile	4.03	0.562	74	1.66	279
62	S-DSC	spiro-OMeTAD	2.27	0.80	37	0.68	280
63 ^a	L-DSC	volatile	9.76	0.400	61	2.4	281

Table 8 (continued)

64	S-DSC	spiro-OMeTAD	3.7	0.540	46	0.9	128
65 ^b	L-DSC	volatile	11.3	0.667	72	5.4	282
66 ^c	L-DSC	volatile	17.6	0.696	70	8.65	249
66 ^d	S-DSC	P3HT	10.75	0.550	55	3.2	283
67	L-DSC	volatile	12.60	0.740	74	6.8	285
67	S-DSC	spiro-OMeTAD	2.83	0.838	75	1.78	285
68	L-DSC	low volatile	4.2	0.440	66	1.2	286
68 ^e	S-DSC	spiro-OMeTAD	8.7	0.640	57	3.2	286
69 ^f	L-DSC	low volatile	15.6	0.512	63	6.3	284
70 ^g	L-DSC	volatile	22.10	0.540	48	7.62	287
71 ^h	L-DSC	volatile	15.9	0.690	75	8.2	288
72	L-DSC	volatile	11.1	0.510	60	3.4	275
73	L-DSC	volatile	12.9	0.500	64	4.1	275
74 ^h	L-DSC	volatile	14.0	0.600	71	6.0	339
75	L-DSC	volatile	15.1	0.470	50	3.5	275
76 ^h	L-DSC	volatile	14.7	0.670	73	7.2	336
77 ^h	L-DSC	volatile	14.3	0.730	74	7.7	336
78	L-DSC	volatile	11.6	0.680	67	5.3	340
79 ⁱ	L-DSC	volatile	18.56	0.717	72	9.52	289
79	L-DSC	ionic liquid	13.73	0.728	72	7.18	344
80	S-DSC	spiro-OMeTAD	7.7	0.866	61	4.1	290
81	S-DSC	spiro-OMeTAD	6.6	0.885	72	4.2	291
81 ^j	S-DSC	PEDOT	9.3	0.860	75	6.1	127
82 ^b	L-DSC	volatile	14.0	0.753	77	8.01	252
82	S-DSC	spiro-OMeTAD	3.85	1.088	68	3.17	103
83	L-DSC	volatile	17.45	0.664	74	8.60	274
84	L-DSC	volatile	17.94	0.770	73	10.1	117

Table 8 (continued)

84	L-DSC	ionic liquid	14.96	0.693	74	7.6	¹¹⁷
85 ⁱ	S-DSC	spiro-OMeTAD	9.06	0.860	61	4.8	²⁹²
86	S-DSC	spiro-OMeTAD	7.52	0.910	71	4.86	²⁹³

^a The volatile electrolyte additionally contained an ionic liquid (1-methyl-3-*n*-hexylimidazolium iodide). Formally, it was reported, that the adsorption of cationic species like ionic liquids enhances the diffusion coefficient of the TiO₂ electrodes^{313, 318}. Additionally, it was assumed that the ionic liquid reduces recombination at the polymer/electrolyte interface and an increase in surface contacts between them²⁸¹. ^b CDCA was used to reduce aggregation. ^c Co-sensitized L-DSC (**66** + **82**) based on a novel film architecture (TiO₂/Dye1/Al₂O₃/Dye2). ^d Average performance of nanotube L-DSCs measured under 90 mW/cm² (the champion cell reached about 3.8 %). ^e The spiro-OMeTAD HTM did not contain any *t*BP. ^f The L-DSC on the basis of propylene carbonate was measured under 80 mW/cm². ^g Measured at 75 mW/cm² under Xe lamp irradiation. ^h DCA was used as co-adsorbent to reduce aggregation; the efficiency without DCA was 5.0 % for **71**. ⁱ CDCA was used as co-adsorbent. ^j The optimized thickness of the mesoporous TiO₂ layer was found to be 5.8 μm. ^k Volatile solvents for the electrolyte are typically on the basis of acetonitrile/valeronitrile/methoxyacetonitrile and low volatile ones mainly rest upon 3-methoxypropionitrile.

5 CONCLUSION

To conclude, an overview of the operation principle of liquid- and solid-state dye-sensitized solar cells and the different types of metal-organic and organic sensitizers are given. Furthermore, the concepts behind the dye designs were presented and the state of the art performances of the diverse types of sensitizers were listed in tables.

The main difference between L- and S-DSCs is the hole transport material and the associated thickness of the mesoporous semiconductor layer ($\sim 10\text{-}20\ \mu\text{m}$ for L-DSCs, $\sim 2\ \mu\text{m}$ for S-DSCs). Regarding L-DSCs typically, the I^-/I_3^- redox couple is used to mediate the electron/hole transport between cathode and sensitizer. Commonly, it is dissolved in a volatile solvent (on the basis of acetonitrile and/or valeronitrile), a low volatile solvent (mostly 3-methoxypropionitrile) or an ionic liquid which can penetrate the porous semiconductor network entirely leading to high solar energy to electricity conversion efficiencies. In contrast to that, S-DSCs show an intrinsically lower efficiency due to the solid standard hole conductor spiro-OMeTAD (Figure 1). This can be ascribed to the lower hole transport mobility of the organic semiconductor, the high recombination between TiO_2 and the HTM, the poor wetting/bad contact between dye and HTM, the less efficient pore-filling and hence the use of thinner mesoporous layers which causes less light harvesting and thus a lower photocurrent output. Nevertheless, it is possible to overcome the typical disadvantages of L-DSC such as solvent leakage/evaporation, corrosion (due to the aggressive nature of the redox couple) by using a solid HTM.

The sensitizers for solar energy conversion can be divided into two classes, *viz.* metal-organic and organic sensitizers. The former comprises of ruthenium dyes, phthalocyanines and porphyrins. Ruthenium dyes feature MLCT absorption in the longer wavelength range in combination with MC and LC absorption bands which makes them capable of absorbing over a wide range of the visible spectrum. Furthermore, they facilitate fast injection because of the fact, that the absorption of photons places the excited electron on the anchoring ligand. The positive charge (hole) is thereby distributed over the metal and also to some extent over the NCS group causing a spatial separation between injected electrons and holes thus retarding the rate of recombination. Moreover, ruthenium(II) complexes show favourable photochemical, photophysical, electrochemical properties. However, ruthenium is a rare/expensive metal and the ruthenium complexes can cause undesirable environmental impacts and the lack absorption in the red/IR-region. Nevertheless, ruthenium complexes bearing donor groups belong to the most efficient sensitizers for DSC applications.

In contrast to that, phthalocyanines and porphyrins feature an intense absorption in the red/IR-region (Q band) and on in the blue region (Soret band). Additionally, only large abundant and inexpensive metals (*e.g.* Cu and Zn) are used as central metals. Furthermore, the optical, photophysical and electrochemical properties can be systematically tailored by modifying the peripheral substituents, changing the symmetry of the macrocycles and/or the inner metal center. Moreover, phthalocyanines and porphyrins are known for their excellent chemical, light and thermal stability. But they are transparent over a large region of the visible spectrum.

Organic sensitizers follow the donor- π -bridge-acceptor concept to reach a high light harvesting efficiency and to create directionality. Typical donor groups are electron-rich aryl amines like aminocoumarins, (difluorenyl)phenylamines, triphenylamines and indolines. Cyanoacrylic acid groups are perfect acceptors/anchors and the π -bridges of the most efficient organic sensitizers are often based on thiophenes (*e.g.* oligothiophenes, thienylenevinylenes, dithienothiophenes or dithienolsilole) due to their excellent charge transport properties. Organic dyes in general are very promising for the use as sensitizers for DSCs because they can be synthesised and purified very easily at low costs, they do not contain rare and expensive metal and have high extinction coefficients which facilitate a high light harvesting ability and hence reduce the optical depth so that organic dyes are suitable for thinner semiconductor electrodes. Additionally, the variety of possible functional groups and the facile modifiability provide the opportunity to tune the spectral, photophysical, photochemical and electrochemical properties very well. In contrast to that, they suffer from their narrow absorption bands in the visible region of the electromagnetic spectrum and their tendency towards π - π -stacking (aggregation). Furthermore, the DSC performance is limited by their lower stability, which may arise from the formation of excited triplet states and unstable radicals under illumination.

In conclusion, the general design strategy for any dye follows the donor-acceptor concept. However, each dye class as well as both DSC show advantages and disadvantages. We believe, that in order to manufacture solar cells capable of reaching higher efficiency not only optimization of the dye design and fine tuning of the devices is the key, but rather novel device concepts have to be established such as multilayer co-sensitization, tandem cells or the fluorescence energy transfer approach in order to exploit the complete solar spectrum more efficiently. Here, the basic ideas of light harvesting and photon management as practiced by the nature on photosynthesis have to be better understood and adapted in a bio-inspired nature.

6 BIBLIOGRAPHY

- 1 T. Nordmann, C. Schmidt, *Im Prinzip Sonne: Visionen zum Energiemarkt*, Kontrast Verlag, Zürich, **2000**.
- 2 E. Becquerel, *Comptes rendus hebdomadaires des séances de l'académie des sciences*, **1839**, 9, 561-567.
- 3 W. Hallwachs, *Nachrichten von der Königlichen Gesellschaft der Wissenschaften und der Georg-Augusts-Universität zu Göttingen*, **1888**, 1888, 174-176.
- 4 A. Einstein, *Annalen der Physik*, **1905**, 17, 132-148.
- 5 Available via Database Provider, http://nobelprize.org/nobel_prizes/physics/laureates/1921/einstein-bio.html, accessed 16-08-2010.
- 6 D. M. Chapin, C. S. Fuller, G. L. Pearson, *Journal of Applied Physics*, **1954**, 25, 676-677.
- 7 Available via Database Provider. <http://nssdc.gsfc.nasa.gov/nmc/masterCatalog.do?sc=1958-002B>, accessed 16-08-2010.
- 8 J. Moser, *Monatshefte für Chemie*, **1887**, 8, 373-373.
- 9 H. Gerischer, M. E. Michel-Beyerle, F. Rebentrost, H. Tributsch, *Electrochimica Acta*, **1968**, 13, 1509-1515.
- 10 H. Tributsch, M. Calvin, *Photochemistry and Photobiology*, **1971**, 14, 95-112.
- 11 A. Fujishima, K. Honda, *Nature*, **1972**, 238, 37-38.
- 12 H. Gerischer, *Journal of Electroanalytical Chemistry*, **1975**, 58, 263-274.
- 13 J. Moser, M. Grätzel, *Journal of the American Chemical Society*, **1984**, 106, 6557-6564.
- 14 K. Tennakone, K. P. Hewaparakkrama, M. Dewasurendra, A. H. Jayatissa, L. K. Weerasena, *Semiconductor Science and Technology*, **1988**, 3, 382.
- 15 B. O'Regan, M. Grätzel, *Nature*, **1991**, 353, 737-740.
- 16 M. K. Nazeeruddin, A. Kay, I. Rodicio, R. Humphry-Baker, E. Müller, P. Liska, N. Vlachopoulos, M. Grätzel, *Journal of the American Chemical Society*, **1993**, 115, 6382-6390.
- 17 M. K. Nazeeruddin, P. Liska, J. Moser, N. Vlachopoulos, M. Grätzel, *Helvetica Chimica Acta*, **1990**, 73, 1788-1803.
- 18 R. Amadelli, R. Argazzi, C. A. Bignozzi, F. Scandola, *Journal of the American Chemical Society*, **1990**, 112, 7099-7103.
- 19 K. Tennakone, G. R. R. A. Kumara, A. R. Kumarasinghe, K. G. U. Wijayantha, P. M. Sirimanne, *Semiconductor Science and Technology*, **1995**, 10, 1689-1693.
- 20 J. Hagen, W. Schaffrath, P. Otschik, R. Fink, A. Bacher, H.-W. Schmidt, D. Haarer, *Synthetic Metals*, **1997**, 89, 215-220.
- 21 U. Bach, D. Lupo, P. Comte, J. E. Moser, F. Weissörtel, J. Salbeck, H. Spreitzer, M. Grätzel, *Nature*, **1998**, 395, 583-585.
- 22 J. Krüger, R. Plass, L. Cevey, M. Piccirelli, M. Grätzel, U. Bach, *Applied Physics Letters*, **2001**, 79, 2085-2087.
- 23 F. Cao, G. Oskam, P. C. Searson, *The Journal of Physical Chemistry*, **1995**, 99, 17071-17073.
- 24 K. Murakoshi, R. Kogure, Y. Wada, S. Yanagida, *Solar Energy Materials and Solar Cells*, **1998**, 55, 113-125.

- 25 A. Hagfeldt, G. Boschloo, L. Sun, L. Kloo, H. Pettersson, *Chemical Reviews (Washington, DC, United States)*, **2010**, *110*, 6595-6663.
- 26 S. Ito, N.-L. C. Ha, G. Rothenberger, P. Liska, P. Comte, S. M. Zakeeruddin, P. Péchy, M. K. Nazeeruddin, M. Grätzel, *Chemical Communications*, **2006**, 4004-4006.
- 27 J. H. Park, Y. Jun, H.-G. Yun, S.-Y. Lee, M. G. Kang, *Journal of the Electrochemical Society*, **2008**, *155*, F145-F149.
- 28 C. G. Granqvist, *Solar Energy Materials and Solar Cells*, **2007**, *91*, 1529-1598.
- 29 H. C. Weerasinghe, P. M. Sirimanne, G. P. Simon, Y. B. Cheng, *Journal of Photochemistry and Photobiology A: Chemistry*, **2009**, *206*, 64-70.
- 30 T. Yamaguchi, N. Tobe, D. Matsumoto, T. Nagai, H. Arakawa, *Solar Energy Materials and Solar Cells*, **2010**, *94*, 812-816.
- 31 M. A. Reed, *Scientific American Magazine*, **1993**, *268*, 118-123.
- 32 A. J. Nozik, *Physica E: Low-dimensional Systems and Nanostructures*, **2002**, *14*, 115-120.
- 33 W.-T. Sun, Y. Yu, H.-Y. Pan, X.-F. Gao, Q. Chen, L.-M. Peng, *Journal of the American Chemical Society*, **2008**, *130*, 1124-1125.
- 34 S.-C. Lin, Y.-L. Lee, C.-H. Chang, Y.-J. Shen, Y.-M. Yang, *Applied Physics Letters*, **2007**, *90*, 143517-143513.
- 35 I. Mora-Seró, S. Giménez, F. Fabregat-Santiago, R. Gómez, Q. Shen, T. Toyoda, J. Bisquert, *Accounts of Chemical Research*, **2009**, *42*, 1848-1857.
- 36 P. V. Kamat, *The Journal of Physical Chemistry C*, **2008**, *112*, 18737-18753.
- 37 P. P. Edwards, A. Porch, M. O. Jones, D. V. Morgan, R. M. Perks, *Dalton Transactions*, **2004**, 2995-3002.
- 38 T. Minami, *Semiconductor Science and Technology*, **2005**, *20*, 35-44.
- 39 A. Martínez, L. Huerta, J. M. O. Rueda de León, D. Acosta, O. Malik, M. Aguilar, *Journal of Physics D: Applied Physics*, **2006**, *39*, 5091-5096.
- 40 K. Skupien, P. Putyra, J. Walter, R. H. Kozlowski, G. Khelashvili, A. Hinsch, U. Würfel, *Progress in Photovoltaics: Research and Applications*, **2009**, *17*, 67-73.
- 41 S.-H. Lee, S.-H. Han, H. S. Jung, H. Shin, J. Lee, J.-H. Noh, S. Lee, I.-S. Cho, J.-K. Lee, J. Kim, H. Shin, *The Journal of Physical Chemistry C*, **2010**, *114*, 7185-7189.
- 42 R.-H. Horng, D.-S. Wu, Y.-C. Lien, W.-H. Lan, *Applied Physics Letters*, **2001**, *79*, 2925-2927.
- 43 S. Dai, J. Weng, Y. Sui, S. Chen, S. Xiao, Y. Huang, F. Kong, X. Pan, L. Hu, C. Zhang, K. Wang, *Inorganica Chimica Acta*, **2008**, *361*, 786-791.
- 44 Available via Database Provider, http://www.presseagentur.com/interactivewear/detail.php?pr_id=1391&lang=en, accessed 20-08-2010.
- 45 M. Dürr, A. Schmid, M. Obermaier, S. Rosselli, A. Yasuda, G. Nelles, *Nature Materials*, **2005**, *4*, 607-611.
- 46 F. Pichot, J. R. Pitts, B. A. Gregg, *Langmuir*, **2000**, *16*, 5626-5630.
- 47 L. Kavan, M. Grätzel, *Electrochimica Acta*, **1995**, *40*, 643-652.
- 48 Ö. Duyar, F. Placido, H. Z. Durusoy, *Journal of Physics D: Applied Physics*, **2008**, *41*, 095307.
- 49 M. Thelakkat, C. Schmitz, H.-W. Schmidt, *Advanced Materials*, **2002**, *14*, 577-581.
- 50 K. L. Hardee, A. J. Bard, *Journal of the Electrochemical Society*, **1975**, *122*, 739-742.
- 51 K. L. Hardee, A. J. Bard, *Journal of the Electrochemical Society*, **1977**, *124*, 215-224.

- 52 B. Peng, G. Jungmann, C. Jäger, D. Haarer, H.-W. Schmidt, M. Thelakkat, *Coordination Chemistry Reviews*, **2004**, 248, 1479-1489.
- 53 P. J. Cameron, L. M. Peter, *The Journal of Physical Chemistry B*, **2003**, 107, 14394-14400.
- 54 K. Zhu, E. A. Schiff, N. G. Park, J. van de Lagemaat, A. J. Frank, *Applied Physics Letters*, **2002**, 80, 685-687.
- 55 S. Ito, P. Liska, P. Comte, R. Charvet, P. Péchy, U. Bach, L. Schmidt-Mende, S. M. Zakeeruddin, A. Kay, M. K. Nazeeruddin, M. Grätzel, *Chemical Communications*, **2005**, 4351-4353.
- 56 S. Ito, K. Ishikawa, C.-J. Wen, S. Yoshida, T. Watanabe, *Bulletin of the Chemical Society of Japan*, **2000**, 73, 2609-2614.
- 57 P. J. Cameron, L. M. Peter, S. Hore, *The Journal of Physical Chemistry B*, **2004**, 109, 930-936.
- 58 P. J. Cameron, L. M. Peter, *The Journal of Physical Chemistry B*, **2005**, 109, 7392-7398.
- 59 R. Jose, V. Thavasi, S. Ramakrishna, *Journal of the American Ceramic Society*, **2009**, 92, 289-301.
- 60 K. Hara, T. Horiguchi, T. Kinoshita, K. Sayama, H. Sugihara, H. Arakawa, *Solar Energy Materials and Solar Cells*, **2000**, 64, 115-134.
- 61 K. Sayama, H. Sugihara, H. Arakawa, *Chemistry of Materials*, **1998**, 10, 3825-3832.
- 62 C. Nasr, S. Hotchandani, P. V. Kamat, *Journal of Physical Chemistry B*, **1998**, 102, 4944-4951.
- 63 H. J. Snaith, C. Ducati, *Nano Letters*, **2010**, 10, 1259-1265.
- 64 S. Burnside, J.-E. Moser, K. Brooks, M. Grätzel, D. Cahen, *The Journal of Physical Chemistry B*, **1999**, 103, 9328-9332.
- 65 J. He, H. Lindström, A. Hagfeldt, S.-E. Lindquist, *The Journal of Physical Chemistry B*, **1999**, 103, 8940-8943.
- 66 P. Qin, M. Linder, T. Brinck, G. Boschloo, A. Hagfeldt, L. Sun, *Advanced Materials*, **2009**, 21, 2993-2996.
- 67 C. S. Karthikeyan, M. Thelakkat, *Inorganica Chimica Acta*, **2008**, 361, 635-655.
- 68 N.-G. Park, J. van de Lagemaat, A. J. Frank, *The Journal of Physical Chemistry B*, **2000**, 104, 8989-8994.
- 69 K. Kalyanasundaram, M. Grätzel, *Coordination Chemistry Reviews*, **1998**, 177, 347-414.
- 70 S. Ito, P. Chen, P. Comte, M. K. Nazeeruddin, P. Liska, P. Péchy, M. Grätzel, *Progress in Photovoltaics: Research and Applications*, **2007**, 15, 603-612.
- 71 L. Schmidt-Mende, S. M. Zakeeruddin, M. Grätzel, *Applied Physics Letters*, **2005**, 86, 013504-013503.
- 72 H. J. Snaith, L. Schmidt-Mende, *Advanced Materials*, **2007**, 19, 3187-3200.
- 73 L. Schmidt-Mende, M. Grätzel, *Thin Solid Films*, **2006**, 500, 296-301.
- 74 J. Kroeze, N. Hirata, L. Schmidt-Mende, C. Orizu, S. Ogier, K. Carr, M. Grätzel, J. Durrant, *Advanced Functional Materials*, **2006**, 16, 1832-1838.
- 75 J. Krüger, R. Plass, M. Grätzel, P. J. Cameron, L. M. Peter, *The Journal of Physical Chemistry B*, **2003**, 107, 7536-7539.
- 76 A. Luque, S. Hegedus, *Handbook of photovoltaic science and engineering*, John Wiley & Sons, **2002**.
- 77 A. Ghicov, P. Schmuki, *Chemical Communications*, **2009**, 2791-2808.

- 78 M. Paulose, K. Shankar, O. K. Varghese, G. K. Mor, C. A. Grimes, *Journal of Physics D: Applied Physics*, **2006**, *39*, 2498-2503.
- 79 Y. Liu, B. Zhou, B. Xiong, J. Bai, L. Li, *Chinese Science Bulletin*, **2007**, *52*, 1585-1589.
- 80 K. Zhu, N. R. Neale, A. Miedaner, A. J. Frank, *Nano Letters*, **2006**, *7*, 69-74.
- 81 P. Wang, C. Klein, J.-E. Moser, R. Humphry-Baker, N.-L. Cevey-Ha, R. Charvet, P. Comte, S. M. Zakeeruddin, M. Grätzel, *The Journal of Physical Chemistry B*, **2004**, *108*, 17553-17559.
- 82 W. R. McNamara, R. C. Snoeberger, G. Li, J. M. Schleicher, C. W. Cady, M. Poyatos, C. A. Schmuttenmaer, R. H. Crabtree, G. W. Brudvig, V. S. Batista, *Journal of the American Chemical Society*, **2008**, *130*, 14329-14338.
- 83 E. Galoppini, *Coordination Chemistry Reviews*, **2004**, *248*, 1283-1297.
- 84 K. Kakiage, Y. Nakada, T. Kogure, M. Yamamura, T. Kyomen, M. Unno, M. Hanaya, *Silicon Chemistry*, **2008**, *3*, 303-305.
- 85 M. Unno, K. Kakiage, M. Yamamura, T. Kogure, T. Kyomen, M. Hanaya, *Applied Organometallic Chemistry*, **2010**, *24*, 247-250.
- 86 C. Baik, D. Kim, M.-S. Kang, S. O. Kang, J. Ko, M. K. Nazeeruddin, M. Grätzel, *Journal of Photochemistry and Photobiology A: Chemistry*, **2009**, *201*, 168-174.
- 87 S. M. Zakeeruddin, M. K. Nazeeruddin, R. Humphry-Baker, P. Péchy, P. Quagliotto, C. Barolo, G. Viscardi, M. Grätzel, *Langmuir*, **2002**, *18*, 952-954.
- 88 S. A. Haque, T. Park, A. B. Holmes, J. R. Durrant, *ChemPhysChem*, **2003**, *4*, 89-93.
- 89 M. Grätzel, *Journal of Photochemistry and Photobiology A: Chemistry*, **2004**, *164*, 3-14.
- 90 A. Mishra, M. Fischer, P. Bäuerle, *Angewandte Chemie International Edition*, **2009**, *48*, 2474-2499.
- 91 N. Robertson, *Angewandte Chemie International Edition*, **2006**, *45*, 2338-2345.
- 92 Y. Ooyama, Y. Harima, *European Journal of Organic Chemistry*, **2009**, *2009*, 2903-2934.
- 93 A. J. McEvoy, M. Grätzel, *Solar Energy Materials and Solar Cells*, **1994**, *32*, 221-227.
- 94 A. Juris, V. Balzani, F. Barigelli, S. Campagna, P. Belser, A. Von Zelewsky, *Coordination Chemistry Reviews*, **1988**, *84*, 85-277.
- 95 C. S. Karthikeyan, K. Peter, H. Wietasch, M. Thelakkat, *Solar Energy Materials and Solar Cells*, **2007**, *91*, 432-439.
- 96 T. Renouard, R. A. Fallahpour, M. K. Nazeeruddin, R. Humphry-Baker, S. I. Gorelsky, A. B. P. Lever, M. Grätzel, *Inorganic Chemistry*, **2002**, *41*, 367-378.
- 97 M. K. Nazeeruddin, P. Péchy, M. Grätzel, *Chemical Communications*, **1997**, 1705-1706.
- 98 J. E. Kroeze, N. Hirata, S. Koops, M. K. Nazeeruddin, L. Schmidt-Mende, M. Grätzel, J. R. Durrant, *Journal of the American Chemical Society*, **2006**, *128*, 16376-16383.
- 99 J.-H. Yum, P. Chen, M. Grätzel, M. K. Nazeeruddin, *ChemSusChem*, **2008**, *1*, 699-707.
- 100 S. A. Haque, S. Handa, K. Peter, E. Palomares, M. Thelakkat, J. R. Durrant, *Angewandte Chemie International Edition*, **2005**, *44*, 5740-5744.
- 101 P. Bonhôte, J.-E. Moser, R. Humphry-Baker, N. Vlachopoulos, S. M. Zakeeruddin, L. Walder, M. Grätzel, *Journal of the American Chemical Society*, **1999**, *121*, 1324-1336.
- 102 N. Hirata, J.-J. Lagref, E. J. Palomares, J. R. Durrant, M. K. Nazeeruddin, M. Grätzel, D. Di Censo, *Chemistry - A European Journal*, **2004**, *10*, 595-602.
- 103 P. Chen, J. H. Yum, F. D. Angelis, E. Mosconi, S. Fantacci, S.-J. Moon, R. H. Baker, J. Ko, M. K. Nazeeruddin, M. Grätzel, *Nano Letters*, **2009**, *9*, 2487-2492.

- 104 J. Krüger, U. Bach, M. Grätzel, *Advanced Materials*, **2000**, *12*, 447-451.
- 105 T. Torimoto, T. Tsuda, K.-i. Okazaki, S. Kuwabata, *Advanced Materials*, **2010**, *22*, 1196-1221.
- 106 Y. Wang, *Solar Energy Materials and Solar Cells*, **2009**, *93*, 1167-1175.
- 107 F.-T. Kong, S.-Y. Dai, K.-J. Wang, *Advances in OptoElectronics*, **2007**, 2007, Article ID 75384.
- 108 Z.-S. Wang, K. Sayama, H. Sugihara, *The Journal of Physical Chemistry B*, **2005**, *109*, 22449-22455.
- 109 G. Oskam, B. V. Bergeron, G. J. Meyer, P. C. Searson, *The Journal of Physical Chemistry B*, **2001**, *105*, 6867-6873.
- 110 B. V. Bergeron, A. Marton, G. Oskam, G. J. Meyer, *The Journal of Physical Chemistry B*, **2004**, *109*, 937-943.
- 111 T. C. Li, A. M. Spokoyny, C. She, O. K. Farha, C. A. Mirkin, T. J. Marks, J. T. Hupp, *Journal of the American Chemical Society*, **2010**, *132*, 4580-4582.
- 112 K. M. Son, M. Kang, R. Vittal, J. Lee, K.-J. Kim, *Journal of Applied Electrochemistry*, **2008**, *38*, 1647-1652.
- 113 G. Boschloo, L. Häggman, A. Hagfeldt, *The Journal of Physical Chemistry B*, **2006**, *110*, 13144-13150.
- 114 C. Zhang, Y. Huang, Z. Huo, S. Chen, S. Dai, *Journal of Physical Chemistry C*, **2009**, *113*, 21779-21783.
- 115 A. Kay, M. Grätzel, *The Journal of Physical Chemistry*, **1993**, *97*, 6272-6277.
- 116 D. Kuang, C. Klein, Z. Zhang, S. Ito, J.-E. Moser, S. M. Zakeeruddin, M. Grätzel, *Small*, **2007**, *3*, 2094-2102.
- 117 W. Zeng, Y. Cao, Y. Bai, Y. Wang, Y. Shi, M. Zhang, F. Wang, C. Pan, P. Wang, *Chemistry of Materials*, **2010**, *22*, 1915-1925.
- 118 D. Shi, N. Pootrakulchote, R. Li, J. Guo, Y. Wang, S. M. Zakeeruddin, M. Grätzel, P. Wang, *The Journal of Physical Chemistry C*, **2008**, *112*, 17046-17050.
- 119 G. Boschloo, A. Hagfeldt, *Accounts of Chemical Research*, **2009**, *42*, 1819-1826.
- 120 F. Fabregat-Santiago, J. Bisquert, L. Cevey, P. Chen, M. Wang, S. M. Zakeeruddin, M. Grätzel, *Journal of the American Chemical Society*, **2009**, *131*, 558-562.
- 121 H. J. Snaith, A. J. Moule, C. Klein, K. Meerholz, R. H. Friend, M. Grätzel, *Nano Letters*, **2007**, *7*, 3372-3376.
- 122 M. Wang, S.-J. Moon, D. Zhou, F. Le Formal, N.-L. Cevey-Ha, R. Humphry-Baker, C. Grätzel, P. Wang, S. M. Zakeeruddin, M. Grätzel, *Advanced Functional Materials*, **2010**, *20*, 1821-1826.
- 123 M. Wang, S.-J. Moon, M. Xu, K. Chittibabu, P. Wang, N.-L. Cevey-Ha, R. Humphry-Baker, S. M. Zakeeruddin, M. Grätzel, *Small*, **2010**, *6*, 319-324.
- 124 C.-Y. Chen, M. Wang, J.-Y. Li, N. Pootrakulchote, L. Alibabaei, C.-h. Ngoc-le, J.-D. Decoppet, J.-H. Tsai, C. Grätzel, C.-G. Wu, S. M. Zakeeruddin, M. Grätzel, *ACS Nano*, **2009**, *3*, 3103-3109.
- 125 M. Wang, J. Liu, N.-L. Cevey-Ha, S.-J. Moon, P. Liska, R. Humphry-Baker, J.-E. Moser, C. Grätzel, P. Wang, S. M. Zakeeruddin, M. Grätzel, *Nano Today*, **2010**, *5*, 169-174.
- 126 C. J. Bhongale, M. Thelakkat, *Solar Energy Materials and Solar Cells*, **2010**, *94*, 817-822.

- 127 X. Liu, W. Zhang, S. Uchida, L. Cai, B. Liu, S. Ramakrishna, *Advanced Materials*, **2010**, *22*, E150-E155.
- 128 R. H. Lohwasser, J. Bandara, M. Thelakkat, *Journal of Materials Chemistry*, **2009**, *19*, 4126-4130.
- 129 S. Yanagida, Y. Yu, K. Manseki, *Accounts of Chemical Research*, **2009**, *42*, 1827-1838.
- 130 K. Imoto, K. Takahashi, T. Yamaguchi, T. Komura, J.-I. Nakamura, K. Murata, *Solar Energy Materials and Solar Cells*, **2003**, *79*, 459-469.
- 131 T. N. Murakami, S. Ito, Q. Wang, M. K. Nazeeruddin, T. Bessho, I. Cesar, P. Liska, R. Humphry-Baker, P. Comte, P. Péchy, M. Grätzel, *Journal of the Electrochemical Society*, **2006**, *153*, A2255-A2261.
- 132 B.-K. Koo, D.-Y. Lee, H.-J. Kim, W.-J. Lee, J.-S. Song, H.-J. Kim, *Journal of Electroceramics*, **2006**, *17*, 79-82.
- 133 H. Kusama, H. Orita, H. Sugihara, *Langmuir*, **2008**, *24*, 4411-4419.
- 134 D. Cahen, G. Hodes, M. Grätzel, J. F. Guillemoles, I. Riess, *The Journal of Physical Chemistry B*, **2000**, *104*, 2053-2059.
- 135 M. Grätzel, *Journal of Photochemistry and Photobiology C: Photochemistry Reviews*, **2003**, *4*, 145-153.
- 136 G. Wedler, *Lehrbuch der physikalischen Chemie*, Wiley-VCH, **2004**.
- 137 D. Poplavskyy, J. Nelson, *Journal of Applied Physics*, **2003**, *93*, 341-346.
- 138 H. J. Snaith, M. Grätzel, *Advanced Materials*, **2007**, *19*, 3643-3647.
- 139 D. Kuang, C. Klein, H. J. Snaith, J.-E. Moser, R. Humphry-Baker, P. Comte, S. M. Zakeeruddin, M. Grätzel, *Nano Letters*, **2006**, *6*, 769-773.
- 140 N. W. Duffy, L. M. Peter, R. M. G. Rajapakse, K. G. U. Wijayantha, *Electrochemistry Communications*, **2000**, *2*, 658-662.
- 141 G. P. Smestad, F. C. Krebs, C. M. Lampert, C. G. Granqvist, K. L. Chopra, X. Mathew, H. Takakura, *Solar Energy Materials and Solar Cells*, **2008**, *92*, 371-373.
- 142 AM 1.5 G Data, available via Database Provider, <http://rredc.nrel.gov/solar/spectra/am1.5/>, accessed 20-08-2010.
- 143 S. Ito, K. Nazeeruddin, P. Liska, P. Comte, R. Charvet, P. Péchy, M. Jirousek, A. Kay, S. M. Zakeeruddin, M. Grätzel, *Progress in Photovoltaics*, **2006**, *14*, 589-601.
- 144 R. Argazzi, G. Larramona, C. Contado, C. A. Bignozzi, *Journal of Photochemistry and Photobiology, A: Chemistry*, **2004**, *164*, 15-21.
- 145 Sauv , Genevieve, M. E. Cass, G. Coia, S. J. Doig, I. Lauermann, K. E. Pomykal, N. S. Lewis, *The Journal of Physical Chemistry B*, **2000**, *104*, 6821-6836.
- 146 A. Islam, H. Sugihara, K. Hara, L. P. Singh, R. Katoh, M. Yanagida, Y. Takahashi, S. Murata, H. Arakawa, G. Fujihashi, *Inorganic Chemistry*, **2001**, *40*, 5371-5380.
- 147 E. A. M. Geary, L. J. Yellowlees, L. A. Jack, I. D. H. Oswald, S. Parsons, N. Hirata, J. R. Durrant, N. Robertson, *Inorganic Chemistry*, **2005**, *44*, 242-250.
- 148 Z. Ning, Q. Zhang, W. Wu, H. Tian, *Journal of Organometallic Chemistry*, **2009**, *694*, 2705-2711.
- 149 N. Alonso-Vante, J.-F. Nierengarten, J.-P. Sauvage, *Journal of the Chemical Society, Dalton Transactions*, **1994**, 1649-1654.
- 150 H. Imahori, T. Umeyama, S. Ito, *Accounts of Chemical Research*, **2009**, *42*, 1809-1818.
- 151 X.-F. Wang, H. Tamiaki, *Energy & Environmental Science*, **2010**, *3*, 94-106.

- 152 P. M. Jayaweera, S. S. Palayangoda, K. Tennakone, *Journal of Photochemistry and Photobiology, A: Chemistry*, **2001**, *140*, 173-177.
- 153 F. Cheng, N. Tang, *Inorganic Chemistry Communications*, **2008**, *11*, 243-245.
- 154 T. Rawling, C. Austin, F. Buchholz, S. B. Colbran, A. M. McDonagh, *Inorganic Chemistry*, **2009**, *48*, 3215-3227.
- 155 S. Fukuda, A. Satake, Y. Kobuke, *Thin Solid Films*, **2006**, *499*, 263-268.
- 156 L. Giribabu, C. V. Kumar, C. S. Rao, V. G. Reddy, P. Y. Reddy, M. Chandrasekharam, Y. Soujanya, *Energy & Environmental Science*, **2009**, *2*, 770-773.
- 157 C.-Y. Chen, H.-C. Lu, C.-G. Wu, J.-G. Chen, K.-C. Ho, *Advanced Functional Materials*, **2007**, *17*, 29-36.
- 158 A. Hinsch, J. M. Kroon, R. Kern, I. Uhlendorf, J. Holzbock, A. Meyer, J. Ferber, *Progress in Photovoltaics: Research and Applications*, **2001**, *9*, 425-438.
- 159 M. K. Nazeeruddin, P. Péchy, T. Renouard, S. M. Zakeeruddin, R. Humphry-Baker, P. Comte, P. Liska, L. Cevey, E. Costa, V. Shklover, L. Spiccia, G. B. Deacon, C. A. Bignozzi, M. Grätzel, *Journal of the American Chemical Society*, **2001**, *123*, 1613-1624.
- 160 Y. Chiba, A. Islam, Y. Watanabe, R. Komiyama, N. Koide, L. Han, *Japanese Journal of Applied Physics, Part 2: Letters & Express Letters*, **2006**, *45*, L638-L640.
- 161 M. K. Nazeeruddin, F. De Angelis, S. Fantacci, A. Selloni, G. Viscardi, P. Liska, S. Ito, B. Takeru, M. Grätzel, *Journal of the American Chemical Society*, **2005**, *127*, 16835-16847.
- 162 Y. Cao, Y. Bai, Q. Yu, Y. Cheng, S. Liu, D. Shi, F. Gao, P. Wang, *The Journal of Physical Chemistry C*, **2009**, *113*, 6290-6297.
- 163 H. J. Snaith, *Advanced Functional Materials*, **2010**, *20*, 13-19.
- 164 J. Krüger, R. Plass, M. Grätzel, H.-J. Matthieu, *Applied Physics Letters*, **2002**, *81*, 367-369.
- 165 M. K. Nazeeruddin, S. M. Zakeeruddin, J. J. Lagref, P. Liska, P. Comte, C. Barolo, G. Viscardi, K. Schenk, M. Grätzel, *Coordination Chemistry Reviews*, **2004**, *248*, 1317-1328.
- 166 L. Schmidt-Mende, J. E. Kroeze, J. R. Durrant, M. K. Nazeeruddin, M. Grätzel, *Nano Letters*, **2005**, *5*, 1315-1320.
- 167 P. Wang, S. M. Zakeeruddin, P. Comte, R. Charvet, R. Humphry-Baker, M. Grätzel, *The Journal of Physical Chemistry B*, **2003**, *107*, 14336-14341.
- 168 P. Wang, S. M. Zakeeruddin, R. Humphry-Baker, J. E. Moser, M. Grätzel, *Advanced Materials*, **2003**, *15*, 2101-2104.
- 169 P. Wang, S. M. Zakeeruddin, J. E. Moser, M. K. Nazeeruddin, T. Sekiguchi, M. Grätzel, *Nature Materials*, **2003**, *2*, 402-407.
- 170 C. Sahin, C. Tozlu, K. Ocakoglu, C. Zafer, C. Varlikli, S. Icli, *Inorganica Chimica Acta*, **2008**, *361*, 671-676.
- 171 M. K. Nazeeruddin, C. Klein, P. Liska, M. Grätzel, *Coordination Chemistry Reviews*, **2005**, *249*, 1460-1467.
- 172 S.-R. Jang, J.-H. Yum, C. Klein, K.-J. Kim, P. Wagner, D. Officer, M. Grätzel, M. K. Nazeeruddin, *The Journal of Physical Chemistry C*, **2009**, *113*, 1998-2003.
- 173 J. N. Clifford, E. Palomares, M. K. Nazeeruddin, M. Grätzel, J. Nelson, X. Li, N. J. Long, J. R. Durrant, *Journal of the American Chemical Society*, **2004**, *126*, 5225-5233.
- 174 K. Peter, M. Thelakkat, *Macromolecules*, **2003**, *36*, 1779-1785.
- 175 S. Handa, H. Wietasch, M. Thelakkat, J. R. Durrant, S. A. Haque, *Chemical Communications*, **2007**, 1725-1727.

- 176 H. J. Snaith, C. S. Karthikeyan, A. Petrozza, J. Teuscher, J. E. Moser, M. K. Nazeeruddin, M. Thelakkat, M. Grätzel, *The Journal of Physical Chemistry C*, **2008**, *112*, 7562-7566.
- 177 J. N. Clifford, G. Yahiloglu, L. R. Milgrom, J. R. Durrant, *Chemical Communications*, **2002**, 1260-1261.
- 178 C. S. Karthikeyan, H. Wietasch, M. Thelakkat, *Advanced Materials*, **2007**, *19*, 1091-1095.
- 179 K. Shankar, J. Bandara, M. Paulose, H. Wietasch, O. K. Varghese, G. K. Mor, T. J. LaTempa, M. Thelakkat, C. A. Grimes, *Nano Letters*, **2008**, *8*, 1654-1659.
- 180 **2010**, results not yet published.
- 181 J.-H. Yum, I. Jung, C. Baik, J. Ko, M. K. Nazeeruddin, M. Grätzel, *Energy & Environmental Science*, **2009**, *2*, 100-102.
- 182 K. Willinger, K. Fischer, R. Kisselev, M. Thelakkat, *Journal of Materials Chemistry*, **2009**, *19*, 5364-5376.
- 183 M. K. Nazeeruddin, T. Bessho, L. Cevey, S. Ito, C. Klein, F. De Angelis, S. Fantacci, P. Comte, P. Liska, H. Imai, M. Grätzel, *Journal of Photochemistry and Photobiology, A: Chemistry*, **2007**, *185*, 331-337.
- 184 D. Kuang, C. Klein, S. Ito, J.-E. Moser, R. Humphry-Baker, N. Evans, F. Durrant, C. Grätzel, S. Zakeeruddin, M. Grätzel, *Advanced Materials*, **2007**, *19*, 1133-1137.
- 185 N. Kopidakis, N. R. Neale, A. J. Frank, *The Journal of Physical Chemistry B*, **2006**, *110*, 12485-12489.
- 186 P. Wang, S. M. Zakeeruddin, J. E. Moser, R. Humphry-Baker, P. Comte, V. Aranyos, A. Hagfeldt, M. K. Nazeeruddin, M. Grätzel, *Advanced Materials*, **2004**, *16*, 1806-1811.
- 187 K.-J. Jiang, J.-b. Xia, N. Masaki, S. Noda, S. Yanagida, *Inorganica Chimica Acta*, **2008**, *361*, 783-785.
- 188 F. Gao, Y. Wang, D. Shi, J. Zhang, M. Wang, X. Jing, R. Humphry-Baker, P. Wang, S. M. Zakeeruddin, M. Grätzel, *Journal of the American Chemical Society*, **2008**, *130*, 10720-10728.
- 189 P. Wang, C. Klein, R. Humphry-Baker, S. M. Zakeeruddin, M. Grätzel, *Journal of the American Chemical Society*, **2005**, *127*, 808-809.
- 190 D. Kuang, S. Ito, B. Wenger, C. Klein, J.-E. Moser, R. Humphry-Baker, S. M. Zakeeruddin, M. Grätzel, *Journal of the American Chemical Society*, **2006**, *128*, 4146-4154.
- 191 J. D. Tovar, A. Rose, T. M. Swager, *Journal of the American Chemical Society*, **2002**, *124*, 7762-7769.
- 192 C.-Y. Chen, S.-J. Wu, C.-G. Wu, J.-G. Chen, K.-C. Ho, *Angewandte Chemie International Edition*, **2006**, *45*, 5822-5825.
- 193 S.-J. Wu, C.-Y. Chen, J.-G. Chen, J.-Y. Li, Y.-L. Tung, K.-C. Ho, C.-G. Wu, *Dyes and Pigments*, **2010**, *84*, 95-101.
- 194 J.-J. Kim, H. Choi, C. Kim, M.-S. Kang, H.-S. Kang, J. Ko, *Chemistry of Materials*, **2009**, *21*, 5719-5726.
- 195 Q. Yu, S. Liu, M. Zhang, N. Cai, Y. Wang, P. Wang, *The Journal of Physical Chemistry C*, **2009**, *113*, 14559-14566.
- 196 C.-Y. Chen, S.-J. Wu, J.-Y. Li, C.-G. Wu, J.-G. Chen, K.-C. Ho, *Advanced Materials*, **2007**, *19*, 3888-3891.
- 197 K.-M. Lee, S.-J. Wu, C.-Y. Chen, C.-G. Wu, M. Ikegami, K. Miyoshi, T. Miyasaka, K.-C. Ho, *Journal of Materials Chemistry*, **2009**, *19*, 5009-5015.

- 198 M. Heeney, W. Zhang, D. J. Crouch, M. L. Chabiny, S. Gordeyev, R. Hamilton, S. J. Higgins, I. McCulloch, P. J. Skabara, D. Sparrowe, S. Tierney, *Chemical Communications*, **2007**, 5061-5063.
- 199 A. Ballantyne, L. Chen, J. Nelson, D. Bradley, Y. Astuti, A. Maurano, C. Shuttle, J. Durrant, M. Heeney, W. Duffy, I. McCulloch, *Advanced Materials*, **2007**, *19*, 4544-4547.
- 200 F. Gao, Y. Cheng, Q. Yu, S. Liu, D. Shi, Y. Li, P. Wang, *Inorganic Chemistry*, **2009**, *48*, 2664-2669.
- 201 F. Gao, Y. Wang, J. Zhang, D. Shi, M. Wang, R. Humphry-Baker, P. Wang, S. M. Zakeeruddin, M. Grätzel, *Chemical Communications*, **2008**, 2635-2637.
- 202 S. Södergren, H. Siegbahn, H. Rensmo, H. Lindström, A. Hagfeldt, S.-E. Lindquist, *The Journal of Physical Chemistry B*, **1997**, *101*, 3087-3090.
- 203 M. V. Koudriachova, N. M. Harrison, S. W. de Leeuw, *Solid State Ionics*, **2002**, *152-153*, 189-194.
- 204 L. Kavan, K. Kratochvilova, M. Grätzel, *Journal of Electroanalytical Chemistry*, **1995**, *394*, 93-102.
- 205 A. J. Frank, N. Kopidakis, J. v. d. Lagemaat, *Coordination Chemistry Reviews*, **2004**, *248*, 1165-1179.
- 206 S. Nakade, T. Kanzaki, W. Kubo, T. Kitamura, Y. Wada, S. Yanagida, *The Journal of Physical Chemistry B*, **2005**, *109*, 3480-3487.
- 207 N.-G. Park, S.-H. Chang, J. Van de Lagemaat, K.-J. Kim, A. J. Frank, *Bulletin of the Korean Chemical Society*, **2000**, *21*, 985-988.
- 208 J. R. Jennings, Q. Wang, *The Journal of Physical Chemistry C*, **2009**, *114*, 1715-1724.
- 209 N. Kopidakis, K. D. Benkstein, J. van de Lagemaat, A. J. Frank, *The Journal of Physical Chemistry B*, **2003**, *107*, 11307-11315.
- 210 S. E. Koops, B. C. O'Regan, P. R. F. Barnes, J. R. Durrant, *Journal of the American Chemical Society*, **2009**, *131*, 4808-4818.
- 211 S. A. Haque, E. Palomares, B. M. Cho, A. N. M. Green, N. Hirata, D. R. Klug, J. R. Durrant, *Journal of the American Chemical Society*, **2005**, *127*, 3456-3462.
- 212 T. A. Heimer, E. J. Heilweil, C. A. Bignozzi, G. J. Meyer, *The Journal of Physical Chemistry A*, **2000**, *104*, 4256-4262.
- 213 P. R. F. Barnes, A. Y. Anderson, S. E. Koops, J. R. Durrant, B. C. O'Regan, *The Journal of Physical Chemistry C*, **2008**, *113*, 1126-1136.
- 214 G. Schlichthörl, S. Y. Huang, J. Sprague, A. J. Frank, *The Journal of Physical Chemistry B*, **1997**, *101*, 8141-8155.
- 215 S. Iwamoto, Y. Sazanami, M. Inoue, T. Inoue, T. Hoshi, K. Shigaki, M. Kaneko, A. Maenosono, *ChemSusChem*, **2008**, *1*, 401-403.
- 216 Y. Yang, J. Zhang, C. Zhou, S. Wu, S. Xu, W. Liu, H. Han, B. Chen, X.-z. Zhao, *The Journal of Physical Chemistry B*, **2008**, *112*, 6594-6602.
- 217 B. O'Regan, F. Lenzmann, R. Muis, J. Wienke, *Chemistry of Materials*, **2002**, *14*, 5023-5029.
- 218 K. Hara, T. Horiguchi, T. Kinoshita, K. Sayama, H. Arakawa, *Solar Energy Materials and Solar Cells*, **2001**, *70*, 151-161.
- 219 H. J. Snaith, M. Grätzel, *Applied Physics Letters*, **2006**, *89*, 262114-262113.

- 220 T. Park, S. A. Haque, R. J. Potter, A. B. Holmes, J. R. Durrant, *Chemical Communications*, **2003**, 2878-2879.
- 221 S. Haque, T. Park, C. Xu, S. Koops, N. Schulte, R. Potter, A. Holmes, J. Durrant, *Advanced Functional Materials*, **2004**, 14, 435-440.
- 222 H. J. Snaith, S. M. Zakeeruddin, L. Schmidt-Mende, C. Klein, M. Grätzel, *Angewandte Chemie*, **2005**, 117, 6571-6575.
- 223 D. Kuang, C. Klein, H. J. Snaith, R. Humphry-Baker, S. M. Zakeeruddin, M. Grätzel, *Inorganica Chimica Acta*, **2008**, 361, 699-706.
- 224 D. Kuang, C. Klein, S. Ito, J.-E. Moser, R. Humphry-Baker, S. Zakeeruddin, M. Grätzel, *Advanced Functional Materials*, **2007**, 17, 154-160.
- 225 J.-H. Yum, S.-J. Moon, C. S. Karthikeyan, H. Wietasch, M. Thelakkat, S. Zakeeruddin, M. K. Nazeeruddin, M. Grätzel, **2010**, *submitted*.
- 226 A. Zaban, A. Meier, B. A. Gregg, *The Journal of Physical Chemistry B*, **1997**, 101, 7985-7990.
- 227 X. Li, H. Wang, H. Wu, in *Functional Phthalocyanine Molecular Materials*, Vol. 135 (Ed.: J. Jiang), Springer Berlin / Heidelberg, **2010**, pp. 229-273.
- 228 M. V. Martinez-Diaz, G. de la Torre, T. Torres, *Chemical Communications*, **2010**, 46, 7090-7108.
- 229 M. Gervaldo, F. Fungo, E. N. Durantini, J. J. Silber, L. Sereno, L. Otero, *The Journal of Physical Chemistry B*, **2005**, 109, 20953-20962.
- 230 L. Giribabu, C. Vijay Kumar, V. Gopal Reddy, P. Yella Reddy, C. Srinivasa Rao, S.-R. Jang, J.-H. Yum, M. K. Nazeeruddin, M. Grätzel, *Solar Energy Materials and Solar Cells*, **2007**, 91, 1611-1617.
- 231 M. G. Kang, N.-G. Park, Y. J. Park, K. S. Ryu, S. H. Chang, *Solar Energy Materials and Solar Cells*, **2003**, 75, 475-479.
- 232 R. F. Bailey-Salzman, B. P. Rand, S. R. Forrest, *Applied Physics Letters*, **2006**, 88, 233502-233503.
- 233 P. Reddy, L. Giribabu, C. Lyness, H. Snaith, C. Vijaykumar, M. Chandrasekharam, M. Lakshmikantam, J.-H. Yum, K. Kalyanasundaram, M. Grätzel, M. Nazeeruddin, *Angewandte Chemie International Edition*, **2007**, 46, 373-376.
- 234 M. K. Nazeeruddin, R. Humphry-Baker, M. Grätzel, D. Wohrle, G. Schnurpfeil, G. Schneider, A. Hirth, N. Trombach, *Journal of Porphyrins and Phthalocyanines*, **1999**, 3, 230-237.
- 235 M. K. Nazeeruddin, R. Humphry-Baker, M. Grätzel, M. K. Nazeeruddin, R. Humphry-Baker, M. Grätzel, B. A. Murrer, *Chemical Communications*, **1998**, 719-720.
- 236 H. Deng, H. Mao, H. Zhang, Z. Lu, H. Xu, *Journal of Porphyrins and Phthalocyanines*, **1998**, 2, 171-175.
- 237 J. He, G. Benkö, F. Korodi, T. Polivka, R. Lomoth, B. Åkermark, L. Sun, A. Hagfeldt, V. Sundström, *Journal of the American Chemical Society*, **2002**, 124, 4922-4932.
- 238 E. Palomares, M. V. Martinez-Diaz, S. A. Haque, T. Torres, J. R. Durrant, *Chemical Communications*, **2004**, 2112-2113.
- 239 H. Deng, H. Mao, B. Liang, Y. Shen, Z. Lu, H. Xu, *Journal of Photochemistry and Photobiology A: Chemistry*, **1996**, 99, 71-74.
- 240 H. Deng, Z. Lu, Y. Shen, H. Mao, H. Xu, *Chemical Physics*, **1998**, 231, 95-103.

- 241 N. Zharnikova, N. Usol'tseva, E. Kudrik, M. Thelakkat, *Journal of Materials Chemistry*, **2009**, *19*, 3161-3167.
- 242 J.-J. Cid, J.-H. Yum, S.-R. Jang, M. Nazeeruddin, E. Martínez-Ferrero, E. Palomares, J. Ko, M. Grätzel, T. Torres, *Angewandte Chemie International Edition*, **2007**, *46*, 8358-8362.
- 243 J.-H. Yum, S.-r. Jang, R. Humphry-Baker, M. Grätzel, J.-J. Cid, T. Torres, M. K. Nazeeruddin, *Langmuir*, **2008**, *24*, 5636-5640.
- 244 K. Sayama, S. Tsukagoshi, T. Mori, K. Hara, Y. Ohga, A. Shinpou, Y. Abe, S. Suga, H. Arakawa, *Solar Energy Materials and Solar Cells*, **2003**, *80*, 47-71.
- 245 Y. Chen, Z. Zeng, C. Li, W. Wang, X. Wang, B. Zhang, *New Journal of Chemistry*, **2005**, *29*, 773-776.
- 246 J. Bandara, H. Weerasinghe, *Solar Energy Materials and Solar Cells*, **2006**, *90*, 864-871.
- 247 D. Kuang, P. Walter, F. Nüesch, S. Kim, J. Ko, P. Comte, S. M. Zakeeruddin, M. K. Nazeeruddin, M. Grätzel, *Langmuir*, **2007**, *23*, 10906-10909.
- 248 J.-H. Yum, S.-R. Jang, P. Walter, T. Geiger, F. Nüesch, S. Kim, J. Ko, M. Grätzel, M. K. Nazeeruddin, *Chemical Communications*, **2007**, 4680-4682.
- 249 H. Choi, S. Kim, S. O. Kang, J. Ko, M.-S. Kang, J. Clifford, A. Forneli, E. Palomares, M. Nazeeruddin, M. Grätzel, *Angewandte Chemie*, **2008**, *120*, 8383-8387.
- 250 J. N. Clifford, E. Palomares, M. K. Nazeeruddin, R. Thampi, M. Grätzel, J. R. Durrant, *Journal of the American Chemical Society*, **2004**, *126*, 5670-5671.
- 251 V. P. S. Perera, P. K. D. D. P. Pitigala, M. K. I. Senevirathne, K. Tennakone, *Solar Energy Materials and Solar Cells*, **2005**, *85*, 91-98.
- 252 S. Kim, J. K. Lee, S. O. Kang, J. Ko, J.-H. Yum, S. Fantacci, F. De Angelis, D. Di Censo, M. K. Nazeeruddin, M. Grätzel, *Journal of the American Chemical Society*, **2006**, *128*, 16701-16707.
- 253 S.-Q. Fan, B. Fang, H. Choi, S. Paik, C. Kim, B.-S. Jeong, J.-J. Kim, J. Ko, *Electrochimica Acta*, **2010**, *55*, 4642-4646.
- 254 J.-J. Cid, M. García-Iglesias, J.-H. Yum, A. Forneli, J. Albero, E. Martínez-Ferrero, P. Vázquez, M. Grätzel, M. Nazeeruddin, E. Palomares, T. Torres, *Chemistry - A European Journal*, **2009**, *15*, 5130-5137.
- 255 S. Mori, M. Nagata, Y. Nakahata, K. Yasuta, R. Goto, M. Kimura, M. Taya, *Journal of the American Chemical Society*, **2010**, *132*, 4054-4055.
- 256 N. B. McKeown, S. Makhseed, K. J. Msayib, L.-L. Ooi, M. Helliwell, J. E. Warren, *Angewandte Chemie International Edition*, **2005**, *44*, 7546-7549.
- 257 S. Cherian, C. C. Wamser, *The Journal of Physical Chemistry B*, **2000**, *104*, 3624-3629.
- 258 T. Ma, K. Inoue, H. Noma, K. Yao, E. Abe, *Journal of Photochemistry and Photobiology A: Chemistry*, **2002**, *152*, 207-212.
- 259 F. Odobel, E. Blart, M. Lagree, M. Villieras, H. Boujtita, N. El Murr, S. Caramori, C. Alberto Bignozzi, *Journal of Materials Chemistry*, **2003**, *13*, 502-510.
- 260 W. M. Campbell, A. K. Burrell, D. L. Officer, K. W. Jolley, *Coordination Chemistry Reviews*, **2004**, *248*, 1363-1379.
- 261 Y. Tachibana, S. A. Haque, I. P. Mercer, J. R. Durrant, D. R. Klug, *The Journal of Physical Chemistry B*, **2000**, *104*, 1198-1205.

- 262 W. M. Campbell, K. W. Jolley, P. Wagner, K. Wagner, P. J. Walsh, K. C. Gordon, L. Schmidt-Mende, M. K. Nazeeruddin, Q. Wang, M. Grätzel, D. L. Officer, *The Journal of Physical Chemistry C*, **2007**, *111*, 11760-11762.
- 263 H.-P. Lu, C.-L. Mai, C.-Y. Tsia, S.-J. Hsu, C.-P. Hsieh, C.-L. Chiu, C.-Y. Yeh, E. W.-G. Diau, *Physical Chemistry Chemical Physics*, **2009**, *11*, 10270-10274.
- 264 H. Imahori, Y. Matsubara, H. Iijima, T. Umeyama, Y. Matano, S. Ito, M. Niemi, N. V. Tkachenko, H. Lemmetyinen, *The Journal of Physical Chemistry C*, **2010**, *114*, 10656-10665.
- 265 S.-L. Wu, H.-P. Lu, H.-T. Yu, S.-H. Chuang, C.-L. Chiu, C.-W. Lee, E. W.-G. Diau, C.-Y. Yeh, *Energy & Environmental Science*, **2010**, *3*, 949-955.
- 266 C.-P. Hsieh, H.-P. Lu, C.-L. Chiu, C.-W. Lee, S.-H. Chuang, C.-L. Mai, W.-N. Yen, S.-J. Hsu, E. W.-G. Diau, C.-Y. Yeh, *Journal of Materials Chemistry*, **2010**, *20*, 1127-1134.
- 267 N. Xiang, X. Huang, X. Feng, Y. Liu, B. Zhao, L. Deng, P. Shen, J. Fei, S. Tan, *Dyes and Pigments*, **2010**, *in press*, doi: 10.1016/j.dyepig.2010.05.003.
- 268 A. Kira, Y. Matsubara, H. Iijima, T. Umeyama, Y. Matano, S. Ito, M. Niemi, N. V. Tkachenko, H. Lemmetyinen, H. Imahori, *The Journal of Physical Chemistry C*, **2010**, *114*, 11293-11304.
- 269 T. Bessho, S. M. Zakeeruddin, C.-Y. Yeh, E. W.-G. Diau, M. Grätzel, *Angewandte Chemie International Edition*, **2010**, *in press*, doi:10.1002/anie.201002118.
- 270 H. Imahori, S. Hayashi, H. Hayashi, A. Oguro, S. Eu, T. Umeyama, Y. Matano, *The Journal of Physical Chemistry C*, **2009**, *113*, 18406-18413.
- 271 S. Eu, S. Hayashi, T. Umeyama, A. Oguro, M. Kawasaki, N. Kadota, Y. Matano, H. Imahori, *The Journal of Physical Chemistry C*, **2007**, *111*, 3528-3537.
- 272 H. Zollinger, *Color chemistry: Syntheses, properties, and applications of organic dyes and pigments*, Wiley-VCH, **2003**.
- 273 K. Sayama, S. Tsukagoshi, K. Hara, Y. Ohga, A. Shinpou, Y. Abe, S. Suga, H. Arakawa, *The Journal of Physical Chemistry B*, **2002**, *106*, 1363-1371.
- 274 H. Choi, C. Baik, S. Kang, J. Ko, M.-S. Kang, M. Nazeeruddin, M. Grätzel, *Angewandte Chemie International Edition*, **2008**, *47*, 327-330.
- 275 K. Hara, T. Sato, R. Katoh, A. Furube, Y. Ohga, A. Shinpo, S. Suga, K. Sayama, H. Sugihara, H. Arakawa, *The Journal of Physical Chemistry B*, **2003**, *107*, 597-606.
- 276 A. C. Khazraji, S. Hotchandani, S. Das, P. V. Kamat, *The Journal of Physical Chemistry B*, **1999**, *103*, 4693-4700.
- 277 H. N. Ghosh, J. B. Asbury, T. Lian, *The Journal of Physical Chemistry B*, **1998**, *102*, 6482-6486.
- 278 J. M. Rehm, G. L. McLendon, Y. Nagasawa, K. Yoshihara, J. Moser, M. Grätzel, *The Journal of Physical Chemistry*, **1996**, *100*, 9577-9578.
- 279 S. Erten-Ela, M. D. Yilmaz, B. Icli, Y. Dede, S. Icli, E. U. Akkaya, *Organic Letters*, **2008**, *10*, 3299-3302.
- 280 S. Kolemen, Y. Cakmak, S. Erten-Ela, Y. Altay, J. Brendel, M. Thelakkat, E. U. Akkaya, *Organic Letters*, **2010**, *12*, 3812-3815.
- 281 G. K. R. Senadeera, K. Nakamura, T. Kitamura, Y. Wada, S. Yanagida, *Applied Physics Letters*, **2003**, *83*, 5470-5472.

- 282 T. Geiger, S. Kuster, J.-H. Yum, S.-J. Moon, M. K. Nazeeruddin, M. Grätzel, F. Nüesch, *Advanced Functional Materials*, **2009**, *19*, 2720-2727.
- 283 G. K. Mor, S. Kim, M. Paulose, O. K. Varghese, K. Shankar, J. Basham, C. A. Grimes, *Nano Letters*, **2009**, *9*, 4250-4257.
- 284 Q.-H. Yao, L. Shan, F.-Y. Li, D.-D. Yin, C.-H. Huang, *New Journal of Chemistry*, **2003**, *27*, 1277-1283.
- 285 L. Chen, J.-H. Yum, S.-J. Moon, A. Herrmann, F. Eickemeyer, N. G. Pschirer, P. Erk, J. Schöneboom, K. Müllen, M. Grätzel, M. K. Nazeeruddin, *ChemSusChem*, **2008**, *1*, 615-618.
- 286 U. B. Cappel, M. H. Karlsson, N. G. Pschirer, F. Eickemeyer, J. Schöneboom, P. Erk, G. Boschloo, A. Hagfeldt, *The Journal of Physical Chemistry C*, **2009**, *113*, 14595-14597.
- 287 X. Ma, J. Hua, W. Wu, Y. Jin, F. Meng, W. Zhan, H. Tian, *Tetrahedron*, **2008**, *64*, 345-350.
- 288 Z.-S. Wang, Y. Cui, Y. Dan-oh, C. Kasada, A. Shinpo, K. Hara, *The Journal of Physical Chemistry C*, **2007**, *111*, 7224-7230.
- 289 S. Ito, H. Miura, S. Uchida, M. Takata, K. Sumioka, P. Liska, P. Comte, P. Péchy, M. Grätzel, *Chemical Communications*, **2008**, 5194-5196.
- 290 L. Schmidt-Mende, U. Bach, R. Humphry-Baker, T. Horiuchi, H. Miura, S. Ito, S. Uchida, M. Grätzel, *Advanced Materials*, **2005**, *17*, 813-815.
- 291 H. J. Snaith, A. Petrozza, S. Ito, H. Miura, M. Grätzel, *Advanced Functional Materials*, **2009**, *19*, 1810-1818.
- 292 M. Wang, M. Xu, D. Shi, R. Li, F. Gao, G. Zhang, Z. Yi, R. Humphry-Baker, P. Wang, S. M. Zakeeruddin, M. Grätzel, *Advanced Materials*, **2008**, *20*, 4460-4463.
- 293 D.-Y. Chen, Y.-Y. Hsu, H.-C. Hsu, B.-S. Chen, Y.-T. Lee, H. Fu, M.-W. Chung, S.-H. Liu, H.-C. Chen, Y. Chi, P.-T. Chou, *Chemical Communications*, **2010**, *46*, 5256-5258.
- 294 K. Hara, M. Kurashige, S. Ito, A. Shinpo, S. Suga, K. Sayama, H. Arakawa, *Chemical Communications*, **2003**, 252-253.
- 295 K. R. J. Thomas, J. T. Lin, Y.-C. Hsu, K.-C. Ho, *Chemical Communications*, **2005**, 4098-4100.
- 296 S. Hwang, J. H. Lee, C. Park, H. Lee, C. Kim, C. Park, M.-H. Lee, W. Lee, J. Park, K. Kim, N.-G. Park, C. Kim, *Chemical Communications*, **2007**, 4887-4889.
- 297 G. Ulrich, R. Ziessel, A. Harriman, *Angewandte Chemie International Edition*, **2008**, *47*, 1184-1201.
- 298 A. Loudet, K. Burgess, *Chemical Reviews*, **2007**, *107*, 4891-4932.
- 299 A. C. Benniston, G. Copley, *Physical Chemistry Chemical Physics*, **2009**, *11*, 4124-4131.
- 300 A. Treibs, F.-H. Kreuzer, *Justus Liebigs Annalen der Chemie*, **1968**, *718*, 208-223.
- 301 T. L. Arbeloa, F. L. Arbeloa, I. L. Arbeloa, I. García-Moreno, A. Costela, R. Sastre, F. Amat-Guerri, *Chemical Physics Letters*, **1999**, *299*, 315-321.
- 302 F. J. Monsma, A. C. Barton, H. Chol Kang, D. L. Brassard, R. P. Haugland, D. R. Sibley, *Journal of Neurochemistry*, **1989**, *52*, 1641-1644.
- 303 S. Hattori, K. Ohkubo, Y. Urano, H. Sunahara, T. Nagano, Y. Wada, N. V. Tkachenko, H. Lemmetyinen, S. Fukuzumi, *The Journal of Physical Chemistry B*, **2005**, *109*, 15368-15375.
- 304 D. Kumaresan, R. Thummel, T. Bura, G. Ulrich, R. Ziessel, *Chemistry - A European Journal*, **2009**, *15*, 6335-6339.
- 305 C. Y. Lee, J. T. Hupp, *Langmuir*, **2009**, *26*, 3760-3765.

- 306 T. Rousseau, A. Cravino, T. Bura, G. Ulrich, R. Ziessel, J. Roncali, *Chemical Communications*, **2009**, 1673-1675.
- 307 T. Rousseau, A. Cravino, T. Bura, G. Ulrich, R. Ziessel, J. Roncali, *Journal of Materials Chemistry*, **2009**, *19*, 2298-2300.
- 308 B. Kim, B. Ma, V. R. Donuru, H. Liu, J. M. J. Frechet, *Chemical Communications*, **2010**, *46*, 4148-4150.
- 309 J. Karolin, L. B.-A. Johansson, L. Strandberg, T. Ny, *Journal of the American Chemical Society*, **1994**, *116*, 7801-7806.
- 310 Y. Hao, M. Yang, C. Yu, S. Cai, M. Liu, L. Fan, Y. Li, *Solar Energy Materials and Solar Cells*, **1998**, *56*, 75-84.
- 311 Y.-G. Kim, J. Walker, L. A. Samuelson, J. Kumar, *Nano Letters*, **2003**, *3*, 523-525.
- 312 G. K. R. Senadeera, W. M. T. C. Pathirathne, *Current Science*, **2004**, *87*, 339-342.
- 313 G. K. R. Senadeera, T. Kitamura, Y. Wada, S. Yanagida, *Solar Energy Materials and Solar Cells*, **2005**, *88*, 315-322.
- 314 J. K. Mwaura, X. Zhao, H. Jiang, K. S. Schanze, J. R. Reynolds, *Chemistry of Materials*, **2006**, *18*, 6109-6111.
- 315 K. Shankar, G. K. Mor, H. E. Prakasam, O. K. Varghese, C. A. Grimes, *Langmuir*, **2007**, *23*, 12445-12449.
- 316 X. Liu, R. Zhu, Y. Zhang, B. Liu, S. Ramakrishna, *Chemical Communications*, **2008**, 3789-3791.
- 317 G. K. R. Senadeera, *Current Science*, **2005**, *88*, 145-148.
- 318 W. Kubo, S. Kambe, S. Nakade, T. Kitamura, K. Hanabusa, Y. Wada, S. Yanagida, *The Journal of Physical Chemistry B*, **2003**, *107*, 4374-4381.
- 319 H. Sirringhaus, N. Tessler, R. H. Friend, *Science*, **1998**, *280*, 1741-1744.
- 320 A. Treibs, K. Jacob, *Angewandte Chemie International Edition in English*, **1965**, *4*, 694.
- 321 S. Sreejith, P. Carol, P. Chithra, A. Ajayaghosh, *Journal of Materials Chemistry*, **2008**, *18*, 264-274.
- 322 J.-H. Yum, P. Walter, S. Huber, D. Rentsch, T. Geiger, F. Nüesch, F. De Angelis, M. Grätzel, M. K. Nazeeruddin, *Journal of the American Chemical Society*, **2007**, *129*, 10320-10321.
- 323 S. Alex, U. Santhosh, S. Das, *Journal of Photochemistry and Photobiology A: Chemistry*, **2005**, *172*, 63-71.
- 324 S. Ferrere, B. A. Gregg, *New Journal of Chemistry*, **2002**, *26*, 1155-1160.
- 325 C. Zafer, M. Kus, G. Turkmen, H. Dincalp, S. Demic, B. Kuban, Y. Teoman, S. Icli, *Solar Energy Materials and Solar Cells*, **2007**, *91*, 427-431.
- 326 T. Dentani, K. Funabiki, J.-Y. Jin, T. Yoshida, H. Minoura, M. Matsui, *Dyes and Pigments*, **2007**, *72*, 303-307.
- 327 Y. Shibano, T. Umeyama, Y. Matano, H. Imahori, *Organic Letters*, **2007**, *9*, 1971-1974.
- 328 T. Edvinsson, C. Li, N. Pschirer, J. Schöneboom, F. Eickemeyer, R. Sens, G. Boschloo, A. Herrmann, K. Müllen, A. Hagfeldt, *The Journal of Physical Chemistry C*, **2007**, *111*, 15137-15140.
- 329 U. Bach, Y. Tachibana, J.-E. Moser, S. A. Haque, J. R. Durrant, M. Grätzel, D. R. Klug, *Journal of the American Chemical Society*, **1999**, *121*, 7445-7446.
- 330 S. Tatay, S. A. Haque, B. O'Regan, J. R. Durrant, W. J. H. Verhees, J. M. Kroon, A. Vidal-Ferran, P. Gavina, E. Palomares, *Journal of Materials Chemistry*, **2007**, *17*, 3037-3044.

- 331 Y.-S. Chen, C. Li, Z.-H. Zeng, W.-B. Wang, X.-S. Wang, B.-W. Zhang, *Journal of Materials Chemistry*, **2005**, *15*, 1654-1661.
- 332 M. Guo, P. Diao, Y.-J. Ren, F. Meng, H. Tian, S.-M. Cai, *Solar Energy Materials and Solar Cells*, **2005**, *88*, 23-35.
- 333 A. Ehret, L. Stuhl, M. T. Spitler, *The Journal of Physical Chemistry B*, **2001**, *105*, 9960-9965.
- 334 K. Sayama, K. Hara, Y. Ohga, A. Shinpou, S. Suga, H. Arakawa, *New Journal of Chemistry*, **2001**, *25*, 200-202.
- 335 W.-J. Wu, W.-H. Zhan, J.-L. Hua, H. Tian, *Research on Chemical Intermediates*, **2008**, *34*, 241-248.
- 336 K. Hara, M. Kurashige, Y. Dan-oh, C. Kasada, A. Shinpo, S. Suga, K. Sayama, H. Arakawa, *New Journal of Chemistry*, **2003**, *27*, 783-785.
- 337 Z.-S. Wang, Y. Cui, K. Hara, Y. Dan-oh, C. Kasada, A. Shinpo, *Advanced Materials*, **2007**, *19*, 1138-1141.
- 338 X. Zhang, J.-J. Zhang, Y.-Y. Xia, *Journal of Photochemistry and Photobiology A: Chemistry*, **2008**, *194*, 167-172.
- 339 K. Hara, Y. Tachibana, Y. Ohga, A. Shinpo, S. Suga, K. Sayama, H. Sugihara, H. Arakawa, *Solar Energy Materials and Solar Cells*, **2003**, *77*, 89-103.
- 340 K. Hara, K. Miyamoto, Y. Abe, M. Yanagida, *The Journal of Physical Chemistry B*, **2005**, *109*, 23776-23778.
- 341 S. E. Koops, P. R. F. Barnes, B. C. O'Regan, J. R. Durrant, *The Journal of Physical Chemistry C*, **2010**, *114*, 8054-8061.
- 342 T. Horiuchi, H. Miura, S. Uchida, *Chemical Communications*, **2003**, 3036-3037.
- 343 T. Horiuchi, H. Miura, K. Sumioka, S. Uchida, *Journal of the American Chemical Society*, **2004**, *126*, 12218-12219.
- 344 D. Kuang, S. Uchida, R. Humphry-Baker, S. Zakeeruddin, M. Grätzel, *Angewandte Chemie*, **2008**, *120*, 1949-1953.
- 345 Y. Saito, N. Fukuri, R. Senadeera, T. Kitamura, Y. Wada, S. Yanagida, *Electrochemistry Communications*, **2004**, *6*, 71-74.
- 346 A. Mishra, C.-Q. Ma, P. Bäuerle, *Chemical Reviews*, **2009**, *109*, 1141-1276.
- 347 K. R. Justin Thomas, Y.-C. Hsu, J. T. Lin, K.-M. Lee, K.-C. Ho, C.-H. Lai, Y.-M. Cheng, P.-T. Chou, *Chemistry of Materials*, **2008**, *20*, 1830-1840.
- 348 H. Qin, S. Wenger, M. Xu, F. Gao, X. Jing, P. Wang, S. M. Zakeeruddin, M. Grätzel, *Journal of the American Chemical Society*, **2008**, *130*, 9202-9203.
- 349 Z.-S. Wang, N. Koumura, Y. Cui, M. Takahashi, H. Sekiguchi, A. Mori, T. Kubo, A. Furube, K. Hara, *Chemistry of Materials*, **2008**, *20*, 3993-4003.
- 350 S. Kim, D. Kim, H. Choi, M.-S. Kang, K. Song, S. O. Kang, J. Ko, *Chemical Communications*, **2008**, 4951-4953.
- 351 K. Tanaka, K. Takimiya, T. Otsubo, K. Kawabuchi, S. Kajihara, Y. Harima, *Chemistry Letters*, **2006**, *35*, 592-593.
- 352 S. Tan, J. Zhai, H. Fang, T. Jiu, J. Ge, Y. Li, L. Jiang, D. Zhu, *Chemistry - A European Journal*, **2005**, *11*, 6272-6276.
- 353 R. Katoh, A. Furube, S. Mori, M. Miyashita, K. Sunahara, N. Koumura, K. Hara, *Energy & Environmental Science*, **2009**, *2*, 542-546.

- 354 H.-Y. Yang, Y.-S. Yen, Y.-C. Hsu, H.-H. Chou, J. T. Lin, *Organic Letters*, **2010**, *12*, 16-19.
- 355 N. Koumura, Z.-S. Wang, S. Mori, M. Miyashita, E. Suzuki, K. Hara, *Journal of the American Chemical Society*, **2006**, *128*, 14256-14257.
- 356 Y. Liang, B. Peng, J. Chen, *The Journal of Physical Chemistry C*, **2010**, *114*, 10992-10998.
- 357 C. Teng, X. Yang, C. Yang, S. Li, M. Cheng, A. Hagfeldt, L. Sun, *The Journal of Physical Chemistry C*, **2010**, *114*, 9101-9110.
- 358 P. Shen, Y. Liu, X. Huang, B. Zhao, N. Xiang, J. Fei, L. Liu, X. Wang, H. Huang, S. Tan, *Dyes and Pigments*, **2009**, *83*, 187-197.
- 359 H. Choi, S. O. Kang, J. Ko, G. Gao, H. S. Kang, M.-S. Kang, M. K. Nazeeruddin, M. Grätzel, *Angewandte Chemie International Edition*, **2009**, *48*, 5938-5941.
- 360 H. Im, S. Kim, C. Park, S.-H. Jang, C.-J. Kim, K. Kim, N.-G. Park, C. Kim, *Chemical Communications*, **2010**, *46*, 1335-1337.
- 361 S.-J. Moon, J.-H. Yum, R. Humphry-Baker, K. M. Karlsson, D. P. Hagberg, T. Marinado, A. Hagfeldt, L. Sun, M. Grätzel, M. K. Nazeeruddin, *The Journal of Physical Chemistry C*, **2009**, *113*, 16816-16820.
- 362 M. K. R. Fischer, S. Wenger, M. Wang, A. Mishra, S. M. Zakeeruddin, M. Grätzel, P. Bäuerle, *Chemistry of Materials*, **2010**, *22*, 1836-1845.
- 363 H. Choi, C. Baik, S. Kang, J. Ko, M.-S. Kang, M. Nazeeruddin, M. Grätzel, *Angewandte Chemie*, **2008**, *120*, 333-336.

LIST OF PUBLICATIONS

1. **K. Willinger**, K. Fischer, R. Kisselev, M. Thelakkat:
Synthesis, spectral, electrochemical and photovoltaic properties of novel heteroleptic polypyridyl ruthenium(II) donor-antenna dyes
Journal of Materials Chemistry, **2009**, 19, 5364-5376.
2. J. Bandara, **K. Willinger**, M. Thelakkat
Multichromophore light harvesting in hybrid solar cells
Physical Chemistry Chemical Physics, **2011**, 13, 12906–12911.
3. M. Pärs, C. C. Hofmann, **K. Willinger**, P. Bauer, M. Thelakkat, J. Köhler
An organic optical transistor operated under ambient conditions
Angewandte Chemie International Edition, **2011**, 50, 11405 –11408.
4. T. Yokong, V. Ahsen
Photosensitizers in medicine, environment, and security
Chapter 11 “Photosensitizers in solar energy conversion” by **K. Willinger**, M. Thelakkat
Springer **2012**, print ISBN 978-90-481-3870-8, online ISBN 978-90-481-3872-2, doi:
10.1007/978-90-481-3872-2

LIST OF CONTRIBUTIONS

1. **K. Willinger**, R. Lohwasser, J. Bandara, M. Thelakkat
Symposium Nanostrukturierte Polymer, 09.-10. October **2008**, Bayreuth (Germany)
Poster presentation: Novel concepts in solid-state dye-sensitized solar cells.
2. **K. Willinger**, M. Thelakkat
Light Harvesting Processes, 10.-14. March **2009**, Banz Monastery (Germany)
Poster presentation: Synthesis and properties of ruthenium(II) donor-antenna dyes.
3. **K. Willinger**, J. Brendel, Y. Lu, M. Thelakkat
DPG spring meeting, 25.-27. March **2009**, Dresden (Germany)
Poster presentation: Novel concepts in solid-state dye-sensitized solar cells.
4. **K. Willinger**, C. S. Karthikeyan, M. Thelakkat
SFB481 Closing Symposium, 10.-11. June **2010**, Weingarten Abbey (Germany)
Poster presentation: Donor-antenna dyes for solid-state dye sensitized solar cells.
5. **K. Gräf**, M. Thelakkat
Conference on Hybrid and Organic Photovoltaics, 06.-09. May **2012**, Uppsala (Sweden)
Poster presentation: Tailor-made synthesis of BODIPY dyes as panchromatic sensitizers.
6. **K. Gräf**, M. A. Rahim, J. Bandara, S. Das, M. Thelakkat
Conference on Hybrid and Organic Photovoltaics, 06.-09. May **2012**, Uppsala (Sweden)
Oral presentation (20 min): Co-sensitization and multichromophore light harvesting in hybrid devices.

DANKSAGUNG

Abschließend möchte ich mich herzlich bei all denjenigen bedanken, die direkt oder indirekt zum Gelingen dieser Arbeit beigetragen haben.

Bei meinem Betreuer Prof. Thelakkat möchte ich mich für die Möglichkeit bedanken diese Arbeit in seiner Gruppe durchführen zu dürfen. Weiterhin möchte ich mich bei ihm für die Finanzierung und die Bereitstellung eines sehr gut ausgestatteten Synthese-/Solarzellenlabors bedanken. Ferner bedanke ich mich bei ihm für die große Freiheit bezüglich der Planung und Umsetzung der Forschungsarbeiten. Für die Gelegenheit zur aktiven Teilnahme an nationalen und internationalen Konferenzen sowie eines Forschungsaufenthaltes an der École polytechnique fédérale de Lausanne (EPFL, Schweiz) bin ich ihm zu großem Dank verpflichtet.

Großer Dank gilt auch meinen Kooperationspartnern aus dem Fachbereich Physik für Messungen, Berechnungen und fachliche Diskussionen. Dazu zählen Dr. Thomas Körzdörfer und Prof. Stephan Kümmel (Universität Bayreuth, Theoretische Physik IV), sowie Nils Bösch und Prof. Jürgen Köhler (Universität Bayreuth, Experimentalphysik IV). Ferner möchte ich mich bei Moochikkadavath A. Rahim und Dr. Suresh Das (National Institute for Interdisciplinary Science and Technology – India, Photosciences and Photonics group) für die Bereitstellung des Squarain Farbstoffs (SQ-dye) bedanken sowie für die praktische und fachliche Mitwirkung bezüglich Untersuchungen an cosensibilisierten Solarzellen. Besonderer Dank gilt Dr. Jayasundera Bandara für die Einführung in die Solarzellenpräparation sowie für zahlreiche Diskussionen und die Zusammenarbeit auf dem Gebiet der multichromophoren Solarzellen. Ferner möchte ich mich ganz speziell bei Torben Daeneke und Prof. Udo Bach (Monash University – Australia, Faculty of Engineering) für die Fortsetzung der Forschung an meinen BODIPY Farbstoffen bedanken.

Weiterhin gilt mein Dank auch unseren Gastwissenschaftlern aus dem Ausland (Chetan Jagdish Bhongale, Dr. Devrim Atilla, Dr. Guodong Fu, Assoc. Prof. Dr. Sule Erten-Ela und Moochikkadavath A. Rahim) die durch ihre Forschungsaufenthalte sowie zahlreiche Gespräche über Wissenschaft, Kultur, Politik und Essen mein Leben auf vielfältige Weise bereichert haben.

Ein herzliches Dankeschön gilt meinen Praktikanten und Bachelor Studenten für ihre motivierte und tatkräftige Mitarbeit an vielen Synthesen, bei der Herstellung von Solarzellen und der

Durchführung vieler Messungen: Martin Hufnagel, Kathrin Lange, Samuel Shehata, Kristin Kühr, Andreas Edenharter und Fabian Pooch.

Dem gesamten Team aus der Makromolekularen Chemie I, sowie ganz speziell meiner Arbeitsgruppe den AFuPos, möchte ich ein großes Dankeschön aussprechen. Ich bin ihnen für viele anregende Gespräche und das freundschaftliche Klima in der Gruppe zu großem Dank verpflichtet. Ferner möchte ich mich bei allen Gerätebetreuern bedanken, die mit ihrer Einsatzbereitschaft den reibungslosen Verlauf meiner Messungen ermöglicht haben. Für die Unterstützung hinsichtlich organisatorischer Belange, möchte ich mich auch bei Petra Weiß bedanken. Ganz besonders möchte ich mich aber bei meinen „Jungs“ Johannes Brendel und Martin Hufnagel für die gute Zusammenarbeit und die nette Atmosphäre im Büro bedanken sowie für das Korrekturlesen so mancher Manuskripte, Poster etc. und die konstruktive Kritik daran. Bei Helga Wietasch, die mit ihrer herzlichen und frischen Art nicht nur für eine kontinuierliche Versorgung mit destillierten Lösungsmitteln, sondern auch für so manche Aufheiterung gesorgt hat, möchte ich mich ebenfalls bedanken.

Abschließend möchte ich mich aufs herzlichste bei meinen „Mädels“ Andrea Wolf, Katja Trenkenschuh und Julia Gensel für die mittwöchlichen Kaffeerunden inklusive der Unterstützung in allen fachlichen und nicht-fachlichen Belangen danken – ihr wart mir eine große Stütze. Ganz besonderer Dank gilt meiner Familie, die mir immer einen starken Rückhalt und die nötigen Erdung schenkte.

Zuletzt möchte ich mich bei meinem Ehemann Harald für seine unermüdliche Unterstützung, sein grenzenloses Verständnis und seine endlose Liebe bedanken. *Alles hat seine Zeit.*

ERKLÄRUNG

Hiermit erkläre ich, dass ich die vorliegende Arbeit selbstständig verfasst und keine anderen als die von mir angegebenen Quellen und Hilfsmittel verwendet habe.

Ferner erkläre ich, dass ich weder anderweitig mit oder ohne Erfolg versucht habe, diese Dissertation einzureichen, noch eine gleichartige Doktorprüfung an einer anderen Hochschule endgültig nicht bestanden habe.

Bayreuth, den

Katja Gräf geb. Willinger